Compact Object Binaries in the Multiwavelength and Time Domain Sky

Thesis by

Antonio C. Rodriguez

In Partial Fulfillment of the Requirements for the
Degree of
Doctor of Philosophy

CALIFORNIA INSTITUTE OF TECHNOLOGY
Pasadena, California

2025
Defended May 6, 2025

Antonio C. Rodriguez
ORCID: [0000-0003-4189-9668]

Para mí y para mi familia; pasada, presente, y futura.

ACKNOWLEDGEMENTS

My PhD journey would not have been possible without the incredible support I have had from so many people. I'd like to first and foremost thank my advisor, Professor Shri Kulkarni, for having been a constant source of enthusiasm and encouragement. I admired his approach to astronomy from the beginning, and only now, as a more mature scientist, do I truly see the value in many of the early lessons he instilled in me. Thanks to his mentorship and advising style, he gave me the freedom and flexibility to take ownership of my own projects and gave me the chance to be a real, independent scientist. I will forever be grateful for fostering my growth and your respect in allowing me to pursue my own journey, Shri. Thank you.

I am also grateful to Professor Kareem El-Badry, effectively my co-advisor in the second half of my PhD. His careful and systematic approach to science is inspirational, and gave me an entirely new perspective while basically saving various projects in this thesis. Thank you for flying me out to Harvard back in 2022, and for all of your support, encouragement, and guidance ever since.

I also thank Professor Tom Prince for his mentorship, especially during my transition to the world of binary stars in my second year. Group meetings at the Keck Center were truly instrumental to my learning, and live among my most treasured academic memories. I additionally thank Professors Jim Fuller and Fiona Harrison for their valuable feedback as members of my thesis committee. I benefited greatly from discussions at Jim's group meetings and always came out with a new persepctive.

I wish to thank my first advisor at Caltech, Professor Lynne Hillenbrand, for providing a rich and educational SURF project that served as my undergraduate thesis and carried on into my early graduate studies. Thank you for your continued support and mentorship throughout grad school. I am also grateful to the current and former members of the "ZTF Stellar Group" — Ilaria Caiazzo, Jan van Roestel, Kevin Burdge, and Zach Vanderbosch. I learned so many critical skills that shaped my entire PhD from all of you. I also extend particular gratitude to Przemek Mróz, from whom I learned a great deal as my first-year project mentor.

I thank Ilkham Galiullin for his longstanding collaboration and encouragement throughout my PhD journey. I have sincerely enjoyed working on papers together and admire your enthusiasm and high goals for our work. Thank you for being a great friend and academic companion.

Another thing that made my PhD especially fun was all the travel, particularly to Europe (thank you so much, Shri!). From the start, Boris Gaensicke took an interest in my work and helped foster my growth. Thank you for all of the excellent, expert feedback and willingness to work together on proposals, Boris. I'd like to thank the rest of my European colleagues (grouping in the UK as well) — Ingrid Pelisoli, Anna Pala, Tim Cunningham, Pasi Hakala, Gav Ramsay, Paul Groot, Simo Scaringi, Arnab Sarkar, among many others. In the few conversations I had with the late Tom Marsh, I learned a great deal about how to always remember the big picture in science. I am also grateful to JJ Hermes, Warren Brown, Edo Berger, and Josh Grindlay for always being welcoming during my visits to the Boston area.

I would also like to thank Rashid Sunyaev and Marat Gilfanov for hosting me at MPA and providing a unique look into my X-ray astronomy endeavors. I must extend a special thanks to Kaya Mori — thank you for being such a great host at Columbia, for introducing me to such an incredible network of CV and LPT enthusiasts, and for your willingness to collaborate on proposals together. I wouldn't have learned as much as I did in the last few years of my PhD had it not been for your support.

Closer to home, I also thank all members of the ZTF collaboration, including, but not limited to Matthew Graham, Mansi Kasliwal, Mike Rich, Eric Bellm, Paula Szkody, Andrew Drake, and the entire crew of engineering, data scientists, and support staff that make this incredible machine possible. I thank the night (and day) crews of Palomar Observatory and Keck Observatory for their support. It has truly been an honor and a privilege to get to use the largest telescopes in the world.

I also thank the Caltech Astronomy faculty, postdocs, and graduate students for fostering such a wonderful community, and to the administrative staff (Ruth, Gita, Judy, JoAnn, Mika, and Nam, among others) that have made everything always run smoothly. I thank the National Science Foundation, Ford Foundation, and France A. Córdova Foundation for providing me with fellowships that gave me the freedom to participate in multiple projects throughout my PhD. I also thank Adam Miller and the LSST Data Science Fellowship Program for that great community.

I also wish to thank my mentors from my Stanford days — Roger Romani, Bruce Macintosh, and Roger Blandford — for bringing me into the world of astrophysics and supporting my applications to graduate school. I also thank Mr. Philip, my high school astronomy teacher, for helping kickstart this journey that took me from a tiny telescope in Salinas to a summer in New Mexico with SSP, to the mighty Keck telescopes in the middle of the Pacific.

I thank all of my friends, near and far, who have been there for me throughout this journey: Keaton, Raul, Nik, Shivnash, Shraddha, Sandip, Édgar, Adolfo, Albert, among others. I couldn't have remained sane without you guys. I'm grateful to my newest friends and supporters as well — Vanessa, Jacob, Fernando, and of course, Ivy, for your warm and always fun company.

Last, but certainly not least, I thank my parents, Magdalena Moncada Cuevas and Antonio Moncada Rodriguez, and my brother, Jorge, for shaping the person and academic that I am today. Their simple lessons and unwavering encouragement stay with me every day and have made my entire journey possible. I cannot express how grateful I am to have them in my life. Finally, I thank my beautiful partner and best friend, Valeria, for her humor, advice, support, companionship, and encouragement to always be the best that I can be. Thank you for propelling me to heights I never imagined possible.

ABSTRACT

Compact objects are natural laboratories to study the most extreme physics under conditions unable to be replicated anywhere on Earth. White dwarfs (WDs) are the most abundant compact objects, and when located in binaries, it becomes possible to measure physical properties such as mass and density. Remarkable phenomena result from interacting WD binaries; for instance, Type Ia supernovae, which established the existence of dark energy, likely result from the coalescence of two WDs or the accretion of matter by a WD in a binary.

This thesis focuses primarily on interacting WD binaries, in the form of cataclysmic variables (CVs) and their ultracompact cousins, AM CVns. The main product of this thesis is the deepest X-ray survey of CVs and AM CVns to date, assembled using a multiwavelength crossmatch of the SRG/eROSITA all-sky X-ray catalog, *Gaia*, and time-domain photometry from the Zwicky Transient Facility (ZTF). I present a rejuvenated version of a tool used for the discovery of such systems in the X-ray + optical sky that would be missed in purely optical surveys. I calculated CV and AM CVn space densities and luminosity functions, and showed that 1) observations indeed reveal a dearth of accreting WDs compared to population synthesis predictions, and 2) the mean X-ray luminonsity of CVs was overestimated by a factor of 10–100 in the past.

Along the way, several single-object papers shine a new light on the diverse physics of binary star evolution. I report the discovery of the second-nearest eclipsing AM CVn and, by constraining binary parameters, show that the "evolved CV" formation channel, which only involves one episode of common envelope evolution, is most likely. I include work on multiwavelength follow-up of the nearest black holes to Earth, *Gaia* BH1 and BH2, and show that the the lack of a detection confirms predictions of hot accretion flows in the extreme sub-Eddington regime. Later, I present a muilti-year, multiwavelength campaign of an enigmatic accreting WD, and argue that it is a missing link between rapidly spinning WD pulsars and slowly rotating polars. This object serves as strong evidence for the dynamo theory of WD magnetism in CVs, where a WD must be spun up by accretion to generate a strong magnetic field. Finally, I report optical spectroscopy of a new radio source pulsing on a 2.9-hr timescale, the slowest at the time of publication. I show that this is a WD + M dwarf binary with a particularly massive ($\sim 1 M_{\odot}$) WD, likely representing a new subclass of long period radio transients.

PUBLISHED CONTENT AND CONTRIBUTIONS

TABLE OF CONTENTS

LIST OF ILLUSTRATIONS

Number *Page*

LIST OF TABLES

Chapter 1

INTRODUCTION

Humanity's understanding of compact objects and binary stars has been historically intertwined with the development in multiwavelength and time-domain observations of the Heavens. Compact objects are the most extreme natural laboratories, serving as testbeds of physics unable to be reproduced on Earth or in our Solar System.

The fundamental difference between main-sequence stars and compact objects lies in the first equation of stellar structure (hydrostatic equilibrium):

$$\frac{dP}{dr} = -\frac{GM(r)\rho(r)}{r^2}. \tag{1.1}$$

Simply put, the right-hand term in Equation 1.1 is the downwards pressure of gravity from the mass of the star itself, while the left-hand term represents a pressure source to balance it out. In main-sequence stars like the Sun, thermal pressure supplied by hydrogen fusion is the main source of pressure, though the story is different for all three types of compact objects.

White dwarfs (WDs) are the most common compact objects, with our nearest star poised to become one in about five billion years. WDs are held up by degeneracy pressure — the pressure originating from the Pauli exclusion principle applied to fermions. In WDs, electrons are the fermions to which this principle applies, and the fact that at most two electrons (assuming different spin states) can occupy the same energy state means that a WD is supported by this electron degeneracy pressure.

Neutron stars (NSs) and black holes (BHs) make up the other two flavors of compact objects. NSs are also held up by degeneracy pressure, though in this case, applied to the fermions known as neutrons. NSs are in fact so dense, that Equation 1.1 must be corrected with general relativity via the Tolman-Oppenheimer-Volkoll (TOV) equation. In BHs, Equation 1.1 is not even properly defined; instead the Schwartzchild or Kerr metric must be used to compute the effective "radius" of a BH — the event horizon. Within that distance from a BH, nothing is causally connected to our Universe. Table 1.1 summarizes the general properties of compact objects, and highlights how each class was initially discovered.

1.1 The History of Compact Objects and Binaries

White Dwarfs

Two of the three types of compact objects were first discovered in a binary system. In the case of WDs, the first such object was discovered in a binary pair with the brightest star in the night sky: Sirius. Detections by F.W. Bessel in 1844 of periodic wobbles (with a $\sim$ 50 year period) in the astrometric motion of the A type star in

Compact Object	Number in Milky Way	Radius (assuming $M \sim M_\odot$)	Wavelength of light that led to discovery	In this thesis?
White Dwarf	$\sim 10^9$	$\sim R_{\rm Earth}$	Visible	Yes, main topic
Neutron Star	$\sim 10^8$	10 km	Radio	Briefly in Ch. 5
Black Hole	$\sim 10^7$	3 km	X-ray	In Chs. 4 and 5

Table 1.1: Summary of compact objects and their general properties.

the system, Sirius A, pointed at a binary companion, later resolved by A.G. Clark in 1862 to be Sirius B (Holberg and Wesemael, 2007). A particular quote from Bessel deserves paraphrasing due to its general application to compact objects and this thesis: "Light is no real property of mass — the existence of countless visible stars proves nothing about an existence of countless invisible stars."

However, the first *confirmed* WD was found in the *triple* system: 40 Eridiani. Williamina Fleming was the first to classify 40 Eri B as an A type star in the early 1900s (Russell, 1944). By the early 1910s, plotting it on the earliest version of the Hertzsprung-Russell diagram demonstrated it to be a an outlier. A few years later, in 1915, W.S. Adams obtained an optical spectrum of Sirius B, and found that the spectrum of Sirius B resembled that of Sirius A (Adams, 1915). This was undisputed evidence that WDs were a new class of small, hot, underluminous objects that were different from any of the stars known to date.

A final curiosity in the history of WDs: the first known exoplanetary material was discovered in the spectrum of the third-known WD, van Maanen 2 (van Maanen, 1919). This star was noted to be of spectral type F, very faint, and with a large proper motion, and thus recognized as a WD. A note was made about unusual absorption lines in its spectrum, which have since been clarified to be iron, calcium, and magnesium lines (Zuckerman, 2015).

Neutron Stars and Black Holes

Neutron stars were discovered as variable sources in a part of the electromagnetic spectrum that was the first to give Humanity a new pair of glasses into the multi-wavelength Universe: radio light (radio waves were first discovered from space by Karl G. Jansky in 1932). In 1968, pulsars were discovered by Jocelyn Bell Burnell as radio sources that repeated nearly once every second (Hewish et al., 1968). It

was rapidly established that a new type of compact object, an NS, was required to explain such rapid and stable pulsations (Gold, 1968; Pacini, 1968). In 1982, my advisor, Shri Kulkarni, discovered millisecond pulsars — the fastest spinning celestial bodies in the Heavens (Hewish et al., 1968). Subsequent studies demonstrated that millisecond pulsars often have a binary companion, and that it is binary interaction which leads to such rapid rotation (e.g.,, Phinney and Kulkarni, 1994). More recently, optical spectroscopy of the binary companions to the oldest millisecond pulsars in binary systems, known as "spider" binaries, have revealed what may be the most massive NSs known to date (Romani et al., 2022).

Finally, the first black hole was discovered when the a window to the X-ray sky was opened in the 1960s. Cygnus X-1 was initially discovered through an X-ray sounding rocket in 1964 (Bowyer et al., 1965). However, it remained uncharacterized for over half a decade until an optical (and radio) source was associated with the X-ray position in 1971 (Murdin and Webster, 1971; Braes and Miley, 1971). Precise radial velocity measurements of the optically bright star at the position of Cygnus X-1 were the only way to securely establish that it was a binary companion to a stellar-mass black hole (Webster and Murdin, 1972; Bolton, 1972).

Especially in the latter two cases, the motivation for a *multiwavelength* thesis is clear — the discovery of compact objects is facilitated outside of the visible spectrum, though optical spectroscopy still proves to be superior in ultimately characterizing the nature of the system, when in a binary. The rest of this introduction will focus on the main topic of this thesis — WDs in close binaries. For additional background on selected topics within NSs and BHs, see Chs. 4 and 5.

1.2 The Science: Landscape of Close White Dwarf Binaries in 2020

Classification of CVs and Subtypes

Cataclysmic Variables (CVs) are composed of a white dwarf (WD) accreting from a Roche-lobe filling donor, which is typically a late-type star (e.g., Warner, 1995b; Hellier, 2001b). In magnetic CVs, where the WD magnetic field is strong enough that the Alfvén radius (defined in Chapter 7) extends well past the surface of the WD, the disk is either substantially truncated (intermediate polars; $B \approx 1$–10 MG) or entirely prevented from forming (polars; $B \approx 10$–230 MG de Martino et al., 2020a; Ferrario et al., 2020). In both cases, matter is channeled via magnetic field lines onto the WD surface, rather than flowing through the disk boundary layer onto the WD as in non-magnetic CVs (e.g., Mukai, 2017). Non-magnetic CVs are then

separated into two main classes — novalikes (high accretion rate systems that rarely outburst since their accretion disks are in a stable, fully ionized state) and dwarf novae (moderate to low accretion rate systems that outburst on timescales which could range from every few weeks to hundreds or thousands of years). Further details on disk physics are outlined below.

AM Canum Venaticorum (AM CVn) binaries are the ultracompact analogs of classical CVs, which are highly evolved, having undergone one or two common envelope events (e.g., Warner, 1995b; Solheim, 2010; Ramsay et al., 2018). As a result they have have helium-dominated donors and orbital periods in the range of 5–65 min (Ramsay et al., 2018). Because of their short orbital periods, some AM CVns will be among the strongest sources of millihertz gravitational waves as seen by the upcoming Laser Space Interferometer Antenna (e.g., Nelemans et al., 2004b; Kupfer et al., 2024).

The "cataclysmic" nature of CVs refers to their variability — CVs can undergo both regular and irregular outbursts with a range of luminosities, and sometimes pulse on short timescales, and can even "flicker" unpredictably due to the complex physics of mass transfer (Hellier, 2001b). For a modern overview of CV subtypes and phenomenology, see Inight et al. (2023a).

Discovery of CVs Before 2020

Dozens of CVs were known by the start of the 1980s, and around a hundred by the 1990s, by which point most of the phenomenology of CVs was thought to be known and categorized. However, the *majority* of CVs are actually not cataclysmic — low-accretion rate CVs (WZ Sge type) undergo dwarf novae at most once every few hundred years, and constitute the majority of CVs. Magnetic CVs tend to be high-amplitude variables if they are polars, and only when in a high accretion state. Most IPs and polars do not undergo dwarf nova outbursts and are missed by typical CV surveys. A summary of CV evolution below outlines the main motivation behind this thesis.

Formation and Evolution of CVs and AM CVns

CVs are outcomes of one of the most mysterious physical processes in binary star evolution — the common envelope (CE) phase. Believed to only last a few days to years, this is the phase when the more massive of the binary pair swells up as a red giant and engulfs its companion. Figure 1.1, adapted from Postnov and Yungelson (2014), shows that CVs and AM CVns constrain the unknown physics of CE and

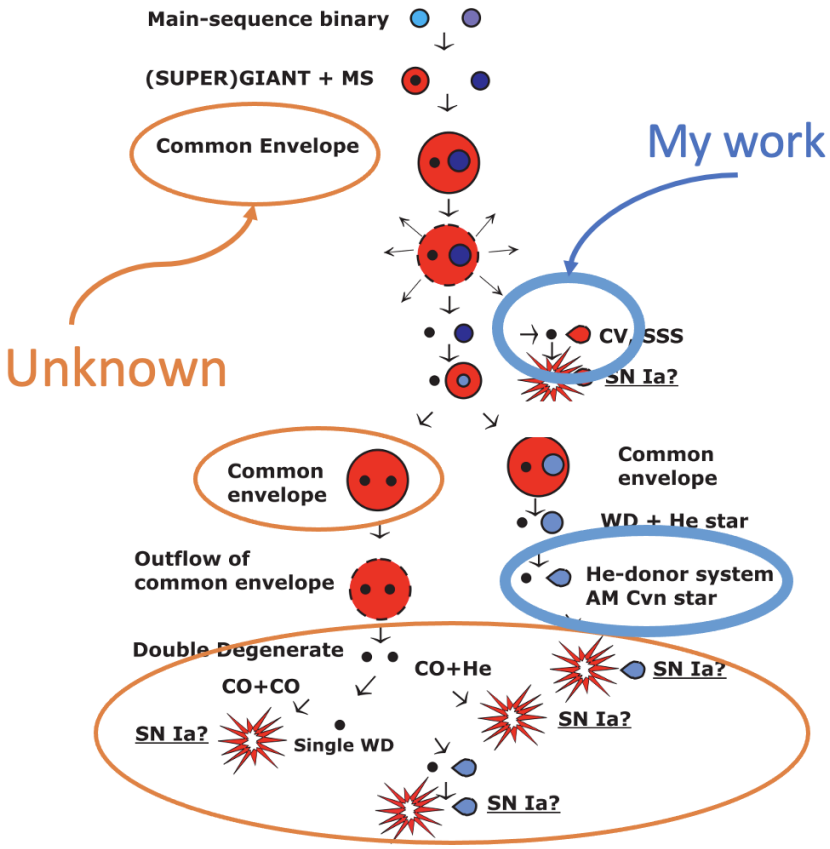

Figure 1.1: CVs and AM CVns probe intermediate stages of binary star evolution. Understanding the magnetic fraction of CVs constrains magnetic field formation during the common envelope phase, and estimating the space density of AM CVns constrains the rate of thermonuclear supernovae they produce. Adapted from Postnov and Yungelson (2014).

supernovae resulting from these systems.

After CE, a close binary composing of a WD and its companion star, remains once the envelope is ejected. CVs are then "born" when the companion star fills its Roche lobe and starts mass transfer to the WD. Depending mainly on the nature of the donor star, most CVs are born at orbital periods of $P_{\rm orb}$ = 6–10 hr (e.g., Knigge et al., 2011). The full evolutionary process is visually outlined in Figure 1.2. *Stage 1*: From this point, down to $P_{\rm orb} \approx$ 3–4 hr, mass transfer is high, reaching levels of $\dot{M} \approx 10^{-8} M_{\odot}$ yr^{-1}. Non-magnetic CVs in this evolutionary state are usually discovered as novalikes (e.g., Inight et al., 2023a), while magnetic systems in this evolutionary state are typically X-ray bright ($L_X \sim 10^{31} - 10^{33}$ erg s^{-1}) intermediate polars (IPs) (e.g., Suleimanov et al., 2019). As mass transfer continues, angular

momentum loss (AML) is high, driven mostly by magnetic braking of the donor star, and the accretion disk in non-magnetic CVs remains permanently ionized. *Stage 2*: As CVs evolve to shorter periods, $\dot{M}$ is reduced, which leads to the onset of a thermal instability (Pringle, 1976; Lasota, 2001)[1]. This is believed to be the cause of dwarf nova outbursts, which observationally manifest themselves as a 2–8 mag transient brightening at optical wavelengths lasting a few tens of days (e.g., Hellier, 2001b; Inight et al., 2023a).

Stage 3: At $P_{\rm orb} \approx$ 2–3 hr, there has been observational evidence and theoretical explanations for the (contested) existence of a "period gap." It is believed that mass transfer halts, presumably due to the donor star becoming fully convective causing magnetic braking to become much weaker (Spruit and Ritter, 1983a; Howell et al., 2001; Zorotovic et al., 2016a; Schreiber et al., 2024a). *Stage 4*: AML due to gravitational wave radiation brings CVs back into contact at $P_{\rm orb} \approx 2$ hr, and mass transfer rates remain high enough for dwarf nova outbursts to be seen until CVs approach the canonical orbital period minimum of $\approx$ 78 min (Paczynski and Sienkiewicz, 1983; Knigge et al., 2011). At this stage in their evolution, mass transfer rates reduce to $\dot{M} \approx 10^{-11} - 10^{-10} M_{\odot}$ yr^{-1}, and the timescale required for the onset of the thermal instability at such low accretion rates is typically much longer than observational timescales. At such low mass transfer rates, the X-ray luminosity is also dramatically reduced, reaching values as low as $L_X \sim 10^{29}$ erg s^{-1} (Reis et al., 2013). Once enough mass is depleted from the donor, nuclear burning halts, and the donor becomes degenerate. This means that the donor radius *increases* as mass is lost. This causes CVs to "bounce" and evolve to longer periods at the canonical period minimum of $P_{\rm orb} \approx 78$ min, leading to these low mass transfer rate ($\dot{M} \approx 10^{-11} M_{\odot}$ yr^{-1}) systems with degenerate donors being called "period bouncers."

At this point, it is clear that CVs at different evolutionary stages have very different observed phenomenology, and have historically been detected in different ways: 1) X-ray surveys (especially hard X-ray surveys sensitive to $E \gtrsim 10$ keV) have mainly discovered magnetic CVs: IPs and nearby polars, though nearby non-magnetic CVs

[1]This is an important concept in CVs and accretion disk physics in general. In brief, the dominant H^- opacity in accretion disks scales as $\propto T^4$ (not to a negative power as is the case in stars where the Kramers' opacity is introduced in classwork). This means that an accretion disk is stable only if its fully ionized or fully neutral. In the partial regime, the disk opacity is sensitive to small changes in temperature, which can lead to outbursts. The relationship between disk temperature and surface density is often described by an "S-curve", which describes the evolution of these various regimes. See Hellier (2001b) for a concise, but more thorough explanation.

with high mass transfer rates have also been discovered this way (e.g., using the ROSAT all-sky soft X-ray mission and the *Swift*/BAT and *INTEGRAL* hard X-ray missions; Verbunt et al., 1997; Schwope et al., 2000; Suleimanov et al., 2022); 2) Optical photometric surveys have mainly discovered (non-magnetic) dwarf novae (e.g., using the Catalina Real-time Transient Facility and Zwicky Transient Facility; Breedt et al., 2014; Szkody et al., 2020); and 3) large spectroscopic surveys have mainly discovered low-accretion rate CVs near the orbital period minimum (e.g., using the Sloan Digital Sky Survey; Gänsicke et al., 2009; Szkody et al., 2011; Inight et al., 2023a). This has led to present CV catalogs such as the Ritter and Kolb catalog (Ritter and Kolb, 2003a) and the International Variable Star Index (VSX) catalog[2] being comprised of systems from many different surveys, each with their own biases.

A similar story applies to AM CVns, though they evolve from short to long orbital periods given the degenerate nature of their donor stars. Short orbital period ($P_{\rm orb}$ = 5 – 20 min) systems do not undergo optical outbursts due to their high mass transfer rates, but are X-ray bright[3] and have been identified since the ROSAT era (e.g., Israel et al., 2002; Ramsay et al., 2018). At intermediate periods ($P_{\rm orb}$ = 20 – 50 min), accretion disks in AM CVns are subject to thermal instabilities, leading to dwarf nova outbursts which enable easy identification through optical photometric surveys (e.g., van Roestel et al., 2021). However, the majority of AM CVns are expected to be long-period ($P_{\rm orb}$ = 50 – 65 min) systems, since they remain at low mass transfer rates for ∼ few Gyr (e.g., Nelemans et al., 2001; Wong and Bildsten, 2021). These systems, like low accretion rate CVs, do not outbust frequently, and have only been identified through large spectroscopic surveys from SDSS (Roelofs et al., 2007; Carter et al., 2013) or through their eclipses in large optical photometric surveys (van Roestel et al., 2022).

Outstanding Questions Surroudning CVs and AM CVns

The biggest problems with CV and AM CVn surveys prior to 2020 were incompleteness and inhomogeneity: no single survey method, aside from large spectroscopic surveys, had been sensitive to all subtypes. Combining systems from various photometric and spectroscopic surveys as was done in the seminal work by Pala et al. (2020a) was possible, but requires hard work and led to a selection function that

[2] `https://www.aavso.org/vsx/index.php?view=search.top`

[3] Aside from the shortest period AM CVns, HM Cnc and V407 Vul, the rest of the population is X-ray faint, reaching only $L_X \sim 10^{30} - 10^{31}$ erg s^{-1} as seen from X-ray follow-up observations (e.g., Ramsay et al., 2005, 2006; Begari and Maccarone, 2023).

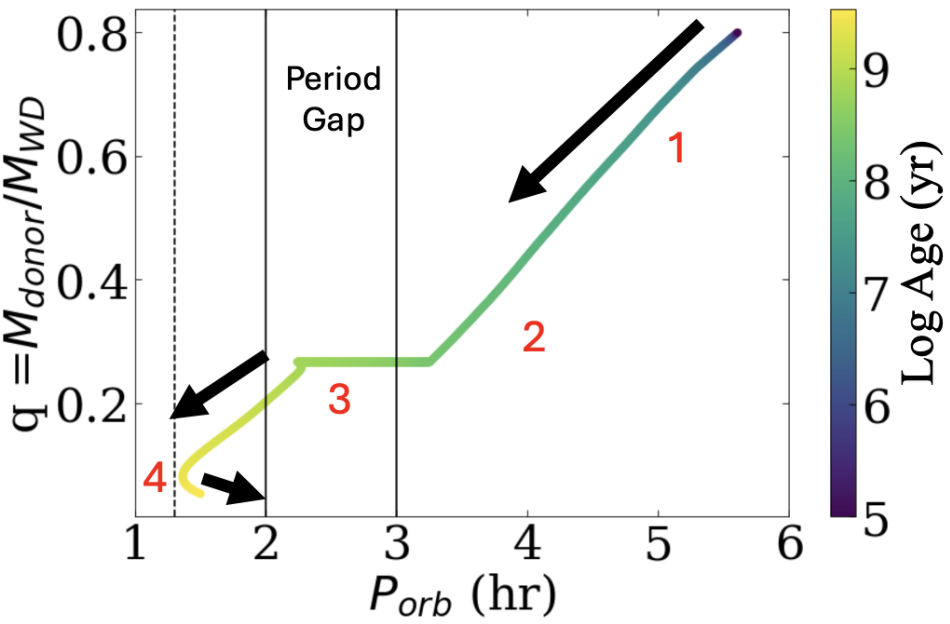

Figure 1.2: The CV evolutionary tracks of Knigge et al. (2011) demonstrate why homogeneous surveys have been difficult in the past. Approximate stages are shown as red numbers. At stage 1, CVs have high mass transfer rates, keeping the accretion disk permanently ionized, and are bright optical and X-ray sources. As the donor loses mass and reaches stage 2, CVs have moderate mass transfer rates, but undergo frequent dwarf novae. At stage 3, the donor star may temporarily detach, leading to no observed outbursts or accretion features. Finally, in the longest lived (~few Gyr) stage 4, mass transfer rates are low, leading to a faint X-ray source and highly infrequent outbursts.

was difficult to characterize (e.g., Pala et al., 2020a; Inight et al., 2021). In reality, by 2020, many of the most important questions of the previous 30 years in the field of CVs and AM CVns had not been fully answered. Some of the major questions in CVs were:

1. What is the true space density and magnetic fraction of CVs? (e.g., Goliasch and Nelson, 2015; Belloni et al., 2018)

2. Where are the missing period bouncers, and are they affected by an incomplete understanding of the physics of AML? (e.g., Rappaport et al., 1983; Gänsicke et al., 2009; El-Badry et al., 2022; Inight et al., 2023b)

3. What does the low X-ray luminosity (L_X) end of CVs look like? (e.g., Reis et al., 2013)

4. What is the origin of magnetism in magnetic CVs? (e.g., Pala et al., 2020a; Schreiber et al., 2021a)

5. How common are the magnetic oddballs: the WD pulsar (AR Sco) and WD propeller (AE Aqr)? (e.g., Wynn et al., 1997; Marsh et al., 2016)

6. What is the dominant formation channel of AM CVns? (e.g., van Roestel et al., 2021; Sarkar et al., 2023a; Belloni and Schreiber, 2023)

7. What is the space density of AM CVns? (e.g., Nelemans et al., 2001; Carter et al., 2013)

Between 2010 and 2020, some works had tackled questions 1, 2, and 6, but all relied on a critical completeness correction to existing surveys that was difficult to model. The problem was with the datasets that formed the basis of these studies. In 2020:

1. About a 1,500 known CVs were known, with only a handful having had system parameters solved for (Ritter and Kolb, 2003a)[4].

2. ~10,000 CV candidates were known, but most of which are not placed into sub-classes[5].

3. ~few ×1,000 CVs which should be in optical and X-ray datasets, but have gone undiscovered due to their low X-ray luminosity and/or quiescent optical lightcurves.

At this point, it was clear what was needed: a homogeneous, uniform survey of CVs, including AM CVns, to tackle the questions above.

1.3 The Data: Landscape of Astronomical Surveys and "Big Data" in 2020

There is no better time to be doing astronomy than now. Within twenty years (2000–2020), astronomy went from being a completely data-starved field, to an incredibly data-rich field. Most of this explosion took place in the late 2010s, when two of the most important surveys, which made this thesis possible, had their first data releases: the Zwicky Transient Facility (ZTF) and *Gaia* (Bellm et al., 2019b; Gaia Collaboration et al., 2016). By 2020, ZTF had observed nearly a billion sources for

[4] 1,429 are in the Ritter and Kolb catalog, but not all are well studied. 939 (66%) of those have known orbital periods, and at most 50 (3%) have well-measured WD masses.

[5] Over 10,000 systems exist in the "Open CV Catalog", with the majority being labeled as "candidates"Jackim et al. (2020b)

over two years. *Gaia* EDR3 had also been released, providing distances and proper motions for hundreds of millions of sources, and detections for nearly all billion ZTF sources. However, ZTF was a preview to what would come with the Rubin Observatory Legacy Survey of Space and Time (LSST) — a large time-domain survey with too much data to handle unless a specific search strategy was proposed. With ZTF, that could have meant running a period search, searching for explosive transients, or finding examples of specific variable stars such as RR Lyrae. In my first year project, I focused on the discovery of microlensing events within ZTF[6]. For my thesis, the goal was to crossmatch ZTF with the X-ray sky in search of compact object binaries.

In 2020, the last all-sky soft X-ray survey had been undertaken nearly 30 years prior, with ROSAT having launched in 1990 (Truemper, 1982). A large problem had been in the Galactic Plane, where ROSAT localization errors of nearly 40" made it impossible to associate X-ray sources with optical counterparts (e.g., Agüeros et al., 2009). By 2020, the *Chandra*, *XMM-Newton*, and *Swift*/XRT catalogs with ~few arcsecond localization had grown immensely, though still cumulatively covered only a few percent of the sky (Brunner et al., 2022). However, the eROSITA telescope aboard the SRG mission launched in 2019, promising eight all-sky surveys that would lead to a final depth forty times deeper than ROSAT and with average localization errors less than 10 arcsec (Sunyaev et al., 2021; Predehl et al., 2021a). At the time of writing, 4.4 surveys were taken, scheduled for full release in 2028, which led to a cumulative depth of twenty times deeper than ROSAT. In Figure 1.3, the SRG/eROSITA survey is shown in comparison to previous X-ray surveys.

1.4 Contributions of this Thesis

This thesis tells a personal story of scientific development, that concludes with the most uniformly created CV survey to date and is the deepest in the X-ray sky. Along the way, novel contributions include:

1. A rejuvenated version of a discovery tool, including proof-of-concept discoveries and an application to the largest X-ray survey ever undertaken, used for the efficient discovery of compact object binaries in the X-ray + optical sky (Chs. 2, 5, and 6).

[6]Though not tied to the bulk of my thesis work, it laid the groundwork for skills that I would use later on, and provided an opportunity to mentor an undergraduate student. Further details surrounding this work are in Rodriguez et al. (2022) and Zhai et al. (2025).

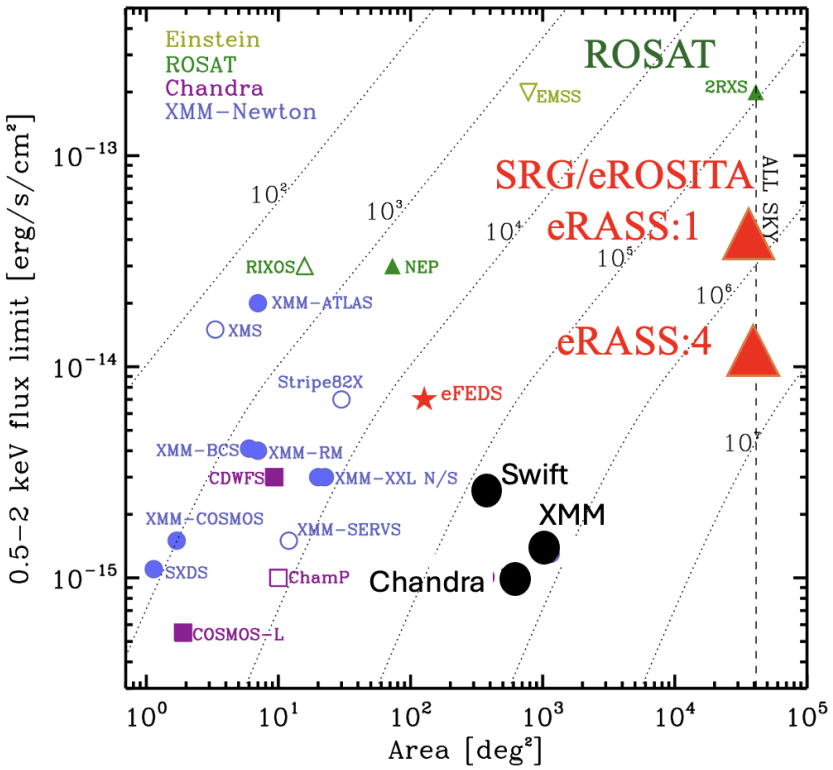

Figure 1.3: The SRG/eROSITA eRASS1 survey, released in January 2024, was the deepest all-sky X-ray survey in nearly thirty years, going five times deeper than ROSAT, and with a comparable increase in localization of sources. While *Chandra*, *XMM-Newton*, and *Swift*/XRT catalogs are deeper than SRG/eROSITA, their limited sky coverage hinders a large, homogeneous survey, though are still useful for discovery and proof-of-concept studies. Adapted from Brunner et al. (2022).

2. A small, directed survey of the X-ray sky that revealed the richness of the low-L_X end of CVs and revealed that the "evolved CV" channel for AM CVns continued to explain the formation of the nearest such systems (Ch. 3).

3. A multiwavelength look at the two nearest BHs to Earth that confirms predictions of the physics of ultra-low accretion, and provides upper limits on the detectability of similar and isolated objects in the X-ray sky (Ch. 4).

4. The finding that the average L_X of CVs is 10–100 times lower than previously believed, the observed space density of both CVs and AM CVns is still lower than that predicted by theory. Elusive period bouncers are revealed in X-rays, but still do not make up the large fraction of CVs predicted by theory (Ch. 6).

5. An observational confirmation that WD pulsars may indeed evolve into polars in a rapid WD spin-down process (Ch. 7).

6. The discovery that a new type of ultra-long period radio source, known as a long period radio transient, is not a single star, but in fact a WD + M dwarf detached binary that will evolve into a magnetic CV (Ch. 8).

Additional work that I contributed significantly to were: 1) the discovery of the first eclipsing magnetic period bouncer, demonstrating that WD magnetic fields are able to be sustained for ~Gyr (Galiullin et al., 2024b), and 2) a catalog of new CVs in the *Chandra* Source Catalog (Galiullin et al., 2024a).

In brief, this thesis highlights the importance of large datasets in astronomy — given a sufficiently large and deeper dataset, one can make a sufficiently interesting discovery. At the same time, the importance lies in asking the right questions along the way and in designing the data search in a way that leads to fundamental understanding of a given population of objects in the Universe.

Chapter 2

DISCOVERY OF TWO POLARS FROM A CROSSMATCH OF ZTF AND THE SRG/EFEDS X-RAY CATALOG

Antonio C. Rodriguez, Shrinivas R. Kulkarni, Thomas A. Prince, Paula Szkody, Kevin B. Burdge, Ilaria Caiazzo, Jan van Roestel, Zachary P. Vanderbosch, Kareem El-Badry, Eric C. Bellm, Boris T. Gänsicke, Matthew J. Graham, Ashish A. Mahabal, Frank J. Masci, Przemek Mróz, Reed Riddle, and Ben Rusholme. Discovery of Two Polars from a Crossmatch of ZTF and the SRG/eFEDS X-Ray Catalog. *The Astrophysical Journal*, 945(2):141, March 2023. doi: 10.3847/1538-4357/acbb6f.

Author List

Antonio C. Rodriguez[1,*], Shrinivas R. Kulkarni[1], Thomas A. Prince[2], Paula Szkody[3], Kevin B. Burdge[4], Ilaria Caiazzo[1], Jan van Roestel[1], Zachary P. Vanderbosch[1], Kareem El-Badry[5], Eric C. Bellm[6], Boris T. Gänsicke[7], Matthew J. Graham[1], Ashish A. Mahabal[2,8], Frank J. Masci[9], Przemek Mróz[10], Reed Riddle[1], Ben Rusholme[9]

[1]Department of Astronomy, California Institute of Technology, 1200 E. California Blvd, Pasadena, CA 91125, USA
[2]Division of Physics, Mathematics and Astronomy, California Institute of Technology, Pasadena, CA 91125, USA
[3]Department of Astronomy, University of Washington, 3910 15th Avenue NE, Seattle, WA 98195, USA
[4]MIT-Kavli Institute for Astrophysics and Space Research, 77 Massachusetts Ave, Cambridge, MA 02139, USA
[5]Center for Astrophysics | Harvard & Smithsonian, 60 Garden Street, Cambridge, MA 02138, USA
[6]DIRAC Institute, Department of Astronomy, University of Washington, 3910 15th Avenue NE, Seattle, WA 98195, USA
[7]Department of Physics, University of Warwick, Coventry CV4 7AL, UK
[8]Center for Data Driven Discovery, California Institute of Technology, Pasadena, CA 91125, USA
[9]IPAC, California Institute of Technology, 1200 E. California Blvd, Pasadena, CA 91125, USA
[10]Astronomical Observatory, University of Warsaw, Al. Ujazdowskie 4, 00-478, Warszawa, Poland

[*]Corresponding author: acrodrig@caltech.edu

ABSTRACT

Magnetic cataclysmic variables (CVs) are luminous Galactic X-ray sources but have been difficult to find in purely optical surveys due to their lack of outburst behavior. The eROSITA telescope aboard the Spektr-RG (SRG) mission is conducting an all-sky X-ray survey and recently released the public eROSITA Final Equatorial Depth Survey (eFEDS) catalog. We crossmatched the eFEDS catalog with photometry from the Zwicky Transient Facility (ZTF) and discovered two new magnetic CVs. We obtained high-cadence optical photometry and phase-resolved spectroscopy for each magnetic CV candidate and found them both to be polars. Among the newly discovered magnetic CVs is eFEDS J085037.2+044359/ZTFJ0850+0443, an eclipsing polar with orbital period $P_{\rm orb} = 1.72$ hr and WD mass $M_{\rm WD} = 0.81 \pm 0.08 M_{\odot}$. We suggest that eFEDS J085037.2+044359/ZTFJ0850+0443 is a low magnetic field strength polar, with $B_{\rm WD} \lesssim 10$ MG. We also discovered a non-eclipsing polar, eFEDS J092614.1+010558/ZTFJ0926+0105, with orbital period $P_{\rm orb} = 1.47$ hr and magnetic field strength $B_{\rm WD} = 36 - 42$ MG.

2.1 Introduction

Magnetic cataclysmic variables (CVs) are compact object binaries in which a highly magnetized white dwarf (WD) accretes from a Roche-lobe filling donor, typically a late-type main-sequence star. Magnetic CVs are interesting for two reasons: 1) they may be the dominant contributors to the Galactic ridge hard X-ray emission (Hailey et al., 2016) and 2) the origin of the strong ($B \sim 1$–100 MG) magnetic fields in accreting WDs is uncertain (Wickramasinghe and Ferrario, 2000; Schreiber et al., 2021b). More broadly, they are rich laboratories for studying accretion under the influence of a strong magnetic field.

CVs typically consist of a WD accreting from a donor via an accretion disk (e.g., Warner, 1995c; Hellier, 2001b). In non-magnetic CVs, the secondary fills its Roche lobe and develops a teardrop-like shape with the tip positioned at the Lagrangian L1 point. Matter leaves the secondary star through this point and forms an accretion stream after exiting the donor star. This stream extends out until a point known as the “circularization radius". The circularization radius is the point where the matter in the accretion stream intersects itself as it orbits the primary. The material then forms an accretion disk around the WD and makes its way to the surface through viscous dissipation of energy.

In magnetic CVs known as intermediate polars (IPs; $B_{\rm WD} \approx 1-10\,{\rm MG}$), the magnetic field pressure is comparable to the ram pressure of the accreted material. As a result, the disk is truncated at the Alfvén radius (also known as the magnetospheric radius). In IPs, the Alfvén radius is smaller than the circularization radius so that a partial disk forms. The accreted material initially flows through the disk but is channeled along field lines onto the WD surface inside the Alfvén radius.

In magnetic CVs known as polars ($B_{\rm WD} \gtrsim 10$ MG), the magnetic field is strong enough that the Alfvén radius is larger than the circularization radius (e.g., Hellier, 2001b; Mukai, 2017). Matter can build up at the Alfvén radius, in a region called the stagnation region (also referred to as the threading region), before being channeled by WD magnetic field lines onto the surface (e.g., Cropper, 1990; Mukai, 2017).

Extensive literature and evolutionary models exist for non-magnetic CVs (e.g., Knigge et al., 2011). In the canonical picture of non-magnetic CVs, these systems are formed through common envelope evolution. Angular momentum loss (AML) of the binary system then drives its evolution as the WD accretes matter from its secondary companion. At orbital periods above ≈ 3 hrs, magnetic braking dominates over gravitational radiation as the dominant contributor to AML. Mag-

netic braking is thought to shut off at the point when the donor star becomes fully convective, leading to the observed period gap ($P_{\rm orb} \approx$ 2–3 hrs). Below this gap, gravitational radiation dominates the loss of angular momentum. Few CVs have been found at orbital periods below $\approx$ 80 mins (known as the "period bounce"), thought to correspond to the point where the donor star becomes degenerate and expands as it loses mass.

There is typically no mention of WD magnetic fields in this evolutionary model of CVs. The discovery of many magnetic CVs within the period gap, and the large number of polars, at periods below 2 hours, has led to new ideas on how magnetic CVs form and evolve (e.g., Belloni et al., 2020; Schreiber et al., 2021b).

Magnetic CVs have previously been difficult to find via optical surveys alone. Both magnetic and non-magnetic CVs have historically been discovered through their novae or dwarf novae outburst behavior. The former occurs when a thermonuclear ignition of hydrogen occurs on or near the surface of the accreting WD. The latter occurs when a thermal instability in the accretion disk leads to a temporary increase in accretion rate (Hellier, 2001b). However, searching via optical outbursts alone is inefficient for finding magnetic CVs. The magnetic field disrupts the disk or eliminates it entirely, which prevents a thermal instability (Hameury and Lasota, 2017b). Novae can still occur in magnetic CVs, but are rare. As a result, optical-only surveys lead to a $\sim 1/100$ rate of discovery for magnetic CVs (e.g., Szkody et al., 2021). However, a recent volume-limited ($d < 150$ pc) study of CVs discovered via various techniques found 36% of CVs to be magnetic (Pala et al., 2020b).

Both magnetic and non-magnetic CVs are strong X-ray emitters. The source of X-rays in magnetic CVs is typically thermal bremsstrahlung from the shock of material accreting onto the magnetic poles of the WD (e.g., Cropper, 1990; Wickramasinghe and Ferrario, 2000; Mukai, 2017).

The source of X-rays in non-magnetic CVs can be difficult to disentangle: the hot WD photosphere of a recent nova, the optically thick boundary layer, or accretion disk wind shock of non-magnetic CVs can also lead to X-ray emission (Mukai, 2017).

X-ray surveys help overcome the observational bias of optical-only surveys in finding CVs by uncovering both the magnetic and non-magnetic populations (e.g., Motch et al., 1996; Bernardini et al., 2017; Halpern et al., 2018). Many magnetic CVs were discovered through the all-sky Roentgensatellit X-ray survey (ROSAT; Truemper,

1982; Voges et al., 1999a; Boller et al., 2016c). Hard X-ray surveys such as the *Swift*/BAT and *INTEGRAL*/IBIS surveys also led to the discovery of many CVs, primarily magnetic CVs (e.g., Mukai, 2017; Lutovinov et al., 2020; de Martino et al., 2020b). The ongoing eROSITA telescope aboard the Spektr-RG mission (SRG; Schwope, 2012; Sunyaev et al., 2021; Predehl et al., 2021b) is projected to go ~30 times deeper than ROSAT with improved localization (~5 arcsec) of X-ray sources, guaranteeing discoveries of new magnetic CVs, among other objects, all over the sky.

In this work, we crossmatched the eROSITA Final Equatorial Depth Survey (eFEDS; Salvato et al., 2022) catalog with forced photometry of ZTF Data Release 5 (DR5)[1]. We discovered two new polars: eFEDS J085037.2+044359/ZTFJ0850+0443 and eFEDS J092614.1+010558/ZTFJ0926+0105 (henceforth ZTFJ0850+0443 and ZTFJ0926+0105, respectively). In Section 2.2, we present an overview of the SRG/eFEDS catalog and ZTF archival photometry. In Section 2.3, we outline our methodology for finding notable objects within the crossmatched dataset. In Section 2.4, we present follow-up high-cadence photometry and spectroscopy and analyze all data for ZTFJ0850+0443. We present data and analysis for ZTFJ0926+0105 in Section 2.5. Finally, in Section 8.4, we place this work in the context of previous CV studies and discuss the utility of X-ray/optical searches for finding otherwise elusive CVs.

2.2 Catalog Data

eFEDS Catalog

We began with the catalog of eFEDS Galactic sources. The “Main" catalog consists of all detections detected in the 0.2–2.3 keV band with a detection likelihood larger than 6, while the “Hard" catalog consists of all sources in the 2.3–5 keV range with a detection likelihood larger than 10 (Brunner et al., 2022). Salvato et al. (2022) searched for optical counterparts to the eFEDS X-ray sources by crossmatching to the DECam Legacy Survey (DECaLS) LS8 catalog, part of the DESI Legacy Imaging Survey version DR8 (Dey et al., 2019). The the mean X-ray positional error (i.e. the eROSITA/SRG uncertainty in the localization of the X-ray source) in the eFEDS catalog is 4".7 (Salvato et al., 2022). The median separation between the X-ray source and optical counterpart, divided by the mean X-ray positional error, is 1.22 (Salvato et al., 2022). For the crossmatch to ZTF data, we use the coordinates of the LS8 optical counterpart. Given the superior depth of DECaLS (23.4 mag), we crossmatch the sources to the LS8 catalog instead of the ZTF catalog (21 mag).

[1] `https://www.ztf.caltech.edu/ztf-public-releases.html`

Galactic sources in eFEDS are mainly identified through two methods as described in Salvato et al. (2022): 1) SDSS redshifts being $z < 0.002$ and/or 2) *Gaia* parallaxes with good significance: $\pi/\sigma_\pi > 3$. The Renormalised Unit Weight Error (RUWE) < 1.4 can also be used. The actual method described in Salvato et al. (2022) is complex, and uses a combination of NWAY, a tool based on Bayesian statistics, and ASTROMATCH, a tool based on the Maximum Likelihood Ratio.

In the eFEDS Main Catalog, 24774/27369 (90.5%) of X-ray sources are reported to have a reliable optical counterpart. Of those sources, 2976 are classified with the label `LIKELY GALACTIC` or `SECURE GALACTIC`. It is this sample that we further investigate with ZTF.

ZTF Data

The Zwicky Transient Facility (ZTF) is a photometric survey that uses a wide 47 deg^2 field-of-view camera mounted on the Samuel Oschin 48-inch telescope at Palomar Observatory with g, r, and i filters (Bellm et al., 2019b; Graham et al., 2019; Dekany et al., 2020; Masci et al., 2019). In its first year of operations, ZTF carried out a public nightly Galactic Plane Survey in g-band and r-band (Bellm et al., 2019a; Kupfer et al., 2021). This survey was in addition to the Northern Sky Survey which operated on a 3 day cadence (Bellm et al., 2019b). Since entering Phase II, the public Northern Sky Survey is now at a 2-day cadence. The pixel size of the ZTF camera is 1" and the median delivered image quality is 2.0" at FWHM.

We use forced photometry from ZTF Data Release 5 (DR5). Lightcurves have a photometric precision of 0.01 mag at 13–14 mag down to a precision of 0.1–0.2 mag for the faintest objects at 20–21 mag. While both raw photometry and forced photometry are PSF-fit photometry, the forced photometry calculates photometry of the object on difference images by forcing the location of the PSF to remain fixed according to the ZTF absolute astrometric reference. This allows one to obtain flux estimates below the detection threshold and therefore probe deeper than the standard photometry. For bulk download, we use a database of forced photometry files (Mróz, Burdge, et al. in prep).

Objects of Interest

It is useful to plot the X-ray to optical flux ratio for the entire eFEDS catalog. A similar exercise was carried out by various studies (e.g., Agüeros et al., 2009; Greiner and Richter, 2015) for the ROSAT catalog and proved to be an effective way for disentangling CVs from other Galactic X-ray sources such as M dwarfs and

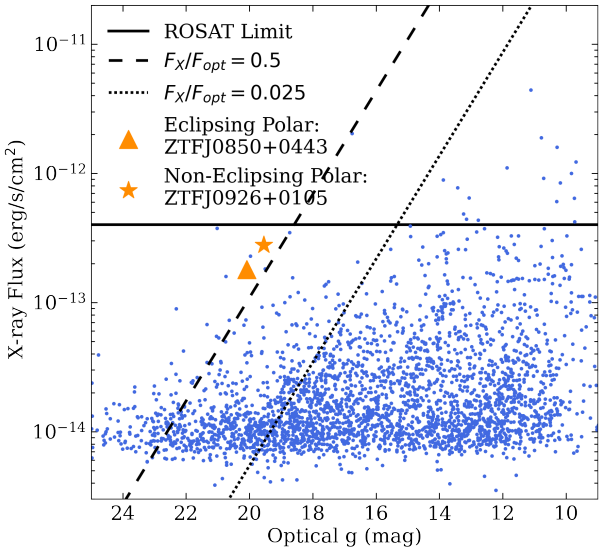

Figure 2.1: X-ray flux compared to DECaLS LS8 optical flux with lines of constant $F_X/F_{\rm opt}$ shown. All SRG/eFEDS Galactic objects are shown in blue, virtually all of which were below the detection threshold of the ROSAT all-sky X-ray survey. The two polars stand out as systems with some of the largest $F_X/F_{\rm opt}$ ratios in the catalog.

chromospherically active binaries: BY Dra and RS CVn systems[2]. Figure 2.1 shows the eFEDS X-ray flux versus DECaLS LS8 optical flux plot (neither corrected for intervening Galactic absorption due to eFEDS being located outside the Galactic Plane: $b > 20°$) along with ZTFJ0850+0443 and ZTFJ0926+0105. Both systems stand out as being amongst the systems with the highest $F_X/F_{\rm opt}$ ratio.

Figure 2.2 shows the advantage of a color cut in picking out CVs from active M dwarfs. By supplementing the X-ray to optical flux ratio with optical color information, M dwarfs cluster towards the upper right, while CVs cluster towards the upper left. The population in the lower center of the figure is generally comprised of the chromsopherically and coronally active BY Dra/RS CVn systems. The labeled objects in Figure 2.2 have been identified through optical spectroscopy that will be presented in a follow-up study of the eFEDS field.

[2]The term BY Dra refers to chromospherically active binary stars on the main sequence, and should be distinguished from RS CVn binary stars which are evolved and therefore above the main sequence. However, the term RS CVn has been used in the literature to refer to both; see Eker (1992) for a summary of the nomenclature.

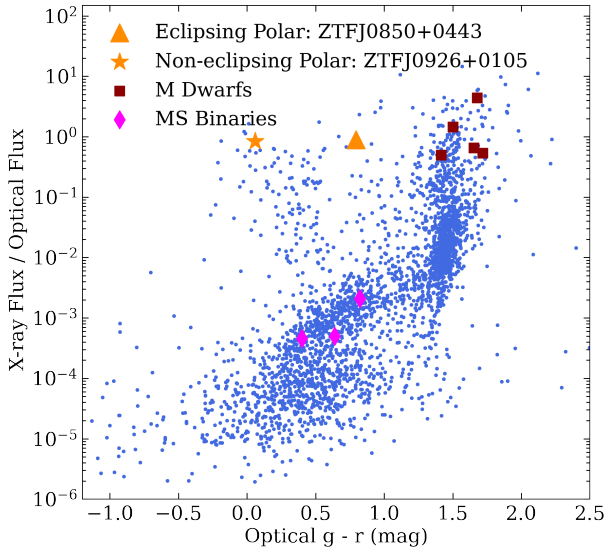

Figure 2.2: Ratio of X-ray flux to DECaLS LS8 optical flux as a function of optical color. The two polars cluster towards the upper left. Active M dwarfs dwarfs cluster towards the upper right and active main sequence binaries (known as BY Dra or RS CVn) below.

2.3 Sample Selection

The goal of our study is to classify Galactic eFEDS/ZTF sources, with an emphasis on those with a high X-ray to optical flux ratio and a strong periodic signal in ZTF.

We adopt the value of optical flux, $F_{\rm opt}$, for our entire study, as the standard conversion of the DECaLS LS8 g magnitude from the AB magnitude system. We assume a flat SED and a reference wavelength of 5000 Angstrom. We define the following samples:

1. High X-ray to optical flux ratio. We obtain spectra for all objects with $F_X/F_{\rm opt} > 0.5$.

2. Moderate X-ray to optical flux ratio and strong periodicity. We obtain spectra for all objects with $0.5 > F_X/F_{\rm opt} > 0.025$ percent that feature strong periodicity and pass a color cut. Our color cut eliminates the reddest objects which are likely to be active M dwarfs. We also report best-fit periods for the objects that do not pass the color cut.

3. Low X-ray to optical flux ratio and strong periodicity. We compile a list periods for all objects that have $F_X/F_{\rm opt} < 0.025$.

We define the significance of periodicity as the maximum Lomb-Scargle power subtracted by the median power, all divided by the median absolute deviation. We define “strong periodicity" as lightcurves where the significance is in the 86^{th} quantile. By this metric, approximately 10 percent of all objects in the eFEDS/ZTF footprint show strong periodicity. We define our color cut in the LS8 color bands and exclude objects with $g - r > 1.4$ as likely M dwarfs.

ZTFJ0850+0443 and ZTFJ0926+0105 stood out immediately from the first cut, with values of $F_X/F_{\text{opt}} > 0.5$. The Lomb-Scargle periodogram search of their lightcurves using `gatspy` also showed strong periodicity (VanderPlas, 2016b, 2018). Both criteria prompted follow-up spectroscopy.

The full analysis of our findings from the above cuts will be reported in an upcoming study.

2.4 ZTFJ0850+0443

Data

ZTFJ0850+0443 was found in both ZTF r and g band data to be a periodic source with high amplitude. The best-fit Lomb-Scargle period is 103.44 minutes (1.72 hr) in both bands. The approximate uncertainty (in both bands) based on the frequency grid oversampling, is 0.01 minutes. The folded lightcurve is shown in Figure 2.3. The optical position in ZTF (average FWHM: 2”) is RA (J2000): 08h 50m 37.19s, DEC(J2000): +04° 43’ 57.04", which corresponds to Gaia DR3 581892477184063232. The X-ray position in the SRG/eROSITA eFEDS catalog (positional uncertainty of source: 1.75”) is RA (J2000): 08h 50m 37.22s, DEC (J2000): +04° 43’ 59.38", which is 2" away from the optical counterpart. No other optical or X-ray sources are present within 2".

We followed up ZTFJ0850+0443 with high-cadence photometry in r and g bands using the Caltech HIgh-speed Multi-color camERA (CHIMERA; Harding et al., 2016) and u band using the Wafer-Scale Imager for Prime (WASP; Bilgi, 2019). The WASP u-band data were only acquired over a single period, while the CHIMERA r-and g-band data were both acquired simultaneously over two orbital periods. The high-cadence data revealed the eclipse in ZTFJ0850+0443 as well as cyclotron beaming at two points during a single orbit as seen in Figure 2.4.

An identification spectrum of ZTFJ0850+0443 was acquired using the Dual Imaging Spectrograph on the 3.5-m Apache Point telescope on 03 January 2022. That spectrum revealed strong He II 4686 compared to the Hβ Balmer line. This is

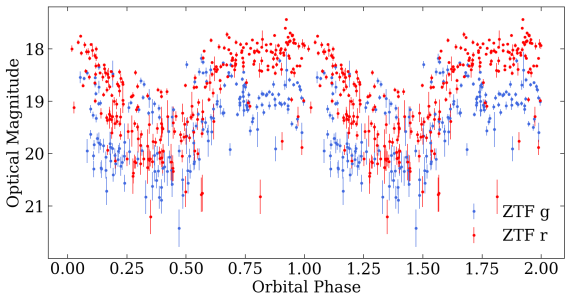

Figure 2.3: Folded lightcurve of ZTFJ0850+0443 (top, $P_{\rm orb}$ = 1.72 hr) over ZTF forced photometry. Large amplitude variations (1–2 mag) are characterstic of cyclotron beaming in polars.

strong evidence of a magnetic CV, although non-magnetic CVs can sometimes show this line behavior (Silber, 1992; Oliveira et al., 2020). Additional spectra at three orbital phases were obtained on the Keck telescope using the Low-Resolution Imaging Spectrometer (LRIS; Oke et al., 1995b) on 01 February 2022. A full orbit of ZTFJ0850+0443 was acquired on 07 March 2022 using LRIS. A summary of all data acquired for ZTF0850+0443 is presented in Table 8.3.

Table 2.1: Data Acquired for ZTFJ0850+0443

Data Type	**Date**	**Instrument**	**Specifications**	**Finding**
Identification Spectrum	08 Jan. 2022	Apache Point 3.5-m Telescope/DIS	Blue: 3770–5030 Å, 0.75 Å resolution, 900s exp. Red: 6200–7380 Å, 0.60 Å resolution, 900s exp.	Strong He II indicative of magnetic nature
High-cadence *u* band Photometry	27 Jan. 2022	Hale Telescope/WASP	10s exp. for 1.8 hr	Eclipse and Cyclotron Beaming Revealed
Multi-phase spectra	01 Feb. 2022	Keck I/LRIS	Blue: 3140–5640 Å, 1.1 Å resolution, 3×900s exp. Red: 5530–8830 Å, 0.80 Å resolution, 3×900s exp.	Emission/Absorption Line Reversals and Multi-Component Emission
High-cadence *r* and *g* band Photometry	04 Feb. 2022	Hale Telescope/CHIMERA	10s exp. for 3.5 hr	High-cadence photometry at simultaneous orbital phases
Multi-phase spectra	07 Mar. 2022	Keck I/LRIS	Blue: 3140–5640 Å, 1.1 Å resolution, 16×900s exp. Red: 5530–8830 Å, 0.80 Å resolution, 16×900s exp.	Full Orbit for Doppler Tomography and Radial Velocities

General Lightcurve Features

In Figure 2.4 we present the high-cadence photometry and spectroscopy of ZTF0850+0443 during notable orbital phases. The most prominent features of the high-cadence lightcurve are 1) the eclipse and 2) the two broad bumps per orbital phase in the u, g, and r bands, one of which occurs around the eclipse and the other at phase $\phi \approx 0.6$.

As described in the Introduction, the magnetic field in polars channels accreted material directly from the threading region. The material is directed by the magnetic field out of the orbital plane through the “accretion curtain" and onto the WD surface via one or two magnetic poles; see Figure 11 of Littlefield et al. (2018). Furthermore, the strong magnetic fields in polars lead to beamed cyclotron emission as non-relativistic spiral around magnetic field lines. Cyclotron emission can manifest itself in optical lightcurves as broad 1–2 mag bumps (e.g., Cropper, 1990; Hellier, 2001b). The data on ZTFJ0850+0443 points to it being an eclipsing polar. A visual aid to describe the system configuration is presented in Figure 8.8.

In most polars ($\approx$ 95 percent), the WD spin is locked with the orbit. We searched to see if ZTFJ0850+0443 is an “asynchronous" polar (i.e. the WD spin period is not locked to the orbital period). After Gaussian smoothing of the high-cadence lightcurves, no separate WD spin period is seen, suggesting that ZTFJ0850+0443 is a (typical) tidally locked polar. Furthermore, we see no signs of a beat period (a periodogram peak above 3σ from the median) aside from the sidereal day, which could indicate a WD spin period close to the orbital period as seen in most asynchronous polars. The period obtained from the high-speed CHIMERA photometry over two orbits is the same, further suggesting against any asynchronism. For the most part, orbital periods of polars range between 1.5 and 4 hours, placing the 1.72 hr period of ZTFJ0850+0443 well within the range of most polars (e.g., Halpern et al., 2018; Pala et al., 2020b; Abril et al., 2020).

In the following subsections, we walk through the orbit of ZTFJ0850+0443 and incorporate photometric and spectroscopic data to support our analysis.

Pre-Eclipse

CVs, both magnetic and non-magnetic, typically feature strong emission lines due to accretion. ZTFJ0850+0443 is now one of eight polars (Littlefield et al., 2018, private communication) where line inversions are seen in the pre-eclipse phase. Other polars that show pre-eclipse line inversions are Howell et al. (2008) and

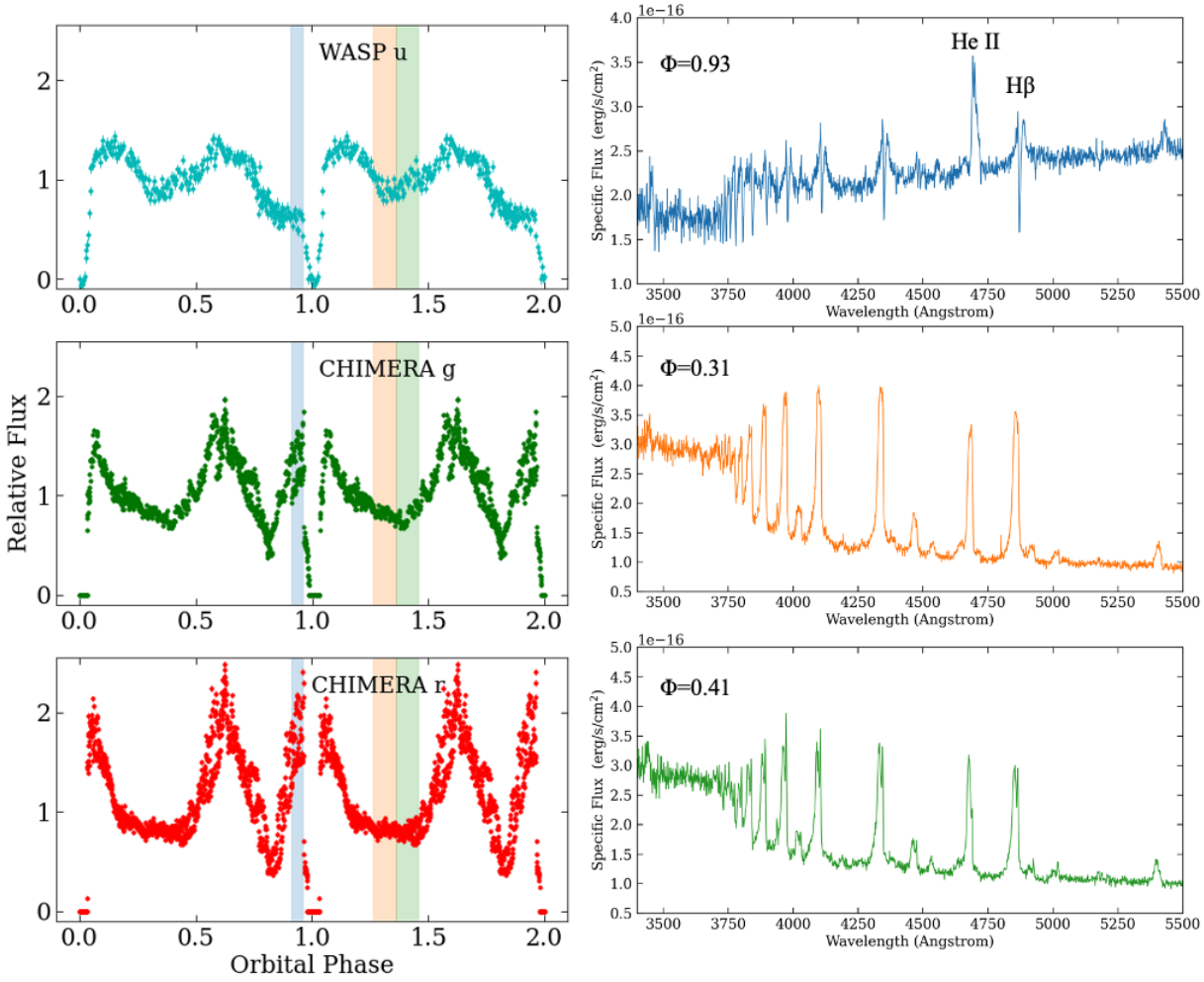

Figure 2.4: High-cadence photometry taken over two orbits (left) and multi-phase spectroscopy (right) of ZTFJ0850+0443. The highlights on the left panels correspond to the spectrum of the same color on the right. At phase $\phi = 0.93$, pre-eclipse line inversion is seen. At phase $\phi = 0.31$, the emission lines begin to split, revealing the irradiated face of the secondary star. At $\phi = 0.41$, the emission lines completely split and the irradiated .

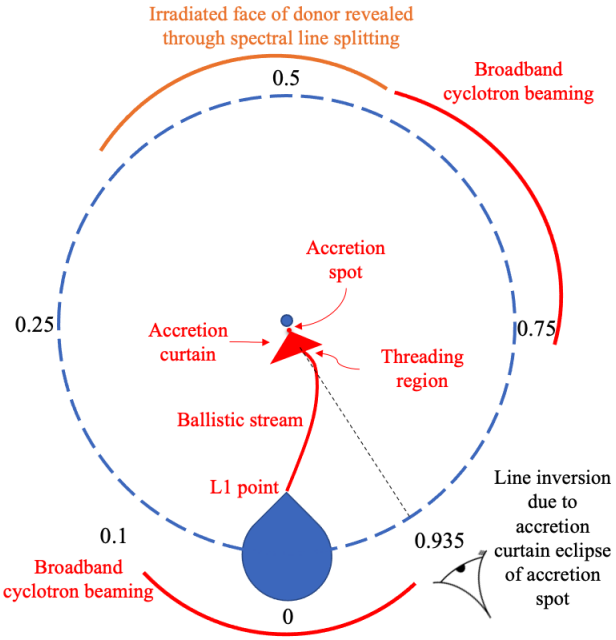

Figure 2.5: Cartoon of the orbit of ZTF0850+0443, based on Figure 12 of Schmidt et al. (2005). The observer can be imagined as rotating along the dashed circle as a function of orbital phase.

Fuchs et al. (2016). Figures 2.4 and 2.6 show that at phase $\phi = 0.93$, the H Balmer and He I lines are absorbed redward of line center. The He II 4686 line is only slightly absorbed. This also the case in the non-eclipsing polar MASTER OT J132104.04+560957.8 (Littlefield et al., 2018) as well as the eclipsing polar FL Cet (SDSS J015543.40+002807.2) (Schmidt et al., 2005). Littlefield et al. (2018) attribute this phenomenon to absorption within the accretion curtain (i.e. within the magnetosphere), not the threading region as was suspected before MASTER OT J132104.04+560957.8 was discovered. The main reason for this is that threading region is confined to the orbital plane, while the accretion curtain comes out of the plane along with the WD magnetic field lines. Since ZTFJ0850+0443 is an eclipsing system, the presence of line inversions supports the idea that this phenomenon is more common at higher inclinations ($i \rightarrow 90°$). We choose to adopt the extended "accretion curtain" as opposed to the thin "accretion column" geometry to be more general. We do not attempt to model this geometry in this study so we leave the innermost part of the accretion region as having an abritrary width: either a curtain or a column.

Another notable feature seen at pre-eclipse is that the u-band flux drops while the r- and g-band flux increase (Figure 2.4). This is due to the u passband being centered

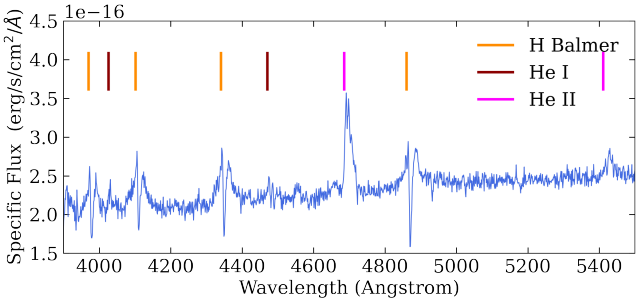

Figure 2.6: Zoomed-in spectrum of ZTFJ0850+0443 at $\phi = 0.93$. He II is less broad than H Balmer lines and hardly absorbed. H Balmer lines are absorbed redward of line center.

blueward of the Balmer jump. In the pre-eclipse occultation of accretion spot emission by the accretion curtain, cooler material passes in front of the dominant source of radiation. Thus, the Balmer jump transitions from emission to absorption.

Eclipse: A Likely One-Pole System

The lightcurve near eclipse can often be used to identify whether a polar has one or two accreting poles. We present the high-cadence lightcurve zoomed in around the eclipse in Figure 2.7. The data favors ZTFJ0850+0443 being a one-pole system, but we cannot discard the possibility of a second low-luminosity accreting pole.

In the single-pole case, the pole is eclipsed at $\phi = 0.966$ as indicated by the sharp decline in the g- and r-band data. The sampling of the u-band data is insufficient to resolve this. The first shaded region ($\phi = 0.966 - 0.988$) in Figure 2.7 corresponds to the gradual ingress of the ballistic stream. The pole exits eclipse at $\phi = 1.033$ as indicated by the sharp rise in the g- and r-band data. The second shaded window ($\phi = 1.033 - 1.05$) shows the gradual egress of the accretion curtain. We denote $\phi = 1.05$ as the end of the accretion stream eclipse as that is the point where the total flux returns to its pre-eclipse value in r- and g-band data. The u-band flux is larger during post-eclipse due to the absence of pre-eclipse self-absorption by the accretion curtain. Previous observations and numerical simulations have been able to reproduce remarkably similar lightcurves (Breytenbach et al., 2019; Zhilkin et al., 2019).

In the case of two-pole accretion, two “steps" in the ingress and egress of the magnetic poles are often seen. However, our photometric sampling cadence (10 seconds) is too low to detect that. For example, a $\sim$ 0.1-second cadence was needed to see this in FL Cet (O’Donoghue et al., 2006) and a 1-second cadence for

eRASSt J192932.9–560346 (Schwope et al., 2022b). It could also be that the second pole is so faint at optical wavelengths that it would not appear in optical photometry at all. After all, no spectroscopic evidence aside from weak evidence in the Doppler tomograms (see Section 2.4) of a second pole is seen. Additional data (e.g., optical polarimetry, X-ray lightcurves, or higher cadence optical photometry) are needed to definitively classify this as a one- or two-pole system, although the current data more strongly support the one-pole model.

On the whole, the eclipse is shallowest in the u band and deepest in the r band. This has been attributed to the accreted material being channeled in the lowest energy configuration, which concentrates cooler material towards the center of the accretion stream. Hotter material is therefore more sparse and can still be seen while the cooler, concentrated material is eclipsed (see Figure 5 of Harrop-Allin et al., 1999) for the modeling of HU Aquarii). We note that in the case of HU Aquarii, modeling of this feature alone in optical lightcurves was insufficient to determine whether the system is accreting at one or two poles.

Donor Star Revealed

At phase $\phi \approx 0.3$, the H Balmer, He I, and He II emission lines begin to split before being distinguishably separated at $\phi \approx 0.4$ (Figure 2.4). The broad (FWHM ≈20Å), blueshifted component traces the accretion onto the WD. The narrow (FWHM ≈5Å) component, which at this phase is slightly redshifted, traces the irradiated face of the donor star. At phase $\phi \approx 0.5$, the narrow component in the H Balmer, He I, and He II emission lines is at line center and stronger than the blueshifted accretion spot emission lines (Figure 2.8).

At this point in the orbital phase, we are seeing directly into the irradiated face of the donor, confirming the origin of the narrow emission component. This phenomenon has been known since early studies of polars (e.g., Cropper, 1990) and used to constrain binary parameters of the eclipsing polar BS Tri (Kolbin et al., 2022) when the traditionally used Na I 8183, 8195 doublet could not be spotted. The Na I 8183, 8195 doublet is not seen in ZTFJ0850+0443 due to the strong accretion continuum that dominates out to red optical wavelengths. At the same orbital phases that H Balmer, He I, and He II emission lines are split into broad and narrow components (center around $\phi = 0.5$), Ca II 8498 and 8542 from the irradiated donor are seen in emission above the accretion continuum (Figure 2.8).

Na I, Ca II, H Balmer, He I, and He II lines from the donor star do not all arise from

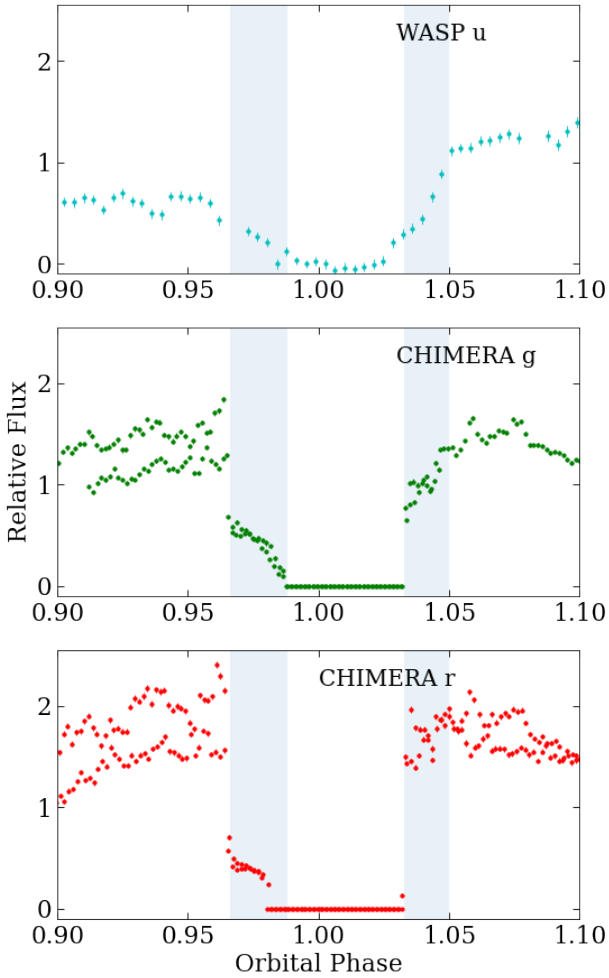

Figure 2.7: High-cadence lightcurve (two stacked orbits) of ZTFJ0850+0443 around the eclipse. Highlights indicate the following phases: In the one-pole accretion model, the accretion spot on the WD is eclipsed by the donor star at $\phi = 0.966$. The accretion stream is gradually eclipsed until totally disappearing at $\phi = 0.988$. The accretion spot exits eclipse at $\phi = 1.033$ and the accretion stream gradually re-emerges until being fully exposed at $\phi = 1.05$.

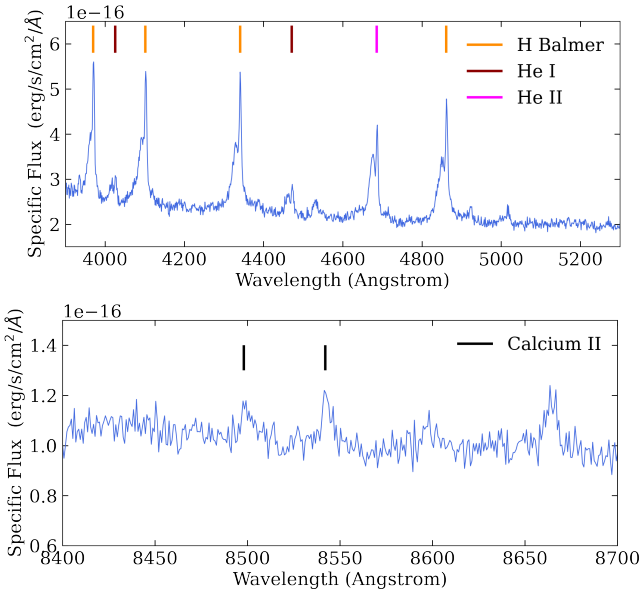

Figure 2.8: The narrow component of H Balmer and He I/II emission lines roughly trace the tip of the Roche lobe of the donor star (top). Ca II lines trace the irradiated face at the center-of-light (bottom). Spectra shown are taken near $\phi = 0.5$.

the same location. The H Balmer, He I, and He II lines likely arise from the tip of the Roche lobe and possibly into the accretion stream (e.g., Schwope et al., 2011). The Ca II lines roughly trace the center-of-light of the irradiated donor, somewhere between the center-of-mass and the tip of the Roche Lobe. The Na I lines tend to arise from deeper within the donor and more reliably trace the center-of-mass (e.g., Schwope et al., 2011). Therefore, in order to correctly use the Ca II lines to trace the radial velocity of the donor, we must apply a correction which we explain in detail in Section 2.4.

Doppler Tomography

Spectral lines in CVs vary as a function of orbital phase, often containing information about all system parameters which can be blended together. In CVs with an accretion disk, the disk, the accretion hot spot (where the accretion stream hits the disk), and irradiated face of the donor star can all contribute to the observed emission. Doppler tomography converts phase-resolved spectroscopy into a plot of observed radial velocity and line strength as a function of orbital phase. Doppler tomograms disentangle the contribution of the various CV components (e.g., accretion disk, accretion hot spot, donor star) to a given spectral line; see Marsh (2005) for a review of the method of Doppler tomography. We present Doppler tomogams and radial

velocity curves of He II 4686 and Hβ in Figure 2.9.

We use the `doptomog`[3] code developed by Kotze et al. (2015b). We show the "inverse" Doppler tomograms, which better illustrate the high-velocity components in magnetic CVs. Higher velocities are located closer in to the center of the diagram, while lower velocities are farther from center (traditional Doppler tomography flips this around).

The feature with an amplitude of 1000 km/s is the dominant component. The free-fall velocity at the surface of a WD, assuming typical parameters ($M_{\rm WD} = 0.8 M_{\odot}$, $R_{\rm WD} = R_{\rm Earth}$) is ≈ 4000 km/s. By observing emission at 1000 km/s, we can infer that this emission is due to material within the accretion curtain as it approaches the WD surface. We do not know enough about the magnetic field configuration near the surface to know exactly where in the accretion curtain we are probing. A weak, diffuse component can also be seen towards the bottom right, which could be indicative of a second magnetic pole. This is the only possible evidence for a second pole that we have in our current data.

The irradiated face of the secondary is clearly shown roughly between 300–400 km/s in both Doppler tomograms as well near $\phi = 0.5$ in the radial velocity curves. The gap near $\phi = 0.3$ is due to a small gap in our data acquisition. The radial velocity curves clearly show the pre-eclipse line inversion, where He II 4686 is hardly split, but Hβ is split into two components due to the intervening redshifted absorption.

Binary Parameters

In order to solve for the full mass and radius parameters of the system, we assume a circular orbit. Our constraining equations are the following: 1) the Roche lobe equation from Eggleton (1983c), 2) the binary star mass function, 3) the relationship between the mass ratio and the correction applied to the RVs derived from Ca II lines, 4) an $R(M)$ relation derived from modern CV evolutionary tracks, and 5) the eclipse of the system.

The Roche lobe equation (Eggleton, 1983c) is:

$$\frac{R_L}{a} = \frac{0.49 q^{2/3}}{0.6 q^{2/3} + \ln\left(1 + q^{1/3}\right)} = f(q) \tag{2.1}$$

where a is the orbital separation of the system: $a^3 = G(M_1 + M_2) P_{\rm orb}^2 / 4\pi^2$ and q is the ratio of the donor star mass to the WD mass: $q = M_2/M_1$. We adopt this mass ratio convention consistently throughout this study.

[3] `https://www.saao.ac.za/~ejk/doptomog/main.html`

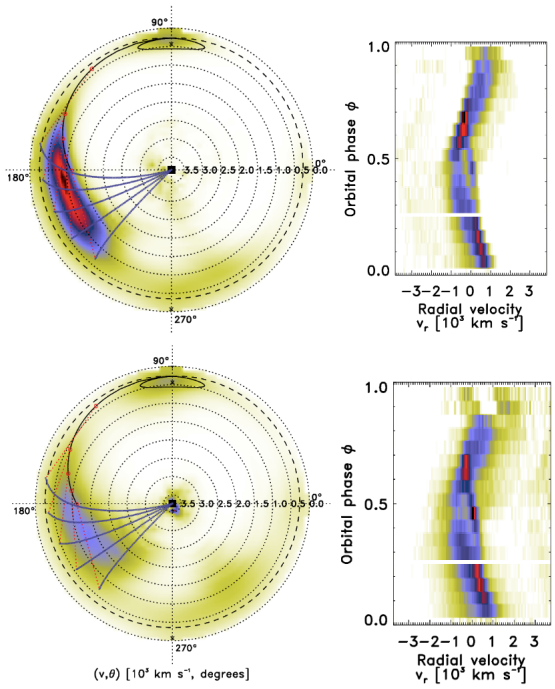

Figure 2.9: "Inverse" Doppler tomograms and radial velocity curves for ZTF0850+0443 using He II 4686 (top) and Hβ (bottom). Redder color indicates stronger line strength. Model magnetic field threading is shown for clarity using generic parameters. The dominant component is that of the accretion curtain. The irradiated face of the secondary can also be seen towards the top.

The binary star mass function is:

$$\frac{(M_1 \sin i)^3}{(M_1 + M_2)^2} = \frac{P_{\rm orb} K_2^3}{2\pi G} \tag{2.2}$$

where M_1 is the mass of the accreting WD and M_2 is the mass of the donor. K_2 is the radial velocity of the donor, which we must infer from the observed radial velocity of the Ca II lines, K_2'. As discussed earlier, these lines originate from the center-of-light of the irradiated (day) side of the donor star, which is not a good approximation for the center-of-mass of the donor star. We obtain $K_2' = 360 \pm 15$ km/s from a least-squares fit to the observed line profiles (Figure 8.1). The statistical error of 15 km/s arises from instrumental precision and low signal-to-noise in measuring the line position at certain phases. We assume the entire donor star is co-rotating around the center of mass of the system at the same orbital period. To determine the relationship between K_2 and K_2', we assume the center-of-light of the donor star is located εR_L from the center-of-mass of the donor star. The factor ε can be

thought as being the coordinate on the axis between the donor center-of-mass and the tip of the Roche lobe. Therefore, the semi-major axis of the center-of-light is $a_2' = a_2 - \varepsilon R_L$ and the observed radial velocity is $K_2' = 2\pi(a_2 - \varepsilon R_L)/P_{\rm orb}$. Since $K_2 = 2\pi a_2/P_{\rm orb}$, we can solve for the correction factor: $K_2'/K_2 = 1 - \varepsilon R_L/a_2$. Since $a = a_2(1+q)$, we write:

$$\frac{K_2'}{K_2} = 1 - \varepsilon f(q) \times (1+q) \tag{2.3}$$

and therefore the RV correction is a function of the mass ratio $q = M_1/M2$ and ε, the coordinate on the axis between the donor center-of-mass and the tip of the Roche lobe. A value of $\varepsilon = 0$ corresponds to the donor center-of-light being located at the donor center-of-mass and a value of $\varepsilon = 1$ corresponds to the donor center-of-light being located at the tip of the Roche lobe.

In order to determine reasonable values of ε, we constructed a simple binary star model using `PHOEBE` (Prsa and Zwitter, 2005; Prsa et al., 2016) consisting of a 15,000 K primary star (average of WDs in CVs at this orbital period, e.g., Pala et al., 2022b) irradiating a 3000 K donor star at a typical CV orbital separation. This model with a single source of radiation serves as the lower limit of possible radiation for the donor. In polars, radiation from the accretion stream, accretion curtain, and accretion pole can also irradiate the donor. Modeling of the accretion-induced X-ray flux is beyond the scope of our work. However, in our simple two-star model, the center-of-light (location of mean intensity) at $\varepsilon = 0.45$, serves as a lower limit.

We then turn to empirical findings to place an upper limit on ε. We consider the analysis of He II, Ca II, and Na I lines of the donor star in HU Aquarii (Schwope et al., 2011). Doppler tomography of those lines showed that the Ca II lines precisely probe the center-of-light, located approximately at values of $\varepsilon = 0.5 - 0.85$.

Therefore, we adopt the range $\varepsilon = 0.45 - 0.85$, combining the simple analytical model and empirical results. We overplot this range on our `PHOEBE` model in Figure 2.10. A full treatment of radiation from the WD, accretion spot, accretion curtain, accretion stream, and efficiency of irradiation of the donor are beyond the scope of this study.

In order to obtain an $R(M)$ relation, we use the CV donor star evolutionary tracks from the Knigge et al. (2011) set of models. They account for the inflated radius of the donor star due to the rotation it undergoes and tidal forces it experiences while in the binary system. The Knigge et al. (2011) models also account for inflation of the secondary due to irradiation by the primary.

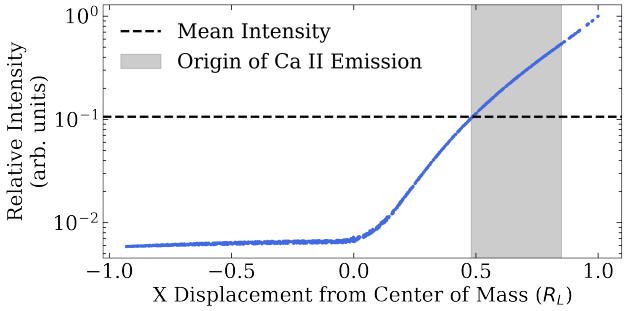

Figure 2.10: Output of a PHOEBE model of a late-type donor being irradiated by a 15,000K WD. The mean intensity (center-of-light) is located at $\varepsilon = 0.45$, while an empirical analysis of the donor in a similar polar places the origin of Ca II emission lines to be as far away from the center-of-mass as $\varepsilon = 0.85$.

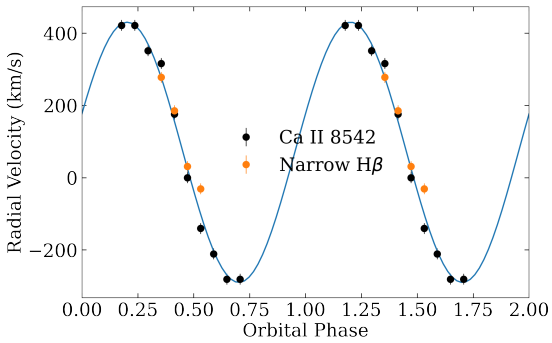

Figure 2.11: Radial velocity (RV) measurements of the irradiated face of the donor star as a function of orbital phases, K_2'. RV measurements are obtained at orbital phases where 1) Ca II is strong enough to be seen above the continuum or 2) the narrow component of H Balmer lines is not blended with the broad accretion component.

The final component is the eclipsing nature of the system. Given the typical system parameters of polars, we know the inclination of the system must be $i \gtrsim 78°$ for the system to be eclipsing. Chanan et al. (1976) showed that if the eclipse timing is well-constrained, then the mass ratio q is a function of the inclination i in Roche lobe filling systems. We find the eclipse duration to be 415 ± 5 sec, measured at the sharp dropoff and sharp rise as described in Section 2.4.

The Chanan et al. (1976) geometry, however, assumes a point source located at the center of the WD and not on the surface, as is that case in polars. This however, leads to a negligible systematic that is contained within the statistic error bars on the measurement of all system parameters. Finally, we note that the deep eclipse places upper limits on the temperature of the donor star, but does not significantly

tighten our final constraints on the donor star properties. The CHIMERA zero point magnitude in the r filter is approximately 27 (Harding et al., 2016) at time of instrument commissioning. Based on the comparison star photometry in our data, however, we estimate a zero point magnitude of no greater than $r = 26$. At the distance of ZTFJ0850+0443 (1080^{+350}_{-250} pc), a null detection in the CHIMERA r filter places the donor star at M5 or later based on SDSS colors.

We then solve for all equations simultaneously via a vectorized least-squares approach implemented with `scipy` to find the final best-fit values. This is equivalent to minimizing the error in Equation 2.2, Equation 2.4, $R_L = R(M_2)$, and the eclipse timing equation from Chanan et al. (1976) simultaneously. We present the final values for the binary system in Table 2.4.

Table 2.2: System Parameters for ZTFJ0850+0443

System Parameter	**Estimated Value**
M_1 ($M_\odot$)	0.81 ± 0.08
M_2 ($M_\odot$)	0.119 ± 0.002
R_2 ($R_\odot$)	0.163 ± 0.002
K_2 ($\mathrm{km\,s^{-1}}$)	434 ± 15
i (degrees)	$83.3° \pm 1.2°$
P_{orb} (hr)	1.724
Δt_{ecl} (s)	415 ± 5
$\dot{M}$ ($M_\odot\,\mathrm{yr^{-1}}$)	$\sim 10^{-11}$
$\varepsilon = (a_2 - a_2')/R_L$	0.65 ± 0.20

The largest uncertainty in our WD mass estimate stems from the uncertainty in radial velocity (which scales to the third power in Kepler's binary system equation). While this is limited by our estimates of the location of the donor center-of-light (parameterized by ε), we find that we can still reasonably constrain the mass of the WD.

Magnetic Field Strength

There are three common ways to determine the magnetic field strength of a polar as outlined by Cropper (1990): 1) Cyclotron humps in the optical spectrum, 2) Zeeman splitting of emission lines in the optical spectrum, 3) Optical polarization measurements. In the case of ZTF0850+0443, we do not detect the first two and have not acquired optical polarization data to test the third criterion.

Why don't we see any cyclotron harmonics? The wavelengths of cyclotron har-

monics (e.g., Ferrario et al., 2015; Mason et al., 2019) are given by the following formula:

$$\lambda_n = \frac{10710}{n}\left(\frac{100\ \mathrm{MG}}{B}\right)\sin\theta\ \text{Å} \tag{2.4}$$

where λ_n is in Angstrom and θ is the viewing angle of the cyclotron beaming. In cases where cyclotron humps are seen in the optical, it is usually the $n = 3$ or $n = 4$ harmonics that are seen (Cropper, 1990; Wickramasinghe and Ferrario, 2000). Since lower-order harmonics are less prominent, the absence of cyclotron harmonics at optical wavelengths often implies low magnetic field strength. Ferrario et al. (1993) and (Wickramasinghe and Ferrario, 2000) showed that in polars with field strengths of $B \lesssim 20$ MG, cyclotron harmonics ($n = 2, 3, 4$) can only be seen in near-infrared spectra and not at all in optical spectra.

When infrared spectra are not available, infrared photometry has been shown to be insightful for magnetic field characterization of low-field polars (Harrison and Campbell, 2015; Wickramasinghe and Ferrario, 2000). Mason et al. (2019) discovered CRTS J035010.7 +323230, a polar that did not show any of the typical magnetic field diagnostics outlined by Cropper (1990). CRTS J035010.7 +323230 stood out by showing a strong infrared excess with WISE W3 and W4 magnitudes higher than W2 and W1 points. The authors argued this was indicative of a low-field ($\lesssim 10$ MG) polar. Similarly, Bernardini et al. (2019) inferred that WISE photometric excess of 2PBC J0658.0–1746 was indicative of a low magnetic field in a polar. We see exactly the same behavior in ZTF0850+0443, with a clear infrared excess in the WISE W3 and W4 bands. We reproduce a spectral energy distribution in Figure 7.10 compiled from GALEX, PanSTARRS, 2MASS, and WISE.

We propose that ZTF0850+0443 must be viewed at a high enough angle ($\sin\theta \sim 1$) from the magnetic pole so that cyclotron beaming can be observed in its optical lightcurve. What we see in the optical is likely a blend of many low-order cyclotron harmonics in the lightcurve bumps peaking at phase $\phi = 0.6$ and $\phi = 1$ (the second peak in the lightcurve would be at $\phi = 1$, but the WD is eclipsed in this system). The fundamental ($n = 1$) harmonic is then in the mid-infared ($\sim 10 - 20\mu$m) with strong $n = 2, 3, 4$ harmonics in the near-infrared. We suggest that ZTF0850+0443 is a low-field ($B \lesssim 10$ MG) polar, potentially adding to a small pool of polars with such low magnetic field strengths.

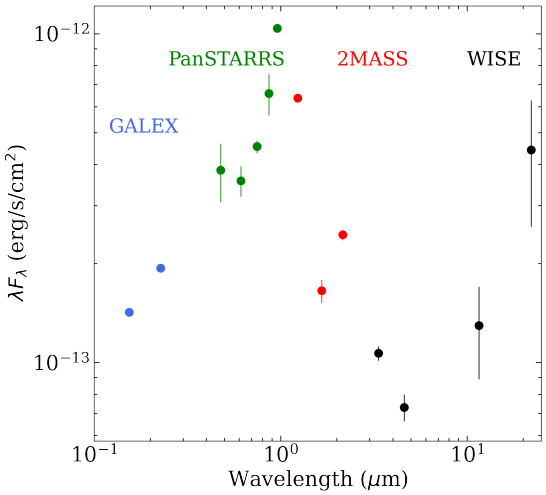

Figure 2.12: Extinction-corrected ($A_V = 0.19$; Schlafly and Finkbeiner (2011a)) spectral energy distribution of ZTFJ0850+0443 reproduced using average photometry from GALEX, PanSTARRS, 2MASS, and WISE data. The mid-infrared excess of ZTFJ0850+0443 suggests it is a low-field ($B \lesssim 10$ MG) polar.

2.5 ZTFJ0926+0105

Data

ZTFJ0926+0105 was found in ZTF data to be a periodic source with high amplitude in both r and g bands (Figure 2.13). The optical position in ZTF (average FWHM: 2") is RA (J2000): 09h 26m 14.30s, DEC (J2000): +01° 05' 57.40", which corresponds to Gaia DR3 3844016380122912640. The X-ray position in the SRG/eROSITA eFEDS catalog (positional uncertainty: 1.26") is RA (J2000): 09h 26m 14.20s, DEC (J2000): +01° 05'58.43" , which is 1.3" away from the optical counterpart. No other optical or X-ray sources are present within 2".

We followed up ZTFJ0926+0105 with high-cadence photometry using CHIMERA. Data were acquired over 3.5 hours, but all orbital phases could not be completely covered due to transient clouds. The best-fit period of the r and g-band data is 88.34 min (1.47 hr). The approximate uncertainty based on the frequency grid oversampling is 0.01 minutes. Furthermore, as with ZTFJ0850+0443, we see no signs of a beat period (a periodogram peak above 3σ from the median) aside from the sidereal day, which could indicate a WD spin period close to the orbital period as seen in most asynchronous polars.

An identification spectrum was acquired using the Double Spectrograph (DBSP; Oke and Gunn, 1982b) on the Hale telescope on 08 January 2022. This spectrum showed strong H Balmer, He I, and He II lines in emission. He II 4686 fulfilled

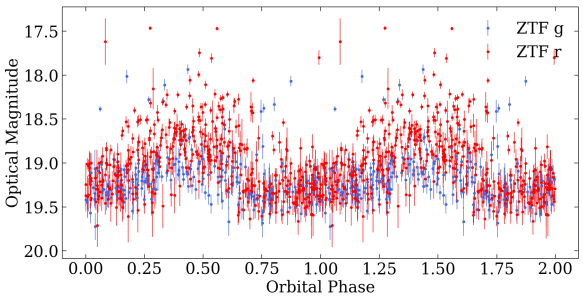

Figure 2.13: Folded lightcurve of ZTF0926+0105 ($P_{\rm orb}$ = 1.47 hr) over ZTF forced photometry.

the criteria of Silber (1992) for being a magnetic CV candidate, prompting us to acquire follow-up spectroscopy. Phase-resolved spectra were taken on the Keck telescope using the Echelle Spectrograph and Imager (ESI; Sheinis et al., 2002) on 01 February 2022. Eight 10-minute spectra were taken consecutively with ~11 minutes between the starting point of each spectrum. Table 2.5 summarizes all data taken and the contribution of each dataset.

Table 2.3: Data Acquired for ZTFJ0926+0105

Data Type	**Date**	**Instrument**	**Specifications**	**Finding**
Identification Spectrum	07 Jan. 2022	Hale Telescope/DBSP	Blue: 3700–5870 Å, 1.5 Å resolution, 900s exp. Red: 5700–10,200 Å, 1.1 Å resolution, 900s exp.	Strong He II indicative of magnetic nature
High-cadence r and g band Photometry	05 Feb. 2022	Hale Telescope/CHIMERA	10s exp. for 3.5 hr	High-cadence photometry at all orbital phases
Multi-phase Spectra	06 Feb. 2022	Keck II/ESI	Echelle mode: 3920–11,000 Å (not continuous); 8×600s exp.	Full orbit for Doppler tomography and radial velocities

Lightcurve and Spectral Analysis with Doppler Tomography

We see cyclotron beaming once per orbital phase in the g and r high-cadence lightcurves of ZTFJ0926+0105 (Figure 2.14). The large factor by which the flux increases, combined with the orbital period of 1.47 hr, is characteristic of few objects other than polars. No eclipse or any other notable features are seen. We also see a prominent cyclotron bump in the phase-resolved spectra of ZTFJ0926+0105 (Figure 2.14). The phase where the bump is most prominent coincides with the maximum in the photometry, confirming cyclotron beaming as the source of the high-amplitude variation. We only see one cyclotron harmonic around 8800 Angstrom, and discuss the implications for determining the magnetic field strength in Section 2.5.

Aside from the prominent cyclotron bump, the phase-resolved spectroscopy of ZTFJ0926+0105 is much like that of ZTFJ0850+0443, revealing emission from both the accretion curtain and the face of the irradiated donor star. We produce Doppler tomograms for ZTFJ0926+0105 in order to disentangle the two components (Figure 2.15).

Both Doppler tomograms of ZTFJ0926+0105 reveal the irradiated face of the donor star at approxmiately 300 km/s, particularly the Hβ tomogram. This coincides with the presence of Ca II lines (see Figure 2.14) which also stem from the irradiated face of the donor star like in ZTFJ0850+0443. While we could estimate radial velocity measurements of the donor star in ZTFJ0926+0105, the lack of an eclipse prevents us from obtaining a precise estimate of the mass ratio and component masses. Both the He II 4686 and Hβ tomograms reveal large, approximately 750 km/s amplitude radial velocities. We attribute such large radial velocities to the accretion curtain, as was the case with 1000 km/s radial velocities in ZTFJ0850+0443. Since ZTFJ0926+0105 is viewed at a more face-on inclination (no eclipse is seen in the lightcurve), the observed radial velocity should be lower.

Magnetic Field Strength

Three cyclotron harmonics are present in the spectrum of ZTFJ0926+1015 at maximum beaming (Φ = 0.64 in Figure 2.14). We fit a polynomial continuum to the un-beamed spectrum (Φ = 0.78 in Figure 2.14), scale it by an additive factor, and subtract it from the beamed spectrum to find cyclotron features. We find three features: a large, prominent one (180 times the continuum) peaking around 8600 Å, a smaller one (20 times the continuum) at 6450 Å, and another small one (30 time the continuum) at 5160 Å.

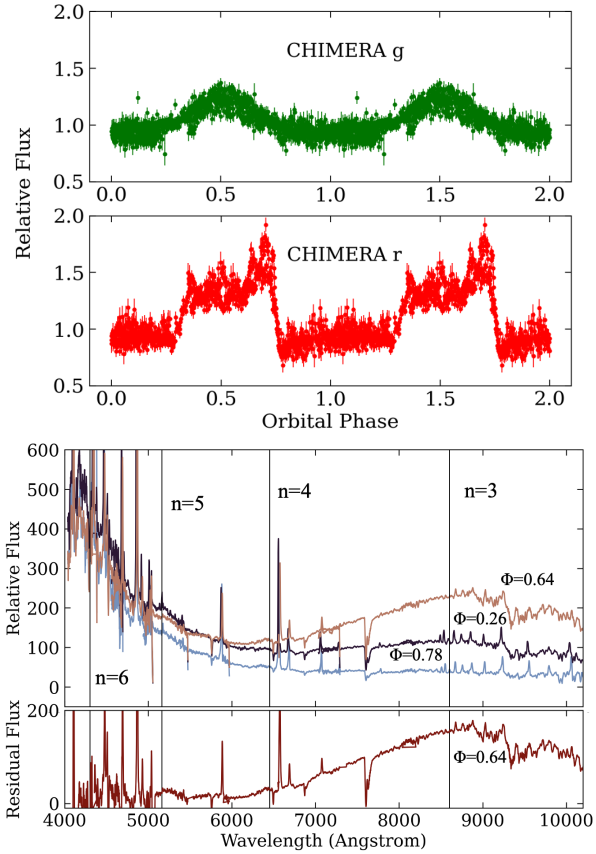

Figure 2.14: Cyclotron beaming is seen once per orbital phase in the high-cadence CHIMERA photometry (top) as well as phase-resolved spectroscopy (bottom).

Using Equation 2.4, we must assume both a viewing angle and obtain cyclotron harmonic numbers to find the magnetic field strength. From the spacing of the three cyclotron features (8600 Å, 6450 Å, 5160 Å), we deduce them to correspond to the $n = 3, 4, 5$ harmonics, respectively. There should be a $n = 6$ harmonic also present in the wavelength range of the data, but harmonics that high are usually optically thick (e.g., Cropper, 1990), and the spectrum at those wavelengths is dominated by emission lines anyway. The viewing angle must also be large ($\theta \gtrsim 60°$) for the beaming to be as high amplitude as we see in the spectroscopy and photometry (e.g., Cropper, 1990). We therefore adopt a viewing angle range of $\theta = 60° - 90°$, leading to a magnetic field of $B = 36 - 42$ MG. Follow-up X-ray and optical studies could be used to determine magnetic field orientation and viewing angle of cyclotron features.

We conclude this section by presenting an SED of ZTFJ0926+0105 (Figure 2.16). There are no significant WISE W3 or W4 detections, consistent with ZTFJ0926+0105

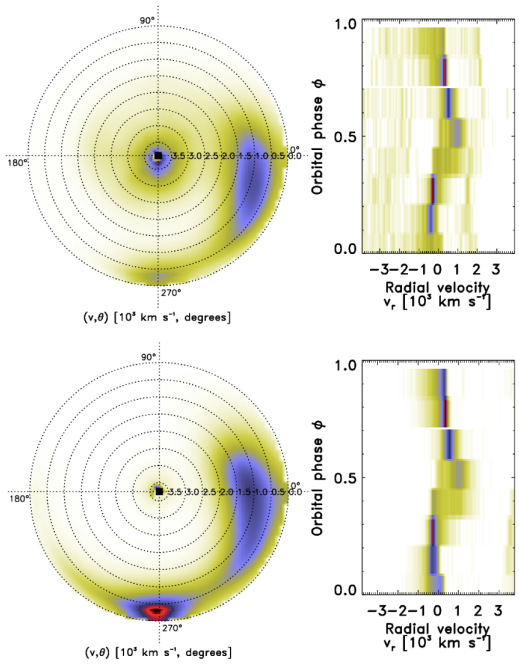

Figure 2.15: "Inverse" Doppler tomograms and radial velocity curves for ZTF0926+0105 using He II 4686 (top) and Hβ (bottom). Redder color indicates stronger line strength. The dominant component is that of the accretion curtain. The irradiated face of the secondary can also be seen at the bottom, appearing stronger in Hβ compared to He II 4686.

having a magnetic field strength of $B = 36 - 42$ MG.

2.6 Discussion

Previous Classifications and X-ray Detections

ZTFJ0850+0443 was previously misclassified as a quasar based on its GALEX color information (Warwick et al., 2012). That same work reported a marginal XMM Slew Survey detection (with 40 percent flux errors), where it was listed as XMMSL1 J085036.8+044354. Had they existed at the time, Gaia proper motions or parallax would have likely prevented the misclassification.

ZTFJ0926+0105 was previously classified as a WD + M dwarf binary in Augusteijn et al. (2008) based on SDSS colors. It is likely to have been observed in a state of cyclotron beaming, during which the increase in flux at red optical wavelengths gives the impression of a late-type donor (note Figure 2.14 at phase $\Phi = 0.64$). ZTFJ0926+0105 is also in the Gaia WD Catalog (Gentile Fusillo et al., 2021b).

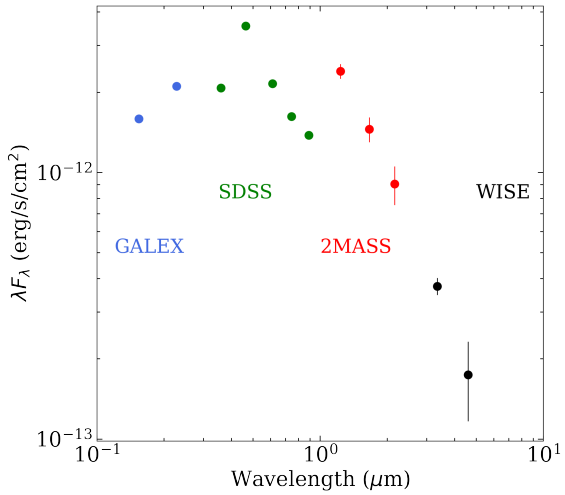

Figure 2.16: Extinction-corrected ($A_V = 0.12$; Schlafly and Finkbeiner (2011a)) spectral energy distribution of ZTFJ0926+0105 reproduced using average photometry from GALEX, SDSS, 2MASS, and WISE data. Unlike ZTFJ0850+0443, there is no mid-infrared excess which could indicate this is a low-field polar.

Distances and X-ray Luminosities

The Gaia EDR3 distances calculated in Bailer-Jones et al. (2021d) for ZTFJ0850+0443 and ZTFJ0926+0105 are 1080^{350}_{-250} pc and 385^{+45}_{-40} pc, respectively.

We estimate the X-ray luminosities of ZTFJ0850+0443 and ZTFJ0926+0105 in the eROSITA Main range (0.2–2.3 keV) using the eFEDS co-added fluxes and Gaia distances. The fluxes of ZTFJ0850+0443 and ZTFJ0926+0105 are $1.80 \pm 0.16 \times 10^{-13}$erg/s/cm^2 and $2.80 \pm 0.16 \times 10^{-13}$erg/s/cm^2, respectively. The X-ray luminosities (in the 0.2–2.3 keV range) of ZTFJ0850+0443 and ZTFJ0926+0105 are $2^{+2}_{-1} \times 10^{31}$ erg/s and $4.7^{+1.1}_{-1.0} \times 10^{30}$ erg/s, respectively. We also note that ZTFJ0850+0443 and ZTFJ0926+0105 fulfill at least one of the criteria to be classified as X-ray variable in the eFEDS data release (Salvato et al., 2022) and are also present in the Hard (2.3–5 keV) sample.

Placement on the HR Diagram

We overplot ZTFJ0850+0443 and ZTFJ0926+0105 (corrected for extinction) on a Gaia Hertzsprung-Russell (HR) diagram (Figure 2.17). We note that ZTFJ0850+0443 has a parallax divided by parallax error (π/σ_π) value of 2.8. This is lower than the value adopted by some authors to claim a precise distance measurement ($\pi/\sigma_\pi > 3$ or even $\pi/\sigma_\pi > 10$, depending on the study). We plot all sources in Gaia EDR3 within 100 pc of the Sun with parallax $\pi/\sigma_\pi > 10$. On average, the locations

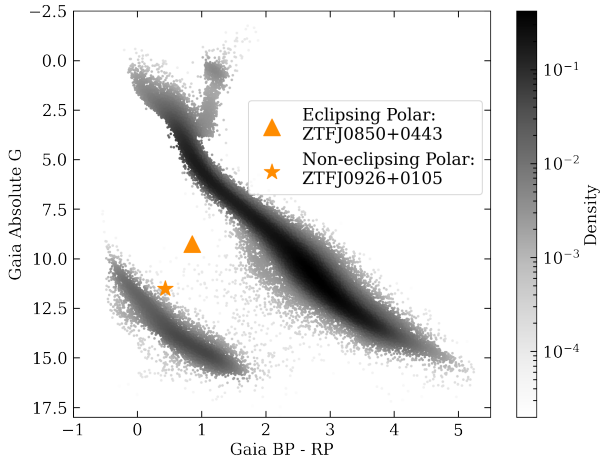

Figure 2.17: Gaia EDR3 HR diagram composed of sources within 100 pc with an exceptional parallax measurement ($\pi/\sigma_\pi > 10$). The two polars are located between the main sequence and WD tracks, consistent with typical polars.

of ZTFJ0850+0443 and ZTFJ0926+0105 are consistent with the mean position of polars as found by Abril et al. (2020).

Current CV Population and SRG

All CVs are X-ray emitters, to some extent (Mukai, 2017). While magnetic CVs typically have higher X-ray luminosities than their non-magnetic counterparts, the eFEDS dataset is deep enough to reveal new X-ray detections of non-magnetic CVs. Even from this modest sample, the efficiency of discovery of magnetic CVs is greatly increased by incorporating X-ray data from eFEDS/SRG. Neither of the two polars were listed as SDSS CVs. A complete analysis of all CVs in the eFEDS field will be presented in a follow-up study.

An all-sky eROSITA/SRG release will be vital for constructing a volume-limited survey similar to that of Pala et al. (2020b). Volume-limited samples are one way of eliminating observational bias from constructing a full picture of CVs and their evolution, as was shown by Pala et al. (2020b). Introducing X-ray information eliminates another observational bias and provides another property that can be used to study CVs.

Schwope et al. (2022b) identified an eclipsing polar through an eROSITA/SRG crossmatch with Gaia using a proprietary eRASS dataset. We showed here that the public eFEDS dataset revealed a similarly interesting object when crossmatched with ZTF.

Our findings show that the eROSITA/SRG X-ray survey is vital in supplementing ZTF for the discovery of new CVs. Making use of Gaia, we can obtain precise luminosities of the objects we find.

2.7 Conclusion

We have discovered two polars: ZTFJ0850+0443 (eclipsing, $P_{\rm orb}$ = 1.72 hr) and ZTFJ0926+0105 (non-eclipsing, $P_{\rm orb}$ = 1.47 hr), through a crossmatch of the eFEDS dataset and ZTF archival photometry. We suggest that ZTFJ0850+0443 is likely a low-field polar with magnetic field $B_{\rm WD} \lesssim 10$ MG. The accreting WD in ZTFJ0850+0443 has a mass of $M_{\rm WD} = 0.81 \pm 0.08 M_{\odot}$, and the donor is a M5.5 dwarf typical of CV donors at short orbital periods. ZTFJ0850+0443 is now one of eight polars in the literature that shows pre-eclipse emission line reversals, possibly due to absorption within the accretion curtain. Further study of these systems could help constrain the geometry of the accretion in polars near the central WD. Our second system, ZTFJ0926+0105, is not eclipsing, so we cannot place robust measurements on the WD mass. However, we identify cyclotron harmonics in the spectra of ZTFJ0926+0105 to determine a magnetic field strength of 36–42 MG.

This study is part of a larger follow-up analysis of the eFEDS/ZTF footprint. Studies such as this are useful in overcoming observational biases in previous optical-only searches for CVs, and will directly lead to accurate volume-limited studies of CVs such as that by Pala et al. (2020b). This in turn will test our knowledge of the origin of magnetic fields in WDs, compact object accretion, and binary star evolution.

2.8 Acknowledgements

ACR thanks the ZTF Variable Star Group for useful comments and discussions. ACR also thanks Axel Schwope, Paul Groot, Frank Verbunt, and Jim Fuller for insightful conversations that led to an improved final manuscript. We thank Colin Littlefield for clarifying the complete census of polars with emission-line reversals in the literature. We acknowledge the staffs of the Palomar, Keck, and Apache Point observatories for their work. We thank E. Kotze for making his Doppler tomography codes public. We are grateful to the referee for useful comments and suggestions.

This work is based on observations obtained with the Samuel Oschin Telescope 48-inch and the 60-inch Telescope at the Palomar Observatory as part of the Zwicky Transient Facility project. Major funding has been provided by the U.S National Science Foundation under Grant No. AST-1440341 and by the ZTF partner institutions: the California Institute of Technology, the Oskar Klein Centre, the Weizmann

Institute of Science, the University of Maryland, the University of Washington, Deutsches Elektronen-Synchrotron, the University of Wisconsin-Milwaukee, and the TANGO Program of the University System of Taiwan.

The ZTF forced-photometry service was funded under the Heising-Simons Foundation grant #12540303 (PI: Graham).

Some observations were made with the Apache Point 3.5m telescope, which is owned and operated be the Astrophysical Research Corporation.

This work has made use of data from the European Space Agency (ESA) mission Gaia (`https://www.cosmos.esa.int/gaia`), processed by the Gaia Data Processing and Analysis Consortium (DPAC, `https://www.cosmos.esa.int/web/gaia/dpac/consortium`). Funding for the DPAC has been provided by national institutions, in particular, the institutions participating in the Gaia Multilateral Agreement.

This work is based on data from eROSITA, the soft X-ray instrument aboard SRG, a joint Russian-German science mission supported by the Russian Space Agency (Roskosmos), in the interests of the Russian Academy of Sciences represented by its Space Research Institute (IKI), and the Deutsches Zentrum für Luft- und Raumfahrt (DLR). The SRG spacecraft was built by Lavochkin Association (NPOL) and its subcontractors, and is operated by NPOL with support from the Max Planck Institute for Extraterrestrial Physics (MPE). The development and construction of the eROSITA X-ray instrument was led by MPE, with contributions from the Dr. Karl Remeis Observatory Bamberg & ECAP (FAU Erlangen-Nuernberg), the University of Hamburg Observatory, the Leibniz Institute for Astrophysics Potsdam (AIP), and the Institute for Astronomy and Astrophysics of the University of Tübingen, with the support of DLR and the Max Planck Society. The Argelander Institute for Astronomy of the University of Bonn and the Ludwig Maximilians Universität Munich also participated in the science preparation for eROSITA.

Chapter 3

SRGEJ045359.9+622444: A 55-MIN PERIOD ECLIPSING AM CVN DISCOVERED FROM A JOINT SRG/EROSITA + ZTF SEARCH

Antonio C. Rodriguez, Ilkham Galiullin, Marat Gilfanov, Shrinivas R. Kulkarni, Irek Khamitov, Ilfan Bikmaev, Jan van Roestel, Lev Yungelson, Kareem El-Badry, Rashid Sunayev, Thomas A. Prince, Mikhail Buntov, Ilaria Caiazzo, Andrew Drake, Mark Gorbachev, Matthew J. Graham, Rustam Gumerov, Eldar Irtuganov, Russ R. Laher, Frank J. Masci, Pavel Medvedev, Josiah Purdum, Nail Sakhibullin, Alexander Sklyanov, Roger Smith, Paula Szkody, and Zachary P. Vanderbosch. SRGeJ045359.9+622444: A 55 Minute Period Eclipsing AM Canum Venaticorum Star Discovered from a Joint SRG/eROSITA + ZTF Search. *The Astrophysical Journal*, 954(1):63, September 2023. doi: 10.3847/1538-4357/ace698.

Author List

Antonio C. Rodriguez[1,*], Ilkham Galiullin[2], Marat Gilfanov[3,4], Shrinivas R. Kulkarni[1], Irek Khamitov[2,5], Ilfan Bikmaev[2,5], Jan van Roestel[6], Lev Yungelson[7], Kareem El-Badry[8,1], Rashid Sunayev[3,4], Thomas A. Prince[9], Mikhail Buntov[3], Ilaria Caiazzo[1], Andrew Drake[1], Mark Gorbachev[2], Matthew J. Graham[1], Rustam Gumerov[2,5], Eldar Irtuganov[2], Russ R. Laher[10], Frank J. Masci[10], Pavel Medvedev[3], Josiah Purdum[1], Nail Sakhibullin[2,5], Alexander Sklyanov[2], Roger Smith[1], Paula Szkody[11], Zachary P. Vanderbosch[1]

[1]Department of Astronomy, California Institute of Technology, 1200 E. California Blvd, Pasadena, CA 91125, USA

[2]Kazan Federal University, Kremlevskaya Str.18, 420008, Kazan, Russia

[3]Space Research Institute, Russian Academy of Sciences, Profsoyuznaya 84/32, 117997 Moscow, Russia

[4]Max Planck Institute for Astrophysics, Karl-Schwarzschild-Str 1, Garching b. Muenchen D-85741, Germany

[5]Academy of Sciences of Tatarstan Rep., Baumana Str. 20, Kazan 420111, Russia

[6]Anton Pannekoek Institute for Astronomy, University of Amsterdam, 1090 GE Amsterdam, The Netherlands

[7]Institute of Astronomy, Russian Academy of Sciences, 48 Pyatnitskaya str., Moscow 109017, Russia

[8]Center for Astrophysics | Harvard & Smithsonian, 60 Garden Street, Cambridge, MA 02138, USA

[9]Division of Physics, Mathematics, and Astronomy, California Institute of Technology, Pasadena, CA 91125, USA

[10]IPAC, California Institute of Technology, 1200 E. California Blvd, Pasadena, CA 91125, USA

[11]Department of Astronomy, University of Washington, 3910 15th Avenue NE, Seattle, WA 98195, USA

[*]Corresponding author: acrodrig@caltech.edu

ABSTRACT

AM CVn systems are ultra-compact binaries where a white dwarf accretes from a helium-rich degenerate or semi-degenerate donor. Some AM CVn systems will be among the loudest sources of gravitational waves for the upcoming Laser Interferometer Space Antenna (LISA), yet the formation channel of AM CVns remains uncertain. We report the study and characterisation of a new eclipsing AM CVn, SRGeJ045359.9+622444 (hereafter SRGeJ0453), discovered from a joint SRG/eROSITA and ZTF program to identify cataclysmic variables (CVs). We obtained optical photometry to confirm the eclipse of SRGeJ0453 and determine the orbital period to be $P_{\rm orb} = 55.0802 \pm 0.0003$ min. We constrain the binary parameters by modeling the high-speed photometry and radial velocity curves and find $M_{\rm donor} = 0.044 \pm 0.024 M_{\odot}$ and $R_{\rm donor} = 0.078 \pm 0.012 R_{\odot}$. The X-ray spectrum is approximated by a power-law model with an unusually flat photon index of $\Gamma \sim 1$ previously seen in magnetic CVs with SRG/eROSITA, but verifying the magnetic nature of SRGeJ0453 requires further investigation. Optical spectroscopy suggests that the donor star of SRGeJ0453 could have initially been a He star or a He white dwarf. SRGeJ0453 is the ninth eclipsing AM CVn system published to date, and its lack of optical outbursts have made it elusive in previous surveys. The discovery of SRGeJ0453 using joint X-ray and optical surveys highlights the potential for discovering similar systems in the near future.

3.1 Introduction

AM Canum Venaticorum stars (AM CVn) are ultra-compact binaries, where a white dwarf (WD) accretes material from a helium-dominated, Roche lobe-filling donor. The orbital period of these systems lies in the 5.4–67.8 minutes range (for recent reviews, see Solheim, 2010; Ramsay et al., 2018). These ultra-compact binaries are potential laboratories to study accretion processes under extreme conditions. Due to the short orbital periods of AM CVn systems, their evolution is governed by the angular momentum loss (AML) via gravitational wave (GW) radiation (Paczyński, 1967). Hellings (1996) recognized that AM CVn stars may be detected by space-based GW antennas. Indeed, many AM CVns are expected to be detected by LISA (e.g., Amaro-Seoane et al., 2023; Kupfer et al., 2024).

AM CVns, like other cataclysmic variables (henceforth, CVs), originate from initially more widely separated binaries via common envelope evolution (Paczynski, 1976). Currently, three evolutionary channels are suggested for their formation. In the Helium WD donor (He WD) channel (Paczyński, 1967), two common envelope (CE) episodes leave behind a detached system composed by a more massive carbon-oxygen WD and a less massive helium WD. This system evolves to shorter orbital periods due to GW radiation. Once it reaches $P_{\rm orb} \approx 5$ minutes, the WD donor fills its Roche lobe, and mass transfer begins. Since degenerate donors expand as they lose mass, the system evolves to longer orbital periods.

Two CE episodes in the Helium star (He star) channel (Iben and Tutukov, 1987) leave behind a carbon-oxygen WD and a low mass He-star, which may be non-degenerate or weakly degenerate (Sarkar et al., 2023b). GW radiation brings the helium star to Roche lobe overflow. Mass transfer then results in the decrease of the orbital period to a minimum of about 10 minutes, after which $P_{\rm orb}$ starts to increase. Conventionally, binaries that evolved past $P_{\rm orb}$ minimum are considered AM CVn stars.

In the evolved CV channel, a single CE episode leaves behind a carbon-oxygen WD with a main-sequence companion. In this model, initially suggested by Tutukov et al. (1985), the donor fills its Roche lobe when hydrogen in its core is almost exhausted ($X_c \lesssim 0.1$). Such an inhomogeneous star becomes completely convective only when its mass decreases to several 0.01 $M_\odot$ and, hence, AML via magnetic braking may be at work. Later, evolution is governed by GW emission. Such a system does not bounce at $P_{\rm orb} \approx 80$ minutes like "ordinary" CVs, but may evolve to $P_{\rm orb} \approx 30$ minutes, if the Verbunt and Zwaan (1981) empirical AML mechanism

is assumed (see Podsiadlowski et al., 2003). In the double-dynamo governed evolution model (Sarkar et al., 2023c), the driving force of evolution is magnetic braking due to the field generated in the boundary layer at $P_{orb} \geq 3$ hr. Evolution is also governed by GW emission and the magnetic field, owing to differential rotation between core and outer layer at $P_{orb} \leq 2$ hr. In this model, the system may reach $P_{orb} \approx$10 minutes.

AM CVns exhibit a wide range of observed phenomena, often analogous to longer periods CVs with Roche lobe-filling main-sequence donors. In the He WD channel, the system immediately after contact may be so close that no accretion disk can form, and instead, direct impact accretion takes place. The possibility of stable mass exchange depends on the efficiency of tidal synchronization (Webbink, 1984; Nelemans et al., 2001; Marsh et al., 2004; Dan et al., 2011). Furthermore, at the high mass transfer rates that occur during direct impact accretion, the matter is ionized and no thermal instabilities can occur. Thus, systems with the lowest orbital periods do not show optical outbursts and can only be discovered through their periodic optical or X-ray emission (e.g., HM Cancri; Ramsay et al., 2002).

Systems with orbital periods in the range $P_{\rm orb} \approx 20 - 50$ minutes transfer mass through an accretion disk and are subject to thermal instabilities (Cannizzo and Nelemans, 2015). This leads to the vast majority of AM CVn systems being discovered through their optical outbursts and having periods in this range (e.g., Levitan et al., 2013; van Roestel et al., 2021).

Long-period AM CVn systems ($P_{orb} \gtrsim$ 50 minutes) have such low mass transfer rates that outbursts are extremely rare. Furthermore, their low mass transfer rates make them optically dim and almost impossible to distinguish from WDs in a Hertzsrpung-Russell diagram. These systems have only been identified in the past using two methods: 1) large-scale optical spectroscopic surveys with color cuts (Carter et al., 2013) and 2) eclipsing systems in all-sky photometric surveys (van Roestel et al., 2022). Each method has inefficiencies, as the former yielded only two new systems out of 2000 candidates; the latter approach is only sensitive to eclipsing systems and yielded five systems after performing a computationally expensive Box Least Squares (Kovács et al., 2002) search of 200,000 objects. Theoretical models suggest that the Galaxy may harbor up to $\simeq 3.4 \times 10^7$ AM CVn stars (e.g.,, Nelemans et al., 2004a), most of which should have long periods. Results of the above-mentioned surveys may suggest that the models overpredict the number of Galactic AM CVns and they are really rare objects or that our current methods do

not allow to detect majority of them.

All-sky surveys provide unique possibilities to probe the Galactic population of compact object binaries. We are in the age of precise all-sky astrometry with Gaia and thousands of epochs of Northern sky photometric coverage with the Zwicky Transient Facility (ZTF) (Gaia Collaboration et al., 2016; Bellm et al., 2019b). While these surveys are useful on their own, they contain billions of targets. Such a large dataset is intractable without initial pre-selection, such as X-ray counterparts. CVs and AM CVns among them were discovered in the past through the all-sky Roentgensatellit X-ray survey (ROSAT; Truemper, 1982; Voges et al., 1999a; Verbunt et al., 1997; Ramsay et al., 2002). The ongoing eROSITA telescope aboard the Spektr-RG mission (SRG; Sunyaev et al., 2021; Predehl et al., 2021b) goes ∼15 times deeper than ROSAT, with improved localization of X-ray sources, and has already led to the discovery of new CVs (e.g., Schwope et al., 2022a; Bikmaev et al., 2022; Rodriguez et al., 2023d). Some CVs were discovered using the Mikhail Pavlinsky ART-XC telescope (Pavlinsky et al., 2021) on board of SRG observatory (e.g., Zaznobin et al., 2022).

SRGeJ0453 is one of the sources discovered from a joint program to search for Galactic CVs from a cross-match of SRG/eROSITA and ZTF data in a 1200 deg^2 patch of the sky. The parameters and procedures of this CV search program will be described in full in future publications. Its first results of the discovery and optical identification of several new Galactic CVs will be presented in upcoming work (Galiullin et al. in prep). At the time of writing, no AM CVn system has been published using SRG/eROSITA data.

In this paper, we present the study and characterisation of the new long-period, eclipsing AM CVn, SRGeJ0453. In Section 8.2, we present X-ray and optical observations with data reduction. In Section 3.3, we outline the discovery and the optical and X-ray properties of SRGeJ0453. In Section 8.4, we discuss our results, the binary parameters, the possible evolutionary channel of the donor, and compare it to the known population of AM CVns in the Hertzsprung-Russell diagram. We summarize our results in Section 3.5.

3.2 Observations and data reduction

SRG/eROSITA

On July 13, 2019, the Spektr–Roentgen–Gamma orbital observatory was successfully launched from the Baikonur Cosmodrome (Sunyaev et al., 2021; Predehl et al.,

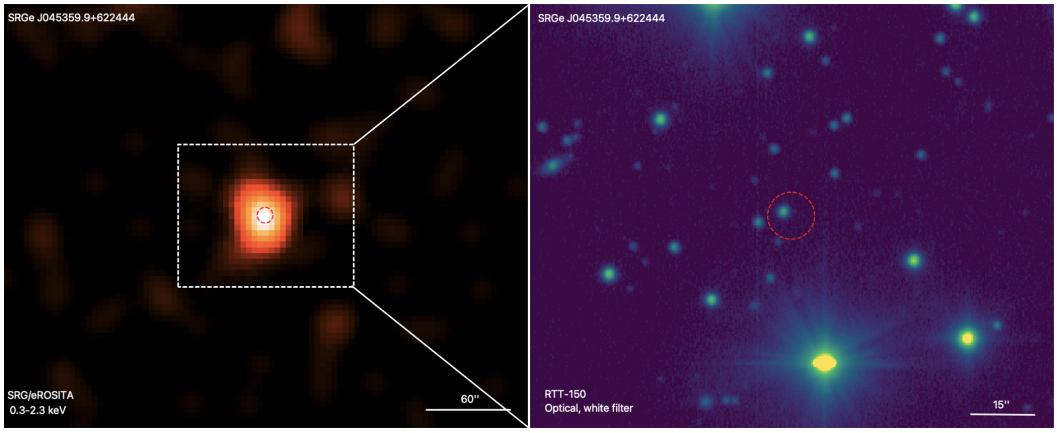

Figure 3.1: Left: False-colour X-ray image of SRGeJ0453 in the 0.3–2.3 keV energy band from combined data of four all-sky surveys of SRG/eROSITA. The image was smoothed with a 15 Gaussian kernel. The white box shows the field of view of the optical image on the right. Right: Optical image around SRGeJ0453 based on RTT-150 data with a white filter. The red circle with a radius of 5.6 (98% localization error, R98) is centred at the X-ray position of SRGeJ0453.

2021b). SRG observatory carries two X-ray telescopes with grazing incidence optics: the ART-XC telescope, named after M. N. Pavlinsky (Pavlinsky et al., 2021), its operating range is 4–30 keV, and the eROSITA telescope, operating in the 0.2–8 keV energy band (Predehl et al., 2021b). We use all data collected by SRG/eROSITA in the survey mode between December 2019 and February 2022, which comprised $\approx$ 4.4 all-sky surveys. The initial data processing and calibration of the eROSITA data were carried out at the Space Research Institute of the Russian Academy of Sciences (IKI RAS) using the software developed in the eROSITA X-ray source catalogue science working group of the RU consortium with the use of the calibration tasks, and calibration database of the eSASS package (eROSITA Science Analysis Software) developed at the Max Planck Institute of Extraterrestrial Physics (MPE), Garching, Germany. The data were preprocessed using the results of ground pre-flight calibrations and flight calibration observations performed in October-November 2019 and throughout 2020–2022. The data from all sky surveys were combined to increase the sensitivity of the final source catalog. Figure 3.1 shows the X-ray image of the SRGeJ0453 obtained from combined data from four all-sky surveys of the SRG/eROSITA and an optical image of the same sky region from RTT-150.

To extract the X-ray spectrum of the source, we used a circle with a radius of 40,

and an annulus with inner and outer radii of 120 and 300, respectively, for the background region. The X-ray spectrum was analysed using XSPEC v.12 software (Arnaud, 1996). Due to the low number of source spectrum counts, we approximated it using the C-statistics (Cash, 1979). The spectrum was grouped to have at least three counts per spectral channels[1].

ZTF

The Zwicky Transient Facility (ZTF) is a photometric survey that uses a wide 47 deg^2 field-of-view camera mounted on the Samuel Oschin 48-inch telescope at Palomar Observatory with g, r, and i filters (Bellm et al., 2019b; Graham et al., 2019; Dekany et al., 2020; Masci et al., 2019). In its first year of operations, ZTF carried out a public nightly Galactic Plane Survey in g-band and r-band (Bellm et al., 2019a; Kupfer et al., 2021). This survey was in addition to the Northern Sky Survey which operated on a 3 day cadence (Bellm et al., 2019b). Since entering Phase II, the public Northern Sky Survey is now at a 2-day cadence. The pixel size of the ZTF camera is 1 and the median delivered image quality is 2.0 at FWHM.

We use ZTF forced photometry taken through February 1, 2023, processed by IPAC at Caltech[2]. Light curves have a photometric precision of 0.015–0.02^m at 14^m down to a precision of 0.1–0.2^m for the faintest objects at 20–21^m. While both the default photometry and forced photometry from ZTF use PSF-fit photometry, the forced photometry calculates the flux of the object on difference images by *forcing the location of the PSF to remain fixed* according to the ZTF absolute astrometric reference. This allows one to obtain flux estimates below the detection threshold and therefore probe deeper than the standard photometry.

We present archival ZTF data (SNR > 5; no upper limits shown) for SRGeJ0453 in Figure 3.2. The lack of optical points is due to the object consistently falling on the edge of a ZTF camera chip. This coincidence led to poor quality data taken after JD 2459000 and a subsequent deficiency in observing epochs.

RTT-150 photometry

We observed SRGeJ0453 with the 1.5-meter Russian-Turkish Telescope (RTT-150) as part of the optical follow-up program of SRG/eROSITA sources. The observations were performed using the TFOSC instrument ANDOR CCD camera, model iKon-L

[1] See note for work in XSPEC: `https://heasarc.gsfc.nasa.gov/xanadu/xspec/manual/XSappendixStatistics.html`

[2] `https://irsa.ipac.caltech.edu/data/ZTF/docs/ztf_forced_photometry.pdf`

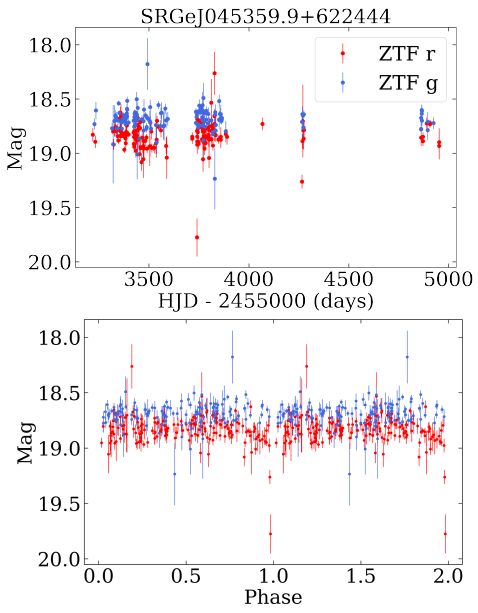

Figure 3.2: ZTF light curves of SRGeJ0453 on g, r filters: long-term (top), and folded at the 55.08 minutes orbital period (bottom). No significant outbursts are seen over the ≈5 yr-long baseline.

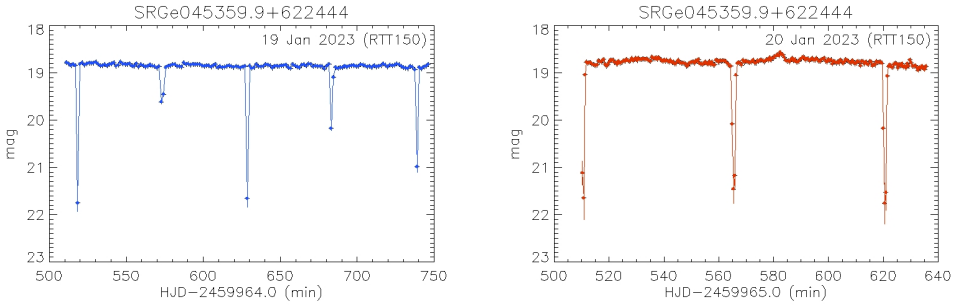

Figure 3.3: Optical light curve of SRGeJ0453 observed by RTT-150, where axes are G-magnitude versus the time from the start of the observations in units of minutes (*top* – the first; and *bottom* – the second nights of observations).

936 and BEX2-DD-9ZQ (a 2048 × 2048 pixels) chip. The resolution element is 0.326 at 1 × 1 binning. Two sets of observations were carried out on January 19 and 20, 2023. The weather was clear, and the average seeing was 1.5–2.0. All images were pre-processed using ATROLIB/IDL packages and the standard method: bias subtracted and flat-field corrected. In addition, astrometric alignment was performed for all images and forced photometry.

A total of 160 images (with 60 seconds of exposure time and 28 seconds of readout

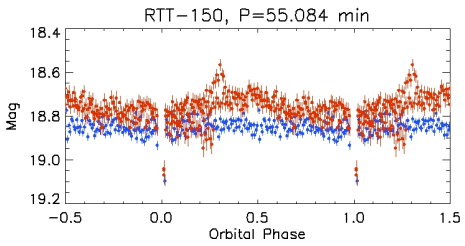

Figure 3.4: Phase-folded light curve of RTT-150 data. *Blue circles* corresponds to January 19, 2023 data, *red circles* – January 20, 2023 data. The light curve shows low amplitude ($\approx 0.1 - 0.3^m$) flickering. Only the upper part of the light curve is shown out of eclipses.

time) were obtained on January 19 with a sub-frame size of 2048 x 600 pixels and binning 1 x 1. The total duration of observations was 245 minutes, and the time resolution was 88 seconds on the first night of observations. Five minima (eclipses) were detected with different depths of minima. Two possible periods were found (55 or 110 minutes) by using the first night's light curve. We found that eclipses were very narrow ($\approx$ 60 seconds); therefore, different depths of minima were produced due to insufficient time resolution during the first night observations. On the second night (January 20, 2023), 258 images with 20 seconds of exposure time and 9 seconds of readout time were obtained with the sub-frame size 1024 x 200 pixels (binning 2×2). The total duration of observations was 135 minutes, and the time resolution was 29 seconds. The three minima (eclipses) were detected with the same depths of minima, confirming 55 and excluding the 110 minutes period.

Having eight minima within both nights' light curves, we searched for an accurate period by using a combined approach (for more details, see Appendix 3.7). We found the period to be 55.084 ± 0.015 minutes. The optical light curves of SRGeJ0453 obtained by RTT-150 are shown in Figures 3.3 (long term), and Figure 3.4 (folded at the orbital period).

LRIS spectroscopy

We obtained an identification spectrum of SRGeJ0453 on the Keck I telescope using the Low-Resolution Imaging Spectrometer (LRIS; Oke et al., 1995b) on January 15, 2023 (UT). We used the 600/4000 grism on the blue side with 2x2 binning (spatial, spectral), and the 600/7500 grating on the red side with 2x1 binning. We used a 1.0 slit, and the seeing during the portion of the night was approximately 0.7, leading to minimal slit losses. Phase-resolved spectroscopy over the entire orbit was

acquired on March 25, 2023 (UT) using LRIS. In that case, the 600/4000 grism (2x2 binning) was used on the blue side, and the 400/8500 grating on the red side (2x1 binning). A 1.0 slit was used, and the seeing during the portion of the night was approximately 0.9. Wavelength coverage and resolution are shown in the timeline of all observations in Table 8.3.

On the night of March 25, 2023, observations were affected by telescope vignetting, resulting in a loss of throughput. In early January 2023, the Keck I bottom shutter drive sustained damage, forcing it to remain stationary at its park position of 24 degrees elevation. In this condition, all observations taken below an elevation of 38 degrees are affected by vignetting. That night, all 6 exposures were forced to be taken at an elevation below 30 degrees (corresponding to airmass $\approx$ 1.9) as the object was quickly setting.

All Keck I/LRIS data were reduced with `lpipe`, an IDL-based pipeline optimized for LRIS long slit spectroscopy and imaging (Perley, 2019). All data were flat fielded and sky-subtracted using standard techniques. Internal arc lamps were used for the wavelength calibration and a standard star for overall flux calibration.

CHIMERA high-speed photometry

We acquired high-speed photometry in Sloan r and g bands using the Caltech HIgh-speed Multi-color camERA (CHIMERA; Harding et al., 2016) on three occasions. In all cases, CHIMERA r-and g-band data were both acquired at a 10 second cadence simultaneously over two orbital periods. We are clearly able to identify eclipses in all CHIMERA data sets, but it may be difficult to interpret out of eclipse variability due to abnormally poor seeing on every night: 3 on January 23, 2023 (UT), 4 on January 27, 2023 (UT), and 3 on February 17, 2023 (UT). Data from the night of January 27, 2023 (UT) was most strongly affected by poor seeing, and the overall flux level surrounding the eclipse was affected. In all the light curve analysis, we only use data from January 23, 2023 (UT) and February 17, 2023 (UT). We show all light curves in Figure 3.5 and summarize this information in Table 8.3.

All CHIMERA data were bias-subtracted and flat-fielded using standard techniques in the `PyCHIMERA` pipeline[3]. The ULTRACAM pipeline was used to do aperture photometry (Dhillon et al., 2007a). A differential light curve was created by dividing the counts of the target by those of a standard star. We experimented with different standard stars to ensure we were not affected by standard star variability.

[3] `https://github.com/caltech-chimera/PyChimera`

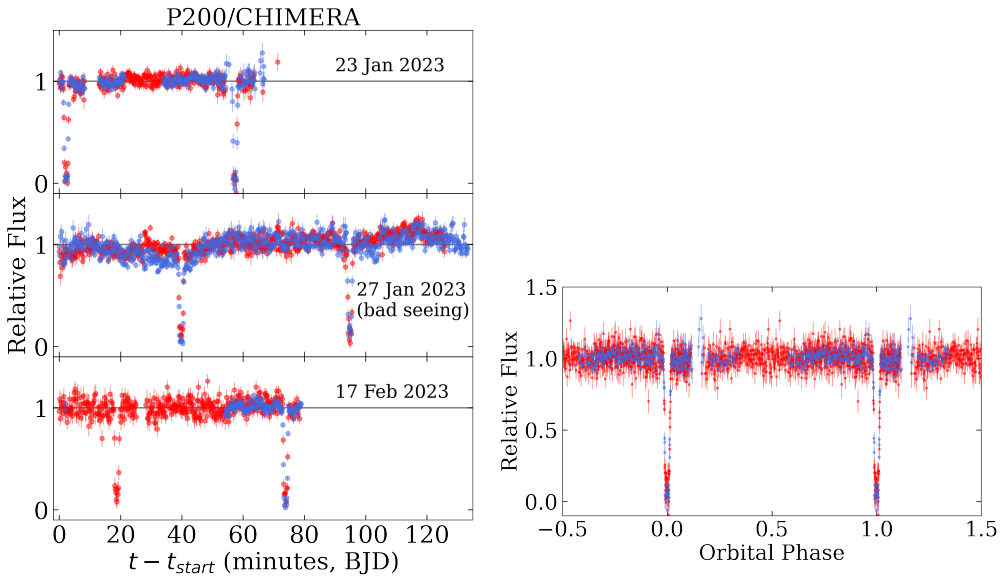

Figure 3.5: CHIMERA *r* (red) and *g* (blue) 10-sec cadence photometry reveal deep eclipses. *Upper three panels*: The entire observation on each occasion. Gaps are due to large error bars in the data where cloud cover or highly variable seeing prevented a good extraction of the data. *Bottom panel*: Data from January 23 and February 17, 2023 are folded over the 55.08 minutes orbital period.

Table 3.1: Data Acquired for SRGeJ0453

Data Type	**Date (UT)**	**Instrument**	**Specifications**	**Finding**
Identification Spectrum	15 Jan. 2023	Keck I/LRIS	Blue: 3140–5640 Å, $\Delta\lambda$ = 1.1 Å, 1×900s exp. Red: 5530–8830 Å, $\Delta\lambda$ = 0.80 Å, 1×900s exp.	Helium emission lines over a blue continuum; central absorption suggesting high inclination
Photometry, no filter	19, 20 Jan. 2023	RTT-150/TFOSC	60s and 20s exp. for 4.1 and 2.2 hrs	Photometry revealed deep (3 mag) eclipse and 55.084 minute period
High-cadence *r* and *g* band Photometry	23, 27 Jan. 2023 17 Feb. 2023	Hale Telescope/CHIMERA	10s exp. for 2 hr	High-cadence photometry at simultaneous orbital phases
Multi-phase spectra	25 Mar. 2023	Keck I/LRIS	Blue: 3240–5640 Å, $\Delta\lambda$ = 2.0 Å, 6×600s exp. Red: 5530–10,200 Å, $\Delta\lambda$ = 1.2 Å, 6×600s exp.	Doppler tomograms reveal bright spots and "central spike" in He II 4686

3.3 Discovery and Results

SRGeJ0453 is one of the objects identified as a CV candidate in a cross-match of a 1200 deg^2 patch of sky of SRG/eROSITA X-ray data with Gaia proper motion data and the optical ZTF database. SRGeJ0453 was called to our attention by its proper motion statistically significantly detected by Gaia, high ratio of X-ray flux to optical flux, $F_X/F_{opt} \approx 0.12$, and placement in the Gaia color-magnitude diagram near the WD region. This is a pilot study, and more targets identified from this program will be presented in future work (Galiullin et al. in prep.).

Period Determination

We detected eight deep eclipses in two observing nights with RTT-150, determining the system's orbital period as 55.084 ± 0.015 minutes (see Section 3.2). The light curve shows low amplitude ($\approx (0.1 - 0.3)^m$) flickering, possibly caused by an accretion disk. During eclipses, the light curve shows deep dips ($\approx 3^m$) separated by ≈ 55.08 minutes (see Figures 3.3 and 3.4).

We ran the Box Least Squares (BLS) algorithm (Kovács et al., 2002) on the ZTF data to find the orbital period of SRGeJ0453. We used the exposure time as an oversampling factor when creating our frequency grid to search for possible periods and durations of the eclipse. We found the best-fit period of 55.1±0.5 minutes using the ZTF forced photometry data, where the uncertainty is determined by exposure time. The ZTF optical light curves of SRGeJ0453 folded with a best-fit period are shown in Figure 3.2.

To clarify and better constrain the period of SRGeJ0453, we ran the BLS algorithm on all CHIMERA light curves, recovering a period of 55.08±0.08 minutes. Starting with the 55.08 minutes period determined from a single CHIMERA observation, we assume there is no significant period derivative and calculate precisely 652 orbits to transpire between the first (January 23, 2023) and last eclipses (February 17, 2023) measured with CHIMERA. By matching the observed mid-eclipse time of all CHIMERA eclipses to the expected mid-eclipse time within 10 seconds (exposure time of individual CHIMERA exposure), we can obtain a much more precise period measurement. Using this method, we obtain a period estimate of $P_{\rm orb} = 55.0802 \pm 0.0003$ minutes. We present all good quality CHIMERA data folded on this period in Figure 3.5.

All periods estimated from different optical data agree with each other within their respective error bars. In all analysis, we adopted the orbital period based

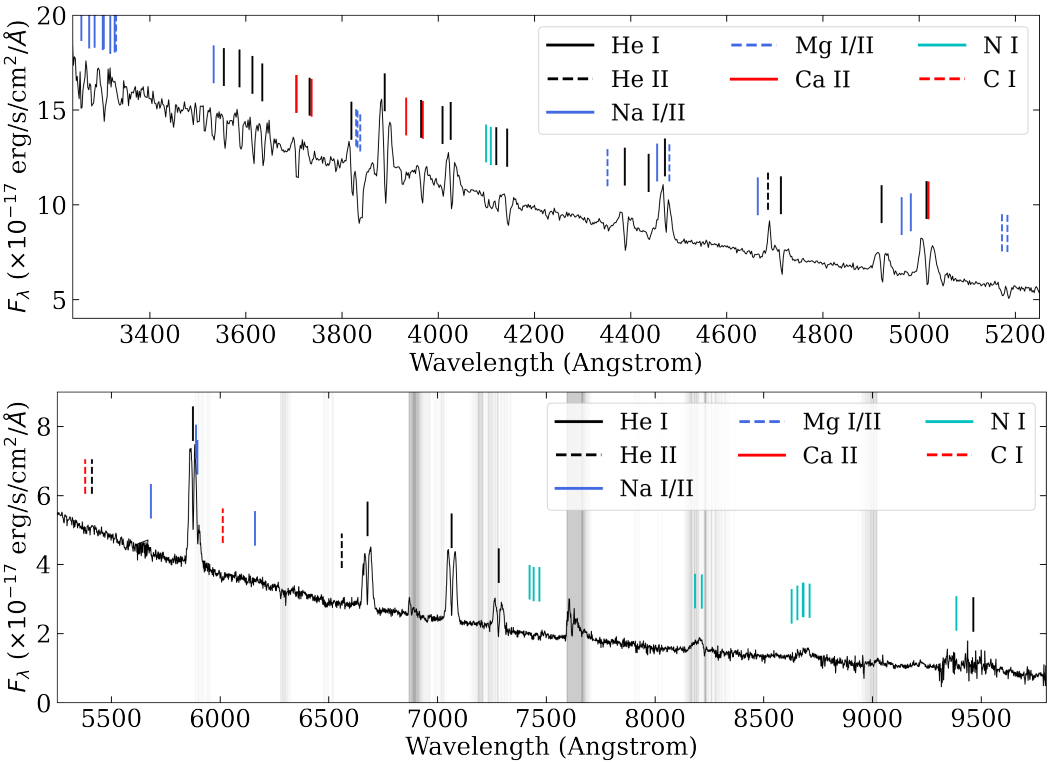

Figure 3.6: LRIS phase-averaged spectrum of SRGeJ0453. The characteristic features of an AM CVn are clear: helium emission lines imposed over a blue continuum. Metals such as Mg, Ca, N, and Na are present. Grey lines are locations where there are telluric features from the Keck Telluric Line List.

on CHIMERA and RTT-150 light curves $P_{\rm orb} \approx 55.08$ minutes, and ephemeris t_0(BJD)= 2459967.726794129(1).

Optical Spectral Features

We present the optical spectrum of SRGeJ0453 in Figure 3.6. We show the average of the first five spectra taken on March 25, 2023 with LRIS, which cover an entire orbit (with approximately 10 percent gap due to read out time). The phase coverage of the sixth spectrum overlaps with that of the first, and was taken near the limiting elevation of 24 degrees, so it is omitted from all analysis.

The archetypal features of an AM CVn system are clear: a blue continuum with He lines (in emission and/or absorption) and an absence of H lines. There is no Balmer jump (or inverse thereof, as commonly present in CVs) in the spectrum. All He I emission lines redward of 3800 Å are clearly doubled, originating from the helium rich accretion disk around the WD. All He I emission lines show a narrow central absorption commonly seen in nearly edge-on (high inclination) AM CVns. This

Table 3.2: Equivalent widths (EWs) of selected lines

Line (Å)	LRIS 25 Mar. EW (Å)
Emission features	
He I 4387.9	-1.68 ± 0.02
He I 4921.9	-3.0 ± 0.1
He I 5876.5	-28.7 ± 0.3
He I 6678.2	-24.5 ± 0.1
He I 7065.2	-34.3 ± 0.2
He I 7281.4	-11.6 ± 0.5
He II 4685.7	-1.7 ± 0.1
Absorption features	
C I 6013.2	0.2 ± 0.2
N I 7442.3	0.8 ± 0.2
N I 7468.3	0.5 ± 0.1
Na II 3304.96	1.35 ± 0.03
Mg I 5183.6	1.3 ± 0.2
Ca II 3933.7	0.6 ± 0.1

phenomenon has been explained by WD light passing through an accretion disk that is optically thick at central He I wavelengths, but optically thin in the wings.

We see a single-peaked emission line of He II 4685.7 Å, which we discuss in detail in Section 3.4. Table 3.2 shows equivalent widths (EWs) for prominent lines identified in the optical spectrum of SRGeJ0453, which we calculate from the averaged spectrum.

Metal lines are also present in the spectrum, which can tell us about the formation channel of this system. We present the most prominent elements below:

em C: There is at best marginal (1σ) evidence for C I 6013.2 Å in absorption in the phase-averaged spectrum of SRGeJ0453. The dip in the spectrum at that position is around 5 percent below the continuum, which is only marginally above the noise level. Therefore, we do not claim this as a significant detection of carbon in SRGeJ0453. No other C I or C II lines are present. em N: We see N I in both emission (8629.2, 8655.8, 8680.28, 8683.4, 8711.7 Å) and absorption (7442.3, 7468.3 Å). The complex around 8184.9, 8188.0, and 8216.30 Å are all near telluric features, making their clear identification difficult. em O: No O I or O II lines are present. em Other metals: We detect Na I/II lines, Mg I/II, and Ca II lines, all in absorption.

With a confident detection of various lines of nitrogen, we are able to place constraints on the formation channel of SRGeJ0453. The lack of oxygen and the high nitrogen to carbon ratio favors either the He star or He WD formation channel, and makes the evolved CV channel unlikely. A detailed discussion and connection to formation channel is in Section 3.4.

Distance, Extinction, and N_H

The only Gaia source associated with SRGeJ0453 within 5.6 search radius (98% localization error, R98) has an ID 4778293709721120000 (Gaia EDR3) and celestial coordinates of RA=$04^h54^m00^s.1$ and DEC=+$6224'45''.6$. The distance calculated using Gaia EDR3 parallaxes is $d = 239^{+11}_{-8}$ pc (Bailer-Jones et al., 2021b). We adopt an extinction value of $E(B-V) = 0.01 \pm 0.004$ using the Bayestar19 dust map (Green et al., 2019b). We use the extinction law of Cardelli et al. (1989) and a value of $R_V = 3.1$ to calculate the flux correction from UV to IR wavelengths. We can now calculate the intervening hydrogen column, $N_H = (6.8 \pm 2.8) \times 10^{19}\mathrm{cm}^{-2}$, using the relation from Güver and Özel (2009a).

SED Modeling and WD Mass

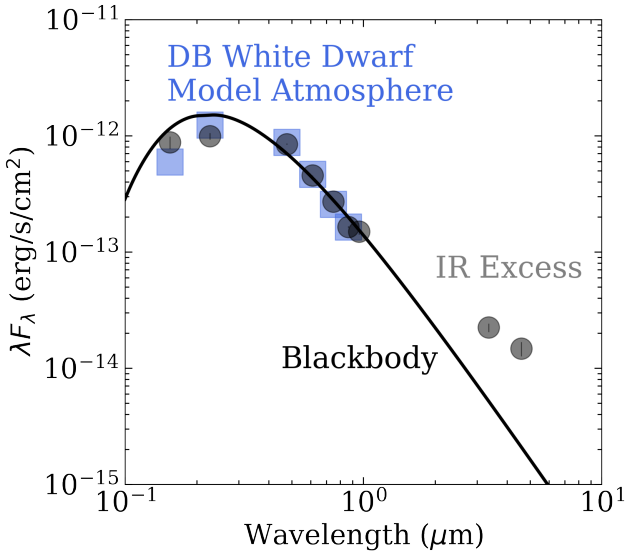

Figure 3.7: The SED of SRGeJ0453 is well fit by a $T_{\rm eff} = 16,570$ K black body (solid, black line) or $T_{\rm eff} = 12,210$ K DB WD model atmosphere (blue squares) at UV/optical wavelengths. There is an IR contribution from the donor and/or accretion disk.

We construct the SED of SRGeJ0453 using photometry from GALEX (Martin et al., 2005), PanSTARRS (Chambers et al., 2016), and WISE (Wright et al., 2010),

compiled from the VizieR[4] and Barbara A. Mikulski Archive for Space Telescopes (MAST)[5] databases. For the WISE data, we make use of the CatWISE (Eisenhardt et al., 2020) catalog, which accounts for proper motions and uses stacked WISE images to go deeper than the AllWISE catalog (in which SRGeJ0453 is not present).

We model the SED, excluding CatWISE data, with a black body corresponding to the accreting WD. Since SRGeJ0453 is a long-period AM CVn ($P_{\rm orb} \gtrsim 50$ minutes), we assume the accretion disk contribution in the optical wavelengths is negligible due to the low accretion rate. We do not model the bright spot since its contribution is also negligible at optical wavelengths (though this may not be true in the UV). Two other long-period AM CVn systems ZTFJ0220+21 ($P_{\rm orb} = 53.5$ minutes) and ZTFJ0003+14 ($P_{\rm orb} = 55.5$ minutes) were found to have the disk and bright spot contribute to the continuum < 8 percent at optical wavelengths (g and r bands) (van Roestel et al., 2022). The light curve of SRGeJ0453 similarly does not show any evidence of a significant disk or bright spot contribution, justifying our approximation.

We perform a Bayesian analysis using the Markov Chain Monte Carlo (MCMC) technique to sample the posterior distribution of the WD radius, WD effective temperature, and extinction, A_V. We use an affine invariant sampler as implemented in `emcee` (Foreman-Mackey et al., 2013). We assume a Gaussian likelihood and set a uniform prior on $R_{\rm WD}$ $(0.005 - 0.5)R_\odot$, a uniform prior $T_{\rm eff}$ (8,000 – 30,000) K, and a Gaussian prior on the extinction ($E(B-V) = 0.010 \pm 0.004$). We run the sampler for 4000 steps, taking half as the burn-in period. The χ^2/dof from the black body approximation is 14.67/5. We determine the WD radius to be (with errors from the 16th and 84th percentiles): $R_{\rm WD} = 7.39^{+0.09}_{-0.08} \times 10^{-3} R_\odot$. From this radius, we determine the mass to be $M_{\rm WD} = 0.854^{+0.04}_{-0.05} M_\odot$, following the WD mass-radius relation from Shipman (1972). We chose this WD relation because the accretion rate is so low that it is unlikely to inflate the WD of order more than a few percent (see Section 6.2). We determine the WD effective temperature to be $T_{\rm eff} = 16,570^{+240}_{-250}$ K. In Figure 7.10, we present the SED of SRGeJ0453 with the WD model resulting from the MCMC analysis. There is clear evidence of an IR excess in WISE W1 and W2 bands. This has been seen in other AM CVns and attributed to the donor and/or accretion disk (e.g., van Roestel et al., 2022).

In addition to the black body modeling, we also modeled the UV/optical photometry

[4] `https://vizier.cds.unistra.fr/viz-bin/VizieR`
[5] `https://archive.stsci.edu/`

of SRGeJ0453 using DB (pure helium) WD atmosphere models. We used the `WDPhotTools`[6] package (Lam et al., 2022), which uses the DB model atmospheres from Bergeron et al. (2011). We leave $T_{\rm eff}$ and $M_{\rm WD}$ as free parameters in this code, which uses the `emcee` MCMC sampler to explore the parameter space and generate the posterior distribution. The χ^2/dof from the DB atmosphere model approximation is 14.78/5. Using this approach, we determine the WD temperature to be $T_{\rm eff} = 12,200^{+420}_{-400}$ K. The WD mass is $M_{\rm WD} = 0.60^{+0.05}_{-0.05} M_{\odot}$, and also computed is the surface gravity: $\log g = 8.02^{+0.08}_{-0.08}$. With these two values, the WD radius is $R_{\rm WD} = 1.2^{+0.1}_{-0.1} \times 10^{-2} R_{\odot}$ (not accounting for any inflation due to accretion heating). Consequently, any parameters computed in this paper that depend on $M_{\rm WD}$ could be scaled by a factor of 0.71 to account for the difference between the black body and DB atmosphere models.

However, we emphasize that DB model atmospheres still constitute an approximation. Various metals (N, Na, Mg, Ca) are detected in the optical spectrum of SRGeJ0453, all of which have strong resonance lines in the UV that are not modeled in the pure helium atmospheres (Bergeron et al., 2011). We note that both the black body and DB atmosphere models lead to a sub-optimal reduced chi-squared of about 3. This could be explained by neither model actually being a good approximation to the true WD atmosphere in this system. Additionally, it is unclear if there is any contribution from the hot spot or boundary layer in the UV, which DB model atmospheres cannot reproduce. Rather than add the complications associated with assuming a DB model atmosphere, we proceed with all calculations using the black body estimates.

X-ray Properties

The X-ray spectrum of SRGeJ0453 is shown in Figure 7.8. The spectrum was obtained by combining four SRG/eROSITA all-sky survey data. We approximated the spectrum of the sources using two models: the power-law model (powerlaw in XSPEC) and the optically thin thermal plasma model (mekal in XSPEC) with solar abundance. To take into account interstellar absorption, we used the Tubingen-Boulder ISM absorption model (tbabs model in XSPEC, Wilms et al. 2000). We used cflux task in XSPEC to compute the unabsorbed fluxes. The results of the approximation of the X-ray spectrum of SRGeJ0453 are shown in Table 3.3. The hydrogen column densities estimated from the approximation of the X-ray spectrum are low and agree with the Galactic absorption column density in the direction of

[6] `https://github.com/cylammarco/WDPhotTools`

Table 3.3: Results of approximation of X-ray spectrum of SRGeJ0453 by different models.

Model: $tbabs \times (powerlaw)$	
Parameters:	
$N_H(\times 10^{22}\mathrm{cm}^2)$	0.03
Γ	$0.63^{+0.27}_{-0.25}$
$C-stat$/(d.o.f)	11.5/16
Model: $tbabs \times (mekal)$	
Parameters:	
$N_H(\times 10^{22}\mathrm{cm}^2)$	$0.19^{+0.17}_{-0.11}$
kT_{mekal}(keV)	3.2
$C-stat$/(d.o.f)	13.4/16
$F_{0.3-2.3\ keV}$ $(\times 10^{-14}\ erg\ cm^{-2}\ s^{-1})$	9.0 ± 0.6
$L_{0.3-2.3\ keV}$ $(\times 10^{29}\ erg\ s^{-1})$	6.2 ± 0.4

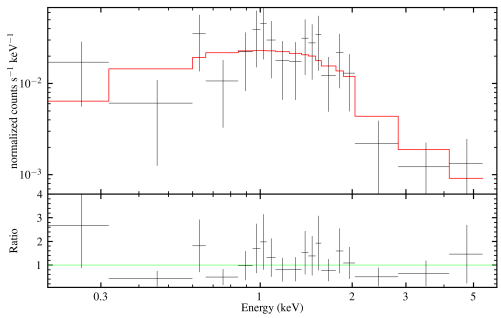

Figure 3.8: The X-ray spectrum of SRGeJ0453 over four SRG/eROSITA all-sky surveys data (top panel). A red line shows the best-fit power-law model from Table 3.3. The bottom panel shows the residuals (ratio of the data divided by the model) in each energy channel.

SRGeJ0453. Only a lower limit of the palsma temperature 3.2 keV (1σ confidence) is estimated from the X-ray spectroscopy.

The absorption-corrected X-ray flux of SRGeJ0453 in the 0.3–2.3 keV energy band is $(9.0\pm0.6)\times10^{-14}$ erg s^{-1}cm^{-2}, computed from the power-law model approximation. Given the well-constrained distance from *Gaia*, the X-ray luminosity is $(6.2\pm0.4)\times 10^{29}$ erg s^{-1}.

Assuming half of the gravitational potential energy is radiated away in the boundary layer, as in non-magnetic CVs, the accretion luminosity is:

$$L_{\rm acc} = \frac{\eta}{2}\frac{GM_{\rm WD}\dot{M}}{R_{\rm WD}} \tag{3.1}$$

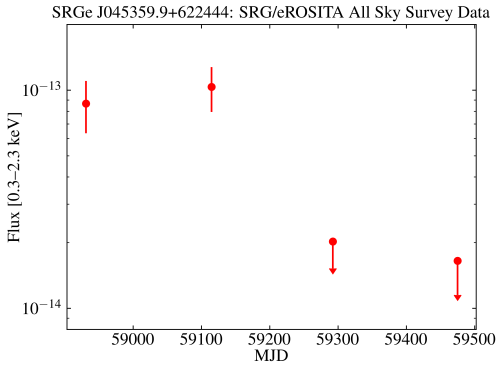

Figure 3.9: The 0.3–2.3 keV X-ray light curve of SRGeJ0453 during four SRG/eROSITA all-sky surveys. Arrows show 3σ upper limits for X-ray fluxes.

where $M_{\rm WD}$ and $R_{\rm WD}$ are the mass and radius of the WD from the results of SED modelling (see Section 3.3), and η is the radiative efficiency of accretion ($\eta = 1$). We assumed the canonical bremsstrahlung model to compute the bolometric correction (BC) factor for the X-ray luminosity in the 0.3–2.3 keV energy band. For the fixed temperature in the 2–50 keV range, we compute the BC factor in the $\approx 1.8 - 11.1$ range. Taking this into account, we obtain an accretion rate of $\dot{M} \approx (2 - 10) \times 10^{-12}\ M_{\odot}\ {\rm yr}^{-1}$, where uncertainties are caused by the BC factor.

Figure 3.9 shows the X-ray light curve of SRGeJ0453 within four sky surveys of SRG/eROSITA. We see the variability in X-rays, where the 3σ lower limit for the ratio between maximum and minimum fluxes is 6.3. X-ray variability could correlate with the system's orbital period, but this needs to be investigated by further X-ray and optical follow-up.

We note that the approximation of the X-ray spectrum of SRGeJ0453 by the power-law model gives a photon index of $\Gamma \sim 1$. Previous studies of a dozen classical novae in the Galaxy observed by SRG/eROSITA in quiescence revealed a dichotomy between their photon indexes (e.g.,, Galiullin and Gilfanov, 2021). X-ray spectra of several intermediate polars (magnetic CVs believed to harbor WDs with magnetic field strengths $B \approx 1 - 10$ MG Mukai, 2017) and candidate IPs are approximated by photon index $\Gamma \sim 1$. Non-magnetic systems are approximated by photon index $\Gamma \sim 2$. The hard spectrum of SRGeJ0453 may suggest that it harbors a magnetized WD, however, any meaningful conclusion would require further observations, including polarimetric studies.

Table 3.4: Radial Velocity Measurements of He Lines

Line (Å)	γ (km/s)	K_x (km/s)	K_y (km/s)
He I 6678.2	11 ± 4	29 ± 5	39 ± 7
He I 7065.2	17 ± 3	-29 ± 4	58 ± 5
He II 4685.7[7]	192 ± 5	-5 ± 8	7 ± 6

Phase-Resolved Spectroscopy

Systemic Velocity

We first constrain the system radial velocity (RV) by identifying He I disk emission lines. We choose several lines that are not blended with other elements (e.g., this eliminates He I 5875.6 Å due a strong blend with Na I). We also exclude lines that are affected by telluric features or show deep central absorption (see Appendix 3.8). The remaining He I lines that fit these criteria are centered at 6678.2 and 7065.2 Å. We fit two Gaussian profiles to each of the two peaks of the He I emission lines. We then produce RV curves using the center of each of the two Gaussians. We only analyze the middle four orbital phases, since spectra centered at orbital phases between 0.9–1.1 are affected by the donor eclipsing the disk. Spectra centered at these orbital phases, unless centered perfectly at conjunction, will show the donor star preferentially eclipsing a component of the disk that is blue/redshifted (see Appendix 3.9).

We assume a circular orbit with a RV equation of the form:

$$\mathrm{RV} = \gamma + K_x \sin(2\pi\phi) + K_y \cos(2\pi\phi), \tag{3.2}$$

where K_x and K_y are the two components of the RV, and γ is systemic velocity. We use an MCMC technique to sample the posterior distribution, assuming a uniform prior on γ, K_x, and K_y (all ranging between –300 and +300 km/s), and a Gaussian likelihood. We take the standard error of the mean (of the fit to the Gaussians) as the error of each RV. The median value of all parameters and error (16th, 84th quartiles) are in Table 3.4. The weighted average of the systemic velocity of both He I lines represents the systemic velocity of the binary system as whole: $\gamma_{\mathrm{binary}} = 14 \pm 5$ km/s.

We also present the RV results for the He II 4685.7 Å line in Table 3.4, which we discuss in more detail in Section 3.4.

Doppler Tomograms

Doppler tomography converts phase-resolved spectroscopy into a plot of observed RV and line strength as a function of orbital phase. In other words, spectral line information is converted from time and wavelength space to phase and velocity space. In this process, Doppler tomograms disentangle the contribution of the various CV components (e.g., accretion disk, accretion hot spot, donor star) to a given spectral line; see Marsh (2005) for a review of the method of Doppler tomography. We use the `doptomog`[8] code developed by Kotze et al. (2015b) to construct Doppler tomograms shown here.

We use 5 Keck LRIS spectra from a single orbit to create Doppler tomograms for the He I 5876.5 Å , 6678.2 Å and 7065.2 Å lines. We use the systemic RV offset calculated after performing a double Gaussian fit to the emission line throughout the entire orbit (see Table 3.4). However, there is strong blending present in He I 5876.5 Å and there could be an artifact in one of the spectra of 6678.2 Å so we discuss those Doppler tomograms in Appendix 3.10. The He I 7065.2 Å Doppler tomograms, along with trailed spectra, are shown in Figure 3.10. We present a Doppler tomogram for the other He I lines in Appendix 3.10.

The He I 7065.2 Doppler tomogram shows that line traces the accretion disk, and a prominent bright spot located approximately 45 degrees ahead of the donor star (second quadrant of the plot). We do not see a significant second bright spot as has been seen in previous studies for other AM CVn systems (e.g., Green et al., 2019c), but other studies have suggested that the second bright spot may be weak (e.g., van Roestel et al., 2022).

We also create a Doppler tomogram for He II 4685.7 Å (Figure 3.10), using the average systemic RV offset of that line. The He II 4685.7 Å tomogram shows neither a disk nor the bright spot seen in the He I tomograms. Instead, the He II tomogram shows clear evidence that this line originates near the center of mass of the system — the “central spike" seen in other AM CVn systems. We present a detailed analysis of this feature in Section 3.4.

3.4 Discussion

Binary Parameters

We used two techniques to compute the binary parameters of SRGeJ0453: 1) modelling of the optical light curve, and 2) RV measurements of the He II 4685.7

[8] `https://www.saao.ac.za/~ejk/doptomog/main.html`

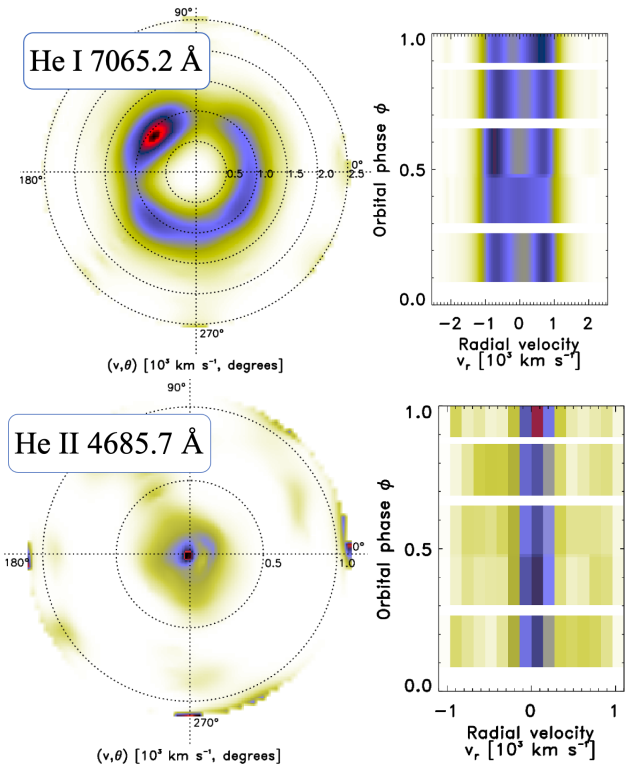

Figure 3.10: Doppler tomograms and trailed spectra of He I 7065.2 Å reveal a disk with at least one prominent bright spot (upper panel). The He II 4685.7 Å Doppler tomogram (lower panel) shows the line to originate near the system center of mass, indicating it is the “central spike" seen in other AM CVn systems.

Å line. The results of these methods are discussed below.

Light curve Modeling

We modeled the optical light curve using the PHysics Of Eclipsing BinariEs code PHOEBE (Prsa and Zwitter, 2005; Prsa et al., 2016). This code allows to model and fit optical light curves, RV curves, and spectral line profiles of binary systems. PHOEBE constructs 3D models of each star using a triangular mesh and incorporates the physics of irradiation, ellipsoidal modulation, spots, and most relevant to our work, a complete Roche geometry.

When comparing our PHOEBE models to data, we only made use of the CHIMERA g band light curve, since any emission from the disk and/or bright spot is minimal in that passband. Helium disk emission lines contribute minimally in the CHIMERA g band (equivalent to Sloan g: 4000 – 5500 Å): The integrated flux over the entire passband (average spectrum) is $\approx 10^{-13}$ erg/s/cm^2, while the integrated flux over the

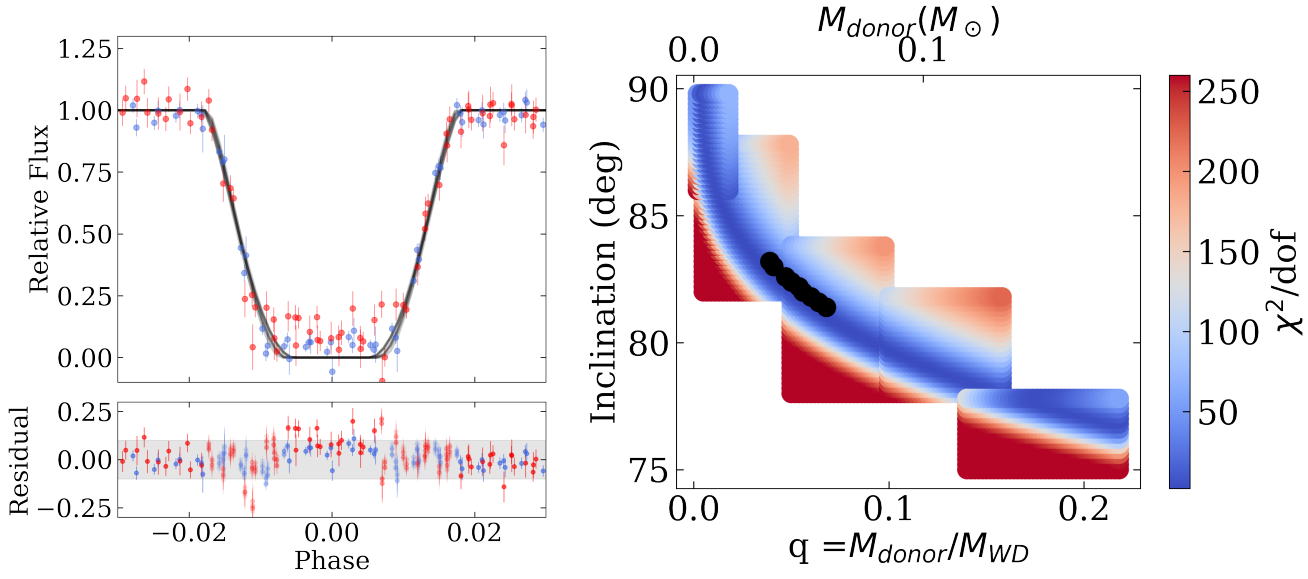

Figure 3.11: PHOEBE modeling of the eclipsing allows us to constrain model parameters of SRGeJ0453. *Left*: CHIMERA r (red) and g (blue) light curves plotted alongside best-fitting PHOEBE models. *Right*: Goodness-of-fit (χ^2/dof) for all PHOEBE models. In black, we show model parameters where χ^2/dof < 2.3, indicating a good fit to the data.

most prominent He I emission line, He I 5015.7 Å, is $\approx 8 \times 10^{-16}$ erg/s/cm^2. The contribution of all emission lines in the CHIMERA g passband is therefore $\lesssim 10^{-15}$ erg/s/cm^2, around one percent of the continuum flux, which is dominated by the WD.

With the above argument in mind, we neglected the emission from the accretion disk and bright spot in our approximation of the g band light curve. Indeed, the contribution of a bright spot does not distort the optical light curve of SRGeJ0453, as expected for non-magnetic CVs (e.g., McAllister et al., 2019). As mentioned in Section 3.3, previous results of modelling the g band optical light curve of other long period AM CVns show that the contribution of the accretion disk and bright spot to the integrated emission of the system is usually less than 10 per cent (van Roestel et al., 2022).

We fixed the WD's mass, radius, and temperature using the SED modelling results (see Section 3.3). The optical spectrum and SED of SRGeJ0453 suggests that the donor temperature should be less than 3000 K, since any object at that temperature should be seen in either the spectrum or SED. We fixed the temperature of the

donor star at 1500 K. PHOEBE modeling is unaffected by varying the donor star temperature in the 1000–3000 K range or varying the WD temperature between 15,000–18,000 K. The donor star is assumed to fill its Roche lobe, and its radius is computed based on the Eggleton (1983a) approximation:

$$\frac{R_L}{a} = \frac{0.49q^{2/3}}{0.6q^{2/3} + \ln\left(1 + q^{1/3}\right)}, \tag{3.3}$$

where the semi-major axis of the system a was calculated based on Kepler's law using a best-fit period from section 3.3 as $a^3 = G(M_1 + M_2)P_{\rm orb}^2/4\pi^2$. The ratio of the donor star mass to the WD mass: $q = M_2/M_1$. Therefore, the two free parameters that we aim to fit are the mass ratio, q, and inclination, i.

Outside the eclipse, light curves show flickering at the < 10 percent level, possibly produced by the accretion disk (see Figures 3.3, 3.4 and 3.5). To compare the PHOEBE model to data, we used only the eclipse in the 0.97–1.03 phase range to minimize the contribution of flickering in parameter estimation.

We created a grid of PHOEBE models with 0.2° steps in i and 0.002 steps in q, in the range: $75° \leq i \leq 90°$ and $0.002 \leq q \leq 0.22$. After initially experimenting with a coarser grid over the entire parameter range, we only created PHOEBE models for values of q and i that lead to the best fits to the data due to the high computational cost of creating such a fine grid. In Figure 3.11, we present the resulting fits along with χ^2/dof values. In the left panel of the figure, we present both in-eclipse CHIMERA g and r data (although the fit is only to the g band data) along with the PHOEBE models for which $\chi^2/\mathrm{dof} < 2.3$. The residuals show better than 10 percent agreement for the entire range of CHIMERA g band data, while some r band points in eclipse disagree with PHOEBE models at the ≈20 percent level. It is unclear if the CHIMERA r band points are due to disk contribution or contamination from the poor seeing that was present during data acquisition.

In the right panel of Figure 3.11, we present the χ^2/dof values for the grid of q vs. i used in our PHOEBE models. The best fitting models ($\chi^2/\mathrm{dof} < 2.3$) allow us to obtain the following parameter range: i (°) = 82.5 ± 1.5, $q = 0.052 \pm 0.024$. Lower inclinations (and therefore higher values of q) are disfavored by the depth of the eclipse, while higher inclinations (and therefore lower values of q) are disfavored by the length of WD ingress/egress in the high speed photometry.

The error bars we report q and i reflect the > 99.9% confidence limit. We choose the $\chi^2/\mathrm{dof} < 2.3$ range to ensure we do not underestimate our final parameter

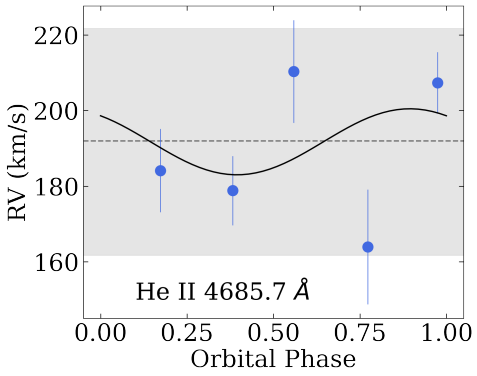

Figure 3.12: RV measurements of the He II 4686 Å line show a systemic offset (dotted line; $\gamma = 192$ km/s) and an RV amplitude of $K = 9 \pm 7$ km/s (3σ confidence limit shown in grey). This low amplitude suggests that the emission originates near the binary center of mass, and therefore the surface of the WD. For more details, see Section 3.4.

uncertainties. Visually, all models in this range fit the CHIMERA g band data equally well, which implies that enforcing a lower χ^2/dof value would carry little meaning. This also implies that additional high cadence photometry is needed to place tighter constraints on the binary parameters.

"Central Spike": He II 4685.7 Å

The central spike lines are observed features in the optical spectra of AM CVns. The central-spike lines are thought to originate on the WD surface or close to it (e.g.,, Marsh, 1999; Kupfer et al., 2016; Green et al., 2019c). Therefore, RV measurements for the central spike lines could be used to place limits on the binary parameters of the system.

From the average optical spectrum of SRGeJ0453, we identified the central spike line at He II 4686 Å (see Figure 3.6). A similar line was found in the optical spectra of other long-period AM CVns (see, for example, Kupfer et al., 2016; Green et al., 2019c; van Roestel et al., 2022). We perform a Gaussian fit to the He II 4686 Å line at every orbital phase. We experiment by trying different sets of initial positions of the line and bounds to find a best-fit line position. The estimated best-fit line positions are independent of initial guesses and bounds. Figure 3.12 shows the RV measurements for the central-spike line at He II 4686 Å.

The best-fit by Eq. (3.2) does not give statistically significant measurements for RVs of the central-spike line, where a systemic velocity of $\gamma_{\rm sys} = 192 \pm 5$ km/s

and RVs of $K_x = -5 \pm 8$ km/s and $K_y = 7 \pm 6$ km/s. The systemic velocity is highly significant, but a similar result might be obtained by fitting the RVs of the central-spike line by a flat line. The chi-squared for a flat line model at the weighted average RV values is χ^2/d.o.f= $11.5/4 = 2.8$, and for the sinusoid function from Eq. (3.2) is χ^2/d.o.f= $9.4/2 = 4.7$. F–test suggests that both models give an acceptable fit (p-value is 0.82) for RV measurements of He II 4686 line.

No significant detection of the RV of the central-spike line at He II 4686 Å is likely due to the low resolution of our data, yet we can still use the amplitude to calculate upper limits ($K = \sqrt{K_x^2 + K_y^2} = 9 \pm 7$ km/s). To constrain the binary parameters, we used a 3σ upper limit to the RV amplitude of $K \lesssim 30$ km/s. Assuming that the central-spike line is produced at the WD surface, and its RV is equal to the RV of the WD ($K \approx K_1$), we compute the binary mass function as:

$$\frac{P_{\rm orb} K_1^3}{2\pi G} = \frac{(M_2 \sin i)^3}{(M_1 + M_2)^2} = \frac{M_1 (q \sin i)^3}{(1+q)^2}, \tag{3.4}$$

where the mass of the WD is equal to $M_1 = 0.85\ M_\odot$ (see Section 3.3), the orbital period is $P_{orb} = 55.08$ minutes (see Section 3.3), and the inclination angle is $i \approx 82$ (see Section 3.4). Using Eq. (3.4), we compute $q < 0.052$, which allows us to place limits on both the donor mass and radius: $M_2 < 0.044\ M_\odot$ and $R_2 \lesssim 0.078\ R_\odot$, assuming a Roche-lobe filling star.

The systemic velocity of the He II 4686 line shows the offset from the *system* velocity of the binary ($\gamma_{\rm binary} = 14 \pm 5$ km/s) by $\gamma_{\rm He\ II\ 4686} = 178 \pm 7$ km/s. A similar excess of the systematic velocities was found in other AM CVns (e.g., Green et al., 2019c). We emphasize that this systemic redshift is present at *all* orbital phases, ruling out orbital motion as a possible source. This leaves only the gravitational redshift of the WD as a source of the systemic redshift. However, given our measured WD mass and radius, we would only expect a gravitational redshift of $v = GM_{\rm WD}/(cR_{\rm WD}) \approx 72$ km/s, which is substantially lower than our measured value. A WD mass $\approx 1.1 M_\odot$ is required to obtain a gravitational redshift of $\approx$ 180 km/s, but a WD of this mass seems unlikely given our SED analysis (Section 3.3). Further investigation is needed to confirm the large systemic redshift observed in the He II 4685.7 Å line and determine its origin.

Evolutionary History

We discuss the evolutionary history of the system using lines of H, C, N, and O. We do not detect H in the optical spectrum of SRGeJ0453. In the Tutukov et al. (1985)

Table 3.5: Summary of system parameters of SRGeJ0453.

Parameter	Value	Origin
Distance, d (pc)	239^{+11}_{-8}	Gaia Parallax
Orbital period, $P_{\rm orb}$ (min)	55.0802 ± 0.0003	Optical Photometry
Extinction, A_V	0.03 ± 0.01	SED Fit
Accretor mass, $M_{\rm WD}$ ($M_\odot$)	$0.85^{+0.04}_{-0.05}$	SED Fit
Accretor temperature, $T_{\rm eff,WD}$ (K)	$16,570^{+240}_{-250}$	SED Fit
Inclination, i ($^\circ$)	82.5 ± 1.5	PHOEBE Model
Mass ratio, q	0.052 ± 0.024	PHOEBE Model
	0.052	Spectroscopy
Accretion rate, $\dot{M}$ ($M_\odot$ yr^{-1})	$\approx (2-10) \times 10^{-12}$	X-ray
Donor mass, $M_{\rm donor}$ ($M_\odot$)	0.044 ± 0.020	SED Fit + PHOEBE
	0.044	SED Fit + Spectroscopy
Donor radius, $R_{\rm donor}$ ($R_\odot$)	0.078 ± 0.012	SED Fit + PHOEBE
	0.078	SED Fit + Spectroscopy

evolved donor channel model, based on the empirical Verbunt and Zwaan (1981) magnetic braking picture, the surface mass abundance of hydrogen of systems with $P_{\rm orb}$ ≈55 minutes never drops below several 0.01 in a Hubble time (see Table A1 in Podsiadlowski et al., 2003). In this scenario, H should be detected by modern techniques (T. Marsh, private communication). However, in the $\alpha - \Omega$ dynamo picture for magnetic braking in the evolved CV model (Sarkar et al., 2023c), and in the modeling done in El-Badry et al. (2021b), the hydrogen mass fraction in long-period AM CVns may be present at a non-detectable level. Thus, our non-detection of H in SRGeJ0453 cannot rule out the evolved donor channel.

Nelemans et al. (2010) calculated abundances for systems evolving through all three postulated AM CVn formation channels. A useful diagnostic from that work is the N/O ratio, which in the evolved CV channel, is N/O≈1 (see Figure 6 of Nelemans et al., 2010). In the He WD and He star channels, it is possible to have N/O>1. (see Figure 11 of Nelemans et al., 2010). Since there is a clear non-detection of oxygen and a strong detection of nitrogen, we can discard the evolved CV channel for SRGeJ0453. This leaves us with the He star and He WD channels as possibilities.

The N/C ratio may be also informative in distinguishing between formation channels (Nelemans et al., 2010). For the He star channel, Nelemans et al. (2010), using the "standard" magnetic braking model and Sarkar et al. (2023b), using the double-dynamo model, predict N/C≈5 and 120–200, respectively, while for the He WD and

evolved CV channels N/C$\gtrsim$ 100 in both models. However, based on the equivalent widths of the N and C lines, we are able only to estimate for SRGeJ0453 a lower limit of N/C$\gtrsim$1, thus allowing for both He WD and He star channels.

It is not surprising that it is difficult to distinguish between the He star and He WD formation channels, since at long orbital periods, donors in systems forming from either channel have nearly identical entropies. This is due to the thermal timescale becoming nearly equal to the mass-transfer timescale, leading to the donor in the He-star channel becoming nearly degenerate (e.g., Solheim, 2010).

We conclude that even with precise abundance or donor mass and radius estimates, the uncertainties in current evolutionary models of any formation channel are large enough to accommodate more than one channel for some AM CVn systems (e.g., van Roestel et al., 2022).

Comparison to Other AM CVns and Future Work

SRGeJ0453 is the ninth published eclipsing AM CVn — YZ LMi/SDSSJ0926+3624 was the first (Anderson et al., 2005), Gaia 14aae the second (Campbell et al., 2015), ZTFJ1905+3134 the third (Burdge et al., 2020), and the fourth through eighth were discovered through a dedicated search for eclipsing AM CVns in ZTF (van Roestel et al., 2022). Like *in all other* eclipsing AM CVns with WD mass measurements, the WD in SRGeJ0453 has a mass equal to or greater than that of single WDs ($\overline{M}_{\rm WD} \approx 0.6 M_{\odot}$; Kepler et al., 2007a), regardless of the black body or DB model atmosphere approximation. This presents further evidence that the mean mass of the WD in AM CVns is greater than that of single WDs, as has been found for CVs (see Pala et al. (2022a) and references therein).

We plot the location of SRGeJ0453 in a 100 pc Gaia Hertzsprung-Russell diagram (Gaia Collaboration et al., 2022) along with other other known AM CVn systems assembled from the catalogs by Ramsay et al. (2018) and van Roestel et al. (2022) in Figure 3.13. We only plot systems for which a significant Gaia parallax is known (`parallax_over_error` > 3). Only systems for which a period is known are then color-coded. We make a distinction between systems that show frequent *optical* outbursts and those that spend the vast majority of their time in optical quiescence.

Figure 3.13 shows the progression of AM CVn systems throughout their accreting lifetimes. They start as non-outbursting, short period ($P_{\rm orb}$ = 5 − 10 minutes), whose high luminosity makes them easy to discover. As they evolve to moderate periods ($P_{\rm orb}$ = 20 − 50 minutes), they become less luminous, but undergo frequent

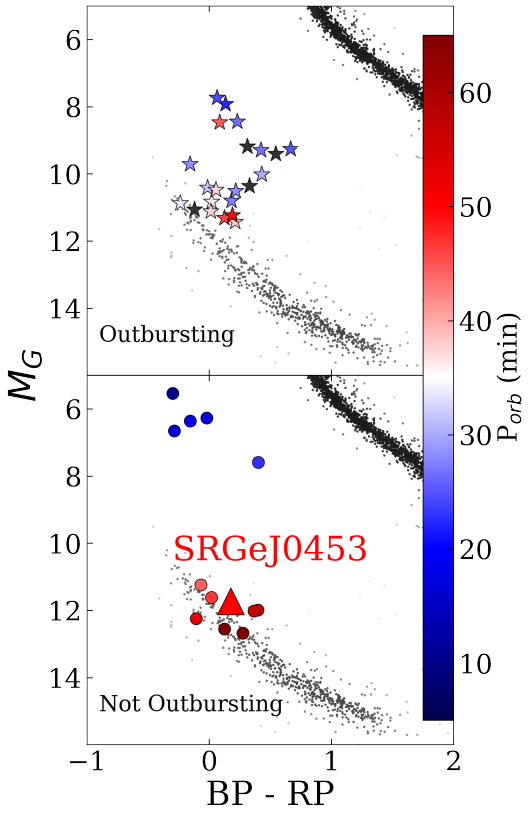

Figure 3.13: Position of SRGeJ0453 in the 100 pc Gaia Hertzsprung-Russell diagram alongside previously known AM CVn systems with a significant Gaia parallax (`parallax_over_error` > 3). The non-outbursting population occupies distinct portions of phase space.

outbursts which can be discovered by all-sky optical surveys. Finally, AM CVns become long-period ($P_{\rm orb} \gtrsim 50$ minutes) systems such as SRGeJ0453, which blend in with the WD track.

We have shown that our multiwavelength analysis has led to the discovery of a long period AM CVn system, due to it being an X-ray source in the SRG/eROSITA sky. With its observed flux of 9×10^{-14} erg s^{-1}cm^{-2} in the 0.3–2.3 keV energy band, SRGeJ0453 is not present in the Second ROSAT All Sky Survey Source Catalog, which had a flux limit of $\sim 2 \times 10^{-13}$erg s^{-1}cm^{-2} (2RXS; Boller et al., 2016b). Furthermore, this system was missed in a search for eclipsing AM CVn systems in the ZTF database of optical photometry due to the requirement that several in-eclipse points be present in the light curve (van Roestel et al., 2022).

Finally, we note that while many AM CVn systems emit GWs that will be detectable by *LISA*, it is unlikely that SRGeJ0453 will be detectable in the initial 4 year long

campaign. We use `LEGWORK` (Wagg et al., 2022a,b), a package designed to calculate *LISA* signal-to-noise ratios for GWs emitted from inspiraling binary systems. We estimate that SRGeJ0453 will be observed with a signal-to-noise ratio ≈ 1 in the initial 4 year long campaign.

3.5 Summary and Conclusion

We have presented the first discovery from a joint SRG/eROSITA and ZTF program to search for CVs and related objects in the Milky Way. SRGeJ0453 is an eclipsing, long period AM CVn system which was identified through its high X-ray to optical flux ratio ($F_X/F_{\rm opt} \approx 0.12$). Our results are summarised as follows:

em[–] The optical spectrum of SRGeJ0453 shows common features for AM CVn systems: a blue continuum with prominent He lines and an absence of H lines. All He I lines have a narrow central absorption commonly seen in nearly edge-on CVs and AM CVns among them. He II 4685.7 Å is only seen as a narrow emission feature (see Figure 3.6). em[–] The optical light curves from observations done with RTT-150/TFOSC, ZTF, and P200/CHIMERA show deep eclipses ($\approx 3^m$). Low amplitude ($\approx 0.1 - 0.3^m$) flickering, possibly caused by an accretion disk, is also seen (see Figures 3.2–3.5). High-speed photometry allows us to tightly constrain the orbital period to be $P_{\rm orb} = 55.0802 \pm 0.0003$ minutes. em[–] Using Keck I/LRIS spectra, we created Doppler tomograms for several prominent lines (Figure 3.17). The He I 7065.2 Å Doppler tomogram shows a bright spot located ≈45 degrees ahead of the donor star, but we see at most weak evidence for a second bright spot in other helium lines. The He II 4685.7 Å tomogram indicates that this line traces the “central spike" seen in other AM CVn systems. em[–] To estimate the binary parameters, we modelled the optical light curve using PHOEBE and used the RV measurements of the central spike line at He II 4685.7 Å. The computed binary parameters are presented in Table 8.2. em[–] SRGeJ0453 has an X-ray luminosity $\approx 6.2 \times 10^{29}$ erg s^{-1} in the 0.3–2.3 keV energy band. The X-ray spectrum of the source can be approximated by a power law model with a photon index of $\Gamma \sim 1$, while the optically thin thermal plasma model gives a lower limit on the plasma temperature of $\gtrsim 3.2$ keV (1σ confidence, see Table 3.3). Intermediate polars (magnetic CVs with $B \approx 1 - 10$ MG) observed with SRG/eROSITA show similarly hard photon indexes. This could tentatively suggest a possible magnetic nature of SRGeJ0453, but such a hypothesis requires further investigation. em[–] The

lower limit of abundance ratio of N/C $\gtrsim 1$ and the absence of oxygen lines suggests that the He WD and He star evolutionary channels could both be possible for SRGeJ0453 (Section 3.4).

A multi-wavelength campaign such as our combination of X-ray and optical information enables the possibility to efficiently search for and discover AM CVns. This method is particularly useful to identify systems that remain quiescent without any outburst activity. This work is a pilot study, and more systems discovered from a joint SRG/eROSITA and ZTF program to identify CVs will be presented in the near future.

3.6 Acknowledgements

This work is based on observations with eROSITA telescope onboard SRG observatory. The SRG observatory was built by Roskosmos in the interests of the Russian Academy of Sciences represented by its Space Research Institute (IKI) in the framework of the Russian Federal Space Program, with the participation of the Deutsches Zentrum für Luft- und Raumfahrt (DLR). The SRG/eROSITA X-ray telescope was built by a consortium of German Institutes led by MPE, and supported by DLR. The SRG spacecraft was designed, built, launched and is operated by the Lavochkin Association and its subcontractors. The science data are downlinked via the Deep Space Network Antennae in Bear Lakes, Ussurijsk, and Baykonur, funded by Roskosmos. The eROSITA data used in this work were processed using the eSASS software system developed by the German eROSITA consortium and proprietary data reduction and analysis software developed by the Russian eROSITA Consortium.

Based on observations obtained with the Samuel Oschin Telescope 48-inch and the 60-inch Telescope at the Palomar Observatory as part of the Zwicky Transient Facility project. ZTF is supported by the National Science Foundation under Grants No. AST-1440341 and AST-2034437 and a collaboration including current partners Caltech, IPAC, the Weizmann Institute of Science, the Oskar Klein Center at Stockholm University, the University of Maryland, Deutsches Elektronen-Synchrotron and Humboldt University, the TANGO Consortium of Taiwan, the University of Wisconsin at Milwaukee, Trinity College Dublin, Lawrence Livermore National Laboratories, IN2P3, University of Warwick, Ruhr University Bochum, Northwestern University and former partners the University of Washington, Los Alamos National Laboratories, and Lawrence Berkeley National Laboratories. Operations

are conducted by COO, IPAC, and UW. The ZTF forced-photometry service was funded under the Heising-Simons Foundation grant #12540303 (PI: Graham).

We are grateful to the staffs of the Palomar and Keck Observatories for their work in help us carry out our observations. We thank TÜBİTAK, the Space Research Institute of the Russian Academy of Sciences, the Kazan Federal University, and the Academy of Sciences of Tatarstan for their partial support in using RTT-150 (Russian - Turkish 1.5-m telescope in Antalya).

This work has made use of data from the European Space Agency (ESA) mission Gaia (`https://www.cosmos.esa.int/gaia`), processed by the Gaia Data Processing and Analysis Consortium (DPAC, `https://www.cosmos.esa.int/web/gaia/dpac/consortium`). Funding for the DPAC has been provided by national institutions, in particular the institutions participating in the Gaia Multilateral Agreement.

This research made use of matplotlib, a Python library for publication quality graphics (Hunter, 2007); NumPy (Harris et al., 2020); Astroquery (Ginsburg et al., 2019); Astropy, a community-developed core Python package for Astronomy (**?**Astropy Collaboration et al., 2013a); and the VizieR catalogue access tool, CDS, Strasbourg, France. The authors wish to thank E. Kotze for making his Doppler tomography code, `doptomog`, public (Kotze et al., 2015b).

ACR acknowledges support from the National Academies of Science via a Ford Foundation Predoctoral Fellowship. IG acknowledges support from Kazan Federal University. The work of IB, MG, IKh, AS, PM supported by the RSF grant N 23-12-00292.

3.7 Period estimation using RTT-150 data

To calculate RTT-150 optical photometry, five stars with good signal-to-noise ratio were used to estimate the position and perform photometric calibration of SRGeJ0453 to the Gaia *G* band. Fluxes were computed using a 2 aperture, and the accuracy of RTT-150 differential photometry is 0.02 mag.

A combined approach was used to determine the period of SRGeJ0453. Based on the frequency analysis, a preliminary period was determined and refined by comparing two epochs of observations on different nights. Even though the eclipse profiles for each night in the RTT-150 data are highly smoothed, the two observational epochs differ by about 25 cycles. Thus, the available cycles of eclipse coverage are sufficient to estimate the eclipse center and, therefore, to correct the period itself.

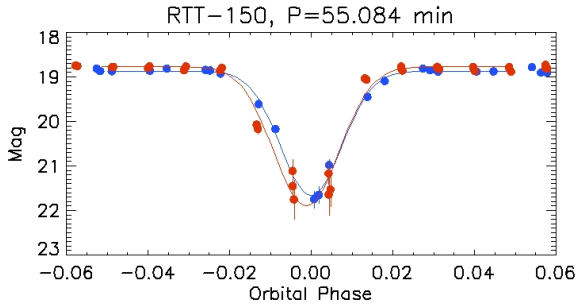

Figure 3.14: Period determination with two epochs of RTT-150 data comparison. *Blue circles* corresponds to January 19, 2023 data, *red circles* – January 20, 2023 data with Gaussian fit as solid lines.

For the frequency analysis, we used the Stellingwerf method implemented in the ISDA code (Stellingwerf, 1978). This method is one of many variations of the PDM (Phase Dispersion Minimization) method. The period that gives the smallest possible dispersion of the obtained light curve is chosen in the PDM method. This is achieved by minimizing the sum of the squares of ordinate differences from one data point to the next. The periods giving the smallest sum are taken as true periods.

The following algorithm was used to correct the obtained period: (i) The phase curve with the given period is constructed for each night separately; (ii) A phase interval of ±0.05 around the phase, corresponding to the maximum magnitude value, is determined. A Gaussian with a constant fitting of the eclipse region is constructed separately for each night; (iii) The difference modulus between the displacement parameters of the two Gaussians is determined; (iv) Finally, the period corresponding to the minimum of the difference modulus is the best calculated period. The period estimation error is computed as the square root of the sum of the squares of the mean square errors of the Gaussian displacement parameters.

Newton's method finds the minimum of the displacement modulus, dividing the interval in half, where the interval bounds are taken from the preliminary estimation of the period by the Stellingwerf method. The computed period is 55.084 ± 0.015 min.

3.8 Selection of He I Lines

We elaborate on why we omit the He I 4387.9 Å and 4921.9 Å lines in the analysis presented in Section 3.3. In Figure 3.15, we present phase resolved spectra of the He I 4387.9 Å line, together with the best-fit made up of two Gaussians. We also show

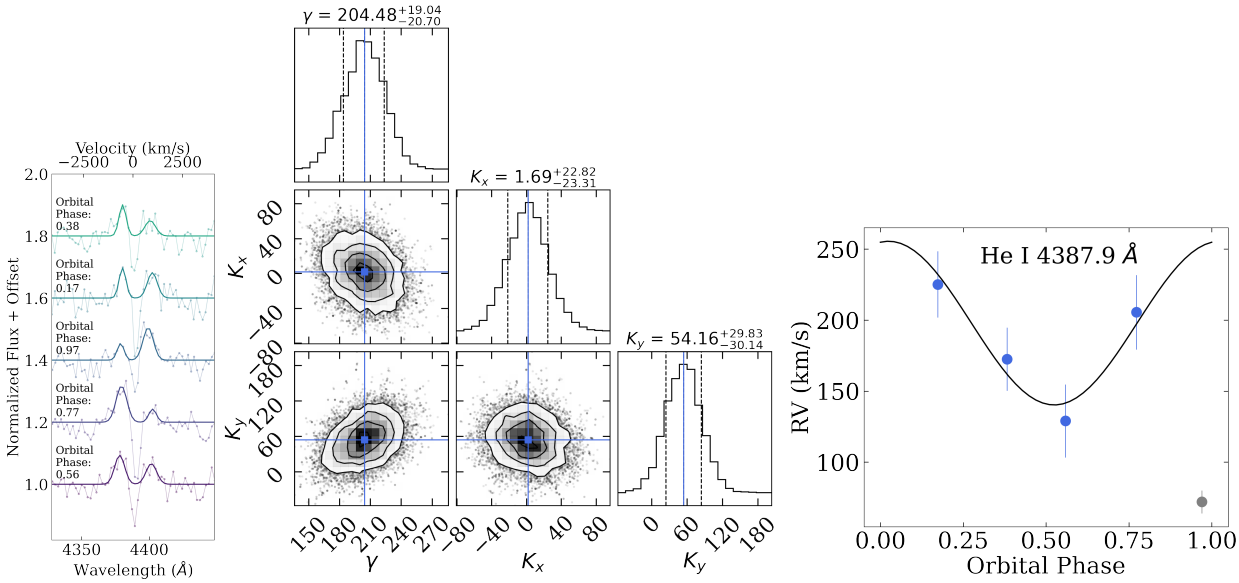

Figure 3.15: Phase-resolved spectra of He I 4387.9 Å with resulting MCMC parameter estimates of radial velocities. The He I 4387.9 Å line is poorly fit due to the strong central absorption feature, which affects the final parameter estimates. Stronger He I Å lines, however, are not affected by low signal-to-noise or strong absorption (see Figure 3.16).

MCMC corner plots to show the constraints on γ, K_x, and K_y, and the resulting RV curves. We show that the He I 4387.9 Å line is affected by both low signal above the continuum and deep central absorption. This absorption seems to be overall redshifted with respect to line center, and has the effect of redshifting the systemic velocity of the line. We attempted to use another fitting procedure where the widths of two Gaussians are held equal, and the central absorption core is omitted from the fit (e.g., Green et al., 2019c). However, this leaves too few points to fit since the peak of the He I 4387.9 Å line is less than 10% above the continuum, which results in a poor fit. Exactly the same feature is present in the He I 4921.9 Å line.

This effect is not seen in the 6678.2 Å and 7065.2 Å lines, which are much stronger (see Figure 3.16). In that case, the lines are more than 50% above the continuum and the absorption core is not deep enough to affect the Gaussian fits (i.e. the absorption does not go below the continuum).

3.9 He I Radial Velocity Curves

We present phase-resolved spectroscopy of the He I 6678.2 and 7065.2 Å lines, along with corresponding MCMC corner plots and RV curves in Figure 3.16. Our

process is the following: we independently fit two Gaussians (letting the amplitude, mean, and variance be free for each) to the two peaks of a He I emission line. Using the `curve_fit` routine from `scipy`, we obtain the best-fit parameters and covariance matrix for each of the two fits. To compute radial velocity of a given line, we take the average of the two peaks as the central wavelength of the line at that orbital phase.

Furthermore, we argue that spectra taken near the WD eclipse (phase $\approx 0.9 - 1.1$) can lead to an incorrect RV analysis. From the photometry, we know that there is an eclipse, at which point both the WD and the disk are eclipsed. Since emission lines originate in the disk surrounding the WD, at this orbital phase the donor star eclipses the disk in an asymmetric manner with respect to our line of sight. In other words, the donor obscures the part of the disk where the lines are blueshifted, causing a velocity distribution that does not reflect the actual disk velocity.

Note: there is a clear feature in the He I 6678 Å line at phase 0.38, with a strong absorption feature in the left peak. It is unclear if this is a cosmic ray or a real feature. The Gaussian fit to that peak does not change significantly if the affected points are omitted, and we keep the feature there for transparency.

3.10 Doppler Tomogram for Other He I Lines

We present a Doppler tomogram and trailed spectra for the strongest He I line at 5875.6 Å. Due to the strong blending with Na I, we cannot perform an adequate RV analysis to find the systemic velocity of the line, γ. In making this Doppler tomogram, we use $\gamma = 17$ km/s, used for the He I 7065.2 Å line. The accretion disk is seen in the Doppler tomogram along with a prominent bright spot 45 degrees ahead of the donor star (second quadrant). There is no strong evidence of another bright spot located 135–180 degrees ahead of the donor star (third quadrant of the plot). The emission seen in yellow at apparently high velocities is likely due to blending with the Na I doublet at 5890.0 and 5895.9 Å.

We also present the Doppler tomogram and trailed spectra of the He I 6678.2 Å line. The Doppler tomogram shows strong evidence there could be another bright spot located 135 degrees ahead of the donor star (third quadrant of the plot). In Figure 3.16, we show that one of the spectra of this line could be affected by a cosmic ray, which may artificially lead to a second bright spot. Overall, the He I 6678.2 Å tomogram reveals the disk to be more patchy, but further spectra are needed to verify the true structure of the disk. In short, because we do not see strong evidence

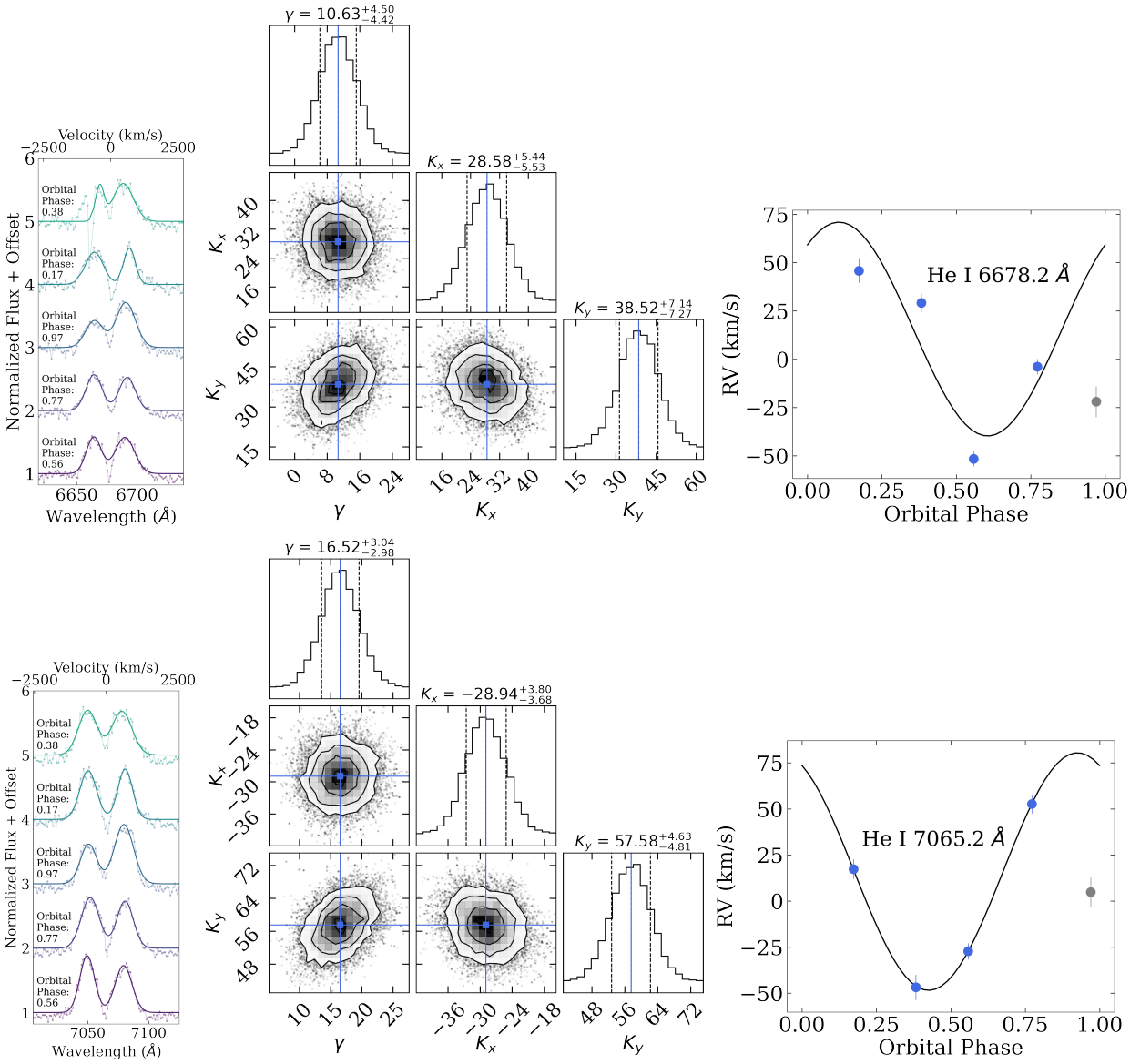

Figure 3.16: Phase-resolved spectra of He I 6678.2 Å (above) and 7065.2 Å (below) with resulting MCMC parameter estimates of radial velocities. The spectrum at phase 0.97 is clearly asymmetric in both lines, confirming the disk is eclipsed by the donor at the orbital phase. The MCMC parameter estimates are therefore done without the spectrum at that orbital phase, and result in a good fit that would not be possible if that point were included. The in-eclipse RV measurement is shown in grey to indicate it is not used in the MCMC analysis.

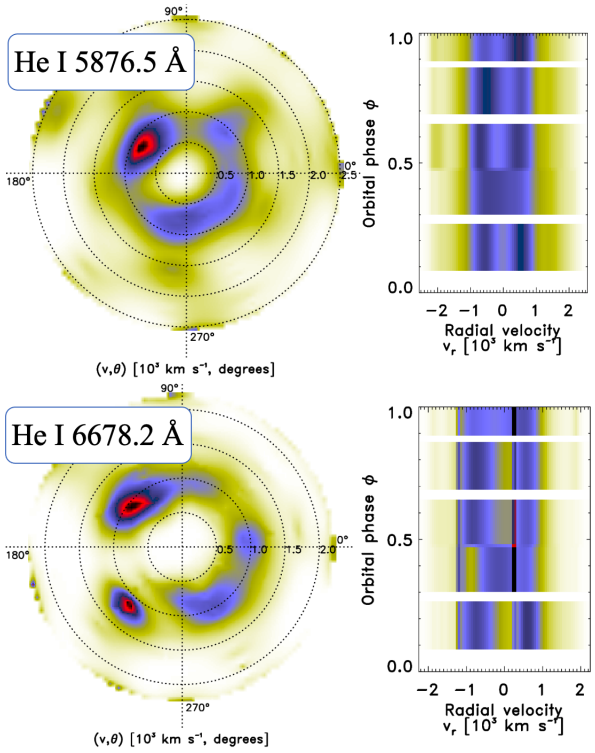

Figure 3.17: Doppler tomogram and trailed spectra for He I 5876.5 Å reveals a disk with at least one prominent bright spot. The Doppler tomogram of He I 6678.2 Å suggests there could be a second bright spot, but this could be an artifact due to a possible cosmic ray in one of the spectra.

for a second bright spot in *all* He I emission lines, we do not conclusively determine if it exists or not.

Chapter 4

NO X-RAYS OR RADIO FROM THE NEAREST BLACK HOLES AND IMPLICATIONS FOR FUTURE SEARCHES

Antonio C. Rodriguez, Yvette Cendes, Kareem El-Badry, and Edo Berger. No X-Rays or Radio from the Nearest Black Holes and Implications for Future Searches. *Publications of the Astronomical Society of the Pacific*, 136(2):024203, February 2024. doi: 10.1088/1538-3873/ad228e.

Author List

Antonio C. Rodriguez[1,*], Yvette Cendes[2,3], Kareem El-Badry[1], Edo Berger[2]

[1]Department of Astronomy, California Institute of Technology, 1200 E. California Blvd, Pasadena, CA 91125, USA
[2]Center for Astrophysics | Harvard & Smithsonian, 60 Garden Street, Cambridge, MA 02138, USA
[3]Department of Physics, University of Oregon, Eugene, OR 97403, USA

[*]Corresponding author: acrodrig@caltech.edu

ABSTRACT

Astrometry from the *Gaia* mission was recently used to discover the two nearest known stellar-mass black holes (BHs), Gaia BH1 and Gaia BH2. These objects are among the first stellar-mass BHs not discovered via X-rays or gravitational waves. Both systems contain $\sim 1\,M_\odot$ stars in wide orbits ($a \approx$1.4 AU, 4.96 AU) around $\sim 9\,M_\odot$ BHs, with both stars (solar-type main sequence star, red giant) well within their Roche lobes in Gaia BH1 and BH2, respectively. However, the BHs are still expected to accrete stellar winds, leading to potentially detectable X-ray or radio emission. Here, we report observations of both systems with the *Chandra* X-ray Observatory, the VLA (for Gaia BH1) and MeerKAT (for Gaia BH2). We did not detect either system, leading to X-ray upper limits of $L_X < 9.4 \times 10^{28}$ and $L_X < 4.0 \times 10^{29}\,erg\,s^{-1}$ and radio upper limits of $L_r < 1.6 \times 10^{25}$ and $L_r < 1.0 \times 10^{26}\,erg\,s^{-1}$ for Gaia BH1 and BH2, respectively. For Gaia BH2, the non-detection implies that the the accretion rate near the horizon is much lower than the Bondi rate, consistent with recent models for hot accretion flows. We discuss implications of these non-detections for broader BH searches, concluding that it is unlikely that isolated BHs will be detected via ISM accretion in the near future. We also calculate evolutionary models for the binaries' future evolution using Modules for Experiments in Stellar Astrophysics (MESA), and find that Gaia BH1 will be visible as a symbiotic BH X-ray binary for 5–50 Myr. Since no symbiotic BH X-ray binaries are known, this implies either that fewer than $\sim 10^4$ Gaia BH1-like binaries exist in the Milky Way, or that they are common but have evaded detection.

4.1 Introduction

Understanding the full demographics of the stellar-mass black hole (BH) population provides key insights into stellar and galactic evolution. BHs are created by the deaths of some stars with initial masses $M_* \gtrsim 20 M_\odot$. Precisely which stars form BHs, and which leave behind neutron stars or no remnant at all, is uncertain (e.g., O'Connor and Ott, 2011; Sukhbold et al., 2016; Laplace et al., 2021). The Milky Way has formed $\sim 10^{11}$ stars in its lifetime, and the stellar initial mass function (IMF; e.g., Salpeter, 1955) dictates that the number of massive stars that have formed, died, and left behind a BH stands at $\sim 10^7 - 10^8$ (e.g., Sweeney et al., 2022).

Most ($\gtrsim 70\%$) of these massive stars exist with a binary companion, with triple and higher order systems also being common (Kobulnicky and Fryer, 2007; Sana et al., 2012; Moe and Di Stefano, 2017). However, the binary fraction of BHs is unknown. Virtually all known or suspected stellar-mass BHs today are in close binaries, in which a stellar companion to a BH is close enough that the BH is accreting significant quantities of gas from it, and the accretion flow produces observable emission across the electromagnetic spectrum. ~20 dynamically confirmed BHs exist in X-ray binaries, ~50 X-ray sources are suspected to contain a BH based on their X-ray properties (e.g., McClintock and Remillard, 2006; Corral-Santana et al., 2016), and a few X-ray quiet binaries have been reported in which a BH is suspected on dynamical grounds (e.g., Giesers et al., 2018a, 2019; Shenar et al., 2022; Mahy et al., 2022). Just one isolated BH candidate has been discovered via microlensing (Sahu et al., 2022; Lam et al., 2022; Mróz et al., 2022).

In X-ray bright systems, a BH accretes material from a close companion through stable Roche lobe overflow or stellar winds (e.g., McClintock and Remillard, 2006). These systems are called X-ray binaries (XRBs), and are often placed into three distinct spectral/temporal states: 1) the soft state, where the system is X-ray bright ($L_X \sim L_{\rm Edd}$) and dominated by thermal emission from the accretion disk; 2) the hard state, which can be seen across an intermediate range of luminosities ($L_X \sim 10^{-5.5} - 10^{-2} L_{\rm Edd}$) and is dominated by power-law emission; and the 3) quiescent state, where the system is very faint ($L_X \lesssim 10^{-5.5} L_{\rm Edd}$) and still dominated by power-law emission (e.g., Remillard and McClintock, 2006). All BH XRBs have been discovered in either a persistent high lumionsity state or through transient X-ray nova (outburst) events (e.g., Corral-Santana et al., 2016). X-ray novae are caused by a sudden increase of mass transfer onto the BH, which leads to a dramatic increase in X-ray luminosity from quiescence (e.g., McClintock and Remillard, 2006). All-

sky X-ray monitors (e.g., MAXI, Swift/BAT; Matsuoka et al., 2009; Burrows et al., 2005) have been effective at discovering BH candidates from their X-ray novae across the entire Milky Way for those whose luminosities approach $L_{\rm Edd}$, and out to a few kpc for those that reach $\sim 10^{-2} L_{\rm Edd}$ (e.g., Corral-Santana et al., 2016). However, the recurrence timescale of these outbursts is under strong debate, and so the total number of BH XRBs in the Galaxy is still quite uncertain (Tanaka and Shibazaki, 1996; Maccarone et al., 2022; Mori et al., 2022).

In the last few years, a handful of BHs orbited by luminous stars have been discovered in wider orbits (Giesers et al., 2018b; Shenar et al., 2022; El-Badry et al., 2023b,a). These systems are still outnumbered by XRBs, but this is likely a consequence of the very different selection functions of X-ray and optical searches. The few wide systems discovered so far likely represent the tip of a substantial iceberg. In this paper, we focus on Gaia BH1 and BH2, the newest and nearest of these systems. Precision astrometry from the third data release of the *Gaia* mission (DR3) enabled their discovery, and optical high-resolution spectroscopy confirmed their nature. Gaia BH1 and BH2 are systems with a BH in an orbit with a sun-like main-sequence star, and a red giant likely in its first ascent of the giant branch, respectively. These systems are unique in currently being the BH binaries with the longest known orbital periods (186 days, 1277 days), largest binary separations (a =1.4 AU, 4.96 AU), and also the closest to Earth (480 pc, 1.16 kpc).

Since both sun-like stars and red giants have stellar winds (e.g., Parker, 1958; Faulkner and Iben, 1966), we asked: can we see evidence of wind accretion in Gaia BH1 and BH2? In Section 8.2, we describe our observations and calculate upper limits for both Gaia BH1 and BH2 based on X-ray data from *Chandra*/ACIS-S, and radio data from the Very Large Array (VLA) and MeerKAT. In Section 8.3, we show that under the assumption of Bondi-Hoyle-Littleton (BHL) accretion, we should have seen X-rays and radio from Gaia BH2. We argue that a lack thereof signals that radiatively inefficient accretion is responsible for reduced accretion rates and the subsequent lack of multiwavelength emission. Finally, in Section 4.4, we explore the prospects of detecting wind accretion onto BHs using rates and efficiencies assuming inefficient accretion flow, either through a red giant companion or from the interstellar medium (ISM). We show that surveys such as SRG/eROSITA and pointed observations from *Chandra* are at best sensitive to 1) BHs accreting from $\sim 100 R_\odot$ red giants and 2) BHs accreting from high density ($n \gtrsim 10^3$ cm^{-3}) H_2 regions while traveling at very low ($\lesssim$ 5 km/s) speeds. Finally, we present

MESA models for the future evolution of both systems and their expected X-ray luminosities. Based on these models and the lack of detections of symbiotic BH XRBs from all-sky surveys, we conclude that at most $\sim 10^4$ systems similar to either Gaia BH1 or BH2 exist in the Milky Way, unless a substantial population of symbiotic BH XRBs have evaded detection so far.

4.2 Data

X-Ray

We observed Gaia BH1 with the *Chandra* X-ray Observatory (ObsID: 27524; PI: Rodriguez) using the Advanced CCD Imaging Spectrometer (ACIS; Garmire et al. 2003) on 31 October 2022 (UT) for a cumulative time of 21.89 ks (sum of two observations: 12.13 ks and 9.76 ks). The ACIS-S instrument was used in pointing mode, chosen over ACIS-I for its slight sensitivity advantage. The observations were taken about 9 days before apastron, when the separation between the BH and star was ≈2.01 AU.

We observed Gaia BH2 for 20ks with Chandra on 25 January 2023 (proposal ID 23208881; PI: El-Badry). We also used the ACIS-S configuration, with a spatial resolution of about 1 arcsec. The observations were timed to occur near the periastron passage, when the separation between the BH and the star was ≈ 2.47 AU.

The X-ray images of both sources are shown in Figure 4.1. We first ran the `chandra_repro` tool to reprocess the observations; this creates a new bad pixel file and de-streaks the event file. Since the observation of Gaia BH1 was split into two, we then ran the `reproject_obs` tool to merge both observations with respect to a common World Coordinate System (WCS). We then used the `srcflux` tool to estimate the 90% upper limit for detecting a source at the optical positions of Gaia BH1 and BH2. We created a 1" radius source region (1, 0 counts in Gaia BH1, BH2, respectively) at the optical positions of each source, and a 15" background region (156, 171 counts in Gaia BH1, BH2, respectively) to the side, away from any obvious sources. This tool uses Poisson statistics, as pertinent to X-ray observations and described in (Kashyap et al., 2010), to calculate upper flux limits. This is unique from estimating the (false negative) case in which a source is not detected due to confusion with the background rate; in both observations the background rate is very low and the upper limit obtained this way with the `aplimits` tool is similar to our reported value. We detect no significant flux at the location of either system

and obtain a 90% upper limit of (1.94×10^{-4}, 1.45×10^{-4} cts s^{-1}), for Gaia BH1 and BH2 respectively. We note that these values are consistent with the 90% upper limits obtained when detecting $n = 1, 0$ photons in the source region in a 20ks exposure, as tabulated by (Gehrels, 1986).

In order to convert to unabsorbed flux, we assume a power-law spectrum with index of 2, and calculate the Galactic hydrogen column density using the relation from Güver and Özel (2009c) and the value of A_V from Lallement et al. (2022) — $A_V = 0.93 \pm 0.1, 0.62 \pm 0.1$ for BH1, BH2, respectively. Using the `PIMMS` tool, we calculate an unabsorbed X-ray flux of $F_X = 3.58 \times 10^{-15}$erg s^{-1}cm^{-2} (BH1) and $F_X = 2.58 \times 10^{-15}$erg s^{-1}cm^{-2} (BH2) in the 0.5–7 keV energy range. With the *Gaia* distances, we can calculate the upper limit of the luminosity, which we present in Table 8.3.

Radio

We observed Gaia BH1 for 4 hr with the Very Large Array (VLA) in C band (4–8 GHz) in the "C" configuration on 27–28 November 2022 (DDT 22B-294; PI: Cendes). At this time, Gaia BH1 was 17 days past apastron, and the separation between the BH and star was ≈1.98 AU. We used the flux calibrator 3C286 and the gain calibrator J1743-0350. Data was calibrated using the Common Astronomy Software Applications (CASA) software. We measured the flux density using the imtool package within pwkit (Williams et al., 2017) at the location of Gaia BH1. The RMS at the source's position is 3.4 μJy, and we present flux and luminosity 3σ upper limits in Table 8.3.

We observed Gaia BH2 for 4 hr with the MeerKAT radio telescope in L band (0.86–1.71 GHz) on 13 January 2023 (DDT-20230103-YC01; PI: Cendes), when the separation between the BH and the star was ≈ 2.54 AU. We used the flux calibrator J1939-6342 and the gain calibrator J1424-4913, and used the calibrated images obtained via the SARAO Science Data Processor (SDP)4 for our analysis. We measured the flux density using the imtool package within pwkit (Williams et al., 2017) at the location of Gaia BH2. The RMS at the source's position is 17 μJy, and we present X-ray flux, radio flux density, and luminosity 3σ upper limits in Table 8.3. Luminosities are calculated using $L = 4\pi d^2 F$, where $F = \nu S_\nu$ and ν is the central frequency of the radio band.

We show cutouts of all X-ray and radio images in Figure 4.1. No significant source of flux is detected at the position of Gaia BH1 or BH2 in either X-rays or radio.

Table 4.1: X-ray and Radio Upper Limits on Flux and Luminosity (90% upper limits in X-ray, 3σ in radio)

Object	Facility	Energy Range	BH–star separation	Flux Limit	Luminosity Limit
Gaia BH1	Chandra/ACIS-S	0.5–7 keV	2.01 AU	$< 3.6 \times 10^{-15}$ erg s^{-1}cm^{-2}	$< 9.4 \times 10^{28}$ erg s^{-1}
Gaia BH1	VLA/C band	4–8 GHz	1.98 AU	< 10.2 μJy	$< 1.6 \times 10^{25}$ erg s^{-1}
Gaia BH2	Chandra/ACIS-S	0.5–7 keV	2.47 AU	$< 2.6 \times 10^{-15}$ erg s^{-1}cm^{-2}	$< 4.0 \times 10^{29}$ erg s^{-1}
Gaia BH2	MeerKAT/L band	0.86–1.71 GHz	2.54 AU	< 51 μJy	$< 1.0 \times 10^{26}$ erg s^{-1}

4.3 Theoretical predictions

X-ray Estimates

We first calculate the X-ray luminosity expected if the BHs accrete their companion stars' winds at the Bondi-Hoyle-Littleton (BHL) rate:

$$\dot{M}_{\rm BHL} = \frac{4\pi G^2 M_{\rm BH}^2 \rho}{(v^2 + c_s^2)^{3/2}} = \frac{G^2 M_{\rm BH}^2 \dot{M}_{\rm wind}}{v_{\rm wind}^4 d_{\rm sep}^2} \tag{4.1}$$

where $d_{\rm sep}$ is the separation between the star and BH (which varies as a function of position along the orbit in an elliptical orbit), $M_{\rm BH}$ is the mass of the BH, ρ is the density of accreted material, $\dot{M}_{\rm wind}$ is the mass loss rate of the donor, c_s is the sound speed, v is the relative velocity between the BH and the accreted material, and $v_{\rm wind}$ is the wind speed. We note that the second equality assumes the relative velocity between the BH and accreted material (i.e., the wind speed) greatly exceeds the sound speed. We assume that a fraction η of the accreted rest mass is converted to X-rays, leading to an observable X-ray flux:

$$F_{\rm X,\,BHL} = \frac{\eta \dot{M}_{\rm BHL} c^2}{4\pi d^2} = \frac{G^2 c^2 M_{\rm BH}^2}{4\pi d^2 d_{\rm sep}^2} \frac{\eta \dot{M}_{\rm wind}}{v_{\rm wind}^4} \tag{4.2}$$

where d is the distance to the system from Earth. We are left with an X-ray flux that depends on three unknown physical quantities: $\dot{M}_{\rm wind}$, the mass loss rate of the donor star due to winds, $v_{\rm wind}$, the wind speed, and η, the radiative efficiency of accretion. It is important to note that η may vary with accretion rate, or with other properties of the accretion flow.

The donor star in Gaia BH1 is a main-sequence Sun-like star (G dwarf), while the donor in Gaia BH2 is a lower red giant ($R \sim 8\,R_\odot$). Since the donor in Gaia BH1 closely resembles the Sun, and abundance measurements point to it being $\gtrsim 4$ Gyr old, we adopt a solar mass loss rate: $\dot{M}_{\rm wind} \approx 2 \times 10^{-14} M_\odot {\rm yr}^{-1}$ (Wang, 1998). Gaia BH2, however, hosts a red giant donor star, which has a mass loss rate strongly dependent on stellar properties. We adopt a simple estimate for its mass loss rate from Reimers (1975):

$$\dot{M}_{\rm wind} = 4 \times 10^{-13} \beta_R \left(\frac{L_\star}{L_\odot}\right) \left(\frac{R_\star}{R_\odot}\right) \left(\frac{M_\star}{M_\odot}\right)^{-1} M_\odot \ {\rm yr}^{-1} \tag{4.3}$$

where β_R is a scaling parameter for the mass loss rate. We set $\beta_R = 0.1$, following empirical estimates for red giant branch stars (Reimers, 1975; Choi et al., 2016a).

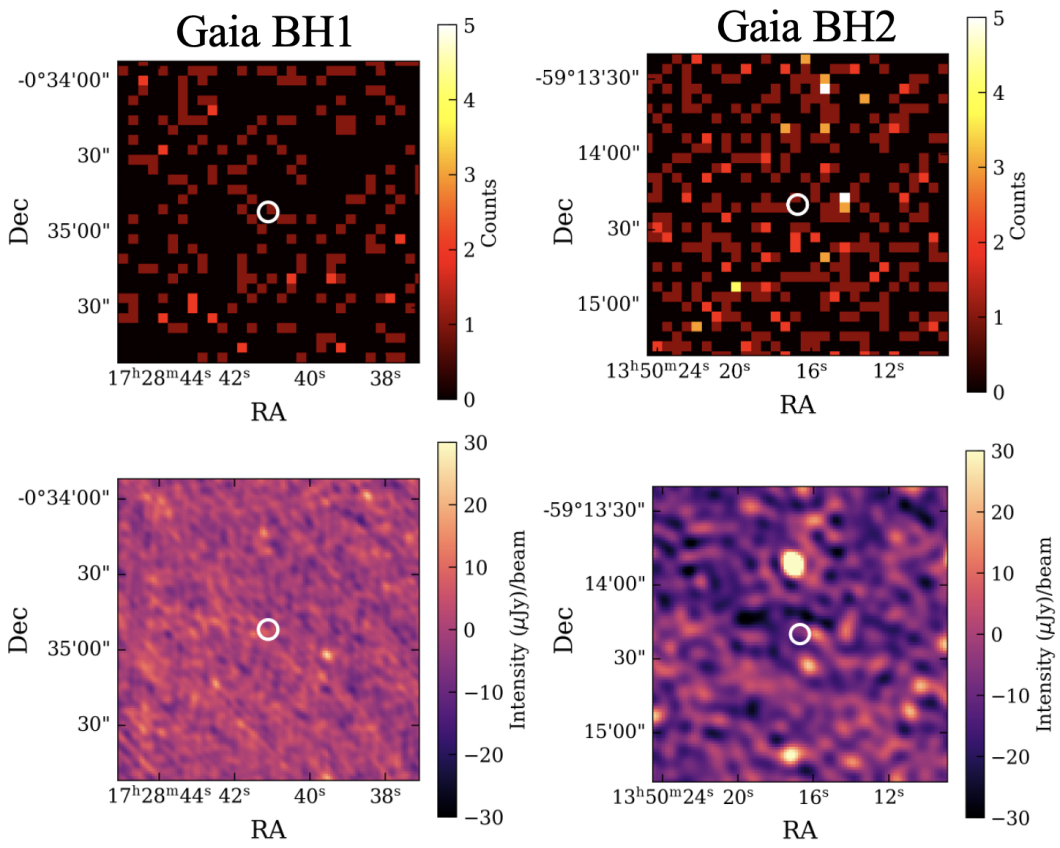

Figure 4.1: Images of Gaia BH1 (left panels) and Gaia BH2 (right panels) in the X-ray (upper panels) and the radio (lower panels). Both sources were observed for ≈ 20 ks with *Chandra*/ACIS-S, corresponding to a flux limit of $\sim 4 \times 10^{-15}$erg s^{-1}cm^{-2}. Gaia BH1 was observed with the VLA for ≈4 hrs, and Gaia BH2 was observed with *MeerKAT* for ≈4 hrs. No significant source of flux is detected at the position of Gaia BH1 or BH2 in either X-rays or radio.

We approximate the wind speed as the escape velocity times a scaling parameter, $\beta_{\rm wind}$:

$$v_{\rm wind} = 600\beta_{\rm wind}\left(\frac{M_\star}{M_\odot}\right)^{1/2}\left(\frac{R_\star}{R_\odot}\right)^{-1/2}\ {\rm km\ s^{-1}} \tag{4.4}$$

We can then write a scaling relation for Equation 4.2, assuming fiducial values for Gaia BH1:

$$\begin{aligned} F_{X,BHL} = 10^{-18}\, erg\, s^{-1}\, cm^{-2}\left(\frac{\eta}{10^{-4}}\right)\left(\frac{M_{BH}}{10\,M_\odot}\right)^2 \times \\ \left(\frac{d_{sep}}{2.03\,AU}\right)^{-2}\left(\frac{d}{480\,pc}\right)^{-2} \times \\ \left(\frac{\dot{M}_{\rm wind}}{2\times10^{-14}M_\odot\ {\rm yr^{-1}}}\right)\times\left(\frac{v_{\rm wind}}{600{\rm km\ s^{-1}}}\right)^{-4} \end{aligned} \tag{4.5}$$

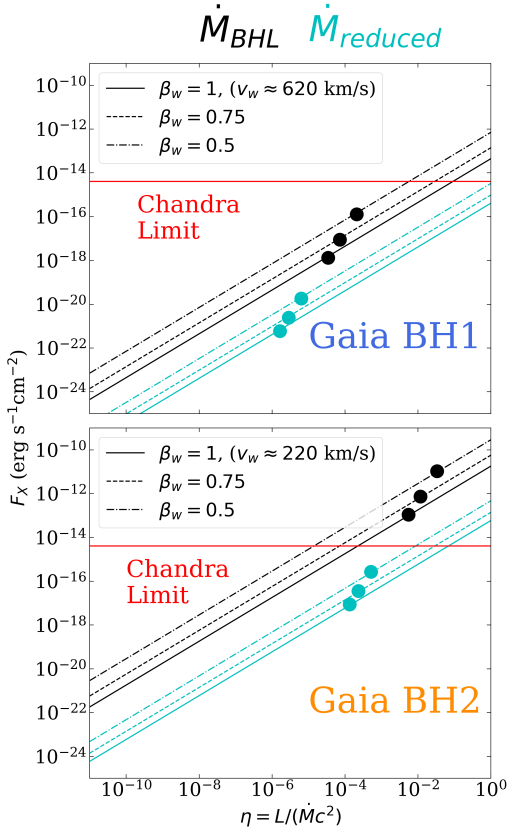

Figure 4.2: For all plausible wind speeds under the assumption of BHL accretion (black lines), *Chandra* should have detected X-rays from Gaia BH1 if the accretion flow were radiatively efficient ($\eta \gtrsim 0.1$; top panel) and from Gaia BH2 if the accretion flow were radiatively *in*efficient down to $\eta \gtrsim 10^{-4}$ (bottom panel). Black dots show expected efficiencies from models of hot accretion flows, but assuming the BHL accretion rate. Neither system is detected in X-rays, due to a combination of reduced accretion rates compared to the BHL assumption (cyan lines), and ensuing lower radiative efficiencies (cyan dots).

and Equations 4.3 and 4.4 can be substituted in for Gaia BH2. We plot the expected X-ray flux from Gaia BH1 and BH2 for a range of possible wind speeds and accretion efficiencies in Figure 4.2.

Figure 4.2 shows that a 20 ks *Chandra* observation should only be able to detect Gaia BH1 if accretion were radiatively efficient ($\eta \gtrsim 0.1$, depending on wind speed). Due to the high wind speed and low mass loss rate, Gaia BH1 is nowhere near its Eddington luminosity and should not experience radiatively efficient accretion. Indeed, no X-rays are detected from Gaia BH1, which supports this prediction.

Because of the much stronger wind expected for Gaia BH2, it should have ap-

proximately 100 times the X-ray flux of Gaia BH1 under the assumption of BHL accretion. This is despite Gaia BH2 being over twice as distant as Gaia BH1. Remarkably, Gaia BH2 would be within the detection threshold of a 20 ks *Chandra* ACIS observation for any values of $\eta_X \gtrsim 10^{-4}$. This also applies for any wind slower than the escape velocity ($\beta_w < 1$), which is to be expected as the wind slows down farther from the star. Figure 4.2 shows that a 20 ks *Chandra* observation should be able to detect Gaia BH2 down to the case of radiatively *in*efficient flow: $\eta \gtrsim 3 \times 10^{-3}$ if the wind speed is the escape velocity and $\eta \gtrsim 10^{-4}$ if the wind slows by the time it escapes from the star and reaches the BH. However, no X-rays were detected from Gaia BH2, indicating that the radiative efficiency is $\eta < 3 \times 10^{-3}$. In Figure 4.2, we show the expected accretion efficiencies (black dots; assuming BHL accretion rates) using the hot accretion flow models of Xie and Yuan (2012), which we will further describe in the following subsection. While these models may not be appropriate for obtaining estimates of accretion efficiency under BHL accretion, the X-ray non-detection of Gaia BH2 shows that reduced *accretion rates*, not just low efficiency at BHL rates, must be invoked to explain this non-detection.

Evidence of Reduced Accretion Rate and Inefficient Accretion in Gaia BH2

The nondetection of X-rays in Gaia BH2 can be explained by going back to Equation 4.5. The two most uncertain parameters in that equation are the accretion rate at the BH event horizon, $\dot{M}$, as well as the accretion efficiency, η. Indeed, the former causes a change in the latter (e.g., Xie and Yuan, 2012). We suggest that in Gaia BH2, the X-ray non-detection is due to $\dot{M}$ being lower than the BHL assumption, which also leads to a lower radiative efficiency. This has been seen in other highly sub-Eddington accreting BHs such as the Milky Way's supermassive BH, Sgr A* (e.g., Yuan et al., 2003), as well as two stellar mass BHs in LMXBs which have been famously well-studied in quiescence: A0620-00 and V404 Cyg (e.g., Narayan et al., 1996, 1997).

In all of these systems, a similar reduction in X-rays is seen, and explained by either advection dominated accretion flows (ADAF), or luminous hot accretion flows (LHAF), both of which fall under the class of hot accretion flows (e.g., Yuan et al., 2012; Xie and Yuan, 2012). Most of the energy dissipated by viscosity is stored as entropy rather than being radiated away (e.g., through X-rays).

Models of hot accretion flows lead to a reduced accretion rate near the BH event horizon, with $\dot{M} \propto r^s$, where $0 < s < 1$. A general description is presented in

Yuan et al. (2012), where it is found that $s \approx 0.5$ and that the accretion rate within $10R_s$ (R_s being the Schwarzschild radius) is approximate constant. This leads to the following reduction to BHL accretion:

$$\dot{M}_{\rm horizon} = \dot{M}_{\rm BHL}\left(\frac{10R_s}{R_{\rm acc}}\right)^{0.5} = \frac{\sqrt{20}v_{\rm wind}}{c}\dot{M}_{\rm BHL} \tag{4.6}$$

where $R_{\rm acc} = GM_{\rm BH}/v_{\rm w}^2$ is the characteristic radius of accretion. In the case of Gaia BH1, this leads to $\dot{M} \approx 0.009\dot{M}_{\rm BHL}$ in Gaia BH1 and $\dot{M} \approx 0.003\dot{M}_{\rm BHL}$ in Gaia BH2.

With a more realistic accretion rate in hand, there is one more correction that we can make, which is to use values of radiative efficiency, η, computed for hot accretion flows by Xie and Yuan (2012). Both accretion rates are highly sub-Eddington: $L_{\rm Edd} = 0.1\dot{M}_{\rm Edd}c^2 \implies \dot{M}_{\rm Edd} \approx 2 \times 10^{-7} M_\odot$ yr^{-1} for both Gaia BH1 and BH2. Gaia BH1 has a predicted accretion rate at the horizon of $\dot{M} \approx 0.009\dot{M}_{\rm BHL} \approx 5 \times 10^{-12}\dot{M}_{\rm Edd}$ and Gaia BH2 has an accretion rate of $\dot{M} \approx 0.003\dot{M}_{\rm BHL} \approx 5\times10^{-9}\dot{M}_{\rm Edd}$. The same fitting equation is appropriate for both systems:

$$\eta \approx 1.58\left(100 \times \frac{\dot{M}}{\dot{M}_{\rm Edd}}\right)^{0.65} \tag{4.7}$$

which leads to $\eta \approx 10^{-6} - 10^{-5}$ for Gaia BH1 and $\eta \approx 10^{-4} - 10^{-3}$ for Gaia BH2 (cyan dots in Figure 4.2).

Finally, by substituting both (1) the reduced accretion rate and (2) the corresponding radiative efficiency into Equation 4.5, we obtain X-ray flux estimates of Gaia BH1 and BH2 to be $10^{-22} - 10^{-20}\, erg\, s^{-1}\, cm^{-2}$ and $10^{-18} - 10^{-16}\, erg\, s^{-1}\, cm^{-2}$, respectively, which we show with cyan curves in Figure 4.2. This places both systems well under the *Chandra* detection limit, but may be within the limits of future missions.

Radio Estimates

The empirical Fundamental Plane of black hole activity relates X-ray luminosity, radio luminosity and BH mass of Galactic black holes and their supermassive analogues (Plotkin et al., 2012). By placing BHs on the Fundamental Plane, the physical process behind BH X-ray and radio emission can be understood. We reproduce the most current compilation of hard state Galactic BHs with measured X-ray and radio luminosities (Bahramian et al., 2018; Plotkin et al., 2021) with upper limits of Gaia BH1 and BH2 overplotted in Figure 4.3. There is a minor correction to convert to the same X-ray energy ranges and radio frequency ranges, which we

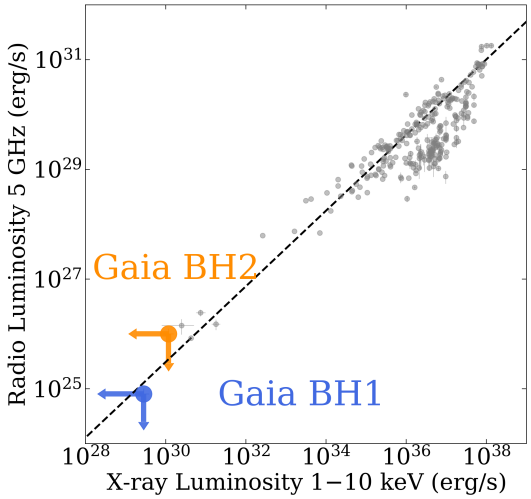

Figure 4.3: Gaia BH1 and BH2 could lie on the BH "Fundamental Plane". In gray are all measurements of hard state galactic BHs. The dotted line shows the BH fundamental plane from Plotkin et al. (2012) for 10 $M_\odot$ BHs.

omit since it is of order unity. We plot a dotted line to represent the Fundamental Plane for $10M_\odot$ BHs, and note that BH masses have been estimated (with a $\sim$ 1 dex uncertainty) from X-ray and radio luminosities (e.g., Gültekin et al., 2019).

If we assume that the Fundamental Plane holds for our systems, and our assumptions of reduced accretion rate and inefficient accretion flow, we can calculate the expected radio luminosities/fluxes: $\sim 10^{21}$erg s^{-1}/ $\sim$ 1 nJy at 5 GHz (BH1) and $\sim 10^{23}$erg s^{-1}/ $\sim$ 10 nJy at 5 GHz (BH2). These radio flux densities are well under the projections for future facilities such as the Next Generation Very Large Array (ngVLA; Murphy et al., 2018). Other works, however, have focused on the radio regime and outlined the prospects of detecting isolated BHs in radio surveys, which strongly depends on the Fundamental Plane ($L_X - L_r-$mass relation) for radio luminosity calculations (e.g., Maccarone, 2005; Fender et al., 2013). We therefore proceed with a discussion of finding BHs solely in the X-ray.

4.4 Implications for X-ray Searches of BHs

If no X-ray or radio signatures of accretion are seen from targeted observations of the two nearest known BHs, then what can we expect from blind searches? In the following subsections, we explore the prospects of detecting in the X-ray, (1) wind-accreting BHs in binary systems similar to Gaia BH2, and (2) isolated BHs accreting from the ISM. While other studies have done similar computations in the past (e.g., Agol and Kamionkowski, 2002), we incorporate the modern models of

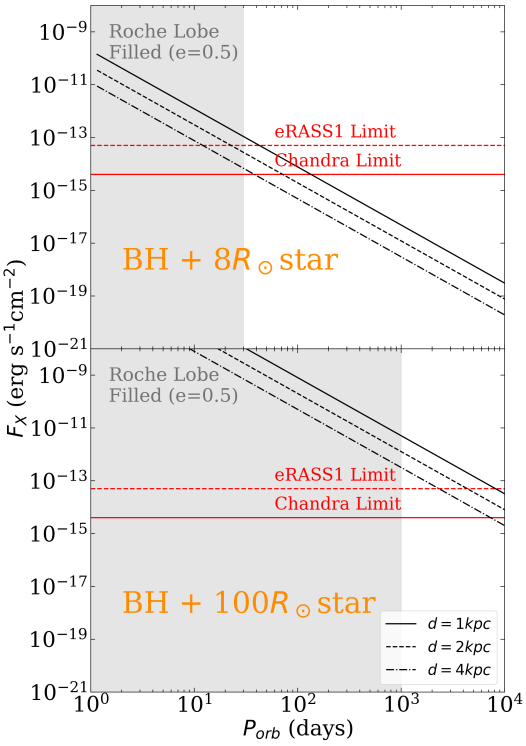

Figure 4.4: Even if Gaia BH2-like system had a shorter orbital period, it would not be detectable in X-rays before filling its Roche lobe (gray shaded area; *upper panel*). A BH in a binary with a tip of the red giant branch star ($R_* \sim 100R_\odot$) can be bright enough in X-rays for the system to be detectable before the star fills its Roche lobe ($P_{\rm orb} \approx 10^3 - 10^4$ days; *bottom panel*).

inefficient accretion flow and reduced accretion rates (compared to BHL) which we used to explain the X-ray non-detection of Gaia BH2.

Wind Accreting BHs in Binaries

Are wind-accreting binaries like Gaia BH2 detectable by current X-ray missions? From Equations 4.3, 4.4 and 4.5, it is clear that systems with (1) a closer separation or (2) a star with a larger radius will lead to a larger X-ray luminosity.

Since sun-like stars that ascend the red giant branch keep their temperatures roughly constant but swell up to $\sim 100R_\odot$, one could expect systems like this to be strong X-ray emitters. In Figure 4.4, we show the prospects of finding systems similar to Gaia BH2 from X-ray searches alone. We use Equations 4.4 and 4.3, to calculate wind speeds and mass loss rates, and Equations 4.6 and 4.7 to calculate efficiency and reduced accretion rate corrections from hot accretion flows, as we did for Gaia BH2. In the top panel of Figure 4.4, we plot the X-ray flux as a function of orbital

period for a system with all other parameters the same as Gaia BH2 ($M_{\rm BH} = 9M_\odot$, $R_* = 8R_\odot$, $e = 0.5$, $d = 1.16$ kpc), and observed at periastron.

Even if a Gaia BH2-like system (i.e., a BH and an $8R_\odot$ giant) were in a shorter period orbit, it would not be detectable before filling its Roche lobe ($P_{\rm orb} \approx 30$ days). At this point, an accretion disk could form, which could lead to higher radiative efficiency and/or outbursts that could lead to the system being more easily detectable in X-rays. Such calculations are the subject of Section 4.5, where we explore the prospects of detecting systems similar to Gaia BH1 and BH2 when filling their Roche lobes.

In the bottom panel of Figure 4.4, we plot the X-ray flux as a function of orbital period for a system that could resemble what Gaia BH2 will look like in 100 Myr, when the red giant reaches the tip of the red giant branch ($M_{\rm BH} = 9M_\odot$, $R_* = 100R_\odot$, $e = 0.5$). We plot the X-ray flux for a system at 1, 2, and 4 kpc. Such a system would fill its Roche lobe at $P_{\rm orb} \sim 10^3$ days, but systems in the range of $P_{\rm orb} \sim 10^3 - 10^4$ days are detectable by *Chandra* out to a few kpc, depending on the exact orbital period. In Figure 4.4 and following figures, we adopt a *Chandra* flux limit of 4×10^{-15}erg s^{-1}cm^{-2}, approximately corresponding to the 90% flux limits presented in this paper in a 20 ks exposure, We also show a flux limit of 5×10^{-14}erg s^{-1}cm^{-2} from a single all-sky scan of the SRG/eROSITA mission — eRASS1 is the name of the first all sky scan, though co-adds of multiple scans go deeper (Sunyaev et al., 2021; Predehl et al., 2021a). This means that wind-accreting BHs in binaries could be detectable in X-rays before the donor stars fill their Roche lobes. However, this is only the case for appreciable eccentricities $e \gtrsim 0.5$. Circular orbits (as might be more likely for $R_* \sim 100R_\odot$ donors due to tidal circularization), would lead to a 75% decease in flux, pushing the limits of *Chandra*.

BHs Accreting from the ISM

We compute the observed X-ray flux from a BH accreting from the ISM. This could be either an isolated BH or a BH in a binary or higher-order system, as long as it is accreting from the ISM. Previous works assumed a BHL accretion rate (e.g., Agol and Kamionkowski, 2002), whereas we use the corrected accretion rates and efficiencies from Yuan et al. (2012) and Xie and Yuan (2012), respectively, as supported by the non-detection of Gaia BH2.

The ISM is made up of at least 5 phases, ordered from most to least dense: gravitationally bound giant molecular clouds (GMCs) made up of molecular hydrogen, diffuse H_2 regions, the cold neutral medium (CNM), warm neutral medium (WNM),

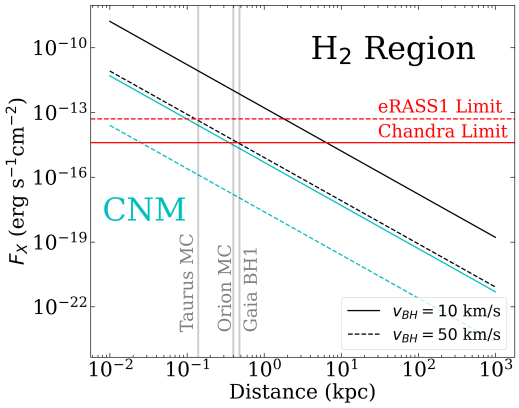

Figure 4.5: A BH accreting from the ISM in an H_2 region is detectable by current X-ray missions out to a few kpc. However, given that the nearest BH, Gaia BH1, is 480 pc away, it is unlikely to find BHs much nearer than that. With that in mind, the plot above shows that the prospects for detecting BHs accreting from the CNM or any lower density ISM phase are slim to none with current capabilities.

and warm ionized medium (WIM) (e.g., Draine, 2011). All phases of the ISM have been found to be roughly in pressure equilibrium (i.e., $\rho \times T \sim$ constant; though with a $\sim$ 1 dex spread). Given that sound speed in a medium is proportional to the square root of temperature: $c_s \propto \sqrt{T}$, from Equation 4.1, it is already clear that ISM-accreting BHs will be more X-ray bright when passing through the densest regions of the ISM.

We calculate the expected X-ray flux due to a BH accreting from an H_2 region ($\overline{n} \approx 10^3$ cm^{-3}, $T \approx 30$ K) and from the CNM ($\overline{n} \approx 30$ cm^{-3}, $T \approx 100$ K). We take $\rho = m_p n$ and calculate the sound speed as $c_s = \sqrt{k_B T / m_p}$. We then use the left hand sides of Equations 4.1 and 4.2 and additionally incorporate the hot accretion flow corrections to the accretion rate (Equation 4.6) and accretion efficiency (Equation 4.7).

We plot the X-ray flux as a function of distance for a BH accreting from the ISM in Figure 4.5. We present curves for a BH accreting from an H_2 region and the CNM, for BH space velocities of 5 km/s and 50 km/s. We do not plot curves for higher velocities since the flux levels are reduced dramatically. In other words, isolated BHs with space velocities that exceed 50 km/s are virtually impossible to detect by current X-ray capabilities. While a few isolated BHs within 100 pc may be detectable as faint X-ray sources, it would be difficult to distinguish them from other astrophysical sources at larger distances.

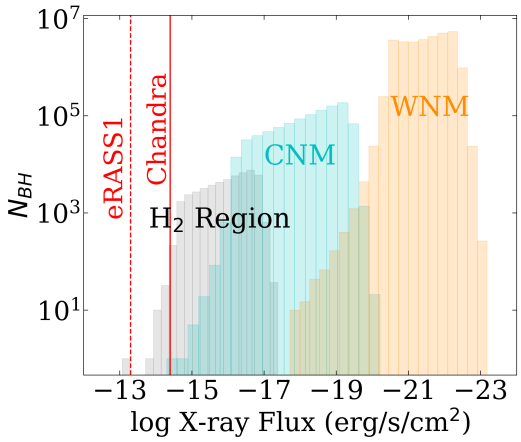

Figure 4.6: A simple model assuming a distribution of 10^8 stellar-mass BHs passing through the various phases of the ISM in the Milky Way show that the most X-ray bright will be those passing through low density H_2 regions. However, even generous model assumptions suggest that the chances of detecting BHs accreting from the ISM are unlikely after adopting models of hot accretion flows.

Figure 4.5 shows that a *very* slow-moving BH (v = 10 km/s) can be detectable if passing through a high-density H_2 region. Such systems are detectable out to $\sim$ 2 kpc in eRASS1, and $\sim$ 5 kpc in a 20 ks *Chandra* pointing. We note that Figure 4.5 makes the prospects of finding such systems deceptively promising, given the low volume filling factors of H_2 regions. Furthermore, the high column density of hydrogen in H_2 regions is likely to reduce the flux by an appreciable amount, further challenging the prospects of detection.

Given the above calculations for single systems, how many ISM-accreting BHs can be found in the Milky Way? From Equation 4.1 and Figure 4.5, it is clear that that $\dot{M}_{\rm BHL} \propto v_{BH}^{-3}$ scaling relation makes the X-ray flux of BHs dramatically decrease given a slight increase in BH space velocity. Currently, the velocity distribution of BHs in binaries is unknown, both due to low-number statistics (only $\sim$ 20 systems are dynamically confirmed) (Corral-Santana et al., 2016; Atri et al., 2019; Zhao et al., 2023) and due to selection effects in samples of detectable BHs. It is still uncertain if BHs are born with kicks (e.g., Stevenson, 2022; Kimball et al., 2023). Furthermore, because there are only a few known BHs in wide binaries and one candidate isolated BH from microlensing, we must assume a velocity distribution.

To investigate an optimistic scenario, we assume the space velocity of ISM-accreting BHs is uniformly distributed between 10 and 50 km/s. We assume that 10^8 BHs are distributed axisymmetrically throughout the Milky Way, exponentially in cylin-

drical (h, s, ϕ are vertical, radial, and azimuthal coordinates, respectively) h and s coordinates with characterstic scales of 410 pc and 1 kpc, respectively (e.g., van Paradijs and White, 1995). We then use the filling factor of each component of the ISM (H_2 region: 0.05%, CNM: 1%, WMN: 30%) to calculate the total number of BHs passing through each region (e.g., Draine, 2011). We present the resulting distributions in Figure 4.6. Based on those results, virtually no ISM-accreting BHs are detectable in eRASS1, but ~ 10 could be detectable in 20 ks *Chandra* observations of *all* H_2 regions. However, this number is almost certainly inflated due to the effects of a high column density in H_2 regions and our uncertain assumptions on the BH velocity distribution. It appears improbable to detect X-rays from ISM-accreting BHs passing through the CNM or WMN, given current capabilities.

Comparison with Previous Work

Previous analyses have been done to estimate the detectability of isolated NSs or BHs accreting from the ISM in the X-ray and/or radio. An early study by Agol and Kamionkowski (2002) projected that all-sky X-ray surveys with the depth of *Chandra* should detect thousands of isolated BHs. That study, however, operated under the assumption of Bondi accretion, which we have shown is insufficient. Work by Perna et al. (2003) arrived at the same conclusion when calculating the number of isolated NSs detectable by the *ROSAT* all-sky X-ray survey. As mentioned earlier, works focused on the radio regime strongly rely on the Fundamental Plane ($L_X - L_r-$mass relation) for radio luminosity calculations, and initially predicted that $\sim 10^2$ isolated BHs could be found in the LOFAR survey (Maccarone, 2005). However, the more recent work of Fender et al. (2013) found this number to be overestimated and that only systems with high accretion efficiencies could be detectable by the upcoming Square Kilometre Array (SKA) radio survey (we note that SKA will have a depth of $\sim 1\mu$Jy (Dewdney et al., 2009), while we estimate that both Gaia BH1 and BH2 have flux densities of 1–10 nJy, as mentioned earlier).

Finally, we note that the recent study by Paduano et al. (2022) undertook an X-ray and radio survey of the globular cluster NGC 3201, where BHs in wide orbits similar to Gaia BH1 and BH2 have been found (NGC 3201 #12560 in a wide, 166 day orbit; NGC 3201 #21859 in a much smaller 2.2 day orbit) (Giesers et al., 2018a, 2019). Crucially, we note that NGC 3201 #21859 is reported to be only a *candidate BH system*. They placed both systems on the Fundamental Plane, finding their upper limits to be in agreement. Most importantly, they found upper limits on the accretion efficiency of both systems. NGC 3201 #12560 has an upper limit of

$\eta < 0.65$, meaning that our efficiency limits are much deeper. The efficiency limits on NGC 3201 #21859 are much deeper: $\eta < 1.5 \times 10^{-5}$. This means that if that system is indeed a BH system, the efficiency upper limit of Paduano et al. (2022) is consistent with our estimated values for Gaia BH1, which has a main sequence donor star most similar to that in NGC 3201 #21859. In summary, our work shows that due to a combination of reduced accretion rate and radiative efficiency, the chances of detecting ISM- or stellar wind-accreting BHs in blind searches is low, in agreement with recent findings.

4.5 Future evolution of Gaia Black Holes and Detection as Symbiotic BH XRBs

We use the expected future evolution of Gaia BH1 and BH2 to understand how common these systems could be in the Milky Way. The discovery paper of Gaia BH1 used the properties of the Gaia DR3 astrometric sample to infer that $\sim 40,000$ BH1-like systems should exist (El-Badry et al., 2023b). To constrain the population size, we take a different approach and evolve the Gaia BH1 and BH2 systems using Modules for Experiments in Stellar Astrophysics (MESA; Paxton et al., 2011, 2013, 2015, 2018). The donor star in Gaia BH1 will become a red giant in a few Gyr, and will ultimately fill its Roche lobe near the tip of the first giant branch. The donor star in Gaia BH2 is already a red giant, and will swell enough to fill its Roche lobe in ~ 100 Myr at the tip of the asymptotic giant branch (AGB). We show their locations in the HR diagram today and during RLOF in Figure 4.7. We look for the timescales in their evolution when the systems could be visible as symbiotic BH XRBs (i.e., a BH accreting from a red giant filling or nearly filling its Roche lobe).

In the top panels of Figure 4.8, we show the BH mass loss rates ($\dot{M}$) of the donor star in the Gaia BH1 and BH2 systems for approximately 500 Myr and 10 Myr before Roche lobe overflow (RLOF), respectively. The bottom panels of Figure 4.8 zoom in and show where RLOF begins. Before RLOF, wind accretion takes place. For low mass loss rates ($\dot{M} \lesssim 10^{-2} \dot{M}_{\rm Edd,\,BH}$), the BH accretion rate could be much lower than the donor mass loss rate (as we explain through most of this paper). However, for mass loss rates that approach the Eddington accretion rate of the BH and certainly during RLOF, the two should be nearly equal (e.g., Ritter, 1988). It is also worth noting that after RLOF, the donor star will have been stripped of its atmosphere, and the orbit of both systems will expand. The orbital period will increase from 186 days to ≈850 days in Gaia BH1 and from 1277 days to ≈2000 days in Gaia BH2.

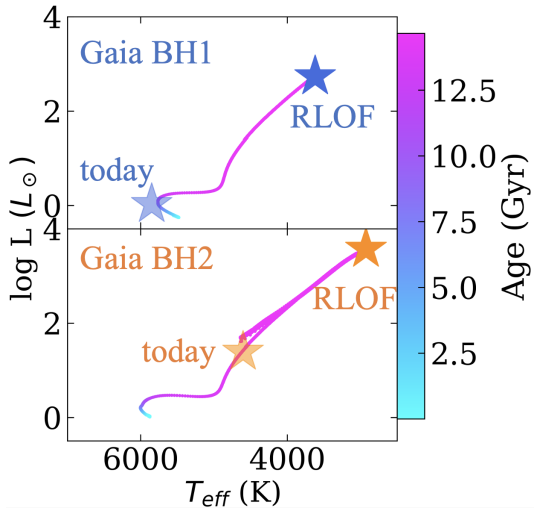

Figure 4.7: Gaia BH1 will fill its Roche lobe near the tip of its first giant branch in a few Gyr. Gaia BH2 will do so near the tip of the AGB in ~ 100 Myr. Leading up to this stage, both systems will likely be detectable as symbiotic BH XRBs, yet no such systems have been confirmed to date.

In the top panels of Figure 4.8, we then shade the region where the accretion rate exceeds $10^{-2}\dot{M}_{\rm Edd}$, where we expect the accretion rate is high enough to lead to frequent outbursts, or a persistent state of high luminosity, that could be observed by all-sky X-ray monitors. This accretion rate corresponds to the X-ray lumionsities at which both currently known symbiotic XRBs (albeit with neutron star accretors) have been seen to outburst (e.g., Kuranov and Postnov, 2015; Yungelson et al., 2019b). We define the timescale during which the Gaia BH systems are seen as symbiotic XRBs as $\tau_{\rm SymXRB}$, which in Gaia BH1 lasts $\approx$ 50 Myr and in Gaia BH2 lasts $\approx$ 2 Myr. X-ray monitors such as the *Swift* Burst Alert Trigger (BAT) (Burrows et al., 2005) and MAXI (Matsuoka et al., 2009) have similar sensitivities of ~100 mCrab (10^{-9}erg s^{-1}cm^{-2}) for ~min long exposures. This means that these monitors are sensitive to essentially all $L_X \sim L_{\rm Edd}$ outbursts in the Galaxy, and sensitive to outbursts $L_X \gtrsim 10^{-2}L_{\rm Edd}$ out to a few kpc.

Both Gaia BH1 and BH2 undergo a very short phase where $\dot{M} \gtrsim \dot{M}_{\rm Edd}$ (Gaia BH1 exceeds $\dot{M}_{\rm Edd}$ by a factor of 10, while BH2 reaches factors of $10^2 - 10^3$). Centaurus X-3 is an example of such a system, where extended periods of low X-ray flux have been observed in a pulsar high mass X-ray binary accreting near the Eddington rate. It has been postulated that at the highest accretion rates, matter gathers at the innermost regions of the accretion disk and absorbs the X-rays, leading to extended lows (Schreier et al., 1976). However, this system is still X-ray bright for the majority

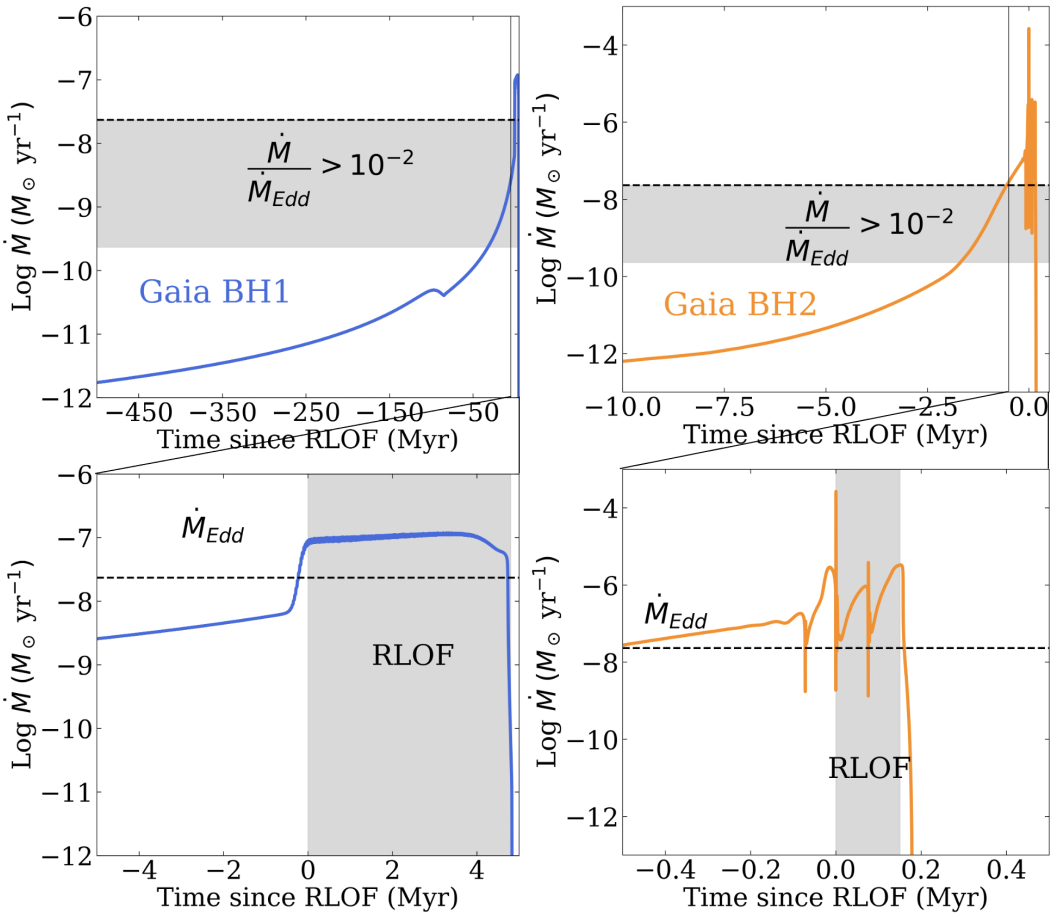

Figure 4.8: MESA models around the time when the donors fill their Roche lobes show that Gaia BH1 will be visible as a symbiotic BH XRB for ≈50 Myr, while $\dot{M} > 10^{-2}\dot{M}_{\rm Edd}$ (upper left) and for ≈5 Myr, while $\dot{M} \sim \dot{M}_{\rm Edd}$ (lower left). Gaia BH2 will be visible as a symbiotic BH XRB for ≈2 Myr, while $\dot{M} > 10^{-2}\dot{M}_{\rm Edd}$ (upper right) and for ≈0.2 Myr, while $\dot{M} \sim \dot{M}_{\rm Edd}$ (lower right). Because no such systems have been discovered through X-ray outbursts, there should be at most $\sim 10^4$ Gaia BH1-like systems in the Milky Way, unless outburst timescales of such systems have been underestimated.

of the time and detectable by all-sky X-ray monitors. Our models show that Gaia BH1 will be in such a phase for $\sim$ 5 Myr, and BH2 for $\sim$ 0.2 Myr. In both cases, this phase lasts for ≈10% the duration of the evolution when the systems are in the symbiotic XRB phase (i.e., accretion is sub-Eddington and is due to winds rather than Roche lobe overflow).

In order to estimate an upper limit on the number of similar systems in the Milky Way, we assume a detection efficiency, $\varepsilon_{\rm detect}$, for all-sky X-ray monitors and take the lifetime of $\sim 1 M_\odot$ stars divided by the time during which these systems are

visible as symbiotic BH XRBs:

$$N_{\rm BH} \sim \frac{\tau_{\rm stars}}{\varepsilon_{\rm detect}\tau_{\rm SymXRB}}$$
$$N_{\rm BH1} \approx 2\times10^{2}/\varepsilon_{\rm detect}, \quad N_{\rm BH2} \approx 5\times10^{3}/\varepsilon_{\rm detect} \tag{4.8}$$

In the case where we use the short-lived phase where the donors are Roche lobe overflowing, the above becomes:

$$N_{\rm BH} \sim \frac{\tau_{\rm stars}}{\varepsilon_{\rm detect}\tau_{\rm RLOF}}$$
$$N_{\rm BH1} \approx 2\times10^{3}/\varepsilon_{\rm detect}, \quad N_{\rm BH2} \approx 5\times10^{4}/\varepsilon_{\rm detect} \tag{4.9}$$

During the last ~50 years, all-sky X-ray surveys have been sensitive to X-ray outbursts from such systems, but no symbiotic BH XRBs have been discovered. From *Uhuru* (Forman et al., 1978) to MAXI, it is highly unlikely that the brightest X-ray outbursts have been missed. From Equation 4.9, even if we assume a 10% efficiency ($\varepsilon_{\rm detect} = 0.1$) of all-sky X-ray monitors in detecting such systems, this places Gaia BH1-like systems at $N \lesssim 2\times10^{3}$ and BH2-like systems at $N \lesssim 2\times10^{4}$ in our galaxy. If we assume that systems are only detectable during RLOF, the corresponding limits are $N \lesssim 2\times10^{4}$ and $N \lesssim 2\times10^{5}$.

There is at least one candidate symbiotic XRB proposed to host a BH, IGR J17454-2919 (Paizis et al., 2015). The most accurate *Chandra* localization of the X-ray source coincides with a red giant (K- to M-type), while the X-ray outburst properties of the system do not securely point to either a NS or BH accretor. Ongoing work is being conducted to determine the nature of this system. A handful of symbiotic XRBs hosting NSs have been detected as X-ray sources even though the donors have not yet overflowed their Roche lobes (e.g., Hinkle et al., 2006; Masetti et al., 2007; Bozzo et al., 2018; Hinkle et al., 2019; De et al., 2022). That being said, the radiative efficiencies of accreting NSs are likely to be larger than those of BHs (e.g., Garcia et al., 2001b), and the accretion rate above which BH symbiotic XRTs are likely to be recognized as such is uncertain.

4.6 Discussion and conclusions

We have analyzed X-ray and radio observations of the two nearest known BHs: Gaia BH1 and BH2. For both sources, we only detect upper limits in both the X-ray and radio. Due to the relatively strong, low-velocity winds from the red giant in Gaia BH2, BHL accretion predicts that we should have seen X-rays from the system.

We interpret our non-detection as a sign of reduced accretion rates as seen in hot accretion flows, and an ensuing lower radiative efficiency than predicted by BHL accretion. We found that these hot accretion flow corrections lead to X-ray (and radio) fluxes well below the limit of current facilities.

We then used the corrected accretion rates and efficiencies to compute the observed flux from a BH accreting from a $R_* \sim 100 R_\odot$ red giant (i.e., what Gaia BH2 will become in 100 Myr). We found that a relatively nearby system ($d \lesssim 4$ kpc) of that type could be detectable in X-rays *before* filling its Roche lobe.

We then extended our calculations to wind-accreting BHs passing through the ISM. We found that the only plausible scenario for detecting such a system would be to have a very slowly moving ($v \lesssim 10$ km/s) BH passing through a dense ($n \gtrsim 10^3$ cm^{-3}) H_2 region. Current technologies rule out the possibility of detecting an ISM-accreting BH passing through the CNM or any lower density phase of the ISM, even with generous assumptions about BH velocity and the population distribution.

Finally, we produced MESA models of the future evolution of Gaia BH1 and BH2. We predict that the accretion rate in Gaia BH1 will be high enough ($\dot{M} \sim 10^{-2} \dot{M}_{\rm Edd}$) for the system to be visible as a symbiotic BH XRB for ≈ 50 Myr. The same will be true for Gaia BH2, but only for ≈ 2 Myr. Although the symbiotic BH XRB phase is a relatively short-lived phase in the evolution of these systems, the effective search volume for X-ray bright systems is large. Because all-sky X-ray monitors have been sensitive to X-ray outbursts in a large part of the Galaxy for the last ≈ 50 yrs, the lack of detected symbiotic BH XRBs would seem to imply an upper limit on the number of Gaia BH1-like systems at $N \lesssim 10^3$ (10^4 assuming 10% detection efficiency), assuming BH + giant systems could be detected anywhere in the galaxy when the BH accretes at a rate $\dot{M} > 10^{-2} \dot{M}_{\rm Edd}$.

This limit is somewhat puzzling. El-Badry et al. (2023b) estimated that the effective search volume for Gaia BH1-like systems in Gaia DR3 was only $\sim 3 \times 10^6$ stars, which would seem to suggest that $> 10^4$ similar systems should exist in the Milky Way. There are several possible explanations for these apparently inconsistent limits. One is that symbiotic BH XRBs have already been detected by X-ray surveys but have not been recognized as such. This seems plausible particularly for wind-accretion systems, which may not form disks and undergo outbursts. Such systems would appear as relatively faint X-ray sources coincident with red giants. Many such sources exist in the Galactic plane and have never been studied in detail. These consideration suggest that radial velocity follow-up of giants coincident with X-ray

sources may be a promising search strategy for symbiotic BH XRBs.

Another possibility is that the detection efficiency of symbiotic BH XRBs is simply very low. This could be the case if they have unstable disks with very long outburst recurrence timescales, as has indeed been proposed (e.g., Deegan et al., 2009). Furthermore, reddening and crowding in the Galactic plane have been suggested to bias the observed BH population in low-mass XRBs (e.g., Jonker et al., 2021), which could have an effect on the observability of symbiotic BH XRBs if they were predominantly located there.

The next few years show promise for the discovery of many more BH binaries: SRG/eROSITA in X-rays, *Gaia* through optical astrometry, and the Rubin Legacy Survey of Space and Time (LSST) through optical photometry. X-ray and radio detections (and non-detections) of future systems will provide new clues regarding the nature of accretion around BHs in a wide range of astrophysical scenarios.

4.7 Acknowledgements

We thank Tim Cunningham for a useful discussion on optimal reduction of *Chandra* data. We are grateful to the *Chandra*, VLA, and MeerKAT directorial offices and support staff for prompt assistance with DDT observations. The MeerKAT telescope is operated by the South African Radio Astronomy Observatory, which is a facility of the National Research Foundation, an agency of the Department of Science and Innovation. We thank the referee for useful input that led to an improved final manuscript.

ACR acknowledges support from an NSF Graduate Research Fellowship. ACR thanks the LSSTC Data Science Fellowship Program, which is funded by LSSTC, NSF Cybertraining Grant #1829740, the Brinson Foundation, and the Moore Foundation; his participation in the program has benefited this work. KE was supported in part by NSF grant AST-2307232.

Chapter 5

FROM ACTIVE STARS TO BLACK HOLES: A DISCOVERY TOOL FOR GALACTIC X-RAY SOURCES

Antonio C. Rodriguez. From Active Stars to Black Holes: A Discovery Tool for Galactic X-Ray Sources. *Publications of the Astronomical Society of the Pacific*, 136(5):054201, May 2024. doi: 10.1088/1538-3873/ad357c.

Author List

Antonio C. Rodriguez[1,*]

[1]Department of Astronomy, California Institute of Technology, 1200 E. California Blvd, Pasadena, CA 91125, USA

[*]Corresponding author: acrodrig@caltech.edu

ABSTRACT

Galactic X-ray sources are diverse, ranging from active M dwarfs to compact object binaries, and everything in between. The X-ray landscape of today is rich, with point source catalogs such as those from *XMM-Newton*, *Chandra*, and *Swift*, each with $\gtrsim 10^5$ sources and growing. Furthermore, X-ray astronomy is on the verge of being transformed through data releases from the all-sky SRG/eROSITA survey. Many X-ray sources can be associated with an optical counterpart, which in the era of *Gaia*, can be determined to be Galactic or extragalactic through parallax and proper motion information. Here, I present a simple diagram — the "X-ray Main Sequence", which distinguishes between compact objects and active stars based on their optical color and X-ray-to-optical flux ratio ($F_X/F_{\rm opt}$). As a proof of concept, I present optical spectroscopy of six exotic accreting WDs discovered using the X-ray Main Sequence as applied to the *XMM-Newton* catalog. Looking ahead to surveys of the near future, I additionally present SDSS-V optical spectroscopy of new systems discovered using the X-ray Main Sequence as applied to the SRG/eROSITA eFEDS catalog.

5.1 Introduction

The discovery and characterization of Galactic X-ray sources in the last sixty years opened a new window to the sky and created the field of high energy astrophysics. X-ray observations of M dwarfs, the most common stars in the Milky Way and most common hosts to exoplanets, revealed that these stars are commonly coronally active (e.g., X-rays were detected from 87% of M and K dwarfs within 7 pc of the Sun by Schmitt et al., 1995). X-ray astronomy has also led to the discovery of all of the known accreting neutron star[1] (NS) systems and nearly all stellar-mass black hole (BH) systems (Tauris and van den Heuvel, 2023), informing our understanding of the most extreme physical environments that cannot be replicated on Earth.

However, it often takes multiwavelength information to decipher the true nature of X-ray sources. Famously, the first stellar-mass black hole in the Milky Way, Cygnus X-1, was initially discovered through an X-ray sounding rocket in 1964 (Bowyer et al., 1965). However, it remained uncharacterized for over half a decade until an optical (and radio) source was associated with the X-ray position in 1971 (Murdin and Webster, 1971; Braes and Miley, 1971). Precise radial velocity measurements of the optically bright star at the position of Cygnus X-1 were the only way to securely establish that it was a binary companion to a stellar-mass black hole (Webster and Murdin, 1972; Bolton, 1972).

It is with the goal of combining X-ray + optical data to characterize Galactic astrophysical sources that I write this paper. In the days of Cygnus X-1, large error boxes associated with X-ray sources made it difficult to make multiwavelength associations. The pioneering Roentgensatellit X-ray mission (ROSAT; Truemper, 1982; Voges et al., 1999a; Boller et al., 2016c) was the first to image the entire sky with sub-arcminute resolution[2], and discovered nearly 135,000 X-ray point sources with error circles of radii $\lesssim$ 40" (e.g., Agüeros et al., 2009). However, association with optical sources at that resolution is still difficult, and X-ray + optical association of ROSAT sources in the Galactic plane is nearly impossible (e.g., Salvato et al., 2018).

Today, the landscape of X-ray astronomy is very different. Point source catalogs from X-ray missions that have been active for over 20 years each contain $\gtrsim 10^5$ point sources and have ~few arcsecond localizations (θ): *XMM-Newton* 4XMM-DR13

[1] Radio astronomy has, of course, contributed significantly to our knowledge of neutron stars as well.

[2] Though the High Energy Astrophysical Observatory-2 (HEAO-2), also known as the (*Einstein Observatory;* Giacconi et al., 1979) was the first to image the X-ray sky with 2" resolution, it did not conduct an all-sky survey.

Catalogue (600,000 sources, $\theta \sim 3$"; Webb et al., 2020), Second *Chandra* Source Catalog (350,000 sources, $\theta \sim 2$"; Evans and Civano, 2018), *Swift*/XRT Point Source Catalog (300,000 sources, $\theta \sim 5$"; Evans et al., 2020b). X-ray astronomy is on the verge of being transformed through data releases from the all-sky SRG/eROSITA survey, with millions of X-ray sources localized to a few arcseconds (Predehl et al., 2021b; Sunyaev et al., 2021).

The landscape of optical astronomy is also very different, with precise astrometry from *Gaia* enabling the distinction between Galactic and extra sources (Gaia Collaboration et al., 2016). Large-scale time-domain photometric surveys such as the Zwicky Transient Facility (ZTF; Bellm et al., 2019b), Transiting Exoplanet Survey Satellite (TESS; Ricker et al., 2015), All Sky Automated Survey for Supernovae (ASAS-SN; Kochanek et al., 2017), and Asteroid Terrestrial-impact Last Alert System (ATLAS; Tonry et al., 2018a) provide variability information and add a new dimension to optical datasets. Optical astronomy is also on the verge of transformation thanks to the Rubin Observatory Legacy Survey of Space and Time (LSST), which will obtain photometry for nearly an order of magnitude more sources than current time-domain optical surveys (e.g., Ivezic et al., 2019a). Just as revolutionary are the multiplexed optical spectroscopic surveys. Millions of spectra are already in the catalog of the Sloan Digital Sky Survey (SDSS; York et al., 2000a), and SDSS-V is rapidly increasing that number as well as bringing the advent of multiplex time-domain spectroscopy (Kollmeier et al., 2017). Other surveys include the Dark Energy Spectroscopic Instrument (DESI; DESI Collaboration et al., 2016), the 4-metre Multi-Object Spectrograph Telescope (4MOST; de Jong et al., 2019), and the William Herschel Telescope Enhanced Area Velocity Explorer (WEAVE; Dalton et al., 2012).

In this paper, I crossmatch the *XMM-Newton* 4XMM-DR13 point source catalog and the SRG/eROSITA eFEDS catalog with *Gaia* to just select Galactic sources. I then present a tool I name the “X-ray Main Sequence", which distinguishes between two main types of Galactic X-ray sources: accreting compact objects (containing a WD, NS, or BH) and active stars. I put forth an empirical cut to separate between the two main types of sources. Finally, I discuss the origin of this clean separation, based on the X-ray saturation properties of solar and late-type stars.

In Section 8.2, I present cleaned versions of the *XMM-Newton* and SRG/eROSITA eFEDS catalogs, and the *Gaia* crossmatch. I also describe each of the Galactic X-ray source classes and the catalogs that I use to provide classifications. In Section 6.3, I

present the X-ray Main Sequence. In Section 6.4, I present optical spectroscopy of new sources as a proof of concept demonstration, including a crossmatch with early data from SDSS-V. Finally, in Section 8.4, I provide details on how to make best use of this diagram and why such clean distinction between source classes is possible.

5.2 Data

XMM-Newton Source Catalog

I began with the Fourth *XMM-Newton* Source Catalog, 13th Edition (4XMM-DR13; Webb et al., 2020), which contains 656,997 sources. It is comprised of all publicly available observations taken with the European Photon Imaging Camera (EPIC) in the 0.2–12 keV range between February 13, 2000 and December 31, 2022. Taking overlapping fields into account, this catalog covers ∼1328 deg^2 (3%) of the sky. I selected only point sources that do not have any quality flags by making the following cuts:

- Well localized point sources: `SC_EXTENT` = 0 and `CONFUSED` = 0.
- 5σ detections (with a threshold as described in Webb et al., 2020): `SC_DET_ML` > 14.
- Low probability of being a spurious detection: `SC_SUM_FLAG` ≤ 1.

After these cuts, 368,068 (56% of initial sources) remained. 99% of sources in this final sample have a positional error of (`SC_POSERR`) < 1.95".

Gaia EDR3 Crossmatch

I then crossmatched the cleaned sources from the *XMM-Newton* catalog with *Gaia* Data Release 3 (DR3; Gaia Collaboration et al., 2021, 2023a) within a 2" radius[3]. I did not account for proper motions since only sources with exceptionally high proper motions ($\gtrsim$ 100 milliarcsec) would move more than 2" in the maximum ∼20 year difference between *XMM-Newton* and *Gaia* observations. Additionally, by using the *stacked* XMM catalog, it is difficult to account for proper motions for sources having been observed potentially years apart. I only kept sources for which there is a single match within 2" — 11,161 of the 368,068 clean sources have more than one match, and are predominantly located near the Galactic Center or the centers of clusters, but are excluded here.

[3]The astrometry and photometry in the Early Data Release (EDR3) is identical to that of the newer DR3.

I then performed the following cuts on *Gaia* data to ensure both good quality and that the sources are Galactic:

- Significant parallax and proper motions: `parallax_over_error` > 3 and `pm/pm_error` > 5 in both RA and DEC.
- Significant photometry: `phot_mean_flux_over_error` > 3 in all bands.
- Uncontaminated photometry: `phot_bp_rp_excess_factor_corrected` < 0.05.
- Good astrometry: `RUWE` <1.4.

This cut left 25,050 sources (3.8% of the original 4XMM-DR13 catalog). I note that I employed rather conservative cuts, particularly on the parallax. Many Galactic sources could have significant proper motions, while not a parallax. However, the goal of this work is to create a catalog of high confidence Galactic sources.

Object Classes and Their Catalogs

I used a variety of modern catalogs to provide classifications for known Galactic X-ray objects. As none of these catalogs are by any means complete[4], I instead focused on a high purity fraction for each source classification. I crossmatched all catalogs with the XMM-Newton/*Gaia* catalog described above to obtain consistent X-ray and optical fluxes. X-ray binaries, symbiotics, and spider binaries are exceptions, where the number of sources is low enough that I used X-ray detections from any available detection.

Active Single Stars

Active stars are soft X-ray emitters due to their rapid rotation, which leads to coronal activity (e.g., Pallavicini et al., 1981). Due to their fully convective nature and overall abundance, active M dwarfs are the most common X-ray emitting single stars (Stelzer et al., 2013)[5]. I used the sample of 823 active stars from Wright et al.

[4]For example, I used the classic Ritter and Kolb catalog of cataclysmic variables (CVs), which contains some of the most well known, spectroscopically verified CVs. This catalog contains 1,429 sources, while the larger Open CV Catalog (Jackim et al., 2020a), contains over 10,000 sources (mostly candidates).

[5]Other esoteric classifications also exist: BY Dra stars are K and M dwarfs which show photometric variability on their rotation period (Vogt et al., 1983), and FK Com stars are G and K giants

(2011). These systems are located both in the field and in open clusters, and have X-ray detections originally from the ROSAT Bright Source Catalog (Voges et al., 1999b). After crossmatching with my XMM-Newton/*Gaia* catalog, I was left with 112 sources.

Active Binary Stars: RS CVn Systems

RS CVn stars are binaries typically consisting of a slightly evolved subgiant and a solar or late-type star, which may or may not be evolved (Audard et al., 2003). Their orbital periods range from 5–6 hours to tens of days, inducing fast rotation of the stars. This leads to increased activity and X-ray emission (Walter and Bowyer, 1981). RS CVns have garnered some attention as being contributors to the Galactic Ridge X-ray Excess (Worrall and Marshall, 1983), though the contribution of cataclysmic variables is comparable or even higher (Revnivtsev et al., 2006).

There are a handful of well-studied RS CVn systems that receive much attention in the literature (e.g., Sasaki et al., 2021), but I encountered a dearth of large catalogs of vetted systems. Instead, I assembled a list of objects from the International Variable Star Index (VSX) in the `RS` category, which yields 73,320 sources. After crossmatching with my XMM-Newton/*Gaia* data set, this left only 341 systems. Since various well-known RS CVn systems are catalogued as eclipsing binaries (`EB*`) in the Simbad database, I also included as active binaries systems from my XMM-Newton/*Gaia* crossmatch that are labeled as `EB*` and have $N > 5$ references in Simbad (147 systems). It appears as though the time is right for a dedicated survey of X-ray emitting RS CVn systems.

Young Stellar Objects (YSOs)

YSOs are dynamic environments, with the seeds of planets forming in the circumstellar disk extending to hundreds of stellar radii (e.g., Hartmann et al., 2016). The pre-main sequence star at the center is inflated, highly magnetic, and is born rotating rapidly (e.g., Bouvier et al., 1986). This high rotation makes YSOs perfect candidates for being X-ray sources, which were first discovered to be as such by Feigelson and Kriss (1981). However, the high levels of X-ray luminosity, hot (0.5–5 keV) temperatures, variability on hour timescales pointed to a sources of X-rays in addition to coronal activity, such as magnetic reconnection (Feigelson et al., 2002).

which show similar variability (Bopp and Stencel, 1981). Both subtypes are rapid rotators, some of which show evidence for binarity, though the binary fraction of each subtype is unknown.

I used the catalog of YSO candidates assembled using a crossmatch of *Gaia* and *WISE* mid-infrared data (Marton et al., 2019). That catalog was assembled using a training set of well-vetted YSO catalogs to which a Random Forest classifier was used to infer probability of an object being a YSO. I began with all objects in that catalog that have a 96% probability or greater of being a YSO. Of those, 398 are in my XMM-Newton/*Gaia* crossmatch.

Cataclysmic Variables

Cataclysmic variables (CVs) are close binaries where a WD accretes from (typically) a late-type main sequence companion (e.g., Warner, 1995b). In (non-magnetic) CVs where the accretion disk extends down to the WD surface, X-rays originate from the disk-WD boundary layer, while in magnetic CVs where the field is strong enough ($B \gtrsim 1$ MG) to influence the accretion, X-rays originate from the accretion shock on the WD surface (Mukai, 2017). CVs are particularly interesting X-ray sources since they are thought to be the dominant contributors to the excess of X-rays from the Galactic Ridge and Galactic Center (Revnivtsev et al., 2006; Hailey et al., 2016).

AM CVn systems are ultracompact CVs ($P_{\rm orb} \approx 5 - 65$ min), where a WD accretes from a helium-dominated degenerate or semi-degenerate companion. While less than 100 of these systems are known, they are particularly interesting in that some of these will be among the loudest sources of gravitational waves as seen by the Laser Interferometer Space Antenna (e.g., Nelemans et al., 2001; Amaro-Seoane et al., 2017)

I used the most updated publicly available catalog of cataclysmic variables (CVs) to date, the Final Version (December 31, 2015) of the Ritter and Kolb catalog (Ritter and Kolb, 2003a). This catalog contains 1,429 systems primarily discovered through their optical outbursts and/or X-ray associations. 64 of those systems are present in my XMM-Newton/*Gaia* catalog, including magnetic CVs. Intermediate polars (DQ Her stars) and polars (AM Her stars) are labeled as subtypes `DQ` and `AM`, respectively, and AM CVn systems are labeled as type `AC`.

I also included supersoft X-ray sources (SSSs), which are WDs that have a layer of steadily burning hydrogen on their surface. Their X-ray spectra have equivalent blackbody temperatures ranging from 15–80 eV, which means that little of their bolometric flux overlaps with the *XMM-Newton* energy range. I used the catalog of SSSs from Kahabka and van den Heuvel (1997) and kept only those systems which

have a detection in the *XMM-Newton* source catalog. 4 systems fulfill this condition (one is AG Dra, which is a symbiotic SSS and labled as “symbiotic" in Figure 5.1).

Millisecond Pulsar (Spider) Binaries

Millisecond pulsars have been found in close binaries with either an M dwarf or brown dwarf companion — redbacks and black widows, respectively. These systems are X-ray sources due to the presence of an intrabinary shock which converts the pulsar power to X-rays (e.g., Romani and Sanchez, 2016). While these systems are not accreting, for the purposes of this paper, I will include them in under the umbrella of compact objects, as these systems occupy the upper left portion of the X-ray main sequence. I took the catalog from Koljonen and Linares (2023), which compiles both *Gaia* positions of known redbacks and black widows as well as their X-ray detections in the literature (all detections come from instruments that would lead to at most a factor of 2–3 correction to the flux in the 0.2–12 keV range, so I kept original measurements). I omitted all sources labeled as “candidates", and kept only sources that had an X-ray detection, which yielded 15 redbacks and 4 black widows.

Neutron Star and Black Hole X-ray Binaries: Low-mass, High-mass, and Ultracompact

X-ray binaries (XRBs) are systems in which a neutron star or a black hole accretes from a binary companion. This takes place in the form of Roche lobe overflow from a degenerate donor star in ultracompact XRBs (UCXBs), Roche lobe overflow from a late-type donor star in low-mass XRBs (LMXBs), and wind accretion from an O/B type star in high-mass XRBs (HMXBs) (e.g., Tauris and van den Heuvel, 2023). Most of these systems have been discovered through outburst events, which lead to a transient brightening in both X-rays and optical luminosity (e.g., Lewin et al., 1993). A handful of systems are in a persistent “high" state, accreting near the Eddington limit, and have been visible as bright sources since the early days of X-ray astronomy (e.g., van Paradijs et al., 1988). It is not useful for me to plot LMXBs in outburst, since it defeats the purpose of creating this diagram — to identify *persistent* Galactic X-ray sources. Instead, I just plotted XRBs which are either in quiescence or in a persistent high state.

I assembled a list of quiescent or high state LMXBs and HMXBs from three papers: Menou et al. (1999) has archival X-ray fluxes of NS and BH binaries before *Chandra*

and *XMM-Newton*, Garcia et al. (2001a) reports results primarily of quiescent BH LMXBs from early *Chandra* data, and Russell et al. (2006) assembles all known XRB X-ray measurements, distinguishing between quiescent and outbursting sources, neutron stars and black holes. For the UCXBs, I use thed catalog from Armas Padilla et al. (2023), which exclusively has NS accretors.

In all cases, I only kept sources that 1) have a significant *Gaia* detection and flux measurement (i.e., bright enough and not located in a globular cluster), 2) have detections in a well-defined persistent high state or quiescent state, and 3) have a well-measured X-ray flux (i.e., not an upper limit or marginal detection). This left 2 UCXBs, 4 HMXBs, and 9 LMXBs.

Symbiotic Stars and Symbiotic X-ray Binaries

Symbiotic stars are long-period ($P_{\rm orb} \gtrsim 200$ days) binary systems in which a NS or WD accretes from an evolved, typically a red giant, companion[6] (e.g., Belloni and Schreiber, 2023). The term “symbiotic X-ray binary" is used often in the literature to refer to the subset of systems in which a NS is the accretor. Such systems are prone to X-ray bursts similar to LMXBs and HMXBs.

I used the catalog of WD accretors from Luna et al. (2013) and the catalog NS accretors from Yungelson et al. (2019a). To obtain X-ray detections of a few more systems, I crossmatched my XMM-Newton/*Gaia* catalog with the catalog of symbiotic stars from Akras et al. (2019). I adopted the same quality cuts as in the previous subsection, rendering a total of 11 symbiotic stars with a WD accretor and 4 symbiotic stars with a NS accretor.

SRG/eROSITA eFEDS Catalog

While data releases from SRG/eROSITA are imminent at the time of writing, the eROSITA Final Equatorial Depth Survey (eFEDS) catalog provides a preliminary look at the final projected sensitivity of the mission. A detailed summary of the survey is outlined in Brunner et al. (2022), and the counterpart association in Salvato et al. (2022). The limiting flux of eFEDS is comparable to that of the *XMM-Newton* catalog, $F_X \sim 6.5 \times 10^{-15}$ erg s^{-1}cm^{-2}, though with a slightly larger positional uncertainty of 4.7" (Salvato et al., 2022). The full catlaog contains 27,369 sources. In order to select only Galactic sources, I took the catalog of Salvato et al.

[6]Symbiotic stars with a BH accretor should in principle exist, but no such systems have been confirmed to date.

(2022), and kept only sources with `CTP_Classification` as `SECURE GALACTIC` or `LIKELY GALACTIC`. I enforced the same astrometric quality cuts as in the *XMM-Newton* catalog. Finally, I kept only sources with an X-ray detection likelihood `ERO_DET_ML` greater than 10, as suggested by Salvato et al. (2022). This left 1,385 sources (5.1% of the original catalog).

SDSS-V (SDSS DR18) Crossmatch

SDSS recently released its 18$^{\text{th}}$ data release (SDSS DR18; Almeida et al., 2023), which includes the first publicly available spectra from SDSS-V (Kollmeier et al., 2017). SDSS-V, among other multiplexed spectrographs (DESI, WEAVE, 4MOST), is undertaking time-domain optical spectroscopic surveys. SDSS-V is uniquely targeting SRG/eROSITA targets, and includes spectra in DR18 of 16,548 objects in the eFEDS patch of sky. This means that even objects without an X-ray counterpart are targeted (Almeida et al., 2023). I crossmatched the SDSS-V eFEDS catalog with the Galactic eFEDS sources described above, and kept only sources with `CLASS == STAR` and high signal-to-noise `SN_MEDIAN_ALL > 10`. This left 49 sources, 42 of which pass *Gaia* quality cuts.

5.3 The X-ray Main Sequence

In Figure 5.1, I present the X-ray Main Sequence with two cuts to distinguish between accreting compact objects and active stars: the “empirical cut" and a “theoretical cut". Symbiotic stars occupy their own region of phase space, below active stars. This means that the diagram can be used to easily separate compact objects with low-mass stellar companions from active stars, but further information is needed to separate out symbiotics (compact objects with evolved donors). The “X-ray Main Sequence" name is attractive since main sequence stars follow their own track, while compact objects occupy separate regions of phase space[7].

The empirical cut is drawn by eye (with the functional form $\log_{10} y = x - 3.5$, where y is the vertical axis and x the horizontal axis). This cut encompasses the majority of accreting compact objects, while removing active stars. More detailed analysis of where to place this cut will be presented in future work. Later in the paper, I discuss the construction of the theoretical cut based on the saturation limit of X-rays stemming from coronal activity of solar and late-type stars.

YSOs and active stars reside below the empirical cut, with YSOs occupying the

[7]Though really, this is a color-color diagram.

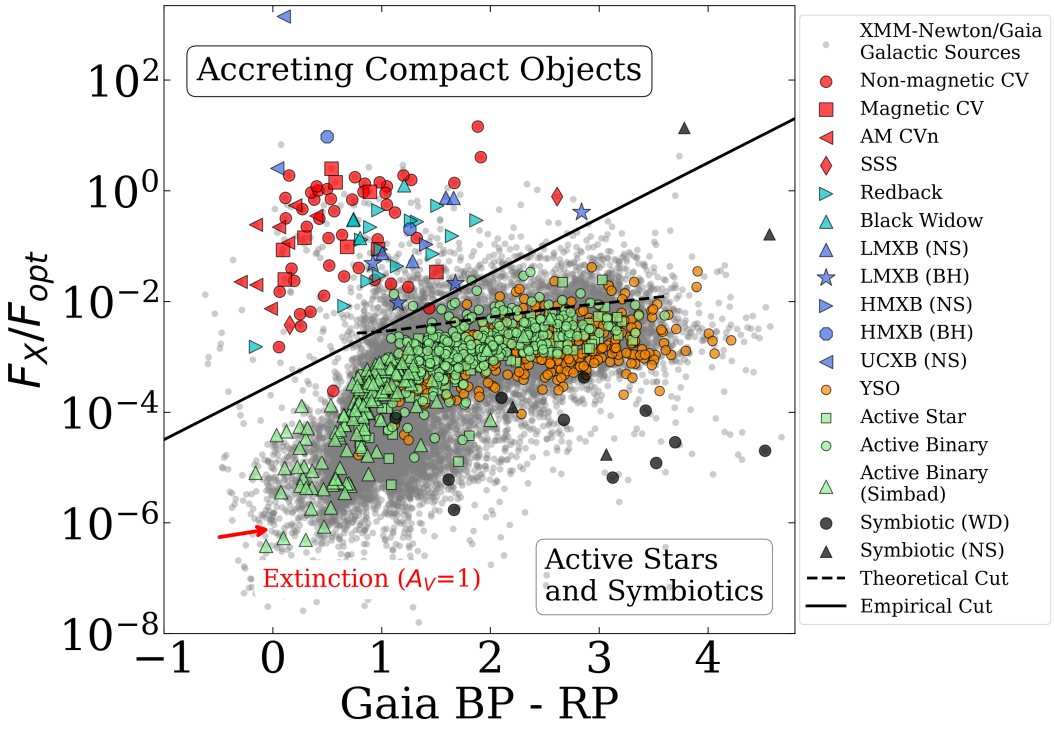

Figure 5.1: The X-ray Main Sequence. Galactic sources from the XMM-Newton/*Gaia* crossmatch is shown in grey. Accreting compact object binaries in the upper left are separated from symbiotic and active stars on the bottom right by the “empirical cut" (solid line) or “theoretical cut" (dotted line). All classifications on the right side panel are from the literature, and described in Section 5.2. No extinction correction is applied here, but the extinction vector is shown (de-reddening slides sources towards the lower left).

reddest regions of the diagram and active (binary) stars dominating the bluest regions. Most of the unclassified sources in the diagram have very low $F_X/F_{\rm opt}$ values, potentially being active binaries that have not been classified as such.

In Figure 5.2, I plot the XMM-Newton/*Gaia* crossmatch, color coded with variability metrics. In the left panel of Figure 5.2, I color code by the X-ray variability flag, `SC_VAR_FLAG` (some sources are missing due to the lack of X-ray counts that can be used to compute the variability metric). While non-variable X-ray sources tend to be located everywhere in the diagram, variable X-ray sources are located either in the upper left accreting compact object corner, or in the active star corner, near the boundary.

In the right panel of Figure 5.2, I color code by an optical variability metric from *Gaia*. This metric is essentially the mean number of standard deviations from the

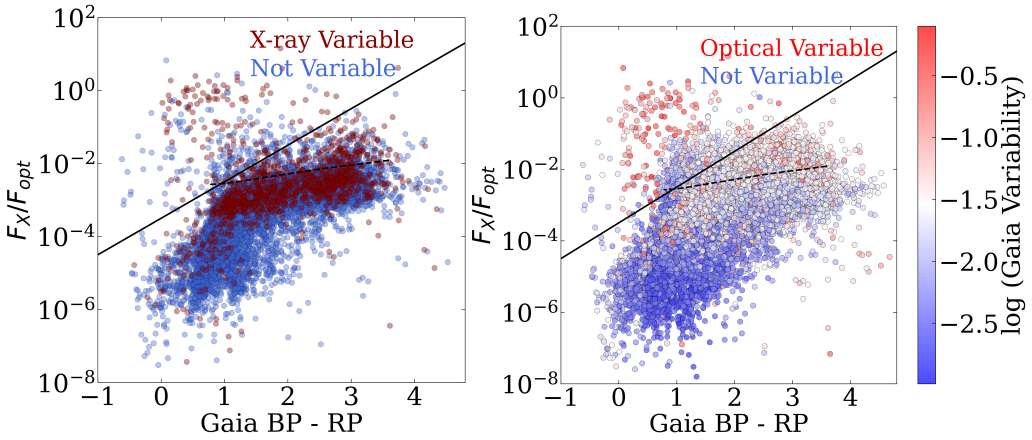

Figure 5.2: The same dataset as in Figure 5.1, but color coded by X-ray variability (*left*) and optical variability (*right*). In both cases, the most variable sources tend to be located above the cut or just below it.

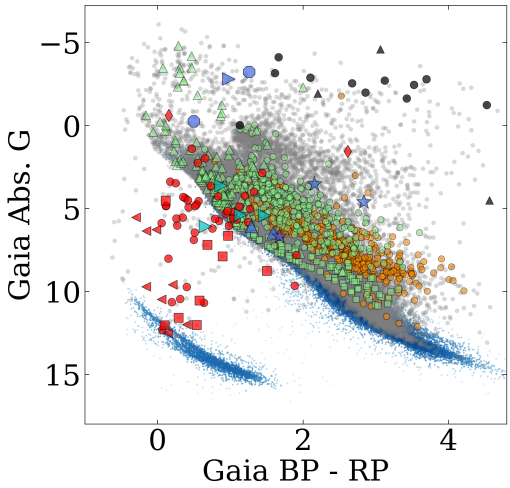

Figure 5.3: Objects from Figure 5.1 (same coloring conventions) plotted atop the 100 pc *Gaia* Hertzsprung-Russell (HR) diagram (light blue). The full XMM-Newton/*Gaia* crossmatch is shown in gray.

median flux by which the source varies: $\sigma_G\sqrt{N_{\rm obs}}/\langle G\rangle$ (e.g., Mowlavi et al., 2021; Guidry et al., 2021). The most optically variable sources are, as with X-ray variable sources, either in the upper left part of the diagram or near the boundary between classes. Finally, in Figure 5.3, I plot all objects with a significant (3σ) parallax in the 100 pc *Gaia* Hertzsprung-Russell diagram.

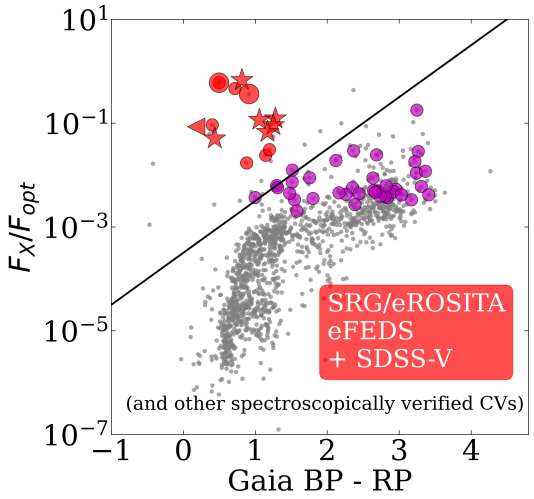

Figure 5.4: Galactic sources from the SRG/eROSITA eFEDS catalog (gray), with colored circles indicating those that have an SDSS-V spectrum. The two larger circles are polars from Rodriguez et al. (2023c). The same empirical cut from Figure 5.1 distinguishes CVs (red) from active stars (magenta). Red stars are spectroscopically confirmed CVs from an ongoing survey using the *XMM-Newton* catalog, and the red triangle is an AM CVn (ultracompact CV) from a separate SRG/eROSITA catalog (Rodriguez et al., 2023a).

5.4 Results: Discovery of New Systems as Proof of Concept

In the following subsections, I show the application of this diagram to the discovery of several new objects. This is a pilot study which serves as a proof of concept.

SRG/eROSITA eFEDS + SDSS-V Optical Spectroscopy

In Figure 5.4, I present the SRG/eROSITA eFEDS catalog of Galactic objects, along with those objects that have an SDSS-V spectrum in SDSS DR18. As described in Section 5.2, I only keep objects with a high signal-to-noise ratio that have `CLASS == STAR`. Using the empirical cut (same as in Figure 5.1), I classify all objects below the cut as active stars and all above as CVs. I visually inspect all 42 spectra, and confirm the `SUBCLASS` classifications in SDSS DR18 (28 M stars, 8 K stars, 1 G star, and 5 CVs). This confirms the effectiveness of the X-ray Main Sequence, though a different empirical cut should ideally be adopted depending on the X-ray telescope, which would have a different energy range. I also note that targeted objects are predominantly located at high values of $F_X/F_{\rm opt}$, likely due to a selection of optically faint objects (e.g., no objects in the eFEDS/SDSS-V crossmatch are brighter than $G = 16$).

The objects in the lower right part of Figure 5.4 are predominantly active stars, with

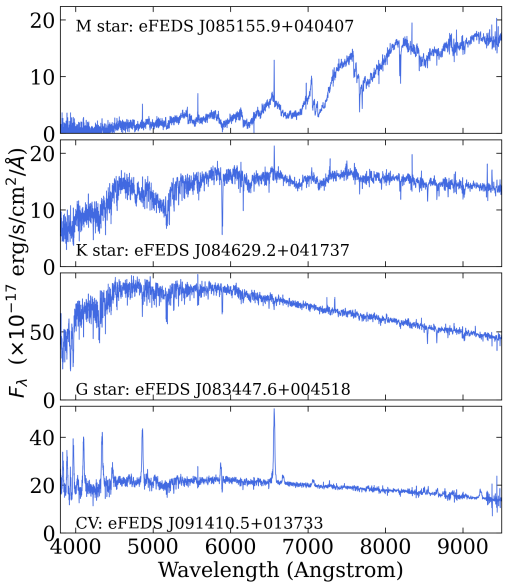

Figure 5.5: SDSS-V spectra of four objects with distinct spectral types in the SRG/eROSITA eFEDS catalog. All objects are new discoveries, with spectroscopy confirming the predicted classification from the X-ray Main Sequence.

most M and K dwarfs showing Balmer emission lines or at least Hα in emission. However, further work is needed to determine the binary nature of these systems. In Figure 5.5, I present SDSS-V co-added spectra of four objects (publicly available in DR18) in the eFEDS/SDSS-V crossmatch, one of each spectral type. All four objects are presumably new, with no references in either Simbad or VSX[8].

Other SRG/eROSITA Systems: Magnetic CVs and AM CVns

I have shown elsewhere that this diagram can be used to discover two important classes of CVs: magnetic CVs and ultracompact AM CVns. In Rodriguez et al. (2023c), we discovered two polars using a crossmatch of the SRG/eROSITA eFEDS catalog with *Gaia* and ZTF. In (Rodriguez et al., 2023a), we discovered an eclipsing AM CVn which showed little optical variability due to poor photometric coverage. We demonstrated that it was the X-ray + optical crossmatch and its placement in the X-ray Main Sequence that enabled the discovery and characterization of that object. I show all three systems in Figure 5.4, with the two polars shown as larger red circles and the AM CVn as a triangle.

[8] At the time of writing, work is being undertaken to identify all CVs in the eFEDS field (Schwope, A. et al, in prep).

XMM-Newton CVs with Keck and Palomar Spectroscopy

To further demonstrate the effectiveness of the X-ray Main Sequence in selecting accreting compact objects, I am undertaking a spectroscopic survey of CV candidates selected from the upper left corner of the XMM-Newton/*Gaia* crossmatch presented in this paper (as well as other X-ray catalogs). To complement this survey, I am also crossmatching with optical photometry from the Zwicky Transient Facility (ZTF; see Appendix 7.8 for details). Here, I present six systems from this ongoing survey to highlight the effectiveness of the X-ray Main Sequence. In particular, the systems I present are “exotic CVs" — CVs which have been particularly rare in purely optical surveys (i.e., those that search for optical outbursts). A description of of all objects and observations is in Appendix 7.8. Optical spectra of all objects are shown in Appendix Figure 5.9, and optical light curves in Appendix Figures 5.10 and 5.11.

5.5 Discussion

How to Interpret This Diagram

As discussed in Section 8.2, the catalogs for all objects types in this sample are almost certainly incomplete. In no way do I claim that this plot perfectly distinguishes between classes of objects. In addition, the majority of objects in the *XMM-Newton* source catalog, even those with optical counterparts, remain unidentified. So, it is difficult to obtain estimates of either purity or completeness without more detailed classification (e.g., from optical spectroscopy). The most that we can say at the present time is that the empirical cut in Figure 5.1 introduces at most a few active stars into the accreting compact object corner, and vice versa. However, there are a few CVs and HMXBs that make their way into the bottom right corner, presumably due to high optical contribution from the donor and/or accretion disk. Despite these caveats, the diagram works very well for classifying objects actually detected by X-ray surveys. That’s the point: not to find every compact object, but the classify the ones that are X-ray sources.

Why This Diagram Works: The Saturation Line

A plausible explanation for the clear clustering in this diagram rests on a well-known empirical result in the study of solar and late-type active stars: the X-ray luminosity “saturates" at the (typically claimed) limit of $L_X/L_{\rm bol} \approx 10^{-3}$.

This existence of this X-ray saturation limit has been proposed to be due to the limit on the magnetic field strength as a result of the dynamo mechanism (Reiners et al., 2022). In the earliest works investigating stellar activity, Skumanich (1972) con-

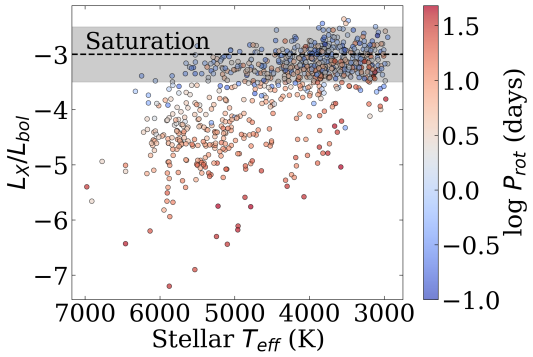

Figure 5.6: All active stars in the sample of Wright et al. (2011) are below the saturation limit of $L_X/L_{\rm bol} = 10^{-2.5}$. The majority of stars in the saturated regime tend to be cooler, with $T_{\rm eff} \lesssim 5000$ K.

nected the strength of the Ca II H and K lines with stellar rotation periods. Pallavicini et al. (1981) was the first to use X-ray fluxes (from the *Einstein Observatory*) as a stellar activity indicator and show a dependence of X-ray luminosity on stellar rotation periods. Later works then used larger X-ray datasets (such as ROSAT) to show that at the fastest rotation periods, X-rays saturate at $L_X/L_{\rm bol} \approx 10^{-3}$ (e.g., Reiners et al., 2014; Magaudda et al., 2020; Johnstone et al., 2021). In most cases, $L_X/L_{\rm bol}$ is plotted versus the Rossby number, *Ro*, which is the ratio of the rotation period over the convective turnover timescale. There is also a "super-saturated" regime at the lowest Rossby numbers where $L_X/L_{\rm bol}$ turns over and decreases from the saturation limit (e.g., Núñez et al., 2023).

In recent years, it has been proposed that stellar activity and magnetism arise from a dynamo mechanism — where it can be most simply stated that kinetic rotational energy is converted to magnetic energy(e.g., Charbonneau, 2014). If the dynamo theory holds, then limits on stellar rotation naturally set a limit on magnetic activity, and therefore X-ray luminosity (Reiners et al., 2022). In Figure 5.6, I present the sample of 823 active stars from Wright et al. (2011). In practice, the saturation limit has a variance of ≈ 0.5 dex, so I adopt a saturation limit of $L_X/L_{\rm bol} = 10^{-2.5}$ when creating the "theoretical cut" in the X-ray Main Sequence.

Now that a limit of $L_X/L_{\rm bol}$ is established, I convert $L_{\rm bol}$ to a more useful observational quanity: an optical color and luminosity in a single optical bandpass, $L_{\rm opt}$. To compute $L_{\rm bol}$, I take a 10 Gyr isochrone from the MESA Isochrones and Stellar Tracks library (MIST; Choi et al., 2016b), at solar metallicity and with $v/v_{\rm crit} = 0.4$. The final step is to obtain an optical luminosity, which can be taken at a single

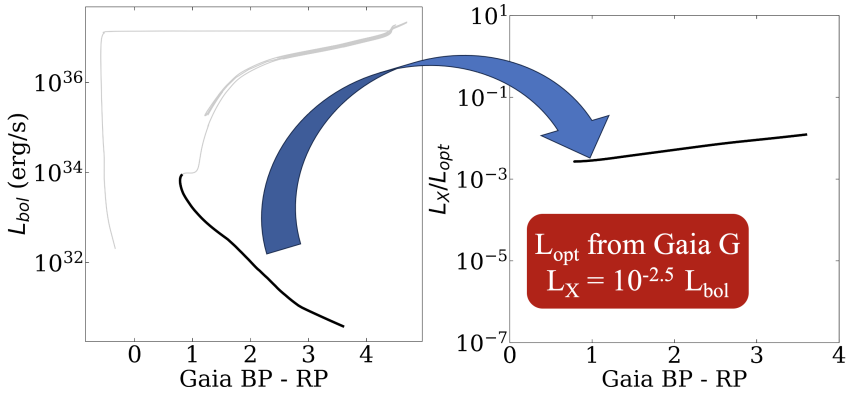

Figure 5.7: A MIST isochrone at the current age of the Milky Way converts between $L_{\rm bol}$, an optical color, and L_X. The main sequence is shown in bold, and we omit the evolved tracks shown in lighter color.

optical passband (i.e., *Gaia* G). I do this by using the Sun's absolute G magnitude as a reference, and computing $L_{\rm opt} = 10^{0.4(M_{G,\odot}-M_G)}L_\odot$. The steps in creating the theoretical cut are visually outlined in Figure 5.7.

Earlier Versions of This Diagram

One of the earliest versions of this diagram appears in Figure 1 of Maccacaro et al. (1988), though it is presented as a way to distinguish extragalactic objects from galactic objects using data from the *Einstein* Observatory. Stocke et al. (1991) later presents this diagram showing only stellar sources, also using *Einstein* data, but only a few dozen points appear in the plot. Nearly 25 years later, the diagram re-appeared in Figure 2 of Greiner and Richter (2015) using ROSAT data, now with a clear distinction between AGN and CVs in the upper left and stars in the lower right. However, just a few dozen sources are plotted, and only a limited explanation given as to why the diagram distinguishes between classes. Discouragingly, there appeared to be no way to distinguish between AGN and CVs, since they both occupied the same region of phase space (Gaia DR1 would come one year later).

Recently, this diagram has appeared more often in the literature thanks to reanalyzed ROSAT and early SRG/eROSITA data, Freund et al. (2022) created this diagram for a catalog of stellar sources in ROSAT data, and present a very thorough explanation for the dearth of sources above $F_X/F_{\rm opt} = 10^{-3}$ (they also invoke the well-known "saturation limit"). However, compact objects are entirely left out. This diagram is also shown in Appendix B of Stelzer et al. (2022), where optical/X-ray counterparts from the eFEDS survey of the SRG/eROSITA telescope are shown. In that figure,

extragalactic and Galactic objects are distinguished, but no further information is presented. Most recently, Schwope et al. (2022a) and Schwope et al. (2023) presented studies of two newly discovered CVs and show their location to be in the upper left corner of this diagram alongside other SRG/eROSITA sources.

I propose three main reasons for the lack of investigation and use of the diagram beyond the studies listed above: 1) there have been fewer X-ray sources in previous surveys compared to today, 2) many of those sources did not even have reliable optical counterparts due to large X-ray error circles, and 3) distinguishing between Galactic and extragalactic sources was much more difficult before *Gaia*. Many of the large catalogs on which I rely to provide classifications have also only come about in the last decade or so.

Applications to Upcoming Large X-ray and Optical Surveys

Given an X-ray detection and identification of an optical counterpart, this tool can efficiently select accreting compact objects candidates for optical spectroscopic follow-up. The efficiency is impressive: of the 25,050 sources in the XMM-Newton/*Gaia* crossmatch, only 562 (2.2%) of sources are above the empirical cut. Furthermore, because the vertical axis is written as $F_X/F_{\rm opt}$, distant or faint objects that may only have a *Gaia* proper motion (and not parallax) can still be selected.

The most obvious application in the immediate future is for large scale spectroscopic surveys (e.g., SDSS-V, DESI, WEAVE, 4MOST). While these surveys are making obtaining optical spectra easier than ever, targeting is still needed to be done based on some prior information. I propose that these spectroscopic surveys inform their targeting strategies based on Figure 5.1. I present a cartoon outlining the main classes in Figure 8.8.

5.6 Conclusion

I have presented a tool for X-ray + optical astronomy that has received little to no attention in the past. The power of this tool is effectively demonstrated thanks to modern datasets — in particular, 2" error circles from the large *XMM-Newton* source catalog, precise astrometry from *Gaia*, and a whole host of catalogs with object classifications in the literature. The “X-ray Main Sequence" distinguishes accreting compact objects in the upper left from active stars and in the lower right. Symbiotic stars appear to occupy a unique portion of phase space as well.

I have presented two cuts to distinguish between accreting compact objects and

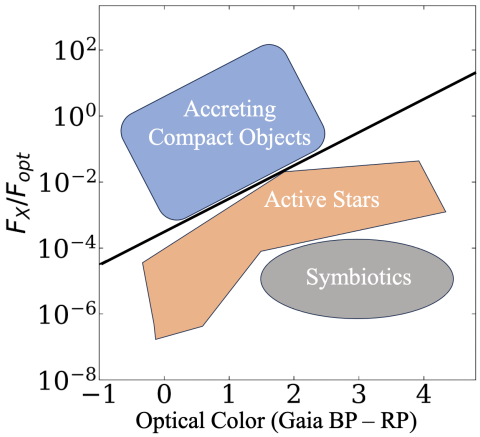

Figure 5.8: A cartoon of Figure 5.1 demonstrating the location of the three main categories of objects in the X-ray Main Sequence.

active stars: an empirical cut and theoretical cut. The latter is based on a well-known relation in active stars, namely that they have a "saturation limit" of $L_X/L_{\rm bol} \lesssim 10^{-2.5}$ (though $L_X/L_{\rm bol} \lesssim 10^{-3}$ is often quoted in the literature). The cuts I present are not perfect by any means, and could be affected by incompleteness in object catalogs that I use.

In brief, the "X-ray Main Sequence" shows promise for being used as an initial classification tool for upcoming surveys. It is highly efficient at selecting accreting compact objects, flagging a mere ∼2% of objects as candidates. Both X-ray and optical astronomy are on the verge of transformation, thanks to SRG/eROSITA, *Gaia*, the Rubin Observatory Legacy Survey of Space and Time (LSST), and the growing optical datasets from ZTF, TESS, ATLAS, and ASAS-SN. Stellar astronomy is entering a new golden era, and tools such as this will be crucial in identifying interesting single objects as well as large systematic surveys.

5.7 Acknowledgements

I wish to thank Shri Kulkarni and Kareem El-Badry for their thorough reading of this manuscript and useful feedback. I also thank Kevin Burdge, Adolfo Carvalho, Jim Fuller, Ilkham Galiullin, Lynne Hillenbrand, Rocio Kiman, Dovi Poznanski, Tom Prince, Axel Schwope, the ZTF Variable Star Group, and the members of various groups to whom I have presented this tool during its inception. I thank Zach Vanderbosch for a well-written tool for downloading SDSS spectra. I thank the staffs of the Palomar and Keck Observatories for their assistance in carrying out observations. I am grateful for support from an NSF Graduate Fellowship.

I thank the LSSTC Data Science Fellowship Program, which is funded by LSSTC, NSF Cybertraining Grant #1829740, the Brinson Foundation, and the Moore Foundation; my participation in the program has benefited this work.

Based on observations obtained with XMM-Newton, an ESA science mission with instruments and contributions directly funded by ESA Member States and NASA. This work has made use of data from the European Space Agency (ESA) mission Gaia (`https://www.cosmos.esa.int/gaia`), processed by the Gaia Data Processing and Analysis Consortium (DPAC, `https://www.cosmos.esa.int/web/gaia/dpac/consortium`). Funding for the DPAC has been provided by national institutions, in particular the institutions participating in the Gaia Multilateral Agreement.

Based on observations obtained with the Samuel Oschin Telescope 48-inch and the 60-inch Telescope at the Palomar Observatory as part of the Zwicky Transient Facility project. ZTF is supported by the National Science Foundation under Grants No. AST-1440341 and AST-2034437 and a collaboration including current partners Caltech, IPAC, the Weizmann Institute of Science, the Oskar Klein Center at Stockholm University, the University of Maryland, Deutsches Elektronen-Synchrotron and Humboldt University, the TANGO Consortium of Taiwan, the University of Wisconsin at Milwaukee, Trinity College Dublin, Lawrence Livermore National Laboratories, IN2P3, University of Warwick, Ruhr University Bochum, Northwestern University and former partners the University of Washington, Los Alamos National Laboratories, and Lawrence Berkeley National Laboratories. Operations are conducted by COO, IPAC, and UW.

Funding for the Sloan Digital Sky Survey V has been provided by the Alfred P. Sloan Foundation, the Heising-Simons Foundation, the National Science Foundation, and the Participating Institutions. SDSS acknowledges support and resources from the Center for High-Performance Computing at the University of Utah. SDSS telescopes are located at Apache Point Observatory, funded by the Astrophysical Research Consortium and operated by New Mexico State University, and at Las Campanas Observatory, operated by the Carnegie Institution for Science. The SDSS web site is `www.sdss.org`.

SDSS is managed by the Astrophysical Research Consortium for the Participating Institutions of the SDSS Collaboration, including Caltech, The Carnegie Institution for Science, Chilean National Time Allocation Committee (CNTAC) ratified researchers, The Flatiron Institute, the Gotham Participation Group, Harvard

University, Heidelberg University, The Johns Hopkins University, L'Ecole polytechnique fédérale de Lausanne (EPFL), Leibniz-Institut für Astrophysik Potsdam (AIP), Max-Planck-Institut für Astronomie (MPIA Heidelberg), Max-Planck-Institut für Extraterrestrische Physik (MPE), Nanjing University, National Astronomical Observatories of China (NAOC), New Mexico State University, The Ohio State University, Pennsylvania State University, Smithsonian Astrophysical Observatory, Space Telescope Science Institute (STScI), the Stellar Astrophysics Participation Group, Universidad Nacional Autónoma de México, University of Arizona, University of Colorado Boulder, University of Illinois at Urbana-Champaign, University of Toronto, University of Utah, University of Virginia, Yale University, and Yunnan University.

This work is based on data from eROSITA, the soft X-ray instrument aboard SRG, a joint Russian-German science mission supported by the Russian Space Agency (Roskosmos), in the interests of the Russian Academy of Sciences represented by its Space Research Institute (IKI), and the Deutsches Zentrum für Luft- und Raumfahrt (DLR). The SRG spacecraft was built by Lavochkin Association (NPOL) and its subcontractors, and is operated by NPOL with support from the Max Planck Institute for Extraterrestrial Physics (MPE). The development and construction of the eROSITA X-ray instrument was led by MPE, with contributions from the Dr. Karl Remeis Observatory Bamberg & ECAP (FAU Erlangen-Nuernberg), the University of Hamburg Observatory, the Leibniz Institute for Astrophysics Potsdam (AIP), and the Institute for Astronomy and Astrophysics of the University of Tübingen, with the support of DLR and the Max Planck Society. The Argelander Institute for Astronomy of the University of Bonn and the Ludwig Maximilians Universität Munich also participated in the science preparation for eROSITA.

5.8 New Cataclysmic Variables form XMM-Newton:Description of Observations and Individual Systems

All systems are summarized in Table 5.1.

4XMM J001830.2+43571 (4XMMJ0018) was observed due to its 2.22 hr periodicity in ZTF. This system shows Balmer emission lines as well as prominent bumps centered at 4000 and 5000 Angstrom. These are reminiscent of cyclotron harmonics in polars, leading me to classify it as a candidate polar (e.g., Warner, 1995b). The narrow emission lines, however, suggest this could be either a low-state polar or low accretion rate polar (e.g., Schwope et al., 2007).

4XMM J001912.5+220732 (4XMMJ0019) stood out due to its placement near the WD track in the *Gaia* HR diagram. This object shows nearly no variability in ZTF, making it unlikely to have been discovered had it not been for its X-ray detection. It features strong, double-peaked Balmer and He emission lines, with weak Hβ and Hγ absoprtion from the WD, leading me to classify it as a candidate WZ Sge CV (e.g., Gilliland et al., 1986; Inight et al., 2023a).

4XMM J021902.2+625713 (4XMMJ0219) stood out due to its placement near the main sequence despite having a 3.85 hr period in ZTF. The lack of strong Balmer emission lines (only weak Hα is seen) as well as the FG-type spectrum is suggestive of the evolved CVs also known as pre-ELMs (El-Badry et al., 2021a). In these systems, the WD accretes from a donor that filled its Roche lobe just before leaving the main sequence, therefore forming an “evolved" CV. Many systems evolve to short ($P_{\rm orb} < 1$ hr) periods before detaching and forming an extremely low mass (ELM) WD (El-Badry et al., 2021a). Virtually all of the criteria are met for me to classify this system as an (pre-ELM) evolved CV.

4XMM J063722.6+054158 (4XMMJ0637) was selected due to its long orbital period ($P_{\rm orb} = 13.8$ hr) dominated by ellipsoidal modulation. It also undergoes regular, triangular outbursts, which last $\sim$ 200 days, in contrast to typical dwarf nova outbursts which last $\sim$ 10 days. At its orbital period, the donor must be an evolved subgiant (e.g., Sokolovsky et al., 2022). The optical spectrum is indeed dominated by the FG-type donor, albeit with He II 4686 and the rare CIII/NIII Bowen blend emission lines. Interestingly, this system is near the “bifurcation period", where depending on the WD and donor parameters, the system may either evolve to longer or shorter orbtial periods (e.g., Belloni and Schreiber, 2023). All of the criteria are met for me to classify this system as an evolved CV, and I will report on extensive spectroscopy in an upcoming study (Rodriguez et al. in prep).

4XMM J085012.5-03163 (4XMMJ0850) stood out due to its 51 min (or doubled, 1.70 hr) period in ZTF data. Phase-resolved spectroscopy is being acquired to determine the true period. Like 4XMMJ0219, this system is also unusually close to the main sequence for so short an orbital period (even if 1.70 hr is the true period). The spectrum is dominated by a K-type donor, which hints at it being an evolved CV. In this system, however, Balmer lines are in emission along with the He II 4686 line, which is not typically seen in pre-ELMs, but suggestive of magnetism (Silber, 1992; El-Badry et al., 2021a). While some characteristics lead me to classify this system as a candidate evolved CV, further work is needed to determine its true nature.

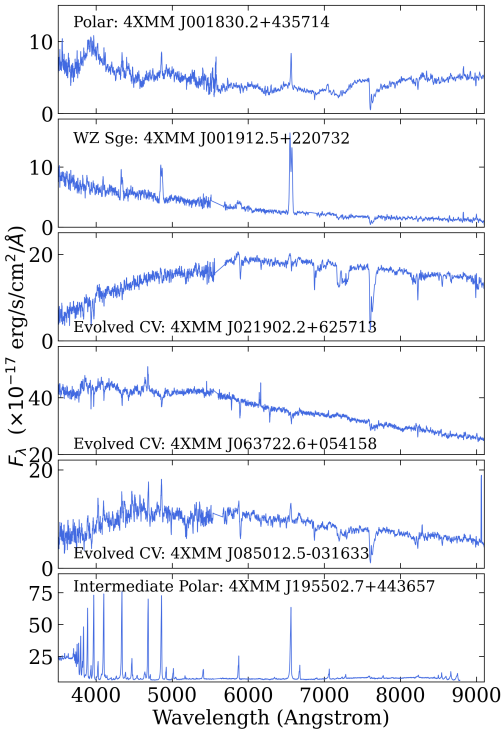

Figure 5.9: Keck and Palomar spectra of six CVs which are part of an ongoing spectroscopic survey of the 4XMM-*Gaia* catalog. All sources were predicted to be accreting compact objects using the X-ray Main Sequence, and confirmed through optical spectroscopy. Sub-classes shown are preliminary, yet all systems are distinct from archetypal CVs (dwarf novae such as that shown in Figure 5.5), demonstrating the richness that X-ray + optical surveys can reveal.

4XMM J195502.7+443657 (4XMMJ1955) features unusual variability in ZTF — low amplitude ($<$ 1 mag) variability with high amplitude ($\sim$ 3 mag), short ($\sim$ 20 day) dips. High-cadence ZTF data also reveals a 20–30 min period, suggestive of a WD spin period in intermediate polars (Mukai, 2017). Remarkably, its optical spectrum shows the strongest Balmer and He emission lines of any object in the sample. He II 4686 is also nearly as strong as Hβ, which is typically seen in intermediate polars (Silber, 1992). Despite fulfilling some of the necessary criteria, I am cautious to label this system as a candidate intermediate polar since extensive X-ray and optical timing data as well as phase-resolved spectroscopy as usually needed to securely classify such systems.

Of the six systems reported above, four were observed with the Double Spectrograph (DBSP; Oke and Gunn, 1982a) on the Hale telescope (4XMMJ0018, 4XMMJ0019 4XMMJ0219, and 4XMMJ0850). I used the 600/4000 grism on the blue side and the

316/7500 grating on the red side. A 1.5" slit was used, and the seeing throughout all observations varied between 1.5 – 2.0", leading to some slit losses. All P200/DBSP data were reduced with `DBSP-DRP`[9], a Python-based pipeline optimized for DBSP built on the more general `PypeIt` pipeline (Prochaska et al., 2020).

4XMMJ0637 and 4XMMJ1955 were observed with the Keck I telescope using the Low-Resolution Imaging Spectrometer (LRIS; Oke et al., 1995a). I used the 600/4000 grism on the blue side with 2x2 binning (spatial, spectral), and the 600/7500 grating on the red side with 2x1 binning. I used a 1.0 slit, and the seeing each night was approximately 0.7–1, leading to minimal slit losses. All Keck I/LRIS data were reduced with `lpipe`, an IDL-based pipeline optimized for LRIS long slit spectroscopy and imaging (Perley, 2019). All data (for both DBSP and LRIS) were flat fielded sky-subtracted using standard techniques. Internal arc lamps were used for the wavelength calibration and a standard star for overall flux calibration.

In Figure 5.10, I present long term ZTF light curves for all CVs in Section 5.4, from Data Release 19 (covering March 2018 – July 2023). ZTF is a photometric survey that uses a wide 47 deg^2 field-of-view camera mounted on the Samuel Oschin 48-inch telescope at Palomar Observatory with g, r, and i filters (Bellm et al., 2019b; Graham et al., 2019; Dekany et al., 2020; Masci et al., 2019). In its first year of operations, ZTF carried out a public nightly Galactic Plane Survey in g-band and r-band (Bellm et al., 2019a; Kupfer et al., 2021). This survey was in addition to the Northern Sky Survey which operated on a 3 day cadence (Bellm et al., 2019b). Since entering Phase II, the public Northern Sky Survey is now at a 2-day cadence. The pixel size of the ZTF camera is 1 and the median delivered image quality is 2.0 at FWHM.

In Figure 5.11, I present phase-folded light curves for four objects: 4XMMJ0018, 4XMMJ0219, 4XMMJ0850, and 4XMMJ0637. I used the `gatspy` software (Vanderplas, 2015) to compute a Lomb-Scargle periodogram (Scargle, 1982), searching for periods between 4 minutes and 10 days with an oversampling factor of 5. For all four systems that show a significant (10σ above the median) periodicity, I plot twice the best period, which in 4XMMJ0219 and 4XMMJ0637 reveals ellipsoidal modulations (minima of different depths). However, in the case of 4XMMJ0018 and 4XMMJ0850, the difference between two different minima is unclear and phase-resolved spectroscopy is needed to reveal the true period. Finally, I present the

[9] `https://dbsp-drp.readthedocs.io/en/stable/index.html`

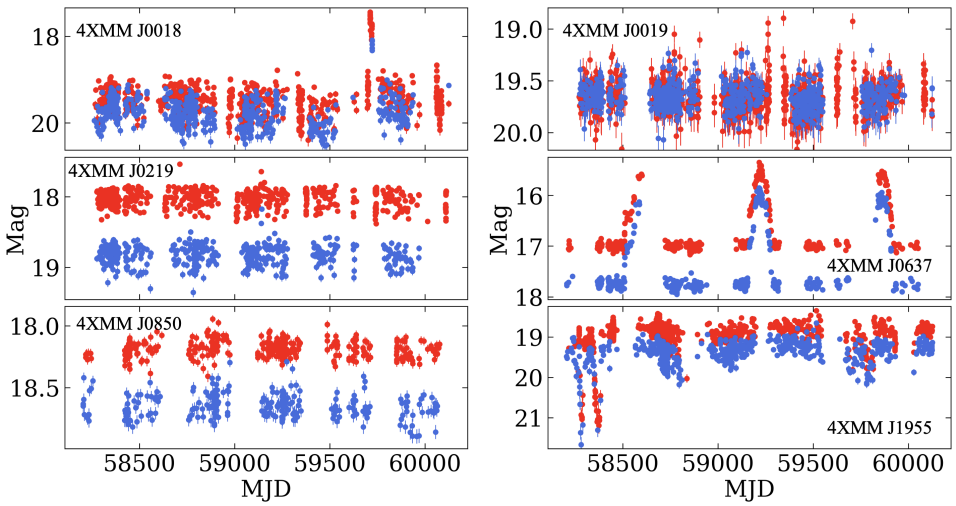

Figure 5.10: Long term (5 year) ZTF light curves in *r* band (red) and *g* band (blue) of all newly discovered XMM CVs.

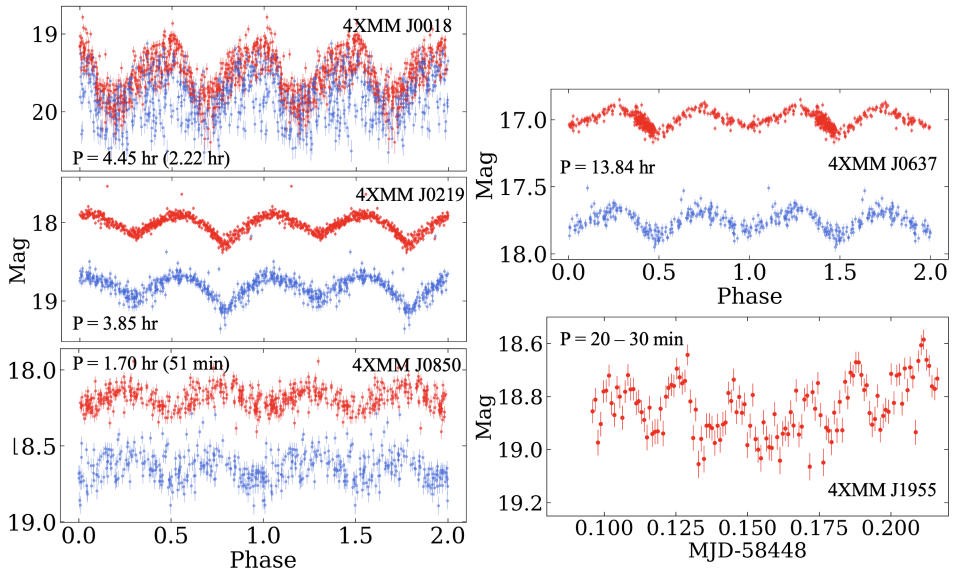

Figure 5.11: Folded ZTF light curves (excluding outbursts) in *r* band (red) and *g* band (blue) of 4 newly discovered XMM CVs. On the bottom right are the high-cadence continuous observations of 4XMMJ1955 from the ZTF Galactic Plane Survey.

high-cadence data from the ZTF Galactic Plane Survey for 4XMMJ1955, which reveals pulsations on a 20–30 min timescale.

Name	Gaia RA (deg)	Gaia DEC (deg)	Classification	Orbital Period (hr)
4XMM J001830.2+435714	4.626476	43.954572	CV (Polar)	2.22 (4.45)
4XMM J001912.5+220732	4.802370	22.125808	CV (WZ Sge)	-
4XMM J021902.2+625713	34.760214	62.953643	CV (evolved)	3.85
4XMM J063722.6+054158	99.344615	5.699567	CV (evolved)	13.8
4XMM J085012.5-031633	132.552197	-3.276101	CV (evolved)	1.70 (0.85)
4XMM J195502.7+443657	298.761724	44.616101	CV (Intermediate Polar)	-

Table 5.1: Summary of all newly discovered XMM CVs. The most likely orbital period is listed first, and the one in parentheses cannot be ruled out without additional data.

5.9 Catalog Data

In Table 5.2, I list all of the objects used from external catalogs and references to the papers in which X-ray fluxes were reported. In Table 5.3, I show a preview of the entire XMM-*Gaia* crossmatched catalog, which I make available in machine readable format.

Name	Class	Gaia DR3 ID	X-ray Reference
J0212+5320	Redback	455282205716288384	(1)
J1048+2339	Redback	3990037124929068032	(1)
J1306-40	Redback	6140785016794586752	(1)
J1431-4715	Redback	6098156298150016768	(1)
J1622-0315	Redback	4358428942492430336	(1)
J1628-3205	Redback	6025344817107454464	(1)
J1723-2837	Redback	4059795674516044800	(1)
J1803-6707	Redback	6436867623955512064	(1)
J1816+4510	Redback	2115337192179377792	(1)
J1908+2105	Redback	4519819661567533696	(1)
J1910-5320	Redback	6644467032871428992	(1)
J2039-5618	Redback	6469722508861870080	(1)
J2129-0429	Redback	2672030065446134656	(1)
J2215+5135	Redback	2001168543319218048	(1)
J2339-0533	Redback	2440660623886405504	(1)
J1311-3430	Black Widow	6179115508262195200	(1)
J1653-0158	Black Widow	4379227476242700928	(1)
J1810+1744	Black Widow	4526229058440076288	(1)
B1957+20	Black Widow	1823773960079216896	(1)
GROJ0422+32	LMXB (BH)	172650748928103552	(2)
A0620-00	LMXB (BH)	3118721026600835328	(2)
V404 Cyg	LMXB (BH)	2056188624872569088	(2)
XTE J1118+480	LMXB (BH)	789430249033567744	(2)
GROJ1655-40	LMXB (BH)	5969790961312131456	(2)
4U 2129+47	LMXB (NS)	1978241050130301312	(3)
Cen X-4	LMXB (NS)	6205715168442046592	(3)
Aql X-1	LMXB (NS)	4264296556603631872	(3)
SAX J1808.4-3658	LMXB (NS)	4037867740522984832	(3)
A0535+26	HMXB (NS)	3441207615229815040	(4)
KS 1947+300	HMXB (NS)	2031939548802102656	(4)
V4641 Sgr	HMXB (BH)	4053096388919082368	(4)
Cyg X-1	HMXB (BH)	2059383668236814720	(4)
GX 1+4	Symbiotic (NS)	4110236324513030656	(5)
4U 1954+319	Symbiotic (NS)	2034031438383765760	(5)
CXOGBS J173620.2–293338	Symbiotic (NS)	4060066227422719872	(5)
4U 1700+24	Symbiotic (NS)	4571810378118789760	(5)
NQ Gem	Symbiotic (WD)	868424696282795392	(6)
UV Aur	Symbiotic (WD)	180919213811383680	(6)
ZZ CMi	Symbiotic (WD)	3155368612444708096	(6)
ER Del	Symbiotic (WD)	1750795043999682304	(6)
CD -283719	Symbiotic (WD)	5608089951177429120	(6)
RX J0019.8+2156	SSS	2800287654443977344	(7)
RX J0925.7-4758	SSS	5422337322910734080	(7)
RR Tel	SSS	6448785024330499456	(7)

Table 5.2: All systems shown in Figure 5.1 with literature X-ray detections. (1): Koljonen and Linares (2023), (2): Garcia et al. (2001a), (3): Menou et al. (1999), (4): Russell et al. (2006), (5): Yungelson et al. (2019a), (6): Luna et al. (2013), (7): 4XMM-DR13 Catalog.

4XMM-DR13 ID	IAUNAME	Gaia DR3 ID	Non-magnetic CV	YSO	Active Binary . . .
201253101010037	4XMM J000009.8-251920	2335010480014243328	False	False	False
204033901010033	4XMM J000012.9+622946	429950007577101952	False	False	False
207009901010018	4XMM J000014.6+675337	528609770043800832	False	False	False
206584004010005	4XMM J000024.9+443634	385045506010558336	False	False	False
207009901010019	4XMM J000030.3+681159	528996042222710016	False	False	False
207009901010001	4XMM J000032.0+681500	528996591978497408	False	False	False
206935404010007	4XMM J000047.9+233216	2848395067729986688	False	False	False
206584004010038	4XMM J000102.0+442809	385041279762788608	False	False	False
206584004010048	4XMM J000110.9+443700	385043405769547136	False	False	False
204033901010077	4XMM J000129.2+622456	429945643890463488	False	False	False
200161401010017	4XMM J000130.0+625236	430053396031738112	False	False	False
206584004010017	4XMM J000139.7+442610	385028910256998528	False	False	True
206935404010018	4XMM J000146.9+233512	2848232133851323264	False	False	False
200417501010032	4XMM J000153.4-300612	2320841520343862400	False	False	False
204033901010016	4XMM J000153.6+623220	429947499316231808	False	False	False
200417501010078	4XMM J000154.4-301038	2320834614036455424	False	False	False
200417501010007	4XMM J000154.4-300741	2320835576109126400	False	False	False
204033901010056	4XMM J000155.6+622800	429946812121535488	False	False	False
200417501010112	4XMM J000157.0-301209	2320834304798813568	False	False	False
200417501010138	4XMM J000157.6-300929	2320834751475799808	False	False	False
. . .					

Table 5.3: I make the full XMM-*Gaia* crossmatch freely available in machine readable format. The first twenty rows, and select columns are shown here as a preview.

Chapter 6

CATACLYSMIC VARIABLES AND AM CVN BINARIES IN SRG/EROSITA + *GAIA*: VOLUME LIMITED SAMPLES, X-RAY LUMINOSITY FUNCTIONS, AND SPACE DENSITIES

Antonio C. Rodriguez, Kareem El-Badry, Valery Suleimanov, Anna F. Pala, Shrinivas R. Kulkarni, Boris Gaensicke, Kaya Mori, R. Michael Rich, Arnab Sarkar, Tong Bao, Raimundo Lopes de Oliveira, Gavin Ramsay, Paula Szkody, Matthew Graham, Thomas A. Prince, Ilaria Caiazzo, Zachary P. Vanderbosch, Jan van Roestel, Kaustav K. Das, Yu-Jing Qin, Mansi M. Kasliwal, Avery Wold, Steven L. Groom, Daniel Reiley, and Reed Riddle. Cataclysmic Variables and AM CVn Binaries in SRG/eROSITA + Gaia: Volume Limited Samples, X-Ray Luminosity Functions, and Space Densities. *Publications of the Astronomical Society of the Pacific*, 137(1):014201, January 2025. doi: 10.1088/1538-3873/ada185.

Author List

Antonio C. Rodriguez[1,*], Kareem El-Badry[1], Valery Suleimanov[2], Anna F. Pala[3], Shrinivas R. Kulkarni[1], Boris Gaensicke[4], Kaya Mori[5], R. Michael Rich[6], Arnab Sarkar[7], Tong Bao[8], Raimundo Lopes de Oliveira[9,10], Gavin Ramsay[11], Paula Szkody[12], Matthew Graham[1], Thomas A. Prince[1], Ilaria Caiazzo[13,1], Zachary P. Vanderbosch[1], Jan van Roestel[14], Kaustav K. Das[1], Yu-Jing Qin[1], Mansi M. Kasliwal[1], Avery Wold[15], Steven L. Groom[15], Daniel Reiley[16], Reed Riddle[16]

[1]Department of Astronomy, California Institute of Technology, 1200 East California Blvd, Pasadena, CA, 91125, USA

[2]Institut für Astronomie und Astrophysik, Universität Tübingen, Sand 1, 72076, Tübingen, Germany

[3]European Space Agency, European Space Astronomy Centre, Camino Bajo del Castillo s/n, Villanueva de la Cañada, E-28692 Madrid, Spain

[4]Department of Physics, University of Warwick, Coventry CV4 7AL, UK

[5]Columbia Astrophysics Laboratory, Columbia University, New York, NY, USA

[6]Department of Physics and Astronomy, UCLA, 430 Portola Plaza, Box 951547, Los Angeles, CA, 90095-1547, USA

[7]Institute of Astronomy, The Observatories, Madingley Road, Cambridge, CB3 OHA, UK

[8]INAF – Osservatorio Astronomico di Brera, Via E. Bianchi 46, 23807 Merate (LC), Italy

[9]Departamento de Física, Universidade Federal de Sergipe, Av. Marechal Rondon, S/N, 49100-000, São Cristóvão, SE, Brazil

[10]Observatório Nacional, Rua Gal. José Cristino 77, 20921-400, Rio de Janeiro, RJ, Brazil

[11]Armagh Observatory and Planetarium, College Hill, Armagh, BT61 9DG, N. Ireland, UK

[12]Department of Astronomy, University of Washington, 3910 15th Avenue NE, Seattle, WA 98195, USA

[13]Institute of Science and Technology Austria (ISTA), Am Campus 1, 3400 Klosterneuburg, Austria

[14]Anton Pannekoek Institute for Astronomy, University of Amsterdam, 1090 GE Amsterdam, The Netherlands

[15]IPAC, California Institute of Technology, 1200 E. California Blvd, Pasadena, CA 91125, USA

[16]Caltech Optical Observatories, California Institute of Technology, Pasadena, CA 91125, USA

[*]Corresponding author: acrodrig@caltech.edu

ABSTRACT

We present volume-limited samples of cataclysmic variables (CVs) and AM CVn binaries jointly selected from SRG/eROSITA eRASS1 and *Gaia* DR3 using an X-ray + optical color-color diagram (the “X-ray Main Sequence"). This tool identifies all CV subtypes, including magnetic and low-accretion rate systems, in contrast to most previous surveys. We find 23 CVs, 3 of which are AM CVns, out to 150 pc in the Western Galactic Hemisphere. Our 150 pc sample is spectroscopically verified and complete down to $L_X = 1.3 \times 10^{29}$ erg s^{-1} in the 0.2–2.3 keV band, and we also present CV candidates out to 300 pc and 1000 pc. We discovered two previously unknown systems in our 150 pc sample: the third nearest AM CVn and a magnetic period bouncer. We find the mean L_X of CVs to be $\langle L_X \rangle \approx 4.6 \times 10^{30}$ erg s^{-1}, in contrast to previous surveys which yielded $\langle L_X \rangle \sim 10^{31} - 10^{32}$ erg s^{-1}. We construct X-ray luminosity functions that, for the first time, flatten out at $L_X \sim 10^{30}$ erg s^{-1}. We infer average number, mass, and luminosity densities of $\rho_{\mathrm{N,\,CV}} = (3.7 \pm 0.7) \times 10^{-6}\mathrm{pc}^{-3}$, $\rho_M = (5.0 \pm 1.0) \times 10^{-5} M_\odot^{-1}$, and $\rho_{L_X} = (2.3 \pm 0.4) \times 10^{26}\mathrm{erg\ s}^{-1} M_\odot^{-1}$, respectively, in the solar neighborhood. Our uniform selection method also allows us to place meaningful estimates on the space density of AM CVns, $\rho_{\mathrm{N,\,AM\,CVn}} = (5.5 \pm 3.7) \times 10^{-7}\mathrm{pc}^{-3}$. Magnetic CVs and period bouncers make up 35% and 25% of our sample, respectively. This work, through a novel discovery technique, shows that the observed number densities of CVs and AM CVns, as well as the fraction of period bouncers, are still in tension with population synthesis estimates.

6.1 Introduction

Cataclysmic Variables (CVs) are the most numerous accreting compact object binaries in the Milky Way. They serve as important laboratories of accretion physics and binary evolution which extend to many other types of binaries (e.g., Tauris and van den Heuvel, 2023). CVs are important in a broader astrophysical context since they likely dominate the hard X-ray excess seen from the Galactic Center (GCXE; Hailey et al., 2016) and Galactic Ridge (GRXE; Revnivtsev et al., 2006). CVs are composed of a white dwarf (WD) accreting from a Roche-lobe filling donor, which is typically a late-type star (e.g., Warner, 1995b; Hellier, 2001b). In magnetic CVs, where the WD magnetic field is strong enough that the Alfvén radius extends well past the surface of the WD, the disk is either substantially truncated (intermediate polars; $B \approx 1$–10 MG) or entirely prevented from forming (polars; $B \approx 10$–230 MG de Martino et al., 2020a; Ferrario et al., 2020). In both cases, matter is channeled via magnetic field lines onto the WD surface, rather than flowing through the disk boundary layer onto the WD as in non-magnetic CVs (e.g., Mukai, 2017).

AM Canum Venaticorum (AM CVn) binaries are the ultracompact analogs of classical CVs, which are highly evolved, having undergone one or two common envelope events (e.g., Warner, 1995b; Solheim, 2010; Ramsay et al., 2018). As a result they have have helium-dominated donors and orbital periods in the range of 5–65 min (Ramsay et al., 2018). Because of their short orbital periods, some AM CVns will be among the strongest sources of millihertz gravitational waves as seen by the upcoming Laser Space Interferometer Antenna (e.g., Nelemans et al., 2004b; Kupfer et al., 2024).

The most fundamental questions surrounding CVs and AM CVns can only be answered through population studies: 1) What is the true space density and total number of CVs and AM CVns in the Milky Way? (e.g., Goliasch and Nelson, 2015; Belloni et al., 2018; Nelemans et al., 2001; Carter et al., 2013); 2) What fraction of CVs are magnetic, and what is the origin of their magnetism? (e.g., Pala et al., 2020a; Schreiber et al., 2021a); 3) Why is the mean mass of WDs in CVs $\approx 30\%$ higher than that of single WDs? (e.g., Zorotovic and Schreiber, 2020; Pala et al., 2022a); 4) Where are all of the “period bouncers" — systems that have a degenerate, brown dwarf donor, and are predicted to constitute 40–70% of all CVs? (e.g., Goliasch and Nelson, 2015; Belloni et al., 2018; Pala et al., 2020a); and 5) What role does magnetic braking play in angular momentum loss (AML), which drives the evolution of CVs and AM CVn progenitors? (e.g., Rappaport et al., 1983;

Andronov et al., 2003; El-Badry et al., 2022). Regarding AM CVns specifically, their formation channel is a major question that has garnered recent interest (e.g., van Roestel et al., 2021; Sarkar et al., 2023a; Belloni and Schreiber, 2023).

The biggest problems with CV and AM CVn surveys are incompleteness and inhomogeneity: no single survey method, aside from large spectroscopic surveys, has been sensitive to all subtypes. Combining systems from various photometric and spectroscopic surveys as was done in the seminal work by Pala et al. (2020a) is possible, but requires hard work and leads to a selection function that is difficult to characterize (e.g., Pala et al., 2020a; Inight et al., 2021). This has strongly encumbered estimates of completeness, which have led to contrasting estimates of space densities and the relative number of CVs in different evolutionary stages. A brief summary of CV evolution reveals which surveys are biased towards the discovery of different CV subtypes.

CVs are “born" when the companion star in a post common envelope binary (PCEB) fills its Roche lobe and starts mass transfer to the WD. Depending mainly on the nature of the donor star, most CVs are born at orbital periods of $P_{\rm orb}$ = 6–10 hr (e.g., Knigge et al., 2011). From this point, down to $P_{\rm orb} \approx$ 3–4 hr, mass transfer is high, reaching levels of $\dot{M} \approx 10^{-8} M_{\odot}$ yr^{-1}. Non-magnetic CVs in this evolutionary state are usually discovered as novalikes (e.g., Inight et al., 2023a), while magnetic systems in this evolutionary state are typically X-ray bright ($L_X \sim 10^{31} - 10^{33}$ erg s^{-1}) intermediate polars (IPs) (e.g., Suleimanov et al., 2019). As mass transfer continues, AML is high, driven mostly by magnetic braking of the donor star, and the accretion disk in non-magnetic CVs remains permanently ionized. As CVs evolve to shorter periods, $\dot{M}$ is reduced, which leads to the onset of a thermal instability (Pringle, 1976; Lasota, 2001). This is believed to be the cause of dwarf nova outbursts, which observationally manifest themselves as a 2–8 mag transient brightening at optical wavelengths lasting a few tens of days (e.g., Hellier, 2001b; Inight et al., 2023a).

At $P_{\rm orb} \approx$ 2–3 hr, there has been observational evidence and theoretical explanations for the (contested) existence of a “period gap". It is believed that mass transfer halts, presumably due to the donor star becoming fully convective causing magnetic braking to turn off (Spruit and Ritter, 1983a; Howell et al., 2001; Zorotovic et al., 2016a; Schreiber et al., 2024a). AML due to gravitational wave radiation brings CVs back into contact at $P_{\rm orb} \approx$ 2 hr, and mass transfer rates remain high enough for dwarf nova outbursts to be seen until CVs approach the canonical orbital period minimum

of $\approx$ 78 min (Paczynski and Sienkiewicz, 1983; Knigge et al., 2011). At this stage in their evolution, mass transfer rates reduce to $\dot{M} \approx 10^{-11} - 10^{-10} M_{\odot}$ yr^{-1}, and the timescale required for the onset of the thermal instability at such low accretion rates is typically much longer than observational timescales. At such low mass transfer rates, the X-ray luminosity is also dramatically reduced, reaching values as low as $L_X \sim 10^{29}$ erg s^{-1} (Reis et al., 2013). Once enough mass is depleted from the donor, nuclear burning halts, and the donor becomes degenerate. This means that the donor radius *increases* as mass is lost. This causes CVs to "bounce" and evolve to longer periods at the canonical period minimum of $P_{\rm orb} \approx 78$ min, leading to these low mass transfer rate ($\dot{M} \approx 10^{-11} M_{\odot}$ yr^{-1}) systems with degenerate donors being called "period bouncers".

At this point, it is clear that CVs at different evolutionary stages have very different observed phenomenology, and have historically been detected in different ways: 1) X-ray surveys (especially hard X-ray surveys sensitive to $E \gtrsim 10$ keV) have mainly discovered magnetic CVs: IPs and nearby polars, though nearby non-magnetic CVs with high mass transfer rates have also been discovered this way (e.g., using the ROSAT all-sky soft X-ray mission and the *Swift*/BAT and *INTEGRAL* hard X-ray missions; Verbunt et al., 1997; Schwope et al., 2000; Suleimanov et al., 2022); 2) Optical photometric surveys have mainly discovered (non-magnetic) dwarf novae (e.g., using the Catalina Real-time Transient Facility and Zwicky Transient Facility; Breedt et al., 2014; Szkody et al., 2020); and 3) large spectroscopic surveys have mainly discovered low-accretion rate CVs near the orbital period minimum (e.g., using the Sloan Digital Sky Survey; Gänsicke et al., 2009; Szkody et al., 2011; Inight et al., 2023a). This has led to present CV catalogs such as the Ritter and Kolb catalog (Ritter and Kolb, 2003a) and the International Variable Star Index (VSX) catalog[1] being comprised of systems from many different surveys, each with their own biases.

A similar story applies to AM CVns, though they evolve from short to long orbital periods given the degenerate nature of their donor stars. Short orbital period ($P_{\rm orb}$ = 5 – 20 min) systems do not undergo optical outbursts due to their high mass transfer rates, but are X-ray bright[2] and have been identified since the ROSAT era (e.g., Israel et al., 2002; Ramsay et al., 2018). At intermediate periods ($P_{\rm orb}$ = 20 – 50

[1] `https://www.aavso.org/vsx/index.php?view=search.top`

[2] Aside from the shortest period AM CVns, HM Cnc and V407 Vul, the rest of the population is X-ray faint, reaching only $L_X \sim 10^{30} - 10^{31}$ erg s^{-1} as seen from X-ray follow-up observations (e.g., Ramsay et al., 2005, 2006; Begari and Maccarone, 2023).

min), accretion disks in AM CVns are subject to thermal instabilities, leading to dwarf nova outbursts which enable easy identification through optical photometric surveys (e.g., van Roestel et al., 2021). However, the majority of AM CVns are expected to be long-period ($P_{\rm orb} = 50 - 65$ min) systems, since they remain at low mass transfer rates for $\sim$ few Gyr (e.g., Nelemans et al., 2001; Wong and Bildsten, 2021). These systems, like low accretion rate CVs, do not outbust frequently, and have only been identified through large spectroscopic surveys from SDSS (Roelofs et al., 2007; Carter et al., 2013) or through their eclipses in large optical photometric surveys (van Roestel et al., 2022).

Here, we present the first volume-limited survey of CVs, including AM CVns, selected using a single tool which is sensitive to all subtypes. We construct volume-limited samples of CV candidates out to 1000 pc, 300 pc, and 150 pc. The 150 pc sample is confirmed with optical spectroscopy, complete down to $L_X = 1.3 \times 10^{29}$erg s^{-1} in the 0.2–2.3 keV range, and the main focus of this paper. This survey is made possible using a tool recently presented by Rodriguez (2024b) — an X-ray + optical color-color diagram dubbed the “X-ray Main Sequence" which efficiently distinguishes accreting compact objects from coronally active stars. Rodriguez (2024b) applied this tool to discover new CVs in a crossmatch of the *XMM-Newton* catalog and *Gaia*, and recently, Galiullin et al. (2024a) incorporated this tool to discover new CVs in a crossmatch between the *Chandra* Source Catalog and *Gaia*. Here, we construct the X-ray Main Sequence through a crossmatch of the recently released SRG/eROSITA eRASS1 soft X-ray survey of the Western Galactic Hemisphere (Merloni et al., 2024) with *Gaia* Data Release 3 (DR3; Gaia Collaboration et al., 2023a).

In Section 6.2, we show that given a sensitive enough X-ray survey, CVs of all subtypes can be detected. In Section 6.3, we present the crossmatch between the eRASS1 catalog and *Gaia* DR3 to identify optical counterparts. We outline the construction of CV samples out to 150, 300, and 1000 pc, as well as a reference sample of CVs created from the VSX catalog. In Section 6.4, we compare the X-ray luminosity distributions of volume-limited samples to those of our VSX reference samples. We also present new space densities and X-ray luminosity functions based on the 150 pc sample. In that section, we also present the two new CVs discovered within 150 pc using our method and summarize global properties of all CVs in the 150 pc sample. Finally, in Section 8.4, we discuss our sample completeness. We compare our inferred space densities of CVs and AM CVns to those of previous

surveys as well as theoretical predictions.

6.2 X-ray Emission from Cataclysmic Variables

All CVs are X-ray emitters. Assuming that half of the gravitational potential energy associated with accretion is radiated away as X-rays[3], the X-ray luminosity can be expressed as in Patterson and Raymond (1985):

$$\begin{aligned} L_X &= \eta \varepsilon_X \varepsilon_{\rm out} \frac{1}{2} \frac{G M_{\rm WD} \dot{M}}{R_{\rm WD}} \\ &= 6.9 \times 10^{30} \left(\frac{\eta}{0.1}\right) \left(\frac{\varepsilon_X}{0.3}\right) \left(\frac{\varepsilon_{\rm out}}{0.5}\right) \left(\frac{M_{\rm WD}}{0.8 M_\odot}\right) \times \\ &\left(\frac{\dot{M}}{10^{-10} M_\odot \ {\rm yr}^{-1}}\right) \left(\frac{R_{\rm WD}}{0.0105 R_\odot}\right)^{-1} \ {\rm erg \ s^{-1}} \end{aligned} \tag{6.1}$$

where L_X is the X-ray luminosity in the 0.2–2.3 keV range, η is the radiative efficiency, ε_X is the correction factor for observing X-rays only in the 0.2–2.3 energy band (a power-law model with $\Gamma = 2$ is assumed to calculate the above value of 0.3), $\varepsilon_{\rm out}$ is the fraction of X-rays that are emitted outward and not absorbed by the WD (we adopt a value of 0.5 as in Patterson and Raymond, 1985), the additional factor of $1/2$ represents the fraction of gravitational potential energy associated with accretion radiated by the boundary layer, and $M_{\rm WD}$ and $R_{\rm WD}$ are the mass and radius of the WD (Bédard et al., 2020), respectively, and $\dot{M}$ is the mass transfer rate.

While there are uncertainties in this simple treatment, particularly in estimating η and $\varepsilon_{\rm out}$, it is clear that the lowest mass transfer rates reached by CVs, $\dot{M} \approx 10^{-11} M_\odot \ {\rm yr}^{-1}$, means that they can reach very low X-ray luminosities, on the order of $L_X \sim 10^{29}$ erg s^{-1}. This is supported by observational evidence, notably the work of Reis et al. (2013), where it was found that the mean X-ray luminosity of an inhomogenously selected sample of low accretion rate CVs discovered by the Sloan Digital Sky Survey (SDSS; York et al., 2000b) reached that value[4].

The first all-sky X-ray survey that is sensitive to such low-L_X systems is eRASS1, carried out by the eROSITA telescope aboard the *SRG* spacecraft (Sunyaev et al., 2021; Merloni et al., 2024). eRASS1 goes nearly six times deeper than the last all-sky soft X-ray survey, ROSAT (Voges et al., 1999a): eRASS1 and the 2RXS ROSAT

[3]This assumes the standard Shakura and Sunyaev (1973) picture that half of the energy is radiated away by the boundary layer, with the other half stored by the accretion disk, though the constant of 1/2 may increase up to 1 when the disk is truncated by a magnetic WD.

[4]These values hold for CVs (i.e., WDs with a Roche-lobe filling donors), whereas wind-accreting systems such as low accretion rate polars (LARPs) have been shown to accrete at even lower rates, producing $L_X \lesssim 8 \times 10^{28}$erg s^{-1} (e.g., Szkody et al., 2004).

catalog have flux limits of $F_X = 5{\times}10^{-14}$erg s^{-1}cm^{-2} and $F_X = 3{\times}10^{-13}$erg s^{-1}cm^{-2} in the 0.2–2.3 and 0.1–2.4 keV bands, respectively (Merloni et al., 2024; Boller et al., 2016a). Another advantage of the eROSITA telescope is the improved localization of sources compared to ROSAT, with a mean positional error of 4.7" and 15", respectively (Salvato et al., 2022; Agüeros et al., 2009).

The added depth of SRG/eROSITA enables the construction of volume-limited, X-ray selected, complete CV samples for the first time. At the $L_X \sim 10^{29}$erg s^{-1} luminosity limit, the 2RXS ROSAT catalog is only complete out to ~50 pc, while the eRASS1 SRG/eROSITA catalog is complete out to ~150 pc, given their respective flux limits. The ROSAT distance limit of 50 pc is not very useful, since the nearest CV to Earth, WZ Sge, at 48 pc, is the only known system within 50 pc, while 42 CVs have been found in the entire sky out to 150 pc (Pala et al., 2020a). Since all CV subtypes are X-ray emitters, and the X-ray Main Sequence selects all CV subtypes without any obvious bias (Rodriguez, 2024b), this likely represents the most effective and complete way to create a CV catalog to date.

6.3 Sample Creation

X-ray + Optical Crossmatching

We aim to create a pure and complete sample of SRG/eROSITA X-ray sources associated with *Gaia* (localized to milliarcseconds) optical counterparts. We first consider the distribution of the separation between X-ray and optical positions, r. Assuming that the distribution of both X-ray and optical positional measurements is Gaussian about the true position, the distribution of r is the well-known Rayleigh distribution (Equation 6.2; e.g., Salvato et al., 2022; Belvedersky et al., 2022; Czesla et al., 2023):

$$p(r;\sigma_{\rm sep}) = \frac{r}{\sigma_{\rm sep}^2}\exp\left(-\frac{1}{2}\frac{r^2}{\sigma_{\rm sep}^2}\right) \tag{6.2}$$

where $\sigma_{\rm sep}$ is the Rayleigh parameter, equivalent to the value of the mode of the distribution (the mean is $\sqrt{\pi/2}$ times that value). Thus, we can use this distribution to characterize the probability that a given optical match is the true counterpart to an X-ray position.

Volume Limited Samples

We start with the eRASS1 "Main" catalog released by the German (DE) consortium of SRG/eROSITA[5]. The eRASS1 release by the DE consortium covers all detections

[5] https://erosita.mpe.mpg.de/dr1/AllSkySurveyData_dr1/Catalogues_dr1/

by SRG/eROSITA covering the Western half (approximately $180° < \ell < 360°$) of the Galactic sky in the first semester of operations (December 2019 – June 2020). Complete details regarding the data footprint and additional information are reported by Merloni et al. (2024). The entire catalog contains 903,203 unique X-ray sources down to an all-sky flux limit of approximately $F_X \sim 5 \times 10^{-14}$ erg s^{-1}cm^{-2} in the 0.2–2.3 keV range as part of the "Main" catalog. We find the mean positional uncertainty (`POS_ERR`) of all sources in eRASS1 to be 4.5".

We keep only point sources, and those with a < 1% chance of being a spurious detection by enforcing `EXT == 0` and `DET_LIKE_0 > 10`, respectively. This reduces the sample size to 427,241 (46% of the original catalog), and reduces the mean positional uncertainty to 3.5". We then crossmatch this catalog with all sources in *Gaia* Data Release 3 (DR3; Gaia Collaboration et al., 2023a) within 20", which gives us 1,850,697 unique optical sources. Not all of those optical sources are expected to be the true counterparts. We use such a large crossmatch radius in order to distinguish the Rayleigh distribution (of likely matches) from the distribution of chance alignments (which increases with r, and requires a large crossmach radius to be well-populated). We also remove X-ray faint objects, keeping only those with `ML_FLUX_1` $> 3 \times 10^{-14}$erg s^{-1}cm^{-2} in the 0.2–2.3 keV range[6].

In order to select Galactic sources with well-measured *Gaia* parallaxes and proper motions, we enforce the following:

- `pmra /pmra_error > 5`
- `pmdec /pmdec_error > 5`
- `parallax_over_error > 3`.

We do not enforce a cut on the astrometric solution using the `RUWE` parameter, since this removes known CVs within 150 pc (see Section 6.4). Rather, we adopt the classifier from Rybizki et al. (2022) to remove spurious astrometric solutions. After some experimenting to recover known CVs within 150 pc (while not losing any known systems), we enforced the following cuts, which have some overlap with those used successfully in other surveys (e.g., El-Badry et al., 2021a):

[6]The presence of these outliers is likely due to the increased eROSITA depth in the ecliptic poles (Merloni et al., 2024). All such systems are beyond 150 pc and this small difference in sensitivity does not affect our final analyses with the 150 pc sample.

- `fidelity_v2 > 0.75`. This corresponds to a < 25 % chance of a spurious astrometric solution for all sources.
- `dist_nearest_neighbor_at_least_4_brighter == 0`. This ensures that the nearest neighbor ≥ 4 mag brighter is over 30 arcsec away[7].
- `norm_dG == NaN OR norm_dG < -3`. This ensures that there are no nearby neighbors or no nearby bright stars which can contaminate the photometry of the source.

The X-ray Main Sequence

Rodriguez (2024b) showed that an empirical cut in the plane of $F_X/F_{\rm opt}$ (vertical axis) vs. *Gaia* BP – RP (horizontal axis) can efficiently select CVs (among other compact object binaries) from other stellar X-ray sources. The cut is defined by $\log_{10}(F_X/F_{\rm opt}) = ({\rm BP} - {\rm RP}) - 3.5$. It was shown that virtually all of the CVs in the Ritter and Kolb catalog (Ritter and Kolb, 2003a) with *Gaia* and *XMM-Newton* counterparts are above the cut, regardless of subtype and without requiring an extinction correction.

We compute the optical flux in the Gaia G band in the same way as in Rodriguez (2024b), with $F_{\rm opt} = 10^{0.4(m_\odot - m)} L_\odot/(4\pi(1\ {\rm AU})^2)$, where $m_\odot = -26.7$ and m is `phot_g_mean_mag`. We take F_X as the X-ray flux in the 0.2–2.3 keV eROSITA band, `ML_FLUX_1`.

In order to improve our selection of CVs, rather than just take all objects above the "empirical cut" from Rodriguez (2024b), we experimented with recovering a highly cleaned sample of CVs (well-vetted systems with known subtypes and orbital periods from photometry and/or spectroscopy) from the International Variable Star Index (VSX) catalog. We describe this procedure in Appendix 6.8. The outcome of this was the adoption of a "modified cut":

- $\log_{10} F_X/F_{\rm opt} > {\rm BP} - {\rm RP} - 3.5$
  if $-0.3 < {\rm BP} - {\rm RP} < 0.7$

[7] We note that this condition could be a bit too strict. Relaxing this condition to allow for ≥ 4 mag neighbors up to 10 arcsec away introduces no new CVs into the 150 pc sample, but does introduce three false matches within a few arcsec of bright (≳ 8 mag stars). Applying this relaxed condition to the 300 pc sample does introduce four recently verified CVs (A. Pala, priv. comm.), albeit with six false matches near bright stars.

- $\log_{10} F_X/F_{\rm opt} > {\rm BP} - {\rm RP} - 3$
  if $0.7 < {\rm BP} - {\rm RP} < 1.5$

We then enforce this “modified cut" as described above, as well as the following:

- BP–RP <1.5. This ensures that a large population of (falsely matched) M dwarfs does not enter the sample while excluding virtually no previously known systems. We elaborate further on this cut in Appendix 6.8.
- BP–RP >-0.3. This ensures that no presumably single hot WDs enter the sample. While these could be true matches, no known CVs are this blue (see Appendix 6.8).

Finally, in Appendix 6.8, we show that at all distances, after enforcing the cuts above, the population of CV candidates is well-modeled by a Rayleigh distribution with $\sigma_{\rm sep} \approx 2.2$”. To ensure > 99% completeness, we keep all systems within a separation of $r < 7.7$” ($3.5\sigma_{\rm sep}$). We also keep all systems out to $r < 11$” ($5\sigma_{\rm sep}$) that are isolated in the field (i.e., *no* other optical sources are present within 30 arcsec). This set of cuts also ensures that all systems in the 150 pc spectroscopically verified sample by Pala et al. (2020a) are recovered in *our* 150 pc sample (see next section). However, such a large separation does introduce some false positives (primarily with background active galactic nuclei), which we are able to remove after manual inspection in the 150 pc sample (see next section).

In Figure 6.1, we present our three volume-limited samples out to distances of 1000 pc, 300 pc, and 150 pc, created from the cuts described above. In the left panels, we show the X-ray Main Sequence constructed from all systems that meet the above cuts. Those that fall above the “modified cut" and color cuts required to be a CV candidate are highlighted in blue. In the middle panels, those same systems are shown on a Hertzsprung-Russell diagram assembled from all systems that meet the cuts above, except for the “modified cut" in the X-ray Main Sequence. The majority of CV candidates selected from the X-ray Main Sequence are located between the WD track and the main sequence, where they would be expected to reside. The right panels show luminosity distributions created from CV candidate systems, showing that the mean observed X-ray luminosity, $\langle \log L_X \rangle$, shifts depending on the survey volume. We describe each of the samples in more detail below. Elaborating on the point made by Rodriguez (2024b), we also emphasize the remarkable efficiency of the X-ray Main Sequence in Table 6.1. At all distance limits, < 1% of sources

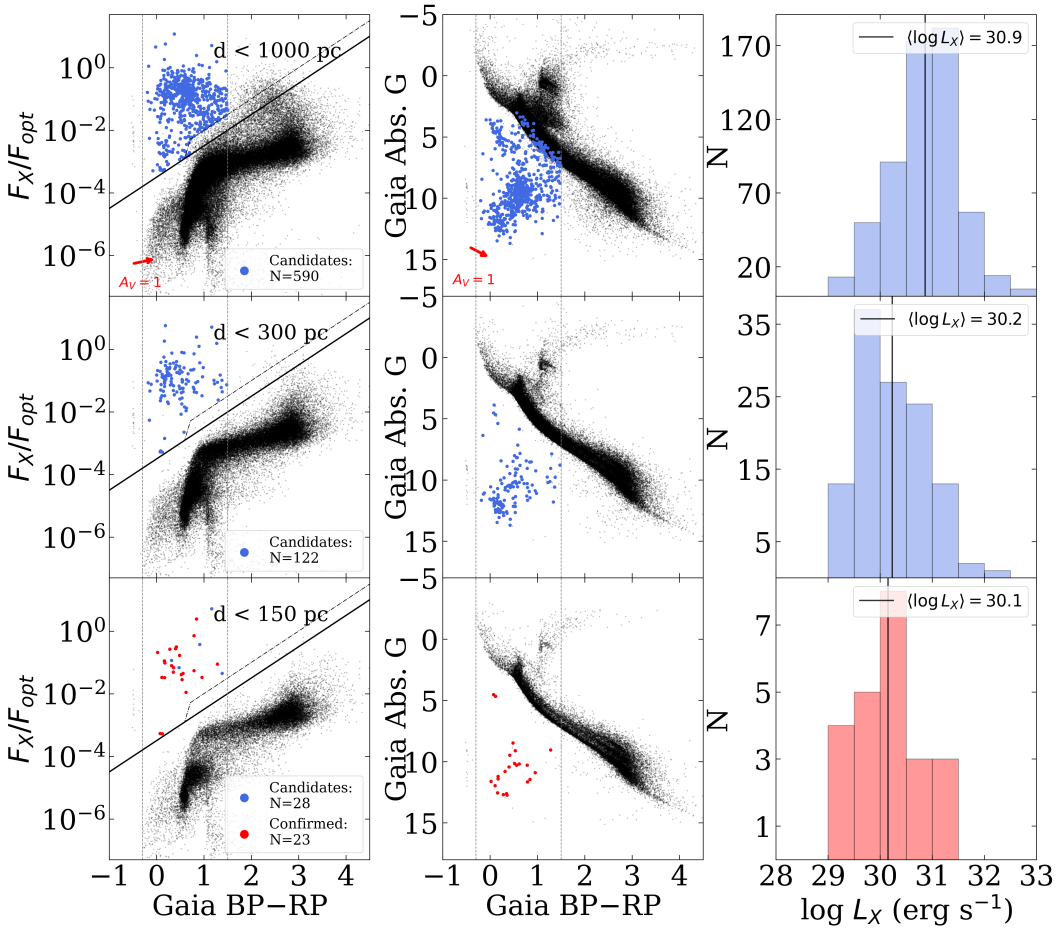

Figure 6.1: Volume-limited samples of CVs in eROSITA selected using the X-ray Main Sequence are shown out to distances of 150, 300, and 1000 pc (from bottom to top; tables available in machine-readable form). All objects in SRG/eROSITA eRASS1 within the given distance are shown in black, CV candidates in blue, and spectroscopically confirmed CVs in red. We select CVs using the dash-dot diagonal line in the X-ray Main Sequence (left), and exclude all objects with BP–RP < -0.3 (hot WDs) and BP–RP > 1.5 (false matches). We plot CVs on an HR diagram constructed using all eRASS1 sources within each volume (center). The X-ray luminosity distribution out to each distance is shown on the right, with the 150 pc sample in red to show it is spectroscopically verified.

are targeted as candidate CVs (or more generally, accreting compact objects) for spectroscopic follow-up.

1000 pc and 300 pc Samples

To create the 1000 pc sample, we enforced all cuts as described in Section 6.3 and 6.3, with the addition of `parallax` $>$ `1`. The total number of systems that pass all cuts

is $N = 590$, with an observed luminosity completeness of $L_X = 5.6 \times 10^{30}$erg s^{-1} in the 0.2–2.3 keV range.

To create the 300 pc sample, we enforce `parallax > 1000/300`. The total number of systems that pass all cuts is $N = 122$, with an observed luminosity completeness of $L_X = 5.1 \times 10^{29}$erg s^{-1} in the 0.2–2.3 keV range. At distances beyond a few hundred pc, the Galactic hydrogen column, N_H, becomes non-negligible and is particularly efficient at absorbing soft X-rays. Therefore, at these distances, the true luminosity completeness starts to depend on the direction of the line of sight. However, because the luminosity limit of these two catalogues does not extend down to the lowest L_X CVs, we do not explore these catalogs further in this work.

However, we make these tables of CV candidates out to 300 pc and 1000 pc publicly available. We note that these samples likely have a high purity rate since they primarily contain objects between the WD track and main sequence on the *Gaia* HR diagram (center panels Figure 6.1), though CVs with an evolved donor and/or bright disk may be near or on the main sequence (e.g., Abril et al., 2020). We are conducting a spectroscopic survey of the 1000 pc and 300 pc catalogs to investigate the demographics of more distant systems, which will be reported elsewhere.

150 pc Sample

Finally, we created a 150 pc sample (`parallax > 1000/150`), which is the main focus of this paper[8]. We focus primarily on this sample for two reasons. Firstly, given the completeness of eRASS1 down to $F_X = 5 \times 10^{-14}$erg s^{-1}cm^{-2}, the X-ray luminosity completeness of a 150 pc catalog is $L_X = 1.3 \times 10^{29}$erg s^{-1}. This is good agreement with the lower limit of L_X observed in CVs in the past — Reis et al. (2013) intentionally targeted low accretion rate WZ Sge-like systems identified with SDSS, and only 1 of 20 systems (5 %) in their sample has an X-ray luminosity below our completeness threshold (even after accounting for the flux difference in *Swift*/XRT and SRG/eROSITA energy bands). In contrast, the luminosity completeness limit of a 300 pc sample constructed with eRASS1 would miss 6 out of 20 systems in the Reis et al. (2013) sample (30%).

Our 150 pc catalog, constructed with the cuts described above, yields 28 candidate CVs. We visually inspect all systems, using the Aladin Lite (Baumann et al., 2022)

[8]In order to best calculate *Gaia* distances, we used the median posteriors from Bailer-Jones et al. (2021a). Even after extending the parallax limit to `parallax > 1000/175`, no new sources were found to be within 150 pc.

Volume Limited Sample Radius (pc)	Complete to L_X Limit (erg/s)	Candidate Galactic X-ray sources	Candidate CVs	Confirmed CVs
1000	5.6×10^{30}	73,129	590 (0.8%)	Future work
300	5.1×10^{29}	43,403	122 (0.3%)	Future work
150	1.3×10^{29}	23,718	28 (0.1%)	23

Table 6.1: The X-ray Main Sequence efficiently selects CV candidates from other Galactic X-ray sources in volume-limited samples. Percentages in the fourth column are taken with respect to sources in the third. The 150 pc sample is the only one complete down to the low L_X end of CVs.

tool to overlay sources from *Gaia* DR3 on images from the PanSTARRS PS1, Digitized Sky Survey (DSS), or DESI Legacy DR10 surveys to search for possible nearby faint contaminants. We first eliminate two systems: 1eRASS J120125.8+084801 since it is $\sim$ 3" away from a known quasar and 1eRASS J170655.5-350631 since there are 6 other *Gaia* sources within a $\sim$ 5" radius, a subset of which could dominate the observed X-ray flux at that position. Moreover, the *Gaia* XP spectrum of that source shows Balmer absorption, but no emission lines. We also eliminate 1eRASS J035319.7-560057 since the DESI Legacy DR10 images reveal that the X-ray position is closer to an extended object $\sim$ 3" away, which is likely an active galaxy or cluster, and therefore the true counterpart to the X-ray source. Moreover, this *Gaia* source is significantly fainter in the optical than the rest of the verified CVs, having a *Gaia* G magnitude of 20.6, whereas the rest of the verified CVs are more commonly between $G \approx 16 - 18$ mag.

After removing the above false matches, we are left with 25 candidate CVs. Of these, there are two true X-ray + optical matches, which are indeed compact object binaries as predicted by the X-ray Main Sequence, but not CVs. The first is 1eRASS J043715.9-471509, which is a known recycled pulsar + WD binary (e.g., Danziger et al., 1993). Previously, *Chandra* observations revealed X-rays from this system (Zavlin et al., 2002), yet it appears that the WD remains poorly studied, likely due to its optical faintness (Durant et al., 2012). The second such system is AR Sco, the prototypical WD "pulsar", in which a rapidly spinning magnetic WD generates

synchrotron emission presumably through interactions with the magnetic field of its M dwarf companion (Marsh et al., 2016). This system is not a CV, since no mass transfer is occurring, though it is close to filling its Roche lobe (Marsh et al., 2016; Pelisoli et al., 2022a). The recovery of these systems reveals the remarkable flexibility of the X-ray Main Sequence in revealing a breadth of compact object binaries.

After removing the above systems, we were left with 23 candidate CVs. Twenty-one of those systems are previously known CVs, and present in the Pala et al. (2020a) catalog. In Table 6.2, we use the classifications from Pala et al. (2020a), with one exception — SDSS J125044.42 +154957.3, which we describe further in Section 6.4. "AM " corresponds to (magnetic) polars, "SU" corresponds to outbursting non-magnetic systems that show SU UMa outburst behavior (i.e., superoutbursts; Osaki, 1989), "UG" corresponds to outbursting non-magnetic systems that show U Gem outburst behavior (i.e., dwarf novae), "NL" corresponds to non-outbursting non-magnetic systems in a high accretion state, "UGWZ" corresponds to non-magnetic systems that only show outburst behavior on very long timescales (and appear quiescent otherwise) in a low accretion state like WZ Sge, "IP" corresponds to intermediate polars, and "AM CVn" corresponds to AM CVns. For further detail, we refer the reader to Pala et al. (2020a) for references to individual systems, and Hellier (2001b) and Inight et al. (2023a) for modern reviews of subtypes and phenomenology. Of the 42 systems in the Pala et al. (2020a) catalog, 24 are located in the Western Galactic Hemisphere and should in principle be recovered by our analysis. However, V379 Vir is one of the three systems in Pala et al. (2020a) not recovered in our 150 pc sample, which an updated *Gaia* DR3 parallax reveals to be located at a distance 155 ± 5 pc and beyond our 150 pc distance limit (Pala et al. (2020a) used *Gaia* DR2). This means that we recover 21 of the 23 CVs within 150 pc in the Western Galactic Hemisphere reported by Pala et al. (2020a), leaving Gaia J154008.28–392917.6 (d = 139 pc) and V379 Tel (d = 131 pc) as the only systems in the Pala et al. (2020a) catalog not recovered by our analysis. We explore possible reasons for this and compare our 150 pc sample to that of Pala et al. (2020a) further in Section 6.5.

This left 2 systems left to verify, both of which we confirm as CVs — 1eRASS J054726.9+132649 is a new magnetic period bouncer and 1eRASS J101328.7-202848 is a new AM CVn. To help characterize those systems, we queried the optical time domain photometric database of the Zwicky Transient Facility (ZTF;

Bellm et al., 2019b; Graham et al., 2019; Dekany et al., 2020; Masci et al., 2019). ZTF is a 47 deg^2 field-of-view camera on the Samuel Oschin 48-inch telescope at Palomar Observatory, which scans the DEC > –28° sky on a two-day cadence. Both new systems and the data associated with them are described in further detail in Section 6.4. In summary, our 150 pc catalog, after visual inspection and removal of other compact object binaries, is comprised of 23 *spectroscopically confirmed* CVs, 2 of which are discoveries made possible thanks to the X-ray Main Sequence.

Table 6.2: Our 150 pc volume-limited sample, created through an X-ray + optical crossmatch of SRG/eROSITA eRASS1 and *Gaia* DR3 (table with additional columns available in machine-readable form). All 25 systems that pass our cuts and visual inspection are shown, along with 23 confirmed CVs, 3 of which are AM CVns. We highlight newly confirmed systems and provide subtypes and orbital periods ($P_{\rm orb}$) for previously known systems following Pala et al. (2020a), where a volume-limited sample was created primarily from optically-identified systems. The star (*) symbol indicates a system is a period bouncer.

eROSITA Name	Other Name	$P_{\rm orb}$ (min)	F_X ($\times 10^{13}$ erg s^{-1}cm^{-2})	Distance (pc)	L_X ($\times 10^{30}$ erg s^{-1})	Gaia G mag	$r_{\rm sep}$ (arc-sec)	Type
150 pc CVs + AM CVns								
1eRASS J014100.5-675326	BL Hyi	113.64	26.54 ± 1.15	$129.29^{+0.83}_{-0.82}$	$5.02^{+0.40}_{-0.37}$	17.2	1.25	AM
1eRASS J040911.6-711741	VW Hyi	106.85	35.17 ± 0.91	$53.74^{+0.06}_{-0.05}$	$1.15^{+0.05}_{-0.05}$	13.8	1.42	UGSU
1eRASS J054726.9+132649	New (this work)	93.948	0.91 ± 0.30	$132.06^{+3.06}_{-2.66}$	$0.18^{+0.10}_{-0.10}$	18.3	3.38	AM*
1eRASS J075505.1+220003	U Gem	254.74	68.94 ± 3.09	$93.06^{+0.31}_{-0.34}$	$6.75^{+0.50}_{-0.54}$	13.9	1.26	UG
1eRASS J082418.3+380104	ZTF J0824+3801	84.46	1.53 ± 0.35	$137.99^{+4.07}_{-3.80}$	$0.35^{+0.17}_{-0.16}$	18.3	2.86	UGWZ*

Continued on next page

Table 6.2 – continued from previous page

eROSITA Name	Other Name	$P_{\rm orb}$ (min)	F_X ($\times 10^{13}$ erg s^{-1}cm^{-2})	Distance (pc)	L_X ($\times 10^{30}$ erg s^{-1})	Gaia G mag	$r_{\rm sep}$ (arc-sec)	Type
1eRASS J084858.1+491055	ZTF J0848+4910	95.11	1.97 ± 0.41	$122.67^{+2.83}_{-2.65}$	$0.35^{+0.15}_{-0.14}$	17.9	1.55	AM
1eRASS J085019.6+121340	ZTF J0850+1213	97.96	2.17 ± 0.38	$120.84^{+1.47}_{-1.40}$	$0.38^{+0.14}_{-0.13}$	18.0	2.04	AM
1eRASS J092751.5-040131	WZ Sge	81.63	20.23 ± 1.16	$45.39^{+0.06}_{-0.06}$	$0.50^{+0.04}_{-0.04}$	15.2	2.17	UGWZ*
1eRASS J093946.7-263257	New (this work)	94.657	3.22 ± 0.53	$130.14^{+2.55}_{-2.41}$	$0.65^{+0.24}_{-0.22}$	18.1	3.38	AM
1eRASS J102638.3-444947	GW Lib	76.78	11.99 ± 0.63	$108.74^{+0.30}_{-0.30}$	$1.70^{+0.14}_{-0.14}$	16.3	2.52	UGWZ
1eRASS J115527.4+191855	V405 Peg	255.45	4.02 ± 0.61	$104.62^{+0.47}_{-0.47}$	$0.53^{+0.13}_{-0.12}$	14.1	2.28	DN
1eRASS J123831.5+210845	SDSS J1238+2108	80.52	1.73 ± 0.34	$119.82^{+2.00}_{-1.89}$	$0.30^{+0.12}_{-0.11}$	17.6	2.61	UGWZ*
1eRASS J132124.5+010934	CRTS J1321+0109	108.7	0.97 ± 0.27	$127.69^{+2.77}_{-2.60}$	$0.19^{+0.10}_{-0.09}$	17.6	2.09	UGSU
1eRASS J140454.7-102702	V396 Hya	65.1	3.83 ± 0.65	$92.92^{+0.57}_{-0.56}$	$0.38^{+0.12}_{-0.11}$	17.6	2.14	AM*
1eRASS J141539.5+231540	ZTF J1415+2315	76.47	1.21 ± 0.32	$132.24^{+3.03}_{-2.78}$	$0.25^{+0.13}_{-0.12}$	18.6	2.31	AM*
1eRASS J145003.6+584511	ZTF J1450+5845	74.89	0.87 ± 0.27	$132.65^{+3.44}_{-3.14}$	$0.18^{+0.10}_{-0.09}$	18.6	2.47	AM*
1eRASS J150137.2+550123	QZ Ser	119.46	3.56 ± 0.41	$123.36^{+0.53}_{-0.53}$	$0.65^{+0.08}_{-0.08}$	17.6	2.27	UGSU
1eRASS J151900.2+135409	CRTS J1519+1354	89.29	0.94 ± 0.27	$124.53^{+2.12}_{-2.00}$	$0.18^{+0.09}_{-0.08}$	18.1	2.08	AM
1eRASS J152333.3-013013	ZTF J1523-0130	72.62	1.26 ± 0.30	$133.34^{+3.82}_{-3.45}$	$0.27^{+0.14}_{-0.13}$	18.6	2.13	AM*
1eRASS J155531.3+210229	New (this work)	93.388	1.29 ± 0.29	$118.84^{+2.76}_{-2.53}$	$0.23^{+0.11}_{-0.10}$	18.2	2.40	AM
1eRASS J162501.4+390927	V844 Her	78.69	3.41 ± 0.39	$119.00^{+0.68}_{-0.66}$	$0.58^{+0.10}_{-0.09}$	17.3	1.88	UGWZ
1eRASS J170818.9-254833	V2051 Oph	89.9	2.22 ± 0.47	$107.98^{+0.40}_{-0.50}$	$0.29^{+0.10}_{-0.10}$	15.4	2.91	UGSU

Continued on next page

Table 6.2 – continued from previous page

eROSITA Name	Other Name	$P_{\rm orb}$ (min)	F_X ($\times 10^{13}$ erg s^{-1}cm^{-2})	Distance (pc)	L_X ($\times 10^{30}$ erg s^{-1})	Gaia G mag	$r_{\rm sep}$ (arc-sec)	Type
1eRASS J194740.7-420026	V3885 Sgr	298.31	12.08 ± 1.25	$128.57^{+0.56}_{-0.53}$	$2.26^{+0.39}_{-0.34}$	10.2	3.00	NL
1eRASS J235301.0-385147	BW Scl	78.23	8.53 ± 0.96	$93.32^{+0.55}_{-0.54}$	$0.84^{+0.16}_{-0.15}$	16.3	2.28	UGWZ*
Other Compact Object Binaries								
1eRASS J043715.9-471509	PSR J0437-47	8208	10.57 ± 0.46	$142.08^{+10.83}_{-10.84}$	$2.40^{+0.69}_{-0.60}$	20.3	1.64	Pulsar + WD
1eRASS J162147.2-225311	AR Sco	213.6	12.04 ± 0.97	$122.77^{+0.47}_{-0.38}$	$2.05^{+0.27}_{-0.26}$	14.6	1.90	WD Pulsar

Reference Samples

In order to highlight the importance of volume-limited samples as well as the power of the X-ray Main Sequence in generating an unbiased sample of CVs, we construct two reference samples to which to compare our volume limited samples: the International Variable Star Index (VSX) catalog of CVs crossmatched with ROSAT as well as the VSX catalog crossmatched with eRASS1. The VSX catalog contains well-vetted CVs confirmed either through a publication or a human expert verifying an amateur discovery. However, CVs may be submitted from time-domain optical surveys, spectroscopic surveys, X-ray surveys, near-infrared surveys, and from both sample papers and individual object papers[9]. The VSX catalog is representative of how CV catalogs have been created in the past, since it suffers from a selection function that is virtually impossible to characterize. Additionally, we emphasize that this catalog is likely not 100% pure and can contain non-CV systems. We simply use this catalog as a *reference* to which to compare our volume-limited catalogs, but encourage further exploration to vet the purity of this catalog. However, previous CV studies have successfully made use of systems from this catalog (e.g., Ak et al., 2015; Abrahams et al., 2022).

To create this catalog, we query the VSX database [10] for all CVs with the following classifications: AM (polar), DQ (intermediate polar), NL (novalike), ZAND ("Z And" types), UG (all "U Gem" types including UGSU, UGER, UGSS, UGWZ, etc.), and CV (no subtype known). This yields a total of 14,756 systems. In order to eliminate some likely false positives, we eliminate all of those with an uncertain subtype, as indicated by the ":" symbol in VSX. We are left with a total of 11,047 systems, which we show in Figure 8.2.

We show the distribution of the separation between the X-ray and optical positions, r, of all sources in the VSX catalog crossmatched against the ROSAT 2RXS and SRG/eROSITA eRASS1 catalogs in Figure 6.3. We also shift all VSX positions by 2 arcmin, repeat the crossmatch with eRASS1, and plot the distribution of r with the dash-dot line (false matches). To determine if an eROSITA point is a true crossmatch with a VSX CV, we require that $r < 3\sigma_{\text{sep, eROSITA}} = 6.6$". According to Equation 6.2, this criterion ensures that $\sim 98\%$ of real associations are selected, assuming r indeed follows a Rayleigh distribution. Beyond this separation, Figure 6.3 shows that over half of potential crossmatches are more likely to be chance

[9] `https://www.aavso.org/vsx/index.php?view=about.faq`

[10] `https://www.aavso.org/vsx/index.php`

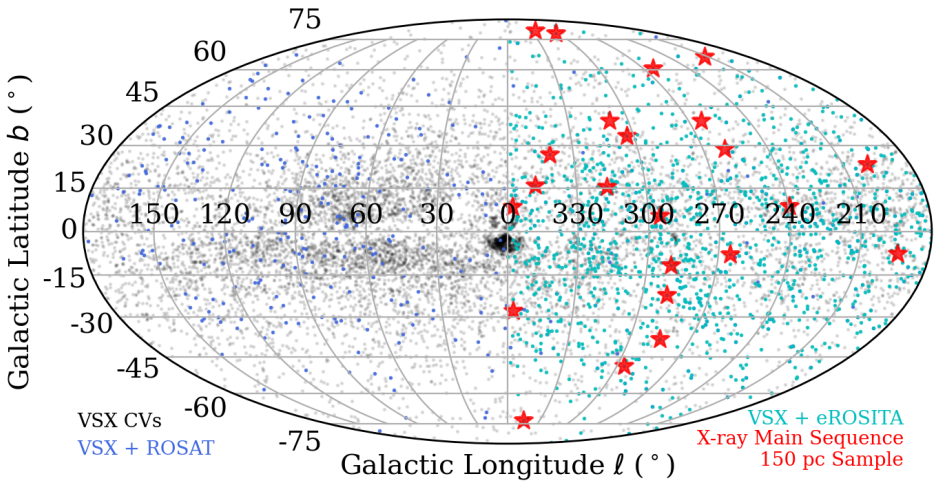

Figure 6.2: All-sky map of optically-selected CVs from the VSX database (black), VSX CVs with ROSAT detections (blue), and VSX CVs with eROSITA detections (cyan). We show our 150 pc sample of CVs identified by applying the X-ray Main Sequence to a crossmatch of SRG/eROSITA eRASS1 with *Gaia* DR3 in red. The increase in density of X-ray detections from ROSAT (launched 1990) to SRG/eROSITA (launched 2019) is obvious. Catalogs assembled from optically-selected CVs suffer from a selection function that is difficult to characterize (e.g., the overdensity of CVs in the Galactic Bulge identified by OGLE).

alignments. To construct our reference sample of VSX + ROSAT crossmatches, because of the larger positional error of ROSAT, we adopt a more conservative separation of $r < 1.5\sigma_{\text{sep, ROSAT}} = 12.15$". According to Equation 6.2, this criterion ensures that $\sim 67\%$ of real associations are selected.

This exercise alone demonstrates the advantage of SRG/eROSITA over ROSAT. Using the criteria above, we find 983 VSX CV systems with an SRG/eROSITA counterpart, whereas only 134 systems have one in ROSAT. In order to create meaningful X-ray luminosity distributions in the following section, we require systems to have a well-measured (3σ) *Gaia* parallax. This leaves 668 VSX CVs with an SRG/eROSITA counterpart and 129 systems with a ROSAT counterpart. To have a fair comparison with the public release of SRG/eROSITA eRASS1, we only reported here the number of ROSAT matches in the Western Galactic Hemisphere.

6.4 Population Properties of the 150 pc Sample

General Trends by CV Subtype

We first present the global properties of the 150 pc sample. In Table 6.3, we list general trends seen in X-ray luminosity and orbital period by CV subtype. We also

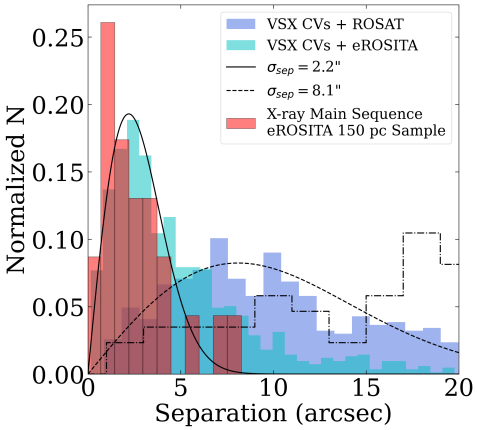

Figure 6.3: Distributions of r, the separation between the optical positions of VSX CVs and the nearest X-ray counterpart in the ROSAT 2RXS (blue) and SRG/eROSITA eRASS1 (cyan) catalogs. Our 150 pc sample is shown in red. Best-fit theoretical distributions (Equation 6.2) are shown as black dashed and solid lines, respectively. The distribution of r for VSX optical points shifted by 2' is shown as a dash-dot line, demonstrating that the VSX CV + eROSITA catalog is dominated by true associations.

list where they tend to be located in the X-ray Main Sequence and HR diagram (Figure 6.10), if there are sufficient systems to make such a claim. Some of the obvious trends are the clustering of novalikes away from the rest of the CVs in both the X-ray Main Sequence and the HR diagram, owing to the bright disk in these systems. Also robust is the location of (long period) AM CVns and period bouncers up against the WD track in the HR diagram. These systems are also located furthest in the upper left corner of the X-ray Main Sequence, due to the minimal contribution from the disk and donor. Generally, long period AM CVns and period bouncers also have the lowest X-ray luminosities of the entire sample, with all systems having $L_X \lesssim 2 \times 10^{30}$erg s^{-1} and four of the five period bouncers having $L_X \lesssim 3 \times 10^{29}$erg s^{-1}.

We also note the obvious lack of high-L_X ($\sim 10^{33}$ erg s^{-1}) IPs in our sample — only EX Hya, the closest IP to Earth is present. There has been some attention paid to so-called "low-luminosity IPs" (LLIPs), which have lower X-ray luminosities than those found abundantly in hard X-ray surveys (Pretorius and Mukai, 2014; Mukai and Pretorius, 2023). EX Hya, like other LLIPs, has an X-ray luminosity of $\sim 10^{31}$erg s^{-1}. Based on the catalog of LLIPs available on the website of K. Mukai[11], it is clear that LLIPs tend to be located below the period gap ($P_{\rm orb} \lesssim 2$

[11] https://asd.gsfc.nasa.gov/Koji.Mukai/iphome/catalog/llip.html

hr) and at much closer distances ($d \lesssim 500$ pc) compared to their high-luminosity counterparts ($P_{\rm orb} \gtrsim 4$ hr; $d \gtrsim 1$ kpc). This could signal that LLIPs are actually the dominant population of IPs and that the 300 pc and 1000 pc samples we present here could harbor several previously unknown LLIPs.

There is also a lack of short-period ($\lesssim 50$ min) AM CVns. These systems are believed to be rare, with AM CVns that have $P_{\rm orb} \lesssim 20$ min existing for only ~0.1 Gyr, those that have $P_{\rm orb} \lesssim 50$ min existing for only ~1 Gyr and long period systems ($P_{\rm orb} \gtrsim 50$ min) existing up to a Hubble time (e.g., Wong and Bildsten, 2021). Therefore, it is not surprising that we only find long-period systems in our sample. This means that our survey indeed targets the dominant population of AM CVns (e.g., Carter et al., 2013; van Roestel et al., 2022). Most of these systems have been difficult to find in the past since they are optically and X-ray faint (G>18 mag; $F_X \lesssim 10^{-13}$erg s^{-1}cm^{-2}) , particularly beyond a few hundred pc where they are most easily discovered through rapid follow-up after a transient outburst (e.g., van Roestel et al., 2021).

CV Subtype (23 total systems)	Typical L_X (erg/s)	Typical $P_{\rm orb}$	X-ray Main Sequence Location	HR Diagram Location
Non-magnetic (16)				
AM CVn (3)	10^{29} – 10^{30}	50–60 min	Uppermost left	On WD track
SU UMa-type (7)	10^{29} – 10^{31}	78 min–2 hr	Scattered	Between WD and MS tracks
U Gem-type (1)	$\sim 10^{31}$	$\gtrsim$ 4 hr	Right	Between WD and MS tracks, closer to MS track
WZ Sge-type Period Bouncer (3)	10^{29} – 10^{30}	78–110 min hr	Middle Left	On or just above WD track
Novalikes (2)	$\sim 10^{30}$	4–5 hr	Lower left	High Abs. G, near MS track
Magnetic (7)				
Intermediate Polar (1)	$\gtrsim 10^{31}$	-	-	Between WD and MS track
Polar (4)	10^{29} – 10^{31}	78 min–2 hr	Scattered/upper center	Between WD and MS track, redder than non-magnetic CVs
Polar Period Bouncer (2)	$\sim 10^{29}$	78–95 min	Center	On WD track

Table 6.3: Summary of CV subtypes and observed properties. If there are not enough systems to make a claim, or if the single system is not representative of the overall population, we denote it with a “-" symbol. Also presented are the location in the X-ray Main Sequence (within the upper left corner) and on the HR diagram.

In Figure 6.4, we split all CVs into subclasses using different symbols, and into magnetic, non-magnetic, and AM CVns using different colors. The left panels show all systems on the X-ray Main Seqeunce as well as the *Gaia* HR diagram. On the right panel, we plot the orbital period of CVs in our sample versus X-ray luminosity. In gray, we show systems from the VSX + eROSITA sample that have well-measured periods. We show magnetic systems (IPs and polars) as squares and non-magnetic systems as circles.

To provide a comparison to theoretical L_X estimates, we overlay the CV evolutionary tracks by Pala et al. (2017)[12] in Figure 6.4. Those tracks produce the donor mass loss rate[13] as a function of orbital period, and are effectively an updated version of the classic Knigge et al. (2011) tracks, but created using Modules for Experiments in Stellar Astrophysics (MESA; Paxton et al., 2011, 2013, 2015, 2018). We call the track that assumes AML only due to gravitational radiation below the period gap "standard" (gray) and that which includes additional AML due to magnetic braking below the period gap "optimal", following the convention of Knigge et al. (2011). These tracks have been computed assuming $M_{\rm WD} = 0.8 M_\odot$ (unlike the tracks of Knigge et al. (2011), which assume $M_{\rm WD} = 0.7 M_\odot$), $R_{\rm WD} = 0.0105 R_\odot$ (Bédard et al., 2020), and convert to X-ray luminosity in the 0.2–2.3 keV range following Equation 6.2. We plot two versions of each track, one assuming an accretion efficiency of $\eta = 0.3$ (solid lines) and another assuming $\eta = 0.02$ (dashed lines), which roughly encompass the X-ray luminosity of all CVs within our sample. However, we note that a different choice of η_X (which depends on the X-ray spectral profile of a CV) and $\eta_{\rm out}$ (which depends on the geometry of a CV) could lead to a different range of accretion efficiencies. For now, we show that a range of accretion efficiencies $\eta \approx 0.02 - 0.3$ reproduces the observed X-ray luminosity of CVs in our sample, but defer more detailed studies to future work.

We also provide a comparison to theoretical L_X estimates of AM CVns in Figure 6.4. We estimate L_X under the same assumptions as in Equation 6.2, taking the donor mass loss rates from the evolutionary tracks of Wong and Bildsten (2021) and Sarkar et al. (2023a), adopting $M_{\rm WD} = 0.75 M_\odot$ and $M_{\rm WD} = 0.8 M_\odot$ and the corresponding $R_{\rm WD}$ from Bédard et al. (2020), respectively. Wong and Bildsten (2021) (blue lines in Figure 6.4) carried out AM CVn evolutionary models based

[12] `https://zenodo.org/records/2592806`

[13] Especially in long period systems (above the period gap), there is some uncertainty in these estimates that arises from uncertainties in the strength of magnetic braking (e.g., El-Badry et al., 2022).

on the He WD channel, where two common envelope phases lead to the creation of two WDs that commence accretion and lead to an AM CVn binary. We present the highest entropy model from that work, assuming a donor WD initial central temperature of $T_c = 3 \times 10^7$ K. Sarkar et al. (2023a) (cyan lines in Figure 6.4) carried out AM CVn evolutionary models based on the evolved CV channel, where a single common envelope phase leads a WD accreting from an evolved donor star, draining its hydrogen envelope and leading to the creation of an AM CVn binary. We present the most hydrogen exhausted model from that work, assuming a donor WD initial central temperature of $T_c = 3 \times 10^7$ K. As with the CV evolutionary tracks, we plot the expected L_X assuming efficiencies of $\eta = 0.3$ (solid lines) and $\eta = 0.02$ (dashed lines). We see that the "He WD progenitor" tracks of Wong and Bildsten (2021) underestimate long period AM CVn L_X values, and that the "evolved CV progenitor" AM CVn tracks of Sarkar et al. (2023a) match the observed L_X values under reasonable assumptions of accretion efficiency. This could provide additional observational basis for recent claims made that most long-period AM CVns are created through the evolved CV channel (though short period systems could more likely originate from the He WD or He star channels), though more detailed analysis of more systems is needed to make such a claim (e.g., Sarkar et al., 2023a; Belloni and Schreiber, 2023).

X-ray Luminosity Distributions

We present the *observed* X-ray luminosity distribution of three samples: the VSX + eROSITA, VSX + ROSAT, and our 150 pc sample, in Figure 6.5. These are observed luminosity distributions because the X-ray fluxes are *not* corrected for Galactic hydrogen column density, N_H. The 150 pc sample can safely be treated as the approximately equal to the *true* X-ray luminosity distribution, though, since the proximity of those systems means that the intervening Galactic hydrogen column density, N_H, is minimal. However, we note that detailed X-ray modeling of CVs has revealed intrinsic absorption, exceeding that predicted by optical/UV extinction estimates (e.g., Mukai, 2017). That would mean that *every* CV would require X-ray spectral modeling to determine its true L_X, which is beyond the scope of this paper. Given this caveat, we estimate the maximum difference between the true and observed luminosities of the 150 pc sample to be a factor of < 0.07. Based on the Bayestar19 map (Green et al., 2019a), even the most distant systems in the 150 pc sample have an upper limit of $A_V < 0.03$ mag, which corresponds to $N_H < 6 \times 10^{19} \mathrm{cm}^{-2}$ Güver and Özel (2009b). We use the WebPIMMS tool (Mukai,

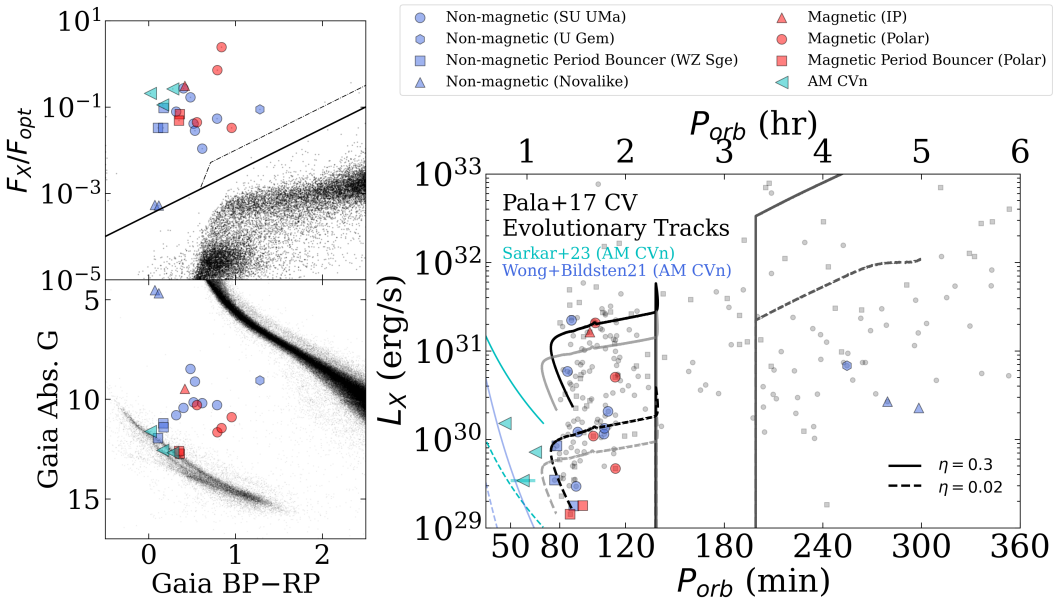

Figure 6.4: Our 150 pc sample in the X-ray Main Sequence (upper left, with all systems in our 150 pc crossmatch in black), *Gaia* HR diagram (lower left, with the 100 pc *Gaia* catalog in black), and in the $P_{\rm orb}$–L_X parameter space (right, with the VSX + eROSITA CV sample in gray). Theoretical L_X values are plotted as a function of period, using donor mass loss estimates from the CV evolutionary tracks ("standard" in gray and "optimal" in black) of Pala et al. (2017), "He WD progenitor"/"evolved CV progenitor" AM CVn tracks of Wong and Bildsten (2021)/Sarkar et al. (2023a) and Equation 1. Accretion efficiencies in the range of $\eta \approx 0.02 - 0.3$ (dashed and solid tracks) best fit the data, which could be confirmed through X-ray spectral analyses that likely depend on CV subclass. Observations of trends in these parameter spaces by CV subclass are presented in Table 6.3.

1993) to calculate the true flux of those systems, assuming a power law model with index $\Gamma \sim 2$. This leads to a difference between observed and true flux of 0.07, though assuming harder X-ray spectra (either through power law models with lower values of Γ or thermal bremsstrahlung models with $kT \sim 10$ keV) leads to even smaller differences (< 0.03).

We do not attempt to correct the observed luminosity distributions of the VSX samples, though, since this would require X-ray spectral fitting of each system. This would be difficult for the majority of systems that are in the low-count regime. We used the Bayestar19 (Green et al., 2019a) map to approximate the value of A_V for some of the most distant systems, along with the WebPIMMS tool to calculate the difference between the true and observed flux. We find that the most distant systems would require at most a correction of 2–3 in the 0.2–2.3 keV range. With most

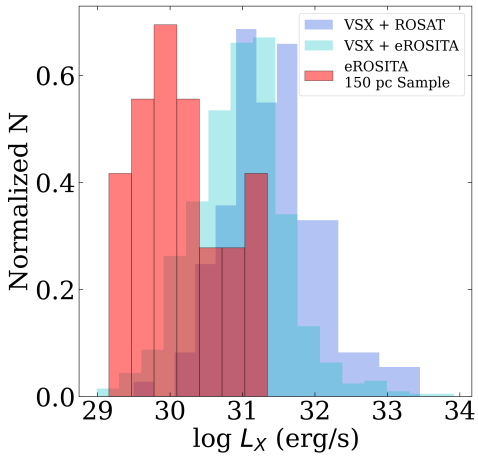

Figure 6.5: Observed L_X distributions of CVs. L_X distributions of primarily optically-identified systems that have eROSITA (cyan) and ROSAT (blue) X-ray counterparts suggest that CVs have $\langle L_X \rangle \sim 10^{31-32}$erg s^{-1}. Our 150 pc volume limited sample of systems selected using the X-ray Main Sequence (red) instead reveals that $\langle L_X \rangle \sim 10^{30}$erg s^{-1}.

systems in the VSX sample located at a few hundreds of pc, we can safely assume that the observed luminosity distributions can be treated as lower limits, which are no more than a factor of $\sim$ 2–3 offset from the true distribution, though further work would be needed to clarify this.

X-ray Luminosity Functions and Space Densities

Galactic Model

Three space densities can fully describe the global properties of CVs in the Milky Way, and can be used to construct luminosity functions — space densities as a function of X-ray luminosity. The number density, ρ_N, is the total number of systems in a given effective volume[14] (units of pc^{-3}). The mass density, ρ_M, is the total number of systems per mass contained in a given effective volume (units of $M_\odot^{-1}$). The luminosity density, ρ_L, is the average X-ray luminosity per mass contained in a given volume (units of erg s$^{-1} M_\odot^{-1}$).

We closely follow the method of Suleimanov et al. (2022), who calculated luminosity functions of hard X-ray emitting CVs. Though that work focused on flux-limited surveys, the method can be applied directly (and more easily) to volume-limited surveys. Suleimanov et al. (2022) integrated over the entire Galactic mass dis-

[14] An “effective" volume assumes a density profile (not necessarily uniform as in a sphere), typically modeled as exponential for the disks of the Milky Way.

tribution (Grimm et al., 2002), whereas other works (e.g., Pretorius and Knigge, 2012; Schwope, 2018) use the $1/V_{\max}$ method outlined by Tinney et al. (1993). This method was developed for flux-limited surveys on photographic plates, which assumed all objects were observed at approximately the same Galactic latitude[15]. Because we enforce a volume limit, the integration over the full Galactic mass distribution is straightforward to do numerically. As in Suleimanov et al. (2022), we adopt a modern estimate of the Galactic stellar mass distribution computed by Barros et al. (2016).

In order to compute the above space densities, we first calculate the amount of mass δM contained in the volume of the Milky Way that we probe (i.e., in our case, how much mass is contained within 150 pc):

$$\delta M = \int d\ell \int d\cos b \int \rho(z, R)\ r^2 dr \tag{6.3}$$

where ℓ, b are Galactic coordinates[16], z is the height above the Galactic plane, R is the distance from a system to the Galactic Center, and r is the distance from a system to the Sun. Since we only work with the Western Galactic Hemisphere, we integrate between $0 < \ell < \pi$ and $-1 < \cos b < 1$. We integrate from $0 < r < d_{\max}$, where $d_{\max}$ is the limiting distance of our survey (150 pc in our case). $\rho(z, R)$ is the mass density profile as calculated by Barros et al. (2016):

$$\rho(z, R) = \frac{\Sigma_0}{2h} \exp\left[-\left(\frac{R - R_0}{R_d} + R_{\rm ch}\left(\frac{1}{R} - \frac{1}{R_0}\right) + \frac{|z|}{h}\right)\right] \tag{6.4}$$

where $\rho(z, R)$ has units of $M_\odot \mathrm{pc}^{-3}$. We adopt the values from Barros et al. (2016) of the surface density near the Sun as $\Sigma_0 = 30.2\ M_\odot \mathrm{pc}^{-2}$, the half thickness of the thin disk as $h = 205$pc, the disk radius of $R_d = 2.12$ kpc, and the central hole in the thin disk at $R_{\rm ch} = 2.07$ kpc[17]. R_0 is the distance from the Sun to the Galactic Center, $R_0 = 8.1$ kpc.

Finally, we express the values of z and R in observable quantities:

$$z = r \sin b; R^2 = (r \cos b)^2 = R_0^2 - 2R_0(r \cos b) \cos \ell \tag{6.5}$$

[15]Though it is noted in Pretorius and Knigge (2012) that the ROSAT RBS survey that was used observed in slices of b, and that they compute the corresponding $1/V_{\max}$ for each slice.

[16]Note the change in coordinates needed for the spherical integral since Galactic b is measured from the Galactic equator, unlike the typical θ used in spherical coordinates which is measured from the North pole.

[17]At our 150 pc radius, the first two terms of Equation 6.4 contribute only one percent to the total, but we include the full equation here for completeness.

We note that the Milky Way model by Barros et al. (2016) implies thin disk stellar masses of $2.49 \times 10^{10} M_{\odot}$ and $4.02 \times 10^{5} M_{\odot}$ for the entire Galaxy and within 150 pc, respectively.

Final Values

After having done the above calculations, we compute three space densities:

$$\rho_M = \sum_i \frac{1}{\delta M_i}; \rho_N = \rho_* \sum_i \frac{1}{\delta M_i}; \rho_L = \sum_i \frac{L_{X,i}}{\delta M_i} \tag{6.6}$$

where ρ_* is the midplane stellar mass density[18] (in $M_{\odot}\mathrm{pc}^{-3}$), and $L_{X,i}$ is the X-ray luminosity for the i^{th} system. Because we calculate the number density at the midplane, we report the quantity as $\rho_{N,0}$. The sum is then carried out for all systems in the sample. If a sample out to greater distances is indeed complete and assumptions satisfied, repeating this calculation should converge to the same space densities. We calculate space densities for AM CVns separately, since they have different formation channels than CVs (i.e., space densities calculated for CVs have AM CVns removed).

We assume Poisson uncertainties (adopting 68% confidence intervals) in obtaining the total number of systems, and report all space densities in Table 6.4, noting that our uncertainties can accommodate $N_{\mathrm{CV}} = 20 \pm 4$ CVs and $N_{\mathrm{AM\,CVn}} = 3 \pm 2$ AM CVns within 150 pc (in half of the sky). We note that the above calculation effectively assumes that CVs trace the Galactic thin disk — and therefore a CV scale height of 205 pc. We explore the effect of adopting different scale heights in Appendix 6.9.

We present X-ray luminosity functions in L_X, in Figure 6.6. We only include CVs, not AM CVns. As a comparison, we also plot previous X-ray luminosity functions of non-magnetic CVs (Pretorius and Knigge, 2012) and magnetic CVs (Pretorius et al., 2013). We have chosen these two works since the ROSAT 0.1–2.4 keV energy range is most similar to the 0.2–2.3 eROSITA energy range; other studies have focused on CVs in hard X-rays (e.g., Revnivtsev et al., 2008; Suleimanov et al., 2022). We note that the samples in Pretorius and Knigge (2012) and Pretorius et al. (2013) were created differently, which does not allow for us to unite both samples. However, they do represent the most uniformly created, soft X-ray luminosity functions of CVs in

[18] We use the midplane value of $0.0736 M_{\odot}\mathrm{pc}^{-3}$ from Barros et al. (2016), whereas Suleimanov et al. (2022) convert to the local stellar mass density at the solar height of 20.8 pc above the midplane.

the literature before our work, and are useful to present for comparison. We adopt the values of effective volume and X-ray luminosity reported in those papers, to provide a fair comparison, and compute X-ray luminosity functions using Equation 6.6. We note that those works use pre-*Gaia* distances and compute effective volumes using the "$1/V_{\rm max}$" method (Tinney et al., 1993). We just use this as a *comparison* sample, mainly to highlight our sensitivity to low L_X systems.

Figure 6.6 shows, for the first time, a "flattening" in the X-ray luminosity function of CVs — i.e., they no longer keep increasing as one goes to lower values of L_X as they have been in every previous plot of CV X-ray luminosity functions (e.g., Revnivtsev et al., 2008; Pretorius and Knigge, 2012; Pretorius et al., 2013; Schwope, 2018; Suleimanov et al., 2022). This is due to the increased sensitivity of eROSITA — seven CVs are detected with $L_X < 10^{30}$erg s^{-1}, whereas only one such system was present in the samples by Pretorius and Knigge (2012) and Pretorius et al. (2013). Nevertheless, we recognize that a larger number of systems from future, deeper eROSITA releases are needed to solidify this claim. We also note that the X-ray luminosity function presented by Sazonov et al. (2006) revealed a flattening and a turn over, though only when both CVs and active binary stars were included. The number and mass density panels show that low X-ray luminosity ($L_X \sim 10^{30}$erg s^{-1}) make up the dominant population of CVs.

The luminosity density panel shows that our sample of these low-L_X systems increases their contribution to the total L_X budget of CVs by a factor of a few, while the high X-ray luminosity ($L_X \sim 10^{32} - 10^{33}$ erg s^{-1}) make up the dominant X-ray output of CVs. Thus, in any given population of CVs, it will be the low L_X systems that will be greatest in number, but it will be the high L_X systems that dominate the overall X-ray luminosity. We compute upper limits in the $10^{28.5} < L_X < 10^{29}$erg s^{-1} are assuming one system within 94 pc (dark red bar) or two systems within 150 pc (light red bar). The former assumes there is at most one system out to the distance where eRASS1 is complete for $L_X = 10^{28.5}$erg s^{-1}, which is 94 pc. The latter assumes that the two systems in the Pala et al. (2020a) sample that we do not detect in eRASS1 are the only two systems within 150 pc that have $L_X < 10^{29}$erg s^{-1}.

As a final note, we emphasize that the space densities and luminosity functions presented here are representative of the solar neighborhood, but likely do not extend to other Galactic environments such as regions of the thin disk closer to the Galactic Center, the nuclear star cluster, globular clusters, etc. For that reason, we cannot reliably estimate the total number of CVs in the Galactic Center and/or Galactic

Ridge. Other works, for example, Suleimanov et al. (2022), were able to do so, since the hard X-ray flux limited survey used in that study was sensitive to more distant systems. In our case, changes in the initial mass function, star formation rate, and binary fraction in different Galactic environments would likely lead to different number densities of CVs (per volume or per solar mass) as well as a different distribution of L_X compared to our local sample.

Sample	$\langle L_X \rangle$ (erg s^{-1})	$\langle \log L_X \rangle$	$\rho_{N,0}$ (pc^{-3})	ρ_M ($M_\odot$pc^{-3})	ρ_{L_X} (erg s^{-1}pc^{-3})
150 pc CVs (no AM CVns; 20)	$4.6 \pm 1.5 \times 10^{30}$	30.19 ± 0.15	$3.7 \pm 0.7 \times 10^{-6}$	$5.0 \pm 1.0 \times 10^{-5}$	$2.3 \pm 0.4 \times 10^{26}$
150 pc AM CVns (3)	$8.6 \pm 3.5 \times 10^{29}$	29.86 ± 0.19	$5.5 \pm 3.7 \times 10^{-7}$	$7.5 \pm 5.0 \times 10^{-6}$	$6.4 \pm 4.3 \times 10^{24}$
150 pc Non-magnetic CVs (13)	$3.6 \pm 1.6 \times 10^{30}$	30.19 ± 0.16	$2.4 \pm 0.7 \times 10^{-6}$	$3.2 \pm 1.0 \times 10^{-5}$	$1.2 \pm 0.4 \times 10^{26}$
150 pc Magnetic CVs (7)	$6.3 \pm 3.3 \times 10^{30}$	30.19 ± 0.34	$1.3 \pm 0.5 \times 10^{-6}$	$1.7 \pm 0.7 \times 10^{-5}$	$1.1 \pm 0.5 \times 10^{26}$
150 pc Period Bouncers (5)	$3.4 \pm 1.3 \times 10^{29}$	29.42 ± 0.14	$9.2 \pm 2.7 \times 10^{-7}$	$1.2 \pm 0.5 \times 10^{-5}$	$4.2 \pm 2.7 \times 10^{24}$
VSX CVs + ROSAT	$1.1 \pm 0.3 \times 10^{32}$	31.42 ± 0.06	-	-	-
VSX CVs + eROSITA	$4.8 \pm 1.3 \times 10^{31}$	30.97 ± 0.02	-	-	-
150 pc CVs (+ AM CVns; 23)	$4.0 \pm 1.4 \times 10^{30}$	30.15 ± 0.14	-	-	-

Table 6.4: Average X-ray luminosities and space densities for all CVs, AM CVns, and CV subtypes in our sample. Our average L_X value of CVs is at least a factor of 10 lower than that computed from samples of optically identified systems (VSX) with X-ray counterparts (ROSAT and eROSITA). Magnetic CVs and period bouncers make up 35% and 25% of CVs in our sample, respectively.

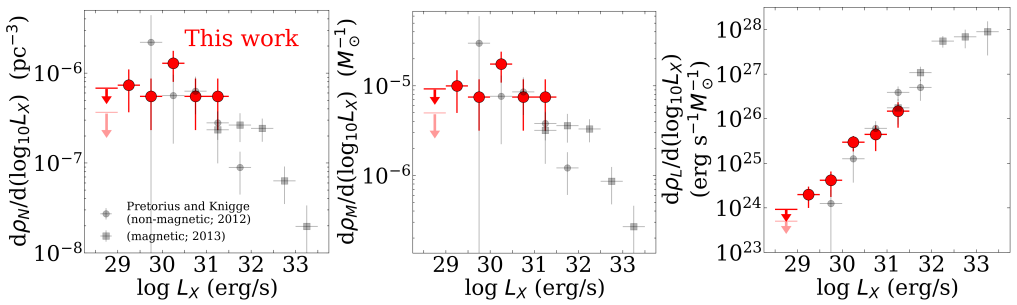

Figure 6.6: X-ray luminosity functions of the CVs in our 150 pc sample (red points), with AM CVns excluded. A clear flattening is seen around $L_X \sim 10^{30}$erg s^{-1} in all number and mass luminosity functions (left and center panels), demonstrating that we are probing the lowest L_X end of CVs. A significant number of low L_X systems lead to smaller error bars compared to previous work (gray points). Low L_X ($\lesssim 10^{30}$erg s^{-1}) CVs dominate in number over high L_X ($\gtrsim 10^{30}$erg s^{-1}) systems (left and center panels), while the right panel shows that the few high L_X systems dominate the total luminosity budget of the population.

New CVs Within 150 pc

We discovered two new systems within 150 pc in the Western Galactic Hemisphere: 1eRASS J101328.7-202848, a new AM CVn which is the third closest known AM CVn (and ultracompact binary) to Earth at 140 pc, and 1eRASS J054726.9+132649, a new magnetic period bouncer.

1eRASS J101328.7-202848: A New AM CVn

We obtained a single 600 sec optical spectrum of 1eRASS J101328.7-202848 (*Gaia* DR3 ID: 5668919328172331904) with the Low Resolution Imaging Spectrometer (LRIS; Oke et al., 1995a) on the Keck I telescope on 31 March 2024. The 400/3400 grism was used and 400/8500 grating with the D55 dichroic. The seeing was <1", and the 1" long slit was used, leading to minimal slit losses. Data were wavelength calibrated with internal lamps, flat fielded, and cleaned for cosmic rays using `lpipe`, a pipeline for LRIS optimized for long slit spectroscopy (Perley, 2019).

1eRASS J101328.7-202848 is an AM CVn located 139±3 pc away. The spectrum of 1eRASS J101328.7-202848 (Figure 6.7) shows a blue continuum with prominent He I lines, some of which are double-peaked (e.g., He I 7065, 7281), and even single-peaked He II 4686. There are no H lines. There are also Ca II and Mg I/II lines in absorption and N I lines in emission, as have been seen in other long-period AM CVns and attributed to WD pollution by the donor (e.g., van Roestel et al., 2022; Rodriguez et al., 2023b).

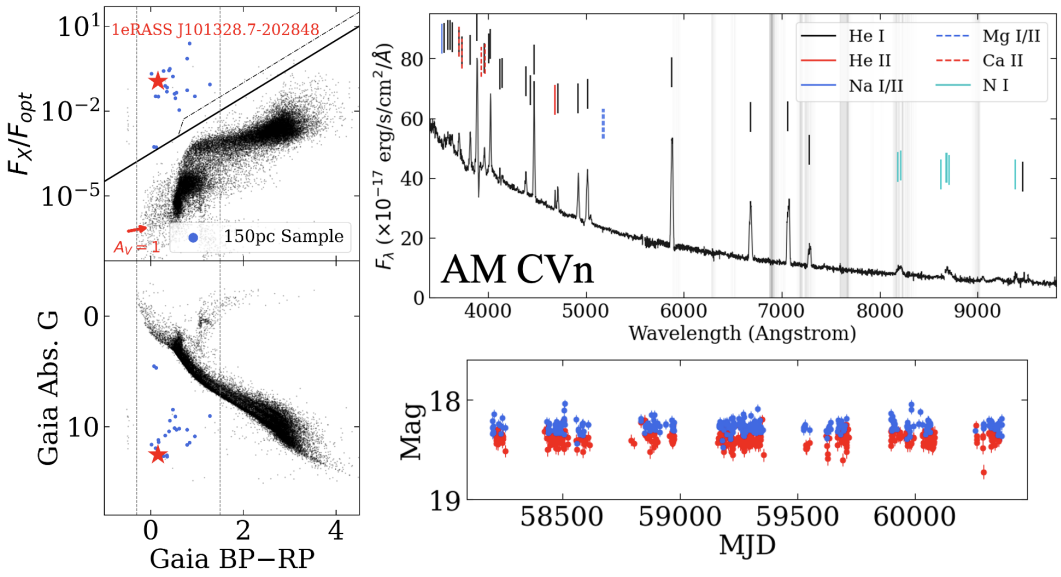

Figure 6.7: 1eRASS J101328.7-202848 is a newly-discovered AM CVn, selected thanks to the X-ray Main Sequence (upper left). The optical spectrum (upper right) shows prominent He I/II emission lines, an absence of H lines, and the presence of metals resulting from the donor polluting the WD. Gray lines indicate telluric features. It appears near the WD track on the HR diagram (lower left), and shows no outbursts in six years of ZTF data (lower right). Those properties suggest it is a long-period ($P_{\rm orb} \gtrsim 50$ min) AM CVn.

This system is likely a long-period ($P_{\rm orb} \gtrsim 50$ min) AM CVn, but follow-up spectroscopy and/or high cadence photometry are needed to confirm the orbital period. A Lomb-Scargle periodicity analysis of both the ZTF and TESS archives does not reveal any statistically significant periods. However, the location of this system near the WD track (see Figure 13 in Rodriguez et al. (2023b)) implies that it is a long-period ($P_{\rm orb} \gtrsim 50$ min) system. In addition, the lack of outbursts in the five year long archive of ZTF data is indicative of a low mass transfer rate, and therefore a long orbital period. Previous works have shown that $P_{\rm orb} \gtrsim 50$ min systems tend to not show outbursts on the timescales of current photometric surveys (e.g., Ramsay et al., 2018; Duffy et al., 2021; van Roestel et al., 2022; Rodriguez et al., 2023b). We will report on phase-resolved spectroscopy and high-cadence photometry of this object in a future study.

Figure 6.7 reveals the location of 1eRASS J101328.7-202848 in the X-ray Main Sequence, clearly above the cut to select accreting compact object binaries. We also show its location in the *Gaia* HR diagram and its quiescent behavior in the five year long ZTF archive.

1eRASS J054726.9+132649: A New Magnetic Period Bouncer

We obtained a single 900 sec optical spectrum of 1eRASS J054726.9+132649 (*Gaia* DR3 ID: 3346524412647596032) with the Double Spectrograph (DBSP; Oke and Gunn, 1982a) on the Hale 200-inch telescope at Palomar Observatory on 21 March 2024. The 600/4000 grism was used and 316/7600 grating with the D55 dichroic. The seeing was <2", and the 1.5" long slit was used, leading to minimal slit losses. Data were wavelength calibrated with internal lamps, flat fielded, and cleaned for cosmic rays using `DBSP-DRP`[19], a Python-based pipeline optimized for DBSP built on the more general `PypeIt` pipeline (Prochaska et al., 2020).

1eRASS J054726.9+132649 is a magnetic period bouncer with a 93.95-min (1.565 hr) orbital period, 132±3 pc away. Its magnetic classification comes from the obvious Zeeman splitting of the Hβ and Hγ lines in the spectrum (Figure 6.8). We present the ZTF r and g light curves of this system in Figure 6.8, which reveal its clear periodicity. We found this period based on a Lomb-Scargle periodogram using the `gatspy` tool (VanderPlas, 2016a). We searched for periods between 5 minutes and 10 days, with a linear frequency grid oversampled by a factor of 10 and found no other significant periods. The ephemeris we report based on the ZTF data is t_0 (BJD)= 2458381.3339(2) + $T\times$ 0.06524(1).

This system bears a remarkable similarity to SDSS J125044.42+154957.3, a polar also in our 150 pc sample. SDSS J125044.42+154957.3 has an 86.3 min orbital period and its white dwarf has a magnetic field strength of 21 MG. SDSS J125044.42+154957.3 has a solid classification based on phase-resolved spectroscopy as a polar near the CV period minimum (Breedt et al., 2012), but has been recently labeled as a period bouncer due to its low X-ray luminosity and late M (near L) spectral type (Muñoz-Giraldo et al., 2023).

In Figure 6.8, we show the location of 1eRASS J054726.9+132649 in the X-ray Main Sequence, clearly above the cut to select accreting compact object binaries. We also show its location in the *Gaia* HR diagram and its quiescent behavior in the five year long ZTF archive. It would not be detectable in a search for outbursting systems, but its periodicity would clearly be revealed in a search for systems showing such behavior.

Now, we justify why 1eRASS J054726.9+132649 1) is a true polar with a Roche lobe filling donor instead of a wind-accreting, low accretion rate polar, and 2) has

[19] `https://dbsp-drp.readthedocs.io/en/stable/index.html`

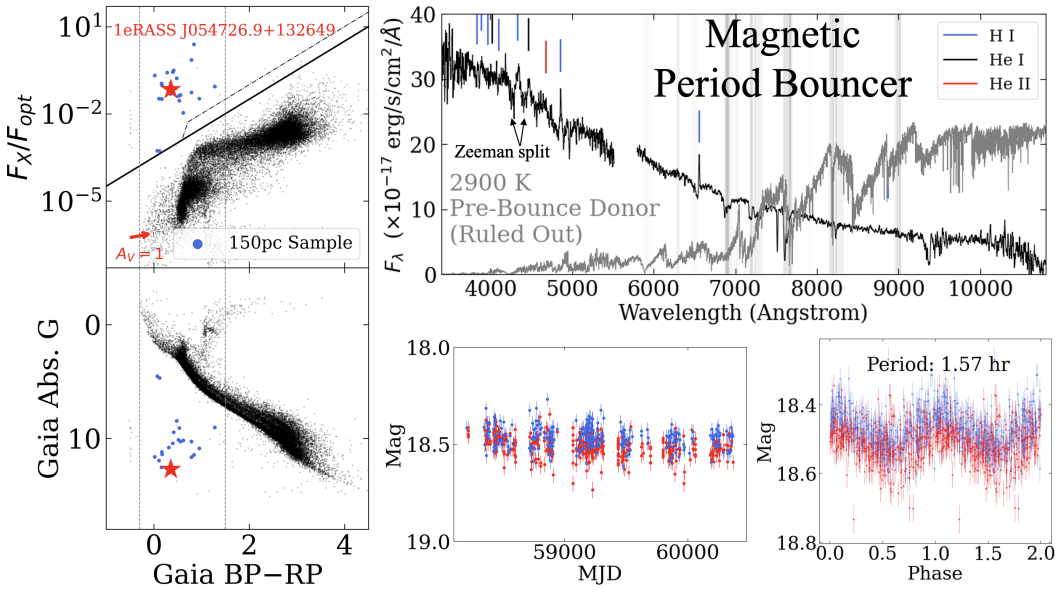

Figure 6.8: 1eRASS J054726.9+132649 is a newly-discovered magnetic period bouncer, selected thanks to the X-ray Main Sequence (upper left). It is located near the WD track (bottom left), and shows no outbursts in six years of data (bottom center), indicative of low mass transfer rates. ZTF optical photometry (r-band in red, g-band in blue) reveals a 1.57 hr orbital period (bottom right). The optical spectrum (upper right) shows that a 2900 K donor star predicted by CV evolutionary tracks (see Figure 6.9) at this orbital period is not seen, thus confirming this system as a period bouncer. Balmer emission lines show clear Zeeman splitting (particularly Hβ and Hγ), which reveal the magnetic nature of the WD.

evolved past the period minimum. To address the first point, we note the arguments put forth by Breedt et al. (2012): Roche lobe filling CVs should show a hotter WD than those in wind-accreting systems. High states of accretion in Roche lobe filling systems regulate the temperature of the WD (Townsley and Bildsten, 2003) and keep it higher than those in wind accreting (or detached) systems. Moreover, the orbital periods of wind accreting systems is generally $\gtrsim$2 hr, since some of these could be pre-polars that have not yet filled their Roche lobes (Breedt et al., 2012; Hakala et al., 2022). The spectrum of 1eRASS J054726.9+132649 in Figure 6.8 shows a blue continuum characteristic of an accretion-heated WD, but quantitative proof of this is clear from the *Gaia* BP–RP color of this system being nearly equal to that of SDSS J125044.42+154957.3. In Figure 6.4, they nearly overlap on the HR diagram and are remarkably close together in the X-ray Main Sequence due to their similar values of X-ray luminosity. We thus conclude that 1eRASS J054726.9+132649 is a true polar, with a Roche lobe filling donor.

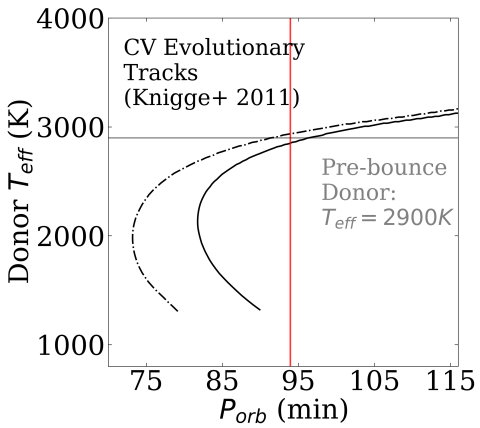

Figure 6.9: The orbital period of 1eRASS J054726.9+132649 is shown in red, and CV “optimal" and “standard" evolutionary tracks are shown by the solid and dot-dashed lines, respectively. If this were a pre-bounce system, its donor $T_{\rm eff}$ would be 2900K. Since we do not see this in the spectrum in Figure 6.8, we determine it must be a period bouncer.

To address the second point, we include Figure 6.9. At the orbital period of 1eRASS J054726.9+132649, if the system evolves according to the evolutionary tracks of Knigge et al. (2011), then the donor star should have an effective temperature of $T_{\rm eff} \approx 2900$ K in either the “standard" or “optimal" track. In Figure 6.8, we plot a BT-DUSTY model atmosphere (Allard et al., 2011b) of that effective temperature, with the corresponding radius in the Knigge et al. (2011) tracks of $0.15 R_{\odot}$, at the *Gaia* median distance of 132 pc. In Figure 6.8, the observed spectrum does not show evidence of such a donor, particularly redward of ≈ 7000 Å. The presence of an accretion stream would only increase the flux level, so we take this as conclusive evidence that a donor star with the temperature and radius that we would expect at the orbital period of 1eRASS J054726.9+132649 is not present. This means that if 1eRASS J054726.9+132649 follows standard CV evolutionary tracks, it must be a period bouncer. Similar arguments have been put forth for other period bouncers in the literature: QZ Lib and SRGe J041130.3+685350 (Pala et al., 2018; Galiullin et al., 2024b). Finally, we show in Figure 6.4 that its low X-ray luminosity is consistent with that of other period bouncers (both magnetic and non-magnetic) at similar orbital periods.

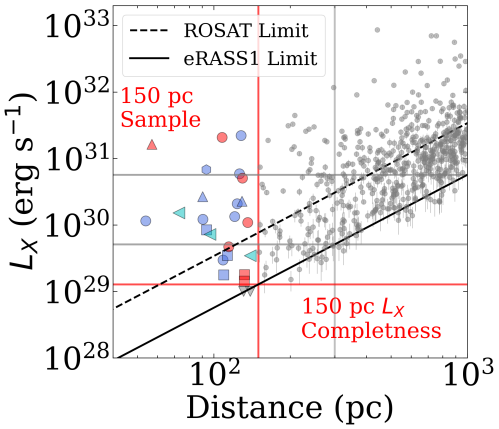

Figure 6.10: All CVs in the 150 pc sample are shown using the same colors/markers as in Figure 6.4, with the two systems in the Pala et al. (2020a) sample not in eRASS1 shown as downward pointing gray triangles. All CV candidates in our 1000 pc sample are shown as gray circles. Gray lines indicate the L_X completeness limits at 300 pc and 1000 pc, demonstrating that our 150 pc sample at the depth of eRASS1 is the only combination of distance/survey to obtain a complete CV catalog.

6.5 Discussion

Sample Completeness and No Very Low L_X CVs

In Figure 6.10, we plot the SRG/eROSITA eRASS1 0.2–2.3 keV X-ray luminosity, L_X as a function of distance, d, of all systems in the 1000 pc sample. We emphasize that a CV survey at the depth of eRASS1 out to a distance of 150 pc is the *only* current combination of survey/distance that can be sensitive to all CVs. The flux limit of the ROSAT 2RXS catalog renders it complete down to only $L_X \sim 8 \times 10^{29}$ erg s^{-1}, at 150 pc, missing nearly half of all objects in our sample. Crucially, two of the three AM CVns and four of the five period bouncers would be missed, both of which are arguably the most poorly-understood CV subtypes and critical to our understanding of CV evolution.

Figure 6.10 also demonstrates that low L_X CVs do not make up a significant fraction of all systems. At ~100 pc, we reach an X-ray completeness of $L_X = 5 \times 10^{28}$erg s^{-1}. This means that if there were a dominant population of CVs at such low X-ray luminosities, which was not able to be ruled out by previous CV surveys (e,g, Pretorius and Knigge, 2012), we would have certainly detected it.

At the luminosity limit of eRASS1 out to 300 pc, nearly a third of the CVs in our 150 pc sample would be missed, including four of the five period bouncers. At the L_X limit at 1000 pc, a full 80% of CVs in our 150 pc sample would be missed,

demonstrating that complete samples of CVs can only be carried out to nearby distances.

In order to quantify the completeness of our sample, we compare the cumulative number of CVs (as a function of distance) to the effective volume probed by our calculated number density, in a similar manner to El-Badry et al. (2021a). In upper panels of Figure 6.11, we show the cumulative number of CVs in our 1000 pc sample, as well as the VSX + ROSAT and VSX + eROSITA comparison samples. There are more CVs in our 1000 pc sample compared to either of the VSX sample, signalling that we have likely constructed the largest sample of X-ray selected CV candidates to date. The cumulative number of our 1000 pc is overall higher, meaning that the primarily optically-constructed VSX catalog is incomplete at all distances.

We also overplot the effective volume, multiplied by the space density we derive for CVs. This is effectively the theoretical total number we expect as a function of distance, which agrees with the cumulative number of systems in our sample up until a distance of $\approx$ 180 pc. Beyond that distance, the completeness plummets. Neither of the VSX samples are complete at any distance. We demonstrate this graphically in the bottom panels of Figure 6.11, plotting the percent difference between the theoretical and observed cumulative numbers of each sample, assuming Poisson counting errors.

Comparison to Previous Estimates of Average L_X

CVs

One of the major findings of this work is that the mean X-ray luminosity of most CVs is $\langle L_X \rangle \sim 10^{30}$erg s^{-1} in the 0.2–2.3 keV range. We also showed that the naive construction of an X-ray luminosity distribution based on X-ray detections of previously known, *primarily optically-identified* systems leads to an overestimate of this, with $\langle L_X \rangle \sim 10^{31} - 10^{32}$erg s^{-1}. This implies that our 1000 pc sample is likely rich with true CVs that have been missed by previous X-ray surveys.

An important exception to this, of course, are targeted X-ray observations (with *Swift*, *XMM-Newton*, *Chandra*, etc.) of systems identified by other means. An example of such a study was conducted by Reis et al. (2013). That study mainly targeted low accretion rate (WZ Sge-type) CVs discovered by SDSS, the majority of which had orbital periods near the period minimum $P_{\rm orb} < 90$ min. Reis et al. (2013) obtained *Swift*/XRT follow-up of ~20 systems, and found $\langle \log L_X (\mathrm{erg\ s^{-1}}) \rangle = 29.78$, and $\langle L_X \rangle = 8 \times 10^{29}$erg s^{-1} in the 0.5–10 keV range. In Figure 6.4, we show that

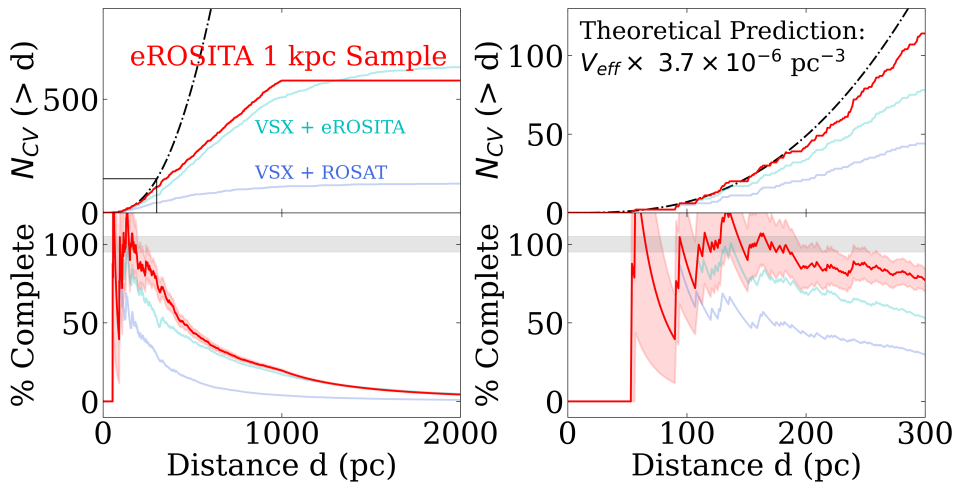

Figure 6.11: The cumulative distribution of CVs is plotted as a function of distance (upper panels) for our 1000 pc sample (red), and VSX samples. The predicted number of systems given our estimate of $\rho_{N,0}$ (black) indicates that both VSX samples are incomplete, even at $d \lesssim 100$ pc. The percentage of the difference between the predicted and observed cumulative distributions is shown in the lower panels. At distances beyond ≈ 180 pc, even our eROSITA + *Gaia* sample starts to become incomplete.

many of our systems in a similar period range also have similarly low values of L_X. However, the systems used to make up the Reis et al. (2013) sample were primarily non-magnetic CVs, not selected homogeneously, so a one-to-one comparison to our result is not possible.

Interestingly, Pretorius and Knigge (2012) note that applying a classic model of CV X-ray emission (Patterson and Raymond, 1985) to a synthetic population that (correctly) predicts the majority of CVs should be low accretion rate systems below the period gap (Kolb, 1993), predicts the majority of systems should have X-ray luminosities between a few $\times 10^{29}$erg s^{-1} and a few $\times 10^{30}$erg s^{-1}, which is similar to what we have found here. In short, while various earlier studies have postulated that there should be a large population of low L_X CVs, a secure discovery of this has not been possible until now.

While this work was in preparation, Schwope et al. (2024a) independently reported on SRG/eROSITA detections of CVs from known catalogs, and calculated $\langle \log L_X \rangle$ for each catalog. However, that work only reported on detections of previously known CVs, and did not conduct a search for new systems as we have done here, so those average L_X values cannot be taken to be representative of CVs. For example, we have shown here that the Pala et al. (2020a) sample, is missing two systems

within 150 pc.

AM CVns

The largest catalog of X-ray detections of AM CVns was compiled by Begari and Maccarone (2023), who searched the *XMM-Newton*, *Chandra* and *Swift* archives for X-ray counterparts to known AM CVns. They showed a clear trend of decreasing X-ray luminosity as a function of orbital period. Our average L_X of $8.6 \pm 3.5 \times 10^{29}$ erg s^{-1} is consistent with that of their longest period systems. Crucially, Ramsay et al. (2006) found that as AM CVns evolve to longer orbital periods, a large fraction luminosity is emitted in the ultraviolet, dominating over the X-ray. At this point, larger samples of AM CVns, particularly X-ray bright, short period systems, are needed to determine the average luminosity density, and if, as is the case with CVs, that the few X-ray bright systems dominate the total luminosity output over the dominant population of low L_X systems.

Synergy with Flux-Limited Surveys

Volume-limited surveys are by no means the only way to discover CVs. X-ray flux-limited and optical magnitude-limited surveys are the only way to discover intrinsically rare, yet scientifically interesting CVs that probe short evolutionary stages. In Figure 6.5, it is clear that CVs with $L_X \gtrsim 10^{32}$ erg s^{-1} are only found at $d \gtrsim 300$ pc. Indeed, many of these systems are long-period IPs, which are abundant in (hard) X-ray surveys and form a crucial part of understanding of magnetism in CVs (Suleimanov et al., 2019).

As mentioned previously, this is especially the case for AM CVns, where the moderate period $P_{\rm orb} \lesssim 50$ min systems, and particularly the short period $P_{\rm orb} \lesssim 20$ min systems, are only found at distances beyond a few hundred pc (Ramsay et al., 2018). These systems tend to have higher L_X values (Begari and Maccarone, 2023), and many have indeed been discovered through X-ray surveys.

The point of this work (and volume-limited surveys in general) is not to be sensitive to *all* CVs, but to conduct a systematic survey that detects all nearby CVs, which should be representative of the population in all regions of the Milky Way that resemble the solar neighborhood. In Figure 6.5, it is clear that low L_X systems, like long-period AM CVns and period bouncers, cannot be detected beyond 150–300 pc given the flux limit of eRASS1. These CV subtypes, once believed to be rare, are actually abundant in the Milky Way, but will remain invisible until the advent of

deeper all-sky X-ray and optical surveys such as future releases from SRG/eROSITA and the upcoming Rubin Observatory Legacy Survey of Space and Time (LSST).

Comparison to Pala et al. (2020a)

We wish to emphasize the importance of the 150 pc survey carried out by Pala et al. (2020a) in this work. 21 of the 23 CVs in our sample were already compiled by Pala et al. (2020a), spectroscopically verified either by that work or before, and had orbital periods determined. We acknowledge that most of the conclusions we reach here echo those of Pala et al. (2020a), though 1) all X-ray analysis presented here is new, and 2) we have made use of a novel selection tool, the X-ray Main Sequence, which has single-handedly recovered virtually all systems in the Pala et al. (2020a) sample, regardless of subtype. Crucially, the latter allows us to derive space densities without adopting a completeness correction, which is sensitive to the targeting strategy of SDSS (Pala et al., 2020a; Inight et al., 2023a).

We now speculate as to why we may have missed two systems in the Pala et al. (2020a) sample within 150 pc in the Western Galactic Hemisphere: Gaia J154008.28–392917.6 (d = 139 pc) and V379 Tel (d = 131 pc). Visual inspection of the eRASS1 images confirms they are not detected. Given the flux limit of eRASS1 and the well-measured distance, it is possible that Gaia J154008.28–392917.6 has an X-ray luminosity of $L_X \lesssim 1.0 \times 10^{29}$erg s^{-1}. Pala et al. (2020a) showed that this system is a WZ Sge-type low accretion rate CV that has shown no outbursts, so the possibility of a low X-ray luminosity is likely. Such low values of L_X, though rare, have been seen in CVs — as mentioned previously, one of the twenty CVs in the sample of Reis et al. (2013) indeed has $L_X < 1.3 \times 10^{29}$erg s^{-1}. In the case of V379 Tel, there are two possible scenarios. Firstly, since this system is an *eclipsing* polar (Potter et al., 2005), it is possible that it was missed by the single eROSITA scan of this part of the sky. Using the eROSITA upper limit calculator[20], the exposure time at this position was 85 sec, while the duration of an eclipse of this system is ≈300 sec (starting from the stream ingress), and its orbital period is 101 min (Potter et al., 2005). The probability that at least 20% of that 85 sec observation took place during eclipse is ∼6%, which is non-negligible. The second possibility is that it may have been observed in a period of low accretion state, as is commonly seen in magnetic CVs (Bernardini et al., 2019). Flickering and state changes have been observed in V379 Tel (Iłkiewicz et al., 2022), making it a possibility that it was in a low accretion state, with $L_X < 9.8 \times 10^{28}$erg s^{-1} during the eRASS1 observation.

[20] `https://erosita.mpe.mpg.de/dr1/erodat/upperlimit/single/`

However, we checked the Asteroid Terrestrial-impact Last Alert System (ATLAS; Tonry et al., 2018b) light curve of both systems near the epoch when their positions were observed by eROSITA in the eRASS1 survey, and do not notice an obvious low state (>1 mag prolonged average state compared to the rest of the light curve). This suggests that if being in a low state is the reason for their non-detection, that is must have been short ($\lesssim$ few days) or longer and missed by ATLAS due to bad weather or data quality. Finally, in both systems, it could be possible that they are being viewed at an inclination such that the X-ray emitting region is obscured (by the disk in Gaia J154008.28–392917 or by the accretion stream in V379 Tel), leading to the absorption of X-ray photons (e.g., Mukai, 2017).

Estimation of Systematic Uncertainties

Importantly, we note that the non-detection of these two systems does not pose a challenge to our estimation of space densities as we present them throughout the text, as the total number of systems is well within our 1σ Poisson counting uncertainties. However, their non-detection does raise the possibility that a small fraction of CVs could be emitting at $L_X < 10^{29}$erg s^{-1}.

Nevertheless, these non-detections are useful and allow us to estimate systematic uncertainties. Since 21 of 23 (91%) of systems in the Pala et al. (2020a) sample are detected in our sample, we could be underestimating our inferred space densities by a factor of 9%. Applying this to our estimate of CV space density (and propagating it with the statistical uncertainty in quadrature) would modify it from $\rho_{\rm N,\,CV} = (3.7 \pm 0.7) \times 10^{-6}$pc^{-3} to $\rho_{\rm N,\,CV} = (4.1 \pm 0.8) \times 10^{-6}$pc^{-3}. As outlined in the above paragraph, the mean value of the space density remains within the original statistical uncertainty.

In this work, since our goal is to create a CV and AM CVn sample selected using a single technique — the X-ray Main Sequence — we cannot in good faith report all space densities by applying a 9% systematic uncertainty across the board since this estimate comes from attempting to recover systems from another survey which itself is incomplete. Rather, future, deeper eRASS releases will shine a light on the true number of systems with $L_X < 10^{29}$erg s^{-1} and reveal the true systematic uncertainty needed to be adopted here. We also note that there are negligible systematic uncertainties in using the Western Galactic Hemisphere, rather than an all-sky sample. By using the VSX + ROSAT catalog as a reference, we note that the number of systems only found in the Western Galactic Hemisphere differs from

half of the all-sky number by at most several percent, which is within the statistical uncertainty reported above.

Comparison to Theoretical Predictions and Previous Estimates of Space Densities

All CVs

All population synthesis results predict an overabundance of CVs compared to observations. To get around this, it has been postulated that the majority of CVs are very faint, with $L_X < 4 \times 10^{28}$erg s^{-1}(e.g., Pretorius and Knigge, 2012), but our work rules that out since we are compete down to that value out to 90 pc. Our midplane number density is $\rho_{N,0} \approx 3.7 \pm 0.7 \times 10^{-6}$ pc^{-3}, yet modern population synthesis analyses predict number densities of $\rho_N \approx 9 \times 10^{-5}$ pc^{-3} (Belloni et al., 2018)[21], assuming a classical canonical angular momentum loss (CAML) prescription, around 20 times higher than our inferred value. Adjusting the AML prescription to "empirical" CAML, the predicted value drops to $\approx 2^{+2}_{-1} \times 10^{-5}$ pc^{-3}, which is still 5 times higher than our observed value (Belloni et al., 2018, 2020) and in $\gtrsim 2\sigma$ tension with our results. Goliasch and Nelson (2015) predict a number density of $1.0 \pm 0.5 \times 10^{-5}$ pc^{-3}, which is also in $\gtrsim 2\sigma$ tension with our results.

Previously, number densities of CVs were obtained in three different ways: 1) X-ray flux limited surveys, 2) large-scale optical spectroscopic surveys, and 3) the volume-limited sample of Pala et al. (2020a), which assembled all known CVs out to 150 pc and based their completeness on SDSS targeting and CRTS observations.

We obtain more precise estimates than those carried out by previous X-ray surveys since they suffer from incompleteness. Pretorius and Knigge (2012) predicted a number density of non-magnetic CVs of $\rho_N = 4^{+6}_{-2} \times 10^{-6}$ pc^{-3}, and Pretorius et al. (2013) a number density of magnetic CVs of $8^{+4}_{-2} \times 10^{-7}$ pc^{-3}. Both analyses were carried out using data from the ROSAT catalogs, but an estimate of completeness could not be carried out due to a nonuniform selection and the challenge of isolating ROSAT sources at low Galactic latitudes ($|b| \lesssim 20°$). Later, Schwope (2018) revisited systems from these samples, and obtained distances using newly available *Gaia* parallaxes. Schwope (2018) obtained number densities ranging between $0.96 - 10.9 \times 10^{-6}$ pc^{-3}, depending on the particular sample used and the assumption of

[21] We report all of our inferred space densities of CVs in powers of 10^{-6} and those of AM CVns in powers of 10^{-7}, in order to be consistent with the majority of the literature. In cases where different powers are used in the literature, we report those values in order to faithfully reproduce the numbers reported by that work.

CV scale height, though individual estimates obtained similarly small error bars as the ones we show here (e.g., the use of the RASS sample with a 200 pc scale height yielded a number density of $4.7^{+0.7}_{-0.4} \times 10^{-6}$ pc^{-3}.

We obtain similarly precise estimates than those carried out by optical spectroscopic surveys, yet those surveys suffer from incompleteness, different than that of X-ray surveys. Inight et al. (2021) calculated a midplane number density of $\rho_0 = 2.2^{+1.0}_{-0.6} \times 10^{-6}$ pc^{-3}, assuming a scale height of 280 pc. They revisited their calculation in Inight et al. (2023a), with new systems, and estimated a completeness factor of 2.14 which was used to compute a number density of $\rho_0 = 7.23 \times 10^{-6}$ pc^{-3} assuming a scale height of 260 pc (this means that before incorporating their completeness factor, they obtained a value of $\rho_0 = 3.37 \times 10^{-6}$ pc^{-3}). This is similar to the work of Pala et al. (2020a), where a value of $\rho_0 = 3.7^{+0.6}_{-0.8} \times 10^{-6}$ pc^{-3} was obtained, and then a completeness factor of 1.4 was incorporated to obtain a number density of $\rho_0 = 4.8^{+0.6}_{-0.8} \times 10^{-6}$ pc^{-3}, all assuming a scale height of 280 pc.

All aforementioned X-ray campaigns have obtained number densities similar to ours and remarkably, the number densities derived by spectroscopic campaigns best agree with ours *before* their application of a correction factor for completeness. The latter possibly suggests that such a correction has been overapplied. All in all, our results echo the conclusion of Inight et al. (2023a), where it appears that various CV observational campaigns using independent methods are converging on a midplane number density of $\rho_{N,0} \approx 4 - 5 \times 10^{-6}$ pc^{-3}. However, our work is unique in not needing to employ a completeness factor and appearing to be unbiased towards any CV subtype.

We also note the work of Canbay et al. (2023), where a cleaned version of the VSX catalog, together with *Gaia* DR3, was used to infer CV space densities and space heights. The local space density of all CVs was found to be $6.8^{+1.3}_{-1.1} \times 10^{-6}$ pc^{-3}, which is about fifty percent higher than the value obtained in our work. While this difference is not egregious, the VSX catalog suffers from incompleteness (as we show in this work), which would lead to a *lower* estimate than ours. Since Canbay et al. (2023) use the older Galactic model from Bilir et al. (2006), it is possible that that, in combination with a different method of calculating the space density ("partial spherical volumes"), leads to this discrepancy.

Magnetic CVs

We calculate the midplane number density of magnetic CVs to be $\rho_{\rm N,\,magnetic} = (1.3\pm0.5)\times10^{-6}$ pc^{-3}. The only theoretical estimate of magnetic CV space densities has been carried out by Belloni et al. (2020), where it was predicted that the space density of polars should be $5^{+5}_{-3} \times 10^{-6}$ pc^{-3} ($1.5^{+1.5}_{-0.6} \times 10^{-6}$ pc^{-3} excluding period bouncers), though the authors initially fix the fraction of polars relative to the entire CV population at 28 percent. Our number density is technically in disagreement with that, since our sample includes one IP (not considered by that analysis) and two magnetic period bouncers.

It is most meaningful to compare our number density to that derived by Pretorius et al. (2013), $8^{+4}_{-2} \times 10^{-7}$ pc^{-3}, which agrees with ours within 1σ. However, that sample is rich with more IPs and lacks period bouncers. Further analysis of our 300 pc and 1000 pc samples will reveal larger numbers of magnetic CVs and show at what distance the classic, high L_X IPs will start to appear (≈500 pc is suggested by Suleimanov et al. (2019)).

Period Bouncers

We calculate the midplane number density of period bouncers to be $\rho_{\rm N,\,PB} = 0.9 \pm 0.4\times10^{-6}$ pc^{-3}. All population synthesis results predict an overabundance of period bouncers compared to observations. Our work is the observational campaign that has found the largest space density of period bouncers to date, thanks to our sensitivity to low L_X systems, where period bouncers live (Table 6.3). However, we do note the possibility that additional period bouncers could still be present, albeit with very low X-ray luminosities ($L_X < 10^{29}$erg s^{-1}). Early works by Kolb (1993) predicted that ≈ 70 % of CVs should be period bouncers, whereas modern works accommodate a range as low as ≈ 38% (Goliasch and Nelson, 2015) to ≈ 82%. (Belloni et al., 2020). Applying these percentages to global space densities, Goliasch and Nelson (2015) place the number density of period bouncers to be $\rho_{\rm N,PB} \approx 4-7\times10^{-6}$ pc^{-3} (at least 4 times higher than our value), and Belloni et al. (2020) estimate it to be 16×10^{-6} pc^{-3} (nearly 20 times higher than our value), assuming the eCAML prescription.

Only a handful of observational campaigns have placed meaningful constraints on the space density of period bouncers: 1) Hernández Santisteban et al. (2018) searched for eclipsing systems in the Palomar Transient Factory data archive and quantified their completeness using SDSS targeting to obtain an upper limit of

$\rho_{\mathrm{N,\,PB}} \lesssim 20 \times 10^{-6}$ pc^{-3}, 2) Pala et al. (2020a) estimated the fraction of period bouncers in their sample to be 7–14%, yielding a number density of $\approx 0.3 - 0.6 \times 10^{-6}$ pc^{-3}, and 3) Inight et al. (2023a) analyzed SDSS I–V data to estimate a value of $\approx 0.2 \times 10^{-6}$ pc^{-3}.

In contrast to virtually all previous studies, we obtain a value of $\rho_{\mathrm{N,\,PB}} = 0.9 \pm 0.4 \times 10^{-6}$ pc^{-3}. This high value is due to the inclusion of two magnetic period bouncers not mentioned in the Pala et al. (2020a) sample: 1) the reclassification of SDSS J125044.42+154957.3 by Muñoz-Giraldo et al. (2023) as a magnetic period bouncer (this was not the case in Pala et al. (2020a)), and 2) our discovery of 1eRASS J054726.9+132649. This suggests that other nearby magnetic period bouncers may be lurking, and could be revealed by deeper eROSITA surveys (e.g., Galiullin et al., 2024b). If this lack of period bouncers is confirmed, as our work seems to suggest, a modification to the standard CV evolutionary picture — for example, either through a different magnetic braking prescription (Sarkar et al., 2024) or through the detachment of CVs as they pass through the period minimum (Schreiber et al., 2023) — could be invoked to explain such a phenomenon.

AM CVns

We calculate the midplane number density of AM CVns to be $\rho_{\mathrm{N,\,AM\,CVn}} = 5.5 \pm 3.7 \times 10^{-7}$ pc^{-3}. We are able to place meaningful constraints on the space density of AM CVns because of our straightforward selection function. Even with three systems in our sample, our 68% Poisson intervals place the errors of our number density estimates on par with those of other observational campaigns. Only a handful of studies have estimated the space density of AM CVns due to 1) the intrinsic rarity of systems and 2) the difficulty in setting up a systematic survey to identify long-period, low accretion rate systems. Because, like CVs, all AM CVns are X-ray emitters (e.g., Ramsay et al., 2005, 2006; Begari and Maccarone, 2023), it is difficult for nearby systems to be missed with the X-ray Main Sequence.

Early work on population synthesis of AM CVns predicted space densities of $\rho_{\mathrm{N,\,AM\,CVn}} = 0.4 - 1.7 \times 10^{-4}$ pc^{-3} (Nelemans et al., 2001), at least 100 times higher than our derived value. This incredibly high number would mean that AM CVns would have higher space densities than CVs.

Two types of observational campaigns have placed meaningful constraints on the space density of AM CVns, with the first being spectroscopic surveys from SDSS. Roelofs et al. (2007) and Carter et al. (2013) calculated number densities of 1 –

3×10^{-7} pc^{-3} and $5 \pm 3 \times 10^{-7}$ pc^{-3}, respectively. The other method has been recently carried out by van Roestel et al. (2022), who systematically searched the ZTF database for eclipsing AM CVns and derived a space density of $6^{+6}_{-2} \times 10^{-7}$ pc^{-3}. That study effectively ruled out a large population of faint, very low accretion rate systems, meaning that our X-ray survey will not miss a large population of AM CVns. In other words, the van Roestel et al. (2022) survey, by targeting *all* eclipsing systems in the period range of AM CVns, should have detected very low accretion rate systems with weak to no emission lines if they indeed existed. Because such systems were not discovered, this suggests that even in the latest stages of their evolution, AM CVns accrete at high enough levels to be detectable in X-rays. It is worth noting that Ramsay et al. (2018) also derived the space density of AM CVns from the collection of all systems known up until that point. There, it was shown that the 1σ lower limit of the AM CVn number density was $> 3 \times 10^{-7}$ pc^{-3}.

Our midplane number density is consistent within 1σ with values derived from both spectroscopic surveys and searches for eclipsing systems. However, it is lower than the expected number density of Nelemans et al. (2001) by at least two orders of magnitude. Our result reinforces the tension with AM CVn population synthesis estimates, and demonstrates the need for a modern recalculation. This is especially important for estimating the population resolved by LISA and that which will make up the gravitational wave background (Nelemans et al., 2004b; Kupfer et al., 2024; Tang et al., 2024).

6.6 Conclusion

We have conducted a systematic, volume-limited survey of CVs down to the lowest X-ray luminosity to date, $L_X = 1.3 \times 10^{29}$ erg s^{-1} in the 0.2–2.3 keV range. Our main survey extends to a distance of 150 pc, and was possible thanks to a crossmatch of the SRG/eROSITA eRASS1 X-ray survey of the Western Galactic Hemisphere and *Gaia* DR3. We employed a novel tool called the “X-ray Main Sequence" — a color-color diagram with *Gaia* BP–RP on the horizontal axis and $F_X/F_{\rm opt}$ on the vertical axis — to create our sample. We recover virtually all previously known CVs within 150 pc in this part of the sky and have discovered two new systems. Our main conclusions are:

1. The X-ray Main Sequence is a highly efficient tool for systematic searches of the X-ray + optical sky (Figure 6.1). Within 150 pc, we selected 28 CV candidates, a mere ≈0.1% of the SRG/eROSITA eRASS1 + *Gaia* parent

sample (Table 6.1). We discarded three false matches, two non-CV compact object binaries, and were left with 23 CVs within 150 pc in the Western Galactic Hemisphere.

2. We discovered two new CVs in the 23 within 150 pc: 1eRASS J054726.9+132649, a magnetic period bouncer (Figure 6.8), and 1eRASS J101328.7-202848, a long-period AM CVn which is now the third closest ultracompact system to Earth, at 140 pc (Figure 6.7).

3. Using our 150 pc sample, we constructed luminosity functions and showed a "flattening" at $L_X \sim 10^{30}$erg s^{-1} for the first time in CVs (Figure 6.6), though larger samples from deeper eROSITA releases are needed to confirm this. We infer the CV number density at the midplane to be $\rho_{\rm N,CV} = 3.7\pm0.7\times10^{-6}$ pc^{-3} (Table 6.4). This number density agrees to within 1σ with most previous estimates from spectroscopic surveys (without completeness correction) and X-ray flux limited surveys. However, it is still lower than that predicted by theory by a factor of ~5–20.

4. We calculated the AM CVn number density at the midplane to be $\rho_{\rm N,AM\ CVn} = 5.5 \pm 3.7 \times 10^{-7}$ pc^{-3} (Table 6.4). Our novel selection method allows us to be complete, even while only having a few systems. This agrees to within 1σ with most previous estimates from spectroscopic and optical photometric surveys. However, it is still lower than that predicted by theory by a factor of ~70–200.

5. The average X-ray luminosity of CVs in our 150 pc sample is $\langle L_X \rangle \approx 4.6 \times 10^{30}$erg s^{-1} in the 0.2–2.3 keV range (Figure 6.5), with a maximum correction of a factor of 0.07 needed to account for interstellar extinction. In contrast, L_X distributions built from X-ray matches to primarily optically-discovered CVs yield $\langle L_X \rangle \sim 10^{31} - 10^{32}$erg s^{-1}, which means that $\langle L_X \rangle$ of CVs has been systematically overrestimated in the past.

6. The fraction of magnetic CVs in our 150 pc sample is 35%, and that of period bouncers is 25%, assuming Poisson counting errors in the main sample. This fraction of period bouncers is higher than all previous observational campaigns, but still lower than the 40–70% predicted by population synthesis. Deeper eROSITA releases are needed to confirm this tension, which could still reveal systems at even lower X-ray luminosities.

By focusing on the volume out to 150 pc from the Sun, this work is somewhat biased to the low-L_X end of CVs. Nevertheless, our local survey should be representative of other regions in the Milky Way that resemble the solar neighborhood. Furthermore, low-L_X systems such as AM CVns and period bouncers have been the most difficult to find in previous surveys, as highlighted by the discovery of two new systems in our sample. It has only been with recent surveys made possible by SRG/eROSITA that such systems have come to light (e.g., Rodriguez et al., 2023b; Galiullin et al., 2024b). In contrast, high-L_X systems like bright IPs have been easier to discover in the past, but are more rare, making them more distant and not recovered by our search (e.g., Suleimanov et al., 2019).

Future work should spectroscopically verify CV candidates in our 300 pc and 1000 pc samples, which we make publicly available. Since the number of systems approaches the hundreds, this could be best accomplished using large spectroscopic surveys such as SDSS-V (Kollmeier et al., 2017; Almeida et al., 2023), the Dark Energy Spectroscopic Instrument (DESI; DESI Collaboration et al., 2016), the 4-metre Multi-Object Spectrograph Telescope (4MOST; de Jong et al., 2019), and the William Herschel Telescope Enhanced Area Velocity Explorer (WEAVE; Dalton et al., 2012).

Upcoming eRASS releases will probe the X-ray variability of these objects, and trends regarding X-ray hardness ratios of CVs and AM CVns should be investigated on a large scale. Co-added eROSITA surveys will go a few times deeper than eRASS1, and will discover many new systems, particularly at larger distances. For example, Schwope et al. (2024b) recently compiled a list of the compact white dwarf binaries in the eFEDS survey of SRG/eROSITA, covering 140 deg^2 of the sky. In that work, of the 23 systems, only 9 systems would pass the flux limit of eRASS1. The remaining systems are at $\gtrsim$ 250 pc, suggesting that our 300 pc sample, and in particular our 1000 pc sample would greatly benefit from deeper eRASS surveys as Figure 6.5 demonstrates. At the eRASS:4/eRASS:8 limit of $F_X = 1{\times}10^{-14}/7{\times}10^{-15}$ erg s^{-1}cm^{-2} (e.g., Sunyaev et al., 2021), a survey complete down to $L_X = 10^{29}$erg s^{-1} can extend out to 300 pc / 360 pc.

New optical surveys will be useful in the near future as well. Releases with updated astrometry, photometry, and ultra low-resolution spectroscopy from *Gaia* DR4/DR5 will also add to the complete picture of CVs and AM CVns. These releases will improve parallaxes to faint, WD-dominated systems at $\gtrsim$ 300 – 400 pc, which are currently difficult to detect due to a combination of large parallax errors and faintness

at that distance (e.g., Gentile Fusillo et al., 2021a). Also on the horizon is the Rubin Observatory Legacy Survey of Space and Time (LSST), which will use large, optically selected samples to provide further data on faint systems, particularly AM CVns and eclipsing and outbursting CVs in the period bounce regime (e.g., Szkody, 2015). In both cases, combining SRG/eROSITA data and employing the X-ray Main Sequence will be a useful tool in identifying candidate compact object binaries and forming large, uniformly selected samples as we have done here.

6.7 Acknowledgements

We thank Roman Krivonos for insightful feedback, Kevin Burdge, Dovi Poznanski, and Jim Fuller for useful discussions, and Sunny Wong for providing AM CVn evolutionary models. ACR acknowledges support from an NSF Graduate Fellowship.

ACR thanks the LSST-DA Data Science Fellowship Program, which is funded by LSST-DA, the Brinson Foundation, and the Moore Foundation; his participation in the program has benefited this work. RLO is a Research Fellow of the Brazilian institution CNPq (PQ-315632/2023-2).

This work is based on data from eROSITA, the soft X-ray instrument aboard SRG, a joint Russian-German science mission supported by the Russian Space Agency (Roskosmos), in the interests of the Russian Academy of Sciences represented by its Space Research Institute (IKI), and the Deutsches Zentrum für Luft- und Raumfahrt (DLR). The SRG spacecraft was built by Lavochkin Association (NPOL) and its subcontractors, and is operated by NPOL with support from the Max Planck Institute for Extraterrestrial Physics (MPE). The development and construction of the eROSITA X-ray instrument was led by MPE, with contributions from the Dr. Karl Remeis Observatory Bamberg & ECAP (FAU Erlangen-Nuernberg), the University of Hamburg Observatory, the Leibniz Institute for Astrophysics Potsdam (AIP), and the Institute for Astronomy and Astrophysics of the University of Tübingen, with the support of DLR and the Max Planck Society. The Argelander Institute for Astronomy of the University of Bonn and the Ludwig Maximilians Universität Munich also participated in the science preparation for eROSITA.

This work presents results from the European Space Agency (ESA) space mission Gaia. Gaia data are being processed by the Gaia Data Processing and Analysis Consortium (DPAC). Funding for the DPAC is provided by national institutions, in particular the institutions participating in the Gaia MultiLateral Agreement (MLA). The Gaia mission website is `https://www.cosmos.esa.int/gaia`. The Gaia

archive website is `https://archives.esac.esa.int/gaia`.

Some of the data presented herein were obtained at Keck Observatory, which is a private 501(c)3 non-profit organization operated as a scientific partnership among the California Institute of Technology, the University of California, and the National Aeronautics and Space Administration. The Observatory was made possible by the generous financial support of the W. M. Keck Foundation. The authors wish to recognize and acknowledge the very significant cultural role and reverence that the summit of Maunakea has always had within the Native Hawaiian community. We are most fortunate to have the opportunity to conduct observations from this mountain. We are also grateful to the staff of Palomar Observatory and that of Lick Observatory for their assistance in carrying out observations used in this work.

Based on observations obtained with the Samuel Oschin Telescope 48-inch and the 60-inch Telescope at the Palomar Observatory as part of the Zwicky Transient Facility project. ZTF is supported by the National Science Foundation under Grants No. AST-1440341 and AST-2034437 and a collaboration including current partners Caltech, IPAC, the Weizmann Institute of Science, the Oskar Klein Center at Stockholm University, the University of Maryland, Deutsches Elektronen-Synchrotron and Humboldt University, the TANGO Consortium of Taiwan, the University of Wisconsin at Milwaukee, Trinity College Dublin, Lawrence Livermore National Laboratories, IN2P3, University of Warwick, Ruhr University Bochum, Northwestern University and former partners the University of Washington, Los Alamos National Laboratories, and Lawrence Berkeley National Laboratories. Operations are conducted by COO, IPAC, and UW.

Software used: Python and the following libraries: `matplotlib` (Hunter, 2007), `scipy` (Virtanen et al., 2020), `astropy` (Astropy Collaboration et al., 2013b), `numpy` (van der Walt et al., 2011). `PypeIt` (Prochaska et al., 2020), `lpipe` (Perley, 2019), and Tool for OPerations on Catalogues And Tables `(TOPCAT)` (Taylor, 2005).

6.8 CV Selection with the X-ray Main Sequence

Here, we justify our choice of enforcing the -0.3 < BP–RP < 1.5 cut , as well as our “modified" cut in the X-ray Main Sequence when creating our samples. At all distances, we crossmatched our volume limited sample with a clean set of CVs from the VSX catalog (see Section 6.3), where we enforced that the orbital period also be well known (no “:" in the period category) to ensure the best selection. We present the results in Figure 6.12.

In Figure 6.12, it is clear that none of the VSX CVs fall under the modified cut (dash dot line) in the 150 pc and 300 pc samples. Less than 3% of systems fall below the cut in the 1000 pc sample, with < 1% falling below the empirical cut from Rodriguez (2024b) (solid diagonal line). No CVs are located in the BP–RP < −0.3 region at any distance. This means that the systems located there are likely hot WDs thermally emitting X-rays, though that should be investigated in future studies.

Finally, no VSX CVs are located in the BP–RP > 1.5 region in the 150 pc sample, while 2 (< 3%) are there in the 300 pc sample and 5 (< 1%) are there in the 1000 pc sample. It is especially clear in the X-ray Main Sequence of the 1000 pc sample (upper left panel of Figure 6.12) that there is a significant amount of objects above the “empirical cut" (Rodriguez, 2024b) as well as “modified cut", redward of BP–RP of 1.5. The distribution of the separation between X-ray and optical points (right panels of Figure 6.12) shows that the distribution of those points (shown in gray), however, does not follow a Rayleigh distribution and is instead consistent with randomly associated matches. In contrast, the distribution of the our CV candidates (shown in blue), clearly follows a Rayleigh distribution, with a best-fit $\sigma_{\rm sep}$ (Equation 6.2) of 2.2" at all distances. We clarify that the blue distributions plotted on the right panels of Figure 6.12 are comprised of *all* possible matches out to 20". The candidates we plot on the left and center panels (and comprise our samples), include only crossmatches out to 7.7" ($3.5\sigma_{\rm sep}$; see Section 6.3), thus being dominated by true associations. This exercise shows the importance of 1) starting with a larger crossmatch radius than the nominal positional error of a survey, and 2)always plotting the distribution of separations when doing a crossmatch. A blind crossmatch, accepting points redward of BP–RP = 1.5 in this case, would have resulted in being dominated by false matches, *even when only keeping points at very low separations* (e.g., < 5 arcsec).

6.9 CV Scale Height Calculation

In order to be self consistent with the Galactic mass profile analysis carried out by Barros et al. (2016), we effectively assumed a CV scale height, $h_{\rm CV}$ of 205 pc. Calculating $h_{\rm CV}$ for CVs is difficult, and technically must be done for different CV subtypes separately to account for their being in different evolutionary stages and therefore having different intrinsic ages (e.g., Pretorius et al., 2007; Ak et al., 2015; Canbay et al., 2023). However, it would likely require a much larger, spectroscopically confirmed sample of systems to undertake such an analysis. We proceed by computing a scale height of CVs for our largest samples, but explain why simply

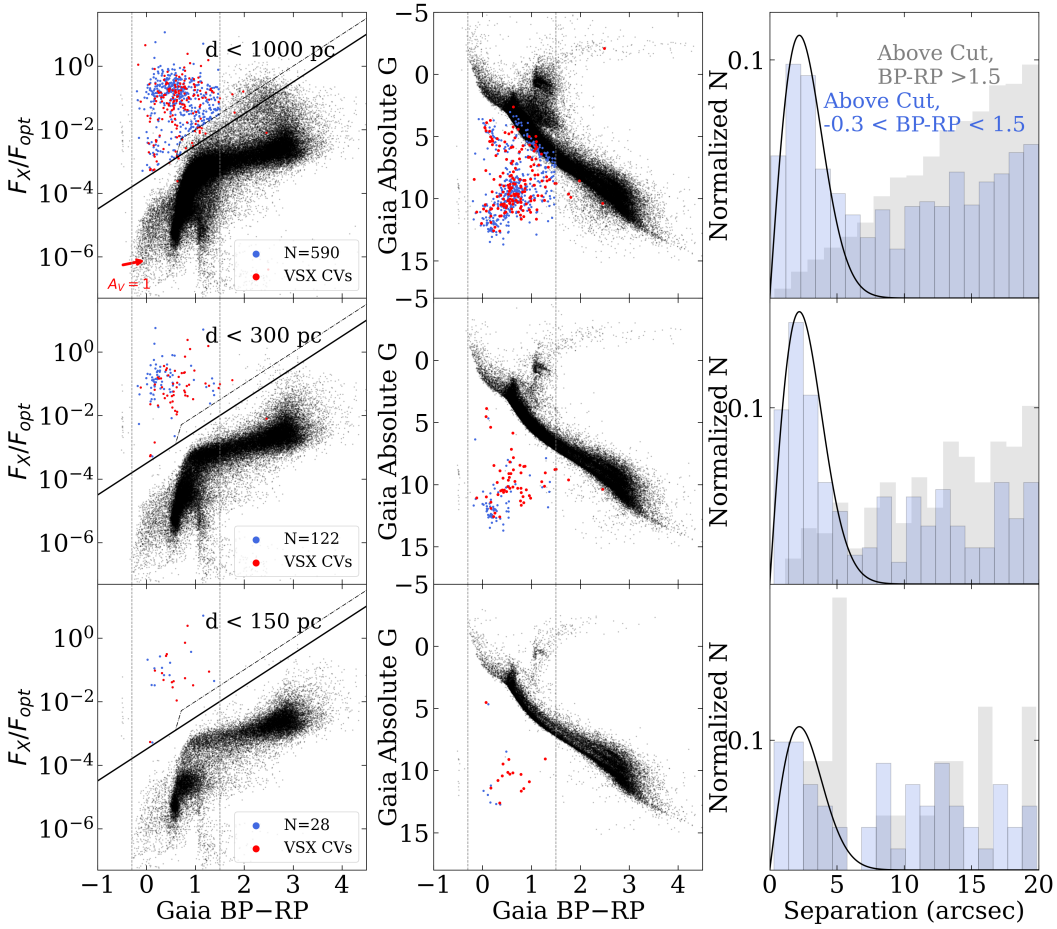

Figure 6.12: Our volume-limited samples are shown on the X-ray Main Sequence (left) and HR diagram (center), with black points denoting all objects in the sample, blue our CV candidates, and red the best vetted CVs from the VSX catalog. Only a few VSX CVs are below the “modified" cut (dash dot line) on the left, meaning that this can be used in place of the cut from Rodriguez (2024b) (solid diagonal line). On the right are distributions of the separation between X-ray and optical points. A Rayleigh distribution with $\sigma_{\rm sep}$ = 2.2” (black line) best fits the final sample at all distances, justifying our choice of cuts.

setting $h_{\rm CV}$ to a fixed value is justified.

Because the scale height of the thin disk is ≈200 pc, we cannot compute a scale height based on the 150 pc sample alone. However, we can make use of three other samples in this study: our 1000 pc sample, the VSX + eROSITA sample, and the VSX + ROSAT sample, which are sensitive to CVs far enough away to trace their characteristic $h_{\rm CV}$. We exclude systems in the VSX samples beyond 1000 pc in order to have a fair comparison to our 1000 pc sample.

We follow a similar approach to Revnivtsev et al. (2008) and Suleimanov et al. (2022), and assume that CVs follow an exponential distribution in the Milky Way, with the probability of a system to be located at a height z above the Galactic place to be:

$$P_i(z_i) = \frac{1}{h_{\rm CV}} \exp\left(\frac{-|z_i|}{h_{\rm CV}}\right) \tag{6.7}$$

where z is defined as in Equation 6.5. We can compute a log-likelihood function:

$$\log \mathcal{L}(z) = \log \prod_i P_i(z_i) = -\sum_i^N \ln h_{\rm CV} - \frac{|z_i|}{h_{\rm CV}} \tag{6.8}$$

We compute the value that maximizes the negative log-likelihood and present that value along with 95% confidence intervals in Figure 6.13. The ROSAT sample suggests that $h_{\rm CV} \approx 185$ pc since it traces X-ray bright systems (e.g., polars, IPs) which are younger, while the VSX + eROSITA and our 1000 pc sample are more sensitive to X-ray faint systems farther along in their evolution, and instead suggest that $h_{\rm CV} \approx 200 - 240$ pc. At the end of the day, neither of those two samples can be taken as ground truth, since the VSX + eROSITA sample suffers from incompleteness and our 1000 pc sample of CV candidates is not spectroscopically verified.

As a final calculation, we determine the midplane number density of CVs assuming different scale heights from our 150 pc sample, assuming a Galactic model as in Equation 6.4. Assuming a extreme values of $h_{\rm CV}$ =100, 500 pc, respectively, we obtain midplane number densities of $\rho_{N,0} \approx 4.7 \times 10^{-6}$ pc^{-3} and 3.2×10^{-6} pc^{-3}, respectively, which lead to no more than ≈ 30% deviations from our calculated values in Table 6.4.

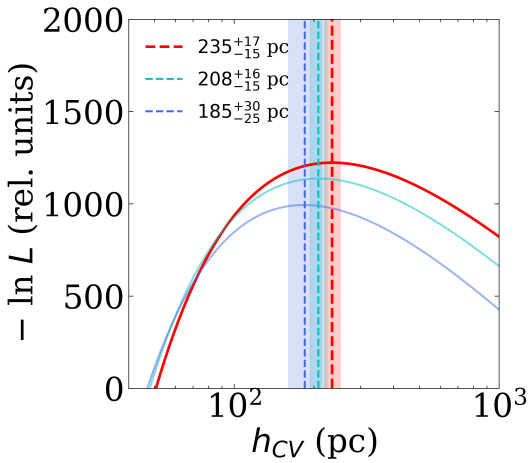

Figure 6.13: Negative log likelihood of the CV characteristic scale height, $h_{\rm CV}$ for the VSX + ROSAT (blue), VSX + eROSITA (cyan), and our 1000 pc sample (red). We plot the most likely value as a dotted line and show 95% confidence intervals as shaded regions. The ROSAT sample likely has a smaller value since it traces X-ray bright systems (e.g., polars, IPs) which are younger, while the VSX + eROSITA and our 1000 pc sample are more sensitive to X-ray faint systems farther along in their evolution. Both the VSX + eROSITA and our 1000 pc sample are consistent with our fixed value of $h_{\rm CV}$ = 205 pc.

Chapter 7

A LINK BETWEEN WHITE DWARF PULSARS AND POLARS: MULTIWAVELENGTH OBSERVATIONS OF THE 9.36-MINUTE PERIOD VARIABLE GAIA22AYJ

Antonio C. Rodriguez, Kareem El-Badry, Pasi Hakala, Pablo Rodríguez-Gil, Tong Bao, Ilkham Galiullin, Jacob A. Kurlander, Casey J. Law, Ingrid Pelisoli, Matthias R. Schreiber, Kevin Burdge, Ilaria Caiazzo, Jan van Roestel, Paula Szkody, Andrew J. Drake, David A. H. Buckley, Stephen B. Potter, Boris Gaensicke, Kaya Mori, Eric C. Bellm, Shrinivas R. Kulkarni, Thomas A. Prince, Matthew Graham, Mansi M. Kasliwal, Sam Rose, Yashvi Sharma, Tomás Ahumada, Shreya Anand, Akke Viitanen, Avery Wold, Tracy X. Chen, Reed Riddle, and Roger Smith. A Link Between White Dwarf Pulsars and Polars: Multiwavelength Observations of the 9.36-minute Period Variable Gaia22ayj. *Publications of the Astronomical Society of the Pacific*, 137(2):024202, February 2025. doi: 10.1088/1538-3873/adb0f1.

Author List

Antonio C. Rodriguez[1,*], Kareem El-Badry[1], Pasi Hakala[2], Pablo Rodríguez-Gil[3,4], Tong Bao[5], Ilkham Galiullin[6], Jacob A. Kurlander[7], Casey J. Law[1,8], Ingrid Pelisoli[9], Matthias R. Schreiber[10], Kevin Burdge[11,12], Ilaria Caiazzo[13], Jan van Roestel[14], Paula Szkody[7], Andrew J. Drake[1], David A. H. Buckley[15,16,17], Stephen B. Potter[15,18], Boris Gaensicke[9], Kaya Mori[19], Eric C. Bellm[7], Shrinivas R. Kulkarni[1], Thomas A. Prince[20], Matthew Graham[1], Mansi M. Kasliwal[1], Sam Rose[1], Yashvi Sharma[1], Tomás Ahumada[1], Shreya Anand[21,22,23], Akke Viitanen[24,25], Avery Wold[26], Tracy X. Chen[26], Reed Riddle[27], Roger Smith[27]

[1]Department of Astronomy, California Institute of Technology, 1200 E. California Blvd, Pasadena, CA 91125, USA

[2]Finnish Centre for Astronomy with ESO (FINCA), Quantum, University of Turku, FI-20014, Finland

[3]Instituto de Astrofísica de Canarias, E-38205 La Laguna, Tenerife, Spain

[4]Departamento de Astrofísica, Universidad de La Laguna, E-38206 La Laguna, Tenerife, Spain

[5]INAF – Osservatorio Astronomico di Brera, Via E. Bianchi 46, 23807 Merate (LC), Italy

[6]Kazan Federal University, Kremlevskaya Str.18, 420008, Kazan, Russia

[7]Department of Astronomy, University of Washington, 3910 15th Avenue NE, Seattle, WA 98195, USA

[8]Owens Valley Radio Observatory, California Institute of Technology, Big Pine CA 93513, USA

[9]Department of Physics, University of Warwick, Coventry CV4 7AL, UK

[10]Departamento de Física, Universidad Técnica Federico Santa María, Av. España 1680, Valparaíso, Chile

[11]Department of Physics, Massachusetts Institute of Technology, Cambridge, MA, USA

[12]Kavli Institute for Astrophysics and Space Research, Massachusetts Institute of Technology, Cambridge, MA, USA

[13]Institute of Science and Technology Austria (ISTA), Am Campus 1, 3400 Klosterneuburg, Austria

[14]Anton Pannekoek Institute for Astronomy, University of Amsterdam, 1090 GE Amsterdam, The Netherlands

[15]South African Astronomical Observatory, PO Box 9, Observatory 7935, Cape

Town, South Africa
[16]Department of Astronomy, University of Cape Town, Private Bag, Rondebosch 7701, Cape Town, South Africa
[17]Department of Physics, University of the Free State, PO Box 339, Bloemfontein 9300, South Africa
[18]Department of Physics, University of Johannesburg, PO Box 524, Auckland Park 2006, South Africa
[19]Columbia Astrophysics Laboratory, Columbia University, New York, NY, USA
[20]Division of Physics, Mathematics, and Astronomy, California Institute of Technology, 1200 E. California Blvd, Pasadena, CA 91125, USA
[21]Department of Physics, California Institute of Technology, 1200 E. California Blvd, Pasadena, CA 91125, USA
[22]Department of Physics, Stanford University, 382 Via Pueblo Mall, Stanford, CA 94305, USA
[23]Kavli Institute for Particle Astrophysics and Cosmology, P.O. Box 2450, Stanford University, Stanford, CA 94305, USA
[24]INAF–Osservatorio Astronomico di Roma, via Frascati 33, 00040 Monteporzio Catone, Italy
[25]Department of Physics and Helsinki Institute of Physics, Gustaf Hällströmin katu 2, 00014 University of Helsinki, Finland
[26]IPAC, California Institute of Technology, 1200 E. California Blvd, Pasadena, CA 91125, USA
[27]Caltech Optical Observatories, California Institute of Technology, Pasadena, CA 91125, USA

[*]Corresponding author: acrodrig@caltech.edu

ABSTRACT

White dwarfs (WDs) are the most abundant compact objects, and recent surveys have suggested that over a third of WDs in accreting binaries host a strong (B $\gtrsim$ 1 MG) magnetic field. However, the origin and evolution of WD magnetism remain under debate. Two WD pulsars, AR Sco and J191213.72–441045.1 (J1912), have been found, which are non-accreting binaries hosting rapidly spinning (1.97-min and 5.30-min, respectively) magnetic WDs. The WD in AR Sco is slowing down on a $P/\dot{P} \approx 5.6 \times 10^6$ yr timescale. It is believed they will eventually become polars, accreting systems in which a magnetic WD (B $\approx$ 10 – 240 MG) accretes from a Roche lobe-filling donor spinning in sync with the orbit ($\gtrsim$ 78 min). Here, we present multiwavelength data and analysis of Gaia22ayj, which outbursted in March 2022. We find that Gaia22ayj is a magnetic accreting WD that is rapidly spinning down ($P/\dot{P} = 6.1^{+0.3}_{-0.2} \times 10^6$ yr) like WD pulsars, but shows clear evidence of accretion, like polars. Strong linear polarization (40%) is detected in Gaia22ayj; such high levels have only been seen in the WD pulsar AR Sco and demonstrate the WD is magnetic. High speed photometry reveals a 9.36-min period accompanying a high amplitude ($\sim$ 2 mag) modulation. We associate this with a WD spin or spin-orbit beat period, not an orbital period as was previously suggested. Fast (60-s) optical spectroscopy reveals a broad "hump", reminiscent of cyclotron emission in polars, between 4000–8000 Å. We find an X-ray luminosity of $L_X = 2.7^{+6.2}_{-0.8} \times 10^{32}$ erg s^{-1} in the 0.3–8 keV energy range, while two VLA radio campaigns resulted in a non-detection with a $F_r < 15.8$ μJy 3σ upper limit. The shared properties of both WD pulsars and polars suggest that Gaia22ayj is a missing link between the two classes of magnetic WD binaries.

7.1 Introduction

Magnetic fields are ubiquitous in the Universe, from planetary scales such as that of the Earth to extragalactic scales of the intergalactic medium. In both cases, dynamos have been proposed to be the origin, and the dynamo theory has recently been invoked as the possible origin of strong magnetic fields in cooling white dwarfs (WDs) undergoing crystallization (e.g.,, Isern et al., 2017; Schreiber et al., 2021a; Ginzburg et al., 2022).

It has been observed that over a third of accreting WDs host a magnetic WD (Pala et al., 2020b; Rodriguez et al., 2024). Such systems, known as magnetic cataclysmic variables (CVs), consist of a magnetic WD accreting from a Roche-lobe filling donor star, in the form of intermediate polars (IPs; $B \approx 1 - 10$ MG) or, more commonly, polars ($B \approx 10 - 240$ MG). Both polars and IPs channel accreted material through the WD magnetic poles onto the surface since, in both cases, the magnetospheric radius extends well past the surface of the WD. In polars, the WD spin is typically locked with the orbital period[1], but in IPs, the WD spins $\sim 10 - 100$ times faster than the orbital period.

Despite the abundance of magnetic CVs, however, only $\sim 2\%$ of their younger progenitors, detached post-common-envelope binaries (PCEBs), host a magnetic WD (e.g.,, Rebassa-Mansergas et al., 2012; Parsons et al., 2021). Because CVs are further evolved and host cooler WDs, this has led to the idea that magnetism arises *as a result* of a crystallization-driven dynamo as the WD cools (e.g.,, Schreiber et al., 2021a). Other channels for WD magnetism, such as 1) the “fossil field" scenario, where the progenitor was a magnetic Ap/Bp star (Braithwaite and Spruit, 2004), 2) a dynamo operating during the common envelope phase (CE) (Tout et al., 2008), and 3) a double WD merger (Garcia-Berro et al., 2012) are also possible, though the former two scenarios would predict a large number of detached PCEBs hosting a magnetic WD. In the dynamo scenario, a crystallizing WD accretes from a donor star, is spun up, and generates a $B \approx 1 - 250$ MG magnetic field (Schreiber et al., 2021a). The WD may then synchronize with the orbit, leading to the creation of a polar. Recent work has suggested that this idea may well lead to some, but not all of the polars hosting $\gtrsim 10$ MG magnetic fields (Ginzburg et al., 2022; Camisassa et al., 2024).

[1] Asynchronous polars are polar-like systems in which there is a $\lesssim 10\%$ difference between the WD spin and the orbital period (e.g.,, Littlefield et al., 2023), which in some systems has been explained by a nova outburst throwing the system out of synchronism (e.g.,, Schmidt and Stockman, 1991).

Furthermore, two WD "pulsars" have been discovered in the last decade: AR Sco (Marsh et al., 2016) and J191213.72–441045.1 (henceforth J1912; Pelisoli et al., 2023b), the first of which motivated a connection from the dynamo theory to reconcile the role of AR Sco in CV evolution (Schreiber et al., 2021a). Curiously, it appears that the WD temperature of J1912 is too high for crystallization to have taken place, potentially calling into question the dynamo origin of magnetic fields or simply showing that this channel may not lead to all magnetic CVs (Pelisoli et al., 2024). Nevertheless, the evolutionary picture of Schreiber et al. (2021a) may still explain the origin of its magnetic field, as the recent work of Camisassa et al. (2024) suggested that dynamo-generated magnetic fields can break out at higher temperatures for more massive WDs.

Regardless of the origin of magnetism in WD pulsars, these systems are close ($P_{\rm orb} \approx 3.5 - 4$ h), *detached, non-accreting* binaries, where fast, pulsed emission ($P_{\rm spin} \approx 2 - 5$ min) out to radio frequencies has been detected. This emission has been attributed to the acceleration of particles in the interaction between the magnetic field ($B \approx 50 - 100$ MG) of the WD and that of the M dwarf companion, though whether the radio pulses are dominated by synchrotron or cyclotron emission is under debate (e.g.,, Marsh et al., 2016; Stanway et al., 2018). Crucially, both AR Sco (Pelisoli et al., 2022b) and J1912 (Woudt, P. et al. in prep) have been observed to be rapidly spinning down, with AR Sco showing $P/\dot{P} = 5.6 \times 10^6$ yr. This suggests that these systems will eventually become polars—the donor star will fill its Roche lobe in a few Gyr due to gravitational wave radiation and magnetic braking , and the WD will spin down to synchronize with the orbital period.

Here, we report the characterization of Gaia22ayj as an accreting magnetic WD which will likely evolve into a polar. Kato (2022) first reported the discovery of Gaia22ayj after it underwent an optical outburst in March 2022, found a 9.36-min period in data from the Zwicky Transient Facility (ZTF) and proposed it to be a WD binary based on the claim that this was the orbital period. We present multiwavelength data to show that the 9.36-min period in Gaia22ayj *is not* the orbital period of a binary system, rather it is likely the WD spin (or spin-orbit beat) period of an accreting magnetic WD. In this sense, Gaia22ayj is like an IP, but its large photometric amplitude and spectroscopic modulation are reminiscent of polars, therefore suggesting this is, at the very minimum, a new empirically-defined subclass of magnetic CVs. The extreme levels of optical linear polarization reaching 40%, as presented in this work, are seen only in AR Sco (Buckley et al.,

2017), further hinting at Gaia22ayj being a possible connection between WD pulsars and polars.

Recently, WD pulsars have gained traction as possible explanations for “long-period radio transients" (LPTs), which are radio sources pulsing on the timescales of minutes to hours (Hurley-Walker et al., 2023b). In two systems, M dwarfs have been seen in optical spectra, though at the time of writing, spectroscopic confirmation of WDs in these systems remains to be obtained (Hurley-Walker et al., 2024b; de Ruiter et al., 2024). The possible connection of Gaia22ayj to WD pulsars that we present here brings to light the likely diversity that exists in WD pulsars and related systems.

In Section 8.2, we present optical photometry and spectroscopy, including polarimetry, that show that Gaia22ayj is an accreting magnetic WD in a close binary. In Section 7.3, we present all multiwavelength data collected on Gaia22ayj in the radio, infrared, X-ray, and (false) γ-ray association. In Section 8.3, we show that the 9.36-min period likely represents the spin of the magnetic WD, and that it is rapidly slowing. In Section 8.4, we argue for a possible interpretation of Gaia22ayj as a link between WD pulsars and polars. We also present estimates of the population of such objects and projections for the discovery of Gaia22ayj-like systems in the upcoming Rubin Observatory Legacy Survey of Space and Time (LSST).

7.2 Optical Photometry and Spectroscopy

A summary of all data is summarized in Table 7.1, with additional details surrounding the optical and multiwavelength data presented in Sections 8.2 and 7.3, respectively.

Telescope	Wavelength	Data	Dates
P48/ZTF	Optical g, r	Long term (~2 day cadence) photometry	2018–2024
Gaia	Optical G	Long term (~60 day cadence) photometry	2014–2024
ATLAS	Optical c, o	Long term (~2 day cadence) photometry	2018–2024 (mostly Mar 2022)
P48/ZTF	Optical g, r	"Deep Drilling" (45s cadence) photometry	10 Jan 2019
NTT/ULTRACAM	Optical u+g+i	High-cadence (10s) photometry	25 Apr 2022
SAAO/SHOC	Optical clear band	High-cadence (30s) photometry	18 May 2023
P200/CHIMERA	Optical g+r, g+i	High-cadence (10s) photometry	13 Nov 2023, 6 Jan 2024
GTC/HiPERCAM	Optical u+g+r+i+z	High-cadence (4s) photometry	6 Mar 2024, 16 Apr 2024
Keck I/LRIS	Optical 3500 – 9000 Å	Single 900s ID spectrum	3 Apr 2022
Magellan Clay/MagE	Optical 4000 – 8000 Å	High-cadence (90s) spectroscopy	10 Apr 2022
Keck I/LRIS	Optical 3500 – 9000 Å	High-cadence (60s) spectroscopy	8,19 Nov 2023
NOT/ALFOSC	Linear optical polarimetry	High-cadence (50s) photometry	1,2 May 2022, 13 Apr 2024
SALT/RSS	Circular spectropolarimetry	2x600s spectra	28 Apr 2022
P200/WIRC	Near-infrared J, H, Ks	High-speed (45s, 9s, 3s) photometry	7 Nov 2023
Swift/XRT	X-ray 0.3–8 keV	Spectral and Timing Data Acquisition	Various in Jun–Dec 2005
VLA	Radio X-band (8–12 GHz)	Continuum Measurement (2x3 h observations)	13, 15 Jan 2024

Table 7.1: Summary of long-term photometry, high cadence photometry, spectroscopy, optical polarimetry, and multiwavelength data acquired for Gaia22ayj, from top to bottom. Further details are presented throughout Sections 8.2 and 7.3.

Archival Photometry

Gaia22ayj was first discovered by Kato (2022) using the *Gaia* alerts stream. In Data Release 3 (DR3), Gaia22ayj has ID 5697000580270393088 and an associated distance of $2.5^{+1.5}_{-1.0}$ kpc as estimated by Bailer-Jones et al. (2021b) from its parallax of $\omega = 0.34 \pm 0.22$ mas. Upon querying the Zwicky Transient Facility (ZTF) photometric database, Gaia22ayj was shown to be periodic, at 9.36 min (Kato, 2022). ZTF is a photometric survey which uses a 47 deg^2 field-of-view camera mounted on the Samuel Oschin 48-inch telescope at Palomar Observatory (Bellm et al., 2019b; Graham et al., 2019; Dekany et al., 2020; Masci et al., 2019). It uses custom g, r, and i filters, taking most of its data in the r filter at 30-s exposure times. Crucial to our characterization of Gaia22ayj was the following: in its first year of operations, ZTF carried out a nightly public Galactic Plane Survey in g and r-band (Bellm et al., 2019a) as well as a partnership survey which obtained continuous (30 sec + 10 sec of read-out time) photometry of a Galactic Plane field for 1.5 hours, though some fields have up to 6 hours of continuous coverage (Kupfer et al., 2021). Since entering Phase II, the public Northern Sky Survey is at a 2-day cadence. The pixel size of the ZTF camera is 1 and the median delivered image quality is 2.0 at FWHM.

We use ZTF forced photometry extracted at the position reported by *Gaia* Data Release 3 (DR3, and corrected to J2000; Gaia Collaboration et al., 2023a) of Gaia22ayj, including proprietary data to be made publicly available in upcoming data releases, taken through 01 Nov, 2024, processed by IPAC at Caltech[2]. This allows one to obtain flux estimates below the detection threshold as well as more realistic error bars on the data.

We also query the forced photometry database of the Asteroid Terrestrial-impact Last Alert System (ATLAS; Tonry et al., 2018a) at the *Gaia* position of Gaia22ayj in both ATLAS c (cyan) and o (orange) bands. Stringent quality cuts were applied to the data, ensuring 5σ flux measurements, a maximum sky brightness of 20.5 mag arcsec^{-2}, and a well-sampled PSF (3.5 pixels in each spatial direction).

We performed a Lomb-Scargle period analysis (Lomb, 1976; Scargle, 1982) of ZTF data using `gatspy` (VanderPlas, 2016b). The strongest peak is at 4.68 minutes, which we confirm as half of the period; folding the light curve on twice that period (9.36 min) reveals two different minima. We show the ZTF light curve of Gaia22ayj (excluding outbursting epochs) in Figure 7.1, and compare the ZTF r light curve

[2]`https://irsa.ipac.caltech.edu/data/ZTF/docs/ztf_forced_photometry.pdf`

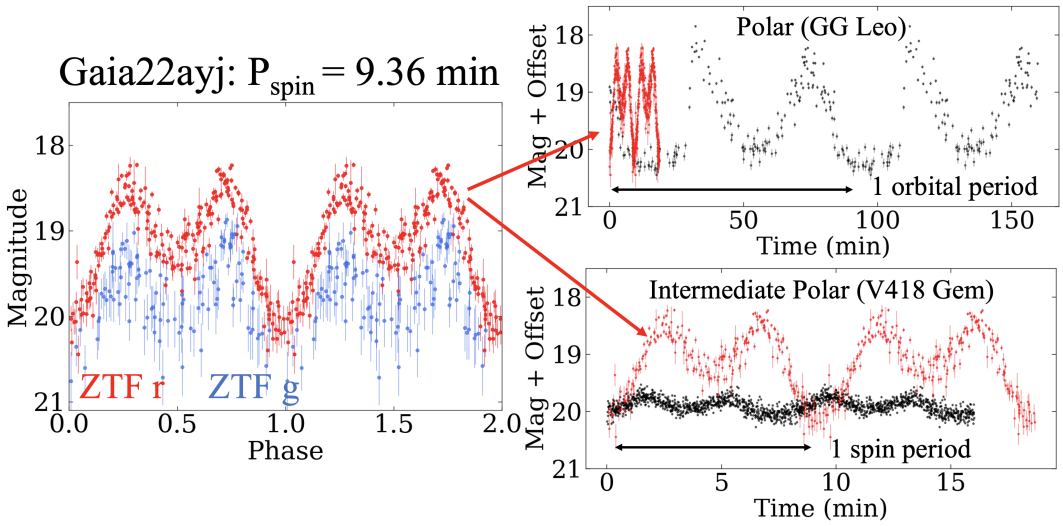

Figure 7.1: *Left:* ZTF light curve of Gaia22ayj in r and g bands folded on the 9.36-min period. *Right:* Comparison of the Gaia22ayj ZTF r band light curve (red) to that of an archetypal polar, GG Leo (top; black points; $P_{\rm spin} = P_{\rm orb} = 1.3$ h) and an archetypal IP, V418 Gem (bottom; black points; $P_{\rm spin} = 8.0$ min). The light curves of GG Leo and V418 are offset to match with the minimum of Gaia22ayj. Gaia22ayj pulsates at the short period of an IP, but at the high amplitude of a polar.

to that of an archetypal polar, GG Leo, as well as to that of an archetypal IP, V418 Gem[3]. Both GG Leo and V418 Gem show double-peaked light curves like Gaia22ayj over a single WD spin period, as do many pre-polars (van Roestel et al., 2024). In brief, Gaia22ayj has the amplitude of a polar, but the rapid spin period of an IP.

Long Term Photometry

In Figure 7.2, we show the long term behavior of Gaia22ayj in both *Gaia*, ZTF photometry, and ATLAS photometry which spans ten years from 2014 to 2024. The ZTF photometric coverage is sparser than average (excluding deep drilling, $\sim$ 50 r-band epochs, whereas the ZTF average across the sky is $\sim$ 850 r-band points) due to the source's low declination. ATLAS photometry firmly establishes that the outburst lasted $\approx$2 days. In Figure 7.2, *Gaia* coverage shows that Gaia22ayj takes $\sim$ 0.75 day to rise to a peak brightness of $\sim$ 16 mag (starting from $\sim$ 19 mag), at which point the light curve is roughly constant for $\sim$ 1 day. ATLAS c and o band photometry shows a rapid decline back to $\sim$ 19 mag two days after outburst.

[3]V418 Gem is one of the IPs with the highest amplitude optical light curve, with some IPs showing little to no detectable variation in the optical on their spin periods (though in some cases they must be seen in the X-ray to confirm their IP nature).

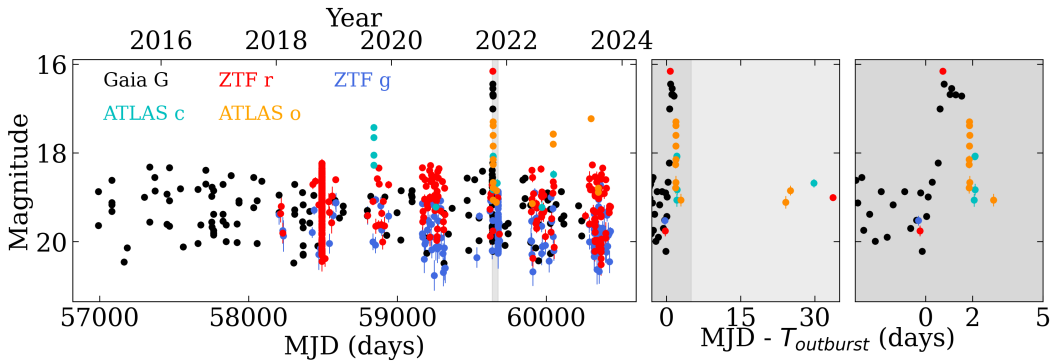

Figure 7.2: *Gaia* coverage from 2014–2024 shows consistent high amplitude modulation, while both ZTF (2018–onwards) and *Gaia* show a ∼ 3-mag outburst beginning on 3 April 2022. ATLAS coverage demonstrates that the outburst lasts two days, during which the high amplitude modulation seen in quiescence disappears. The low amplitude and short duration of the outburst more closely resembles those seen in IPs than those in non-magnetic dwarf novae. In either case, this outburst suggests ongoing accretion in Gaia22ayj.

Approximately 30 days after the outburst, the ZTF and ATLAS data show Gaia22ayj still in quiescence. These outbursts are on the lower amplitude end of dwarf nova outbursts, which typically range between 2–4 mag (though low-accretion rate WZ Sge-like systems can reach 8 mag outbursts; e.g.,, Warner, 1995b).

Instead of typical dwarf nova outbursts, the 2022 outburst of Gaia22ayj more closely resembles very short outbursts seen in IPs, notably in the famous systems V1223 Sgr (Hameury and Lasota, 2017a; Hameury et al., 2022) and TV Col (Hellier and Buckley, 1993). However, those outbursts last less than a day and do not show rapid fading like that of Gaia22ayj. Scaringi et al. (2022) recently suggested that such bursts, increases in brightness by a factor of three over a few hours, are “micronovae" which are localized thermonuclear events associated with magnetic WDs. It is unclear if the 2022 outburst of Gaia22ayj is related to such phenomena. During outburst, Gaia22ayj does not show the characteristic high amplitude modulation it does in quiescence, or the modulation seen in other IPs during outburst, though the *Gaia* temporal cadence may not be high enough to reveal fast variability. There is some evidence of additional outburst-like behavior from the ATLAS light curve in 2019 and 2022, but aside from the outburst of 3 March 2022, no other such events were covered by multiple photometric surveys.

Finally, in Figure 7.3, we show the Lomb-Scargle periodogram constructed from the ZTF r and g light curves, showing clear peaks at 9.36 min (true period) and

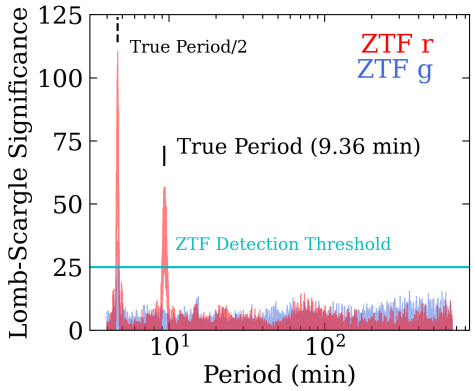

Figure 7.3: A Lomb-Scargle periodogram constructed from ZTF r and g photometry only reveals peaks at 9.36 min (true period) and 4.68 min (half of that). No other peaks, including one corresponding to a possible orbital period, pass the typical ZTF detection threshold of 25 in these units (see text for details).

4.68 min (half of that). In Figure 7.3, we calculate a Lomb-Scargle periodogram using `gatspy` (VanderPlas, 2016b), evenly sampling fifty thousand trial periods in frequency space between four minutes and eleven hours (in order to avoid strong harmonics of the sidereal day around twelve hours). We define the significance as the number of median absolute deviations above the median power. In samples of ≈10,000 ZTF light curves, we have found that a value of 25 in these units corresponds to approximately the 95$^{\text{th}}$ quantile. This means only five percent of ZTF light curves have a significance this high, which typically contain a true periodic signal. There are no significant peaks aside from the 4.68 and 9.36 min ones that pass this threshold, suggesting that long term photometry alone is unsuitable for detecting an orbital period.

High Speed Photometry

We obtained high speed photometry of Gaia22ayj on seven separate occasions: 25 April 2022 with ULTRACAM (Dhillon et al., 2007b) on the 3.58-m New Technology Telescope at La Silla (u, g, i filters simultaneously at 10-s cadence), 18 May 2023 with the Sutherland High Speed Optical Cameras (SHOC) on the 1m SAAO telescope (clear filter), 13 November 2023 and 6 January 2024 with the Caltech HIgh-speed Multi-color camERA (CHIMERA; Harding et al., 2016) on the 5-m Hale Telescope at Palomar Observatory (g, r and g, i filters simultaneously at 10-s cadence), 6 March 2024 and 16 April 2024 with HiPERCAM (Dhillon et al., 2021) on the 10.4-m Gran Telescopio Canarias at the Observatorio del Roque de los

Muchachos on La Palma (u, g, r, i, z filters simultaneously at 3.77-s cadence). All data were acquired along with GPS timestamps to ensure sub-millisecond timing precision, and corrected to a barycentric Julian date in barycentric dynamical time (BJD_{TDB}). All data were extracted using aperture photometry pipelines[4] which computed the flux relative to the same star, Gaia DR3 5697012365660670720.

In Figure 7.4, we show the 5-band simultaneous light curve acquired by HiPERCAM on 16 April 2024. Two maxima per spin period are clearly seen, as in the ZTF light curve, but the multi-band coverage shows that one peak is higher than the other at bluer bands. We show that the amplitude of the higher peak is variable in the full optical high speed light curves taken with P200/CHIMERA and NTT/ULTRACAM in Appendix 7.8.

Optical Polarimetry

Linear optical polarimetry was taken with the Alhambra Faint Object Spectrograph and Camera (ALFOSC) on the 2.56-m Nordic Optical Telescope (NOT), La Palma, on three occasions: 1 May 2022, 2 May 2022, and 13 April 2024. ALFOSC was equipped with WeDoWO, a four-beam polarimetric unit, capable of obtaining a full linear polarimetric observation from a single exposure using a wedged double Wollaston prism. A red pass (OG570) filter was used to select the red part of the spectrum, where the photometric modulation is strongest. This setup produced a bandpass ranging from 5500Å to ~10000Å, where the CCD response effectively tapers off. On all occasions, a comparison star was simultaneously monitored which showed no $> 1\sigma$ changes in linear polarization percentage ($< 1\%$) or angle. In Figure 7.4, we show the linear polarization (percentage and angle) of Gaia22ayj folded on the spin period. Data are taken from the third observing run, which lasted one hour and took place in excellent conditions. The entire dataset is folded on the 9.36-minute period (light blue) and averaged over twenty phase bins (dark blue). Two distinct peaks are seen, with one reaching $\sim$ 20 % polarization and the other $\sim$ 40 % polarization, each coincident with the two minima in total flux. The same behavior is seen two years apart, in the 2022 as well as the 2024 observations of Gaia22ayj. The full light polarimetric light curve is shown in the Appendix Figure 7.20.

[4] `https://github.com/HiPERCAM/hipercam`

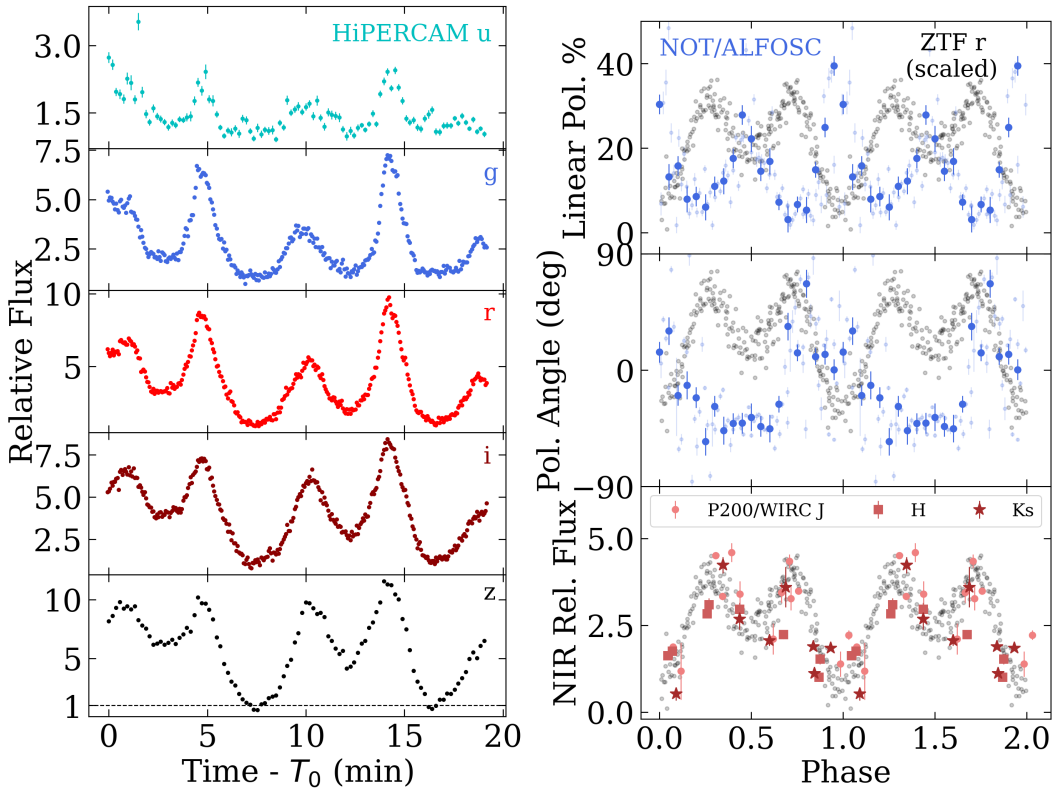

Figure 7.4: All optical and NIR photometry of Gaia22ayj. *Left:* Quintuple-band simultaneous high speed (3.77 s) photometry of Gaia22ayj acquired over 20 min with HiPERCAM on the GTC shows that Gaia22ayj can increase in brightness by a factor of ~ 10 in 2.5 minutes, and that the variability amplitude varies significantly with wavelength, being lowest in the u band. Gaia22ayj also shows high levels of linear polarization (*upper right*), with two peaks (~ 20 % and ~ 40 %) anticorrelated with the peaks of the ZTF light curve (black, arbitrarily scaled). Such high levels of linear polarization are only rivaled by AR Sco. The double-peaked nature of the linear polarization curve, along with the polarization angle swing (*middle right*), may suggest two-pole accretion. Triple-band near-infrared photometry (*lower right*) reveals similar extreme behavior as in the optical (black; arbitrarily scaled).

Spectroscopy

We obtained optical spectroscopy of Gaia22ayj on various occasions. The first spectrum was taken with the Low Resolution Imaging Spectrometer (LRIS; Oke et al., 1995b) on the Keck I telescope on 3 April 2022 through some cloud coverage, but showed emission lines, ruling out a detached WD binary nature. The next set of spectra, acquired on 10 April 2022 with the Magellan Echellete Spectrograph (MagE; Marshall et al., 2008) on the Magellan Clay Telescope in April 2022 confirmed that emission lines were present in Gaia22ayj and showed that an overall modulation across the entire optical band was responsible for the high amplitude photometric modulation.

Most notably, we acquired low-resolution ($\Delta\lambda \approx 0.8$ Å) spectra with Keck I/LRIS on 8 November 2023 (for a total time of 1.6 h) and on 19 November 2023 (for a total time of 1.96 h) at high speed 60-s exposures on the blue channel, 90 s on the red with 2x2 and 2x1 binning (spatial vs spectral), respectively to sample the 9.36-min spin period. The first run had strong winds and some light clouds with 0.9" seeing, while the second run had more favorable conditions with 0.8" seeing that led to higher signal-to-noise ratio. All LRIS data were wavelength calibrated with internal lamps, flat fielded, and cleaned for cosmic rays using `lpipe`, a pipeline for LRIS optimized for long slit spectroscopy (Perley, 2019).

In Figure 7.5, we show phase-resolved and averaged spectra from the second run, which confirm the initial MagE findings, though with higher temporal and spectral resolution. The slightly double-peaked nature of the Balmer, He I, and He ii emission lines suggests either the presence of a disk or face-on viewing of two accretion poles. Metal lines in emission (Mg I and Ca II) are seen only in the phase-averaged spectrum, though even then with just a marginal detection. If indeed present, these lines likely trace the irradiated face of the donor star (e.g.,, Rodriguez et al., 2023d). The Na I doublet at 8183 and 8195 Å in late-type stars is not seen.

In Figure 7.6, we show the trailed Keck I/LRIS spectra of the second run, acquired over 1.96 h. No radial velocity (RV) shifts of the Balmer, He I, or He ii emission lines or suspected donor lines (Mg I and Ca II) are seen. We experimented by binning a different number of individual spectra and using different smoothing levels to probe RV shifts, but none are seen down to the limiting resolution of our LRIS setup ($0.8 = 30$ km s^{-1}).

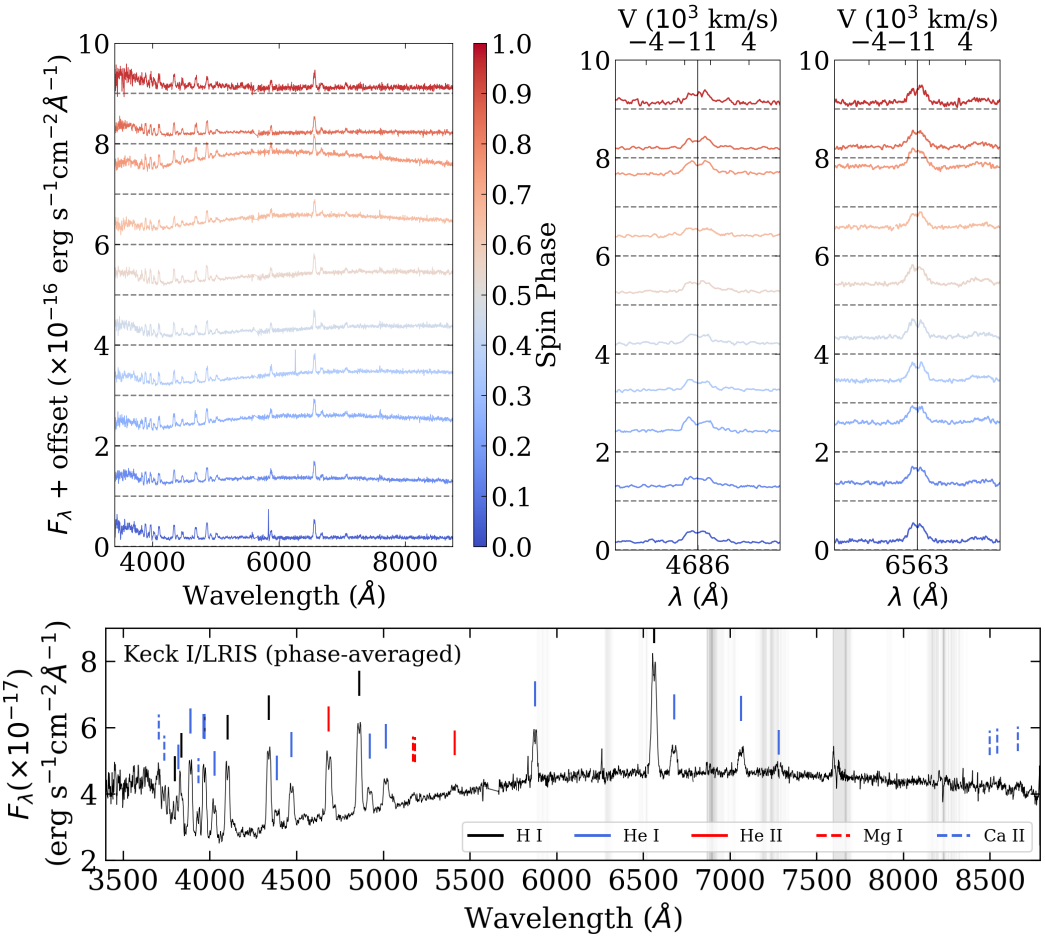

Figure 7.5: Phase-resolved spectroscopy of Gaia22ayj shows that overall modulation between 4000–8000Å leads to the observed high-amplitude photometric variability. Gray shaded areas are telluric features. *Upper left*: Two hours of Keck I/LRIS spectra, stacked into ten bins folded on the 9.36-min period show two distinct maxima that resemble "cyclotron humps", peaking at phases 0.25 and 0.75 (third and eighth sub-panels from the bottom, respectively). *Upper right*: The He ii 4686 and Hα emission lines remain flat or double-peaked (broadened with $v \approx 1200$ km s^{-1}) and show no amplitude or RV modulation on the spin phase. *Bottom*: The phase-averaged, stacked spectrum of Gaia22ayj reveals prominent H and He (slightly double-peaked) emission lines and a Balmer jump in emission, commonly seen in CVs. The high concentration of hydrogen rules out an ultracompact nature. Strong He ii 4686 (He II/H$\beta \approx 1$) is suggestive of a magnetic WD. Ca II and Mg I emission lines are marginally detected, which could trace the irradiated face of the donor star.

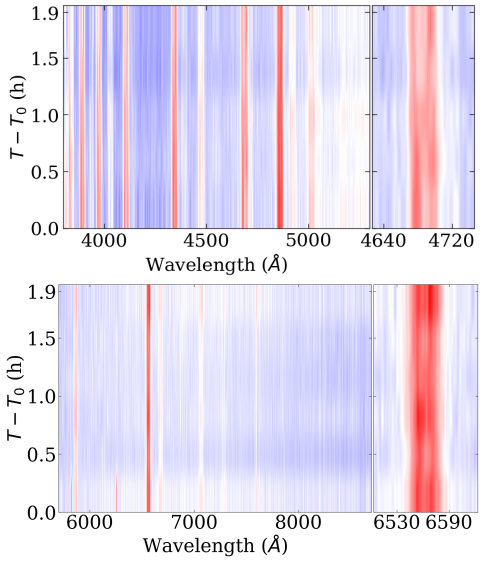

Figure 7.6: Trailed Keck I/LRIS continuum-normalized spectra acquired over ≈ 2 h do not reveal any RV shifts in emission lines down to the limiting resolution of ≈ 30 km s^{-1}.

Spectropolarimetry

We obtained spectropolarimetry of Gaia22ayj on 28 April 2022 using the Robert Stobie Spectrograph (RSS; Burgh et al., 2003; Kobulnicky et al., 2003) in circular spectropolarimetry mode (Brink et al., 2010) on the 10-m Southern African Large Telescope (SALT; Buckley et al., 2006). The observations consisted of two exposures of 600 sec for each of two positions of a 1/4 waveplate retarder, which was repeated once. In Figure 7.7, we show the resulting data: total flux (black) and circularly polarized spectrum (original in light red; smoothed in red). We detect circularly polarized flux, reaching up to ∼5% level at ∼6800Å, with a $> 1\sigma$ significance. A nearby comparison star on the slit showed polarisation consistent with zero percent. Due to the long exposure times, these observations are unable to resolve the 9.3 min spin period. Further data are needed to confirm this detection and search for variability on longer time scales.

7.3 Multiwavelength Observations

Near-Infrared Photometry

We observed Gaia22ayj on 7 November 2023 in J, H, and K_s bands with the Wide field InfraRed Camera (WIRC) on the 200-inch Hale Telescope at Palomar Observatory. A 9-dither observing pattern, tiling the field by shifting 10 in a 3x3 square, was used. We acquired single 45-s J-band exposures, co-added six 9-s

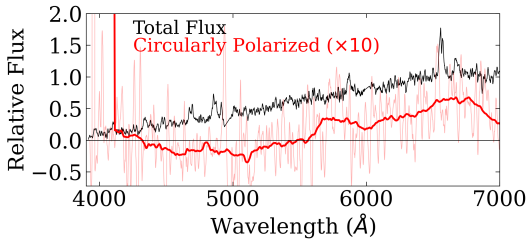

Figure 7.7: Low-resolution spectropolarimetry acquired with SALT reveals a possible ($> 1\sigma$) detection of a circularly polarized continuum, peaking around 6800 Å. The height of the feature corresponds to a five percent level of circular polarization, consistent with magnetic CVs.

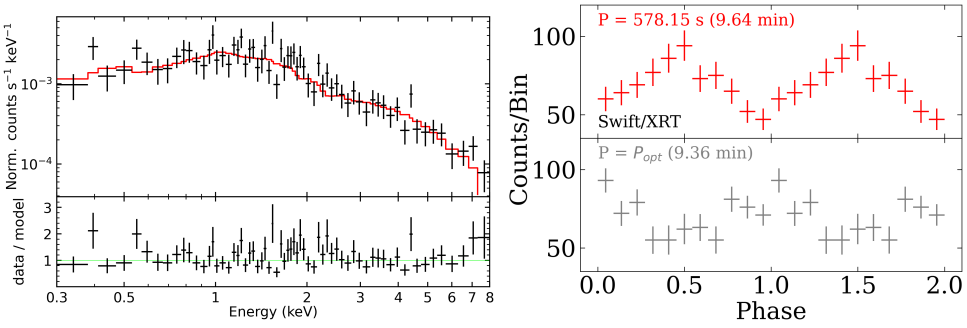

Figure 7.8: X-ray spectra and light curves of Gaia22ayj. *Left:* The combined X-ray spectrum of Gaia22ayj from all 11 Swift/XRT observations (from June 21, 2005 to December 6, 2005). The red line shows the best-fit $tbabs \times pcfabs \times mkcflow$ model. The bottom panel shows the ratio of the data divided by the model spectrum. *Right:* The X-ray light curve folded on the X-ray derived period (*top*) and on the optically derived period (*bottom*) is shown. Due to overlap with harmonics of the *Swift* good time interval (GTI) of the observation, the X-ray period of 9.64 min is tentative and should be tested with further observations.

H-band exposures, and co-added ten 3-s K_s-band exposures, with exposures taken in each filter for a total of forty minutes. Data were dark-subtracted and flat fielded using standard techniques implemented in a custom `wirc_pipe` pipeline (De, K. and Karambelkar, V. in prep.).

In Figure 7.4, we show the WIRC light curves folded on the 9.36-min optical period. Because we had to bin multiple exposures, we could not independently solve for a period using the near infrared data alone. All light curves appear to have a similar behavior as in the optical, peaking twice per spin period.

Table 7.2: The best-fit spectral parameters and their errors for the different models applied to analyze the combined Swift/XRT X-ray spectrum of Gaia22ayj.

Model: $tbabs \times powerlaw$	
Parameters:	
N_H ($\times 10^{22}$ cm^{-2})	0.09
Γ	$1.27^{+0.15}_{-0.14}$
χ^2_{red} (dof)	0.99(62)
Model: $tbabs \times mekal$	
Parameters:	
N_H ($\times 10^{22}$ cm^{-2})	$0.03^{+0.04}_{-0.03}$
kT (keV)	15
χ^2_{red} (dof)	0.98(62)
Model: $tbabs \times mkcflow$	
Parameters:	
N_H ($\times 10^{22}$ cm^{-2})	$0.07^{+0.05}_{-0.04}$
kT_{min} (keV)	0.1 ($fixed$)
kT_{max} (keV)	64
$\dot{M}$ ($\times 10^{-12}$ $M_\odot$ yr^{-1})	$28.2^{+5.1}_{-2.4}$
χ^2_{red} (dof)	1.12(62)
Model: $tbabs \times pcfabs \times mkcflow$	
N_H ($\times 10^{22}$ cm^{-2})	$0.02^{+0.05}_{-0.02}$
$N_{H,pc}$ ($\times 10^{22}$ cm^{-2})	$1.96^{+4.10}_{-1.36}$
pcf (per cent)	38^{+32}_{-20}
kT_{min} (keV)	0.1 ($fixed$)
kT_{max} (keV)	13
$\dot{M}$ ($\times 10^{-12}$ $M_\odot$ yr^{-1})	$38.1^{+130.2}_{-8.4}$
χ^2_{red} (dof)	1.01(60)
F_{obs} ($\times 10^{-13}$ $erg\ s^{-1} cm^{-2}$)	3.3 ± 0.3
F_{un} ($\times 10^{-13}$ $erg\ s^{-1} cm^{-2}$)	3.9 ± 0.9
F_{bol} ($\times 10^{-13}$ $erg\ s^{-1} cm^{-2}$)	5.3 ± 1.0
L_{un} ($\times 10^{32}$ $erg\ s^{-1}$)	$2.7^{+4.3}_{-1.8}$
L_{bol} ($\times 10^{32}$ $erg\ s^{-1}$)	$3.7^{+5.8}_{-2.4}$

Notes: Upper and lower limits are computed for a 90% confidence level. Observed (F_{obs}) and absorption-corrected (F_{un}) fluxes in the 0.3–8 keV energy band. Bolometric flux (F_{bol}) in the 0.001–100 keV energy band. F_{un} and F_{bol} are computed for the mkcflow component of the $tbabs \times pcfabs \times mkcflow$ model.

X-ray Detection

Gaia22ayj is listed in the Second Swift-XRT Point Source Catalog (2SXPS) as 2SXPS J082526.4–223212 (Evans et al., 2020a). The angular separation between the ZTF optical and Swift X-ray centroids is 1.2, and the Swift X-ray 90% error circle is 2.2, strongly suggesting this as the true X-ray counterpart. Swift/XRT serendipitously observed this source for a total of 86-ks exposure (at the location of the source on the detector), separated into 11 different observations. This was due to a bright and well-studied BL Lac, QSO B0823–223, 8.25 away, which was the target of the Swift/XRT observations.

X-ray Spectral Analysis

We used the online web tool[5] to build Swift-XRT products (Goad et al., 2007; Evans et al., 2009, 2020a) and extract a single combined spectrum from all 11 observations of Swift/XRT (PC mode). To analyze X-ray spectra, we used the XSPEC v12.13 spectral modeling package (Arnaud, 1996). We grouped spectral channels using the grppha tool from FTOOLS (Nasa High Energy Astrophysics Science Archive Research Center (Heasarc), 2014) to have a minimum of 10 counts per channel. We used the χ^2 test statistic and performed spectral analysis in the 0.3–8 keV energy band. To compute 90% confidence intervals for the best-fit parameters, we used the error tool in XSPEC. We used the Tuebingen-Boulder ISM absorption model (tbabs in XSPEC, the solar elemental abundances from Wilms et al. 2000) to account for interstellar absorption. The unabsorbed fluxes were computed by using the cflux convolution model in XSPEC.

We initially approximated the X-ray spectrum with power-law (powerlaw) and optically thin thermal emission models (mekal with fixed metal abundance at solar value). Both power-law ($\Gamma = 1.27$) and mekal ($kT \gtrsim 15$ keV) models give an acceptable fit to our spectrum, resulting in reduced chi-square (χ^2_{red}) values of 0.99 and 0.98, respectively (see Table 7.2). We used an isobaric cooling flow model (mkcflow; Mushotzky and Szymkowiak 1988) to fit the X-ray spectrum of Gaia22ayj. The mkcflow[6] provides a good approximation of the X-ray spectrum of non-magnetic CVs (e.g.,,, Mukai, 2017). The single fit with the mkcflow results in an unacceptable fit ($\chi^2_{red} = 1.12$) and gives only the lower limit for the temperature (kT64 keV). Along with the resulting photon index of the power-law model ($\Gamma = 1.27$), this indicates that the X-ray spectrum of Gaia22ayj is hard. X-ray spectra of some magnetic CVs cannot be fitted well with the single mkcflow model, showing a steep photon index ($\Gamma \sim 1$) for a power-law model (e.g.,,, Mukai, 2017; Galiullin and Gilfanov, 2021). The X-ray spectrum of magnetic CVs might be affected by local absorbers, so we added the partial covering absorption component (pcfabs) to the mkcflow model (e.g.,, Mukai, 2017). The final model $tbabs \times pcfabs \times mkcflow$ approximates well the observed spectrum of Gaia22ayj and gives an acceptable fit ($\chi^2_{red} = 1.01$; see Figure 7.8).

The X-ray spectrum of some polars shows a soft component along with the thermal

[5] `https://www.swift.ac.uk/user\_objects/`

[6] To properly use the mkcflow model, the redshift parameter can not be set at zero value (see for more details Mukai 2017). We fixed the redshift parameter at 5.84×10^{-7} (equal to the 2,500 pc distance) using the cosmological Hubble constant of 70 $km\ s^{-1}\ Mpc^{-1}$.

plasma emission model (e.g.,, Mukai, 2017). We approximated the X-ray spectrum by including the black-body component (bbody) in the final model, having $tbabs * pcfabs * (mkcflow + bbody)$. However, the fit gives no meaningful result for the black-body temperature.

Table 7.2 shows the best-fit spectral parameters for different models. The hydrogen column density, $N_{\rm H}$, from our fit is consistent with the Galactic value for Gaia22ayj from the Bayestar dust map ($\sim 2 \times 10^{20}\ cm^{-2}$;E(g–r) = 0.03;Green et al. 2019b). To compute the bolometric flux in the 0.001–100 keV energy band, we used the cflux model for the mkcflow component. We converted the fluxes into luminosities by assuming the 2.5 kpc *Gaia*-estimated distance to the object. Gaia22ayj shows an observed X-ray luminosity of $\approx 2.5 \times 10^{32}$ erg s^{-1} and a bolometric X-ray luminosity of $\approx 4 \times 10^{32}$ erg s^{-1}. We extracted the X-ray spectrum for 11 Swift/XRT observations to find possible X-ray variability. The current analysis shows no change of spectral parameters between six months of the observation with Swift/XRT (from June 21, 2005 to December 6, 2005).

X-ray Timing Analysis

Finally, we performed a timing analysis on the combined Swift data. This required downloading the raw data and performing a barycentric correction, converting all photon arrival times to $\rm BJD_{TDB}$. We used the Gregory-Loredo algorithm (GL; Gregory and Loredo, 1992), which is a phase-folding Bayesian algorithm that performs well in the regime of low to moderate counts, which is common in X-ray data like that which we present here. For a full explanation of the implementation and application of this algorithm to other sources, we refer the reader to Bao et al. (2023, 2024). In Figure 7.8, we show the folded light curve at the best X-ray period obtained with the GL algorithm: 9.635(2) min. We also show the X-ray light curve folded on the optical period (9.36 min), which shows that modulation is still detected on that period, though not as clear and significant as on the 9.64-min period. However, we strongly emphasize that the period we obtain has significant overlap with harmonics of the "Good Time Interval" (GTI) of the *Swift* observation, meaning that this analysis is subject to scrutiny and further X-ray observations and timing analyses should be done to confirm this period.

Radio Observation

We observed Gaia22ayj with the Very Large Array (VLA) for 3 h on two separate occasions: 13 and 15 Jan, 2024 (UT), both in X-band (8–12 GHz) with the VLA in the "D" array configuration. Weather conditions were good (at most 20% cloud cover) on both occasions. We used the flux calibrator 3C138 and the gain calibrator J0826–2230. Data were calibrated using the Common Astronomy Software Applications software (CASA; McMullin et al., 2007) and deconvolved using the `clean` algorithm with the `tclean` command. We measured the flux density using the Cube Analysis and Rendering Tool for Astronomy (CARTA; Comrie et al., 2021) and found no detection in either the dirty or deconvolved image. To deconvolve the image, we used the `clean` algorithm (Clark, 1980) within CASA. The rms at the source position was 5.0 μJy, which corresponds to a 3σ upper limit of 15 μJy. We show the cleaned image in Figure 7.9, which shows no significant source in the vicinity of Gaia22ayj, but reveals an unassociated radio source (likely a radio galaxy) 1.45' to the south west and another 1.5' to the north. The apparent fringes in the radio image are due to the nearby (7.91') bright quasar, J0826–2230.

In Figure 7.9, we show that we expected Gaia22ayj to have a radio flux of $F_\nu = 30^{+50}_{-20}$ μJy. This was calculated based on a least-squares fit to the radio fluxes of AR Sco (Marsh et al., 2016) and J1912 (Pelisoli et al., 2023b), assuming that Gaia22ayj was powered by the same physical mechanism. The uncertainties on our estimates of the radio flux of Gaia22ayj are large due to the distance uncertainty from *Gaia*. Figure 7.9 shows that the radio non-detection of Gaia22ayj is inconsistent with it having a similar radio luminosity as the known WD pulsars at the 3σ (2σ) level, assuming a distance of 2.5 kpc (4 kpc).

Near-Infrared Spectroscopy

We observed Gaia22ayj on 30 April 2023 with the Near-Infrared Echellette Spectrometer (NIRES) on the Keck II telescope on Mauna Kea. We obtained an ABBA dither sequence of four 180-s exposures. Spectra were reduced using standard techniques with the NSX pipeline[7]. We find a significant detection of the He i emission line at 1.083 μm, but no other discernible lines above the sky background.

Gamma-Ray False Association

Gaia22ayj is located 7.91 away from the well-studied BL Lacertae source PKS 0823–223 (Allen et al., 1982), also known as 4FGL J0825.9–2230 in the *Fermi*

[7] `https://sites.astro.caltech.edu/~tb/nsx/`

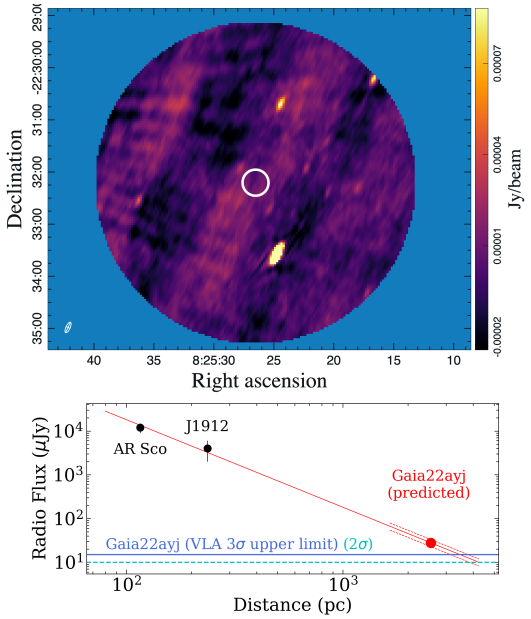

Figure 7.9: Radio data of Gaia22ayj. *Top:* VLA non-detection (3σ upper limit of 15 μJy) of Gaia22ayj (a 15 arcsec radius white circle is shown around the optical position). A bright, unassociated radio source is located approximately 1.45 arcmin to the south west of the field center, with the synthesized beam shown on the lower left. *Bottom:* If the same radio emission mechanism were present as in the known WD pulsars, AR Sco and J1912, we should have seen a radio flux of $F_\nu = 30^{+50}_{-20}$ μJy from Gaia22ayj. VLA observations rule this out.

4FGL catalog (Ballet et al., 2023). Gaia22ayj is within the 27.5×26.6 *Fermi* error ellipse (68% confidence intervals). However, Gaia22ayj can be confidently discarded as being associated with the gamma-ray source since the 4FGL catalog reports a >99.9% likelihood of PKS 0823–223 being associated with the gamma-ray source. A search for gamma-ray pulsations on the 9.36-min period could still be conducted, but is beyond the scope of this work.

7.4 Results and Interpretation

An Accreting Binary System

Kato (2022) first suggested Gaia22ayj to be an eclipsing double WD system, but the optical spectrum in Figure 7.5 shows clear emission lines. No absorption lines are seen anywhere in the spectrum at any orbital phase, which provides clear evidence against a *detached* double WD system. Furthermore, Figure 7.5 shows that the He ii 4686 and Hα lines are double-peaked, and have a characteristic broadening of $v \approx 1200$ km s^{-1}. This discards the possibility of a chromospheric origin of the emission lines (which would be broadened at the 10-20 km s^{-1} level), meaning that

accretion must be taking place in a semi-detached binary system (i.e., one star fills its Roche lobe).

The 9.36-min Period: Not an Ultracompact System

In the absence of additional information, the observed 9.36-min period could either be attributed to the binary orbit or to the spin of the accreting star. However, there is also the possibility that this is the beat period between the spin and the orbit (i.e., $1/P_{\rm beat} = 1/P_{\rm spin} \pm 1/P_{\rm orbit}$). The spectrum in Figure 7.5 shows that this cannot be an orbital period because the spectrum is dominated by hydrogen emission lines and a clear Balmer jump in emission (inverse Balmer jump) at 3645 Å.

CVs have an observed orbital period minimum of approximately 78–82 minutes (Gänsicke et al., 2009), which has been explained by calculating the minimum orbital period that a hydrogen-rich donor star can remain in thermal equilibrium and continue hydrogen burning while filling its Roche lobe (e.g.,, Paczyński and Sienkiewicz, 1983). However, this orbital period minimum can reach $\approx$ 51 minutes for the smallest, lowest metallicity stars (Stehle et al., 1997). Even more generally, a degenerate companion object (i.e., a gas giant planet or a brown dwarf) can reach orbital periods as low as 37 minutes (Rappaport et al., 2021).

Gaia22ayj, with a photometric period of 9.36 min, is well below this limit and shows no evidence of helium-rich accretion that would suggest a high-density donor[8], so the observed period *must* be related to the spin period of the WD. The overall modulation of the spectrum on this period and the lack of emission-line RV shifts (Figure 7.5) also support this claim.

Spectral Energy Distribution and Upper Limits on the Donor Star

In Figure 7.10, we show the interstellar extinction-corrected spectral energy distribution (SED) of Gaia22ayj. We use the $E(g-r)$ value of 0.03 from Green et al. (2019b), which, given the Galactic coordinates of Gaia22ayj (ℓ: 243.93762°, b : 8.80238°) where interstellar extinction is low, should be a reliable estimate. UV (GALEX GR6/7; upper limits), optical (PanSTARRS PS1), near-IR (VISTA), and mid-IR (WISE) points are shown, along with the phase-averaged Keck I/LRIS spectrum. ZTF photometry is plotted at the light curve maximum and minimum. The

[8]It is worth nothing that though hydrogen has been seen in ultraviolet spectra of ultracompact (AM CVn) WD binaries (such as the 5.4-min orbital period HM Cnc; Munday et al., 2023), the amount of hydrogen is estimated to be very low, meaning optical spectra are still dominated by helium lines.

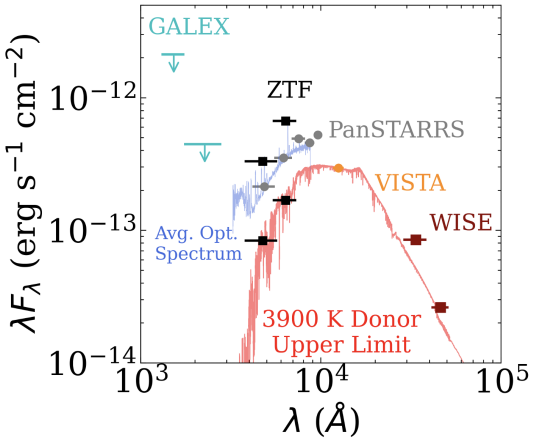

Figure 7.10: A 3900-K donor, with $R_{\rm donor} = 0.62\ R_\odot$ best fits the optical light curve minimum of Gaia22ayj. This is consistent with near-IR and mid-IR photometry from VISTA and WISE, respectively, and allows us to place upper limits on the orbital period of Gaia22ayj (Figure 8.8). The ZTF minima and maxima represent the limits of the variable light curve in quiescence (i.e., not the 2022 outburst), and the average optical spectrum is the Keck I/LRIS spectrum presented in Figure 7.5.

minimum of the ZTF photometry allows us to place an upper limit on the temperature of the donor star. We take a grid of stellar atmospheres at a given temperature (at solar metallicity) from the BT-Settl library (Allard et al., 2011c) and corresponding stellar radii from the models of Knigge et al. (2011), and compare to the ZTF g and r points at light curve minimum. Assuming a donor behaving according to the Knigge et al. (2011) tracks (i.e., not evolved), we find that a donor with $T_{\rm eff} = 3900$ K, $R_{\rm donor} = 0.62\ R_\odot$ best fits the observed limits, given the median *Gaia* distance of $d \approx 2500$ pc. In Section 7.5, we elaborate on how this finding could inform the potential orbital period of the system and its evolutionary stage.

Polarization Confirms a Magnetic White Dwarf

Linear polarization in Gaia22ayj confirms the magnetic nature of the object. Most interestingly, the only system to date that has shown such high levels (40%) of linear polarization is AR Sco, the prototypical WD pulsar, which also showed up to 40% linear polarization (Buckley et al., 2017). In AR Sco, the linear polarization is in phase with the total optical modulation, whereas in Gaia22ayj (Figure 7.4), the two are clearly in antiphase.

Polars are typically polarized to at most a few percent in linear polarization, and can only reach high levels of *circular* polarization (e.g.,, Schaich et al., 1992). *No* IP is known to exhibit linear polarization at the level observed in Gaia22ayj (e.g.,, Ferrario

et al., 2020), suggesting that this system has a high magnetic field and could have at most a small truncated disk. Two distinct peaks in linear polarization percentage and a swing in polarization angle across spin phase, however, may suggest the presence of two accretion poles, as famously seen in the prototypical polar CV, AM Her, though circular polarization will tell for certain (Wickramasinghe et al., 1991).

This may also be supported by the nearly double-peaked nature of the He ii 4686 and Hα emission lines, that remain constant throughout the spin phase (Figure 7.5) and even during $\approx$ 2-h long integrations (Figure 7.6). This suggests that either 1) a disk is present or 2) that we are always viewing down one accretion pole in a two-pole system, with the second pole behind the WD also contributing to the observed emission. The high velocity of each peak ($v \approx 1200$ km s^{-1} broadening) suggests that in the former scenario, those lines trace matter in a disk in Keplerian rotation at $r \approx 0.1\,R_\odot$ around a $0.8\,M_\odot$ WD, or in the latter scenario, material in free-fall down the accretion stream traveling at that speed. The absence of RV shifts in the emission lines slightly favors the two-pole scenario, as the disk around the WD in the first scenario would display some motion relative to the center of mass. In the two-pole accretion stream scenario, if a pole is viewed head-on, the emission region would exhibit minimal motion as the WD rotates.

Optical Spectroscopy Suggests a High Magnetic Field Strength

The high-amplitude optical modulation seen in the spectrum (see Figure 7.5, upper left panel) is reminiscent of cyclotron “humps" in polar CVs. Setting the magnetic force equal to the centripetal force leads to the derivation of cyclotron harmonics:

$$\lambda = \frac{10710\,\text{Å}}{n}\left(\frac{100\,\text{MG}}{B}\right)\sin\theta\,, \tag{7.1}$$

where n is the cyclotron harmonic number, B the WD magnetic field strength, and θ the angle of the magnetic pole with respect to our line of sight.

The following two observations are critical for determining the magnetic field strength of the WD: 1) individual cyclotron humps are not observed, and 2) there is high-amplitude optical modulation, with two distinct “humps" spanning nearly the entire optical spectrum peaking at spin phases 0.25 and 0.75 (Figure 7.5). The former provides a clue that the magnetic field should be weak enough such that only high harmonics should be present at optical wavelengths. Cyclotron modeling and observations reveal that $n \gtrsim 7$ harmonics are difficult to discern as single features (e.g.,, Campbell et al., 2008). The latter suggests that the viewing angle must be

high enough for high amplitude modulation to be seen (e.g.,, Campbell et al., 2008). Therefore, we set $\theta = 60^\circ$ in Equation 7.1 as a lower limit for the viewing angle. Because the $n = 7$ feature is not seen at $\lambda < 8800$, we infer an upper limit on the WD magnetic field strength of $B \lesssim 15$ MG (Equation 7.1).

In order to place a lower limit on B, we assume that $n > 20$ harmonics must be present at optical wavelengths, which implies $B \gtrsim 5$ MG. The lowest measured magnetic field of a polar CV showing Zeeman splitting has been 7 MG in V2301 Oph (Ferrario et al., 1995), though its optical variability (out of eclipse) does not exceed 0.5 mag in ZTF. This shows that our 5 MG lower limit is quite conservative, and that Gaia22ayj likely has a stronger magnetic field.

Is the Accretion Stable?

The magnetospheric radius is the point where the ram pressure of infalling material equals the magnetic pressure due to the WD. At this point, accreted matter is forced to follow the magnetic field lines of the WD, and is channeled onto its surface. The magnetospheric radius is:

$$r_A = \left(\frac{B^4 R^{12}}{2GM\dot{M}^2}\right)^{1/7} \tag{7.2}$$
$$= 0.62 R_\odot \left(\frac{B}{10\,\mathrm{MG}}\right)^{4/7} \left(\frac{R}{0.0105\,R_\odot}\right)^{12/7} \times$$
$$\left(\frac{M}{0.8\,M_\odot}\right)^{-1/7} \left(\frac{\dot{M}}{10^{-9}\,M_\odot\ \mathrm{yr}^{-1}}\right)^{-2/7},$$

where M is the WD mass, $\dot{M}$ is the accretion rate, B is the WD field strength, and R is the WD radius. As matter makes its way to the magnetospheric radius, two possible scenarios can occur. If the centrifugal force on a piece of matter exceeds the gravitational force from the WD, then it will be flung out, removing angular momentum from the system (i.e., a “propeller" phase). Otherwise, it will be accreted onto the WD, transferring angular momentum to the WD. This leads to a condition of “spin equilibrium" (e.g.,, Patterson, 1994), and involves finding the

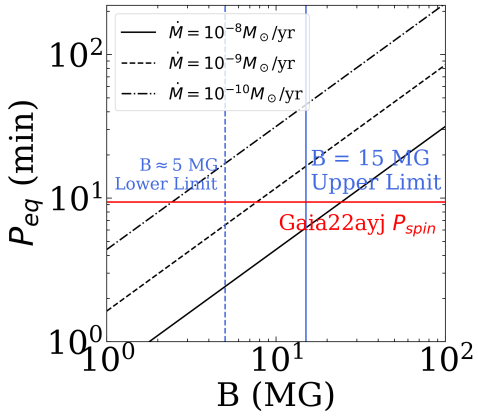

Figure 7.11: Equilibrium spin period as a function of magnetic field strength, for different accretion rates (Equation 7.3). Limits on magnetic field strength from Equation 7.1 are shown as vertical blue lines, and the 9.36-min spin period as a horizontal red line. Given the magnetic field constraints, $\dot{M} \gtrsim 5 \times 10^{-10}\, M_\odot\ \mathrm{yr}^{-1}$ is required for $P_{\mathrm{eq}} < P_{\mathrm{spin}}$, the condition required for stable accretion.

orbital period of material at the magnetospheric radius:

$$P_{\mathrm{eq}}^2 = \frac{4\pi^2 r_A^3}{GM} = \frac{4\pi^2}{GM}\left(\frac{B^4 R^{12}}{2GM\dot{M}^2}\right)^{3/7} \tag{7.3}$$

$$\implies P_{\mathrm{eq}} = 11.7\ \mathrm{min}\left(\frac{B}{10\ \mathrm{MG}}\right)^{6/7}\left(\frac{R}{0.0105\, R_\odot}\right)^{18/7} \times \left(\frac{M}{0.8\, M_\odot}\right)^{-17/14}\left(\frac{\dot{M}}{10^{-9}\, M_\odot\ \mathrm{yr}^{-1}}\right)^{-3/7}.$$

We plot the result of this analysis in Figure 7.11. In order to sustain accretion in such a fast-spinning WD, either the magnetic field must be weak or the accretion rate must be high. In IPs, the 1–10 MG magnetic field allows for stability across a wide range of accretion rates: low-luminosity IPs (LLIPs; Pretorius and Mukai, 2014) are below the CV orbital period gap, and are thought to have $\dot{M} \lesssim 10^{-10}\, M_\odot\ \mathrm{yr}^{-1}$, while typical IPs are above the gap and accrete at $\dot{M} \gtrsim 10^{-9}\, M_\odot\ \mathrm{yr}^{-1}$ (e.g.,, Suleimanov et al., 2019).

We proceed with the assumption that Gaia22ayj is indeed accreting (i.e., not in a propeller phase). This is justified by the following: 1) the X-ray luminosity exceeds that of AE Aqr, the prototypical propeller, by at least an order of magnitude (Patterson et al., 1980); 2) there is no clear optical flaring in the light curve, unlike AE Aqr and LAMOST J0240, the two known WD propellers (Thorstensen, 2020);

and 3) the spin period of Gaia22ayj is twenty times longer than that of the two known propellers (33 and 24 seconds; Patterson, 1979; Pelisoli et al., 2022a).

In the case of Gaia22ayj, we know that $B \gtrsim 5$ MG in order for such strong cyclotron emission and polarization to be observed. In order for stable mass transfer to be taking place, Figure 7.11 suggests that $\dot{M} \gtrsim 5 \times 10^{-10}\, M_\odot\ \mathrm{yr}^{-1}$. Since this is a conservative lower limit, it is likely that $\dot{M} \gtrsim 10^{-9}\, M_\odot\ \mathrm{yr}^{-1}$, placing Gaia22ayj above the CV orbital period gap, as explored further in Section 7.5.

A White Dwarf Rapidly Spinning Down

We folded the entire ZTF light curve of Gaia22ayj, with data between 2018 and 2024, and obtained the best period using a Lomb-Scargle analysis (Lomb, 1976; Scargle, 1982). Based on that, we then computed an "observed minus calculated" ($O-C$) value for each high-speed light curve obtained between 2018 and 2024. We fit a two-component sinusoid to the ZTF r-band light curve and fit the same model to all other high-speed light curves. We computed the deviation of the light curve minimum (phase 1.0 in Figure 7.1) from the original ZTF template, and created the $O-C$ diagram in Figure 7.12. We also show all high-speed light curves along with their best-fit two-component sinusoid, and show how one light curve minimum (phase 0.5) drifts from the original ZTF fixed phase in Figure 7.12.

We then measure $\dot{P}$ by obtaining the best-fit (least squares) quadratic function (red line) to the data in Figure 7.12. $\dot{f}$ is given (e.g.,,, Equation 1 in Burdge et al. 2019) by:

$$\Delta t_{\mathrm{O-C}} = \frac{1}{f_0}\left(\frac{1}{2}\dot{f}_0(t-t_0)^2 + \frac{1}{6}\ddot{f}_0(t-t_0)^3 + \cdots\right), \tag{7.4}$$

where t is an epoch of observation, t_0 the initial epoch, $\Delta t_{\mathrm{O-C}}$ the measured deviation in the light curve, f_0 is the frequency at t_0, $\dot{f}_0$ its first derivative, and $\ddot{f}_0$ its second derivative. Since $\ddot{f}$ is consistent with zero, we only fit a parabola to the observed data. We calculate $\dot{f}_0$ directly, assume that it remains constant throughout the entire span and estimate errors based on the covariance matrix of the best-fit parameters: $\dot{f} = (2.57 \pm 0.11) \times 10^{-15}\,\mathrm{Hz\ s}^{-1}$. Propagating errors to measure $\dot{P}$, we obtain $\dot{P} = (2.89 \pm 0.12) \times 10^{-12}\ \mathrm{s\ s}^{-1}$.

In Figure 7.13, we compare the measured characteristic spin-down timescale of Gaia22ayj ($P/\dot{P} \approx 6.1^{+0.3}_{-0.2} \times 10^6$ yr) to that of other IPs, the propeller system AE Aqr, and the WD pulsar AR Sco. The IPs used as reference are systems that have a consistent spin up/down as determined by Patterson et al. (2020): DQ Her, FO

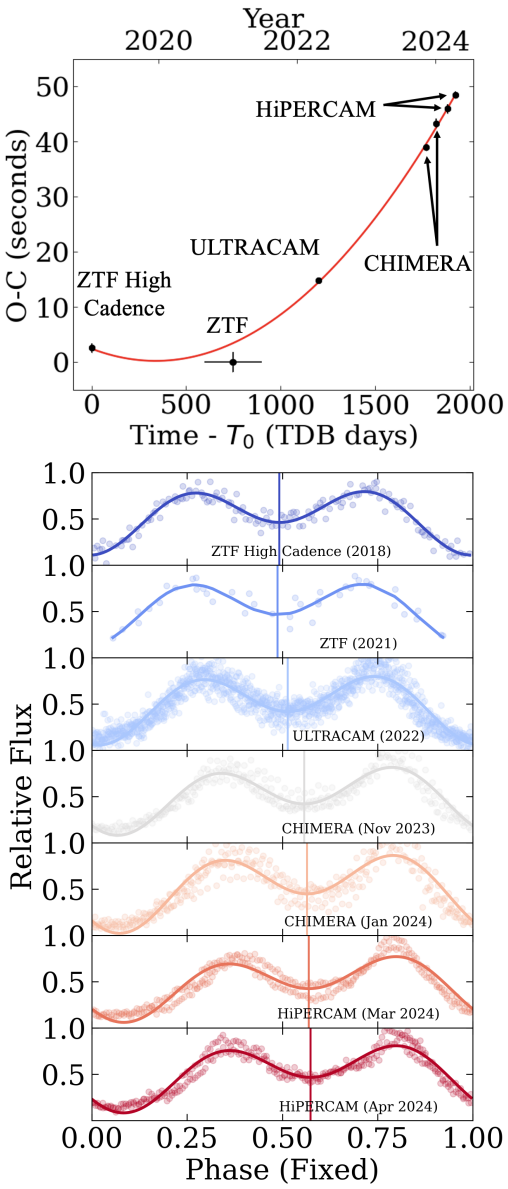

Figure 7.12: The “observed" minus “expected" (O–C) diagram of Gaia22ayj (top) shows that the expected time of the light curve minimum has drifted over six years. A multiyear, high-speed optical photometry campaign demonstrated that Gaia22ayj is spinning down at $\dot{P} = (2.89 \pm 0.12) \times 10^{-12}$ s s^{-1}, about four times higher than AR Sco, though with a similar characteristic timescale $P/\dot{P} \sim 5 \times 10^6$ yr.

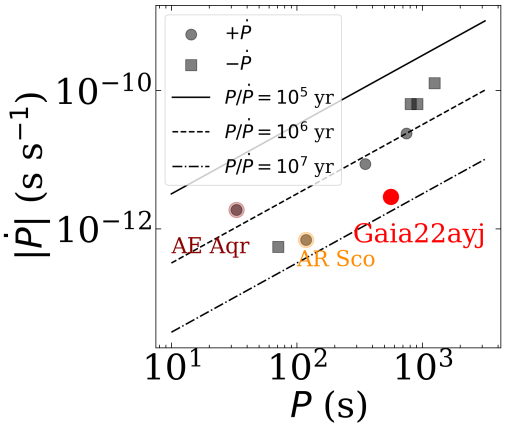

Figure 7.13: IPs that show consistent spin up (squares) or spin down (circles), including the propeller AE Aqr, are shown on the $P - \dot{P}$ diagram. AR Sco and Gaia22ayj are related in having the longest characteristic spin-down times of known systems.

Quantity	Value	Source
RA (hms)	08:25:26.52	*Gaia* DR3
DEC (dms)	-22:32:12.34	*Gaia* DR3
Distance (kpc)	$2.5^{+1.5}_{-1.0}$	*Gaia* DR3
G (mag)	19.2	*Gaia* DR3
$BP - RP$ (mag)	1.11	*Gaia* DR3
Gaia DR3 ID	5697000580270393088	*Gaia* DR3
F_X (erg s^{-1}cm^{-2})	$(3.9 \pm 0.9) \times 10^{-13}$	Swift/XRT[9]
F_r (μJy)	< 15.8 (3σ upper lim.)	VLA[10]
$P_{\rm opt}$ (min)	9.3587(1)	ZTF
$P_{\rm X\text{-}ray}$ (min)	9.635(2)	Swift/XRT[11]
$\dot{P}_{\rm opt}$(s s^{-1})	$(2.89 \pm 0.12) \times 10^{-12}$	ZTF
$P/\dot{P}$ (yr)	$6.1^{+0.3}_{-0.2} \times 10^6$	ZTF

Table 7.3: Summary of observed properties of Gaia22ayj.

Aqr, V1223 Sgr, BG CMi, and GK Per. AE Aqr and AR Sco have separately measured period derivatives, determined by de Jager et al. (1994) and Pelisoli et al. (2022b), respectively. Figure 7.13 shows that no IPs have as high a characteristic spin-down timescale ($\tau = P/\dot{P}$) as AR Sco (5.6×10^6 yr) and Gaia22ayj (6.1×10^6 yr). Curiously, the spin-down timescale of AE Aqr is comparable to that of other IPs.

Finally, in Table 7.3, we summarize all observed and inferred parameters of Gaia22ayj, the latter of which are obtained from arguments and analysis presented above.

7.5 Discussion

Gaia22ayj is observationally a new class of object. It occupies a new region in the phase space of photometric period (spin period) vs. optical amplitude. To empirically show that Gaia22ayj represents a new subclass of CVs, Figure 7.14 situates it in the phase space of WD spin period vs. peak-to-peak optical amplitude for various magnetic WD subtypes. The vertical axis shows the amplitude in ZTF *r* magnitudes for both known WD propellers, both known WD pulsars, a representative sample of IPs taken from the "ironclad list" compiled by Koji Mukai[12], and a representative sample of polar CVs from the Ritter and Kolb catalog (Ritter and Kolb, 2003b). Finally, we show Gaia22ayj on a *Gaia* HR diagram (100-pc sample) compared to polars and IPs from the catalog of Abril et al. (2020), with only systems that have a three σ measurement of parallax shown. Gaia22ayj appears to fit right between IPs and polars, owing to its likely long (but still unknown) orbital period and high accretion luminosity.

Gaia22ayj: A Link Between White Dwarf Pulsars and Polars

The evidence presented thus far suggests that Gaia22ayj is an accreting analog of WD pulsars, since 1) Gaia22ayj is rapidly spinning down, being the only system with a $P/\dot{P}$ comparable to that of AR Sco, 2) has high levels of linear polarization matched only by AR Sco, and 3) is accreting, with a WD spin period slightly longer than that of the known WD pulsars, but not yet synchronized with the orbital period as would be the case in polar CVs.

In considering the radiation mechanisms driving the optical modulations, it is notable that in AR Sco–type systems, the optical and polarimetric signals are largely powered by synchrotron processes (Buckley et al., 2017), whereas in polars and intermediate polars (IPs), cyclotron emission from the white dwarf's accretion shock is dominant (e.g.,, Mukai, 2017). The high levels of linear polarization in Gaia22ayj appear more consistent with AR Sco–type behavior; however, one important caveat is the observed anti-correlation between the linearly polarized pulse and the photometric pulse, which contrasts with the behavior typically seen in AR Sco–type systems (Buckley et al., 2017). Circular polarization and further examination of the polarized flux in Gaia22ayj would help clarify how much of its polarized variability might be driven by unpolarized variability.

Based on our measured value of $\dot{P}$, the WD in Gaia22ayj will slow down to match

[12] `https://asd.gsfc.nasa.gov/Koji.Mukai/iphome/catalog/alpha.html`

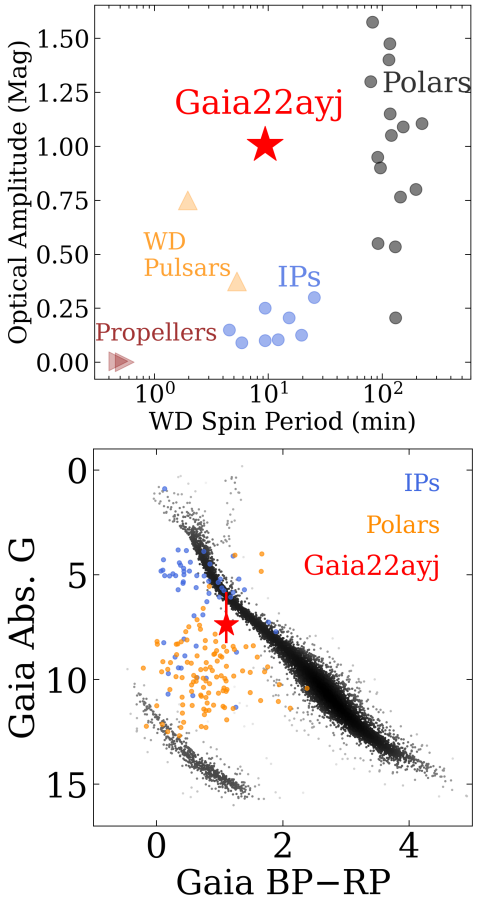

Figure 7.14: Broader context of Gaia22ayj. *Top:* Gaia22ayj occupies a new region in the phase space of WD spin period vs. optical amplitude, suggesting that, at least empirically, it represents a new class of magnetic CVs. *Bottom:* Gaia22ayj is roughly located between IPs and polar CVs in the *Gaia* HR diagram.

the 1.3–4 h orbital periods of polars in ≈ 40 Myr, assuming a constant $\dot{P}$, though it may do so more rapidly if higher order derivatives of the spin period are measured. Curiously, this timescale appears to agree with predictions made by Schreiber et al. (2021a), as seen in Supplementary Material Figure 2, where accretion commences as the WD spins down.

In a similar style to the evolutionary model put forth by Schreiber et al. (2021a), in Figure 8.8, we present a cartoon of the evolution of Gaia22ayj. First, a WD + M dwarf system emerges out of a common envelope phase with an unknown orbital period, presumably longer than 6 h (Knigge et al., 2011). Then, the WD is spun up to 2–5 min through accretion until the binary system reaches orbital periods of 3.5–4 h. At this point, the binary is detached, and a strong WD magnetic field is

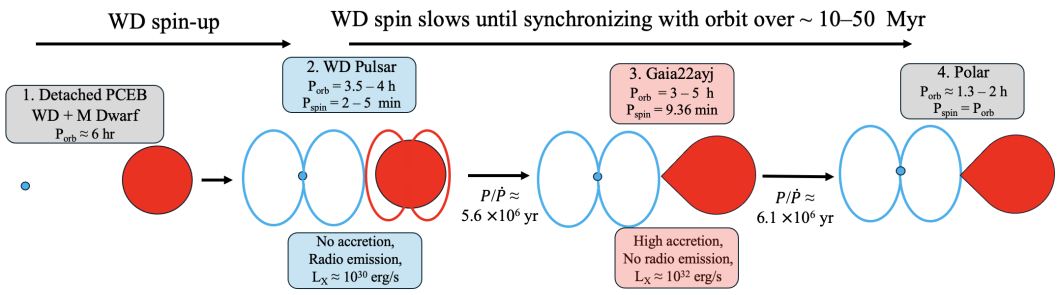

Figure 7.15: Cartoon of the possible evolution of WD pulsars into Gaia22ayj and then into polars. WD pulsars must be products of common envelope evolution, and WDs are likely spun up by an early accretion phase. WD pulsars are detached (non-accreting) systems, which are spinning down. Along the spin-down phase, the donor fills its Roche lobe and accretion begins, resembling Gaia22ayj. In ≈ 40 Myr, Gaia22ayj will spin down to the point where the WD spin is synchronized with the orbit, leading to the creation of a polar CV.

present, which interacts with that of the donor star, leading to pulsed radio emission. Because of the lack of accretion, X-rays are weak. As the WD spins down to $\approx$ 10 min, the donor star fills its Roche lobe and accretion commences. This leads to no radio emission (or at least much weaker emission than that of WD pulsars), and X-rays two orders of magnitude stronger than in the detached phase, over the course of ≈ 40 Myr.

Is Gaia22ayj an Intermediate Polar?

The arguments put forth above suggest that Gaia22ayj is a new class of accreting magnetic WDs, but which could also be considered a new subtype of intermediate polars (IPs). The WD spin period, X-ray luminosity, and possible orbital period are all similar to the majority of IPs (e.g.,, Suleimanov et al., 2019). However, the extreme levels of linear polarization (Figure 7.4), high amplitude optical modulation (Figure 7.14), and rapid spin-down rate (Figure 7.13), are completely unlike any known IP. As more analogous systems are discovered, we suggest usage of the term "Gaia22ayj-like" systems. When an indisputable link between WD pulsars and polars is found, "post-pulsar" could be a suitable term since "pre-polars" already exist.

The Biggest Unknowns: Orbital Period and Magnetic Field Strength of Gaia22ayj

At this point, the biggest question surrounding Gaia22ayj is: what is its orbital period? The known WD pulsars have orbital periods of 3.5 – 4 h, while the majority

of polars have orbital periods between 1.3 – 4 h. Therefore, for Gaia22ayj to be a possible link between the two, it should have an orbital period in the ≈ 3–4 h range. In Figure 7.16, we show the CV evolutionary tracks by Knigge et al. (2011) as a function of orbital period. In the upper panel, we plot the upper limit of the donor luminosity derived from fitting the SED at light curve minimum (Figure 7.10). If a donor star exceeded this luminosity, it would definitely be seen in the optical spectra of Gaia22ayj. This allows us to place an upper limit on the orbital period of ≈ 5.2 h. In the middle panel of that figure, we place a lower limit based on the assumption that the WD in Gaia22ayj is in spin equilibrium. Because we know the WD spin period and have a sense of the magnetic field strength, we place lower limits on the accretion rate (Figure 7.11). Plotting this value of $\dot{M} = 5 \times 10^{-10} M_{\odot}$ yr^{-1} on the CV evolutionary tracks, we obtain an orbital period lower limit of ≈ 3.5 h. We infer that Gaia22ayj could have an orbital period in the range 3.5–5.2 h, though it could be in the CV orbital period gap with an even lower orbital period. Because there is overlap with the periods of the known WD pulsars, we conclude that given the current data, it is likely that Gaia22ayj could indeed be a link between WD pulsars and polars.

In the lower panel of Figure 7.16, we show the absolute value of the derivative of angular momentum, $|\dot{J}|$, as a function of orbital period, assuming the Knigge et al. (2011) CV evolutionary tracks. The black and cyan curves represent the contribution to angular momentum loss from magnetic braking and gravitational wave radiation, respectively. We show a weakened magnetic braking prescription, simply reduced by a factor of ten, since it has been suggested that magnetic braking models in the past have been too strong (e.g.,, Belloni et al., 2020; El-Badry et al., 2022). As Gaia22ayj spins down to match the orbital period of polars, the angular momentum should be transferred to the orbit, which could lead to the system becoming detached. We plot horizontal lines which represent the change in angular momentum transferred to the orbit over 40 Myr timescales, starting from the spin periods of AR Sco (1.97 min, blue) and Gaia22ayj (9.36 min, red), and ending at 2 h. Effectively for all plausible orbital periods of Gaia22ayj (3.5 – 5.2 h), the red line is below both the black and dotted black lines, which suggests that the angular momentum transferred to the orbit during the spin-down phase will not lead to the binary detaching. However, weaker magnetic braking prescriptions could lead to detachment and should be explored in further detail.

Returning to the main question here—how can the orbital period of Gaia22ayj be

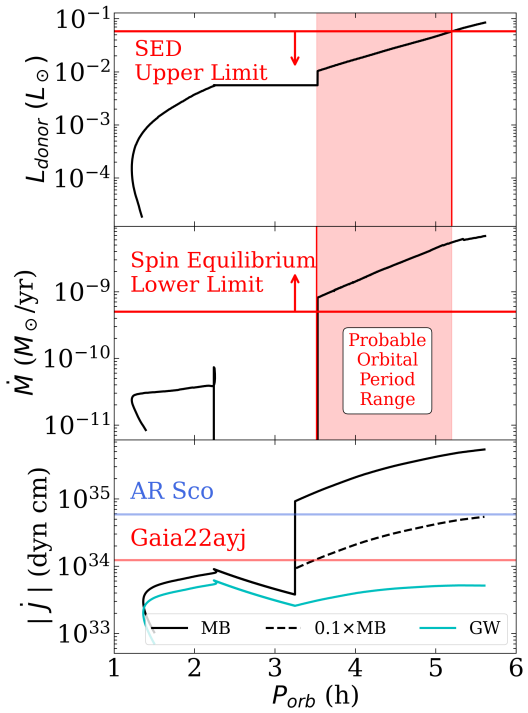

Figure 7.16: The evolutionary models of Knigge et al. (2011) illustrate the possible orbital period of Gaia22ayj. The SED at light curve minimum (Figure 7.10) places upper limits on the donor luminosity (*top*). The fact that Gaia22ayj is accreting and not flinging material out as a "propeller" sets a lower limit on the accretion rate (*middle*). Combined, they constrain $P_{\rm orb} = 3.5 - 5.2$ h, though future observations that detect donor lines and measure RVs are needed to test this. *Bottom:* Even assuming weakened (10%) magnetic braking compared to the Knigge et al. (2011) models, the angular momentum transferred by Gaia22ayj back to the orbit (assuming constant spin-down) will not detach the binary.

detected? We have shown that ≈ 2 h on 10-m class telescope time, unfortunately, is inadequate. Near-infrared spectroscopy with similar class telescopes is another possible option, and should be undertaken in upcoming years. Clearer, low harmonic cyclotron humps should be present in that regime, and it is possible that donor lines (either emission or absorption) will stand out more clearly. Ultraviolet spectroscopy with *HST* may detect the RV shift of the WD with respect to the center of mass, though since this is a long period (few hours) system, this effect is likely to be minimal. The discovery of Gaia22ayj analogs that may exhibit clearer donor lines is likely the best prospect.

X-ray timing of Gaia22ayj, if it confirms a different period than that measured in the optical, may also help solve this mystery. Assuming that the 9.36-min optical period is the WD spin-orbit beat and the 9.64-min X-ray period is the WD spin,

we find that $P_{\rm orb}$ = 5.37 h, in rough agreement with the limits we outline in Figure 7.16. Because of the limitations of the *Swift* GTI in our analysis, however, we can at best report this as a candidate orbital period. An analogy can be drawn to the prototypical diskless IP, V2400 Oph, where an orbital period has never been directly measured, but instead inferred from the WD spin (seen in circular polarization) and spin-orbit beat (seen in optical photometry) (Buckley et al., 1995).

Finally, we emphasize that we have not provided a true measurement of the magnetic field strength of Gaia22ayj due to the lack of visible cyclotron harmonics. Future work modeling the optical light curve and/or optical polarimetry, as well as near-infrared spectroscopy to find lower order (stronger) harmonics could shed light on the true value of the magnetic field strength.

Spin-down Rate of Gaia22ayj, Duration of Evolutionary Phase, and Rarity of Similar Systems

Another big question remains: if Gaia22ayj represents an evolutionary phase between WD pulsars and polar CVs, why is it so much more distant (2.5 kpc) than the two known WD pulsars (116 and 237 pc)? This means that Gaia22ayj-like systems are 1) either rare outcomes or 2) represent very short-lived phases of CV evolution. To address the first point, the main evolutionary model of Schreiber et al. (2021a) argued that WD pulsars first spin down to synchronicity with the orbit, commence wind accretion as low accretion rate polars, and then become true, accreting polars. This would mean that Gaia22ayj systems would just represent rare cases in which Roche-lobe filling occurs before WD spin-orbit synchronicity. Nevertheless, Figure 2 in the Supplementary Material of Schreiber et al. (2021a) did predict a similar synchronization timescale with ongoing accretion, exactly as is seen in Gaia22ayj. To address the second point, it could be that $\dot{P}$ keeps increasing until WD-spin orbit synchronicity is nearly reached. This is supported by the fact that $\dot{P}$ is a factor of ≈ 4 higher in Gaia22ayj than in AR Sco. Ongoing high-speed photometric campaigns of the known WD pulsars and Gaia22ayj are highly encouraged to find evidence for higher order spin period derivatives which could probe this idea.

Gaia22ayj-like Systems in the Rubin Legacy Survey of Space and Time (LSST)

The LSST is expected to reach $\approx$ 24 mag, a factor of 16 deeper than ZTF in flux (Ivezic et al., 2019b). This means that the LSST will be able to detect a system of a given luminosity four times farther away than the farthest system detectable by ZTF. Assuming that Gaia22ayj-like systems are young and concentrated in the disk,

at the very minimum, the LSST will detect dozens more. Based on its extraordinary optical light curve amplitude, we expect that Gaia22ayj-like systems will stand out in LSST, even early on in the 10-year survey. Polars also have high amplitudes, but period searches of LSST data will distinguish them from Gaia22ayj as we have done here with ZTF data.

Taking the simulated ten-year LSST baseline cadence (v3.4) described in Bianco et al. (2022), which is based on the OpSim[13] tool outlined by Delgado and Reuter (2016) (available from the following URL: `https://s3df.slac.stanford.edu/data/rubin/sim-data/sims_featureScheduler_runs3.4/baseline/`), we injected a Gaia22ayj-like signal at the actual position of Gaia22ayj, but $\approx$ 3 mag fainter than was observed by ZTF, with error bars scaled from typical ZTF values near the detection limit. In Figure 7.17, we show the simulated r-band LSST light curve of such a system. We also show the period significance as a function of time elapsed since the start of the LSST, calculated by taking the peak of the Lomb-Scargle periodogram divided by the median absolute deviation. We find that after $\approx$ 3 years into the LSST, such a signal could be detected above a significance threshold of 25. Given the significance defined above, 25 is the typical 95% percentile for ZTF light curves (i.e., only 95 percent of ZTF light curves have such a high periodicity significance). We conclude that while Gaia22ayj-like signals could be reliably detected in the r band in LSST within three years of survey start, it could be possible that through combining multiple filters, such objects could be discovered earlier. A similar claim was made and alternative observing strategies were proposed for other rapidly evolving astronomical phenomena in Bellm et al. (2022), suggesting that a higher LSST cadence could be beneficial for a multitide of science cases.

7.6 Conclusion

Gaia22ayj is a remarkable accreting magnetic WD that empirically represents a new class of magnetic CVs, and could be the missing link between WD pulsars and polar CVs. At the very minimum, Gaia22ayj:

> em Pulses at optical and near-IR wavelengths on a 9.36-min period. High-speed optical photometry over six years reveals that it is slowing down, with $\dot{P} = (2.89 \pm 0.12) \times 10^{-12}$ s s^{-1} and $P/\dot{P} \approx 6.1^{+0.3}_{-0.2} \times 10^6$ yr. em Pulses at extreme levels, changing in brightness by a factor of 7.5–10 at optical wavelengths within the span of 2.5 minutes. Broadband spectral modulation,

[13] `https://github.com/lsst/rubin_sim`

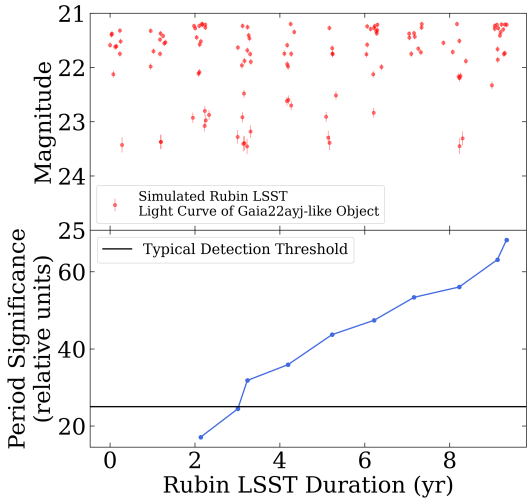

Figure 7.17: Simulated r-band light curve by injecting a Gaia22ayj-like signal into the simulated cadence of the LSST (*top*). Given typical periodicity detection thresholds, tested on real data with ZTF, Gaia22ayj-like systems should be detectable ≈ 3 yr after the start of the LSST, though combining data in multiple filters, such a signal could be detected earlier.

reminiscent of cyclotron emission in polars, is responsible for this. em Likely hosts a magnetic WD accreting from a Roche-lobe-filling donor. Linear polarization levels reaching 40% are a clear sign of magnetism. An outburst seen by ZTF, ATLAS, and *Gaia* resembling outbursts from IPs, as well as broad ($v \sin i \approx 1200$ km s^{-1}) double-peaked Balmer, He i, and He ii emission lines indicate ongoing accretion. em Is a luminous X-ray source, with $L_X = 2.7^{+6.2}_{-0.8} \times 10^{32}$ erg s^{-1} in the 0.3–8 keV band, comparable to most IPs and the most luminous polars. It is not detected in the radio with a 3σ upper limit of 15 μJy. em Does not show any emission-line RV shifts over the course of ≈ 2 h of observations with Keck I/LRIS. Donor lines are only marginally detected after averaging multiple spectra and do not shift on these timescales, impeding a measurement of the orbital period.

Based on these properties, we argued that Gaia22ayj could be a link between WD pulsars and polars, for the following reasons:

em Gaia22ayj is spinning down at nearly the same characteristic timescale as AR Sco, $\sim 5 \times 10^6$ yr. em Gaia22ayj shows extreme levels of linear polarization (40%) only seen in AR Sco, and not in either IPs or polars. em The possible spin period of Gaia22ayj (9.36 min) is longer than that of AR

Sco (1.97 min) and J1912 (5.3 min). Because accretion is ongoing, and the WD in Gaia22ayj is spinning down, in ≈ 40 Myr it will evolve into a polar, where the WD spin is locked with the orbit (assuming constant spin-down). em The orbital period is indirectly constrained, through the nondetection of the donor star and spin equilibrium arguments, to be in the 3.5–5.2 h range, overlapping with the orbital periods of AR Sco (3.6 h) and J1912 (4.0 h).

Other candidates (high brightness amplitude variables with $\sim$ 10-min periods) are emerging from current releases of SRG/eROSITA and ZTF, compiled using the methods outlined in Rodriguez (2024a) and surveys presented in Rodriguez et al. (2024). Future, deeper releases from SRG/eROSITA (Predehl et al., 2021a; Sunyaev et al., 2021) will likely reveal several more systems, though the Rubin LSST (Tyson, 2002; Ivezic et al., 2019b) will enable the optical discovery of at least dozens more systems within the first few years of the start of the survey.

The detailed characterization of Gaia22ayj demonstrates that there were previously missing details regarding the true diversity of magnetic WD binaries. This shows that rare systems could represent short-lived intermediate stages of binary evolution and lead to an improved understanding of magnetic field generation in WD binaries. The discovery of exotic systems like Gaia22ayj could hint at other intermediate stages of magnetic WD systems, which have been proposed to be responsible for the emerging class of long-period radio transients (LPTs). Multiwavelength (radio, X-ray, optical) surveys and follow-up efforts show promise in revealing such systems over the next decade.

7.7 Acknowledgments

We wish to dedicate this work to the memory of our colleague and friend Tom Marsh. Tom's enthusiasm to work on this object and rapid efforts to facilitate data collection truly made this project possible.

ACR acknowledges support from an NSF Graduate Fellowship. ACR thanks the LSST-DA Data Science Fellowship Program, which is funded by LSST-DA, the Brinson Foundation, and the Moore Foundation; his participation in the program has benefited this work. PR–G acknowledges support by the Spanish Agencia Estatal de Investigación del Ministerio de Ciencia e Innovación (MCIN/AEI) and the European Regional Development Fund (ERDF) under grant PID2021–124879NB–I00. MRS is supported by FONDECYT (grant numbers 1221059) and eRO-STEP (SA 2131/15-2 project number 414059771). IP acknowledges support from a Royal

Society University Research Fellowship (URF/R1/231496). We thank the referee for feedback that improved the clarity of this paper.

Based on observations made with the Gran Telescopio Canarias (GTC), installed at the Spanish Observatorio del Roque de los Muchachos of the Instituto de Astrofísica de Canarias, on the island of La Palma. Based on observations obtained with the Samuel Oschin Telescope 48-inch and the 60-inch Telescope at the Palomar Observatory as part of the Zwicky Transient Facility project. ZTF is supported by the National Science Foundation under Grants No. AST-1440341 and AST-2034437 and a collaboration including current partners Caltech, IPAC, the Weizmann Institute of Science, the Oskar Klein Center at Stockholm University, the University of Maryland, Deutsches Elektronen-Synchrotron and Humboldt University, the TANGO Consortium of Taiwan, the University of Wisconsin at Milwaukee, Trinity College Dublin, Lawrence Livermore National Laboratories, IN2P3, University of Warwick, Ruhr University Bochum, Northwestern University and former partners the University of Washington, Los Alamos National Laboratories, and Lawrence Berkeley National Laboratories. Operations are conducted by COO, IPAC, and UW.

Some of the data presented herein were obtained at Keck Observatory, which is a private 501(c)3 non-profit organization operated as a scientific partnership among the California Institute of Technology, the University of California, and the National Aeronautics and Space Administration. The Observatory was made possible by the generous financial support of the W. M. Keck Foundation. The authors wish to recognize and acknowledge the very significant cultural role and reverence that the summit of Maunakea has always had within the Native Hawaiian community. We are most fortunate to have the opportunity to conduct observations from this mountain. We are also grateful to the staff of Palomar Observatory for their assistance in carrying out observations used in this work.

Partly based on observations made with the Nordic Optical Telescope, owned in collaboration by the University of Turku and Aarhus University, and operated jointly by Aarhus University, the University of Turku and the University of Oslo, representing Denmark, Finland and Norway, the University of Iceland and Stockholm University at the Observatorio del Roque de los Muchachos, La Palma, Spain, of the Instituto de Astrofisica de Canarias. The data presented here were obtained with ALFOSC, which is provided by the Instituto de Astrofisica de Andalucia (IAA) under a joint agreement with the University of Copenhagen and NOT. The observation with the Southern African Large Telescope (SALT) was obtained under program 2021-2-

LSP-001 (PI: D. Buckley). Polish participation in SALT is funded by grant No. MEiN nr 2021/WK/01. DAHB acknowledges support from the National Research Foundation.

This work presents results from the European Space Agency (ESA) space mission Gaia. Gaia data are being processed by the Gaia Data Processing and Analysis Consortium (DPAC). Funding for the DPAC is provided by national institutions, in particular the institutions participating in the Gaia MultiLateral Agreement (MLA). The Gaia mission website is `https://www.cosmos.esa.int/gaia`. The Gaia archive website is `https://archives.esac.esa.int/gaia`. This work made use of data supplied by the UK Swift Science Data Centre at the University of Leicester

ECB and JK acknowledge support from the DIRAC Institute in the Department of Astronomy at the University of Washington. The DIRAC Institute is supported through generous gifts from the Charles and Lisa Simonyi Fund for Arts and Sciences, and the Washington Research Foundation.

7.8 Full High-speed Optical Photometry

In Figures 7.18 and 7.19, we show the full high-speed light curves of Gaia22ayj from CHIMERA and ULTRACAM, respectively. Pulsations are stable in time, but not in amplitude, most noticeably in the *g* band. The higher of the two peaks in a given spin period is particularly variable. For example, the peak near minute 7 in the CHIMERA light curve reaches a relative flux of 4, while the peak at minute 42 only reaches a relative flux of 2.5. Similar behavior is seen in the ULTRACAM light curve, where the relative flux in the higher peak reaches a relative flux of 3 at minute 40, but never does so again. In Figure 7.20, we show the full polarimetry light curve, showing that Gaia22ayj regularly reaches 30% polarization and exceeds 40% in four data points. In Figure 7.21, we show high speed photometry from a several-hour campaign carried out with the Sutherland High Speed Optical Cameras (SHOC) on the 1m SAAO telescope.

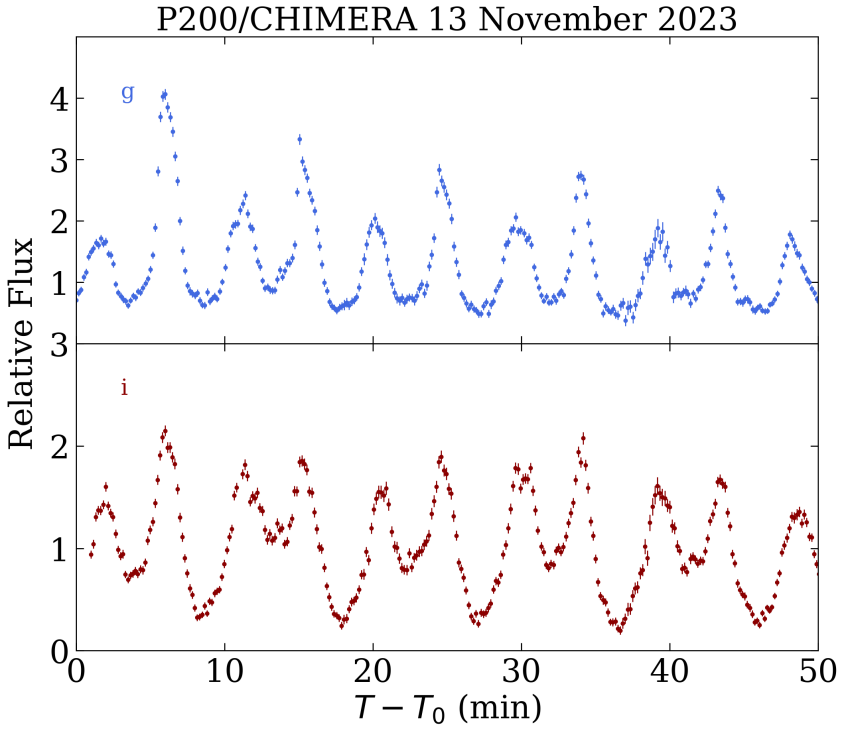

Figure 7.18: P200/CHIMERA light curve from 13 Nov 2023. In *g* band, the second peak of the spin phase (higher of the two peaks) steadily decreases over the course of the observing window, from a relative flux of 4 at minute 7 to a relative flux of 2.5 at minute 42. Similar behavior is seen in the ULTRACAM light curve (Figure 7.19).

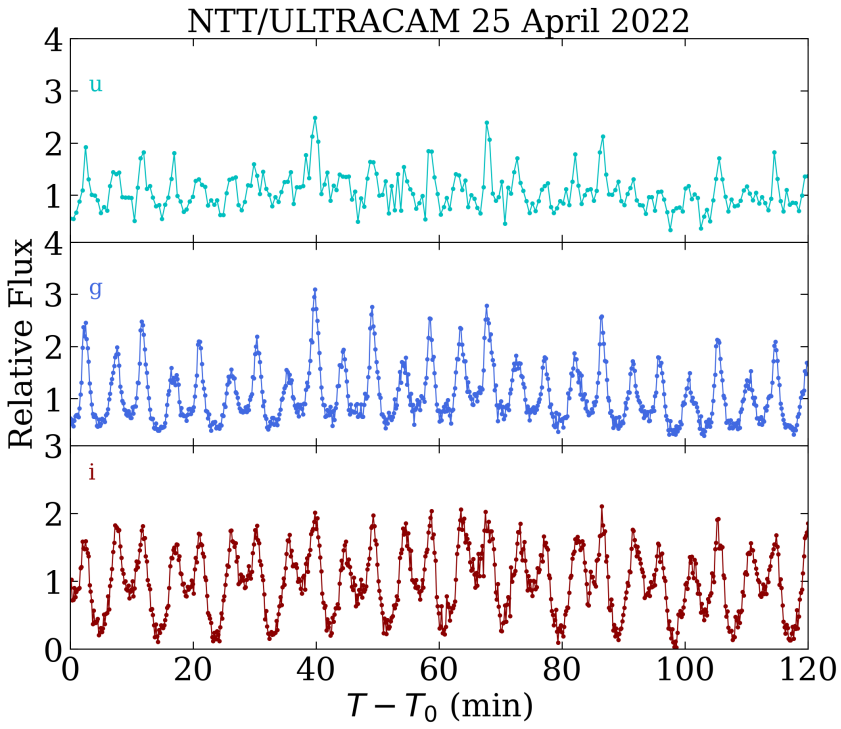

Figure 7.19: NTT/ULTRACAM light curve from 25 Apr 2022. In *g* band, the second peak of the spin phase (higher of the two peaks) is variable throughout the observing window, reaching its highest value at the 40 minute mark.

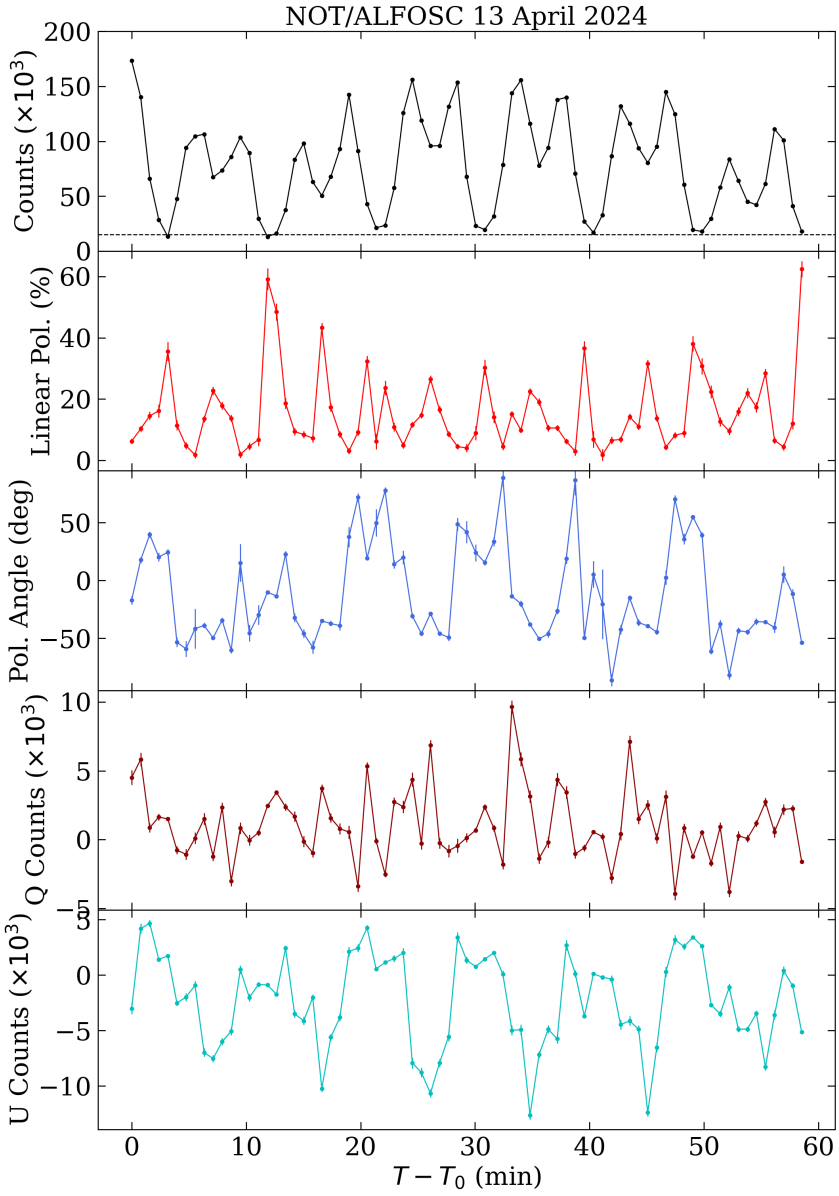

Figure 7.20: NOT/ALFOSC light curve from 13 Apr 2024. The dotted black line in the top panel denotes 15,000 counts, demonstrating that even at light curve minimum, a significant measurement is recorded. Linear polarization percentage regularly reaches 30%, and exceeds 40% in four data points. Variability in Stokes Q and U confirm that the variability in polarization percentage and angle are real and not due to noise bias.

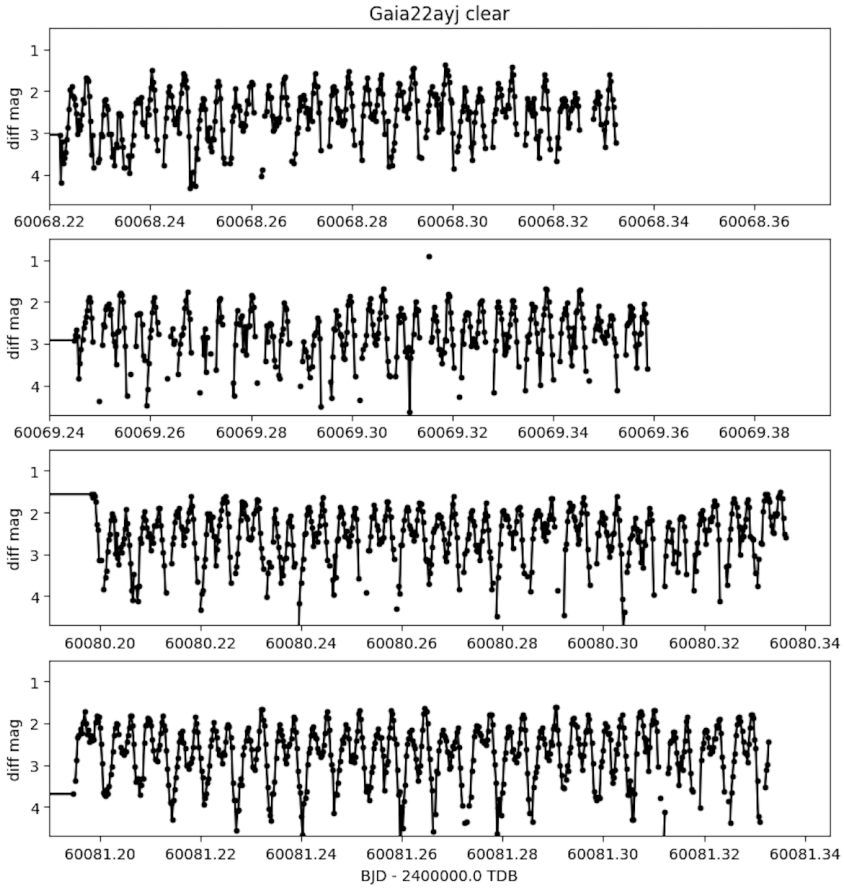

Figure 7.21: High speed photometry carried out with the Sutherland High Speed Optical Cameras (SHOC) on the 1m SAAO telescope reveals consistent modulation similar to that seen in other photometric runs.

Chapter 8

SPECTROSCOPIC DETECTION OF A 2.9-HOUR ORBIT IN A LONG-PERIOD RADIO TRANSIENT

Antonio C. Rodriguez. Spectroscopic detection of a 2.9-hour orbit in a long-period radio transient. *Astronomy & Astrophysics*, 695:L8, March 2025. doi: 10.1051/0004-6361/202553684.

Author List

Antonio C. Rodriguez[1,*]

[1]Department of Astronomy, California Institute of Technology, 1200 E. California Blvd, Pasadena, CA 91125, USA

[*]Corresponding author: acrodrig@caltech.edu

ABSTRACT

Long-period radio transients (LPTs) are a mysterious new class of radio transients pulsating on periods of minutes to hours. To date, nine LPTs have been discovered predominantly at low Galactic latitudes, and yet their nature remains unknown. Here I present the first phase-resolved optical spectroscopy of the 2.9 h LPT GLEAM-X J0704–37, acquired with the 10 m Keck I telescope. Radial velocity (RV) shifts of 189 ± 3 km s^{-1} of an M5-type star in a binary system are detected on a period nearly equal to the radio period. Weak Hα emission is also present, with some of it possibly originating from outside of the M dwarf. Based on the RV amplitude, and assuming a typical M dwarf mass, the companion mass must be $M \geq 0.22 M_{\odot}$. Calibrating the spectra with space-based *Gaia* photometry reveals that the system is nearly four times closer than previously reported, at $d \approx 400$ pc, suggesting that more systems could be nearby and amenable to optical characterization. The optical spectrum between 3500–10,000 Å is well modeled by a binary comprised of a massive white dwarf (WD; $T_{\rm eff}$ ≈7,300 K, $M \approx 0.8 - 1.0 M_{\odot}$) and an M dwarf ($T_{\rm eff}$ ≈3,000 K, $M \approx 0.14 M_{\odot}$). Radio pulses arrive when the WD is at nearly maximum blueshift and the M dwarf at nearly maximum redshift, in contrast to what has been reported for a similar LPT, ILT J1101+5521. GLEAM-X J0704–37 is now the second LPT with an orbital period nearly equal to the radio period, establishing a class of LPTs associated with WD + M dwarf binaries; other LPTs are likely related to WD and/or neutron star spins. This work demonstrates that the precise localization of LPTs, which enables optical follow-up, will be key in uncovering the mechanism(s) that power this new class of phenomena.

8.1 Introduction

Long-period radio transients (LPTs) represent a new era in radio astronomy. Pulsars were the first radio sources discovered to be stably pulsating at ∼1 sec timescales (Hewish et al., 1968), and attributed to rotating neutron stars (NSs; Gold, 1968; Pacini, 1968). Exploring a new range of periodicity has historically proven to be revolutionary in the field. For instance, the discovery of a millisecond pulsar (MSP; Backer et al., 1982) and subsequent studies established the importance of binary interaction in the formation of such rapid rotators (e.g.,, Phinney and Kulkarni, 1994).

Crucially, the association of optical (and other multiwavelength) counterparts with

radio sources has proven to be vital for their characterization. Kulkarni (1986) optically identified white dwarf (WD) binary companions to MSPs, establishing both the old age of MSPs and demonstrating that NS magnetic fields do not strictly decay exponentially. In addition, optical spectroscopy of the faint companions to black widow MSPs (Fruchter et al., 1988) with 10 m class telescopes has revealed what may be the most massive NS known to date, placing useful constraints on the NS equation of state ($\approx 2.35 M_{\odot}$; Romani et al., 2022).

At the time of writing, nine LPTs have been reported[1] (in published form or as a preprint), and are summarized in Table 8.1. Hurley-Walker et al. (2024a) reported the discovery of the 2.915 h LPT known as GLEAM-X J0704–37. The radio source was localized using MeerKAT and is associated with a faint (*Gaia* G $\approx$ 20.78) optical counterpart at that position. An optical spectrum in that work revealed an M dwarf counterpart, similar to the one seen in the LPT ILT J1101+5521 (de Ruiter et al., 2024). Hurley-Walker et al. (2024a) also found a ≈6 yr period in radio timing residuals, and suggested it to be the binary period of a WD + M dwarf system, with the 2.9 h period being the WD spin.

[1]PSR J0901-4046 is an ultra-long-period pulsar (not considered here to be an LPT) that has been established to be a neutron star with a 76 s period (Caleb et al., 2022).

LPT Name	Radio Period (min)	Counterpart?	Reference
GCRT J1745-3009	76.2	None	Hyman et al. (2005)
GLEAM-X J162759.5-523504.3	18.18	None	Hurley-Walker et al. (2022)
GPM J1839-10	21.97	None	Hurley-Walker et al. (2023a)
ASKAP J193505.1+214841.0	53.76	NIR source	Caleb et al. (2024)
CHIME J0630+25	7.017	None	Dong et al. (2024)
ILT J1101+5521	125.5	M dwarf	de Ruiter et al. (2024)
GLEAM-X J0704–37	174.9	M dwarf	Hurley-Walker et al. (2024a)
ASKAP/DART J1832-0911	44.27	X-ray source	Wang et al. (2024); Li et al. (2024)
ASKAP J183950.5-075635.0	387	None	Lee et al. (2025)

Table 8.1: List of the nine known LPTs at the time of writing (reported in published form or as a preprint).

Here I show that GLEAM-X J0704–37 is in fact a compact WD + M dwarf binary, with the 2.9 h radio period matching the orbital period and located only ≈400 pc away. Based on the orbital solution, radio pulses arrive when the WD is nearly at maximum blueshift and M dwarf nearly at maximum redshift.

8.2 Data

GLEAM-X J0704–37 was observed on two occasions using the Low Resolution Imaging Spectrometer (LRIS; Oke et al., 1995b) on the 10 m Keck I telescope on Mauna Kea in Hawai'i. An observing log is provided in Table 8.3. All LRIS data were wavelength calibrated with internal lamps, flat-fielded, and cleaned for cosmic rays using `lpipe`, a pipeline for LRIS optimized for long-slit spectroscopy (Perley, 2019). To calculate radial velocities (RVs), the mid-exposure time of all observations was corrected to the barycentric Julian date ($\mathrm{BJD_{TDB}}$).

The spectrum shown in Figure 3 of Hurley-Walker et al. (2024a), at $\lambda \approx 6000$, ($F_\lambda \approx 3 \times 10^{-18}$erg s^{-1}cm^{-2-1}) appears to be nearly four times lower than the value derived from the average *Gaia* G photometry, $F_\lambda \approx 1.5 \times 10^{-17}$erg s^{-1}cm^{-2-1}. Here, *Gaia* Data Release 3 (DR3; Gaia Collaboration et al., 2023b) average photometry of the source (Gaia DR3 5566254014771398912) was used to calibrate the overall flux level obtained by spectroscopy. The `pyphot` package[2] was used to calculate synthetic photometry from the average spectrum of Night 2 in the *Gaia* BP, G, and RP bandpasses. The average spectrum was then multiplied by a correction factor in order to match the synthetic photometry to the *Gaia* photometry, leading to a smaller inferred distance (≈400 pc) compared to that presented in the discovery paper (≈1,500 pc).[3]

8.3 Analysis

RV fitting and mass constraints on companion star

The radial velocity (RV) measurements traced by the Na I doublet (8183 and 8195) absorption lines in the left panel are shown in the left panel of Figure 8.1. The full sets of spectra are shown in Figure 8.5, and all RV measurements are reported in Table 8.4. The orbital phase is set to coincide with the start of observations on Night 2. The gray vertical lines indicate the observed radio pulses (2018-02-04 at 14:57:02, 2023-10-04 at 02:33:02, and 2023-10-04 at 05:29:59 UT) reported

[2] `https://mfouesneau.github.io/pyphot/index.html`

[3] Curiously, the nearer distance agrees with that derived from the radio dispersion measure using the electron density model of Yao et al. (2017), as reported in the discovery paper.

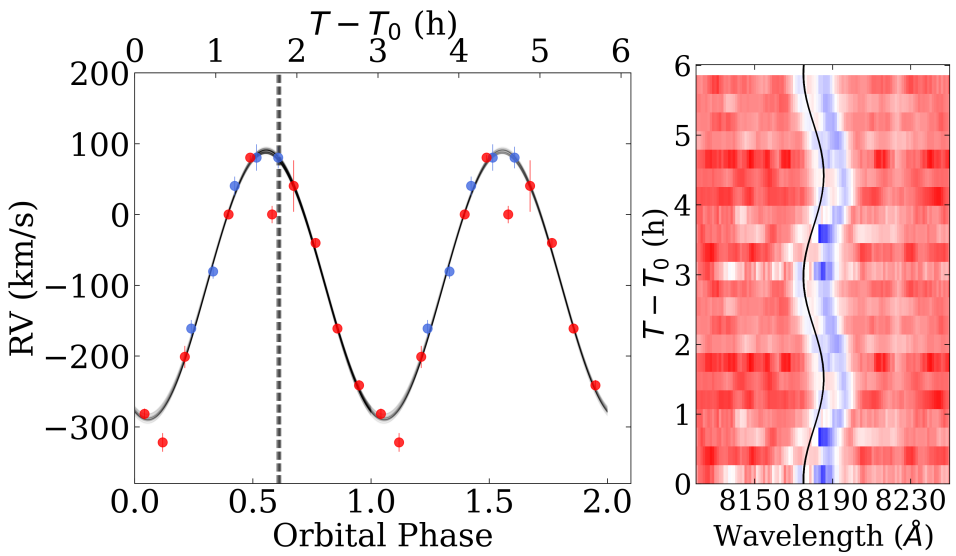

Figure 8.1: Binary nature of GLEAM-X J0704–37*Left:* RVs measured using the Na I absorption doublet from Night 1 (blue) and Night 2 (red) folded on a period of 2.915(1) h and plotted with the best RV model (black; $K_{\rm MD} = 189 \pm 3$ km s^{-1}). This shows that the binary orbital period matches the radio pulse period to within 0.05 percent. Radio pulses (gray) occur just after the maximum redshift of the M dwarf, when it is at the ascending node as viewed from Earth. *Right:* Trailed spectra (Night 2) of the Na I doublet show good agreement with the RV model (black). Two orbital periods are shown for visual aid.

by Hurley-Walker et al. (2024a), folded on the 10496 s period, and barycentric-corrected to BJD$_{\rm TDB}$. Orbital period constraints of 10496 ± 5 s (resp. 10500 ± 500 s) based on RVs from two nights (resp. one night) of data are outlined in Section 8.6.

Equation 8.1 yields a minimum mass constraint on the companion star:

$$\frac{(M_{\rm companion} \sin i)^3}{(M_{\rm companion} + M_{\rm MD})^2} = \frac{P_{\rm orb} K_{\rm MD}^3}{2\pi G}. \tag{8.1}$$

Assuming an edge-on inclination ($i = 90°$) and an M dwarf of zero mass, the minimum companion mass is $M_{\rm companion} \geq 0.087 M_\odot$. Assuming a realistic M dwarf mass of $0.14 M_\odot$, based on the spectral analysis below, yields $M_{\rm companion} \geq 0.22 M_\odot$.[4]

[4]It has been found in M dwarfs in close binaries that the Na I doublet may trace the back of the star, leading to the need for a correction to the RV amplitude of at most ≈ −15 km s^{-1} (e.g.,, Wade and Horne, 1988). This would imply a minimum companion mass of $0.068 M_\odot$ and $0.20 M_\odot$, assuming an M dwarf mass of zero and $0.14 M_\odot$, respectively.

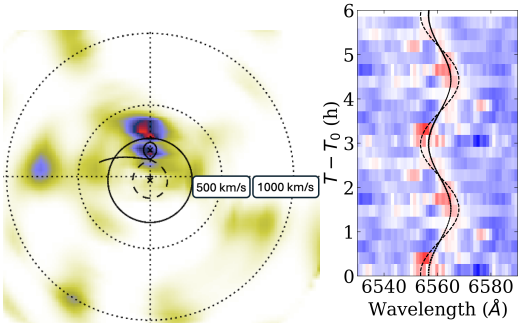

Figure 8.2: Mapping the Hα emission of GLEAM-X J0407–37. *Left:* Doppler tomogram of the Hα line revealing $> 3\sigma$ (red) emission associated with the orbital phase of the M dwarf (Roche potential shown by the solid black teardrop shape). The majority of the emission may originate from outside the M dwarf, with a higher observed velocity. *Right:* Trailed spectra of the Hα emission line shown alongside the M dwarf RV model (black solid line), and the higher velocity component (black dotted line; $K \approx 330$ km s^{-1}).

Hα emission associated with the M dwarf

The origin of the Hα emission is explored by creating a Doppler tomogram[5] (Marsh and Horne, 1988) in Figure 8.2 with the `doptomog` IDL-based code[6] (Kotze et al., 2015a). The systemic offset of $\gamma = -98.9$ km s^{-1} was applied, and the orbital phases were shifted such that inferior conjunction corresponds to a phase of 90° on the resulting map (e.g.,, Kotze et al., 2015a; Rodriguez et al., 2023d). The Roche potentials derived from the inferred masses and system inclination (Table 8.2) are overlaid, showing the Roche potential of the M dwarf as a solid black teardrop.[7] The dotted black teardrop is the Roche potential of the companion star. Other markings are related to accreting systems and can be ignored here. The physical geometry mapped onto these coordinates is illustrated in Figures 1 and 3 of Kotze et al. (2015a).

Figure 8.2 shows that some Hα emission is coincident with the orbital phase and RV of the donor star (inside the Roche potential), but that the bulk of the Hα emission may originate from a higher velocity region outside of the M dwarf. However,

[5] A Doppler tomogram, in polar coordinates, shows RV shift as the radial coordinate and orbital phase as the azimuthal coordinate. Doppler maps are commonly used in the cataclysmic variable (CV) literature to disentangle emission from the donor star and accretion-related components, though they are also useful for detached binaries; see Marsh (2001) for a review of the method of Doppler tomography.

[6] `https://www.saao.ac.za/~ejk/doptomog/main.html`

[7] Typically, in the CV literature, this also represents the actual shape of the star since it fills its Roche lobe in such systems. That is, however, not the case here since the M dwarf in GLEAM-X J0704–37 does not fill its Roche lobe.

this is only seen in the single orbit of spectra presented here, so further data are needed to confirm the presence of this feature. It may very well turn out that all Hα emission is associated with chromospheric activity of the rapidly rotating M dwarf (e.g.,, Delfosse et al., 1998). If this higher velocity feature is indeed present, then its velocity corresponds to $\approx$ 330 km s^{-1}, as represented by the black dashed curve in the right panel of Figure 8.2. Details regarding the possible spatial origin of that emission region and resemblance to the post common envelope WD + M dwarf binary QS Vir are discussed in Section 8.9.

Binary parameters

The spectra of GLEAM-X J0704–37 do not reveal any strong emission lines that could be indicative of accretion, suggesting that this system is a detached binary (M dwarf + companion). Because there is a detection of a blue continuum (shortward of 5500 Å) above the noise, I proceeded with the assumption that the companion star is a white dwarf (WD), also adopted by Hurley-Walker et al. (2024a) based on radio pulse arguments. Further arguments against a NS + M dwarf binary are put forth in Section 8.6.

Proceeding with this assumption, the average spectrum can be described by six parameters, only four of which are independent: the WD effective temperature and radius, $T_{\rm WD}$ and $R_{\rm WD}$; the M dwarf effective temperature and radius, $T_{\rm MD}$ and $R_{\rm MD}$; the distance to the system, d; and the reddening to the system, $E(B-V)$. $T_{\rm MD}$ and $R_{\rm MD}$ are related though the M dwarf isochrones (assuming an age of 10 Gyr) of Baraffe et al. (2015); d and $E(B-V)$ are related through the 3D dust map of Edenhofer et al. (2024). Other dust maps infer slightly different levels of extinction, explored further in Section 8.10. The four independent parameters were constrained using a Markov chain Monte Carlo (MCMC) parameter exploration, described in complete detail in Section 8.6. The resulting parameters are credible intervals, and are shown in Table 8.2.

In Figure 8.3 the average spectrum (rectified using *Gaia* photometry), both *Gaia* and synthetic photometry, and the model obtained from the parameters in Table 8.2 are shown. The residuals do not show any obvious systematic biases across the entire 3500–10,000Å range, aside from features related to telluric subtraction and the Hα emission feature at 6563Å.

The largest uncertainty in the above analysis is the extinction to the system; assuming higher extinction values leads to a larger WD radius (meaning lower mass). The

Parameter	Value
$K_{\rm MD}$ (km s^{-1})	189.4 ± 2.7
ϕ_0	1.3074 ± 0.0021
γ (km s^{-1})	$-98.9^{+1.7}_{-1.8}$
$P_{\rm orb}$ (s)	10496 ± 5
$E(B-V)$	0.119 ± 0.001
$T_{\rm WD}$ (K)	7320^{+800}_{-590}
$R_{\rm WD}$ ($R_\odot$)	$0.0079^{+0.0014}_{-0.0015}$
$T_{\rm MD}$ (K)	3010 ± 20
$R_{\rm MD}$ ($R_\odot$)	$0.165^{+0.003}_{-0.004}$
d (pc)	380 ± 10
$M_{\rm WD}$ ($M_\odot$)	$1.02^{+0.12}_{-0.13}$
$M_{\rm MD}$ ($M_\odot$)	0.136 ± 0.003
a ($R_\odot$)	1.07 ± 0.04
q	$0.133^{+0.019}_{-0.014}$
$R_{\rm MD}/R_L$	0.680 ± 0.001
i ($^\circ$)	28^{+2}_{-1}

Table 8.2: All parameters for the GLEAM-X J0704–37 WD + MD binary system. The first level of parameters are just based on the RV shifts of the MD, while the next level is based on a MCMC parameter exploration of the average spectrum. The final level represents parameters derived from those used in the MCMC analysis.

WD in this system, however, is clearly massive, since it is unlikely for the extinction to exceed $E(B-V) = 0.3$ (see Appendix 8.10). Assuming this leads to a WD mass of $0.82 M_\odot$, lower than that presented in Table 8.2, but still more massive compared to typical single WDs in the field ($0.6 M_\odot$, $0.7 M_\odot$ for DA and DB WDs; Kepler et al., 2007b) or WDs in post common envelope binaries ($0.67 \pm 0.21 M_\odot$; Zorotovic et al., 2011).

8.4 Discussion

A detached WD + M dwarf close binary

I have shown that the optical spectrum of GLEAM-X J0704–37 is well modeled by that of a detached (non-accreting) WD + MD binary with an orbital period of 10496±5 s (2.915 h), which agrees with the radio period (10496.5522) to within 0.05 percent (to within 5 percent at worst if only fitting RVs from Night 2). This allows us to discard a scenario put forth by Hurley-Walker et al. (2024a), where the 2.9 h period was attributed to a NS or WD spin period in a $\approx$ 6 yr orbital period

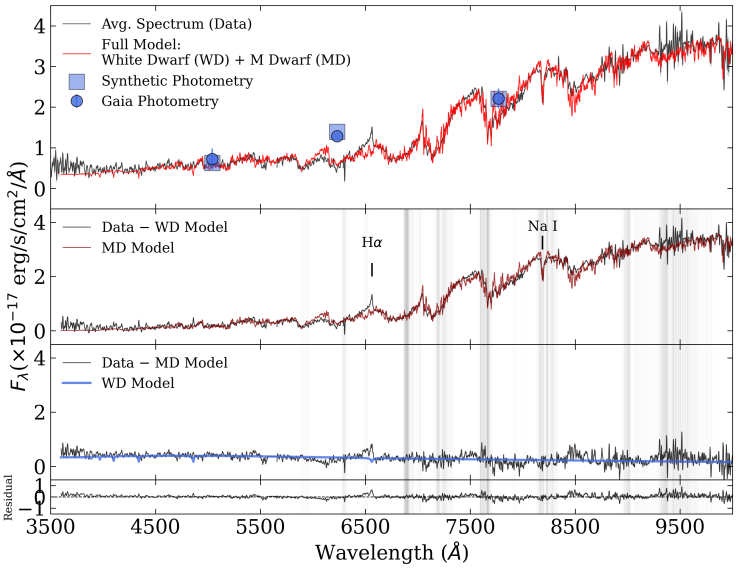

Figure 8.3: Spectral modeling of the binary. *Top:* Average spectrum of GLEAM-X J0704–37 (black) well fit by a WD + MD binary model (red; parameters in Table 8.2). The overall flux level was calibrated by matching synthetic photometry (squares), generated from the spectrum, with *Gaia* average photometry (circles). *Middle:* Each binary component provides a good fit to the data when the other is subtracted. *Bottom:* Residuals show no obvious systematic disagreement, aside from the Hα emission and telluric features (gray bands).

with an M dwarf.[8]

Connections to ILT J1101+5521, WD pulsars, and cataclysmic variables

GLEAM-X J0704–37 bears a strong similarly to another LPT, ILT J1101+5521 (de Ruiter et al., 2024). They both host a cool massive WD (≈7,300 K and ≈5,500 K; $\approx 1.02 M_\odot$ and $\approx 0.77 M_\odot$, respectively). They are both WD + M dwarf binaries, pulsing in the radio on a similar nearly equal to the orbit. WD pulsars (which are also radio emitting detached WD + M dwarf systems, but host a magnetic WD spinning and radio pulsing on 2–5 min timescales, but in a 3.5–4 h orbit) are another class of similar radio sources, though over an order of magnitude less radio luminous than LPTs Marsh et al. (2016); Pelisoli et al. (2022a). All of these systems highlight the unexpected diversity of radio activity and emission processes associated with

[8]A faint third body could still be present in the system orbiting on a 6 yr period. Recent discoveries in close compact object binaries have revealed the presence and evolutionary impact of distant triples (Burdge et al., 2024; Shariat et al., 2024). At the same time timing residuals of approximately a few years seen in CVs have been attributed to magnetic activity in the low-mass companion star (Souza and Baptista, 2024). Both scenarios warrant further investigation to explain the radio timing residuals.

otherwise common detached WD + M dwarf binaries. These systems, including GLEAM-X J0704–37, will eventually begin mass transfer and become cataclysmic variables (CVs; Warner, 1995a; Hellier, 2001a). Magnetic braking in some form (e.g.,, Rappaport et al., 1983; El-Badry et al., 2022) and gravitational wave radiation will drive the binary closer together, with accretion commencing in a few gigayears (e.g.,, Knigge et al., 2011). An extended discussion on the above points is presented in Appendix 8.7.

8.5 Conclusions

I conducted the first phase-resolved spectroscopic observations of GLEAM-X J0704–37, an LPT pulsing on a 2.915 h period. The main conclusions are as follows:

1. RV shifts (189 ± 3 km s^{-1}) of the Na I doublet show that the binary orbital period (10496±5 s) agrees with the 10496.5522 s radio pulse period to within 5 (0.05) percent, fitting spectra from one (both) night(s) (Figure 8.1).

2. Radio pulses nearly coincide with the ascending node of the orbit when the M dwarf is at maximum redshift and WD at maximum blueshift (Figure 8.1). This differs from what has been reported in ILT J1101+5521, where radio pulses arrive near binary conjunction.

3. The average spectrum is well fit by the sum of a ≈3,000 K, $\approx 0.14 M_{\odot}$ M dwarf and a massive ≈7,300 K, ≈ 0.8–$1.0 M_{\odot}$ white dwarf (Figure 8.3; Table 8.2).

4. Weak Hα emission is seen; some is attributed to the M dwarf, though some appears to be localized to a region outside the M dwarf that coincides with it in orbital phase, but orbits at a higher velocity of ≈ 330 km s^{-1} (Figure 8.2).

5. GLEAM-X J0704–37 (≈400 pc) is nearly four times closer than previously thought (≈1500 pc), suggesting that such systems may be relatively common.

6. I propose that GLEAM-X J0704–37, along with ILT J1101+5521, are part of a class of LPTs that are associated with WD binary orbits, while other LPTs are likely associated with WD or NS spins.

This work demonstrates the importance of multiwavelength follow-up in characterizing LPTs: optical spectroscopy has now revealed a class of LPTs associated with WD + M dwarf close binaries (this work; Hurley-Walker et al., 2024a; de Ruiter et al., 2024), and X-ray pulsations along with a spatial association with a supernova

remnant has tentatively connected another LPT to NS or WD spins (Wang et al., 2024; Li et al., 2024). Optical follow-up remains difficult, requiring the biggest telescopes in the world (10 m class) to adequately characterize the optical counterparts. Ongoing searches for new LPTs may discover closer sources or reveal them to be an intrinsically distant rare class of objects, in either case shining light on this exciting new phenomenon.

ACKNOWLEDGEMENTS

I thank Shri Kulkarni and Kareem El-Badry for a close reading of this paper and valuable feedback. I also thank the referee for constructive input that improved the final manuscript. I acknowledge support from an NSF Graduate Student Fellowship. I also thank Matthew Graham and Ilaria Caiazzo for obtaining an early spectrum that demonstrated the feasibility of this campaign and for assistance with observations, respectively. I thank the organizers and attendees of the *XMM-Newton* "The X-ray Mysteries of Neutron Stars and White Dwarfs" Conference, including Natasha Hurley-Walker and Ingrid Pelisoli, for alerting me to the discovery of LPTs and to Myles Sherman, Casey Law, and the Caltech LPT Group for interesting discussions on related objects. I am grateful to the staff of Keck Observatory for their support in carrying out the observations presented here.

Some of the data presented herein were obtained at Keck Observatory, which is a private 501(c)3 non-profit organization operated as a scientific partnership among the California Institute of Technology, the University of California, and the National Aeronautics and Space Administration. The Observatory was made possible by the generous financial support of the W. M. Keck Foundation. I wish to recognize and acknowledge the very significant cultural role and reverence that the summit of Maunakea has always had within the Native Hawaiian community. We are most fortunate to have the opportunity to conduct observations from this mountain.

8.6 Extended analysis: Parameter constraints

Orbital solution

Radial velocities are obtained by cross-correlating a 50 Å window around the Na I doublet with an M5 template from the BT-DUSTY library of theoretical spectral atmospheres (Allard et al., 2011a). The RVs are fit to Equation 8.2 using data from both Night 1 and 2 simultaneously, assuming a circular orbit ($e = 0$):

$$\mathrm{RV}_{\mathrm{MD}} = K_{\mathrm{MD}} \sin(2\pi(\phi - \phi_0)) + \gamma. \tag{8.2}$$

Here MD stands for M dwarf, RV is an individual RV, K is the RV curve amplitude, ϕ is the orbital phase, ϕ_0 sets the zero-point of the orbit (inferior conjunction), and γ is the systemic velocity. To constrain the parameter values, a Markov chain Monte Carlo (MCMC) parameter exploration (Hastings, 1970) was performed using the `emcee` package (Foreman-Mackey et al., 2019); the ensemble sampler was run with twelve walkers for 10,000 runs, taking the first half as the burn-in period. Table 8.2 shows the credible intervals of all parameters, with the most relevant being $K_{\mathrm{MD}} = 189 \pm 3 \mathrm{km\ s^{-1}}$.

To calculate orbital phases, the period was first fixed to be equal to the radio period reported by Hurley-Walker et al. (2024a) of 10496.5522 s[9]. Phases were recalculated based on different candidate orbital periods in the range of 2.8 to 3 h and evaluated the fit to the RV solution derived above. This Monte Carlo trial constrained the orbital period to be $P = 10496 \pm 5$ s. However, since the total number of orbital cycles that transpired between Night 1 and 2 are unknown, performing the above analysis on the Night 2 data lone yields a more conservative error of $P = 10500 \pm 500$ s. Both analyses are consistent with the radio period to within one sigma.

Binary parameters

To create an M dwarf model, T_{MD} is specified, interpolating through the BT-DUSTY library of theoretical stellar atmospheres (Allard et al., 2011a), assuming solar metallicity and $\log g = 5.0$. An inflation factor of 10% is adopted for the radius of the M dwarf, as it has been shown that for binaries this close, fast rotation leads to increased magnetic activity and thus inflation (Parsons et al., 2018). The stellar atmosphere is multiplied by $(R_{\mathrm{MD}}/d)^2$ to obtain a flux as viewed from Earth. The same process is used for the WD, taking the theoretical (DA; H-rich) WD atmospheres of (Koester, 2010) and assuming $\log g = 8.0$.

[9]Other periods were reported by Hurley-Walker et al. (2024a), differing by at most 0.002 s. The current observing baseline yields a level of precision (5 s) which is consistent with all possible periods in Hurley-Walker et al. (2024a).

A Markov chain Monte Carlo (MCMC) parameter exploration was performed using the `emcee` package (Foreman-Mackey et al., 2019) to explore all four simultaneously, adopting uniform priors on all parameters: $5000 < T_{\rm WD}$ (K) < 12000, $2500 < T_{\rm MD}$ (K) < 4000, $0.008 < R_{\rm WD}$ ($R_\odot$) < 0.02, $250 < d$ (pc) < 1000. The MCMC sampler was run for 2000 steps, taking half as the burn-in period. The parameter exploration converged, with a Gelman-Rubin statistic ($\hat{R}$; Gelman and Rubin, 1992) of 1.08 averaged over all chains. Gelman and Rubin (1992) argue that values close to 1, with $\hat{R} \lesssim 1.1$ being a typical threshold, indicate convergence for typical multivariate distributions. The corner plot and marginalized posterior distributions are shown in Figure 8.9.

In Table 8.2, the inferred binary parameters (median values and credible intervals: 16$^{\rm th}$ and 84$^{\rm th}$ percentiles of the posterior distributions) resulting from the MCMC analysis are shown. $M_{\rm WD}$ is obtained from the mass-radius relation of Bédard et al. (2020); $M_{\rm MD}$, from the M dwarf isochrones (assuming an age of 10 Gyr) of Baraffe et al. (2015), assuming solar metallicity. The binary separation, a, and inclination, i, are solved for using Kepler's laws, and the M dwarf Roche lobe filling factor, $R_{\rm MD}/R_L$, (i.e.,, how much of its Roche lobe is filled), is solved for using the Eggleton (1983b) relation

$$\frac{R_L}{a} = \frac{0.49q^{2/3}}{0.6q^{2/3} + \ln\left(1 + q^{1/3}\right)}, \tag{8.3}$$

where $q = M_{\rm MD}/M_{\rm WD}$ is the mass ratio of the two objects.

GLEAM-X J0704–37: WD or NS?

It is unlikely that the primary companion star to the M dwarf could be anything other than a WD. No main sequence star could fit in so compact an orbit. I speculate that in order to produce strong radio emission, the WD must be magnetic. Two known WD pulsars indeed host magnetic WDs in a 3–4 h orbits with an M dwarf (Marsh et al., 2016; Pelisoli et al., 2023a) and are discussed further in Section 8.7. A NS is disfavored, since the blue excess (shortward of ≈6500 Å) in the average optical spectrum would require a exceptionally young and nearby NS to be so optically bright (e.g.,, Walter and Matthews, 1997). Being so nearby, such a NS would also be detectable in X-rays, which has been ruled out (Hurley-Walker et al., 2024a).

8.7 Extended discussion: Connections to cataclysmic variables and white dwarf pulsars

Comparison to ILT J1101+5521: Cool and massive WDs

The discovery of ILT J1101+5521 was reported by de Ruiter et al. (2024) as an LPT with a radio pulse period of 125.5195 min (2.0912 h). Optical spectroscopy of ILT J1101+5521 revealed an M dwarf with RV variability on a very similar period (127.4 min). It is likely that ILT J1101+5521 is indeed a detached WD + MD binary, as suggested by de Ruiter et al. (2024), though absolute confirmation of this model requires spectroscopic observations over the entire period. Furthermore, both systems host rather cool, massive WDs: ≈7,300 K and ≈5,500 K; $\approx 1.02 M_{\odot}$ and $\approx 0.77 M_{\odot}$ for GLEAM-X J0704–37 and ILT J1101+5521, respectively. The WD in both systems appears to be more massive than the average isolated DA (hydrogen-atmosphere) and DB (helium-atmosphere) WDs: $0.6 M_{\odot}$ and $0.7 M_{\odot}$, respectively (Kepler et al., 2007b).

At the time of writing, the origin of radio pulses in LPTs has not been established, though a scenario for ILT J1101+5521 has been put forth (Qu and Zhang, 2024). In that model, electron cyclotron maser emission is responsible for the radio emission, requiring that the WD be strongly magnetic ($B \approx$ MG) and the M dwarf only mildly so ($B \approx$ kG). A similar situation could be the case for GLEAM-X J0704–37, though direct evidence for the magnetic nature of the WD (in either system) has not been established.

Connection to CVs and the period gap

Cataclysmic variables are mass-transferring systems in which a WD accretes from a Roche lobe-filling donor, typically a late-type star (e.g.,, Warner, 1995a; Hellier, 2001a). Magnetic CVs host a WD with a magnetic field strong enough so that the magnetosphere extends well past the WD surface and affects the accretion flow; recently, optical and X-ray surveys have revealed that 35–36% of CVs are magnetic Pala et al. (2020a); Rodriguez et al. (2025b).

CVs typically have orbital periods in the range of ≈78 min–10 h, with an observed (though highly debated) period gap between 2.2–3.2 h (e.g.,, Spruit and Ritter, 1983b; Schreiber et al., 2024b). It is believed that changes in the convective nature of the M dwarf donor star cause magnetic braking to become less efficient and accretion to temporarily stop (Spruit and Ritter, 1983b). This has been supported by a higher observed rate of detached WD + M dwarf binaries in this period range (Zorotovic

et al., 2016b). The overlap of both GLEAM-X J0704–37 and ILT J1101+5521 with the CV period gap is exciting (Figure 8.4), and may indicate that detached magnetic WD + M dwarf binaries in this orbital period range can exhibit a rich variety of radio activity. However, it may very well be the case that GLEAM-X J0704–37 has never undergone accretion, and is instead a post common envelope binary that will eventually become a CV (pre-CV). This is supported by the extremely low WD temperature, which may not have enough time to cool while crossing the gap ($\sim$ 1 Gyr), but would after emerging from common envelope ($\sim$ several Gyr).

LPTs, WD pulsars, and evolutionary links

A connection between LPTs and so-called WD "pulsars" has been made by both Hurley-Walker et al. (2024a) and de Ruiter et al. (2024) regarding GLEAM-X J0704–37 and ILT J1101+5521. The two known WD pulsars, AR Sco and J191213.72–441045.1 (henceforth J1912), show pulsed emission at radio frequencies at 1.97 and 5.30 min, respectively (Marsh et al., 2016; Pelisoli et al., 2023a). Those periods are not the binary orbital period of the system, which are instead 3.56 and 4.03 h for AR Sco and J1912, respectively (Marsh et al., 2016; Pelisoli et al., 2023a). The emission mechanism in WD pulsars is unclear, with it currently being debated whether synchrotron or cyclotron dominates (Buckley et al., 2017; Stanway et al., 2018). Unlike typical NS pulsars, it is thought that radio emission is generated through particle acceleration in the interaction between the WD and M dwarf magnetospheres (Marsh et al., 2016; Pelisoli et al., 2023a). Phenomenologically, there are two major differences between WD pulsars and long LPTs:

1. *Pulse periods in WD pulsars are shorter, and associated with WD spin periods*. In WD pulsars, radio pulses are associated with the spin-orbit beat between the WD spinning at min-long timescales and several hour-long orbits.

2. *Pulses in WD pulsars are 10–100 times fainter*. AR Sco and J1912 have peak radio luminosities of $\approx 2 \times 10^{26}$erg s^{-1} at $\approx$1 GHz. GLEAM-X J0704–37 has a radio luminosity of $\approx 1.5 \times 10^{28}$erg s^{-1} (at 1 GHz, adopting a distance of 400 pc in Equation 1 of Hurley-Walker et al. (2024a)), and ILT J1101+5521 has a typical peak radio luminosity of 2×10^{27}erg s^{-1} with the highest peak reaching 1×10^{28}erg s^{-1} (both at 100 MHz).

I put forth the possibility that long LPTs represent a phase between WD pulsars and polars. Polars are the most abundant magnetic CVs (e.g.,, Pala et al., 2020a;

Rodriguez et al., 2025b), and typically have orbital periods below the period gap, in the 1.3–2.2 h regime (e.g.,, Warner, 1995a; Hellier, 2001a). WD pulsars are detached, with the Roche lobe filling factor ($R_{\rm MD}/R_L$) in AR Sco having been measured to be ≈0.8 Pelisoli et al. (2022a). Since (Pelisoli et al., 2022a) also detected that the WD in AR Sco is spinning down (to longer spin periods), WD pulsars may evolve into long LPTs. Magnetic braking in some form (e.g.,, Rappaport et al., 1983; Knigge et al., 2011; El-Badry et al., 2022) by the M dwarf will then lead it to fill its Roche lobe. At this point, accretion will commence and the system will be a polar Alternatively, accretion could commence before the WD fully spins down, which is consistent with the recent finding of a magnetic CV with a polar-like magnetic field, though with a WD spinning at 9.36 min (Rodriguez et al., 2025a).

This is qualitatively similar to the picture put forth by Schreiber et al. (2021a), further explored by Ginzburg et al. (2022), where WD pulsars are thought to evolve into polars. The WD magnetic field in this evolutionary model is thought to emerge as a result of crystallization in the WD core, which is more easily achieved in cool, massive WDs. Comparing to Figure 2 of Schreiber et al. (2021a), it is clear that both the WD in in GLEAM-X J0704–37 and that in ILT J1101+5521 are cool and massive enough to be at least somewhat crystallized. Optical polarimetry of GLEAM-X J0704–37 should be undertaken in order to assess the magnetic nature of the WD.

Finally, it could be that GLEAM-X J0704–37 and ILT J1101+5521 may be progenitors to magnetic CVs (post common envelope binaries) that have not yet experienced mass transfer. Their unusually cool WD temperatures are significantly cooler than those of WDs in a sample of detached WD + M dwarf binaries in this period range ($T_{\rm eff;\,WD} \gtrsim 10,000$ K; Zorotovic et al., 2016b), and may favor this scenario.

An emerging picture: Two classes of LPTs

I amplify the idea that there are two classes of LPTs: short ($P \lesssim 78$ min) and long' ($P \gtrsim 78$ min).[10] The dividing line between the two types in Figure 8.4 is the CV orbital period minimum of ≈78 min (e.g.,, Hellier, 2001a). Samples of CVs and AM CVns are shown in Figure 8.4, drawn from the catalogs of Ritter and Kolb (2003a) and Ramsay et al. (2018), respectively. However, there are two major caveats: 1) it is obvious that GCRT J1745-3009 is effectively on that line, and 2) the recent discovery of ASKAP J183950.5-075635.0 and its likely association with a NS spin

[10]Other works have also noted this distinction, though the relation to the CV period minimum has not been put forth.

reveals that long LPTs are not exclusively WD binaries. I primarily argue that long LPTs can be plausibly associated with orbital periods, but not short LPTs.

For any mass-transferring system with a main-sequence star as the donor, ≈78 min is the minimum orbital period at which hydrogen burning on the donor star can be sustained (Faulkner, 1971; Paczynski, 1981; Gänsicke et al., 2009). In other words, any binary system with an orbital period lower than this value cannot have a hydrogen-rich donor star.[11] Due to angular momentum losses (from magnetic braking and gravitational wave radiation), long LPTs such as GLEAM-X J0704–37 will commence accretion near the orbital period minimum, and then "bounce" back to longer periods as CVs do (e.g.,, Knigge et al., 2011), meaning they will not overlap with the population of short LPTs.

Based on this, I suggest that in general, long LPTs are associated with WD binary orbital periods, and short LPTs with compact object (WD or NS) spin periods. Short LPTs may still be associated with orbital periods of binary systems, but unlikely with those in which the lower mass component is hydrogen rich.[12] The lack of optical counterparts in short LPTs would instead point to a spin period of an optically faint WD or NS.

8.8 Full spectra and RVs

Individual spectra from Night 1 and 2 are shown in Figure 8.5 with observing logs in Table 8.3. All spectra are dominated by TiO molecular bandheads, characteristic of M dwarfs, as first revealed in the discovery paper by Hurley-Walker et al. (2024a). I detect a clear Na I doublet (8183 and 8195) in absorption in all spectra, not seen in the original discovery paper due to wavelength constraints of the spectroscopic setup. I also detect weak Hα, which was not reported in the discovery paper, demonstrating the advatage of spectroscopy from 10 m class telescopes. The K I doublet (7665 and 7699Å) is also seen in the spectrum, and yield an RV solution that is consistent with that of fitting the Na I doublet alone. However, the K I doublet is excluded from this analysis since it overlaps significantly with airmass-dependent telluric features that can alter the wavelength solution. No other obvious emission or absorption features are present.

[11] An interesting exception to this are hydrogen-rich donor stars with low metallicities, which can reach even shorter orbital periods (Stehle et al., 1997).

[12] AM CVn binaries and ultra-compact X-ray binaries (UCXBs) are examples of systems where donor stars dominated by helium and heavier elements orbit WDs and NSs, respectively, at periods below this minimum (e.g.,, Nelemans et al., 2010).

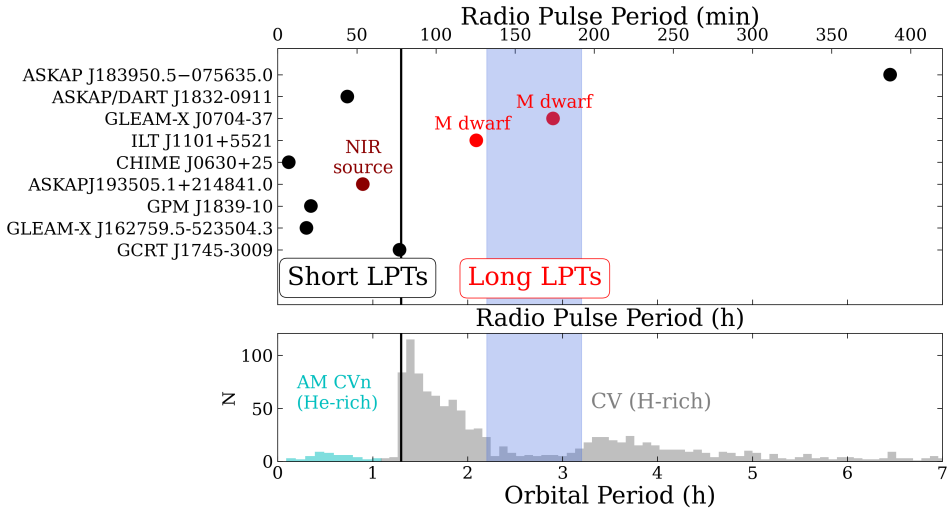

Figure 8.4: Two of the three "long LPTs" ($P \gtrsim 78$ min) are associated with orbital periods of WD + MD binaries, while "short LPTs" ($P \lesssim 78$ min) generally lack optical counterparts. The ≈78 min division (black line) corresponds to the orbital period minimum of any binary containing a Roche lobe-filling H-rich donor star, seen in the observed period distribution of CVs. The recent discovery of ASKAP J183950.5-075635.0 and its likely association with an NS spin suggests that "long LPTs" are not exclusively associated with WD orbits. Two of the three known "long LPTs" nearly coincide with the CV "period gap", where accretion is thought to temporarily shut off (blue band).

Even in the 1.3 h total observation from Night 1, radial velocity (RV) variations of the Na I doublet from the M dwarf are clearly seen. The measured RVs and ensuring MCMC parameter exploration of the RV model (Equation 8.2) are presented in Table 8.4 and Figure 8.6, respectively. The 3 h total observation from Night 2 shows the entire RV curve filled out, although by shallower Na I absorption lines, likely due to the presence of high clouds on that night. Some features in the red spectra of the second night could be attributed to cosmic rays or poor telluric subtraction, but are shown here for full transparency, namely the apparent emission feature at ≈6650–6670Å in the first and seventh spectra of Night 2. Follow-up observations should confirm or refute the presence of such features.

8.9 Origin of the Hα emission, frame shifting, and cartoons of the geometry

Doppler tomography reveals the Hα emission to be coincident with the orbital phase of the donor star, though with a higher RV. This means that the bulk of the Hα emission originates from outside the M dwarf. Figure 8.2, however, is not a spatial representation of the system — rather, I explore two possible scenarios that

Date	Exposures	Total Time (h)	Conditions	Airmass
Night 1: 08 Nov 2024	5×900 s	1.3	Light cirrus; 1.1" seeing	1.8–2.0
Night 2: 30 Nov 2024	11×900 s	3.0	Moderate cirrus; 0.9" seeing	1.8–2.5

Table 8.3: Keck I/LRIS observation log of GLEAM-X J0704–37. The blue (red) side was binned at 2x2 (2x1) (spatial vs spectral axis). The 600/4000 grism was used on the blue side, and 400/8500 grating on the red side, leading to a resolution of approximately 1.2 and 1.1Å , respectively. Total time includes read-out between consecutive exposures.

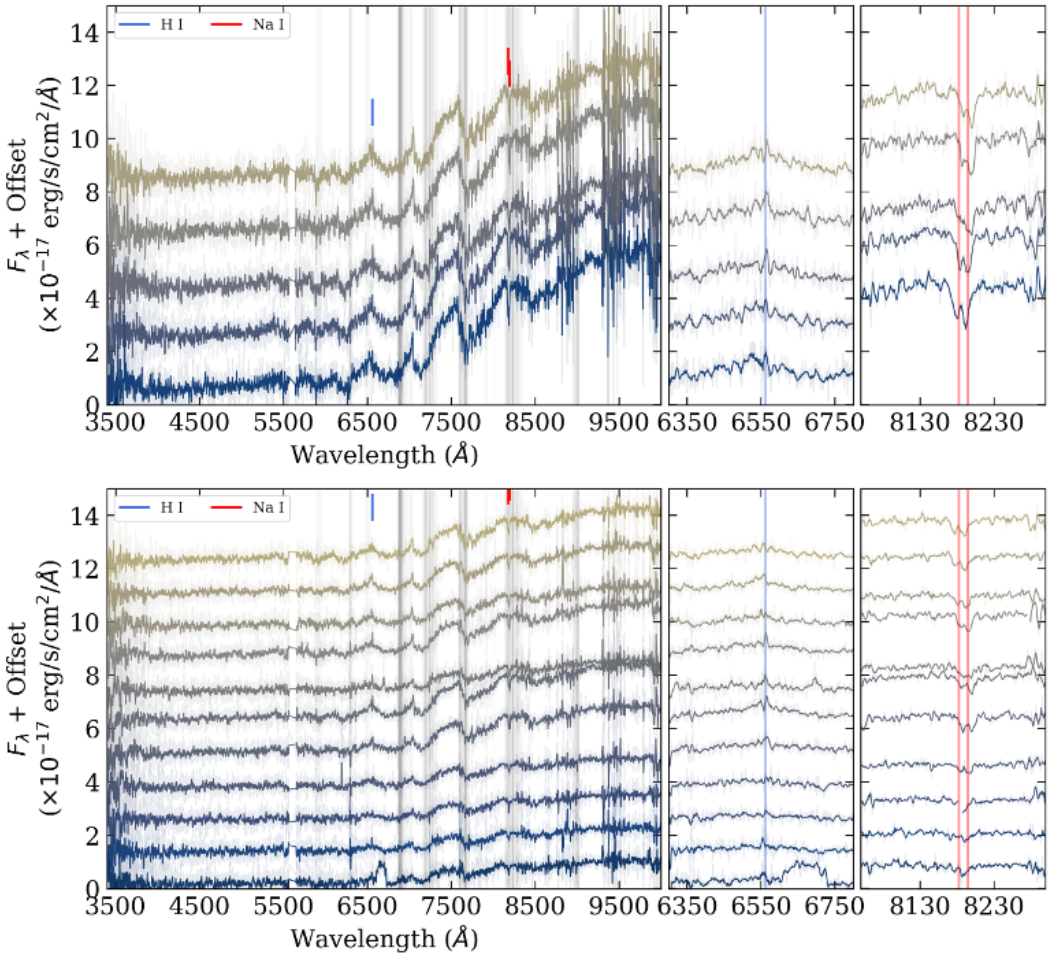

Figure 8.5: Keck I/LRIS 900-s exposures (top: Night 1, bottom: Night 2) of GLEAM-X J0704–37 reveal 2.9 h RV variability of an M dwarf star in the binary system. Gray bands indicate telluric features.

MJD (BJD_{TDB})	RV (km s^{-1})	σ_{RV} (km s^{-1})
60622.579392	-161	10
60622.590561	-80	8
60622.601730	40	11
60622.612899	80	15
60622.624067	80	13
60644.432526	-322	11
60644.443907	-201	13
60644.455099	-	-
60644.466292	0	3
60644.477483	80	3
60644.488663	0	10
60644.499879	40	30
60644.511071	-40	5
60644.522264	-161	5
60644.533444	-241	6
60644.544625	-282	6

Table 8.4: RV measurements and errors of each exposure from Night 1 and Night 2. Times shown are the mid-exposure times (of 900s exposures in all cases), and have been barycentric-corrected.

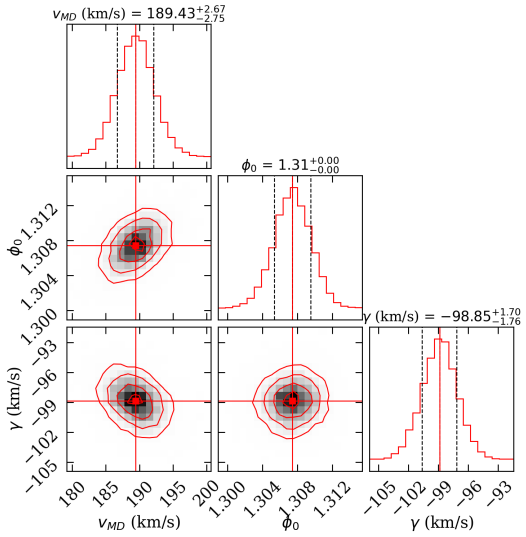

Figure 8.6: Corner plot of the MCMC analysis used to constrain RV parameters.

could lead to the observed $\approx$ 330 km s^{-1} Hα emission (which is higher than the 189 $\pm$ 3 km s^{-1} RV amplitude of the M dwarf):

1. A compact emission region co-rotating with the M dwarf, but at higher orbital separation.

2. Emission from material falling onto the M dwarf.

The geometry of both scenarios is visually outlined below. It is unlikely that the emission region would be located between the WD and M dwarf. The Doppler tomogram shows that the emission region is locked with the M dwarf at the same orbital phase, meaning that they have the same angular velocity, ω. Since $v = r\omega$, where r is the distance from the center of mass, this means that in order to see a higher velocity, the material would have to be located farther from the center of mass than the M dwarf. A way around this would be for the emission region to be in Keplerian orbit (i.e.,, not locked with the M dwarf) around the WD. However, this would mean that the material is localized to a small region (i.e.,, not a disk), and it is highly unlikely that we would see the orbital phase of the emission region coincide with that of the M dwarf in one, much less both observing runs. It could also be possible that the Na I absorption line could emerge from the side of the M dwarf facing the WD while Hα emission originates from the center of mass of the M dwarf; however, this is unlikely given the large difference in velocities and previous findings in the CV literature (e.g.,, Wade and Horne, 1988; Schwope et al., 2011).

In Figure 8.7, I show the average spectrum around the Hα line in the frame of the binary system (adding all spectra without any shifts; black), frame of the M dwarf (adding all spectra by shifting each one by the corresponding M dwarf RV; blue), and frame of the M dwarf but with an RV amplitude of 330km s^{-1} (adding all spectra by shifting each one by 1.7 times the corresponding M dwarf RV; red). This shows that the strongest, sharpest emission is resolved when shifting into the 330km s^{-1} frame, though signal-to-noise also builds up in the frame of the M dwarf. This exercise demonstrates that, independent of any model assumptions made, other than the measurement of the M dwarf RV curve with the Na I doublet, that Hα emission comes from outside of the M dwarf.

In Figure 8.8, I show cartoons of two possible scenarios that could lead to the observed Hα emission. The two criteria to be met are: 1) the emission region must coincide with the orbital phase of the M dwarf and 2) must be seen to have an RV

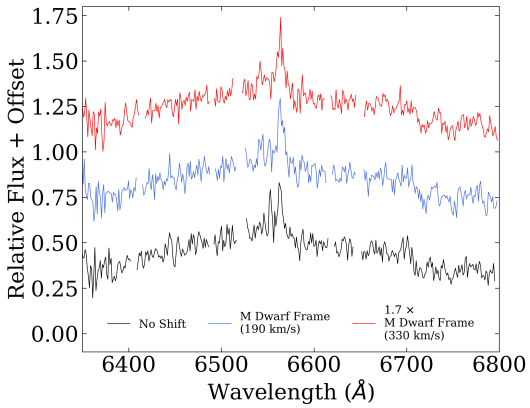

Figure 8.7: Average Hα line profile after shifting into the reference frame of the binary (black), M dwarf (blue), and 1.7 times the velocity of the M dwarf (red). This demonstrates that Hα is strongest and sharpest when shifting into the latter frame. This result only depends on the measured RV curve of the M dwarf from the Na I doublet, and is independent of any M dwarf parameter estimation.

of 330 km s^{-1}, around 1.7 times that of the M dwarf. I speculate that the same phenomenon which powers the radio pulses also powers the Hα emission, and I draw the cartoons in Figure 8.8 in the orbital configuration (ascending node) where the radio pulses are observed (Figure 8.1).

In the first scenario, material would be locked with the M dwarf, but located at a higher orbital separation, $a_{\rm emission} = 1.7 a_{\rm MD}$. Taking $a = 0.99 R_\odot \implies a_{\rm MD} = 0.85 R_\odot$, This corresponds to $a_{\rm emission} = 1.5 R_\odot$ and confirms that the emission must originate from outside of the M dwarf. In the second scenario, the material would be falling in toward the M dwarf, potentially magnetically channeled. At that velocity, the free-fall height from the M dwarf center of mass would be $\sqrt{2GM_{\rm MD}/h}$, corresponding to $h \approx 0.45 R_\odot$, also well outside the surface of the M dwarf.

Connection to the 3.6 h post common envelope WD + M dwarf QS Vir

As a final note, the resemblance of this Hα Doppler tomogram to at least one of QS Vir, a post common envelope WD + M dwarf in a 3.6 h binary only $\approx$ 50 pc away, is intriguing. Figure 7 of Ribeiro et al. (2010) shows a similar picture to Figure 8.2 in this work — some Hα emission is associated with the M dwarf, yet a large fraction of it spills past the Roche lobe and originates from higher velocity. Ribeiro et al. (2010) argued that this was evidence of magnetic confinement in a prominence-like magnetic loop. However, this is not the case in Figure 5 of Parsons et al. (2016), where spectra obtained at a later date revealed no Hα emission at higher velocity,

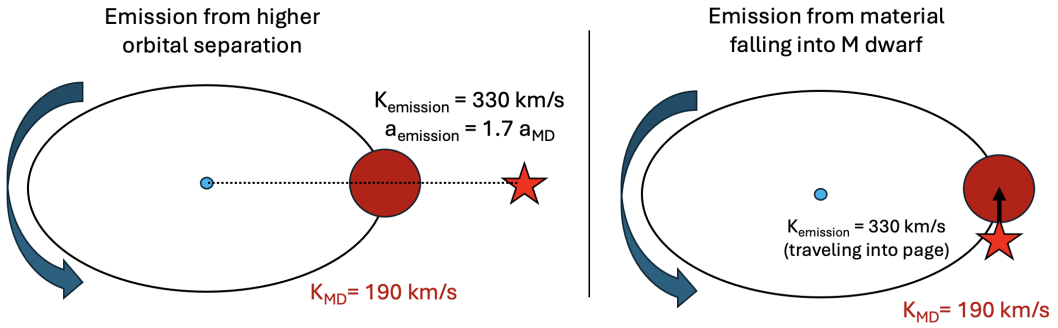

Figure 8.8: I propose two possible scenarios in which Hα emission could be generated: 1) an emission region locked with M dwarf, co-orbiting the WD, though 1.7 times farther away from the WD; 2) an emission region originating from material falling into the WD, either through free-fall or by being magnetically channeled. Both diagrams are shown at the ascending node, where the radio pulses occur.

but instead some emission localized to different orbital phases. Recently, QS Vir was identified as a radio source in the VLA Sky Survey (VLASS) by Ridder et al. (2023). Follow-up of that source revealed a variable circularly polarized component in addition to a constant low-polarization component (Ridder et al., 2023). However, it appears that QS Vir has not been observed for an entire orbital period in the radio, which is necessary to search for pulsations. Upcoming radio campaigns should target post common envelope-binaries to investigate the occurrence rate of LPTs among them. Curiously, a survey of WD candidates in a crossmatch between *Gaia* and VLASS has revealed at most one candidate, suggesting that such systems may be rare, or radio-faint (Pelisoli et al., 2024).

8.10 MCMC corner plots

Prior information on distance and extinction

GLEAM-X J0704–37 is located at Galactic coordinates of $\ell = 247.912298°, b = -13.62183°$. The low Galactic latitude corresponds to low, but non-negligible extinction: the 2D map of Schlafly and Finkbeiner (2011b) estimates a value of $E(B-V) = 0.25$ while the 3D map of Lallement et al. (2022) estimates a value of $A_{550\,\mathrm{nm}} = 0.821$ at its maximum reach of 800 pc, which corresponds to $E(B-V) \approx 0.28$. The map of Edenhofer et al. (2024) is ultimately used, as described in the main text, which leads to $E(B-V) \approx 0.12$.

Notably, the distance to the system is poorly constrained a priori. Its *Gaia* DR3 (DR2) parallax of -0.22 ± 0.98 (0.4 ± 1.1) mas implies a distance of $3.9^{+3.0}_{-1.5}$ ($1.8^{+1.7}_{-0.9}$) kpc as estimated by Bailer-Jones et al. (2021c) (Bailer-Jones et al. (2018)). Hurley-

Parameter	Value
$E(B-V)$	0.3 (fixed)
$T_{\rm WD}$ (K)	7460^{+860}_{-540}
$R_{\rm WD}$ ($R_\odot$)	$0.0103^{+0.0017}_{-0.0017}$
$T_{\rm MD}$ (K)	3050 ± 20
$R_{\rm MD}$ ($R_\odot$)	$0.172^{+0.005}_{-0.004}$
d (pc)	364^{+15}_{-12}
$M_{\rm WD}$ ($M_\odot$)	$0.82^{+0.14}_{-0.12}$
$M_{\rm MD}$ ($M_\odot$)	0.143 ± 0.005
a ($R_\odot$)	$1.01^{+0.05}_{-0.04}$
q	$0.174^{+0.030}_{-0.026}$
$R_{\rm MD}/R_L$	0.698 ± 0.001
i (°)	32^{+2}_{-3}

Table 8.5: Same as Table 8.2, but fixing $E(B-V) = 0.3$. The parameter that is most strongly affected is the inferred WD mass, reducing the median value from 1.02 to $0.82 M_\odot$. Since higher values of extinction are unlikely, it appears that the WD must be above the mean WD mass of single WDs ($0.6 M_\odot$; Kepler et al., 2007b).

Walker et al. (2024a) report that electron density models of the Milky Way report lead to modest distance estimates of 0.4 ± 0.1 (Yao et al., 2017) and 1.8 ± 0.5 kpc (Cordes, 2004). Since *Gaia* does not detect a significant parallax, I favor an a priori assumption that the distances implied by electron density models are favored, and expect the system to be located within 2 kpc, with the extinction to be at most $E(B-V) = 0.3$.

In addition to the MCMC analysis described in the main text, I ran another routine identical to the one adopted in the main text, but fixing $E(B-V) = 0.3$. This was done in order to produce the lowest possible mass WD (since higher extinction values lead to higher WD radii). The table of parameters and ensuing corner plot are shown in Table 8.10 and Figure 8.9, respectively. Even assuming extreme values of extinction, it appears that the WD in the system is massive, taking on a value of $0.82 M_\odot$ with $E(B-V) = 0.3$.

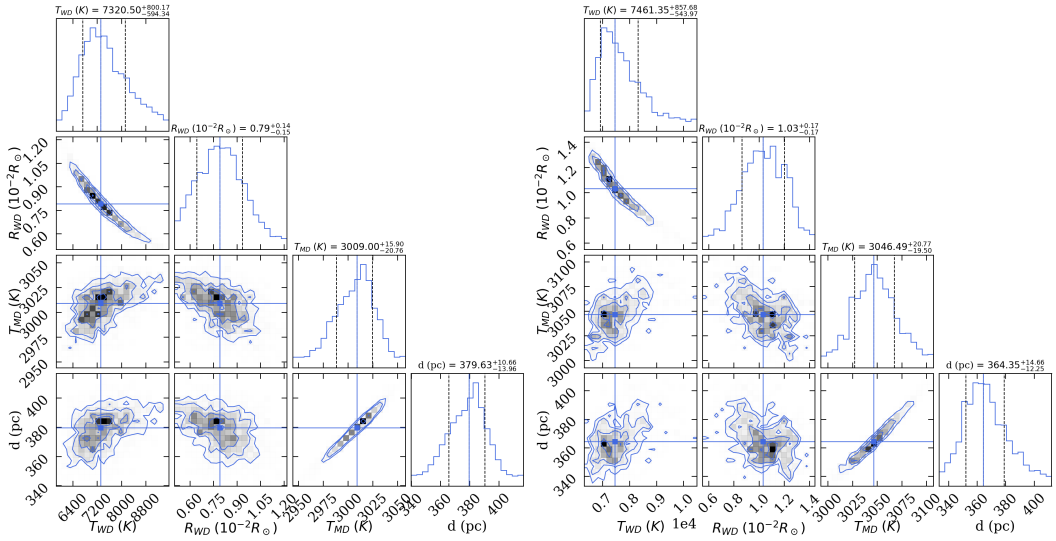

Figure 8.9: Corner plots resulting from the MCMC analysis. *Left:* Letting $E(B-V)$ depend on the distance according to the 3D map of Edenhofer et al. (2024). *Right:* Fixing $E(B-V) = 0.3$, which is likely the highest possible value. This leads to a lower inferred WD mass, though which still exceeds that of the mean single WD in the field (0.6 $M_\odot$ for a DA WD; Kepler et al., 2007b).

Chapter 9

CONCLUSION

Thus we arrive at the end of this PhD thesis. I will conclude with what some of the main takeaways and contributions to the field were, along with some predictions as to how the fields of time-domain optical, X-ray, and radio astronomy will progress over the next decade.

9.1 Novel Contributions

The main contributions of this thesis are the following:

1. *The X-ray Main Sequence*. I rejuvenated this discovery tool and generated the most uniformly created catalog of CVs and AM CVns to date. It takes advantage of the treasure trove of X-ray and optical data available in today's era of "big data" astronomy and allows for efficient discovery. In the next few years, the pipeline is simple: 1) Use the X-ray Main Sequence to make discoveries in (Rubin LSST/ZTF) + SRG/eROSITA, and assign important targets for follow-up spectroscopy with multiplexed spectrographs (SDSS-V/DESI/WEAVE/4MOST) or classical large telescope follow-up.

2. *CVs come in even more flavors than seen before*. My discovery of SRGeJ0411 — the first eclipsing magnetic period bouncer — showed that such systems do exist, but just need to be discovered via X-rays. My characterization of Gaia22ayj as a link between WD pulsars and polars showed that magnetic CVs can undergo rapid changes in their evolution, since such systems are rare. Population synthesis work in the future must account for the formation and evolution of such systems in order to form a holistic view of CV evolution.

3. *On average, CVs are less X-ray luminous than previously observed, but just as elusive.* I showed this through the volume-limited survey and updated X-ray luminosity function that I generated from the SRG/eROSITA eRASS1 survey. This demonstrates that there are no "missing period bouncers" or other low-accretion rate CVs, as had been previously suggested. Instead, the higher numbers of CVs predicted by population synthesis could be explained by mergers, loss of orbital contact, or simply a slower evolution in the latest stages of a CV's life.

4. *Symbiotic BHs must exist, and isolated BHs are nearly impossible to discover with X-rays alone.* My investigations into the nature of accretion in Gaia BH1 and BH2 showed that symbiotic BH XRBs must exist, although rare. They could be masquerading in all-sky surveys as red giants with very weak

signatures of mass transfer. Finally, I showed that reduced accretion rates and efficiencies characterized of hot accretion flows (not Bondi accretion) onto stellar-mass BHs reduces the amount of detectable ISM-accreting systems to nearly zero. Isolated BHs may still be detectable by photometric/astrometric microlensing, or creative X-ray/radio/infrared targeting of the nearest molecular clouds.

5. *Some long period radio transients (LPTs) are WD + M dwarf systems, and harbor massive, crystallized WDs.* I conducted the first optical spectroscopy of an LPT that had been associated with an M dwarf and showed that a binary system was indeed present. This discovery opens up investigations into the evolution and history of such systems, as well as the radiation mechanisms responsible for sharply pulsed radio emission repeating once per orbit. I look forward to upcoming radio surveys that will discover dozens more of these objects in the coming years.

9.2 The Future

Next year, in 2026, the first release of the largest time-domain survey ever conducted, the Rubin Observatory Legacy Survey of Space and Time (LSST), will take place (Tyson, 2002; Ivezic et al., 2019a). It will go about 3 magnitudes deeper than ZTF, though mostly covering the Southern sky. Given the amount of novel ZTF discoveries that are still emerging, it is likely that LSST will provide a large amount of new and exciting sources to study.

In the X-ray sky, SRG/eROSITA will have its second release in mid 2026, presumably of the eRASS2 and stacked eRASS:2 all-sky surveys (Merloni et al., 2024). The final SRG/eROSITA release is scheduled for late 2028, and will include all 4.4 surveys, including the stacked survey, which should reach a depth of $F_X \sim 1 \times 10^{-14}$erg s^{-1}cm^{-2}. AXIS will likely be lauched in the mid 2030s, and will conduct deep surveys of the Galactic Plane and clusters with unprecedented localization (Reynolds et al., 2023). However, given the existing amount of such sources from *Chandra*, it seems that the advent of 30m-class telescopes for optical characterization of faint sources in crowded fields will be more important than the initial detection of X-ray emitters.

Most exciting will probably be the radio sky. Surveys with the DSA-110 are in full force, with funding for DSA-2000 secured and construction proceeding (Ravi et al., 2023). Since Galactic radio sources tend to be faint, it is likely that deeper radio

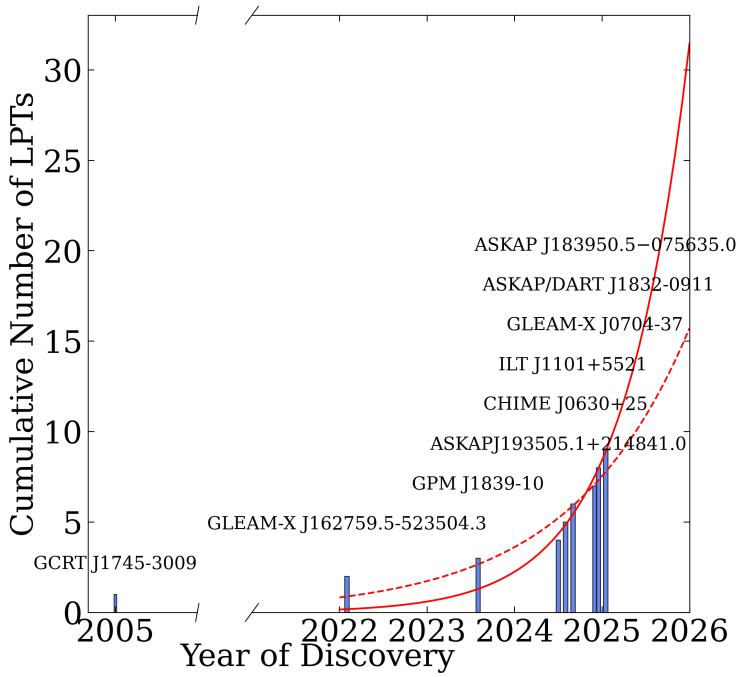

Figure 9.1: The field of LPTs is rapidly growing, showing exponential growth since 2022. An exponential fit to the data starting in 2023 (2022) suggests that 30 (15) LPTs will be be known by the end of 2025, with dozens more over the following years.

surveys hold the key to systematic discovery of stellar radio sources (Ayala et al., 2024). Supplementing radio catalogs with time-domain ZTF data and *Gaia* proper motions and parallaxes, as has been done in the X-ray in this thesis, is an attractive future pursuit. The field of LPTs is also just gearing up. A simple extrapolation of expected LPTs by the end of 2026 predicts that two to three dozen will be known, likely leading to an explosion of understanding in that field. Figure 9.1 presents estimates of the discovered population LPTs in the coming year.

Finally, in the mid- to late-2030s, the Laser Interferometer Space Antenna (*LISA*) will provide a gravitational wave window into ultracompact binaries, with AM CVns making up over half of the current "verification" sources (Kupfer et al., 2024). That will finally lead to a multiwavelength, time-domain, and multimessenger picture of AM CVns, and any remaining very nearby CVs that have not been discovered may additionally show up as new sources (Scaringi et al., 2023).

Given all of these, I hope to conduct the following investigations:

1. A crossmatch of upcoming SRG/eROSITA releases with ZTF and Rubin

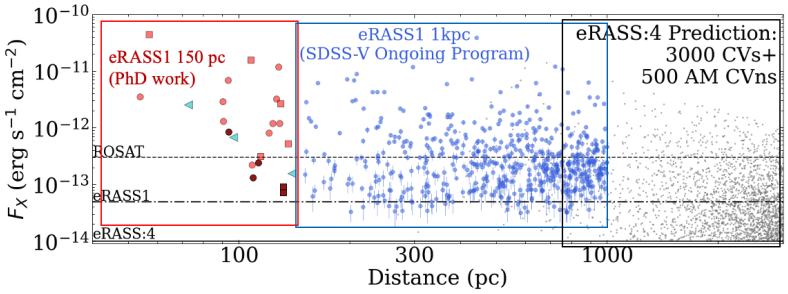

Figure 9.2: The full eRASS:4 catalog will reveal thousands of new CVs and accreting compact binaries. Current SDSS-V spectroscopy of those within 1 kpc will inform the full picture of such systems.

LSST data. Hundreds to thousands of more CVs will be revealed, along with possible quiescent NS and BH systems in close binaries. Figure 9.2 shows the expected number of such systems, which I am already targeting with SDSS-V.

2. Optical follow-up of LPTs and localization of LPTs discovered with large positional uncertainties. Currently, there are CHIME-discovered sources that are localized to arcminutes, not arcseconds, hindering the potential for multiwavelength follow-up. Multiplexed spectrographs and/or high-speed photometry are the most promising tools for localization.

3. Something completely different. New tools and datasets are quickly emerging in astronomy. The world of artificial intelligence (AI) has begun to influence research directions across science, and it could be that deep learning tools are even more powerful for detecting rare and interesting binaries. Within the next ten years, the Roman survey will have taken place, Rubin LSST will be in full force, and early releases of UVEX (ultraviolet) and DSA-2000 (radio) will continue to open up the multiwavelength sky. I hope to continue my mix of large surveys and targeted studies to advance our understanding of stellar and high-energy astrophysics.

Every time a new window is opened into the Universe, it is clear that exciting new discoveries and new understanding will lie ahead. The present time is the best time to be doing astronomy, and for the foreseeable future, astronomy as a field is poised to become more fruitful and exciting than ever.

Bibliography

E. S. Abrahams, J. S. Bloom, P. Szkody, H.-W. Rix, and N. Mowlavi. Informing the Cataclysmic Variable Sequence from Gaia Data: The Orbital-period-Color-Absolute-magnitude Relationship. *The Astrophysical Journal*, 938(1):46, Oct. 2022. doi: 10.3847/1538-4357/ac87ab.

J. Abril, L. Schmidtobreick, A. Ederoclite, and C. López-Sanjuan. Disentangling cataclysmic variables in Gaia's HR diagram. *Monthly Notices of the Royal Astronomical Society*, 492(1):L40–L44, Feb. 2020. doi: 10.1093/mnrasl/slz181.

W. S. Adams. The Spectrum of the Companion of Sirius. *Publications of the Astronomical Society of the Pacific*, 27(161):236, Dec. 1915. doi: 10.1086/122440.

E. Agol and M. Kamionkowski. X-rays from isolated black holes in the Milky Way. *Monthly Notices of the Royal Astronomical Society*, 334(3):553–562, Aug. 2002. doi: 10.1046/j.1365-8711.2002.05523.x.

M. A. Agüeros, S. F. Anderson, K. R. Covey, S. L. Hawley, B. Margon, E. R. Newsom, B. Posselt, N. M. Silvestri, P. Szkody, and W. Voges. X-Ray-Emitting Stars Identified from the ROSAT All-Sky Survey and the Sloan Digital Sky Survey. *The Astrophysical Journal Supplement Series*, 181(2):444–465, Apr. 2009. doi: 10.1088/0067-0049/181/2/444.

T. Ak, S. Bilir, A. Özdönmez, F. Soydugan, E. Soydugan, Ç. Püsküllü, S. Ak, and Z. Eker. The Galactic kinematics of cataclysmic variables. *Astrophysics and Space Science*, 357(1):72, May 2015. doi: 10.1007/s10509-015-2245-3.

S. Akras, L. Guzman-Ramirez, M. L. Leal-Ferreira, and G. Ramos-Larios. A Census of Symbiotic Stars in the 2MASS, WISE, and Gaia Surveys. *The Astrophysical Journal Supplement Series*, 240(2):21, Feb. 2019. doi: 10.3847/1538-4365/aaf88c.

F. Allard, D. Homeier, and B. Freytag. Model Atmospheres From Very Low Mass Stars to Brown Dwarfs. In C. Johns-Krull, M. K. Browning, and A. A. West, editors, *16th Cambridge Workshop on Cool Stars, Stellar Systems, and the Sun*, volume 448 of *Astronomical Society of the Pacific Conference Series*, page 91, Dec. 2011a. doi: 10.48550/arXiv.1011.5405.

F. Allard, D. Homeier, and B. Freytag. Model Atmospheres From Very Low Mass Stars to Brown Dwarfs. In C. Johns-Krull, M. K. Browning, and A. A. West, editors, *16th Cambridge Workshop on Cool Stars, Stellar Systems, and the Sun*, volume 448 of *Astronomical Society of the Pacific Conference Series*, page 91, Dec. 2011b. doi: 10.48550/arXiv.1011.5405.

F. Allard, D. Homeier, and B. Freytag. Model Atmospheres From Very Low Mass Stars to Brown Dwarfs. In C. Johns-Krull, M. K. Browning, and A. A. West,

editors, *16th Cambridge Workshop on Cool Stars, Stellar Systems, and the Sun*, volume 448 of *Astronomical Society of the Pacific Conference Series*, page 91, Dec. 2011c. doi: 10.48550/arXiv.1011.5405.

D. A. Allen, M. J. Ward, and A. R. Hyland. The near-infrared continua of BL Lacertae objects. *Monthly Notices of the Royal Astronomical Society*, 199:969–978, June 1982. doi: 10.1093/mnras/199.4.969.

A. Almeida, S. F. Anderson, M. Argudo-Fernández, C. Badenes, K. Barger, J. K. Barrera-Ballesteros, C. F. Bender, E. Benitez, F. Besser, J. C. Bird, D. Bizyaev, M. R. Blanton, J. Bochanski, J. Bovy, W. N. Brandt, J. R. Brownstein, J. Buchner, E. Bulbul, J. N. Burchett, M. Cano Díaz, J. K. Carlberg, A. R. Casey, V. Chandra, B. Cherinka, C. Chiappini, A. A. Coker, J. Comparat, C. Conroy, G. Contardo, A. Cortes, K. Covey, J. D. Crane, K. Cunha, C. Dabbieri, J. W. Davidson, M. C. Davis, A. B. de Andrade Queiroz, N. De Lee, J. E. Méndez Delgado, S. Demasi, F. Di Mille, J. Donor, P. Dow, T. Dwelly, M. Eracleous, J. Eriksen, X. Fan, E. Farr, S. Frederick, L. Fries, P. Frinchaboy, B. T. Gänsicke, J. Ge, C. González Ávila, K. Grabowski, C. Grier, G. Guiglion, P. Gupta, P. Hall, K. Hawkins, C. R. Hayes, J. J. Hermes, L. Hernández-García, D. W. Hogg, J. A. Holtzman, H. J. Ibarra-Medel, A. Ji, P. Jofre, J. A. Johnson, A. M. Jones, K. Kinemuchi, M. Kluge, A. Koekemoer, J. A. Kollmeier, M. Kounkel, D. Krishnarao, M. Krumpe, I. Lacerna, P. J. A. Lago, C. Laporte, C. Liu, A. Liu, X. Liu, A. R. Lopes, M. Macktoobian, S. R. Majewski, V. Malanushenko, D. Maoz, T. Masseron, K. L. Masters, G. Matijevic, A. McBride, I. Medan, A. Merloni, S. Morrison, N. Myers, S. Mészáros, C. A. Negrete, D. L. Nidever, C. Nitschelm, D. Oravetz, A. Oravetz, K. Pan, Y. Peng, M. H. Pinsonneault, R. Pogge, D. Qiu, S. V. Ramirez, H.-W. Rix, D. Fernández Rosso, J. Runnoe, M. Salvato, S. F. Sanchez, F. A. Santana, A. Saydjari, C. Sayres, K. C. Schlaufman, D. P. Schneider, A. Schwope, J. Serna, Y. Shen, J. Sobeck, Y.-Y. Song, D. Souto, T. Spoo, K. G. Stassun, M. Steinmetz, I. Straumit, G. Stringfellow, J. Sánchez-Gallego, M. Taghizadeh-Popp, J. Tayar, A. Thakar, P. B. Tissera, A. Tkachenko, H. Hernandez Toledo, B. Trakhtenbrot, J. G. Fernández-Trincado, N. Troup, J. R. Trump, S. Tuttle, N. Ulloa, J. A. Vazquez-Mata, P. Vera Alfaro, S. Villanova, S. Wachter, A.-M. Weijmans, A. Wheeler, J. Wilson, L. Wojno, J. Wolf, X.-X. Xue, J. E. Ybarra, E. Zari, and G. Zasowski. The Eighteenth Data Release of the Sloan Digital Sky Surveys: Targeting and First Spectra from SDSS-V. *The Astrophysical Journal Supplement Series*, 267(2):44, Aug. 2023. doi: 10.3847/1538-4365/acda98.

P. Amaro-Seoane, H. Audley, S. Babak, J. Baker, E. Barausse, P. Bender, E. Berti, P. Binetruy, M. Born, D. Bortoluzzi, J. Camp, C. Caprini, V. Cardoso, M. Colpi, J. Conklin, N. Cornish, C. Cutler, K. Danzmann, R. Dolesi, L. Ferraioli, V. Ferroni, E. Fitzsimons, J. Gair, L. Gesa Bote, D. Giardini, F. Gibert, C. Grimani, H. Halloin, G. Heinzel, T. Hertog, M. Hewitson, K. Holley-Bockelmann, D. Hollington, M. Hueller, H. Inchauspe, P. Jetzer, N. Karnesis, C. Killow, A. Klein, B. Klipstein, N. Korsakova, S. L. Larson, J. Livas, I. Lloro, N. Man, D. Mance, J. Martino, I. Mateos, K. McKenzie, S. T. McWilliams, C. Miller,

G. Mueller, G. Nardini, G. Nelemans, M. Nofrarias, A. Petiteau, P. Pivato, E. Plagnol, E. Porter, J. Reiche, D. Robertson, N. Robertson, E. Rossi, G. Russano, B. Schutz, A. Sesana, D. Shoemaker, J. Slutsky, C. F. Sopuerta, T. Sumner, N. Tamanini, I. Thorpe, M. Troebs, M. Vallisneri, A. Vecchio, D. Vetrugno, S. Vitale, M. Volonteri, G. Wanner, H. Ward, P. Wass, W. Weber, J. Ziemer, and P. Zweifel. Laser Interferometer Space Antenna. *arXiv e-prints*, art. arXiv:1702.00786, Feb. 2017. doi: 10.48550/arXiv.1702.00786.

P. Amaro-Seoane, J. Andrews, M. Arca Sedda, A. Askar, Q. Baghi, R. Balasov, I. Bartos, S. S. Bavera, J. Bellovary, C. P. L. Berry, E. Berti, S. Bianchi, L. Blecha, S. Blondin, T. Bogdanović, S. Boissier, M. Bonetti, S. Bonoli, E. Bortolas, K. Breivik, P. R. Capelo, L. Caramete, F. Cattorini, M. Charisi, S. Chaty, X. Chen, M. Chruślińska, A. J. K. Chua, R. Church, M. Colpi, D. D'Orazio, C. Danielski, M. B. Davies, P. Dayal, A. De Rosa, A. Derdzinski, K. Destounis, M. Dotti, I. DuÅ£an, I. Dvorkin, G. Fabj, T. Foglizzo, S. Ford, J.-B. Fouvry, A. Franchini, T. Fragos, C. Fryer, M. Gaspari, D. Gerosa, L. Graziani, P. Groot, M. Habouzit, D. Haggard, Z. Haiman, W.-B. Han, A. Istrate, P. H. Johansson, F. M. Khan, T. Kimpson, K. Kokkotas, A. Kong, V. Korol, K. Kremer, T. Kupfer, A. Lamberts, S. Larson, M. Lau, D. Liu, N. Lloyd-Ronning, G. Lodato, A. Lupi, C.-P. Ma, T. Maccarone, I. Mandel, A. Mangiagli, M. Mapelli, S. Mathis, L. Mayer, S. McGee, B. McKernan, M. C. Miller, D. F. Mota, M. Mumpower, S. S. Nasim, G. Nelemans, S. Noble, F. Pacucci, F. Panessa, V. Paschalidis, H. Pfister, D. Porquet, J. Quenby, A. Ricarte, F. K. Röpke, J. Regan, S. Rosswog, A. Ruiter, M. Ruiz, J. Runnoe, R. Schneider, J. Schnittman, A. Secunda, A. Sesana, N. Seto, L. Shao, S. Shapiro, C. Sopuerta, N. C. Stone, A. Suvorov, N. Tamanini, T. Tamfal, T. Tauris, K. Temmink, J. Tomsick, S. Toonen, A. Torres-Orjuela, M. Toscani, A. Tsokaros, C. Unal, V. Vázquez-Aceves, R. Valiante, M. van Putten, J. van Roestel, C. Vignali, M. Volonteri, K. Wu, Z. Younsi, S. Yu, S. Zane, L. Zwick, F. Antonini, V. Baibhav, E. Barausse, A. Bonilla Rivera, M. Branchesi, G. Branduardi-Raymont, K. Burdge, S. Chakraborty, J. Cuadra, K. Dage, B. Davis, S. E. de Mink, R. Decarli, D. Doneva, S. Escoffier, P. Gandhi, F. Haardt, C. O. Lousto, S. Nissanke, J. Nordhaus, R. O'Shaughnessy, S. Portegies Zwart, A. Pound, F. Schussler, O. Sergijenko, A. Spallicci, D. Vernieri, and A. Vigna-Gómez. Astrophysics with the Laser Interferometer Space Antenna. *Living Reviews in Relativity*, 26(1):2, Dec. 2023. doi: 10.1007/s41114-022-00041-y.

S. F. Anderson, D. Haggard, L. Homer, N. R. Joshi, B. Margon, N. M. Silvestri, P. Szkody, M. A. Wolfe, E. Agol, A. C. Becker, A. Henden, P. B. Hall, G. R. Knapp, M. W. Richmond, D. P. Schneider, G. Stinson, J. C. Barentine, H. J. Brewington, J. Brinkmann, M. Harvanek, S. J. Kleinman, J. Krzesinski, D. Long, J. Neilsen, Eric H., A. Nitta, and S. A. Snedden. Ultracompact AM Canum Venaticorum Binaries from the Sloan Digital Sky Survey: Three Candidates Plus the First Confirmed Eclipsing System. *The Astronomical Journal*, 130(5): 2230–2236, Nov. 2005. doi: 10.1086/491587.

N. Andronov, M. Pinsonneault, and A. Sills. Cataclysmic Variables: An Empirical

Angular Momentum Loss Prescription from Open Cluster Data. *The Astrophysical Journal*, 582(1):358–368, Jan. 2003. doi: 10.1086/343030.

M. Armas Padilla, J. M. Corral-Santana, A. Borghese, V. A. Cúneo, T. Muñoz-Darias, J. Casares, and M. A. P. Torres. UltraCompCAT: A comprehensive catalogue of ultra-compact and short orbital period X-ray binaries. *Astronomy & Astrophysics*, 677:A186, Sept. 2023. doi: 10.1051/0004-6361/202346797.

K. A. Arnaud. XSPEC: The First Ten Years. In G. H. Jacoby and J. Barnes, editors, *Astronomical Data Analysis Software and Systems V*, volume 101 of *Astronomical Society of the Pacific Conference Series*, page 17, Jan. 1996.

Astropy Collaboration, T. P. Robitaille, E. J. Tollerud, P. Greenfield, M. Droettboom, E. Bray, T. Aldcroft, M. Davis, A. Ginsburg, A. M. Price-Whelan, W. E. Kerzendorf, A. Conley, N. Crighton, K. Barbary, D. Muna, H. Ferguson, F. Grollier, M. M. Parikh, P. H. Nair, H. M. Unther, C. Deil, J. Woillez, S. Conseil, R. Kramer, J. E. H. Turner, L. Singer, R. Fox, B. A. Weaver, V. Zabalza, Z. I. Edwards, K. Azalee Bostroem, D. J. Burke, A. R. Casey, S. M. Crawford, N. Dencheva, J. Ely, T. Jenness, K. Labrie, P. L. Lim, F. Pierfederici, A. Pontzen, A. Ptak, B. Refsdal, M. Servillat, and O. Streicher. Astropy: A community Python package for astronomy. *Astronomy & Astrophysics*, 558:A33, Oct. 2013a. doi: 10.1051/0004-6361/201322068.

Astropy Collaboration, T. P. Robitaille, E. J. Tollerud, P. Greenfield, M. Droettboom, E. Bray, T. Aldcroft, M. Davis, A. Ginsburg, A. M. Price-Whelan, W. E. Kerzendorf, A. Conley, N. Crighton, K. Barbary, D. Muna, H. Ferguson, F. Grollier, M. M. Parikh, P. H. Nair, H. M. Unther, C. Deil, J. Woillez, S. Conseil, R. Kramer, J. E. H. Turner, L. Singer, R. Fox, B. A. Weaver, V. Zabalza, Z. I. Edwards, K. Azalee Bostroem, D. J. Burke, A. R. Casey, S. M. Crawford, N. Dencheva, J. Ely, T. Jenness, K. Labrie, P. L. Lim, F. Pierfederici, A. Pontzen, A. Ptak, B. Refsdal, M. Servillat, and O. Streicher. Astropy: A community Python package for astronomy. *Astronomy & Astrophysics*, 558:A33, Oct. 2013b. doi: 10.1051/0004-6361/201322068.

P. Atri, J. C. A. Miller-Jones, A. Bahramian, R. M. Plotkin, P. G. Jonker, G. Nelemans, T. J. Maccarone, G. R. Sivakoff, A. T. Deller, S. Chaty, M. A. P. Torres, S. Horiuchi, J. McCallum, T. Natusch, C. J. Phillips, J. Stevens, and S. Weston. Potential kick velocity distribution of black hole X-ray binaries and implications for natal kicks. *Monthly Notices of the Royal Astronomical Society*, 489(3): 3116–3134, Nov. 2019. doi: 10.1093/mnras/stz2335.

M. Audard, M. Güdel, A. Sres, A. J. J. Raassen, and R. Mewe. A study of coronal abundances in RS CVn binaries%. *Astronomy & Astrophysics*, 398:1137–1149, Feb. 2003. doi: 10.1051/0004-6361:20021737.

T. Augusteijn, R. Greimel, E. J. M. van den Besselaar, P. J. Groot, and L. Morales-Rueda. White dwarf-red dwarf binaries in the Sloan Digital Sky Survey. I.

Sample definition. *Astronomy & Astrophysics*, 486(3):843–853, Aug. 2008. doi: 10.1051/0004-6361:20078584.

C. Ayala, D. Dong, G. Hallinan, I. Davis, Y. Huang, and C. Law. Stellar Radio Transients in the VLA Sky Survey. In *American Astronomical Society Meeting Abstracts*, volume 243 of *American Astronomical Society Meeting Abstracts*, page 359.33, Feb. 2024.

D. C. Backer, S. R. Kulkarni, C. Heiles, M. M. Davis, and W. M. Goss. A millisecond pulsar. *Nature*, 300(5893):615–618, Dec. 1982. doi: 10.1038/300615a0.

A. Bahramian, J. Miller-Jones, J. Strader, A. Tetarenko, R. Plotkin, A. Rushton, V. Tudor, S. Motta, and L. Shishkovsky. Radio/X-ray correlation database for X-ray binaries, May 2018. URL `https://doi.org/10.5281/zenodo.1252036`.

C. A. L. Bailer-Jones, J. Rybizki, M. Fouesneau, G. Mantelet, and R. Andrae. Estimating Distance from Parallaxes. IV. Distances to 1.33 Billion Stars in Gaia Data Release 2. *The Astronomical Journal*, 156(2):58, Aug. 2018. doi: 10.3847/1538-3881/aacb21.

C. A. L. Bailer-Jones, J. Rybizki, M. Fouesneau, M. Demleitner, and R. Andrae. Estimating Distances from Parallaxes. V. Geometric and Photogeometric Distances to 1.47 Billion Stars in Gaia Early Data Release 3. *The Astronomical Journal*, 161(3):147, Mar. 2021a. doi: 10.3847/1538-3881/abd806.

C. A. L. Bailer-Jones, J. Rybizki, M. Fouesneau, M. Demleitner, and R. Andrae. Estimating Distances from Parallaxes. V. Geometric and Photogeometric Distances to 1.47 Billion Stars in Gaia Early Data Release 3. *The Astronomical Journal*, 161(3):147, Mar. 2021b. doi: 10.3847/1538-3881/abd806.

C. A. L. Bailer-Jones, J. Rybizki, M. Fouesneau, M. Demleitner, and R. Andrae. Estimating Distances from Parallaxes. V. Geometric and Photogeometric Distances to 1.47 Billion Stars in Gaia Early Data Release 3. *The Astronomical Journal*, 161(3):147, Mar. 2021c. doi: 10.3847/1538-3881/abd806.

C. A. L. Bailer-Jones, J. Rybizki, M. Fouesneau, M. Demleitner, and R. Andrae. Estimating Distances from Parallaxes. V. Geometric and Photogeometric Distances to 1.47 Billion Stars in Gaia Early Data Release 3. *The Astronomical Journal*, 161(3):147, Mar. 2021d. doi: 10.3847/1538-3881/abd806.

J. Ballet, P. Bruel, T. H. Burnett, B. Lott, and The Fermi-LAT collaboration. Fermi Large Area Telescope Fourth Source Catalog Data Release 4 (4FGL-DR4). *arXiv e-prints*, art. arXiv:2307.12546, July 2023. doi: 10.48550/arXiv.2307.12546.

T. Bao, Z. Li, and Z. Cheng. Periodic X-ray sources in the massive globular cluster 47 Tucanae: Evidence for dynamically formed cataclysmic variables. *Monthly Notices of the Royal Astronomical Society*, 521(3):4257–4276, May 2023. doi: 10.1093/mnras/stad836.

T. Bao, Z. Li, Z. Cheng, and D. Belloni. A Chandra survey of Milky Way globular clusters - IV. Periodic X-ray sources. *Monthly Notices of the Royal Astronomical Society*, 527(3):7173–7190, Jan. 2024. doi: 10.1093/mnras/stad3665.

I. Baraffe, D. Homeier, F. Allard, and G. Chabrier. New evolutionary models for pre-main sequence and main sequence low-mass stars down to the hydrogen-burning limit. *Astronomy & Astrophysics*, 577:A42, May 2015. doi: 10.1051/0004-6361/201425481.

D. A. Barros, J. R. D. Lépine, and W. S. Dias. Models for the 3D axisymmetric gravitational potential of the Milky Way galaxy. A detailed modelling of the Galactic disk. *Astronomy & Astrophysics*, 593:A108, Sept. 2016. doi: 10.1051/0004-6361/201527535.

M. Baumann, T. Boch, F.-X. Pineau, P. Fernique, C. Bot, and M. Allen. Aladin Lite v3: Behind the Scenes of a Major Overhaul. In J. E. Ruiz, F. Pierfedereci, and P. Teuben, editors, *Astronomical Society of the Pacific Conference Series*, volume 532 of *Astronomical Society of the Pacific Conference Series*, page 7, July 2022.

A. Bédard, P. Bergeron, P. Brassard, and G. Fontaine. On the Spectral Evolution of Hot White Dwarf Stars. I. A Detailed Model Atmosphere Analysis of Hot White Dwarfs from SDSS DR12. *The Astrophysical Journal*, 901(2):93, Oct. 2020. doi: 10.3847/1538-4357/abafbe.

T. Begari and T. J. Maccarone. X-ray Luminosity Versus Orbital Period of AM CVn Systems. , 51(2):227, Dec. 2023. doi: 10.48550/arXiv.2312.06007.

E. C. Bellm, S. R. Kulkarni, T. Barlow, U. Feindt, M. J. Graham, A. Goobar, T. Kupfer, C.-C. Ngeow, P. Nugent, E. Ofek, T. A. Prince, R. Riddle, R. Walters, and Q.-Z. Ye. The Zwicky Transient Facility: Surveys and Scheduler. *Publications of the Astronomical Society of the Pacific*, 131(1000):068003, June 2019a. doi: 10.1088/1538-3873/ab0c2a.

E. C. Bellm, S. R. Kulkarni, M. J. Graham, R. Dekany, R. M. Smith, R. Riddle, F. J. Masci, G. Helou, T. A. Prince, S. M. Adams, C. Barbarino, T. Barlow, J. Bauer, R. Beck, J. Belicki, R. Biswas, N. Blagorodnova, D. Bodewits, B. Bolin, V. Brinnel, T. Brooke, B. Bue, M. Bulla, R. Burruss, S. B. Cenko, C.-K. Chang, A. Connolly, M. Coughlin, J. Cromer, V. Cunningham, K. De, A. Delacroix, V. Desai, D. A. Duev, G. Eadie, T. L. Farnham, M. Feeney, U. Feindt, D. Flynn, A. Franckowiak, S. Frederick, C. Fremling, A. Gal-Yam, S. Gezari, M. Giomi, D. A. Goldstein, V. Z. Golkhou, A. Goobar, S. Groom, E. Hacopians, D. Hale, J. Henning, A. Y. Q. Ho, D. Hover, J. Howell, T. Hung, D. Huppenkothen, D. Imel, W.-H. Ip, Z. Ivezic, E. Jackson, L. Jones, M. Juric, M. M. Kasliwal, S. Kaspi, S. Kaye, M. S. P. Kelley, M. Kowalski, E. Kramer, T. Kupfer, W. Landry, R. R. Laher, C.-D. Lee, H. W. Lin, Z.-Y. Lin, R. Lunnan, M. Giomi, A. Mahabal, P. Mao, A. A. Miller, S. Monkewitz, P. Murphy, C.-C. Ngeow, J. Nordin, P. Nugent, E. Ofek, M. T. Patterson, B. Penprase, M. Porter, L. Rauch, U. Rebbapragada,

D. Reiley, M. Rigault, H. Rodriguez, J. van Roestel, B. Rusholme, J. van Santen, S. Schulze, D. L. Shupe, L. P. Singer, M. T. Soumagnac, R. Stein, J. Surace, J. Sollerman, P. Szkody, F. Taddia, S. Terek, A. Van Sistine, S. van Velzen, W. T. Vestrand, R. Walters, C. Ward, Q.-Z. Ye, P.-C. Yu, L. Yan, and J. Zolkower. The Zwicky Transient Facility: System Overview, Performance, and First Results. *Publications of the Astronomical Society of the Pacific*, 131(995):018002, Jan. 2019b. doi: 10.1088/1538-3873/aaecbe.

E. C. Bellm, C. J. Burke, M. W. Coughlin, I. Andreoni, C. M. Raiteri, and R. Bonito. Give Me a Few Hours: Exploring Short Timescales in Rubin Observatory Cadence Simulations. *The Astrophysical Journal Supplement Series*, 258(1):13, Jan. 2022. doi: 10.3847/1538-4365/ac4602.

D. Belloni and M. R. Schreiber. Formation and Evolution of Accreting Compact Objects. In *Handbook of X-ray and Gamma-ray Astrophysics. Edited by Cosimo Bambi and Andrea Santangelo*, page 129. 2023. doi: 10.1007/978-981-16-4544-0_98-1.

D. Belloni, M. R. Schreiber, M. Zorotovic, K. Ilkiewicz, J. R. Hurley, M. Giersz, and F. Lagos. No cataclysmic variables missing: higher merger rate brings into agreement observed and predicted space densities. *Monthly Notices of the Royal Astronomical Society*, 478(4):5626–5637, Aug. 2018. doi: 10.1093/mnras/sty1421.

D. Belloni, M. R. Schreiber, A. F. Pala, B. T. Gänsicke, M. Zorotovic, and C. V. Rodrigues. Evidence for reduced magnetic braking in polars from binary population models. *Monthly Notices of the Royal Astronomical Society*, 491(4):5717–5731, Feb. 2020. doi: 10.1093/mnras/stz3413.

M. I. Belvedersky, A. V. Meshcheryakov, P. S. Medvedev, and M. R. Gilfanov. SRGz: Building an Optical Cross-Match Model for the X-ray SRG/eROSITA Sources Using the Lockman Hole Data. *Astronomy Letters*, 48(2):109–125, Feb. 2022. doi: 10.1134/S1063773722020013.

P. Bergeron, F. Wesemael, P. Dufour, A. Beauchamp, C. Hunter, R. A. Saffer, A. Gianninas, M. T. Ruiz, M. M. Limoges, P. Dufour, G. Fontaine, and J. Liebert. A Comprehensive Spectroscopic Analysis of DB White Dwarfs. *The Astrophysical Journal*, 737(1):28, Aug. 2011. doi: 10.1088/0004-637X/737/1/28.

F. Bernardini, D. de Martino, K. Mukai, D. M. Russell, M. Falanga, N. Masetti, C. Ferrigno, and G. Israel. Broad-band characteristics of seven new hard X-ray selected cataclysmic variables. *Monthly Notices of the Royal Astronomical Society*, 470(4):4815–4837, Oct. 2017. doi: 10.1093/mnras/stx1494.

F. Bernardini, D. de Martino, K. Mukai, M. Falanga, and N. Masetti. 2PBC J0658.0-1746: a hard X-ray eclipsing polar in the orbital period gap. *Monthly Notices of the Royal Astronomical Society*, 489(1):1044–1053, Oct. 2019. doi: 10.1093/mnras/stz1951.

F. B. Bianco, Z. Ivezic, R. L. Jones, M. L. Graham, P. Marshall, A. Saha, M. A. Strauss, P. Yoachim, T. Ribeiro, T. Anguita, A. E. Bauer, F. E. Bauer, E. C. Bellm, R. D. Blum, W. N. Brandt, S. Brough, M. Catelan, W. I. Clarkson, A. J. Connolly, E. Gawiser, J. E. Gizis, R. Hlozek, S. Kaviraj, C. T. Liu, M. Lochner, A. A. Mahabal, R. Mandelbaum, P. McGehee, J. Neilsen, Eric H., K. A. G. Olsen, H. V. Peiris, J. Rhodes, G. T. Richards, S. Ridgway, M. E. Schwamb, D. Scolnic, O. Shemmer, C. T. Slater, A. Slosar, S. J. Smartt, J. Strader, R. Street, D. E. Trilling, A. Verma, A. K. Vivas, R. H. Wechsler, and B. Willman. Optimization of the Observing Cadence for the Rubin Observatory Legacy Survey of Space and Time: A Pioneering Process of Community-focused Experimental Design. *The Astrophysical Journal Supplement Series*, 258(1):1, Jan. 2022. doi: 10.3847/1538-4365/ac3e72.

I. F. Bikmaev, A. I. Kolbin, V. V. Shimansky, I. M. Khamitov, E. N. Irtuganov, E. A. Nikolaeva, N. A. Sakhibullin, R. I. Gumerov, R. A. Burenin, M. R. Gilfanov, I. A. Zaznobin, R. A. Krivonos, P. S. Medvedev, A. V. Meshcheryakov, S. Y. Sazonov, R. A. Sunyaev, G. A. Khorunzhev, A. V. Moiseev, E. A. Malygin, E. S. Shablovinskaya, and S. G. Zheltoukhov. SRGe J214919.3+673634—a Candidate for AM Her Variables Discovered by the eROSITA Telescope onboard the Spectrum-Roentgen-Gamma Orbital Observatory. *Astronomy Letters*, 48(9): 530–541, Sept. 2022. doi: 10.1134/S1063773722090018.

P. Bilgi. *Optimization of CCD charge transfer for ground and space-based astronomy*. PhD thesis, California Institute of Technology, Jan. 2019.

S. Bilir, S. Karaali, S. Ak, E. Yaz, and E. Hamzaoglu. Galactic longitude dependent galactic model parameters. *New Astronomy*, 12(3):234–245, Dec. 2006. doi: 10.1016/j.newast.2006.10.001.

T. Boller, M. J. Freyberg, J. Trümper, F. Haberl, W. Voges, and K. Nandra. Second ROSAT all-sky survey (2RXS) source catalogue. *Astronomy & Astrophysics*, 588: A103, Apr. 2016a. doi: 10.1051/0004-6361/201525648.

T. Boller, M. J. Freyberg, J. Trümper, F. Haberl, W. Voges, and K. Nandra. Second ROSAT all-sky survey (2RXS) source catalogue. *Astronomy & Astrophysics*, 588: A103, Apr. 2016b. doi: 10.1051/0004-6361/201525648.

T. Boller, M. J. Freyberg, J. Trümper, F. Haberl, W. Voges, and K. Nandra. Second ROSAT all-sky survey (2RXS) source catalogue. *Astronomy & Astrophysics*, 588: A103, Apr. 2016c. doi: 10.1051/0004-6361/201525648.

C. T. Bolton. Identification of Cygnus X-1 with HDE 226868. *Nature*, 235(5336): 271–273, Feb. 1972. doi: 10.1038/235271b0.

B. W. Bopp and R. E. Stencel. The FK COM stars. *The Astrophysical Journal Letters*, 247:L131–L134, Aug. 1981. doi: 10.1086/183606.

J. Bouvier, C. Bertout, W. Benz, and M. Mayor. Rotation in T Tauri stars. I. Obervations and immediate analysis. *Astronomy & Astrophysics*, 165:110–119, Sept. 1986.

S. Bowyer, E. T. Byram, T. A. Chubb, and H. Friedman. Cosmic X-ray Sources. *Science*, 147(3656):394–398, Jan. 1965. doi: 10.1126/science.147.3656.394.

E. Bozzo, A. Bahramian, C. Ferrigno, A. Sanna, J. Strader, F. Lewis, D. M. Russell, T. di Salvo, L. Burderi, A. Riggio, A. Papitto, P. Gandhi, and P. Romano. IGR J17329-2731: The birth of a symbiotic X-ray binary. *Astronomy & Astrophysics*, 613:A22, May 2018. doi: 10.1051/0004-6361/201832588.

L. L. E. Braes and G. K. Miley. Detection of Radio Emission from Cygnus X-1. *Nature*, 232:246, July 1971.

J. Braithwaite and H. C. Spruit. A fossil origin for the magnetic field in A stars and white dwarfs. *Nature*, 431(7010):819–821, Oct. 2004. doi: 10.1038/nature02934.

E. Breedt, B. T. Gänsicke, J. Girven, A. J. Drake, C. M. Copperwheat, S. G. Parsons, and T. R. Marsh. The evolutionary state of short-period magnetic white dwarf binaries. *Monthly Notices of the Royal Astronomical Society*, 423(2):1437–1449, June 2012. doi: 10.1111/j.1365-2966.2012.20965.x.

E. Breedt, B. T. Gänsicke, A. J. Drake, P. Rodríguez-Gil, S. G. Parsons, T. R. Marsh, P. Szkody, M. R. Schreiber, and S. G. Djorgovski. 1000 cataclysmic variables from the Catalina Real-time Transient Survey. *Monthly Notices of the Royal Astronomical Society*, 443(4):3174–3207, Oct. 2014. doi: 10.1093/mnras/stu1377.

H. Breytenbach, D. A. H. Buckley, P. Hakala, J. R. Thorstensen, A. Y. Kniazev, M. Motsoaledi, P. A. Woudt, S. B. Potter, V. Lipunov, E. Gorbovskoy, P. Balanutsa, and N. Tyurina. Discovery, observations, and modelling of a new eclipsing polar: MASTER OT J061451.70-272535.5. *Monthly Notices of the Royal Astronomical Society*, 484(3):3831–3845, Apr. 2019. doi: 10.1093/mnras/stz056.

J. D. Brink, D. A. H. Buckley, K. H. Nordsieck, and S. B. Potter. Spectropolarimetry with the SALT RSS. In I. S. McLean, S. K. Ramsay, and H. Takami, editors, *Ground-based and Airborne Instrumentation for Astronomy III*, volume 7735 of *Society of Photo-Optical Instrumentation Engineers (SPIE) Conference Series*, page 773517, July 2010. doi: 10.1117/12.856932.

H. Brunner, T. Liu, G. Lamer, A. Georgakakis, A. Merloni, M. Brusa, E. Bulbul, K. Dennerl, S. Friedrich, A. Liu, C. Maitra, K. Nandra, M. E. Ramos-Ceja, J. S. Sanders, I. M. Stewart, T. Boller, J. Buchner, N. Clerc, J. Comparat, T. Dwelly, D. Eckert, A. Finoguenov, M. Freyberg, V. Ghirardini, A. Gueguen, F. Haberl, I. Kreykenbohm, M. Krumpe, S. Osterhage, F. Pacaud, P. Predehl, T. H. Reiprich, J. Robrade, M. Salvato, A. Santangelo, T. Schrabback, A. Schwope, and J. Wilms. The eROSITA Final Equatorial Depth Survey (eFEDS). X-ray catalogue. *Astronomy & Astrophysics*, 661:A1, May 2022. doi: 10.1051/0004-6361/202141266.

D. A. H. Buckley, K. Sekiguchi, C. Motch, D. O'Donoghue, A.-L. Chen, A. Schwarzenberg-Czerny, W. Pietsch, and M. K. Harrop-Allin. RX J1712.6-2414: a polarized intermediate polar from the ROSAT Galactic Plane Survey. *Monthly Notices of the Royal Astronomical Society*, 275(4):1028–1048, Aug. 1995. doi: 10.1093/mnras/275.4.1028.

D. A. H. Buckley, G. P. Swart, and J. G. Meiring. Completion and commissioning of the Southern African Large Telescope. In *Society of Photo-Optical Instrumentation Engineers (SPIE) Conference Series*, volume 6267 of , page 62670Z, June 2006. doi: 10.1117/12.673750.

D. A. H. Buckley, P. J. Meintjes, S. B. Potter, T. R. Marsh, and B. T. Gänsicke. Polarimetric evidence of a white dwarf pulsar in the binary system AR Scorpii. *Nature Astronomy*, 1:0029, Jan. 2017. doi: 10.1038/s41550-016-0029.

K. B. Burdge, M. W. Coughlin, J. Fuller, T. Kupfer, E. C. Bellm, L. Bildsten, M. J. Graham, D. L. Kaplan, J. v. Roestel, R. G. Dekany, D. A. Duev, M. Feeney, M. Giomi, G. Helou, S. Kaye, R. R. Laher, A. A. Mahabal, F. J. Masci, R. Riddle, D. L. Shupe, M. T. Soumagnac, R. M. Smith, P. Szkody, R. Walters, S. R. Kulkarni, and T. A. Prince. General relativistic orbital decay in a seven-minute-orbital-period eclipsing binary system. *Nature*, 571(7766):528–531, July 2019. doi: 10.1038/s41586-019-1403-0.

K. B. Burdge, T. A. Prince, J. Fuller, D. L. Kaplan, T. R. Marsh, P.-E. Tremblay, Z. Zhuang, E. C. Bellm, I. Caiazzo, M. W. Coughlin, V. S. Dhillon, B. Gaensicke, P. Rodríguez-Gil, M. J. Graham, J. Hermes, T. Kupfer, S. P. Littlefair, P. Mróz, E. S. Phinney, J. van Roestel, Y. Yao, R. G. Dekany, A. J. Drake, D. A. Duev, D. Hale, M. Feeney, G. Helou, S. Kaye, A. A. Mahabal, F. J. Masci, R. Riddle, R. Smith, M. T. Soumagnac, and S. R. Kulkarni. A Systematic Search of Zwicky Transient Facility Data for Ultracompact Binary LISA-detectable Gravitational-wave Sources. *The Astrophysical Journal*, 905(1):32, Dec. 2020. doi: 10.3847/1538-4357/abc261.

K. B. Burdge, K. El-Badry, E. Kara, C. Canizares, D. Chakrabarty, A. Frebel, S. C. Millholland, S. Rappaport, R. Simcoe, and A. Vanderburg. The black hole low-mass X-ray binary V404 Cygni is part of a wide triple. *Nature*, 635(8038): 316–320, Nov. 2024. doi: 10.1038/s41586-024-08120-6.

E. B. Burgh, K. H. Nordsieck, H. A. Kobulnicky, T. B. Williams, D. O'Donoghue, M. P. Smith, and J. W. Percival. Prime Focus Imaging Spectrograph for the Southern African Large Telescope: optical design. In M. Iye and A. F. M. Moorwood, editors, *Instrument Design and Performance for Optical/Infrared Ground-based Telescopes*, volume 4841 of *Society of Photo-Optical Instrumentation Engineers (SPIE) Conference Series*, pages 1463–1471, March 2003. doi: 10.1117/12.460312.

D. N. Burrows, J. E. Hill, J. A. Nousek, J. A. Kennea, A. Wells, J. P. Osborne, A. F. Abbey, A. Beardmore, K. Mukerjee, A. D. T. Short, G. Chincarini, S. Campana,

O. Citterio, A. Moretti, C. Pagani, G. Tagliaferri, P. Giommi, M. Capalbi, F. Tamburelli, L. Angelini, G. Cusumano, H. W. Bräuninger, W. Burkert, and G. D. Hartner. The Swift X-Ray Telescope. *Space Science Reviews*, 120(3-4):165–195, Oct. 2005. doi: 10.1007/s11214-005-5097-2.

M. Caleb, I. Heywood, K. Rajwade, M. Malenta, B. W. Stappers, E. Barr, W. Chen, V. Morello, S. Sanidas, J. van den Eijnden, M. Kramer, D. Buckley, J. Brink, S. E. Motta, P. Woudt, P. Weltevrede, F. Jankowski, M. Surnis, S. Buchner, M. C. Bezuidenhout, L. N. Driessen, and R. Fender. Discovery of a radio-emitting neutron star with an ultra-long spin period of 76 s. *Nature Astronomy*, 6:828–836, May 2022. doi: 10.1038/s41550-022-01688-x.

M. Caleb, E. Lenc, D. L. Kaplan, T. Murphy, Y. P. Men, R. M. Shannon, L. Ferrario, K. M. Rajwade, T. E. Clarke, S. Giacintucci, N. Hurley-Walker, S. D. Hyman, M. E. Lower, S. McSweeney, V. Ravi, E. D. Barr, S. Buchner, C. M. L. Flynn, J. W. T. Hessels, M. Kramer, J. Pritchard, and B. W. Stappers. An emission-state-switching radio transient with a 54-minute period. *Nature Astronomy*, 8: 1159–1168, Sept. 2024. doi: 10.1038/s41550-024-02277-w.

M. Camisassa, J. R. Fuentes, M. R. Schreiber, A. Rebassa-Mansergas, S. Torres, R. Raddi, and I. Dominguez. Main sequence dynamo magnetic fields emerging in the white dwarf phase. *Astronomy & Astrophysics*, 691:L21, Nov. 2024. doi: 10.1051/0004-6361/202452539.

H. C. Campbell, T. R. Marsh, M. Fraser, S. T. Hodgkin, E. de Miguel, B. T. Gänsicke, D. Steeghs, A. Hourihane, E. Breedt, S. P. Littlefair, S. E. Koposov, Ł. Wyrzykowski, G. Altavilla, N. Blagorodnova, G. Clementini, G. Damljanovic, A. Delgado, M. Dennefeld, A. J. Drake, J. Fernández-Hernández, G. Gilmore, R. Gualandi, A. Hamanowicz, B. Handzlik, L. K. Hardy, D. L. Harrison, K. Iłkiewicz, P. G. Jonker, C. S. Kochanek, Z. Kołaczkowski, Z. Kostrzewa-Rutkowska, R. Kotak, G. van Leeuwen, G. Leto, P. Ochner, M. Pawlak, L. Palaversa, G. Rixon, K. Rybicki, B. J. Shappee, S. J. Smartt, M. A. P. Torres, L. Tomasella, M. Turatto, K. Ulaczyk, S. van Velzen, O. Vince, N. A. Walton, P. Wielgórski, T. Wevers, P. Whitelock, A. Yoldas, F. De Angeli, P. Burgess, G. Busso, R. Busuttil, T. Butterley, K. C. Chambers, C. Copperwheat, A. B. Danilet, V. S. Dhillon, D. W. Evans, L. Eyer, D. Froebrich, A. Gomboc, G. Holland, T. W. S. Holoien, J. F. Jarvis, N. Kaiser, D. A. Kann, D. Koester, U. Kolb, S. Komossa, E. A. Magnier, A. Mahabal, J. Polshaw, J. L. Prieto, T. Prusti, M. Riello, A. Scholz, G. Simonian, K. Z. Stanek, L. Szabados, C. Waters, and R. W. Wilson. Total eclipse of the heart: the AM CVn Gaia14aae/ASSASN-14cn. *Monthly Notices of the Royal Astronomical Society*, 452(1):1060–1067, Sept. 2015. doi: 10.1093/mnras/stv1224.

R. K. Campbell, T. E. Harrison, A. D. Schwope, and S. B. Howell. Cyclotron Modeling Phase-Resolved Infrared Spectroscopy of Polars. I. EF Eridani. *The Astrophysical Journal*, 672(1):531–539, Jan. 2008. doi: 10.1086/523632.

R. Canbay, S. Bilir, A. Özdönmez, and T. Ak. Galactic Model Parameters and Spatial Density of Cataclysmic Variables in the Gaia Era: New Constraints on Population Models. *The Astronomical Journal*, 165(4):163, Apr. 2023. doi: 10.3847/1538-3881/acbead.

J. K. Cannizzo and G. Nelemans. Constraining the Physics of AM Canum Venaticorum Systems with the Accretion Disk Instability Model. *The Astrophysical Journal*, 803(1):19, Apr. 2015. doi: 10.1088/0004-637X/803/1/19.

J. A. Cardelli, G. C. Clayton, and J. S. Mathis. The Relationship between Infrared, Optical, and Ultraviolet Extinction. *The Astrophysical Journal*, 345:245, Oct. 1989. doi: 10.1086/167900.

P. J. Carter, T. R. Marsh, D. Steeghs, P. J. Groot, G. Nelemans, D. Levitan, A. Rau, C. M. Copperwheat, T. Kupfer, and G. H. A. Roelofs. A search for the hidden population of AM CVn binaries in the Sloan Digital Sky Survey. *Monthly Notices of the Royal Astronomical Society*, 429(3):2143–2160, Mar. 2013. doi: 10.1093/mnras/sts485.

W. Cash. Parameter estimation in astronomy through application of the likelihood ratio. *The Astrophysical Journal*, 228:939–947, Mar. 1979. doi: 10.1086/156922.

K. C. Chambers, E. A. Magnier, N. Metcalfe, H. A. Flewelling, M. E. Huber, C. Z. Waters, L. Denneau, P. W. Draper, D. Farrow, D. P. Finkbeiner, C. Holmberg, J. Koppenhoefer, P. A. Price, A. Rest, R. P. Saglia, E. F. Schlafly, S. J. Smartt, W. Sweeney, R. J. Wainscoat, W. S. Burgett, S. Chastel, T. Grav, J. N. Heasley, K. W. Hodapp, R. Jedicke, N. Kaiser, R. P. Kudritzki, G. A. Luppino, R. H. Lupton, D. G. Monet, J. S. Morgan, P. M. Onaka, B. Shiao, C. W. Stubbs, J. L. Tonry, R. White, E. Bañados, E. F. Bell, R. Bender, E. J. Bernard, M. Boegner, F. Boffi, M. T. Botticella, A. Calamida, S. Casertano, W. P. Chen, X. Chen, S. Cole, N. Deacon, C. Frenk, A. Fitzsimmons, S. Gezari, V. Gibbs, C. Goessl, T. Goggia, R. Gourgue, B. Goldman, P. Grant, E. K. Grebel, N. C. Hambly, G. Hasinger, A. F. Heavens, T. M. Heckman, R. Henderson, T. Henning, M. Holman, U. Hopp, W. H. Ip, S. Isani, M. Jackson, C. D. Keyes, A. M. Koekemoer, R. Kotak, D. Le, D. Liska, K. S. Long, J. R. Lucey, M. Liu, N. F. Martin, G. Masci, B. McLean, E. Mindel, P. Misra, E. Morganson, D. N. A. Murphy, A. Obaika, G. Narayan, M. A. Nieto-Santisteban, P. Norberg, J. A. Peacock, E. A. Pier, M. Postman, N. Primak, C. Rae, A. Rai, A. Riess, A. Riffeser, H. W. Rix, S. Röser, R. Russel, L. Rutz, E. Schilbach, A. S. B. Schultz, D. Scolnic, L. Strolger, A. Szalay, S. Seitz, E. Small, K. W. Smith, D. R. Soderblom, P. Taylor, R. Thomson, A. N. Taylor, A. R. Thakar, J. Thiel, D. Thilker, D. Unger, Y. Urata, J. Valenti, J. Wagner, T. Walder, F. Walter, S. P. Watters, S. Werner, W. M. Wood-Vasey, and R. Wyse. The Pan-STARRS1 Surveys. *arXiv e-prints*, art. arXiv:1612.05560, Dec. 2016. doi: 10.48550/arXiv.1612.05560.

G. A. Chanan, J. Middleditch, and J. E. Nelson. The Geometry of the Eclipse of a Pointlike Star by a Roche-Lobe Companion. *The Astrophysical Journal*, 208: 512–517, Sept. 1976. doi: 10.1086/154633.

P. Charbonneau. Solar Dynamo Theory. *Annual Review of Astronomy and Astrophysics*, 52:251–290, Aug. 2014. doi: 10.1146/annurev-astro-081913-040012.

J. Choi, A. Dotter, C. Conroy, M. Cantiello, B. Paxton, and B. D. Johnson. Mesa Isochrones and Stellar Tracks (MIST). I. Solar-scaled Models. *The Astrophysical Journal*, 823(2):102, June 2016a. doi: 10.3847/0004-637X/823/2/102.

J. Choi, A. Dotter, C. Conroy, M. Cantiello, B. Paxton, and B. D. Johnson. Mesa Isochrones and Stellar Tracks (MIST). I. Solar-scaled Models. *The Astrophysical Journal*, 823(2):102, June 2016b. doi: 10.3847/0004-637X/823/2/102.

B. G. Clark. An efficient implementation of the algorithm 'CLEAN'. *Astronomy & Astrophysics*, 89(3):377, Sept. 1980.

A. Comrie, K.-S. Wang, S.-C. Hsu, A. Moraghan, P. Harris, Q. Pang, A. Pińska, C.-C. Chiang, T.-H. Chang, Y.-H. Hwang, H. Jan, M.-Y. Lin, and R. Simmonds. CARTA: The Cube Analysis and Rendering Tool for Astronomy, June 2021.

J. M. Cordes. NE2001: A New Model for the Galactic Electron Density and its Fluctuations. In D. Clemens, R. Shah, and T. Brainerd, editors, *Milky Way Surveys: The Structure and Evolution of our Galaxy*, volume 317 of *Astronomical Society of the Pacific Conference Series*, page 211, Dec. 2004.

J. M. Corral-Santana, J. Casares, T. Muñoz-Darias, F. E. Bauer, I. G. Martínez-Pais, and D. M. Russell. BlackCAT: A catalogue of stellar-mass black holes in X-ray transients. *Astronomy & Astrophysics*, 587:A61, Mar. 2016. doi: 10.1051/0004-6361/201527130.

M. Cropper. The Polars. *Space Science Reviews*, 54(3-4):195–295, Dec. 1990. doi: 10.1007/BF00177799.

S. Czesla, P. C. Schneider, J. H. M. M. Schmitt, S. Freund, M. Salvato, J. Buchner, and J. Robrade. Likelihood of the sky. Bayesian treatment of the geometric two-catalog matching problem. *Astronomy & Astrophysics*, 674:A136, June 2023. doi: 10.1051/0004-6361/202244195.

G. Dalton, S. C. Trager, D. C. Abrams, D. Carter, P. Bonifacio, J. A. L. Aguerri, M. MacIntosh, C. Evans, I. Lewis, R. Navarro, T. Agocs, K. Dee, S. Rousset, I. Tosh, K. Middleton, J. Pragt, D. Terrett, M. Brock, C. Benn, M. Verheijen, D. Cano Infantes, C. Bevil, I. Steele, C. Mottram, S. Bates, F. J. Gribbin, J. Rey, L. F. Rodriguez, J. M. Delgado, I. Guinouard, N. Walton, M. J. Irwin, P. Jagourel, R. Stuik, G. Gerlofsma, R. Roelfsma, I. Skillen, A. Ridings, M. Balcells, J.-B. Daban, C. Gouvret, L. Venema, and P. Girard. WEAVE: the next generation wide-field spectroscopy facility for the William Herschel Telescope. In I. S.

McLean, S. K. Ramsay, and H. Takami, editors, *Ground-based and Airborne Instrumentation for Astronomy IV*, volume 8446 of *Society of Photo-Optical Instrumentation Engineers (SPIE) Conference Series*, page 84460P, Sept. 2012. doi: 10.1117/12.925950.

M. Dan, S. Rosswog, J. Guillochon, and E. Ramirez-Ruiz. Prelude to A Double Degenerate Merger: The Onset of Mass Transfer and Its Impact on Gravitational Waves and Surface Detonations. *The Astrophysical Journal*, 737(2):89, Aug. 2011. doi: 10.1088/0004-637X/737/2/89.

I. J. Danziger, D. Baade, and M. della Valle. Optical spectroscopy and photometry of the companion of the bright millisecond pulsar J 0437-4715. *Astronomy & Astrophysics*, 276:382–388, Sept. 1993.

K. De, I. Mereminskiy, R. Soria, C. Conroy, E. Kara, S. Anand, M. C. B. Ashley, M. L. Boyer, D. Chakrabarty, B. Grefenstette, M. J. Hankins, L. A. Hillenbrand, J. E. Jencson, V. Karambelkar, M. M. Kasliwal, R. M. Lau, A. Lutovinov, A. M. Moore, M. Ng, C. Panagiotou, D. R. Pasham, A. Semena, R. Simcoe, J. Soon, G. P. Srinivasaragavan, T. Travouillon, and Y. Yao. SRGA J181414.6-225604: A New Galactic Symbiotic X-Ray Binary Outburst Triggered by an Intense Mass-loss Episode of a Heavily Obscured Mira Variable. *The Astrophysical Journal*, 935(1):36, Aug. 2022. doi: 10.3847/1538-4357/ac7c6e.

O. C. de Jager, P. J. Meintjes, D. O'Donoghue, and E. L. Robinson. The discovery of a brake on the white dwarf in AE Aquarii. *Monthly Notices of the Royal Astronomical Society*, 267:577–588, Apr. 1994. doi: 10.1093/mnras/267.3.577.

R. S. de Jong, O. Agertz, A. A. Berbel, J. Aird, D. A. Alexander, A. Amarsi, F. Anders, R. Andrae, B. Ansarinejad, W. Ansorge, P. Antilogus, H. Anwand-Heerwart, A. Arentsen, A. Arnadottir, M. Asplund, M. Auger, N. Azais, D. Baade, G. Baker, S. Baker, E. Balbinot, I. K. Baldry, M. Banerji, S. Barden, P. Barklem, E. Barthélémy-Mazot, C. Battistini, S. Bauer, C. P. M. Bell, O. Bellido-Tirado, S. Bellstedt, V. Belokurov, T. Bensby, M. Bergemann, J. M. Bestenlehner, R. Bielby, M. Bilicki, C. Blake, J. Bland-Hawthorn, C. Boeche, W. Boland, T. Boller, S. Bongard, A. Bongiorno, P. Bonifacio, D. Boudon, D. Brooks, M. J. I. Brown, R. Brown, M. Brüggen, J. Brynnel, J. Brzeski, T. Buchert, P. Buschkamp, E. Caffau, P. Caillier, J. Carrick, L. Casagrande, S. Case, A. Casey, I. Cesarini, G. Cescutti, D. Chapuis, C. Chiappini, M. Childress, N. Christlieb, R. Church, M. R. L. Cioni, M. Cluver, M. Colless, T. Collett, J. Comparat, A. Cooper, W. Couch, F. Courbin, S. Croom, D. Croton, E. Daguisé, G. Dalton, L. J. M. Davies, T. Davis, P. de Laverny, A. Deason, F. Dionies, K. Disseau, P. Doel, D. Döscher, S. P. Driver, T. Dwelly, D. Eckert, A. Edge, B. Edvardsson, D. E. Youssoufi, A. Elhaddad, H. Enke, G. Erfanianfar, T. Farrell, T. Fechner, C. Feiz, S. Feltzing, I. Ferreras, D. Feuerstein, D. Feuillet, A. Finoguenov, D. Ford, S. Fotopoulou, M. Fouesneau, C. Frenk, S. Frey, W. Gaessler, S. Geier, N. Gentile Fusillo, O. Gerhard, T. Giannantonio, D. Giannone, B. Gibson, P. Gillingham,

C. González-Fernández, E. Gonzalez-Solares, S. Gottloeber, A. Gould, E. K. Grebel, A. Gueguen, G. Guiglion, M. Haehnelt, T. Hahn, C. J. Hansen, H. Hartman, K. Hauptner, K. Hawkins, D. Haynes, R. Haynes, U. Heiter, A. Helmi, C. H. Aguayo, P. Hewett, S. Hinton, D. Hobbs, S. Hoenig, D. Hofman, I. Hook, J. Hopgood, A. Hopkins, A. Hourihane, L. Howes, C. Howlett, T. Huet, M. Irwin, O. Iwert, P. Jablonka, T. Jahn, K. Jahnke, A. Jarno, S. Jin, P. Jofre, D. Johl, D. Jones, H. Jönsson, C. Jordan, I. Karovicova, A. Khalatyan, A. Kelz, R. Kennicutt, D. King, F. Kitaura, J. Klar, U. Klauser, J. P. Kneib, A. Koch, S. Koposov, G. Kordopatis, A. Korn, J. Kosmalski, R. Kotak, M. Kovalev, K. Kreckel, Y. Kripak, M. Krumpe, K. Kuijken, A. Kunder, I. Kushniruk, M. I. Lam, G. Lamer, F. Laurent, J. Lawrence, M. Lehmitz, B. Lemasle, J. Lewis, B. Li, C. Lidman, K. Lind, J. Liske, J. L. Lizon, J. Loveday, H. G. Ludwig, R. M. McDermid, K. Maguire, V. Mainieri, S. Mali, H. Mandel, K. Mandel, L. Mannering, S. Martell, D. Martinez Delgado, G. Matijevic, H. McGregor, R. McMahon, P. McMillan, O. Mena, A. Merloni, M. J. Meyer, C. Michel, G. Micheva, J. E. Migniau, I. Minchev, G. Monari, R. Muller, D. Murphy, D. Muthukrishna, K. Nandra, R. Navarro, M. Ness, V. Nichani, R. Nichol, H. Nicklas, F. Niederhofer, P. Norberg, D. Obreschkow, S. Oliver, M. Owers, N. Pai, S. Pankratow, D. Parkinson, J. Paschke, R. Paterson, A. Pecontal, I. Parry, D. Phillips, A. Pillepich, L. Pinard, J. Pirard, N. Piskunov, V. Plank, D. Plüschke, E. Pons, P. Popesso, C. Power, J. Pragt, A. Pramskiy, D. Pryer, M. Quattri, A. B. d. A. Queiroz, A. Quirrenbach, S. Rahurkar, A. Raichoor, S. Ramstedt, A. Rau, A. Recio-Blanco, R. Reiss, F. Renaud, Y. Revaz, P. Rhode, J. Richard, A. D. Richter, H. W. Rix, A. S. G. Robotham, R. Roelfsema, M. Romaniello, D. Rosario, F. Rothmaier, B. Roukema, G. Ruchti, G. Rupprecht, J. Rybizki, N. Ryde, A. Saar, E. Sadler, M. Sahlén, M. Salvato, B. Sassolas, W. Saunders, A. Saviauk, L. Sbordone, T. Schmidt, O. Schnurr, R. D. Scholz, A. Schwope, W. Seifert, T. Shanks, A. Sheinis, T. Sivov, Á. Skúladóttir, S. Smartt, S. Smedley, G. Smith, R. Smith, J. Sorce, L. Spitler, E. Starkenburg, M. Steinmetz, I. Stilz, J. Storm, M. Sullivan, W. Sutherland, E. Swann, A. Tamone, E. N. Taylor, J. Teillon, E. Tempel, R. ter Horst, W. F. Thi, E. Tolstoy, S. Trager, G. Traven, P. E. Tremblay, L. Tresse, M. Valentini, R. van de Weygaert, M. van den Ancker, J. Veljanoski, S. Venkatesan, L. Wagner, K. Wagner, C. J. Walcher, L. Waller, N. Walton, L. Wang, R. Winkler, L. Wisotzki, C. C. Worley, G. Worseck, M. Xiang, W. Xu, D. Yong, C. Zhao, J. Zheng, F. Zscheyge, and D. Zucker. 4MOST: Project overview and information for the First Call for Proposals. *The Messenger*, 175:3–11, Mar. 2019. doi: 10.18727/0722-6691/5117.

D. de Martino, F. Bernardini, K. Mukai, M. Falanga, and N. Masetti. Hard X-ray cataclysmic variables. *Advances in Space Research*, 66(5):1209–1225, Sept. 2020a. doi: 10.1016/j.asr.2019.09.006.

D. de Martino, F. Bernardini, K. Mukai, M. Falanga, and N. Masetti. Hard X-ray cataclysmic variables. *Advances in Space Research*, 66(5):1209–1225, Sept. 2020b. doi: 10.1016/j.asr.2019.09.006.

I. de Ruiter, K. M. Rajwade, C. G. Bassa, A. Rowlinson, R. A. M. J. Wijers, C. D. Kilpatrick, G. Stefansson, J. R. Callingham, J. W. T. Hessels, T. E. Clarke, W. Peters, R. A. D. Wijnands, T. W. Shimwell, S. ter Veen, V. Morello, G. R. Zeimann, and S. Mahadevan. A white dwarf binary showing sporadic radio pulses at the orbital period. *arXiv e-prints*, art. arXiv:2408.11536, Aug. 2024. doi: 10.48550/arXiv.2408.11536.

P. Deegan, C. Combet, and G. A. Wynn. The outburst duration and duty cycle of GRS1915+105. *Monthly Notices of the Royal Astronomical Society*, 400(3): 1337–1346, Dec. 2009. doi: 10.1111/j.1365-2966.2009.15573.x.

R. Dekany, R. M. Smith, R. Riddle, M. Feeney, M. Porter, D. Hale, J. Zolkower, J. Belicki, S. Kaye, J. Henning, R. Walters, J. Cromer, A. Delacroix, H. Rodriguez, D. J. Reiley, P. Mao, D. Hover, P. Murphy, R. Burruss, J. Baker, M. Kowalski, K. Reif, P. Mueller, E. Bellm, M. Graham, and S. R. Kulkarni. The Zwicky Transient Facility: Observing System. *Publications of the Astronomical Society of the Pacific*, 132(1009):038001, Mar. 2020. doi: 10.1088/1538-3873/ab4ca2.

X. Delfosse, T. Forveille, C. Perrier, and M. Mayor. Rotation and chromospheric activity in field M dwarfs. *Astronomy & Astrophysics*, 331:581–595, Mar. 1998.

F. Delgado and M. A. Reuter. The LSST Scheduler from design to construction. In A. B. Peck, R. L. Seaman, and C. R. Benn, editors, *Observatory Operations: Strategies, Processes, and Systems VI*, volume 9910 of *Society of Photo-Optical Instrumentation Engineers (SPIE) Conference Series*, page 991013, July 2016. doi: 10.1117/12.2233630.

DESI Collaboration, A. Aghamousa, J. Aguilar, S. Ahlen, S. Alam, L. E. Allen, C. Allende Prieto, J. Annis, S. Bailey, C. Balland, O. Ballester, C. Baltay, L. Beaufore, C. Bebek, T. C. Beers, E. F. Bell, J. L. Bernal, R. Besuner, F. Beutler, C. Blake, H. Bleuler, M. Blomqvist, R. Blum, A. S. Bolton, C. Briceno, D. Brooks, J. R. Brownstein, E. Buckley-Geer, A. Burden, E. Burtin, N. G. Busca, R. N. Cahn, Y.-C. Cai, L. Cardiel-Sas, R. G. Carlberg, P.-H. Carton, R. Casas, F. J. Castander, J. L. Cervantes-Cota, T. M. Claybaugh, M. Close, C. T. Coker, S. Cole, J. Comparat, A. P. Cooper, M. C. Cousinou, M. Crocce, J.-G. Cuby, D. P. Cunningham, T. M. Davis, K. S. Dawson, A. de la Macorra, J. De Vicente, T. Delubac, M. Derwent, A. Dey, G. Dhungana, Z. Ding, P. Doel, Y. T. Duan, A. Ealet, J. Edelstein, S. Eftekharzadeh, D. J. Eisenstein, A. Elliott, S. Escoffier, M. Evatt, P. Fagrelius, X. Fan, K. Fanning, A. Farahi, J. Farihi, G. Favole, Y. Feng, E. Fernandez, J. R. Findlay, D. P. Finkbeiner, M. J. Fitzpatrick, B. Flaugher, S. Flender, A. Font-Ribera, J. E. Forero-Romero, P. Fosalba, C. S. Frenk, M. Fumagalli, B. T. Gaensicke, G. Gallo, J. Garcia-Bellido, E. Gaztanaga, N. Pietro Gentile Fusillo, T. Gerard, I. Gershkovich, T. Giannantonio, D. Gillet, G. Gonzalez-de-Rivera, V. Gonzalez-Perez, S. Gott, O. Graur, G. Gutierrez, J. Guy, S. Habib, H. Heetderks, I. Heetderks, K. Heitmann, W. A. Hellwing, D. A. Herrera, S. Ho, S. Holland, K. Honscheid, E. Huff, T. A. Hutchinson, D. Huterer,

H. S. Hwang, J. M. Illa Laguna, Y. Ishikawa, D. Jacobs, N. Jeffrey, P. Jelinsky, E. Jennings, L. Jiang, J. Jimenez, J. Johnson, R. Joyce, E. Jullo, S. Juneau, S. Kama, A. Karcher, S. Karkar, R. Kehoe, N. Kennamer, S. Kent, M. Kilbinger, A. G. Kim, D. Kirkby, T. Kisner, E. Kitanidis, J.-P. Kneib, S. Koposov, E. Kovacs, K. Koyama, A. Kremin, R. Kron, L. Kronig, A. Kueter-Young, C. G. Lacey, R. Lafever, O. Lahav, A. Lambert, M. Lampton, M. Landriau, D. Lang, T. R. Lauer, J.-M. Le Goff, L. Le Guillou, A. Le Van Suu, J. H. Lee, S.-J. Lee, D. Leitner, M. Lesser, M. E. Levi, B. L'Huillier, B. Li, M. Liang, H. Lin, E. Linder, S. R. Loebman, Z. Lukić, J. Ma, N. MacCrann, C. Magneville, L. Makarem, M. Manera, C. J. Manser, R. Marshall, P. Martini, R. Massey, T. Matheson, J. McCauley, P. McDonald, I. D. McGreer, A. Meisner, N. Metcalfe, T. N. Miller, R. Miquel, J. Moustakas, A. Myers, M. Naik, J. A. Newman, R. C. Nichol, A. Nicola, L. Nicolati da Costa, J. Nie, G. Niz, P. Norberg, B. Nord, D. Norman, P. Nugent, T. O'Brien, M. Oh, K. A. G. Olsen, C. Padilla, H. Padmanabhan, N. Padmanabhan, N. Palanque-Delabrouille, A. Palmese, D. Pappalardo, I. Pâris, C. Park, A. Patej, J. A. Peacock, H. V. Peiris, X. Peng, W. J. Percival, S. Perruchot, M. M. Pieri, R. Pogge, J. E. Pollack, C. Poppett, F. Prada, A. Prakash, R. G. Probst, D. Rabinowitz, A. Raichoor, C. H. Ree, A. Refregier, X. Regal, B. Reid, K. Reil, M. Rezaie, C. M. Rockosi, N. Roe, S. Ronayette, A. Roodman, A. J. Ross, N. P. Ross, G. Rossi, E. Rozo, V. Ruhlmann-Kleider, E. S. Rykoff, C. Sabiu, L. Samushia, E. Sanchez, J. Sanchez, D. J. Schlegel, M. Schneider, M. Schubnell, A. Secroun, U. Seljak, H.-J. Seo, S. Serrano, A. Shafieloo, H. Shan, R. Sharples, M. J. Sholl, W. V. Shourt, J. H. Silber, D. R. Silva, M. M. Sirk, A. Slosar, A. Smith, G. F. Smoot, D. Som, Y.-S. Song, D. Sprayberry, R. Staten, A. Stefanik, G. Tarle, S. Sien Tie, J. L. Tinker, R. Tojeiro, F. Valdes, O. Valenzuela, M. Valluri, M. Vargas-Magana, L. Verde, A. R. Walker, J. Wang, Y. Wang, B. A. Weaver, C. Weaverdyck, R. H. Wechsler, D. H. Weinberg, M. White, Q. Yang, C. Yeche, T. Zhang, G.-B. Zhao, Y. Zheng, X. Zhou, Z. Zhou, Y. Zhu, H. Zou, and Y. Zu. The DESI Experiment Part I: Science,Targeting, and Survey Design. *arXiv e-prints*, art. arXiv:1611.00036, Oct. 2016. doi: 10.48550/arXiv.1611.00036.

P. E. Dewdney, P. J. Hall, R. T. Schilizzi, and T. J. L. W. Lazio. The Square Kilometre Array. *IEEE Proceedings*, 97(8):1482–1496, Aug. 2009. doi: 10.1109/JPROC.2009.2021005.

A. Dey, D. J. Schlegel, D. Lang, R. Blum, K. Burleigh, X. Fan, J. R. Findlay, D. Finkbeiner, D. Herrera, S. Juneau, M. Landriau, M. Levi, I. McGreer, A. Meisner, A. D. Myers, J. Moustakas, P. Nugent, A. Patej, E. F. Schlafly, A. R. Walker, F. Valdes, B. A. Weaver, C. Yèche, H. Zou, X. Zhou, B. Abareshi, T. M. C. Abbott, B. Abolfathi, C. Aguilera, S. Alam, L. Allen, A. Alvarez, J. Annis, B. Ansarinejad, M. Aubert, J. Beechert, E. F. Bell, S. Y. BenZvi, F. Beutler, R. M. Bielby, A. S. Bolton, C. Briceño, E. J. Buckley-Geer, K. Butler, A. Calamida, R. G. Carlberg, P. Carter, R. Casas, F. J. Castander, Y. Choi, J. Comparat, E. Cukanovaite, T. Delubac, K. DeVries, S. Dey, G. Dhungana, M. Dickinson, Z. Ding, J. B. Donaldson, Y. Duan, C. J. Duckworth, S. Eftekharzadeh, D. J.

Eisenstein, T. Etourneau, P. A. Fagrelius, J. Farihi, M. Fitzpatrick, A. Font-Ribera, L. Fulmer, B. T. Gänsicke, E. Gaztanaga, K. George, D. W. Gerdes, S. G. A. Gontcho, C. Gorgoni, G. Green, J. Guy, D. Harmer, M. Hernandez, K. Honscheid, L. W. Huang, D. J. James, B. T. Jannuzi, L. Jiang, R. Joyce, A. Karcher, S. Karkar, R. Kehoe, J.-P. Kneib, A. Kueter-Young, T.-W. Lan, T. R. Lauer, L. Le Guillou, A. Le Van Suu, J. H. Lee, M. Lesser, L. Perreault Levasseur, T. S. Li, J. L. Mann, R. Marshall, C. E. Martínez-Vázquez, P. Martini, H. du Mas des Bourboux, S. McManus, T. G. Meier, B. Ménard, N. Metcalfe, A. Muñoz-Gutiérrez, J. Najita, K. Napier, G. Narayan, J. A. Newman, J. Nie, B. Nord, D. J. Norman, K. A. G. Olsen, A. Paat, N. Palanque-Delabrouille, X. Peng, C. L. Poppett, M. R. Poremba, A. Prakash, D. Rabinowitz, A. Raichoor, M. Rezaie, A. N. Robertson, N. A. Roe, A. J. Ross, N. P. Ross, G. Rudnick, S. Safonova, A. Saha, F. J. Sánchez, E. Savary, H. Schweiker, A. Scott, H.-J. Seo, H. Shan, D. R. Silva, Z. Slepian, C. Soto, D. Sprayberry, R. Staten, C. M. Stillman, R. J. Stupak, D. L. Summers, S. Sien Tie, H. Tirado, M. Vargas-Magaña, A. K. Vivas, R. H. Wechsler, D. Williams, J. Yang, Q. Yang, T. Yapici, D. Zaritsky, A. Zenteno, K. Zhang, T. Zhang, R. Zhou, and Z. Zhou. Overview of the DESI Legacy Imaging Surveys. *The Astronomical Journal*, 157(5):168, May 2019. doi: 10.3847/1538-3881/ab089d.

V. S. Dhillon, T. R. Marsh, M. J. Stevenson, D. C. Atkinson, P. Kerry, P. T. Peacocke, A. J. A. Vick, S. M. Beard, D. J. Ives, D. W. Lunney, S. A. McLay, C. J. Tierney, J. Kelly, S. P. Littlefair, R. Nicholson, R. Pashley, E. T. Harlaftis, and K. O'Brien. ULTRACAM: an ultrafast, triple-beam CCD camera for high-speed astrophysics. *Monthly Notices of the Royal Astronomical Society*, 378(3):825–840, July 2007a. doi: 10.1111/j.1365-2966.2007.11881.x.

V. S. Dhillon, T. R. Marsh, M. J. Stevenson, D. C. Atkinson, P. Kerry, P. T. Peacocke, A. J. A. Vick, S. M. Beard, D. J. Ives, D. W. Lunney, S. A. McLay, C. J. Tierney, J. Kelly, S. P. Littlefair, R. Nicholson, R. Pashley, E. T. Harlaftis, and K. O'Brien. ULTRACAM: an ultrafast, triple-beam CCD camera for high-speed astrophysics. *Monthly Notices of the Royal Astronomical Society*, 378(3):825–840, July 2007b. doi: 10.1111/j.1365-2966.2007.11881.x.

V. S. Dhillon, N. Bezawada, M. Black, S. D. Dixon, T. Gamble, X. Gao, D. M. Henry, P. Kerry, S. P. Littlefair, D. W. Lunney, T. R. Marsh, C. Miller, S. G. Parsons, R. P. Ashley, E. Breedt, A. Brown, M. J. Dyer, M. J. Green, I. Pelisoli, D. I. Sahman, J. Wild, D. J. Ives, L. Mehrgan, J. Stegmeier, C. M. Dubbeldam, T. J. Morris, J. Osborn, R. W. Wilson, J. Casares, T. Muñoz-Darias, E. Pallé, P. Rodríguez-Gil, T. Shahbaz, M. A. P. Torres, A. de Ugarte Postigo, A. Cabrera-Lavers, R. L. M. Corradi, R. D. Domínguez, and D. García-Alvarez. HiPERCAM: a quintuple-beam, high-speed optical imager on the 10.4-m Gran Telescopio Canarias. *Monthly Notices of the Royal Astronomical Society*, 507(1):350–366, Oct. 2021. doi: 10.1093/mnras/stab2130.

F. A. Dong, T. Clarke, A. P. Curtin, A. Kumar, I. Stairs, S. Chatterjee, A. M. Cook, E. Fonseca, B. M. Gaensler, J. W. T. Hessels, V. M. Kaspi, M. Lazda, K. W. Masui, J. W. McKee, B. W. Meyers, A. B. Pearlman, S. M. Ransom, P. Scholz, K. Shin, K. M. Smith, and C. M. Tan. The discovery of a nearby 421transient with CHIME/FRB/Pulsar. *arXiv e-prints*, art. arXiv:2407.07480, July 2024. doi: 10.48550/arXiv.2407.07480.

B. T. Draine. *Physics of the Interstellar and Intergalactic Medium*. 2011.

C. Duffy, G. Ramsay, D. Steeghs, V. Dhillon, M. R. Kennedy, D. Mata Sánchez, K. Ackley, M. Dyer, J. Lyman, K. Ulaczyk, D. K. Galloway, P. O'Brien, K. Noysena, L. Nuttall, and D. Pollacco. Evidence that short-period AM CVn systems are diverse in outburst behaviour. *Monthly Notices of the Royal Astronomical Society*, 502(4):4953–4962, Apr. 2021. doi: 10.1093/mnras/stab389.

M. Durant, O. Kargaltsev, G. G. Pavlov, P. M. Kowalski, B. Posselt, M. H. van Kerkwijk, and D. L. Kaplan. The Spectrum of the Recycled PSR J0437-4715 and Its White Dwarf Companion. *The Astrophysical Journal*, 746(1):6, Feb. 2012. doi: 10.1088/0004-637X/746/1/6.

G. Edenhofer, C. Zucker, P. Frank, A. K. Saydjari, J. S. Speagle, D. Finkbeiner, and T. A. Enßlin. A parsec-scale Galactic 3D dust map out to 1.25 kpc from the Sun. *Astronomy & Astrophysics*, 685:A82, May 2024. doi: 10.1051/0004-6361/202347628.

P. P. Eggleton. Aproximations to the radii of Roche lobes. *The Astrophysical Journal*, 268:368–369, May 1983a. doi: 10.1086/160960.

P. P. Eggleton. Aproximations to the radii of Roche lobes. *The Astrophysical Journal*, 268:368–369, May 1983b. doi: 10.1086/160960.

P. P. Eggleton. Aproximations to the radii of Roche lobes. *The Astrophysical Journal*, 268:368–369, May 1983c. doi: 10.1086/160960.

P. R. M. Eisenhardt, F. Marocco, J. W. Fowler, A. M. Meisner, J. D. Kirkpatrick, N. Garcia, T. H. Jarrett, R. Koontz, E. J. Marchese, S. A. Stanford, D. Caselden, M. C. Cushing, R. M. Cutri, J. K. Faherty, C. R. Gelino, A. H. Gonzalez, A. Mainzer, B. Mobasher, D. J. Schlegel, D. Stern, H. I. Teplitz, and E. L. Wright. The CatWISE Preliminary Catalog: Motions from WISE and NEOWISE Data. *The Astrophysical Journal Supplement Series*, 247(2):69, Apr. 2020. doi: 10.3847/1538-4365/ab7f2a.

Z. Eker. Kinematics and Age of RS Canum Venaticorum and BY Draconis Stars. *The Astrophysical Journal Supplement Series*, 79:481, Apr. 1992. doi: 10.1086/191658.

K. El-Badry, H.-W. Rix, E. Quataert, T. Kupfer, and K. J. Shen. Birth of the ELMs: a ZTF survey for evolved cataclysmic variables turning into extremely

low-mass white dwarfs. *Monthly Notices of the Royal Astronomical Society*, 508 (3):4106–4139, Dec. 2021a. doi: 10.1093/mnras/stab2583.

K. El-Badry, H.-W. Rix, E. Quataert, T. Kupfer, and K. J. Shen. Birth of the ELMs: a ZTF survey for evolved cataclysmic variables turning into extremely low-mass white dwarfs. *Monthly Notices of the Royal Astronomical Society*, 508 (3):4106–4139, Dec. 2021b. doi: 10.1093/mnras/stab2583.

K. El-Badry, C. Conroy, J. Fuller, R. Kiman, J. van Roestel, A. C. Rodriguez, and K. B. Burdge. Magnetic braking saturates: evidence from the orbital period distribution of low-mass detached eclipsing binaries from ZTF. *Monthly Notices of the Royal Astronomical Society*, 517(4):4916–4939, Dec. 2022. doi: 10.1093/mnras/stac2945.

K. El-Badry, H.-W. Rix, Y. Cendes, A. C. Rodriguez, C. Conroy, E. Quataert, K. Hawkins, E. Zari, M. Hobson, K. Breivik, A. Rau, E. Berger, S. Shahaf, R. Seeburger, K. B. Burdge, D. W. Latham, L. A. Buchhave, A. Bieryla, D. Bashi, T. Mazeh, and S. Faigler. A red giant orbiting a black hole. *Monthly Notices of the Royal Astronomical Society*, 521(3):4323–4348, May 2023a. doi: 10.1093/mnras/stad799.

K. El-Badry, H.-W. Rix, E. Quataert, A. W. Howard, H. Isaacson, J. Fuller, K. Hawkins, K. Breivik, K. W. K. Wong, A. C. Rodriguez, C. Conroy, S. Shahaf, T. Mazeh, F. Arenou, K. B. Burdge, D. Bashi, S. Faigler, D. R. Weisz, R. Seeburger, S. Almada Monter, and J. Wojno. A Sun-like star orbiting a black hole. *Monthly Notices of the Royal Astronomical Society*, 518(1):1057–1085, Jan. 2023b. doi: 10.1093/mnras/stac3140.

I. N. Evans and F. Civano. The Chandra Source Catalog release 2.0. *Astronomy and Geophysics*, 59(2):2.17–2.18, Apr. 2018. doi: 10.1093/astrogeo/aty079.

P. A. Evans, A. P. Beardmore, K. L. Page, J. P. Osborne, P. T. O'Brien, R. Willingale, R. L. C. Starling, D. N. Burrows, O. Godet, L. Vetere, J. Racusin, M. R. Goad, K. Wiersema, L. Angelini, M. Capalbi, G. Chincarini, N. Gehrels, J. A. Kennea, R. Margutti, D. C. Morris, C. J. Mountford, C. Pagani, M. Perri, P. Romano, and N. Tanvir. Methods and results of an automatic analysis of a complete sample of Swift-XRT observations of GRBs. *Monthly Notices of the Royal Astronomical Society*, 397(3):1177–1201, Aug. 2009. doi: 10.1111/j.1365-2966.2009.14913.x.

P. A. Evans, K. L. Page, J. P. Osborne, A. P. Beardmore, R. Willingale, D. N. Burrows, J. A. Kennea, M. Perri, M. Capalbi, G. Tagliaferri, and S. B. Cenko. 2SXPS: An Improved and Expanded Swift X-Ray Telescope Point-source Catalog. *The Astrophysical Journal Supplement Series*, 247(2):54, Apr. 2020a. doi: 10.3847/1538-4365/ab7db9.

P. A. Evans, K. L. Page, J. P. Osborne, A. P. Beardmore, R. Willingale, D. N. Burrows, J. A. Kennea, M. Perri, M. Capalbi, G. Tagliaferri, and S. B. Cenko. 2SXPS: An Improved and Expanded Swift X-Ray Telescope Point-source Catalog.

The Astrophysical Journal Supplement Series, 247(2):54, Apr. 2020b. doi: 10.3847/1538-4365/ab7db9.

J. Faulkner. Ultrashort-Period Binaries, Gravitational Radiation, and Mass Transfer. I. The Standard Model, with Applications to WZ Sagittae and Z Camelopardalis. *The Astrophysical Journal Letters*, 170:L99, Dec. 1971. doi: 10.1086/180848.

J. Faulkner and J. Iben, Icko. The Evolution of Population II Stars. *The Astrophysical Journal*, 144:995, June 1966. doi: 10.1086/148697.

E. D. Feigelson and G. A. Kriss. Discovery of three X-ray luminous pre-main-sequence stars. *The Astrophysical Journal Letters*, 248:L35–L38, Aug. 1981. doi: 10.1086/183618.

E. D. Feigelson, P. Broos, I. Gaffney, James A., G. Garmire, L. A. Hillenbrand, S. H. Pravdo, L. Townsley, and Y. Tsuboi. X-Ray-emitting Young Stars in the Orion Nebula. *The Astrophysical Journal*, 574(1):258–292, July 2002. doi: 10.1086/340936.

R. P. Fender, T. J. Maccarone, and I. Heywood. The closest black holes. *Monthly Notices of the Royal Astronomical Society*, 430(3):1538–1547, Apr. 2013. doi: 10.1093/mnras/sts688.

L. Ferrario, J. Bailey, and D. T. Wickramasinghe. Detection of cyclotron emission features in the infrared spectrum of ST LMi. *Monthly Notices of the Royal Astronomical Society*, 262:285–288, May 1993. doi: 10.1093/mnras/262.2.285.

L. Ferrario, D. Wickramasinghe, J. Bailey, and D. Buckley. 1H 1752+08: the lowest field AM Herculis system? *Monthly Notices of the Royal Astronomical Society*, 273(1):17–24, Mar. 1995. doi: 10.1093/mnras/273.1.17.

L. Ferrario, D. de Martino, and B. T. Gänsicke. Magnetic White Dwarfs. *Space Science Reviews*, 191(1-4):111–169, Oct. 2015. doi: 10.1007/s11214-015-0152-0.

L. Ferrario, D. Wickramasinghe, and A. Kawka. Magnetic fields in isolated and interacting white dwarfs. *Advances in Space Research*, 66(5):1025–1056, Sept. 2020. doi: 10.1016/j.asr.2019.11.012.

D. Foreman-Mackey, D. W. Hogg, D. Lang, and J. Goodman. emcee: The MCMC Hammer. *Publications of the Astronomical Society of the Pacific*, 125(925):306, Mar. 2013. doi: 10.1086/670067.

D. Foreman-Mackey, W. Farr, M. Sinha, A. Archibald, D. Hogg, J. Sanders, J. Zuntz, P. Williams, A. Nelson, M. de Val-Borro, T. Erhardt, I. Pashchenko, and O. Pla. emcee v3: A Python ensemble sampling toolkit for affine-invariant MCMC. *The Journal of Open Source Software*, 4(43):1864, Nov. 2019. doi: 10.21105/joss.01864.

W. Forman, C. Jones, L. Cominsky, P. Julien, S. Murray, G. Peters, H. Tananbaum, and R. Giacconi. The fourth Uhuru catalog of X-ray sources. *The Astrophysical Journal Supplement Series*, 38:357–412, Dec. 1978. doi: 10.1086/190561.

S. Freund, S. Czesla, J. Robrade, P. C. Schneider, and J. H. M. M. Schmitt. The stellar content of the ROSAT all-sky survey. *Astronomy & Astrophysics*, 664: A105, Aug. 2022. doi: 10.1051/0004-6361/202142573.

A. S. Fruchter, D. R. Stinebring, and J. H. Taylor. A millisecond pulsar in an eclipsing binary. *Nature*, 333(6170):237–239, May 1988. doi: 10.1038/333237a0.

J. T. Fuchs, B. H. Dunlap, E. Dennihy, D. O'Donoghue, J. C. Clemens, D. E. Reichart, J. P. Moore, A. P. LaCluyze, J. B. Haislip, and K. V. Ivarsen. The magnetic cataclysmic variable LSQ1725-64. *Monthly Notices of the Royal Astronomical Society*, 462(3):2382–2395, Nov. 2016. doi: 10.1093/mnras/stw1759.

Gaia Collaboration, T. Prusti, J. H. J. de Bruijne, A. G. A. Brown, A. Vallenari, C. Babusiaux, C. A. L. Bailer-Jones, U. Bastian, M. Biermann, D. W. Evans, L. Eyer, F. Jansen, C. Jordi, S. A. Klioner, U. Lammers, L. Lindegren, X. Luri, F. Mignard, D. J. Milligan, C. Panem, V. Poinsignon, D. Pourbaix, S. Randich, G. Sarri, P. Sartoretti, H. I. Siddiqui, C. Soubiran, V. Valette, F. van Leeuwen, N. A. Walton, C. Aerts, F. Arenou, M. Cropper, R. Drimmel, E. Høg, D. Katz, M. G. Lattanzi, W. O'Mullane, E. K. Grebel, A. D. Holland, C. Huc, X. Passot, L. Bramante, C. Cacciari, J. Castañeda, L. Chaoul, N. Cheek, F. De Angeli, C. Fabricius, R. Guerra, J. Hernández, A. Jean-Antoine-Piccolo, E. Masana, R. Messineo, N. Mowlavi, K. Nienartowicz, D. Ordóñez-Blanco, P. Panuzzo, J. Portell, P. J. Richards, M. Riello, G. M. Seabroke, P. Tanga, F. Thévenin, J. Torra, S. G. Els, G. Gracia-Abril, G. Comoretto, M. Garcia-Reinaldos, T. Lock, E. Mercier, M. Altmann, R. Andrae, T. L. Astraatmadja, I. Bellas-Velidis, K. Benson, J. Berthier, R. Blomme, G. Busso, B. Carry, A. Cellino, G. Clementini, S. Cowell, O. Creevey, J. Cuypers, M. Davidson, J. De Ridder, A. de Torres, L. Delchambre, A. Dell'Oro, C. Ducourant, Y. Frémat, M. García-Torres, E. Gosset, J. L. Halbwachs, N. C. Hambly, D. L. Harrison, M. Hauser, D. Hestroffer, S. T. Hodgkin, H. E. Huckle, A. Hutton, G. Jasniewicz, S. Jordan, M. Kontizas, A. J. Korn, A. C. Lanzafame, M. Manteiga, A. Moitinho, K. Muinonen, J. Osinde, E. Pancino, T. Pauwels, J. M. Petit, A. Recio-Blanco, A. C. Robin, L. M. Sarro, C. Siopis, M. Smith, K. W. Smith, A. Sozzetti, W. Thuillot, W. van Reeven, Y. Viala, U. Abbas, A. Abreu Aramburu, S. Accart, J. J. Aguado, P. M. Allan, W. Allasia, G. Altavilla, M. A. Álvarez, J. Alves, R. I. Anderson, A. H. Andrei, E. Anglada Varela, E. Antiche, T. Antoja, S. Antón, B. Arcay, A. Atzei, L. Ayache, N. Bach, S. G. Baker, L. Balaguer-

Núñez, C. Barache, C. Barata, A. Barbier, F. Barblan, M. Baroni, D. Barrado y Navascués, M. Barros, M. A. Barstow, U. Becciani, M. Bellazzini, G. Bellei, A. Bello García, V. Belokurov, P. Bendjoya, A. Berihuete, L. Bianchi, O. Bienaymé, F. Billebaud, N. Blagorodnova, S. Blanco-Cuaresma, T. Boch, A. Bombrun, R. Borrachero, S. Bouquillon, G. Bourda, H. Bouy, A. Bragaglia, M. A. Breddels, N. Brouillet, T. Brüsemeister, B. Bucciarelli, F. Budnik, P. Burgess, R. Burgon, A. Burlacu, D. Busonero, R. Buzzi, E. Caffau, J. Cambras, H. Campbell, R. Cancelliere, T. Cantat-Gaudin, T. Carlucci, J. M. Carrasco, M. Castellani, P. Charlot, J. Charnas, P. Charvet, F. Chassat, A. Chiavassa, M. Clotet, G. Cocozza, R. S. Collins, P. Collins, G. Costigan, F. Crifo, N. J. G. Cross, M. Crosta, C. Crowley, C. Dafonte, Y. Damerdji, A. Dapergolas, P. David, M. David, P. De Cat, F. de Felice, P. de Laverny, F. De Luise, R. De March, D. de Martino, R. de Souza, J. Debosscher, E. del Pozo, M. Delbo, A. Delgado, H. E. Delgado, F. di Marco, P. Di Matteo, S. Diakite, E. Distefano, C. Dolding, S. Dos Anjos, P. Drazinos, J. Durán, Y. Dzigan, E. Ecale, B. Edvardsson, H. Enke, M. Erdmann, D. Escolar, M. Espina, N. W. Evans, G. Eynard Bontemps, C. Fabre, M. Fabrizio, S. Faigler, A. J. Falcão, M. Farràs Casas, F. Faye, L. Federici, G. Fedorets, J. Fernández-Hernández, P. Fernique, A. Fienga, F. Figueras, F. Filippi, K. Findeisen, A. Fonti, M. Fouesneau, E. Fraile, M. Fraser, J. Fuchs, R. Furnell, M. Gai, S. Galleti, L. Galluccio, D. Garabato, F. García-Sedano, P. Garé, A. Garofalo, N. Garralda, P. Gavras, J. Gerssen, R. Geyer, G. Gilmore, S. Girona, G. Giuffrida, M. Gomes, A. González-Marcos, J. González-Núñez, J. J. González-Vidal, M. Granvik, A. Guerrier, P. Guillout, J. Guiraud, A. Gúrpide, R. Gutiérrez-Sánchez, L. P. Guy, R. Haigron, D. Hatzidimitriou, M. Haywood, U. Heiter, A. Helmi, D. Hobbs, W. Hofmann, B. Holl, G. Holland, J. A. S. Hunt, A. Hypki, V. Icardi, M. Irwin, G. Jevardat de Fombelle, P. Jofré, P. G. Jonker, A. Jorissen, F. Julbe, A. Karampelas, A. Kochoska, R. Kohley, K. Kolenberg, E. Kontizas, S. E. Koposov, G. Kordopatis, P. Koubsky, A. Kowalczyk, A. Krone-Martins, M. Kudryashova, I. Kull, R. K. Bachchan, F. Lacoste-Seris, A. F. Lanza, J. B. Lavigne, C. Le Poncin-Lafitte, Y. Lebreton, T. Lebzelter, S. Leccia, N. Leclerc, I. Lecoeur-Taibi, V. Lemaitre, H. Lenhardt, F. Leroux, S. Liao, E. Licata, H. E. P. Lindstrøm, T. A. Lister, E. Livanou, A. Lobel, W. Löffler, M. López, A. Lopez-Lozano, D. Lorenz, T. Loureiro, I. MacDonald, T. Magalhães Fernandes, S. Managau, R. G. Mann, G. Mantelet, O. Marchal, J. M. Marchant, M. Marconi, J. Marie, S. Marinoni, P. M. Marrese, G. Marschalkó, D. J. Marshall, J. M. Martín-Fleitas, M. Martino, N. Mary, G. Matijevic, T. Mazeh, P. J. McMillan, S. Messina, A. Mestre, D. Michalik, N. R. Millar, B. M. H. Miranda, D. Molina, R. Molinaro,

M. Molinaro, L. Molnár, M. Moniez, P. Montegriffo, D. Monteiro, R. Mor, A. Mora, R. Morbidelli, T. Morel, S. Morgenthaler, T. Morley, D. Morris, A. F. Mulone, T. Muraveva, I. Musella, J. Narbonne, G. Nelemans, L. Nicastro, L. Noval, C. Ordénovic, J. Ordieres-Meré, P. Osborne, C. Pagani, I. Pagano, F. Pailler, H. Palacin, L. Palaversa, P. Parsons, T. Paulsen, M. Pecoraro, R. Pedrosa, H. Pentikäinen, J. Pereira, B. Pichon, A. M. Piersimoni, F. X. Pineau, E. Plachy, G. Plum, E. Poujoulet, A. Prsa, L. Pulone, S. Ragaini, S. Rago, N. Rambaux, M. Ramos-Lerate, P. Ranalli, G. Rauw, A. Read, S. Regibo, F. Renk, C. Reylé, R. A. Ribeiro, L. Rimoldini, V. Ripepi, A. Riva, G. Rixon, M. Roelens, M. Romero-Gómez, N. Rowell, F. Royer, A. Rudolph, L. Ruiz-Dern, G. Sadowski, T. Sagristà Sellés, J. Sahlmann, J. Salgado, E. Salguero, M. Sarasso, H. Savietto, A. Schnorhk, M. Schultheis, E. Sciacca, M. Segol, J. C. Segovia, D. Segransan, E. Serpell, I. C. Shih, R. Smareglia, R. L. Smart, C. Smith, E. Solano, F. Solitro, R. Sordo, S. Soria Nieto, J. Souchay, A. Spagna, F. Spoto, U. Stampa, I. A. Steele, H. Steidelmüller, C. A. Stephenson, H. Stoev, F. F. Suess, M. Süveges, J. Surdej, L. Szabados, E. Szegedi-Elek, D. Tapiador, F. Taris, G. Tauran, M. B. Taylor, R. Teixeira, D. Terrett, B. Tingley, S. C. Trager, C. Turon, A. Ulla, E. Utrilla, G. Valentini, A. van Elteren, E. Van Hemelryck, M. van Leeuwen, M. Varadi, A. Vecchiato, J. Veljanoski, T. Via, D. Vicente, S. Vogt, H. Voss, V. Votruba, S. Voutsinas, G. Walmsley, M. Weiler, K. Weingrill, D. Werner, T. Wevers, G. Whitehead, Ł. Wyrzykowski, A. Yoldas, M. $vZerjal, S. Zucker, C. Zurbach, T. Zwitter, A. Alecu, M. Allen, C. AllendePrieto, A. Amorim, G.$ $A1, Nov.2016. doi : .$

Gaia Collaboration, A. G. A. Brown, A. Vallenari, T. Prusti, J. H. J. de Bruijne, C. Babusiaux, M. Biermann, O. L. Creevey, D. W. Evans, L. Eyer, A. Hutton, F. Jansen, C. Jordi, S. A. Klioner, U. Lammers, L. Lindegren, X. Luri, F. Mignard, C. Panem, D. Pourbaix, S. Randich, P. Sartoretti, C. Soubiran, N. A. Walton, F. Arenou, C. A. L. Bailer-Jones, U. Bastian, M. Cropper, R. Drimmel, D. Katz, M. G. Lattanzi, F. van Leeuwen, J. Bakker, C. Cacciari, J. Castañeda, F. De Angeli, C. Ducourant, C. Fabricius, M. Fouesneau, Y. Frémat, R. Guerra, A. Guerrier, J. Guiraud, A. Jean-Antoine Piccolo, E. Masana, R. Messineo, N. Mowlavi, C. Nicolas, K. Nienartowicz, F. Pailler, P. Panuzzo, F. Riclet, W. Roux, G. M. Seabroke, R. Sordo, P. Tanga, F. Thévenin, G. Gracia-Abril, J. Portell, D. Teyssier, M. Altmann, R. Andrae, I. Bellas-Velidis, K. Benson, J. Berthier, R. Blomme, E. Brugaletta, P. W. Burgess, G. Busso, B. Carry, A. Cellino, N. Cheek, G. Clementini, Y. Damerdji, M. Davidson, L. Delchambre, A. Dell'Oro, J. Fernández-Hernández, L. Galluccio,

P. García-Lario, M. Garcia-Reinaldos, J. González-Núñez, E. Gosset, R. Haigron, J. L. Halbwachs, N. C. Hambly, D. L. Harrison, D. Hatzidimitriou, U. Heiter, J. Hernández, D. Hestroffer, S. T. Hodgkin, B. Holl, K. Janßen, G. Jevardat de Fombelle, S. Jordan, A. Krone-Martins, A. C. Lanzafame, W. Löffler, A. Lorca, M. Manteiga, O. Marchal, P. M. Marrese, A. Moitinho, A. Mora, K. Muinonen, P. Osborne, E. Pancino, T. Pauwels, J. M. Petit, A. Recio-Blanco, P. J. Richards, M. Riello, L. Rimoldini, A. C. Robin, T. Roegiers, J. Rybizki, L. M. Sarro, C. Siopis, M. Smith, A. Sozzetti, A. Ulla, E. Utrilla, M. van Leeuwen, W. van Reeven, U. Abbas, A. Abreu Aramburu, S. Accart, C. Aerts, J. J. Aguado, M. Ajaj, G. Altavilla, M. A. Álvarez, J. Álvarez Cid-Fuentes, J. Alves, R. I. Anderson, E. Anglada Varela, T. Antoja, M. Audard, D. Baines, S. G. Baker, L. Balaguer-Núñez, E. Balbinot, Z. Balog, C. Barache, D. Barbato, M. Barros, M. A. Barstow, S. Bartolomé, J. L. Bassilana, N. Bauchet, A. Baudesson-Stella, U. Becciani, M. Bellazzini, M. Bernet, S. Bertone, L. Bianchi, S. Blanco-Cuaresma, T. Boch, A. Bombrun, D. Bossini, S. Bouquillon, A. Bragaglia, L. Bramante, E. Breedt, A. Bressan, N. Brouillet, B. Bucciarelli, A. Burlacu, D. Busonero, A. G. Butkevich, R. Buzzi, E. Caffau, R. Cancelliere, H. Cánovas, T. Cantat-Gaudin, R. Carballo, T. Carlucci, M. I. Carnerero, J. M. Carrasco, L. Casamiquela, M. Castellani, A. Castro-Ginard, P. Castro Sampol, L. Chaoul, P. Charlot, L. Chemin, A. Chiavassa, M. R. L. Cioni, G. Comoretto, W. J. Cooper, T. Cornez, S. Cowell, F. Crifo, M. Crosta, C. Crowley, C. Dafonte, A. Dapergolas, M. David, P. David, P. de Laverny, F. De Luise, R. De March, J. De Ridder, R. de Souza, P. de Teodoro, A. de Torres, E. F. del Peloso, E. del Pozo, M. Delbo, A. Delgado, H. E. Delgado, J. B. Delisle, P. Di Matteo, S. Diakite, C. Diener, E. Distefano, C. Dolding, D. Eappachen, B. Edvardsson, H. Enke, P. Esquej, C. Fabre, M. Fabrizio, S. Faigler, G. Fedorets, P. Fernique, A. Fienga, F. Figueras, C. Fouron, F. Fragkoudi, E. Fraile, F. Franke, M. Gai, D. Garabato, A. Garcia-Gutierrez, M. García-Torres, A. Garofalo, P. Gavras, E. Gerlach, R. Geyer, P. Giacobbe, G. Gilmore, S. Girona, G. Giuffrida, R. Gomel, A. Gomez, I. Gonzalez-Santamaria, J. J. González-Vidal, M. Granvik, R. Gutiérrez-Sánchez, L. P. Guy, M. Hauser, M. Haywood, A. Helmi, S. L. Hidalgo, T. Hilger, N. Hładczuk, D. Hobbs, G. Holland, H. E. Huckle, G. Jasniewicz, P. G. Jonker, J. Juaristi Campillo, F. Julbe, L. Karbevska, P. Kervella, S. Khanna, A. Kochoska, M. Kontizas, G. Kordopatis, A. J. Korn, Z. Kostrzewa-Rutkowska, K. Kruszyńska, S. Lambert, A. F. Lanza, Y. Lasne, J. F. Le Campion, Y. Le Fustec, Y. Lebreton, T. Lebzelter, S. Leccia, N. Leclerc, I. Lecoeur-Taibi, S. Liao, E. Licata, E. P. Lindstrøm, T. A. Lister, E. Livanou, A. Lobel, P. Madrero Pardo, S. Managau, R. G. Mann, J. M. Marchant,

M. Marconi, M. M. S. Marcos Santos, S. Marinoni, F. Marocco, D. J. Marshall, L. Martin Polo, J. M. Martín-Fleitas, A. Masip, D. Massari, A. Mastrobuono-Battisti, T. Mazeh, P. J. McMillan, S. Messina, D. Michalik, N. R. Millar, A. Mints, D. Molina, R. Molinaro, L. Molnár, P. Montegriffo, R. Mor, R. Morbidelli, T. Morel, D. Morris, A. F. Mulone, D. Munoz, T. Muraveva, C. P. Murphy, I. Musella, L. Noval, C. Ordénovic, G. Orrù, J. Osinde, C. Pagani, I. Pagano, L. Palaversa, P. A. Palicio, A. Panahi, M. Pawlak, X. Peñalosa Esteller, A. Penttilä, A. M. Piersimoni, F. X. Pineau, E. Plachy, G. Plum, E. Poggio, E. Poretti, E. Poujoulet, A. Prsa, L. Pulone, E. Racero, S. Ragaini, M. Rainer, C. M. Raiteri, N. Rambaux, P. Ramos, M. Ramos-Lerate, P. Re Fiorentin, S. Regibo, C. Reylé, V. Ripepi, A. Riva, G. Rixon, N. Robichon, C. Robin, M. Roelens, L. Rohrbasser, M. Romero-Gómez, N. Rowell, F. Royer, K. A. Rybicki, G. Sadowski, A. Sagristà Sellés, J. Sahlmann, J. Salgado, E. Salguero, N. Samaras, V. Sanchez Gimenez, N. Sanna, R. Santoveña, M. Sarasso, M. Schultheis, E. Sciacca, M. Segol, J. C. Segovia, D. Ségransan, D. Semeux, S. Shahaf, H. I. Siddiqui, A. Siebert, L. Siltala, E. Slezak, R. L. Smart, E. Solano, F. Solitro, D. Souami, J. Souchay, A. Spagna, F. Spoto, I. A. Steele, H. Steidelmüller, C. A. Stephenson, M. Süveges, L. Szabados, E. Szegedi-Elek, F. Taris, G. Tauran, M. B. Taylor, R. Teixeira, W. Thuillot, N. Tonello, F. Torra, J. Torra, C. Turon, N. Unger, M. Vaillant, E. van Dillen, O. Vanel, A. Vecchiato, Y. Viala, D. Vicente, S. Voutsinas, M. Weiler, T. Wevers, Ł. Wyrzykowski, A. Yoldas, P. Yvard, H. Zhao, J. Zorec, S. Zucker, C. Zurbach, and T. Zwitter. Gaia Early Data Release 3. Summary of the contents and survey properties. *Astronomy & Astrophysics*, 649:A1, May 2021. 10.1051/0004-6361/202039657.

Gaia Collaboration, A. Vallenari, A. G. A. Brown, T. Prusti, J. H. J. de Bruijne, F. Arenou, C. Babusiaux, M. Biermann, O. L. Creevey, C. Ducourant, D. W. Evans, L. Eyer, R. Guerra, A. Hutton, C. Jordi, S. A. Klioner, U. L. Lammers, L. Lindegren, X. Luri, F. Mignard, C. Panem, D. Pourbaix, S. Randich, P. Sartoretti, C. Soubiran, P. Tanga, N. A. Walton, C. A. L. Bailer-Jones, U. Bastian, R. Drimmel, F. Jansen, D. Katz, M. G. Lattanzi, F. van Leeuwen, J. Bakker, C. Cacciari, J. Castañeda, F. De Angeli, C. Fabricius, M. Fouesneau, Y. Frémat, L. Galluccio, A. Guerrier, U. Heiter, E. Masana, R. Messineo, N. Mowlavi, C. Nicolas, K. Nienartowicz, F. Pailler, P. Panuzzo, F. Riclet, W. Roux, G. M. Seabroke, R. Sordoørcit, F. Thévenin, G. Gracia-Abril, J. Portell, D. Teyssier, M. Altmann, R. Andrae, M. Audard, I. Bellas-Velidis, K. Benson, J. Berthier, R. Blomme, P. W. Burgess, D. Busonero, G. Busso, H. Cánovas, B. Carry, A. Cellino, N. Cheek,

G. Clementini, Y. Damerdji, M. Davidson, P. de Teodoro, M. Nuñez Campos, L. Delchambre, A. Dell'Oro, P. Esquej, J. Fernández-Hernández, E. Fraile, D. Garabato, P. García-Lario, E. Gosset, R. Haigron, J. L. Halbwachs, N. C. Hambly, D. L. Harrison, J. Hernández, D. Hestroffer, S. T. Hodgkin, B. Holl, K. Janßen, G. Jevardat de Fombelle, S. Jordan, A. Krone-Martins, A. C. Lanzafame, W. Löffler, O. Marchal, P. M. Marrese, A. Moitinho, K. Muinonen, P. Osborne, E. Pancino, T. Pauwels, A. Recio-Blanco, C. Reylé, M. Riello, L. Rimoldini, T. Roegiers, J. Rybizki, L. M. Sarro, C. Siopis, M. Smith, A. Sozzetti, E. Utrilla, M. van Leeuwen, U. Abbas, P. Ábrahám, A. Abreu Aramburu, C. Aerts, J. J. Aguado, M. Ajaj, F. Aldea-Montero, G. Altavilla, M. A. Álvarez, J. Alves, F. Anders, R. I. Anderson, E. Anglada Varela, T. Antoja, D. Baines, S. G. Baker, L. Balaguer-Núñez, E. Balbinot, Z. Balog, C. Barache, D. Barbato, M. Barros, M. A. Barstow, S. Bartolomé, J. L. Bassilana, N. Bauchet, U. Becciani, M. Bellazzini, A. Berihuete, M. Bernet, S. Bertone, L. Bianchi, A. Binnenfeld, S. Blanco-Cuaresma, A. Blazere, T. Boch, A. Bombrun, D. Bossini, S. Bouquillon, A. Bragaglia, L. Bramante, E. Breedt, A. Bressan, N. Brouillet, E. Brugaletta, B. Bucciarelli, A. Burlacu, A. G. Butkevich, R. Buzzi, E. Caffau, R. Cancelliere, T. Cantat-Gaudin, R. Carballo, T. Carlucci, M. I. Carnerero, J. M. Carrasco, L. Casamiquela, M. Castellani, A. Castro-Ginard, L. Chaoul, P. Charlot, L. Chemin, V. Chiaramida, A. Chiavassa, N. Chornay, G. Comoretto, G. Contursi, W. J. Cooper, T. Cornez, S. Cowell, F. Crifo, M. Cropper, M. Crosta, C. Crowley, C. Dafonte, A. Dapergolas, M. David, P. David, P. de Laverny, F. De Luise, R. De March, J. De Ridder, R. de Souza, A. de Torres, E. F. del Peloso, E. del Pozo, M. Delbo, A. Delgado, J. B. Delisle, C. Demouchy, T. E. Dharmawardena, P. Di Matteo, S. Diakite, C. Diener, E. Distefano, C. Dolding, B. Edvardsson, H. Enke, C. Fabre, M. Fabrizio, S. Faigler, G. Fedorets, P. Fernique, A. Fienga, F. Figueras, Y. Fournier, C. Fouron, F. Fragkoudi, M. Gai, A. Garcia-Gutierrez, M. Garcia-Reinaldos, M. García-Torres, A. Garofalo, A. Gavel, P. Gavras, E. Gerlach, R. Geyer, P. Giacobbe, G. Gilmore, S. Girona, G. Giuffrida, R. Gomel, A. Gomez, J. González-Núñez, I. González-Santamaría, J. J. González-Vidal, M. Granvik, P. Guillout, J. Guiraud, R. Gutiérrez-Sánchez, L. P. Guy, D. Hatzidimitriou, M. Hauser, M. Haywood, A. Helmer, A. Helmi, M. H. Sarmiento, S. L. Hidalgo, T. Hilger, N. Hładczuk, D. Hobbs, G. Holland, H. E. Huckle, K. Jardine, G. Jasniewicz, A. Jean-Antoine Piccolo, Ó. Jiménez-Arranz, A. Jorissen, J. Juaristi Campillo, F. Julbe, L. Karbevska, P. Kervella, S. Khanna, M. Kontizas, G. Kordopatis, A. J. Korn, Á. Kóspál, Z. Kostrzewa-Rutkowska, K. Kruszyńska, M. Kun, P. Laizeau, S. Lambert, A. F. Lanza, Y. Lasne, J. F. Le Cam-

pion, Y. Lebreton, T. Lebzelter, S. Leccia, N. Leclerc, I. Lecoeur-Taibi, S. Liao, E. L. Licata, H. E. P. Lindstrøm, T. A. Lister, E. Livanou, A. Lobel, A. Lorca, C. Loup, P. Madrero Pardo, A. Magdaleno Romeo, S. Managau, R. G. Mann, M. Manteiga, J. M. Marchant, M. Marconi, J. Marcos, M. M. S. Marcos Santos, D. Marín Pina, S. Marinoni, F. Marocco, D. J. Marshall, L. M. Polo, J. M. Martín-Fleitas, G. Marton, N. Mary, A. Masip, D. Massari, A. Mastrobuono-Battisti, T. Mazeh, P. J. McMillan, S. Messina, D. Michalik, N. R. Millar, A. Mints, D. Molina, R. Molinaro, L. Molnár, G. Monari, M. Monguió, P. Montegriffo, A. Montero, R. Mor, A. Mora, R. Morbidelli, T. Morel, D. Morris, T. Muraveva, C. P. Murphy, I. Musella, Z. Nagy, L. Noval, F. Ocaña, A. Ogden, C. Ordenovic, J. O. Osinde, C. Pagani, I. Pagano, L. Palaversa, P. A. Palicio, L. Pallas-Quintela, A. Panahi, S. Payne-Wardenaar, X. Peñalosa Esteller, A. Penttilä, B. Pichon, A. M. Piersimoni, F. X. Pineau, E. Plachy, G. Plum, E. Poggio, A. Prsa, L. Pulone, E. Racero, S. Ragaini, M. Rainer, C. M. Raiteri, N. Rambaux, P. Ramos, M. Ramos-Lerate, P. Re Fiorentin, S. Regibo, P. J. Richards, C. Rios Diaz, V. Ripepi, A. Riva, H. W. Rix, G. Rixon, N. Robichon, A. C. Robin, C. Robin, M. Roelens, H. R. O. Rogues, L. Rohrbasser, M. Romero-Gómez, N. Rowell, F. Royer, D. Ruz Mieres, K. A. Rybicki, G. Sadowski, A. Sáez Núñez, A. Sagristà Sellés, J. Sahlmann, E. Salguero, N. Samaras, V. Sanchez Gimenez, N. Sanna, R. Santoveña, M. Sarasso, M. Schultheis, E. Sciacca, M. Segol, J. C. Segovia, D. Ségransan, D. Semeux, S. Shahaf, H. I. Siddiqui, A. Siebert, L. Siltala, A. Silvelo, E. Slezak, I. Slezak, R. L. Smart, O. N. Snaith, E. Solano, F. Solitro, D. Souami, J. Souchay, A. Spagna, L. Spina, F. Spoto, I. A. Steele, H. Steidelmüller, C. A. Stephenson, M. Süveges, J. Surdej, L. Szabados, E. Szegedi-Elek, F. Taris, M. B. Taylo, R. Teixeira, L. Tolomei, N. Tonello, F. Torra, J. Torra, G. Torralba Elipe, M. Trabucchi, A. T. Tsounis, C. Turon, A. Ulla, N. Unger, M. V. Vaillant, E. van Dillen, W. van Reeven, O. Vanel, A. Vecchiato, Y. Viala, D. Vicente, S. Voutsinas, M. Weiler, T. Wevers, L. Wyrzykowski, A. Yoldas, P. Yvard, H. Zhao, J. Zorec, S. Zucker, and T. Zwitter. Gaia Data Release 3: Summary of the content and survey properties. *arXiv e-prints*, art. arXiv:2208.00211, July 2022. 10.48550/arXiv.2208.00211.

Gaia Collaboration, A. Vallenari, A. G. A. Brown, T. Prusti, J. H. J. de Bruijne, F. Arenou, C. Babusiaux, M. Biermann, O. L. Creevey, C. Ducourant, D. W. Evans, L. Eyer, R. Guerra, A. Hutton, C. Jordi, S. A. Klioner, U. L. Lammers, L. Lindegren, X. Luri, F. Mignard, C. Panem, D. Pourbaix, S. Randich, P. Sartoretti, C. Soubiran, P. Tanga, N. A. Walton, C. A. L. Bailer-Jones, U. Bastian, R. Drimmel, F. Jansen,

D. Katz, M. G. Lattanzi, F. van Leeuwen, J. Bakker, C. Cacciari, J. Castañeda, F. De Angeli, C. Fabricius, M. Fouesneau, Y. Frémat, L. Galluccio, A. Guerrier, U. Heiter, E. Masana, R. Messineo, N. Mowlavi, C. Nicolas, K. Nienartowicz, F. Pailler, P. Panuzzo, F. Riclet, W. Roux, G. M. Seabroke, R. Sordo, F. Thévenin, G. Gracia-Abril, J. Portell, D. Teyssier, M. Altmann, R. Andrae, M. Audard, I. Bellas-Velidis, K. Benson, J. Berthier, R. Blomme, P. W. Burgess, D. Busonero, G. Busso, H. Cánovas, B. Carry, A. Cellino, N. Cheek, G. Clementini, Y. Damerdji, M. Davidson, P. de Teodoro, M. Nuñez Campos, L. Delchambre, A. Dell'Oro, P. Esquej, J. Fernández-Hernández, E. Fraile, D. Garabato, P. García-Lario, E. Gosset, R. Haigron, J. L. Halbwachs, N. C. Hambly, D. L. Harrison, J. Hernández, D. Hestroffer, S. T. Hodgkin, B. Holl, K. Janßen, G. Jevardat de Fombelle, S. Jordan, A. Krone-Martins, A. C. Lanzafame, W. Löffler, O. Marchal, P. M. Marrese, A. Moitinho, K. Muinonen, P. Osborne, E. Pancino, T. Pauwels, A. Recio-Blanco, C. Reylé, M. Riello, L. Rimoldini, T. Roegiers, J. Rybizki, L. M. Sarro, C. Siopis, M. Smith, A. Sozzetti, E. Utrilla, M. van Leeuwen, U. Abbas, P. Ábrahám, A. Abreu Aramburu, C. Aerts, J. J. Aguado, M. Ajaj, F. Aldea-Montero, G. Altavilla, M. A. Álvarez, J. Alves, F. Anders, R. I. Anderson, E. Anglada Varela, T. Antoja, D. Baines, S. G. Baker, L. Balaguer-Núñez, E. Balbinot, Z. Balog, C. Barache, D. Barbato, M. Barros, M. A. Barstow, S. Bartolomé, J. L. Bassilana, N. Bauchet, U. Becciani, M. Bellazzini, A. Berihuete, M. Bernet, S. Bertone, L. Bianchi, A. Binnenfeld, S. Blanco-Cuaresma, A. Blazere, T. Boch, A. Bombrun, D. Bossini, S. Bouquillon, A. Bragaglia, L. Bramante, E. Breedt, A. Bressan, N. Brouillet, E. Brugaletta, B. Bucciarelli, A. Burlacu, A. G. Butkevich, R. Buzzi, E. Caffau, R. Cancelliere, T. Cantat-Gaudin, R. Carballo, T. Carlucci, M. I. Carnerero, J. M. Carrasco, L. Casamiquela, M. Castellani, A. Castro-Ginard, L. Chaoul, P. Charlot, L. Chemin, V. Chiaramida, A. Chiavassa, N. Chornay, G. Comoretto, G. Contursi, W. J. Cooper, T. Cornez, S. Cowell, F. Crifo, M. Cropper, M. Crosta, C. Crowley, C. Dafonte, A. Dapergolas, M. David, P. David, P. de Laverny, F. De Luise, R. De March, J. De Ridder, R. de Souza, A. de Torres, E. F. del Peloso, E. del Pozo, M. Delbo, A. Delgado, J. B. Delisle, C. Demouchy, T. E. Dharmawardena, P. Di Matteo, S. Diakite, C. Diener, E. Distefano, C. Dolding, B. Edvardsson, H. Enke, C. Fabre, M. Fabrizio, S. Faigler, G. Fedorets, P. Fernique, A. Fienga, F. Figueras, Y. Fournier, C. Fouron, F. Fragkoudi, M. Gai, A. Garcia-Gutierrez, M. Garcia-Reinaldos, M. García-Torres, A. Garofalo, A. Gavel, P. Gavras, E. Gerlach, R. Geyer, P. Giacobbe, G. Gilmore, S. Girona, G. Giuffrida, R. Gomel, A. Gomez, J. González-Núñez, I. González-Santamaría, J. J. González-Vidal, M. Granvik, P. Guillout, J. Guiraud, R. Gutiérrez-Sánchez,

L. P. Guy, D. Hatzidimitriou, M. Hauser, M. Haywood, A. Helmer, A. Helmi, M. H. Sarmiento, S. L. Hidalgo, T. Hilger, N. Hładczuk, D. Hobbs, G. Holland, H. E. Huckle, K. Jardine, G. Jasniewicz, A. Jean-Antoine Piccolo, Ó. Jiménez-Arranz, A. Jorissen, J. Juaristi Campillo, F. Julbe, L. Karbevska, P. Kervella, S. Khanna, M. Kontizas, G. Kordopatis, A. J. Korn, Á. Kóspál, Z. Kostrzewa-Rutkowska, K. Kruszyńska, M. Kun, P. Laizeau, S. Lambert, A. F. Lanza, Y. Lasne, J. F. Le Campion, Y. Lebreton, T. Lebzelter, S. Leccia, N. Leclerc, I. Lecoeur-Taibi, S. Liao, E. L. Licata, H. E. P. Lindstrøm, T. A. Lister, E. Livanou, A. Lobel, A. Lorca, C. Loup, P. Madrero Pardo, A. Magdaleno Romeo, S. Managau, R. G. Mann, M. Manteiga, J. M. Marchant, M. Marconi, J. Marcos, M. M. S. Marcos Santos, D. Marín Pina, S. Marinoni, F. Marocco, D. J. Marshall, L. Martin Polo, J. M. Martín-Fleitas, G. Marton, N. Mary, A. Masip, D. Massari, A. Mastrobuono-Battisti, T. Mazeh, P. J. McMillan, S. Messina, D. Michalik, N. R. Millar, A. Mints, D. Molina, R. Molinaro, L. Molnár, G. Monari, M. Monguió, P. Montegriffo, A. Montero, R. Mor, A. Mora, R. Morbidelli, T. Morel, D. Morris, T. Muraveva, C. P. Murphy, I. Musella, Z. Nagy, L. Noval, F. Ocaña, A. Ogden, C. Ordenovic, J. O. Osinde, C. Pagani, I. Pagano, L. Palaversa, P. A. Palicio, L. Pallas-Quintela, A. Panahi, S. Payne-Wardenaar, X. Peñalosa Esteller, A. Penttilä, B. Pichon, A. M. Piersimoni, F. X. Pineau, E. Plachy, G. Plum, E. Poggio, A. Prsa, L. Pulone, E. Racero, S. Ragaini, M. Rainer, C. M. Raiteri, N. Rambaux, P. Ramos, M. Ramos-Lerate, P. Re Fiorentin, S. Regibo, P. J. Richards, C. Rios Diaz, V. Ripepi, A. Riva, H. W. Rix, G. Rixon, N. Robichon, A. C. Robin, C. Robin, M. Roelens, H. R. O. Rogues, L. Rohrbasser, M. Romero-Gómez, N. Rowell, F. Royer, D. Ruz Mieres, K. A. Rybicki, G. Sadowski, A. Sáez Núñez, A. Sagristà Sellés, J. Sahlmann, E. Salguero, N. Samaras, V. Sanchez Gimenez, N. Sanna, R. Santoveña, M. Sarasso, M. Schultheis, E. Sciacca, M. Segol, J. C. Segovia, D. Ségransan, D. Semeux, S. Shahaf, H. I. Siddiqui, A. Siebert, L. Siltala, A. Silvelo, E. Slezak, I. Slezak, R. L. Smart, O. N. Snaith, E. Solano, F. Solitro, D. Souami, J. Souchay, A. Spagna, L. Spina, F. Spoto, I. A. Steele, H. Steidelmüller, C. A. Stephenson, M. Süveges, J. Surdej, L. Szabados, E. Szegedi-Elek, F. Taris, M. B. Taylor, R. Teixeira, L. Tolomei, N. Tonello, F. Torra, J. Torra, G. Torralba Elipe, M. Trabucchi, A. T. Tsounis, C. Turon, A. Ulla, N. Unger, M. V. Vaillant, E. van Dillen, W. van Reeven, O. Vanel, A. Vecchiato, Y. Viala, D. Vicente, S. Voutsinas, M. Weiler, T. Wevers, Ł. Wyrzykowski, A. Yoldas, P. Yvard, H. Zhao, J. Zorec, S. Zucker, and T. Zwitter. Gaia Data Release 3. Summary of the content and survey properties. *Astronomy & Astrophysics*, 674:A1, June 2023a. 10.1051/0004-6361/202243940.

Gaia Collaboration, A. Vallenari, A. G. A. Brown, T. Prusti, J. H. J. de Bruijne, F. Arenou, C. Babusiaux, M. Biermann, O. L. Creevey, C. Ducourant, D. W. Evans, L. Eyer, R. Guerra, A. Hutton, C. Jordi, S. A. Klioner, U. L. Lammers, L. Lindegren, X. Luri, F. Mignard, C. Panem, D. Pourbaix, S. Randich, P. Sartoretti, C. Soubiran, P. Tanga, N. A. Walton, C. A. L. Bailer-Jones, U. Bastian, R. Drimmel, F. Jansen, D. Katz, M. G. Lattanzi, F. van Leeuwen, J. Bakker, C. Cacciari, J. Castañeda, F. De Angeli, C. Fabricius, M. Fouesneau, Y. Frémat, L. Galluccio, A. Guerrier, U. Heiter, E. Masana, R. Messineo, N. Mowlavi, C. Nicolas, K. Nienartowicz, F. Pailler, P. Panuzzo, F. Riclet, W. Roux, G. M. Seabroke, R. Sordo, F. Thévenin, G. Gracia-Abril, J. Portell, D. Teyssier, M. Altmann, R. Andrae, M. Audard, I. Bellas-Velidis, K. Benson, J. Berthier, R. Blomme, P. W. Burgess, D. Busonero, G. Busso, H. Cánovas, B. Carry, A. Cellino, N. Cheek, G. Clementini, Y. Damerdji, M. Davidson, P. de Teodoro, M. Nuñez Campos, L. Delchambre, A. Dell'Oro, P. Esquej, J. Fernández-Hernández, E. Fraile, D. Garabato, P. García-Lario, E. Gosset, R. Haigron, J. L. Halbwachs, N. C. Hambly, D. L. Harrison, J. Hernández, D. Hestroffer, S. T. Hodgkin, B. Holl, K. Janßen, G. Jevardat de Fombelle, S. Jordan, A. Krone-Martins, A. C. Lanzafame, W. Löffler, O. Marchal, P. M. Marrese, A. Moitinho, K. Muinonen, P. Osborne, E. Pancino, T. Pauwels, A. Recio-Blanco, C. Reylé, M. Riello, L. Rimoldini, T. Roegiers, J. Rybizki, L. M. Sarro, C. Siopis, M. Smith, A. Sozzetti, E. Utrilla, M. van Leeuwen, U. Abbas, P. Ábrahám, A. Abreu Aramburu, C. Aerts, J. J. Aguado, M. Ajaj, F. Aldea-Montero, G. Altavilla, M. A. Álvarez, J. Alves, F. Anders, R. I. Anderson, E. Anglada Varela, T. Antoja, D. Baines, S. G. Baker, L. Balaguer-Núñez, E. Balbinot, Z. Balog, C. Barache, D. Barbato, M. Barros, M. A. Barstow, S. Bartolomé, J. L. Bassilana, N. Bauchet, U. Becciani, M. Bellazzini, A. Berihuete, M. Bernet, S. Bertone, L. Bianchi, A. Binnenfeld, S. Blanco-Cuaresma, A. Blazere, T. Boch, A. Bombrun, D. Bossini, S. Bouquillon, A. Bragaglia, L. Bramante, E. Breedt, A. Bressan, N. Brouillet, E. Brugaletta, B. Bucciarelli, A. Burlacu, A. G. Butkevich, R. Buzzi, E. Caffau, R. Cancelliere, T. Cantat-Gaudin, R. Carballo, T. Carlucci, M. I. Carnerero, J. M. Carrasco, L. Casamiquela, M. Castellani, A. Castro-Ginard, L. Chaoul, P. Charlot, L. Chemin, V. Chiaramida, A. Chiavassa, N. Chornay, G. Comoretto, G. Contursi, W. J. Cooper, T. Cornez, S. Cowell, F. Crifo, M. Cropper, M. Crosta, C. Crowley, C. Dafonte, A. Dapergolas, M. David, P. David, P. de Laverny, F. De Luise, and R. De March. Gaia Data Release 3. Summary of the content and survey properties. *Astronomy & Astrophysics*, 674:A1, June 2023b. 10.1051/0004-6361/202243940.

I. Galiullin, A. C. Rodriguez, K. El-Badry, P. Szkody, A. Anand, J. van Roestel, A. Sibgatullin, V. Dodon, N. Tyrin, I. Caiazzo, M. J. Graham, R. R. Laher, S. R. Kulkarni, T. A. Prince, R. Riddle, Z. P. Vanderbosch, and A. Wold. Searching for new cataclysmic variables in the Chandra Source Catalog. *Astronomy & Astrophysics*, 690:A374, Oct. 2024a. 10.1051/0004-6361/202450734.

I. Galiullin, A. C. Rodriguez, S. R. Kulkarni, R. Sunyaev, M. Gilfanov, I. Bikmaev, L. Yungelson, J. van Roestel, B. T. Gänsicke, I. Khamitov, P. Szkody, K. El-Badry, M. Suslikov, T. A. Prince, M. Buntov, I. Caiazzo, M. Gorbachev, M. J. Graham, R. Gumerov, E. Irtuganov, R. R. Laher, P. Medvedev, R. Riddle, B. Rusholme, N. Sakhibullin, A. Sklyanov, and Z. P. Vanderbosch. A joint SRG/eROSITA + ZTF search: Discovery of a 97-min period eclipsing cataclysmic variable with evidence of a brown dwarf secondary. *Monthly Notices of the Royal Astronomical Society*, 528(1):676–692, Feb. 2024b. 10.1093/mnras/stae012.

I. I. Galiullin and M. R. Gilfanov. X-ray Observations of Historical Classical Nova Counterparts with eROSITA Telescope Onboard the SRG Orbital Observatory during the All-Sky Survey. *Astronomy Letters*, 47(9):587–606, Sept. 2021. 10.1134/S1063773721090048.

B. T. Gänsicke, M. Dillon, J. Southworth, J. R. Thorstensen, P. Rodríguez-Gil, A. Aungwerojwit, T. R. Marsh, P. Szkody, S. C. C. Barros, J. Casares, D. de Martino, P. J. Groot, P. Hakala, U. Kolb, S. P. Littlefair, I. G. Martínez-Pais, G. Nelemans, and M. R. Schreiber. SDSS unveils a population of intrinsically faint cataclysmic variables at the minimum orbital period. *Monthly Notices of the Royal Astronomical Society*, 397(4):2170–2188, Aug. 2009. 10.1111/j.1365-2966.2009.15126.x.

M. R. Garcia, J. E. McClintock, R. Narayan, P. Callanan, D. Barret, and S. S. Murray. New Evidence for Black Hole Event Horizons from Chandra. *The Astrophysical Journal Letters*, 553(1):L47–L50, May 2001a. 10.1086/320494.

M. R. Garcia, J. E. McClintock, R. Narayan, P. Callanan, D. Barret, and S. S. Murray. New Evidence for Black Hole Event Horizons from Chandra. *The Astrophysical Journal Letters*, 553(1):L47–L50, May 2001b. 10.1086/320494.

E. Garcia-Berro, P. Loren-Aguilar, G. Aznar-Siguan, S. Torres, J. Camacho, L. G. Althaus, A. H. Corsico, B. Kulebi, and J. Isern. Double Degenerate Mergers as Progenitors of High-field Magnetic White Dwarfs. *The Astrophysical Journal*, 749 (1):25, Apr. 2012. 10.1088/0004-637X/749/1/25.

N. Gehrels. Confidence Limits for Small Numbers of Events in Astrophysical Data. *The Astrophysical Journal*, 303:336, Apr. 1986. 10.1086/164079.

A. Gelman and D. B. Rubin. Inference from Iterative Simulation Using Multiple Sequences. *Statistical Science*, 7:457–472, Jan. 1992. 10.1214/ss/1177011136.

N. P. Gentile Fusillo, P. E. Tremblay, E. Cukanovaite, A. Vorontseva, R. Lallement, M. Hollands, B. T. Gänsicke, K. B. Burdge, J. McCleery, and S. Jordan. A catalogue of white dwarfs in Gaia EDR3. *Monthly Notices of the Royal Astronomical Society*, 508(3):3877–3896, Dec. 2021a. 10.1093/mnras/stab2672.

N. P. Gentile Fusillo, P. E. Tremblay, E. Cukanovaite, A. Vorontseva, R. Lallement, M. Hollands, B. T. Gänsicke, K. B. Burdge, J. McCleery, and S. Jordan. A catalogue of white dwarfs in Gaia EDR3. *Monthly Notices of the Royal Astronomical Society*, 508(3):3877–3896, Dec. 2021b. 10.1093/mnras/stab2672.

R. Giacconi, G. Branduardi, U. Briel, A. Epstein, D. Fabricant, E. Feigelson, W. Forman, P. Gorenstein, J. Grindlay, H. Gursky, F. R. Harnden, J. P. Henry, C. Jones, E. Kellogg, D. Koch, S. Murray, E. Schreier, F. Seward, H. Tananbaum, K. Topka, L. Van Speybroeck, S. S. Holt, R. H. Becker, E. A. Boldt, P. J. Serlemitsos, G. Clark, C. Canizares, T. Markert, R. Novick, D. Helfand, and K. Long. The Einstein (HEAO 2) X-ray Observatory. *The Astrophysical Journal*, 230:540–550, June 1979. 10.1086/157110.

B. Giesers, S. Dreizler, T.-O. Husser, S. Kamann, G. Anglada Escudé, J. Brinchmann, C. M. Carollo, M. M. Roth, P. M. Weilbacher, and L. Wisotzki. A detached stellar-mass black hole candidate in the globular cluster NGC 3201. *Monthly Notices of the Royal Astronomical Society*, 475(1):L15–L19, Mar. 2018a. 10.1093/mnrasl/slx203.

B. Giesers, S. Dreizler, T.-O. Husser, S. Kamann, G. Anglada Escudé, J. Brinchmann, C. M. Carollo, M. M. Roth, P. M. Weilbacher, and L. Wisotzki. A detached stellar-mass black hole candidate in the globular cluster NGC 3201. *Monthly Notices of the Royal Astronomical Society*, 475(1):L15–L19, Mar. 2018b. 10.1093/mnrasl/slx203.

B. Giesers, S. Kamann, S. Dreizler, T.-O. Husser, A. Askar, F. Göttgens, J. Brinchmann, M. Latour, P. M. Weilbacher, M. Wendt, and M. M. Roth. A stellar census in

globular clusters with MUSE: Binaries in NGC 3201. *Astronomy & Astrophysics*, 632:A3, Dec. 2019. 10.1051/0004-6361/201936203.

R. L. Gilliland, E. Kemper, and N. Suntzeff. WZ Sagittae: Time-resolved Spectroscopy during Quiescence. *The Astrophysical Journal*, 301:252, Feb. 1986. 10.1086/163894.

A. Ginsburg, B. M. Sipőcz, C. E. Brasseur, P. S. Cowperthwaite, M. W. Craig, C. Deil, J. Guillochon, G. Guzman, S. Liedtke, P. Lian Lim, K. E. Lockhart, M. Mommert, B. M. Morris, H. Norman, M. Parikh, M. V. Persson, T. P. Robitaille, J.-C. Segovia, L. P. Singer, E. J. Tollerud, M. de Val-Borro, I. Valtchanov, J. Woillez, Astroquery Collaboration, and a subset of astropy Collaboration. astroquery: An Astronomical Web-querying Package in Python. *The Astronomical Journal*, 157 (3):98, Mar. 2019. 10.3847/1538-3881/aafc33.

S. Ginzburg, J. Fuller, A. Kawka, and I. Caiazzo. Slow convection and fast rotation in crystallization-driven white dwarf dynamos. *Monthly Notices of the Royal Astronomical Society*, 514(3):4111–4119, Aug. 2022. 10.1093/mnras/stac1363.

M. R. Goad, L. G. Tyler, A. P. Beardmore, P. A. Evans, S. R. Rosen, J. P. Osborne, R. L. C. Starling, F. E. Marshall, V. Yershov, D. N. Burrows, N. Gehrels, P. W. A. Roming, A. Moretti, M. Capalbi, J. E. Hill, J. Kennea, S. Koch, and D. vanden Berk. Accurate early positions for Swift GRBs: enhancing X-ray positions with UVOT astrometry. *Astronomy & Astrophysics*, 476(3):1401–1409, Dec. 2007. 10.1051/0004-6361:20078436.

T. Gold. Rotating Neutron Stars as the Origin of the Pulsating Radio Sources. *Nature*, 218(5143):731–732, May 1968. 10.1038/218731a0.

J. Goliasch and L. Nelson. Population Synthesis of Cataclysmic Variables. I. Inclusion of Detailed Nuclear Evolution. *The Astrophysical Journal*, 809(1):80, Aug. 2015. 10.1088/0004-637X/809/1/80.

M. J. Graham, S. R. Kulkarni, E. C. Bellm, S. M. Adams, C. Barbarino, N. Blagorodnova, D. Bodewits, B. Bolin, P. R. Brady, S. B. Cenko, C.-K. Chang, M. W. Coughlin, K. De, G. Eadie, T. L. Farnham, U. Feindt, A. Franckowiak, C. Fremling, S. Gezari, S. Ghosh, D. A. Goldstein, V. Z. Golkhou, A. Goobar, A. Y. Q. Ho, D. Huppenkothen, Z. Ivezic, R. L. Jones, M. Juric, D. L. Kaplan, M. M. Kasliwal, M. S. P.

Kelley, T. Kupfer, C.-D. Lee, H. W. Lin, R. Lunnan, A. A. Mahabal, A. A. Miller, C.-C. Ngeow, P. Nugent, E. O. Ofek, T. A. Prince, L. Rauch, J. van Roestel, S. Schulze, L. P. Singer, J. Sollerman, F. Taddia, L. Yan, Q.-Z. Ye, P.-C. Yu, T. Barlow, J. Bauer, R. Beck, J. Belicki, R. Biswas, V. Brinnel, T. Brooke, B. Bue, M. Bulla, R. Burruss, A. Connolly, J. Cromer, V. Cunningham, R. Dekany, A. Delacroix, V. Desai, D. A. Duev, M. Feeney, D. Flynn, S. Frederick, A. Gal-Yam, M. Giomi, S. Groom, E. Hacopians, D. Hale, G. Helou, J. Henning, D. Hover, L. A. Hillenbrand, J. Howell, T. Hung, D. Imel, W.-H. Ip, E. Jackson, S. Kaspi, S. Kaye, M. Kowalski, E. Kramer, M. Kuhn, W. Landry, R. R. Laher, P. Mao, F. J. Masci, S. Monkewitz, P. Murphy, J. Nordin, M. T. Patterson, B. Penprase, M. Porter, U. Rebbapragada, D. Reiley, R. Riddle, M. Rigault, H. Rodriguez, B. Rusholme, J. van Santen, D. L. Shupe, R. M. Smith, M. T. Soumagnac, R. Stein, J. Surace, P. Szkody, S. Terek, A. Van Sistine, S. van Velzen, W. T. Vestrand, R. Walters, C. Ward, C. Zhang, and J. Zolkower. The Zwicky Transient Facility: Science Objectives. *Publications of the Astronomical Society of the Pacific*, 131(1001):078001, July 2019. 10.1088/1538-3873/ab006c.

G. M. Green, E. Schlafly, C. Zucker, J. S. Speagle, and D. Finkbeiner. A 3D Dust Map Based on Gaia, Pan-STARRS 1, and 2MASS. *The Astrophysical Journal*, 887 (1):93, Dec. 2019a. 10.3847/1538-4357/ab5362.

G. M. Green, E. Schlafly, C. Zucker, J. S. Speagle, and D. Finkbeiner. A 3D Dust Map Based on Gaia, Pan-STARRS 1, and 2MASS. *The Astrophysical Journal*, 887 (1):93, Dec. 2019b. 10.3847/1538-4357/ab5362.

M. J. Green, T. R. Marsh, D. Steeghs, E. Breedt, T. Kupfer, P. Rodríguez-Gil, J. van Roestel, R. P. Ashley, L. Wang, E. Cukanovaite, and S. Outmani. Phase-resolved spectroscopy of Gaia14aae: line emission from near the white dwarf surface. *Monthly Notices of the Royal Astronomical Society*, 485(2):1947–1960, May 2019c. 10.1093/mnras/stz469.

P. C. Gregory and T. J. Loredo. A New Method for the Detection of a Periodic Signal of Unknown Shape and Period. *The Astrophysical Journal*, 398:146, Oct. 1992. 10.1086/171844.

J. Greiner and G. A. Richter. Optical counterparts of ROSAT X-ray sources in two selected fields at low vs. high Galactic latitudes. *Astronomy & Astrophysics*, 575: A42, Mar. 2015. 10.1051/0004-6361/201322844.

H. J. Grimm, M. Gilfanov, and R. Sunyaev. The Milky Way in X-rays for an outside observer. Log(N)-Log(S) and luminosity function of X-ray binaries from RXTE/ASM data. *Astronomy & Astrophysics*, 391:923–944, Sept. 2002. 10.1051/0004-6361:20020826.

J. A. Guidry, Z. P. Vanderbosch, J. J. Hermes, B. N. Barlow, I. D. Lopez, T. M. Boudreaux, K. A. Corcoran, K. J. Bell, M. H. Montgomery, T. M. Heintz, B. G. Castanheira, J. S. Reding, B. H. Dunlap, D. E. Winget, K. I. Winget, and J. W. Kuehne. I Spy Transits and Pulsations: Empirical Variability in White Dwarfs Using Gaia and the Zwicky Transient Facility. *The Astrophysical Journal*, 912(2): 125, May 2021. 10.3847/1538-4357/abee68.

K. Gültekin, A. L. King, E. M. Cackett, K. Nyland, J. M. Miller, T. Di Matteo, S. Markoff, and M. P. Rupen. The Fundamental Plane of Black Hole Accretion and Its Use as a Black Hole-Mass Estimator. *The Astrophysical Journal*, 871(1):80, Jan. 2019. 10.3847/1538-4357/aaf6b9.

T. Güver and F. Özel. The relation between optical extinction and hydrogen column density in the Galaxy. *Monthly Notices of the Royal Astronomical Society*, 400(4): 2050–2053, Dec. 2009a. 10.1111/j.1365-2966.2009.15598.x.

T. Güver and F. Özel. The relation between optical extinction and hydrogen column density in the Galaxy. *Monthly Notices of the Royal Astronomical Society*, 400(4): 2050–2053, Dec. 2009b. 10.1111/j.1365-2966.2009.15598.x.

T. Güver and F. Özel. The relation between optical extinction and hydrogen column density in the Galaxy. *Monthly Notices of the Royal Astronomical Society*, 400(4): 2050–2053, Dec. 2009c. 10.1111/j.1365-2966.2009.15598.x.

C. J. Hailey, K. Mori, K. Perez, A. M. Canipe, J. Hong, J. A. Tomsick, S. E. Boggs, F. E. Christensen, W. W. Craig, F. Fornasini, J. E. Grindlay, F. A. Harrison, M. Nynka, F. Rahoui, D. Stern, S. Zhang, and W. W. Zhang. Evidence for Intermediate Polars as the Origin of the Galactic Center Hard X-ray Emission. *The Astrophysical Journal*, 826(2):160, Aug. 2016. 10.3847/0004-637X/826/2/160.

P. Hakala, S. G. Parsons, T. R. Marsh, B. T. Gänsicke, G. Ramsay, A. Schwope, and J. J. Hermes. Circular polarimetry of suspect wind-accreting magnetic pre-polars. *Monthly Notices of the Royal Astronomical Society*, 513(3):3858–3870, July 2022. 10.1093/mnras/stac1111.

J. P. Halpern, J. R. Thorstensen, P. Cho, G. Collver, M. Motsoaledi, H. Breytenbach, D. A. H. Buckley, and P. A. Woudt. Optical Studies of 15 Hard X-Ray Selected Cataclysmic Binaries. *The Astronomical Journal*, 155(6):247, June 2018. 10.3847/1538-3881/aabfd0.

J. M. Hameury and J. P. Lasota. Dwarf nova outbursts in intermediate polars. *Astronomy & Astrophysics*, 602:A102, June 2017a. 10.1051/0004-6361/201730760.

J. M. Hameury and J. P. Lasota. Dwarf nova outbursts in intermediate polars. *Astronomy & Astrophysics*, 602:A102, June 2017b. 10.1051/0004-6361/201730760.

J. M. Hameury, J. P. Lasota, and A. W. Shaw. Magnetically gated accretion model: Application to short bursts in the intermediate polar V1223 Sgr. *Astronomy & Astrophysics*, 664:A7, Aug. 2022. 10.1051/0004-6361/202243727.

L. K. Harding, G. Hallinan, J. Milburn, P. Gardner, N. Konidaris, N. Singh, M. Shao, J. Sandhu, G. Kyne, and H. E. Schlichting. CHIMERA: a wide-field, multi-colour, high-speed photometer at the prime focus of the Hale telescope. *Monthly Notices of the Royal Astronomical Society*, 457(3):3036–3049, Apr. 2016. 10.1093/mnras/stw094.

C. R. Harris, K. J. Millman, S. J. van der Walt, R. Gommers, P. Virtanen, D. Cournapeau, E. Wieser, J. Taylor, S. Berg, N. J. Smith, R. Kern, M. Picus, S. Hoyer, M. H. van Kerkwijk, M. Brett, A. Haldane, J. F. del R'ιo, $M. Wiebe$, $P. Peterson$, $P. G'erard-$ $Marchant$, $K. Sheppard$, $T. Reddy$, $W. Weckesser$, $H. Abbasi$, $C. Gohlke$, $andT. E. Oliphant. Array$ (7825) : 357 − −362, $Sept.2020.10.1038/s41586 - 020 - 2649 - 2.URL.$

T. E. Harrison and R. K. Campbell. The WISE Light Curves of Polars. *The Astrophysical Journal Supplement Series*, 219(2):32, Aug. 2015. 10.1088/0067-0049/219/2/32.

M. K. Harrop-Allin, M. Cropper, P. J. Hakala, C. Hellier, and T. Ramseyer. Indirect imaging of the accretion stream in eclipsing polars - II. HU Aquarii. *Monthly Notices of the Royal Astronomical Society*, 308(3):807–817, Sept. 1999. 10.1046/j.1365-8711.1999.02780.x.

L. Hartmann, G. Herczeg, and N. Calvet. Accretion onto Pre-Main-Sequence Stars. *Annual Review of Astronomy and Astrophysics*, 54:135–180, Sept. 2016. 10.1146/annurev-astro-081915-023347.

W. K. Hastings. Monte Carlo Sampling Methods using Markov Chains and their Applications. *Biometrika*, 57(1):97–109, Apr. 1970. 10.1093/biomet/57.1.97.

C. Hellier. *Cataclysmic Variable Stars*. 2001a.

C. Hellier. *Cataclysmic Variable Stars*. 2001b.

C. Hellier and D. A. H. Buckley. TV Columbae in outburst : a mass transfer event ? *Monthly Notices of the Royal Astronomical Society*, 265:766–772, Dec. 1993. 10.1093/mnras/265.3.766.

R. W. Hellings. Gravitational wave detectors in space. *Contemporary Physics*, 37 (6):457–469, Dec. 1996. 10.1080/00107519608217536.

J. V. Hernández Santisteban, C. Knigge, M. L. Pretorius, M. Sullivan, and B. Warner. The space density of post-period minimum Cataclysmic Variables. *Monthly Notices of the Royal Astronomical Society*, 473(3):3241–3250, Jan. 2018. 10.1093/mnras/stx2296.

A. Hewish, S. J. Bell, J. D. H. Pilkington, P. F. Scott, and R. A. Collins. Observation of a Rapidly Pulsating Radio Source. *Nature*, 217(5130):709–713, Feb. 1968. 10.1038/217709a0.

K. H. Hinkle, F. C. Fekel, R. R. Joyce, P. R. Wood, V. V. Smith, and T. Lebzelter. Infrared Spectroscopy of Symbiotic Stars. IV. V2116 Ophiuchi/GX 1+4, The Neutron Star Symbiotic. *The Astrophysical Journal*, 641(1):479–487, Apr. 2006. 10.1086/500350.

K. H. Hinkle, F. C. Fekel, R. R. Joyce, J. Mikolajewska, C. Galan, and T. Lebzelter. Infrared Spectroscopy of Symbiotic Stars. XII. The Neutron Star SyXB System 4U 1700+24 = V934 Herculis. *The Astrophysical Journal*, 872(1):43, Feb. 2019. 10.3847/1538-4357/aafba5.

J. B. Holberg and F. Wesemael. The discovery of the companion of Sirius and its aftermath. *Journal for the History of Astronomy*, 38:161–174, May 2007. 10.1177/002182860703800202.

S. B. Howell, L. A. Nelson, and S. Rappaport. An Exploration of the Paradigm for the 2-3 Hour Period Gap in Cataclysmic Variables. *The Astrophysical Journal*, 550 (2):897–918, Apr. 2001. 10.1086/319776.

S. B. Howell, T. E. Harrison, M. E. Huber, P. Szkody, F. M. Walter, and D. Harbeck. Optical and Infrared Observations of Two Magnetic Interacting Binaries: Tau 4 (RXJ0502.8+1624) & SDSS J121209.31+013627.7. *The Astronomical Journal*, 136(6):2541–2551, Dec. 2008. 10.1088/0004-6256/136/6/2541.

J. D. Hunter. Matplotlib: A 2d graphics environment. *Computing in Science & Engineering*, 9(3):90–95, 2007. 10.1109/MCSE.2007.55.

J. D. Hunter. Matplotlib: A 2D Graphics Environment. *Computing in Science and Engineering*, 9(3):90–95, May 2007. 10.1109/MCSE.2007.55.

N. Hurley-Walker, X. Zhang, A. Bahramian, S. J. McSweeney, T. N. O'Doherty, P. J. Hancock, J. S. Morgan, G. E. Anderson, G. H. Heald, and T. J. Galvin. A radio transient with unusually slow periodic emission. *Nature*, 601(7894):526–530, Jan. 2022. 10.1038/s41586-021-04272-x.

N. Hurley-Walker, N. Rea, S. J. McSweeney, B. W. Meyers, E. Lenc, I. Heywood, S. D. Hyman, Y. P. Men, T. E. Clarke, F. Coti Zelati, D. C. Price, C. Horváth, T. J. Galvin, G. E. Anderson, A. Bahramian, E. D. Barr, N. D. R. Bhat, M. Caleb, M. Dall'Ora, D. de Martino, S. Giacintucci, J. S. Morgan, K. M. Rajwade, B. Stappers, and A. Williams. A long-period radio transient active for three decades. *Nature*, 619(7970):487–490, July 2023a. 10.1038/s41586-023-06202-5.

N. Hurley-Walker, N. Rea, S. J. McSweeney, B. W. Meyers, E. Lenc, I. Heywood, S. D. Hyman, Y. P. Men, T. E. Clarke, F. Coti Zelati, D. C. Price, C. Horváth, T. J. Galvin, G. E. Anderson, A. Bahramian, E. D. Barr, N. D. R. Bhat, M. Caleb, M. Dall'Ora, D. de Martino, S. Giacintucci, J. S. Morgan, K. M. Rajwade, B. Stappers, and A. Williams. A long-period radio transient active for three decades. *Nature*, 619(7970):487–490, July 2023b. 10.1038/s41586-023-06202-5.

N. Hurley-Walker, S. J. McSweeney, A. Bahramian, N. Rea, C. Horváth, S. Buchner, A. Williams, B. W. Meyers, J. Strader, E. Aydi, R. Urquhart, L. Chomiuk, T. J. Galvin, F. Coti Zelati, and M. Bailes. A 2.9 hr Periodic Radio Transient with an Optical Counterpart. *The Astrophysical Journal Letters*, 976(2):L21, Dec. 2024a. 10.3847/2041-8213/ad890e.

N. Hurley-Walker, S. J. McSweeney, A. Bahramian, N. Rea, C. Horvath, S. Buchner, A. Williams, B. W. Meyers, J. Strader, E. Aydi, R. Urquhart, L. Chomiuk, T. J. Galvin, F. Coti Zelati, and M. Bailes. A 2.9-hour periodic radio transient with

an optical counterpart. *arXiv e-prints*, art. arXiv:2408.15757, Aug. 2024b. 10.48550/arXiv.2408.15757.

S. D. Hyman, T. J. W. Lazio, N. E. Kassim, P. S. Ray, C. B. Markwardt, and F. Yusef-Zadeh. A powerful bursting radio source towards the Galactic Centre. *Nature*, 434 (7029):50–52, Mar. 2005. 10.1038/nature03400.

J. Iben, Icko and A. V. Tutukov. Evolutionary Scenarios for Intermediate-Mass Stars in Close Binaries. *The Astrophysical Journal*, 313:727, Feb. 1987. 10.1086/165011.

K. Iłkiewicz, S. Scaringi, C. Littlefield, and P. A. Mason. Locating the flickering source in polars. *Monthly Notices of the Royal Astronomical Society*, 516(4): 5209–5215, Nov. 2022. 10.1093/mnras/stac2597.

K. Inight, B. T. Gänsicke, E. Breedt, T. R. Marsh, A. F. Pala, and R. Raddi. Towards a volumetric census of close white dwarf binaries - I. Reference samples. *Monthly Notices of the Royal Astronomical Society*, 504(2):2420–2442, June 2021. 10.1093/mnras/stab753.

K. Inight, B. T. Gänsicke, E. Breedt, H. T. Israel, S. P. Littlefair, C. J. Manser, T. R. Marsh, T. Mulvany, A. F. Pala, and J. R. Thorstensen. A catalogue of cataclysmic variables from 20 yr of the Sloan Digital Sky Survey with new classifications, periods, trends, and oddities. *Monthly Notices of the Royal Astronomical Society*, 524(4):4867–4898, Oct. 2023a. 10.1093/mnras/stad2018.

K. Inight, B. T. Gänsicke, A. Schwope, S. F. Anderson, C. Badenes, E. Breedt, V. Chandra, B. D. R. Davies, N. P. Gentile Fusillo, M. J. Green, J. J. Hermes, I. A. Huamani, H. Hwang, K. Knauff, J. Kurpas, K. S. Long, V. Malanushenko, S. Morrison, I. J. Quiroz C., G. N. A. Ramos, A. Roman-Lopes, M. R. Schreiber, A. Standke, L. Stütz, J. R. Thorstensen, O. Toloza, G. Tovmassian, and N. L. Zakamska. Cataclysmic Variables from Sloan Digital Sky Survey - V. The search for period bouncers continues. *Monthly Notices of the Royal Astronomical Society*, 525(3):3597–3625, Nov. 2023b. 10.1093/mnras/stad2409.

J. Isern, E. García-Berro, B. Külebi, and P. Lorén-Aguilar. A Common Origin of Magnetism from Planets to White Dwarfs. *The Astrophysical Journal Letters*, 836 (2):L28, Feb. 2017. 10.3847/2041-8213/aa5eae.

G. L. Israel, W. Hummel, S. Covino, S. Campana, I. Appenzeller, W. Gässler, K. H. Mantel, G. Marconi, C. W. Mauche, U. Munari, I. Negueruela, H. Nicklas,

G. Rupprecht, R. L. Smart, O. Stahl, and L. Stella. RX J0806.3+1527: A double degenerate binary with the shortest known orbital period (321s). *Astronomy & Astrophysics*, 386:L13–L17, May 2002. 10.1051/0004-6361:20020314.

Z. Ivezic, S. M. Kahn, J. A. Tyson, B. Abel, E. Acosta, R. Allsman, D. Alonso, Y. AlSayyad, S. F. Anderson, J. Andrew, J. R. P. Angel, G. Z. Angeli, R. Ansari, P. Antilogus, C. Araujo, R. Armstrong, K. T. Arndt, P. Astier, É. Aubourg, N. Auza, T. S. Axelrod, D. J. Bard, J. D. Barr, A. Barrau, J. G. Bartlett, A. E. Bauer, B. J. Bauman, S. Baumont, E. Bechtol, K. Bechtol, A. C. Becker, J. Becla, C. Beldica, S. Bellavia, F. B. Bianco, R. Biswas, G. Blanc, J. Blazek, R. D. Blandford, J. S. Bloom, J. Bogart, T. W. Bond, M. T. Booth, A. W. Borgland, K. Borne, J. F. Bosch, D. Boutigny, C. A. Brackett, A. Bradshaw, W. N. Brandt, M. E. Brown, J. S. Bullock, P. Burchat, D. L. Burke, G. Cagnoli, D. Calabrese, S. Callahan, A. L. Callen, J. L. Carlin, E. L. Carlson, S. Chandrasekharan, G. Charles-Emerson, S. Chesley, E. C. Cheu, H.-F. Chiang, J. Chiang, C. Chirino, D. Chow, D. R. Ciardi, C. F. Claver, J. Cohen-Tanugi, J. J. Cockrum, R. Coles, A. J. Connolly, K. H. Cook, A. Cooray, K. R. Covey, C. Cribbs, W. Cui, R. Cutri, P. N. Daly, S. F. Daniel, F. Daruich, G. Daubard, G. Daues, W. Dawson, F. Delgado, A. Dellapenna, R. de Peyster, M. de Val-Borro, S. W. Digel, P. Doherty, R. Dubois, G. P. Dubois-Felsmann, J. Durech, F. Economou, T. Eifler, M. Eracleous, B. L. Emmons, A. Fausti Neto, H. Ferguson, E. Figueroa, M. Fisher-Levine, W. Focke, M. D. Foss, J. Frank, M. D. Freemon, E. Gangler, E. Gawiser, J. C. Geary, P. Gee, M. Geha, C. J. B. Gessner, R. R. Gibson, D. K. Gilmore, T. Glanzman, W. Glick, T. Goldina, D. A. Goldstein, I. Goodenow, M. L. Graham, W. J. Gressler, P. Gris, L. P. Guy, A. Guyonnet, G. Haller, R. Harris, P. A. Hascall, J. Haupt, F. Hernandez, S. Herrmann, E. Hileman, J. Hoblitt, J. A. Hodgson, C. Hogan, J. D. Howard, D. Huang, M. E. Huffer, P. Ingraham, W. R. Innes, S. H. Jacoby, B. Jain, F. Jammes, M. J. Jee, T. Jenness, G. Jernigan, D. Jevremović, K. Johns, A. S. Johnson, M. W. G. Johnson, R. L. Jones, C. Juramy-Gilles, M. Jurić, J. S. Kalirai, N. J. Kallivayalil, B. Kalmbach, J. P. Kantor, P. Karst, M. M. Kasliwal, H. Kelly, R. Kessler, V. Kinnison, D. Kirkby, L. Knox, I. V. Kotov, V. L. Krabbendam, K. S. Krughoff, P. Kubánek, J. Kuczewski, S. Kulkarni, J. Ku, N. R. Kurita, C. S. Lage, R. Lambert, T. Lange, J. B. Langton, L. Le Guillou, D. Levine, M. Liang, K.-T. Lim, C. J. Lintott, K. E. Long, M. Lopez, P. J. Lotz, R. H. Lupton, N. B. Lust, L. A. MacArthur, A. Mahabal, R. Mandelbaum, T. W. Markiewicz, D. S. Marsh, P. J. Marshall, S. Marshall, M. May, R. McKercher, M. McQueen, J. Meyers, M. Migliore, M. Miller, D. J. Mills, C. Miraval, J. Moeyens,

F. E. Moolekamp, D. G. Monet, M. Moniez, S. Monkewitz, C. Montgomery, C. B. Morrison, F. Mueller, G. P. Muller, F. Muñoz Arancibia, D. R. Neill, S. P. Newbry, J.-Y. Nief, A. Nomerotski, M. Nordby, P. O'Connor, J. Oliver, S. S. Olivier, K. Olsen, W. O'Mullane, S. Ortiz, S. Osier, R. E. Owen, R. Pain, P. E. Palecek, J. K. Parejko, J. B. Parsons, N. M. Pease, J. M. Peterson, J. R. Peterson, D. L. Petravick, M. E. Libby Petrick, C. E. Petry, F. Pierfederici, S. Pietrowicz, R. Pike, P. A. Pinto, R. Plante, S. Plate, J. P. Plutchak, P. A. Price, M. Prouza, V. Radeka, J. Rajagopal, A. P. Rasmussen, N. Regnault, K. A. Reil, D. J. Reiss, M. A. Reuter, S. T. Ridgway, V. J. Riot, S. Ritz, S. Robinson, W. Roby, A. Roodman, W. Rosing, C. Roucelle, M. R. Rumore, S. Russo, A. Saha, B. Sassolas, T. L. Schalk, P. Schellart, R. H. Schindler, S. Schmidt, D. P. Schneider, M. D. Schneider, W. Schoening, G. Schumacher, M. E. Schwamb, J. Sebag, B. Selvy, G. H. Sembroski, L. G. Seppala, A. Serio, E. Serrano, R. A. Shaw, I. Shipsey, J. Sick, N. Silvestri, C. T. Slater, J. A. Smith, R. C. Smith, S. Sobhani, C. Soldahl, L. Storrie-Lombardi, E. Stover, M. A. Strauss, R. A. Street, C. W. Stubbs, I. S. Sullivan, D. Sweeney, J. D. Swinbank, A. Szalay, P. Takacs, S. A. Tether, J. J. Thaler, J. G. Thayer, S. Thomas, A. J. Thornton, V. Thukral, J. Tice, D. E. Trilling, M. Turri, R. Van Berg, D. Vanden Berk, K. Vetter, F. Virieux, T. Vucina, W. Wahl, L. Walkowicz, B. Walsh, C. W. Walter, D. L. Wang, S.-Y. Wang, M. Warner, O. Wiecha, B. Willman, S. E. Winters, D. Wittman, S. C. Wolff, W. M. Wood-Vasey, X. Wu, B. Xin, P. Yoachim, and H. Zhan. LSST: From Science Drivers to Reference Design and Anticipated Data Products. *The Astrophysical Journal*, 873(2):111, Mar. 2019a. 10.3847/1538-4357/ab042c.

Z. Ivezic, S. M. Kahn, J. A. Tyson, B. Abel, E. Acosta, R. Allsman, D. Alonso, Y. AlSayyad, S. F. Anderson, J. Andrew, J. R. P. Angel, G. Z. Angeli, R. Ansari, P. Antilogus, C. Araujo, R. Armstrong, K. T. Arndt, P. Astier, É. Aubourg, N. Auza, T. S. Axelrod, D. J. Bard, J. D. Barr, A. Barrau, J. G. Bartlett, A. E. Bauer, B. J. Bauman, S. Baumont, E. Bechtol, K. Bechtol, A. C. Becker, J. Becla, C. Beldica, S. Bellavia, F. B. Bianco, R. Biswas, G. Blanc, J. Blazek, R. D. Blandford, J. S. Bloom, J. Bogart, T. W. Bond, M. T. Booth, A. W. Borgland, K. Borne, J. F. Bosch, D. Boutigny, C. A. Brackett, A. Bradshaw, W. N. Brandt, M. E. Brown, J. S. Bullock, P. Burchat, D. L. Burke, G. Cagnoli, D. Calabrese, S. Callahan, A. L. Callen, J. L. Carlin, E. L. Carlson, S. Chandrasekharan, G. Charles-Emerson, S. Chesley, E. C. Cheu, H.-F. Chiang, J. Chiang, C. Chirino, D. Chow, D. R. Ciardi, C. F. Claver, J. Cohen-Tanugi, J. J. Cockrum, R. Coles, A. J. Connolly, K. H. Cook, A. Cooray, K. R. Covey, C. Cribbs, W. Cui, R. Cutri, P. N. Daly, S. F. Daniel, F. Daruich,

G. Daubard, G. Daues, W. Dawson, F. Delgado, A. Dellapenna, R. de Peyster, M. de Val-Borro, S. W. Digel, P. Doherty, R. Dubois, G. P. Dubois-Felsmann, J. Durech, F. Economou, T. Eifler, M. Eracleous, B. L. Emmons, A. Fausti Neto, H. Ferguson, E. Figueroa, M. Fisher-Levine, W. Focke, M. D. Foss, J. Frank, M. D. Freemon, E. Gangler, E. Gawiser, J. C. Geary, P. Gee, M. Geha, C. J. B. Gessner, R. R. Gibson, D. K. Gilmore, T. Glanzman, W. Glick, T. Goldina, D. A. Goldstein, I. Goodenow, M. L. Graham, W. J. Gressler, P. Gris, L. P. Guy, A. Guyonnet, G. Haller, R. Harris, P. A. Hascall, J. Haupt, F. Hernandez, S. Herrmann, E. Hileman, J. Hoblitt, J. A. Hodgson, C. Hogan, J. D. Howard, D. Huang, M. E. Huffer, P. Ingraham, W. R. Innes, S. H. Jacoby, B. Jain, F. Jammes, M. J. Jee, T. Jenness, G. Jernigan, D. Jevremović, K. Johns, A. S. Johnson, M. W. G. Johnson, R. L. Jones, C. Juramy-Gilles, M. Jurić, J. S. Kalirai, N. J. Kallivayalil, B. Kalmbach, J. P. Kantor, P. Karst, M. M. Kasliwal, H. Kelly, R. Kessler, V. Kinnison, D. Kirkby, L. Knox, I. V. Kotov, V. L. Krabbendam, K. S. Krughoff, P. Kubánek, J. Kuczewski, S. Kulkarni, J. Ku, N. R. Kurita, C. S. Lage, R. Lambert, T. Lange, J. B. Langton, L. Le Guillou, D. Levine, M. Liang, K.-T. Lim, C. J. Lintott, K. E. Long, M. Lopez, P. J. Lotz, R. H. Lupton, N. B. Lust, L. A. MacArthur, A. Mahabal, R. Mandelbaum, T. W. Markiewicz, D. S. Marsh, P. J. Marshall, S. Marshall, M. May, R. McKercher, M. McQueen, J. Meyers, M. Migliore, M. Miller, D. J. Mills, C. Miraval, J. Moeyens, F. E. Moolekamp, D. G. Monet, M. Moniez, S. Monkewitz, C. Montgomery, C. B. Morrison, F. Mueller, G. P. Muller, F. Muñoz Arancibia, D. R. Neill, S. P. Newbry, J.-Y. Nief, A. Nomerotski, M. Nordby, P. O'Connor, J. Oliver, S. S. Olivier, K. Olsen, W. O'Mullane, S. Ortiz, S. Osier, R. E. Owen, R. Pain, P. E. Palecek, J. K. Parejko, J. B. Parsons, N. M. Pease, J. M. Peterson, J. R. Peterson, D. L. Petravick, M. E. Libby Petrick, C. E. Petry, F. Pierfederici, S. Pietrowicz, R. Pike, P. A. Pinto, R. Plante, S. Plate, J. P. Plutchak, P. A. Price, M. Prouza, V. Radeka, J. Rajagopal, A. P. Rasmussen, N. Regnault, K. A. Reil, D. J. Reiss, M. A. Reuter, S. T. Ridgway, V. J. Riot, S. Ritz, S. Robinson, W. Roby, A. Roodman, W. Rosing, C. Roucelle, M. R. Rumore, S. Russo, A. Saha, B. Sassolas, T. L. Schalk, P. Schellart, R. H. Schindler, S. Schmidt, D. P. Schneider, M. D. Schneider, W. Schoening, G. Schumacher, M. E. Schwamb, J. Sebag, B. Selvy, G. H. Sembroski, L. G. Seppala, A. Serio, E. Serrano, R. A. Shaw, I. Shipsey, J. Sick, N. Silvestri, C. T. Slater, J. A. Smith, R. C. Smith, S. Sobhani, C. Soldahl, L. Storrie-Lombardi, E. Stover, M. A. Strauss, R. A. Street, C. W. Stubbs, I. S. Sullivan, D. Sweeney, J. D. Swinbank, A. Szalay, P. Takacs, S. A. Tether, J. J. Thaler, J. G. Thayer, S. Thomas, A. J. Thornton, V. Thukral, J. Tice, D. E. Trilling, M. Turri, R. Van Berg, D. Vanden Berk, K. Vetter, F. Virieux,

T. Vucina, W. Wahl, L. Walkowicz, B. Walsh, C. W. Walter, D. L. Wang, S.-Y. Wang, M. Warner, O. Wiecha, B. Willman, S. E. Winters, D. Wittman, S. C. Wolff, W. M. Wood-Vasey, X. Wu, B. Xin, P. Yoachim, and H. Zhan. LSST: From Science Drivers to Reference Design and Anticipated Data Products. *The Astrophysical Journal*, 873(2):111, Mar. 2019b. 10.3847/1538-4357/ab042c.

R. Jackim, P. Szkody, B. Hazelton, and N. C. Benson. The Open Cataclysmic Variable Catalog. *Research Notes of the American Astronomical Society*, 4(12): 219, Dec. 2020a. 10.3847/2515-5172/abd104.

R. Jackim, P. Szkody, B. Hazelton, and N. C. Benson. The Open Cataclysmic Variable Catalog. *Research Notes of the American Astronomical Society*, 4(12): 219, Dec. 2020b. 10.3847/2515-5172/abd104.

C. P. Johnstone, M. Bartel, and M. Güdel. The active lives of stars: A complete description of the rotation and XUV evolution of F, G, K, and M dwarfs. *Astronomy & Astrophysics*, 649:A96, May 2021. 10.1051/0004-6361/202038407.

P. G. Jonker, K. Kaur, N. Stone, and M. A. P. Torres. The Observed Mass Distribution of Galactic Black Hole LMXBs Is Biased against Massive Black Holes. *The Astrophysical Journal*, 921(2):131, Nov. 2021. 10.3847/1538-4357/ac2839.

P. Kahabka and E. P. J. van den Heuvel. Luminous Supersoft X-Ray Sources. *Annual Review of Astronomy and Astrophysics*, 35:69–100, Jan. 1997. 10.1146/annurev.astro.35.1.69.

V. L. Kashyap, D. A. van Dyk, A. Connors, P. E. Freeman, A. Siemiginowska, J. Xu, and A. Zezas. On Computing Upper Limits to Source Intensities. *The Astrophysical Journal*, 719(1):900–914, Aug. 2010. 10.1088/0004-637X/719/1/900.

T. Kato. Gaia22ayj: outburst from a deeply eclipsing 9.36-min binary? *arXiv e-prints*, art. arXiv:2203.13975, Mar. 2022.

S. O. Kepler, S. J. Kleinman, A. Nitta, D. Koester, B. G. Castanheira, O. Giovannini, A. F. M. Costa, and L. Althaus. White dwarf mass distribution in the SDSS. *Monthly Notices of the Royal Astronomical Society*, 375(4):1315–1324, Mar. 2007a. 10.1111/j.1365-2966.2006.11388.x.

S. O. Kepler, S. J. Kleinman, A. Nitta, D. Koester, B. G. Castanheira, O. Giovannini, A. F. M. Costa, and L. Althaus. White dwarf mass distribution in the SDSS.

Monthly Notices of the Royal Astronomical Society, 375(4):1315–1324, Mar. 2007b. 10.1111/j.1365-2966.2006.11388.x.

C. Kimball, S. Imperato, V. Kalogera, K. A. Rocha, Z. Doctor, J. J. Andrews, A. Dotter, E. Zapartas, S. S. Bavera, K. Kovlakas, T. Fragos, P. M. Srivastava, D. Misra, M. Sun, and Z. Xing. A Black Hole Kicked at Birth: MAXI J1305-704. *The Astrophysical Journal Letters*, 952(2):L34, Aug. 2023. 10.3847/2041-8213/ace526.

C. Knigge, I. Baraffe, and J. Patterson. The Evolution of Cataclysmic Variables as Revealed by Their Donor Stars. *The Astrophysical Journal Supplement Series*, 194 (2):28, June 2011. 10.1088/0067-0049/194/2/28.

H. A. Kobulnicky and C. L. Fryer. A New Look at the Binary Characteristics of Massive Stars. *The Astrophysical Journal*, 670(1):747–765, Nov. 2007. 10.1086/522073.

H. A. Kobulnicky, K. H. Nordsieck, E. B. Burgh, M. P. Smith, J. W. Percival, T. B. Williams, and D. O'Donoghue. Prime focus imaging spectrograph for the Southern African large telescope: operational modes. In M. Iye and A. F. M. Moorwood, editors, *Instrument Design and Performance for Optical/Infrared Ground-based Telescopes*, volume 4841 of *Society of Photo-Optical Instrumentation Engineers (SPIE) Conference Series*, pages 1634–1644, March 2003. 10.1117/12.460315.

C. S. Kochanek, B. J. Shappee, K. Z. Stanek, T. W. S. Holoien, T. A. Thompson, J. L. Prieto, S. Dong, J. V. Shields, D. Will, C. Britt, D. Perzanowski, and G. Pojmański. The All-Sky Automated Survey for Supernovae (ASAS-SN) Light Curve Server v1.0. *Publications of the Astronomical Society of the Pacific*, 129(980):104502, Oct. 2017. 10.1088/1538-3873/aa80d9.

D. Koester. White dwarf spectra and atmosphere models. *Memorie della Società Astronomica Italiana*, 81:921–931, Jan. 2010.

U. Kolb. A model for the intrinsic population of cataclysmic variables. *Astronomy & Astrophysics*, 271:149, Apr. 1993.

A. I. Kolbin, N. V. Borisov, N. A. Serebriakova, V. V. Shimansky, N. A. Katysheva, M. M. Gabdeev, and S. Y. Shugarov. On accretion in the eclipsing polar BS Tri. *Monthly Notices of the Royal Astronomical Society*, 511(1):20–30, Mar. 2022. 10.1093/mnras/stab3676.

K. I. I. Koljonen and M. Linares. A Gaia view of the optical and X-ray luminosities of compact binary millisecond pulsars. *Monthly Notices of the Royal Astronomical Society*, 525(3):3963–3985, Nov. 2023. 10.1093/mnras/stad2485.

J. A. Kollmeier, G. Zasowski, H.-W. Rix, M. Johns, S. F. Anderson, N. Drory, J. A. Johnson, R. W. Pogge, J. C. Bird, G. A. Blanc, J. R. Brownstein, J. D. Crane, N. M. De Lee, M. A. Klaene, K. Kreckel, N. MacDonald, A. Merloni, M. K. Ness, T. O'Brien, J. R. Sanchez-Gallego, C. C. Sayres, Y. Shen, A. R. Thakar, A. Tkachenko, C. Aerts, M. R. Blanton, D. J. Eisenstein, J. A. Holtzman, D. Maoz, K. Nandra, C. Rockosi, D. H. Weinberg, J. Bovy, A. R. Casey, J. Chaname, N. Clerc, C. Conroy, M. Eracleous, B. T. Gänsicke, S. Hekker, K. Horne, J. Kauffmann, K. B. W. McQuinn, E. W. Pellegrini, E. Schinnerer, E. F. Schlafly, A. D. Schwope, M. Seibert, J. K. Teske, and J. L. van Saders. SDSS-V: Pioneering Panoptic Spectroscopy. *arXiv e-prints*, art. arXiv:1711.03234, Nov. 2017. 10.48550/arXiv.1711.03234.

E. J. Kotze, S. B. Potter, and V. A. McBride. Exploring inside-out Doppler tomography: non-magnetic cataclysmic variables. *Astronomy & Astrophysics*, 579: A77, July 2015a. 10.1051/0004-6361/201526381.

E. J. Kotze, S. B. Potter, and V. A. McBride. Exploring inside-out Doppler tomography: non-magnetic cataclysmic variables. *Astronomy & Astrophysics*, 579: A77, July 2015b. 10.1051/0004-6361/201526381.

G. Kovács, S. Zucker, and T. Mazeh. A box-fitting algorithm in the search for periodic transits. *Astronomy & Astrophysics*, 391:369–377, Aug. 2002. 10.1051/0004-6361:20020802.

S. R. Kulkarni. Optical Identification of Binary Pulsars: Implications for Magnetic Field Decay in Neutron Stars. *The Astrophysical Journal Letters*, 306:L85, July 1986. 10.1086/184711.

T. Kupfer, D. Steeghs, P. J. Groot, T. R. Marsh, G. Nelemans, and G. H. A. Roelofs. UVES and X-Shooter spectroscopy of the emission line AM CVn systems GP Com and V396 Hya. *Monthly Notices of the Royal Astronomical Society*, 457(2): 1828–1841, Apr. 2016. 10.1093/mnras/stw126.

T. Kupfer, T. A. Prince, J. van Roestel, E. C. Bellm, L. Bildsten, M. W. Coughlin, A. J. Drake, M. J. Graham, C. Klein, S. R. Kulkarni, F. J. Masci, R. Walters, I. Andreoni, R. Biswas, C. Bradshaw, D. A. Duev, R. Dekany, J. A. Guidry, J. J.

Hermes, R. R. Laher, and R. Riddle. Year 1 of the ZTF high-cadence Galactic plane survey: strategy, goals, and early results on new single-mode hot subdwarf B-star pulsators. *Monthly Notices of the Royal Astronomical Society*, 505(1):1254–1267, July 2021. 10.1093/mnras/stab1344.

T. Kupfer, V. Korol, T. B. Littenberg, S. Shah, E. Savalle, P. J. Groot, T. R. Marsh, M. Le Jeune, G. Nelemans, A. F. Pala, A. Petiteau, G. Ramsay, D. Steeghs, and S. Babak. LISA Galactic Binaries with Astrometry from Gaia DR3. *The Astrophysical Journal*, 963(2):100, Mar. 2024. 10.3847/1538-4357/ad2068.

A. G. Kuranov and K. A. Postnov. Symbiotic X-ray binaries systems in the galaxy. *Astronomy Letters*, 41(3-4):114–127, Mar. 2015. 10.1134/S1063773715040064.

R. Lallement, J. L. Vergely, C. Babusiaux, and N. L. J. Cox. Updated Gaia-2MASS 3D maps of Galactic interstellar dust. *Astronomy & Astrophysics*, 661:A147, May 2022. 10.1051/0004-6361/202142846.

C. Y. Lam, J. R. Lu, A. Udalski, I. Bond, D. P. Bennett, J. Skowron, P. Mróz, R. Poleski, T. Sumi, M. K. Szymański, S. Kozłowski, P. Pietrukowicz, I. Soszyński, K. Ulaczyk, Ł. Wyrzykowski, S. Miyazaki, D. Suzuki, N. Koshimoto, N. J. Rattenbury, M. W. Hosek, F. Abe, R. Barry, A. Bhattacharya, A. Fukui, H. Fujii, Y. Hirao, Y. Itow, R. Kirikawa, I. Kondo, Y. Matsubara, S. Matsumoto, Y. Muraki, G. Olmschenk, C. Ranc, A. Okamura, Y. Satoh, S. I. Silva, T. Toda, P. J. Tristram, A. Vandorou, H. Yama, N. S. Abrams, S. Agarwal, S. Rose, and S. K. Terry. An Isolated Mass-gap Black Hole or Neutron Star Detected with Astrometric Microlensing. *The Astrophysical Journal Letters*, 933(1):L23, July 2022. 10.3847/2041-8213/ac7442.

M. C. Lam, K. W. Yuen, M. J. Green, and W. Li. WDPhotTools – a white dwarf photometric toolkit in Python. *RAS Techniques and Instruments*, 1(1):81–98, 12 2022. ISSN 2752-8200. 10.1093/rasti/rzac006. URL `https://doi.org/10.1093/rasti/rzac006`.

E. Laplace, S. Justham, M. Renzo, Y. Götberg, R. Farmer, D. Vartanyan, and S. E. de Mink. Different to the core: The pre-supernova structures of massive single and binary-stripped stars. *Astronomy & Astrophysics*, 656:A58, Dec. 2021. 10.1051/0004-6361/202140506.

J.-P. Lasota. The disc instability model of dwarf novae and low-mass X-ray binary transients. *New Astronomy Reviews*, 45(7):449–508, June 2001. 10.1016/S1387-6473(01)00112-9.

Y. W. J. Lee, M. Caleb, T. Murphy, E. Lenc, D. L. Kaplan, L. Ferrario, Z. Wadiasingh, A. Anumarlapudi, N. Hurley-Walker, V. Karambelkar, S. K. Ocker, S. McSweeney, H. Qiu, K. M. Rajwade, A. Zic, K. W. Bannister, N. D. R. Bhat, A. Deller, D. Dobie, L. N. Driessen, K. Gendreau, M. Glowacki, V. Gupta, J. N. Jahns-Schindler, A. Jaini, C. W. James, M. M. Kasliwal, M. E. Lower, R. M. Shannon, P. A. Uttarkar, Y. Wang, and Z. Wang. The emission of interpulses by a 6.45-h-period coherent radio transient. *Nature Astronomy*, 2025. 10.1038/s41550-024-02452-z. URL `https://doi.org/10.1038/s41550-024-02452-z`.

D. Levitan, T. Kupfer, P. J. Groot, S. R. Kulkarni, T. A. Prince, G. V. Simonian, I. Arcavi, J. S. Bloom, R. Laher, P. E. Nugent, E. O. Ofek, B. Sesar, and J. Surace. Five new outbursting AM CVn systems discovered by the Palomar Transient Factory. *Monthly Notices of the Royal Astronomical Society*, 430(2):996–1007, Apr. 2013. 10.1093/mnras/sts672.

W. H. G. Lewin, J. van Paradijs, and R. E. Taam. X-Ray Bursts. *Space Science Reviews*, 62(3-4):223–389, Sept. 1993. 10.1007/BF00196124.

D. Li, M. Yuan, L. Wu, J. Yan, X. Lv, C.-W. Tsai, P. Wang, W. Zhu, L. Deng, A. Lan, R. Xu, X. Chen, L. Meng, J. Li, X. Li, P. Zhou, H. Yang, M. Xue, J. Lu, C. Miao, W. Wang, J. Niu, Z. Fang, Q. Fu, Y. Feng, P. Zhang, J. Jiang, X. Miao, Y. Chen, L. Sun, Y. Yang, X. Deng, S. Dai, X. Chen, J. Yao, Y. Liu, C. Li, M. Zhang, Y. Yang, Y. Zhou, Yiyizhou, Y. Zhang, C. Niu, R. Zhao, L. Zhang, B. Peng, J. Wu, and C. Wang. A 44-minute periodic radio transient in a supernova remnant. *arXiv e-prints*, art. arXiv:2411.15739, Nov. 2024. 10.48550/arXiv.2411.15739.

C. Littlefield, P. Garnavich, T. J. Hoyt, and M. Kennedy. MASTER OT J132104.04+560957.8: A Polar with Absorption-Emission Line Reversals. *The Astronomical Journal*, 155 (1):18, Jan. 2018. 10.3847/1538-3881/aa9750.

C. Littlefield, P. A. Mason, P. Garnavich, P. Szkody, J. Thorstensen, S. Scaringi, K. Iłkiewicz, M. R. Kennedy, and N. Wells. SDSS J134441.83+204408.3: A Highly Asynchronous Short-period Magnetic Cataclysmic Variable with a 56 MG Field Strength. *The Astrophysical Journal Letters*, 943(2):L24, Feb. 2023. 10.3847/2041-8213/acaf04.

N. R. Lomb. Least-Squares Frequency Analysis of Unequally Spaced Data. *Astrophysics and Space Science*, 39(2):447–462, Feb. 1976. 10.1007/BF00648343.

G. J. M. Luna, J. L. Sokoloski, K. Mukai, and T. Nelson. Symbiotic stars in X-rays. *Astronomy & Astrophysics*, 559:A6, Nov. 2013. 10.1051/0004-6361/201220792.

A. Lutovinov, V. Suleimanov, G. J. Manuel Luna, S. Sazonov, D. de Martino, L. Ducci, V. Doroshenko, and M. Falanga. INTEGRAL View on cataclysmic variables and symbiotic binaries. *New Astronomy Reviews*, 91:101547, Dec. 2020. 10.1016/j.newar.2020.101547.

T. Maccacaro, I. M. Gioia, A. Wolter, G. Zamorani, and J. T. Stocke. The X-Ray Spectra of the Extragalactic Sources in the Einstein Extended Medium-Sensitivity Survey. *The Astrophysical Journal*, 326:680, Mar. 1988. 10.1086/166127.

T. J. Maccarone. Using radio emission to detect isolated and quiescent accreting black holes. *Monthly Notices of the Royal Astronomical Society*, 360(1):L30–L34, June 2005. 10.1111/j.1745-3933.2005.00039.x.

T. J. Maccarone, N. Degenaar, B. E. Tetarenko, C. O. Heinke, R. Wijnands, and G. R. Sivakoff. On the recurrence times of neutron star X-ray binary transients and the nature of the Galactic Centre quiescent X-ray binaries. *Monthly Notices of the Royal Astronomical Society*, 512(2):2365–2370, May 2022. 10.1093/mnras/stac506.

E. Magaudda, B. Stelzer, K. R. Covey, S. Raetz, S. P. Matt, and A. Scholz. Relation of X-ray activity and rotation in M dwarfs and predicted time-evolution of the X-ray luminosity. *Astronomy & Astrophysics*, 638:A20, June 2020. 10.1051/0004-6361/201937408.

L. Mahy, H. Sana, T. Shenar, K. Sen, N. Langer, P. Marchant, M. Abdul-Masih, G. Banyard, J. Bodensteiner, D. M. Bowman, K. Dsilva, M. Fabry, C. Hawcroft, S. Janssens, T. Van Reeth, and C. Eldridge. Identifying quiescent compact objects in massive Galactic single-lined spectroscopic binaries. *Astronomy & Astrophysics*, 664:A159, Aug. 2022. 10.1051/0004-6361/202243147.

T. R. Marsh. Kinematics of the helium accretor GP COM. *Monthly Notices of the Royal Astronomical Society*, 304(2):443–450, Apr. 1999. 10.1046/j.1365-8711.1999.02323.x.

T. R. Marsh. Doppler Tomography. In H. M. J. Boffin, D. Steeghs, and J. Cuypers, editors, *Astrotomography, Indirect Imaging Methods in Observational Astronomy*, volume 573, page 1. 2001. 10.48550/arXiv.astro-ph/0011020.

T. R. Marsh. Doppler Tomography. *Astrophysics and Space Science*, 296(1-4): 403–415, Apr. 2005. 10.1007/s10509-005-4859-3.

T. R. Marsh and K. Horne. Images of accretion discs - II. Doppler tomography. *Monthly Notices of the Royal Astronomical Society*, 235:269–286, Nov. 1988. 10.1093/mnras/235.1.269.

T. R. Marsh, G. Nelemans, and D. Steeghs. Mass transfer between double white dwarfs. *Monthly Notices of the Royal Astronomical Society*, 350(1):113–128, May 2004. 10.1111/j.1365-2966.2004.07564.x.

T. R. Marsh, B. T. Gänsicke, S. Hümmerich, F. J. Hambsch, K. Bernhard, C. Lloyd, E. Breedt, E. R. Stanway, D. T. Steeghs, S. G. Parsons, O. Toloza, M. R. Schreiber, P. G. Jonker, J. van Roestel, T. Kupfer, A. F. Pala, V. S. Dhillon, L. K. Hardy, S. P. Littlefair, A. Aungwerojwit, S. Arjyotha, D. Koester, J. J. Bochinski, C. A. Haswell, P. Frank, and P. J. Wheatley. A radio-pulsing white dwarf binary star. *Nature*, 537 (7620):374–377, Sept. 2016. 10.1038/nature18620.

J. L. Marshall, S. Burles, I. B. Thompson, S. A. Shectman, B. C. Bigelow, G. Burley, C. Birk, J. Estrada, P. Jones, M. Smith, V. Kowal, J. Castillo, R. Storts, and G. Ortiz. The MagE spectrograph. In I. S. McLean and M. M. Casali, editors, *Ground-based and Airborne Instrumentation for Astronomy II*, volume 7014 of *Society of Photo-Optical Instrumentation Engineers (SPIE) Conference Series*, page 701454, July 2008. 10.1117/12.789972.

D. C. Martin, J. Fanson, D. Schiminovich, P. Morrissey, P. G. Friedman, T. A. Barlow, T. Conrow, R. Grange, P. N. Jelinsky, B. Milliard, O. H. W. Siegmund, L. Bianchi, Y.-I. Byun, J. Donas, K. Forster, T. M. Heckman, Y.-W. Lee, B. F. Madore, R. F. Malina, S. G. Neff, R. M. Rich, T. Small, F. Surber, A. S. Szalay, B. Welsh, and T. K. Wyder. The Galaxy Evolution Explorer: A Space Ultraviolet Survey Mission. *The Astrophysical Journal Letters*, 619(1):L1–L6, Jan. 2005. 10.1086/426387.

G. Marton, P. Ábrahám, E. Szegedi-Elek, J. Varga, M. Kun, Á. Kóspál, E. Varga-Verebélyi, S. Hodgkin, L. Szabados, R. Beck, and C. Kiss. Identification of Young

Stellar Object candidates in the Gaia DR2 x AllWISE catalogue with machine learning methods. *Monthly Notices of the Royal Astronomical Society*, 487(2): 2522–2537, Aug. 2019. 10.1093/mnras/stz1301.

F. J. Masci, R. R. Laher, B. Rusholme, D. L. Shupe, S. Groom, J. Surace, E. Jackson, S. Monkewitz, R. Beck, D. Flynn, S. Terek, W. Landry, E. Hacopians, V. Desai, J. Howell, T. Brooke, D. Imel, S. Wachter, Q.-Z. Ye, H.-W. Lin, S. B. Cenko, V. Cunningham, U. Rebbapragada, B. Bue, A. A. Miller, A. Mahabal, E. C. Bellm, M. T. Patterson, M. Jurić, V. Z. Golkhou, E. O. Ofek, R. Walters, M. Graham, M. M. Kasliwal, R. G. Dekany, T. Kupfer, K. Burdge, C. B. Cannella, T. Barlow, A. Van Sistine, M. Giomi, C. Fremling, N. Blagorodnova, D. Levitan, R. Riddle, R. M. Smith, G. Helou, T. A. Prince, and S. R. Kulkarni. The Zwicky Transient Facility: Data Processing, Products, and Archive. *Publications of the Astronomical Society of the Pacific*, 131(995):018003, Jan. 2019. 10.1088/1538-3873/aae8ac.

N. Masetti, R. Landi, M. L. Pretorius, V. Sguera, A. J. Bird, M. Perri, P. A. Charles, J. A. Kennea, A. Malizia, and P. Ubertini. IGR J16194-2810: a new symbiotic X-ray binary. *Astronomy & Astrophysics*, 470(1):331–337, July 2007. 10.1051/0004-6361:20077509.

P. A. Mason, N. K. Wells, M. Motsoaledi, P. Szkody, and E. Gonzalez. CRTS J035010.7 + 323230, a new eclipsing polar in the cataclysmic variable period gap. *Monthly Notices of the Royal Astronomical Society*, 488(2):2881–2891, Sept. 2019. 10.1093/mnras/stz1863.

M. Matsuoka, K. Kawasaki, S. Ueno, H. Tomida, M. Kohama, M. Suzuki, Y. Adachi, M. Ishikawa, T. Mihara, M. Sugizaki, N. Isobe, Y. Nakagawa, H. Tsunemi, E. Miyata, N. Kawai, J. Kataoka, M. Morii, A. Yoshida, H. Negoro, M. Nakajima, Y. Ueda, H. Chujo, K. Yamaoka, O. Yamazaki, S. Nakahira, T. You, R. Ishiwata, S. Miyoshi, S. Eguchi, K. Hiroi, H. Katayama, and K. Ebisawa. The MAXI Mission on the ISS: Science and Instruments for Monitoring All-Sky X-Ray Images. *Publications of the Astronomical Society of Japan*, 61:999, Oct. 2009. 10.1093/pasj/61.5.999.

M. McAllister, S. P. Littlefair, S. G. Parsons, V. S. Dhillon, T. R. Marsh, B. T. Gänsicke, E. Breedt, C. Copperwheat, M. J. Green, C. Knigge, D. I. Sahman, M. J. Dyer, P. Kerry, R. P. Ashley, P. Irawati, and S. Rattanasoon. The evolutionary status of Cataclysmic Variables: eclipse modelling of 15 systems. *Monthly Notices of the Royal Astronomical Society*, 486(4):5535–5551, July 2019. 10.1093/mnras/stz976.

J. E. McClintock and R. A. Remillard. Black hole binaries. In *Compact stellar X-ray sources*, volume 39, pages 157–213. 2006. 10.48550/arXiv.astro-ph/0306213.

J. P. McMullin, B. Waters, D. Schiebel, W. Young, and K. Golap. CASA Architecture and Applications. In R. A. Shaw, F. Hill, and D. J. Bell, editors, *Astronomical Data Analysis Software and Systems XVI*, volume 376 of *Astronomical Society of the Pacific Conference Series*, page 127, Oct. 2007.

K. Menou, A. A. Esin, R. Narayan, M. R. Garcia, J.-P. Lasota, and J. E. McClintock. Black Hole and Neutron Star Transients in Quiescence. *The Astrophysical Journal*, 520(1):276–291, July 1999. 10.1086/307443.

A. Merloni, G. Lamer, T. Liu, M. E. Ramos-Ceja, H. Brunner, E. Bulbul, K. Dennerl, V. Doroshenko, M. J. Freyberg, S. Friedrich, E. Gatuzz, A. Georgakakis, F. Haberl, Z. Igo, I. Kreykenbohm, A. Liu, C. Maitra, A. Malyali, M. G. F. Mayer, K. Nandra, P. Predehl, J. Robrade, M. Salvato, J. S. Sanders, I. Stewart, D. Tubín-Arenas, P. Weber, J. Wilms, R. Arcodia, E. Artis, J. Aschersleben, A. Avakyan, C. Aydar, Y. E. Bahar, F. Balzer, W. Becker, K. Berger, T. Boller, W. Bornemann, M. Brüggen, M. Brusa, J. Buchner, V. Burwitz, F. Camilloni, N. Clerc, J. Comparat, D. Coutinho, S. Czesla, S. M. Dannhauer, L. Dauner, T. Dauser, J. Dietl, K. Dolag, T. Dwelly, K. Egg, E. Ehl, S. Freund, P. Friedrich, R. Gaida, C. Garrel, V. Ghirardini, A. Gokus, G. Grünwald, S. Grandis, I. Grotova, D. Gruen, A. Gueguen, S. Hämmerich, N. Hamaus, G. Hasinger, K. Haubner, D. Homan, J. Ider Chitham, W. M. Joseph, A. Joyce, O. König, D. M. Kaltenbrunner, A. Khokhriakova, W. Kink, C. Kirsch, M. Kluge, J. Knies, S. Krippendorf, M. Krumpe, J. Kurpas, P. Li, Z. Liu, N. Locatelli, M. Lorenz, S. Müller, E. Magaudda, C. Mannes, H. McCall, N. Meidinger, M. Michailidis, K. Migkas, D. Muñoz-Giraldo, B. Musiimenta, N. T. Nguyen-Dang, Q. Ni, A. Olechowska, N. Ota, F. Pacaud, T. Pasini, E. Perinati, A. M. Pires, C. Pommranz, G. Ponti, K. Poppenhaeger, G. Pühlhofer, A. Rau, M. Reh, T. H. Reiprich, W. Roster, S. Saeedi, A. Santangelo, M. Sasaki, J. Schmitt, P. C. Schneider, T. Schrabback, N. Schuster, A. Schwope, R. Seppi, M. M. Serim, S. Shreeram, E. Sokolova-Lapa, H. Starck, B. Stelzer, J. Stierhof, V. Suleimanov, C. Tenzer, I. Traulsen, J. Trümper, K. Tsuge, T. Urrutia, A. Veronica, S. G. H. Waddell, R. Willer, J. Wolf, M. C. H. Yeung, A. Zainab, F. Zangrandi, X. Zhang, Y. Zhang, and X. Zheng. The SRG/eROSITA all-sky survey. First X-ray catalogues and data release of the western Galactic hemisphere. *Astronomy & Astrophysics*, 682:A34, Feb. 2024. 10.1051/0004-6361/202347165.

M. Moe and R. Di Stefano. Mind Your Ps and Qs: The Interrelation between Period (P) and Mass-ratio (Q) Distributions of Binary Stars. *The Astrophysical Journal Supplement Series*, 230(2):15, June 2017. 10.3847/1538-4365/aa6fb6.

K. Mori, S. Mandel, C. J. Hailey, T. Schutt, K. Heuer, J. E. Grindlay, J. Hong, and J. A. Tomsick. Comment on "On the recurrence times of neutron star X-ray binary transients and the nature of the Galactic Center quiescent X-ray binaries". *arXiv e-prints*, art. arXiv:2204.09812, Apr. 2022. 10.48550/arXiv.2204.09812.

C. Motch, F. Haberl, P. Guillout, M. Pakull, K. Reinsch, and J. Krautter. New cataclysmic variables from the ROSAT All-Sky Survey. *Astronomy & Astrophysics*, 307:459–469, Mar. 1996.

N. Mowlavi, L. Rimoldini, D. W. Evans, M. Riello, F. De Angeli, L. Palaversa, M. Audard, L. Eyer, P. Garcia-Lario, P. Gavras, B. Holl, G. Jevardat de Fombelle, I. Lecœur-Taïbi, and K. Nienartowicz. Large-amplitude variables in Gaia Data Release 2. Multi-band variability characterization. *Astronomy & Astrophysics*, 648:A44, Apr. 2021. 10.1051/0004-6361/202039450.

P. Mróz, A. Udalski, and A. Gould. Systematic Errors as a Source of Mass Discrepancy in Black Hole Microlensing Event OGLE-2011-BLG-0462. *The Astrophysical Journal Letters*, 937(2):L24, Oct. 2022. 10.3847/2041-8213/ac90bb.

D. Muñoz-Giraldo, B. Stelzer, D. de Martino, and A. Schwope. New X-ray detections of magnetic period-bounce cataclysmic variables from XMM-Newton and SRG/eROSITA. *Astronomy & Astrophysics*, 676:A7, Aug. 2023. 10.1051/0004-6361/202346420.

K. Mukai. PIMMS and Viewing: proposal preparation tools. *Legacy*, 3:21–31, May 1993.

K. Mukai. X-Ray Emissions from Accreting White Dwarfs: A Review. *Publications of the Astronomical Society of the Pacific*, 129(976):062001, June 2017. 10.1088/1538-3873/aa6736.

K. Mukai and M. L. Pretorius. The orbital period versus absolute magnitude relationship of intermediate polars: implications for low states and outbursts. *Monthly Notices of the Royal Astronomical Society*, 523(2):3192–3200, Aug. 2023. 10.1093/mnras/stad1603.

J. Munday, T. R. Marsh, M. Hollands, I. Pelisoli, D. Steeghs, P. Hakala, E. Breedt, A. Brown, V. S. Dhillon, M. J. Dyer, M. Green, P. Kerry, S. P. Littlefair, S. G. Parsons, D. Sahman, S. Somjit, B. Sukaum, and J. Wild. Two decades of optical timing of the shortest-period binary star system HM Cancri. *Monthly Notices of the Royal Astronomical Society*, 518(4):5123–5139, Feb. 2023. 10.1093/mnras/stac3385.

P. Murdin and B. L. Webster. Optical Identification of Cygnus X-1. *Nature*, 233 (5315):110, Sept. 1971. 10.1038/233110a0.

E. J. Murphy, A. Bolatto, S. Chatterjee, C. M. Casey, L. Chomiuk, D. Dale, I. de Pater, M. Dickinson, J. D. Francesco, G. Hallinan, A. Isella, K. Kohno, S. R. Kulkarni, C. Lang, T. J. W. Lazio, A. K. Leroy, L. Loinard, T. J. Maccarone, B. C. Matthews, R. A. Osten, M. J. Reid, D. Riechers, N. Sakai, F. Walter, and D. Wilner. The ngVLA Science Case and Associated Science Requirements. In E. Murphy, editor, *Science with a Next Generation Very Large Array*, volume 517 of *Astronomical Society of the Pacific Conference Series*, page 3, Dec. 2018. 10.48550/arXiv.1810.07524.

R. F. Mushotzky and A. E. Szymkowiak. Einstein Observatory Solid State Detector Observations of Cooling Flows in Clusters of Galaxies. In A. C. Fabian, editor, *Cooling Flows in Clusters and Galaxies*, volume 229 of *NATO Advanced Study Institute (ASI) Series C*, page 53, Jan. 1988. 10.1007/978-94-009-2953-1_6.

R. Narayan, J. E. McClintock, and I. Yi. A New Model for Black Hole Soft X-Ray Transients in Quiescence. *The Astrophysical Journal*, 457:821, Feb. 1996. 10.1086/176777.

R. Narayan, D. Barret, and J. E. McClintock. Advection-dominated Accretion Model of the Black Hole V404 Cygni in Quiescence. *The Astrophysical Journal*, 482(1):448–464, June 1997. 10.1086/304134.

Nasa High Energy Astrophysics Science Archive Research Center (Heasarc). HEAsoft: Unified Release of FTOOLS and XANADU. Astrophysics Source Code Library, record ascl:1408.004, Aug. 2014.

G. Nelemans, S. F. Portegies Zwart, F. Verbunt, and L. R. Yungelson. Population synthesis for double white dwarfs. II. Semi-detached systems: AM CVn stars. *Astronomy & Astrophysics*, 368:939–949, Mar. 2001. 10.1051/0004-6361:20010049.

G. Nelemans, L. R. Yungelson, and S. F. Portegies Zwart. Short-period AM CVn systems as optical, X-ray and gravitational-wave sources. *Monthly Notices of the Royal Astronomical Society*, 349(1):181–192, Mar. 2004a. 10.1111/j.1365-2966.2004.07479.x.

G. Nelemans, L. R. Yungelson, and S. F. Portegies Zwart. Short-period AM CVn systems as optical, X-ray and gravitational-wave sources. *Monthly Notices of the Royal Astronomical Society*, 349(1):181–192, Mar. 2004b. 10.1111/j.1365-2966.2004.07479.x.

G. Nelemans, L. R. Yungelson, M. V. van der Sluys, and C. A. Tout. The chemical composition of donors in AM CVn stars and ultracompact X-ray binaries: observational tests of their formation. *Monthly Notices of the Royal Astronomical Society*, 401(2):1347–1359, Jan. 2010. 10.1111/j.1365-2966.2009.15731.x.

A. Núñez, M. A. Agüeros, J. L. Curtis, K. R. Covey, S. T. Douglas, S. R. Chu, S. DeLaurentiis, M. Wang, and J. J. Drake. The Factory and the Beehive. V. Chromospheric and Coronal Activity and Its Dependence on Rotation in Praesepe and the Hyades. *arXiv e-prints*, art. arXiv:2311.18690, Nov. 2023. 10.48550/arXiv.2311.18690.

E. O'Connor and C. D. Ott. Black Hole Formation in Failing Core-Collapse Supernovae. *The Astrophysical Journal*, 730(2):70, Apr. 2011. 10.1088/0004-637X/730/2/70.

D. O'Donoghue, D. A. H. Buckley, L. A. Balona, D. Bester, L. Botha, J. Brink, D. B. Carter, P. A. Charles, A. Christians, F. Ebrahim, R. Emmerich, W. Esterhuyse, G. P. Evans, C. Fourie, P. Fourie, H. Gajjar, M. Gordon, C. Gumede, M. de Kock, A. Koeslag, W. P. Koorts, H. Kriel, F. Marang, J. G. Meiring, J. W. Menzies, P. Menzies, D. Metcalfe, B. Meyer, L. Nel, J. O'Connor, F. Osman, C. Du Plessis, H. Rall, A. Riddick, E. Romero-Colmenero, S. B. Potter, C. Sass, H. Schalekamp, N. Sessions, S. Siyengo, V. Sopela, H. Steyn, J. Stoffels, J. Scholtz, G. Swart, A. Swat, J. Swiegers, T. Tiheli, P. Vaisanen, W. Whittaker, and F. van Wyk. First science with the Southern African Large Telescope: peering at the accreting polar caps of the eclipsing polar SDSS J015543.40+002807.2. *Monthly Notices of the Royal Astronomical Society*, 372(1):151–162, Oct. 2006. 10.1111/j.1365-2966.2006.10834.x.

J. B. Oke and J. E. Gunn. An Efficient Low Resolution and Moderate Resolution Spectrograph for the Hale Telescope. *Publications of the Astronomical Society of the Pacific*, 94:586, June 1982a. 10.1086/131027.

J. B. Oke and J. E. Gunn. An Efficient Low Resolution and Moderate Resolution Spectrograph for the Hale Telescope. *Publications of the Astronomical Society of the Pacific*, 94:586, June 1982b. 10.1086/131027.

J. B. Oke, J. G. Cohen, M. Carr, J. Cromer, A. Dingizian, F. H. Harris, S. Labrecque, R. Lucinio, W. Schaal, H. Epps, and J. Miller. The Keck Low-Resolution Imaging Spectrometer. *Publications of the Astronomical Society of the Pacific*, 107:375, Apr. 1995a. 10.1086/133562.

J. B. Oke, J. G. Cohen, M. Carr, J. Cromer, A. Dingizian, F. H. Harris, S. Labrecque, R. Lucinio, W. Schaal, H. Epps, and J. Miller. The Keck Low-Resolution Imaging Spectrometer. *Publications of the Astronomical Society of the Pacific*, 107:375, Apr. 1995b. 10.1086/133562.

A. S. Oliveira, C. V. Rodrigues, M. Martins, M. S. Palhares, K. M. G. Silva, I. J. Lima, and F. J. Jablonski. Exploratory Spectroscopy of Magnetic Cataclysmic Variables Candidates and Other Variable Objects. II. *The Astronomical Journal*, 159(3):114, Mar. 2020. 10.3847/1538-3881/ab6ded.

Y. Osaki. A model for the superoutburst phenomenon of SU Ursae MAjoris stars. *Publications of the Astronomical Society of Japan*, 41:1005–1033, Jan. 1989.

F. Pacini. Rotating Neutron Stars, Pulsars and Supernova Remnants. *Nature*, 219 (5150):145–146, July 1968. 10.1038/219145a0.

B. Paczyński. Gravitational Waves and the Evolution of Close Binaries. *Acta Astronomica*, 17:287, Jan. 1967.

B. Paczynski. Common Envelope Binaries. In P. Eggleton, S. Mitton, and J. Whelan, editors, *Structure and Evolution of Close Binary Systems*, volume 73, page 75, Jan. 1976.

B. Paczynski. Evolution of cataclysmic binaries. *Acta Astronomica*, 31:1–12, Jan. 1981.

B. Paczynski and R. Sienkiewicz. The minimum period and the gap in periods of cataclysmic binaries. *The Astrophysical Journal*, 268:825–831, May 1983. 10.1086/161004.

B. Paczyński and R. Sienkiewicz. The minimum period and the gap in periods of cataclysmic binaries. *The Astrophysical Journal*, 268:825–831, May 1983. 10.1086/161004.

A. Paduano, A. Bahramian, J. C. A. Miller-Jones, A. Kawka, F. Göttgens, J. Strader, L. Chomiuk, S. Kamann, S. Dreizler, C. O. Heinke, T.-O. Husser, T. J. Maccarone, E. Tremou, and Y. Zhao. The MAVERIC Survey: The first radio and X-ray limits on the detached black holes in NGC 3201. *Monthly Notices of the Royal Astronomical Society*, 510(3):3658–3673, Mar. 2022. 10.1093/mnras/stab3743.

A. Paizis, M. A. Nowak, J. Rodriguez, A. Segreto, S. Chaty, A. Rau, J. Chenevez, M. Del Santo, J. Greiner, and S. Schmidl. Investigating the Nature of IGR J17454-2919 Using X-Ray and Near-infrared Observations. *The Astrophysical Journal*, 808(1):34, July 2015. 10.1088/0004-637X/808/1/34.

A. F. Pala, B. T. Gänsicke, D. Townsley, D. Boyd, M. J. Cook, D. De Martino, P. Godon, J. B. Haislip, A. A. Henden, I. Hubeny, K. M. Ivarsen, S. Kafka, C. Knigge, A. P. LaCluyze, K. S. Long, T. R. Marsh, B. Monard, J. P. Moore, G. Myers, P. Nelson, D. Nogami, A. Oksanen, R. Pickard, G. Poyner, D. E. Reichart, D. Rodriguez Perez, M. R. Schreiber, J. Shears, E. M. Sion, R. Stubbings, P. Szkody, and M. Zorotovic. Effective temperatures of cataclysmic-variable white dwarfs as a probe of their evolution. *Monthly Notices of the Royal Astronomical Society*, 466(3):2855–2878, Apr. 2017. 10.1093/mnras/stw3293.

A. F. Pala, L. Schmidtobreick, C. Tappert, B. T. Gänsicke, and A. Mehner. The cataclysmic variable QZ Lib: a period bouncer. *Monthly Notices of the Royal Astronomical Society*, 481(2):2523–2535, Dec. 2018. 10.1093/mnras/sty2434.

A. F. Pala, B. T. Gänsicke, E. Breedt, C. Knigge, J. J. Hermes, N. P. Gentile Fusillo, M. A. Hollands, T. Naylor, I. Pelisoli, M. R. Schreiber, S. Toonen, A. Aungwerojwit, E. Cukanovaite, E. Dennihy, C. J. Manser, M. L. Pretorius, S. Scaringi, and O. Toloza. A Volume-limited Sample of Cataclysmic Variables from Gaia DR2: Space Density and Population Properties. *Monthly Notices of the Royal Astronomical Society*, 494(3):3799–3827, May 2020a. 10.1093/mnras/staa764.

A. F. Pala, B. T. Gänsicke, E. Breedt, C. Knigge, J. J. Hermes, N. P. Gentile Fusillo, M. A. Hollands, T. Naylor, I. Pelisoli, M. R. Schreiber, S. Toonen, A. Aungwerojwit, E. Cukanovaite, E. Dennihy, C. J. Manser, M. L. Pretorius, S. Scaringi, and O. Toloza. A Volume-limited Sample of Cataclysmic Variables from Gaia DR2: Space Density and Population Properties. *Monthly Notices of the Royal Astronomical Society*, 494(3):3799–3827, May 2020b. 10.1093/mnras/staa764.

A. F. Pala, B. T. Gänsicke, D. Belloni, S. G. Parsons, T. R. Marsh, M. R. Schreiber, E. Breedt, C. Knigge, E. M. Sion, P. Szkody, D. Townsley, L. Bildsten, D. Boyd, M. J. Cook, D. De Martino, P. Godon, S. Kafka, V. Kouprianov, K. S. Long, B. Monard, G. Myers, P. Nelson, D. Nogami, A. Oksanen, R. Pickard, G. Poyner, D. E. Reichart, D. Rodriguez Perez, J. Shears, R. Stubbings, and O. Toloza. Constraining the evolution of cataclysmic variables via the masses and accretion rates of their underlying white dwarfs. *Monthly Notices of the Royal Astronomical Society*, 510 (4):6110–6132, Mar. 2022a. 10.1093/mnras/stab3449.

A. F. Pala, B. T. Gänsicke, D. Belloni, S. G. Parsons, T. R. Marsh, M. R. Schreiber, E. Breedt, C. Knigge, E. M. Sion, P. Szkody, D. Townsley, L. Bildsten, D. Boyd, M. J. Cook, D. De Martino, P. Godon, S. Kafka, V. Kouprianov, K. S. Long, B. Monard, G. Myers, P. Nelson, D. Nogami, A. Oksanen, R. Pickard, G. Poyner, D. E. Reichart, D. Rodriguez Perez, J. Shears, R. Stubbings, and O. Toloza. Constraining the evolution of cataclysmic variables via the masses and accretion rates of their underlying white dwarfs. *Monthly Notices of the Royal Astronomical Society*, 510 (4):6110–6132, Mar. 2022b. 10.1093/mnras/stab3449.

R. Pallavicini, L. Golub, R. Rosner, G. S. Vaiana, T. Ayres, and J. L. Linsky. Relations among stellar X-ray emission observed from Einstein, stellar rotation and bolometric luminosity. *The Astrophysical Journal*, 248:279–290, Aug. 1981. 10.1086/159152.

E. N. Parker. Dynamics of the Interplanetary Gas and Magnetic Fields. *The Astrophysical Journal*, 128:664, Nov. 1958. 10.1086/146579.

S. G. Parsons, C. A. Hill, T. R. Marsh, B. T. Gänsicke, C. A. Watson, D. Steeghs, V. S. Dhillon, S. P. Littlefair, C. M. Copperwheat, M. R. Schreiber, and M. Zorotovic. The crowded magnetosphere of the post-common-envelope binary QS Virginis. *Monthly Notices of the Royal Astronomical Society*, 458(3):2793–2812, May 2016. 10.1093/mnras/stw516.

S. G. Parsons, B. T. Gänsicke, T. R. Marsh, R. P. Ashley, E. Breedt, M. R. Burleigh, C. M. Copperwheat, V. S. Dhillon, M. J. Green, J. J. Hermes, P. Irawati, P. Kerry, S. P. Littlefair, A. Rebassa-Mansergas, D. I. Sahman, M. R. Schreiber, and M. Zorotovic. The scatter of the M dwarf mass-radius relationship. *Monthly Notices of the Royal Astronomical Society*, 481(1):1083–1096, Nov. 2018. 10.1093/mnras/sty2345.

S. G. Parsons, B. T. Gänsicke, M. R. Schreiber, T. R. Marsh, R. P. Ashley, E. Breedt, S. P. Littlefair, and H. Meusinger. Magnetic white dwarfs in post-common-envelope binaries. *Monthly Notices of the Royal Astronomical Society*, 502(3):4305–4327, Apr. 2021. 10.1093/mnras/stab284.

J. Patterson. Rapid oscillations in cataclysmic variables. III. an oblique rotator in AE Aqr. *The Astrophysical Journal*, 234:978–992, Dec. 1979. 10.1086/157582.

J. Patterson. The DQ Herculis Stars. *Publications of the Astronomical Society of the Pacific*, 106:209, Mar. 1994. 10.1086/133375.

J. Patterson and J. C. Raymond. X-ray emission from cataclysmic variables with accretion disks. I. Hard X-rays. *The Astrophysical Journal*, 292:535–549, May 1985. 10.1086/163187.

J. Patterson, D. Branch, G. Chincarini, and E. L. Robinson. 33 second X-ray pulsations in AE Aquarii. *The Astrophysical Journal Letters*, 240:L133–L136, Sept. 1980. 10.1086/183339.

J. Patterson, E. de Miguel, J. Kemp, S. Dvorak, B. Monard, F.-J. Hambsch, T. Vanmunster, D. R. Skillman, D. Cejudo, T. Campbell, G. Roberts, J. Jones, L. M. Cook, G. Bolt, R. Rea, J. Ulowetz, T. Krajci, K. Menzies, S. Lowther, W. Goff, W. Stein, M. A. Wood, G. Myers, G. Stone, H. Uthas, E. Karamehmetoglu, J. Seargeant, and J. McCormick. The Spin-period History of Intermediate Polars. *The Astrophysical Journal*, 897(1):70, July 2020. 10.3847/1538-4357/ab863d.

M. Pavlinsky, A. Tkachenko, V. Levin, N. Alexandrovich, V. Arefiev, V. Babyshkin, O. Batanov, Y. Bodnar, A. Bogomolov, A. Bubnov, M. Buntov, R. Burenin, I. Chelovekov, C. T. Chen, T. Drozdova, S. Ehlert, E. Filippova, S. Frolov, D. Gamkov, S. Garanin, M. Garin, A. Glushenko, A. Gorelov, S. Grebenev, S. Grigorovich, P. Gureev, E. Gurova, R. Ilkaev, I. Katasonov, A. Krivchenko, R. Krivonos, F. Korotkov, M. Kudelin, M. Kuznetsova, V. Lazarchuk, I. Lomakin, I. Lapshov, V. Lipilin, A. Lutovinov, I. Mereminskiy, S. Molkov, V. Nazarov, V. Oleinikov, E. Pikalov,

B. D. Ramsey, I. Roiz, A. Rotin, A. Ryadov, E. Sankin, S. Sazonov, D. Sedov, A. Semena, N. Semena, D. Serbinov, A. Shirshakov, A. Shtykovsky, A. Shvetsov, R. Sunyaev, D. A. Swartz, V. Tambov, V. Voron, and A. Yaskovich. The ART-XC telescope on board the SRG observatory. *Astronomy & Astrophysics*, 650:A42, June 2021. 10.1051/0004-6361/202040265.

B. Paxton, L. Bildsten, A. Dotter, F. Herwig, P. Lesaffre, and F. Timmes. Modules for Experiments in Stellar Astrophysics (MESA). *The Astrophysical Journal Supplement Series*, 192(1):3, Jan. 2011. 10.1088/0067-0049/192/1/3.

B. Paxton, M. Cantiello, P. Arras, L. Bildsten, E. F. Brown, A. Dotter, C. Mankovich, M. H. Montgomery, D. Stello, F. X. Timmes, and R. Townsend. Modules for Experiments in Stellar Astrophysics (MESA): Planets, Oscillations, Rotation, and Massive Stars. *The Astrophysical Journal Supplement Series*, 208(1):4, Sept. 2013. 10.1088/0067-0049/208/1/4.

B. Paxton, P. Marchant, J. Schwab, E. B. Bauer, L. Bildsten, M. Cantiello, L. Dessart, R. Farmer, H. Hu, N. Langer, R. H. D. Townsend, D. M. Townsley, and F. X. Timmes. Modules for Experiments in Stellar Astrophysics (MESA): Binaries, Pulsations, and Explosions. *The Astrophysical Journal Supplement Series*, 220(1):15, Sept. 2015. 10.1088/0067-0049/220/1/15.

B. Paxton, J. Schwab, E. B. Bauer, L. Bildsten, S. Blinnikov, P. Duffell, R. Farmer, J. A. Goldberg, P. Marchant, E. Sorokina, A. Thoul, R. H. D. Townsend, and F. X. Timmes. Modules for Experiments in Stellar Astrophysics (MESA): Convective Boundaries, Element Diffusion, and Massive Star Explosions. *The Astrophysical Journal Supplement Series*, 234(2):34, Feb. 2018. 10.3847/1538-4365/aaa5a8.

I. Pelisoli, T. R. Marsh, S. G. Parsons, A. Aungwerojwit, R. P. Ashley, E. Breedt, A. J. Brown, V. S. Dhillon, M. J. Dyer, M. J. Green, P. Kerry, S. P. Littlefair, D. I. Sahman, T. Shahbaz, J. F. Wild, A. Chakpor, and R. Lakhom. Long-term photometric monitoring and spectroscopy of the white dwarf pulsar AR Scorpii. *Monthly Notices of the Royal Astronomical Society*, 516(4):5052–5066, Nov. 2022a. 10.1093/mnras/stac2391.

I. Pelisoli, T. R. Marsh, S. G. Parsons, A. Aungwerojwit, R. P. Ashley, E. Breedt, A. J. Brown, V. S. Dhillon, M. J. Dyer, M. J. Green, P. Kerry, S. P. Littlefair, D. I. Sahman, T. Shahbaz, J. F. Wild, A. Chakpor, and R. Lakhom. Long-term

photometric monitoring and spectroscopy of the white dwarf pulsar AR Scorpii. *Monthly Notices of the Royal Astronomical Society*, 516(4):5052–5066, Nov. 2022b. 10.1093/mnras/stac2391.

I. Pelisoli, T. R. Marsh, D. A. H. Buckley, I. Heywood, S. B. Potter, A. Schwope, J. Brink, A. Standke, P. A. Woudt, S. G. Parsons, M. J. Green, S. O. Kepler, J. Munday, A. D. Romero, E. Breedt, A. J. Brown, V. S. Dhillon, M. J. Dyer, P. Kerry, S. P. Littlefair, D. I. Sahman, and J. F. Wild. A 5.3-min-period pulsing white dwarf in a binary detected from radio to X-rays. *Nature Astronomy*, 7: 931–942, Aug. 2023a. 10.1038/s41550-023-01995-x.

I. Pelisoli, T. R. Marsh, D. A. H. Buckley, I. Heywood, S. B. Potter, A. Schwope, J. Brink, A. Standke, P. A. Woudt, S. G. Parsons, M. J. Green, S. O. Kepler, J. Munday, A. D. Romero, E. Breedt, A. J. Brown, V. S. Dhillon, M. J. Dyer, P. Kerry, S. P. Littlefair, D. I. Sahman, and J. F. Wild. A 5.3-min-period pulsing white dwarf in a binary detected from radio to X-rays. *Nature Astronomy*, 7: 931–942, Aug. 2023b. 10.1038/s41550-023-01995-x.

I. Pelisoli, S. Sahu, M. Lyutikov, M. Barkov, B. T. Gänsicke, J. Brink, D. A. H. Buckley, S. B. Potter, A. Schwope, and S. H. Ramírez. Unveiling the white dwarf in J191213.72 - 441045.1 through ultraviolet observations. *Monthly Notices of the Royal Astronomical Society*, 527(2):3826–3836, Jan. 2024. 10.1093/mnras/stad3442.

D. A. Perley. Fully Automated Reduction of Longslit Spectroscopy with the Low Resolution Imaging Spectrometer at the Keck Observatory. *Publications of the Astronomical Society of the Pacific*, 131(1002):084503, Aug. 2019. 10.1088/1538-3873/ab215d.

R. Perna, R. Narayan, G. Rybicki, L. Stella, and A. Treves. Bondi Accretion and the Problem of the Missing Isolated Neutron Stars. *The Astrophysical Journal*, 594 (2):936–942, Sept. 2003. 10.1086/377091.

E. S. Phinney and S. R. Kulkarni. Binary and Millisecond Pulsars. *Annual Review of Astronomy and Astrophysics*, 32:591–639, Jan. 1994. 10.1146/annurev.aa.32.090194.003111.

R. M. Plotkin, S. Markoff, B. C. Kelly, E. Körding, and S. F. Anderson. Using the Fundamental Plane of black hole activity to distinguish X-ray processes from

weakly accreting black holes. *Monthly Notices of the Royal Astronomical Society*, 419(1):267–286, Jan. 2012. 10.1111/j.1365-2966.2011.19689.x.

R. M. Plotkin, A. Bahramian, J. C. A. Miller-Jones, M. T. Reynolds, P. Atri, T. J. Maccarone, A. W. Shaw, and P. Gandhi. Towards a larger sample of radio jets from quiescent black hole X-ray binaries. *Monthly Notices of the Royal Astronomical Society*, 503(3):3784–3795, May 2021. 10.1093/mnras/stab644.

P. Podsiadlowski, Z. Han, and S. Rappaport. Cataclysmic variables with evolved secondaries and the progenitors of AM CVn stars. *Monthly Notices of the Royal Astronomical Society*, 340(4):1214–1228, Apr. 2003. 10.1046/j.1365-8711.2003.06380.x.

K. A. Postnov and L. R. Yungelson. The Evolution of Compact Binary Star Systems. *Living Reviews in Relativity*, 17(1):3, Dec. 2014. 10.12942/lrr-2014-3.

S. B. Potter, T. Augusteijn, and C. Tappert. Photopolarimetric observations of the new eclipsing polar CTCVJ1928 - 5001. *Monthly Notices of the Royal Astronomical Society*, 364(2):565–572, Dec. 2005. 10.1111/j.1365-2966.2005.09569.x.

P. Predehl, R. Andritschke, V. Arefiev, V. Babyshkin, O. Batanov, W. Becker, H. Böhringer, A. Bogomolov, T. Boller, K. Borm, W. Bornemann, H. Bräuninger, M. Brüggen, H. Brunner, M. Brusa, E. Bulbul, M. Buntov, V. Burwitz, W. Burkert, N. Clerc, E. Churazov, D. Coutinho, T. Dauser, K. Dennerl, V. Doroshenko, J. Eder, V. Emberger, T. Eraerds, A. Finoguenov, M. Freyberg, P. Friedrich, S. Friedrich, M. Fürmetz, A. Georgakakis, M. Gilfanov, S. Granato, C. Grossberger, A. Gueguen, P. Gureev, F. Haberl, O. Hälker, G. Hartner, G. Hasinger, H. Huber, L. Ji, A. v. Kienlin, W. Kink, F. Korotkov, I. Kreykenbohm, G. Lamer, I. Lomakin, I. Lapshov, T. Liu, C. Maitra, N. Meidinger, B. Menz, A. Merloni, T. Mernik, B. Mican, J. Mohr, S. Müller, K. Nandra, V. Nazarov, F. Pacaud, M. Pavlinsky, E. Perinati, E. Pfeffermann, D. Pietschner, M. E. Ramos-Ceja, A. Rau, J. Reiffers, T. H. Reiprich, J. Robrade, M. Salvato, J. Sanders, A. Santangelo, M. Sasaki, H. Scheuerle, C. Schmid, J. Schmitt, A. Schwope, A. Shirshakov, M. Steinmetz, I. Stewart, L. Strüder, R. Sunyaev, C. Tenzer, L. Tiedemann, J. Trümper, V. Voron, P. Weber, J. Wilms, and V. Yaroshenko. The eROSITA X-ray telescope on SRG. *Astronomy & Astrophysics*, 647:A1, Mar. 2021a. 10.1051/0004-6361/202039313.

P. Predehl, R. Andritschke, V. Arefiev, V. Babyshkin, O. Batanov, W. Becker, H. Böhringer, A. Bogomolov, T. Boller, K. Borm, W. Bornemann, H. Bräuninger,

M. Brüggen, H. Brunner, M. Brusa, E. Bulbul, M. Buntov, V. Burwitz, W. Burkert, N. Clerc, E. Churazov, D. Coutinho, T. Dauser, K. Dennerl, V. Doroshenko, J. Eder, V. Emberger, T. Eraerds, A. Finoguenov, M. Freyberg, P. Friedrich, S. Friedrich, M. Fürmetz, A. Georgakakis, M. Gilfanov, S. Granato, C. Grossberger, A. Gueguen, P. Gureev, F. Haberl, O. Hälker, G. Hartner, G. Hasinger, H. Huber, L. Ji, A. v. Kienlin, W. Kink, F. Korotkov, I. Kreykenbohm, G. Lamer, I. Lomakin, I. Lapshov, T. Liu, C. Maitra, N. Meidinger, B. Menz, A. Merloni, T. Mernik, B. Mican, J. Mohr, S. Müller, K. Nandra, V. Nazarov, F. Pacaud, M. Pavlinsky, E. Perinati, E. Pfeffermann, D. Pietschner, M. E. Ramos-Ceja, A. Rau, J. Reiffers, T. H. Reiprich, J. Robrade, M. Salvato, J. Sanders, A. Santangelo, M. Sasaki, H. Scheuerle, C. Schmid, J. Schmitt, A. Schwope, A. Shirshakov, M. Steinmetz, I. Stewart, L. Strüder, R. Sunyaev, C. Tenzer, L. Tiedemann, J. Trümper, V. Voron, P. Weber, J. Wilms, and V. Yaroshenko. The eROSITA X-ray telescope on SRG. *Astronomy & Astrophysics*, 647:A1, Mar. 2021b. 10.1051/0004-6361/202039313.

M. L. Pretorius and C. Knigge. The space density and X-ray luminosity function of non-magnetic cataclysmic variables. *Monthly Notices of the Royal Astronomical Society*, 419(2):1442–1454, Jan. 2012. 10.1111/j.1365-2966.2011.19801.x.

M. L. Pretorius and K. Mukai. Constraints on the space density of intermediate polars from the Swift-BAT survey. *Monthly Notices of the Royal Astronomical Society*, 442(3):2580–2585, Aug. 2014. 10.1093/mnras/stu990.

M. L. Pretorius, C. Knigge, D. O'Donoghue, J. P. Henry, I. M. Gioia, and C. R. Mullis. The space density of cataclysmic variables: constraints from the ROSAT North Ecliptic Pole survey. *Monthly Notices of the Royal Astronomical Society*, 382 (3):1279–1288, Dec. 2007. 10.1111/j.1365-2966.2007.12461.x.

M. L. Pretorius, C. Knigge, and A. D. Schwope. The space density of magnetic cataclysmic variables. *Monthly Notices of the Royal Astronomical Society*, 432(1): 570–583, June 2013. 10.1093/mnras/stt499.

J. E. Pringle. Thermal instabilities in accretion discs. *Monthly Notices of the Royal Astronomical Society*, 177:65–71, Oct. 1976. 10.1093/mnras/177.1.65.

J. Prochaska, J. Hennawi, K. Westfall, R. Cooke, F. Wang, T. Hsyu, F. Davies, E. Farina, and D. Pelliccia. PypeIt: The Python Spectroscopic Data Reduction Pipeline. *The Journal of Open Source Software*, 5(56):2308, Dec. 2020. 10.21105/joss.02308.

A. Prsa and T. Zwitter. A Computational Guide to Physics of Eclipsing Binaries. I. Demonstrations and Perspectives. *The Astrophysical Journal*, 628(1):426–438, July 2005. 10.1086/430591.

A. Prsa, K. E. Conroy, M. Horvat, H. Pablo, A. Kochoska, S. Bloemen, J. Giammarco, K. M. Hambleton, and P. Degroote. Physics Of Eclipsing Binaries. II. Toward the Increased Model Fidelity. *The Astrophysical Journal Supplement Series*, 227(2):29, Dec. 2016. 10.3847/1538-4365/227/2/29.

Y. Qu and B. Zhang. Magnetic Interaction in White Dwarf Binaries as Mechanism for Long-Period Radio Transients. *arXiv e-prints*, art. arXiv:2409.05978, Sept. 2024. 10.48550/arXiv.2409.05978.

G. Ramsay, P. Hakala, and M. Cropper. RX J0806+15: the shortest period binary? *Monthly Notices of the Royal Astronomical Society*, 332(1):L7–L10, May 2002. 10.1046/j.1365-8711.2002.05471.x.

G. Ramsay, P. Hakala, T. Marsh, G. Nelemans, D. Steeghs, and M. Cropper. XMM-Newton observations of AM CVn binaries. *Astronomy & Astrophysics*, 440(2): 675–681, Sept. 2005. 10.1051/0004-6361:20052950.

G. Ramsay, P. J. Groot, T. Marsh, G. Nelemans, D. Steeghs, and P. Hakala. XMM-Newton observations of AM CVn binaries: V396 Hya and SDSS J1240-01. *Astronomy & Astrophysics*, 457(2):623–627, Oct. 2006. 10.1051/0004-6361:20065491.

G. Ramsay, M. J. Green, T. R. Marsh, T. Kupfer, E. Breedt, V. Korol, P. J. Groot, C. Knigge, G. Nelemans, D. Steeghs, P. Woudt, and A. Aungwerojwit. Physical properties of AM CVn stars: New insights from Gaia DR2. *Astronomy & Astrophysics*, 620:A141, Dec. 2018. 10.1051/0004-6361/201834261.

S. Rappaport, F. Verbunt, and P. C. Joss. A new technique for calculations of binary stellar evolution application to magnetic braking. *The Astrophysical Journal*, 275: 713–731, Dec. 1983. 10.1086/161569.

S. Rappaport, A. Vanderburg, J. Schwab, and L. Nelson. Minimum Orbital Periods of H-rich Bodies. *The Astrophysical Journal*, 913(2):118, June 2021. 10.3847/1538-4357/abf7b0.

V. Ravi, M. Catha, G. Chen, L. Connor, J. T. Faber, J. W. Lamb, G. Hallinan, C. Harnach, G. Hellbourg, R. Hobbs, D. Hodge, M. Hodges, C. Law, P. Rasmussen,

K. Sharma, M. B. Sherman, J. Shi, D. Simard, R. Squillace, S. Weinreb, D. P. Woody, N. Yadlapalli, T. Ahumada, D. Dong, C. Fremling, Y. Huang, V. Karambelkar, and J. M. Miller. Deep Synoptic Array Science: Discovery of the Host Galaxy of FRB 20220912A. *The Astrophysical Journal Letters*, 949(1):L3, May 2023. 10.3847/2041-8213/acc4b6.

A. Rebassa-Mansergas, A. Nebot Gómez-Morán, M. R. Schreiber, B. T. Gänsicke, A. Schwope, J. Gallardo, and D. Koester. Post-common envelope binaries from SDSS - XIV. The DR7 white dwarf-main-sequence binary catalogue. *Monthly Notices of the Royal Astronomical Society*, 419(1):806–816, Jan. 2012. 10.1111/j.1365-2966.2011.19923.x.

D. Reimers. Circumstellar absorption lines and mass loss from red giants. *Memoires of the Societe Royale des Sciences de Liege*, 8:369–382, Jan. 1975.

A. Reiners, M. Schüssler, and V. M. Passegger. Generalized Investigation of the Rotation-Activity Relation: Favoring Rotation Period instead of Rossby Number. *The Astrophysical Journal*, 794(2):144, Oct. 2014. 10.1088/0004-637X/794/2/144.

A. Reiners, D. Shulyak, P. J. Käpylä, I. Ribas, E. Nagel, M. Zechmeister, J. A. Caballero, Y. Shan, B. Fuhrmeister, A. Quirrenbach, P. J. Amado, D. Montes, S. V. Jeffers, M. Azzaro, V. J. S. Béjar, P. Chaturvedi, T. Henning, M. Kürster, and E. Pallé. Magnetism, rotation, and nonthermal emission in cool stars. Average magnetic field measurements in 292 M dwarfs. *Astronomy & Astrophysics*, 662: A41, June 2022. 10.1051/0004-6361/202243251.

R. C. Reis, P. J. Wheatley, B. T. Gänsicke, and J. P. Osborne. X-ray luminosities of optically selected cataclysmic variables and application to the Galactic ridge X-ray emission. *Monthly Notices of the Royal Astronomical Society*, 430(3):1994–2001, Apr. 2013. 10.1093/mnras/stt025.

R. A. Remillard and J. E. McClintock. X-Ray Properties of Black-Hole Binaries. *Annual Review of Astronomy and Astrophysics*, 44(1):49–92, Sept. 2006. 10.1146/annurev.astro.44.051905.092532.

M. Revnivtsev, S. Sazonov, M. Gilfanov, E. Churazov, and R. Sunyaev. Origin of the Galactic ridge X-ray emission. *Astronomy & Astrophysics*, 452(1):169–178, June 2006. 10.1051/0004-6361:20054268.

M. Revnivtsev, S. Sazonov, R. Krivonos, H. Ritter, and R. Sunyaev. Properties of the Galactic population of cataclysmic variables in hard X-rays. *Astronomy & Astrophysics*, 489(3):1121–1127, Oct. 2008. 10.1051/0004-6361:200810213.

C. S. Reynolds, E. A. Kara, R. F. Mushotzky, A. Ptak, M. J. Koss, B. J. Williams, S. W. Allen, F. E. Bauer, M. Bautz, A. Bogadhee, K. B. Burdge, N. Cappelluti, B. Cenko, G. Chartas, K.-W. Chan, L. Corrales, T. Daylan, A. D. Falcone, A. Foord, C. E. Grant, M. Habouzit, D. Haggard, S. Herrmann, E. Hodges-Kluck, O. Kargaltsev, G. W. King, M. Kounkel, L. A. Lopez, S. Marchesi, M. McDonald, E. Meyer, E. D. Miller, M. Nynka, T. Okajima, F. Pacucci, H. R. Russell, S. Safi-Harb, K. G. Strassun, A. Trindade Falcão, S. A. Walker, J. Wilms, M. Yukita, and W. W. Zhang. Overview of the advanced x-ray imaging satellite (AXIS). In O. H. Siegmund and K. Hoadley, editors, *UV, X-Ray, and Gamma-Ray Space Instrumentation for Astronomy XXIII*, volume 12678 of *Society of Photo-Optical Instrumentation Engineers (SPIE) Conference Series*, page 126781E, Oct. 2023. 10.1117/12.2677468.

T. Ribeiro, S. Kafka, R. Baptista, and C. Tappert. Activity On the M Star of QS Vir. *The Astronomical Journal*, 139(3):1106–1116, Mar. 2010. 10.1088/0004-6256/139/3/1106.

G. R. Ricker, J. N. Winn, R. Vanderspek, D. W. Latham, G. Á. Bakos, J. L. Bean, Z. K. Berta-Thompson, T. M. Brown, L. Buchhave, N. R. Butler, R. P. Butler, W. J. Chaplin, D. Charbonneau, J. Christensen-Dalsgaard, M. Clampin, D. Deming, J. Doty, N. De Lee, C. Dressing, E. W. Dunham, M. Endl, F. Fressin, J. Ge, T. Henning, M. J. Holman, A. W. Howard, S. Ida, J. M. Jenkins, G. Jernigan, J. A. Johnson, L. Kaltenegger, N. Kawai, H. Kjeldsen, G. Laughlin, A. M. Levine, D. Lin, J. J. Lissauer, P. MacQueen, G. Marcy, P. R. McCullough, T. D. Morton, N. Narita, M. Paegert, E. Palle, F. Pepe, J. Pepper, A. Quirrenbach, S. A. Rinehart, D. Sasselov, B. Sato, S. Seager, A. Sozzetti, K. G. Stassun, P. Sullivan, A. Szentgyorgyi, G. Torres, S. Udry, and J. Villasenor. Transiting Exoplanet Survey Satellite (TESS). *Journal of Astronomical Telescopes, Instruments, and Systems*, 1:014003, Jan. 2015. 10.1117/1.JATIS.1.1.014003.

M. E. Ridder, C. O. Heinke, G. R. Sivakoff, and A. K. Hughes. Radio detections of two unusual cataclysmic variables in the VLA Sky Survey. *Monthly Notices of the Royal Astronomical Society*, 519(4):5922–5930, Mar. 2023. 10.1093/mnras/stad038.

H. Ritter. Turning on and off mass transfer in cataclysmic binaries. *Astronomy & Astrophysics*, 202:93–100, Aug. 1988.

H. Ritter and U. Kolb. Catalogue of cataclysmic binaries, low-mass X-ray binaries and related objects (Seventh edition). *Astronomy & Astrophysics*, 404:301–303, June 2003a. 10.1051/0004-6361:20030330.

H. Ritter and U. Kolb. Catalogue of cataclysmic binaries, low-mass X-ray binaries and related objects (Seventh edition). *Astronomy & Astrophysics*, 404:301–303, June 2003b. 10.1051/0004-6361:20030330.

A. C. Rodriguez. From Active Stars to Black Holes: A Discovery Tool for Galactic X-Ray Sources. *Publications of the Astronomical Society of the Pacific*, 136(5): 054201, May 2024a. 10.1088/1538-3873/ad357c.

A. C. Rodriguez. From Active Stars to Black Holes: A Discovery Tool for Galactic X-Ray Sources. *Publications of the Astronomical Society of the Pacific*, 136(5): 054201, May 2024b. 10.1088/1538-3873/ad357c.

A. C. Rodriguez, P. Mróz, S. R. Kulkarni, I. Andreoni, E. C. Bellm, R. Dekany, A. J. Drake, D. A. Duev, M. J. Graham, F. J. Masci, T. A. Prince, R. Riddle, and D. L. Shupe. Microlensing Events in the Galactic Plane Using the Zwicky Transient Facility. *The Astrophysical Journal*, 927(2):150, Mar. 2022. 10.3847/1538-4357/ac51cc.

A. C. Rodriguez, I. Galiullin, M. Gilfanov, S. R. Kulkarni, I. Khamitov, I. Bikmaev, J. van Roestel, L. Yungelson, K. El-Badry, R. Sunayev, T. A. Prince, M. Buntov, I. Caiazzo, A. Drake, M. Gorbachev, M. J. Graham, R. Gumerov, E. Irtuganov, R. R. Laher, F. J. Masci, P. Medvedev, J. Purdum, N. Sakhibullin, A. Sklyanov, R. Smith, P. Szkody, and Z. P. Vanderbosch. SRGeJ045359.9+622444: A 55 Minute Period Eclipsing AM Canum Venaticorum Star Discovered from a Joint SRG/eROSITA + ZTF Search. *The Astrophysical Journal*, 954(1):63, Sept. 2023a. 10.3847/1538-4357/ace698.

A. C. Rodriguez, I. Galiullin, M. Gilfanov, S. R. Kulkarni, I. Khamitov, I. Bikmaev, J. van Roestel, L. Yungelson, K. El-Badry, R. Sunayev, T. A. Prince, M. Buntov, I. Caiazzo, A. Drake, M. Gorbachev, M. J. Graham, R. Gumerov, E. Irtuganov, R. R. Laher, F. J. Masci, P. Medvedev, J. Purdum, N. Sakhibullin, A. Sklyanov, R. Smith, P. Szkody, and Z. P. Vanderbosch. SRGeJ045359.9+622444: A 55

Minute Period Eclipsing AM Canum Venaticorum Star Discovered from a Joint SRG/eROSITA + ZTF Search. *The Astrophysical Journal*, 954(1):63, Sept. 2023b. 10.3847/1538-4357/ace698.

A. C. Rodriguez, S. R. Kulkarni, T. A. Prince, P. Szkody, K. B. Burdge, I. Caiazzo, J. van Roestel, Z. P. Vanderbosch, K. El-Badry, E. C. Bellm, B. T. Gänsicke, M. J. Graham, A. A. Mahabal, F. J. Masci, P. Mróz, R. Riddle, and B. Rusholme. Discovery of Two Polars from a Crossmatch of ZTF and the SRG/eFEDS X-Ray Catalog. *The Astrophysical Journal*, 945(2):141, Mar. 2023c. 10.3847/1538-4357/acbb6f.

A. C. Rodriguez, S. R. Kulkarni, T. A. Prince, P. Szkody, K. B. Burdge, I. Caiazzo, J. van Roestel, Z. P. Vanderbosch, K. El-Badry, E. C. Bellm, B. T. Gänsicke, M. J. Graham, A. A. Mahabal, F. J. Masci, P. Mróz, R. Riddle, and B. Rusholme. Discovery of Two Polars from a Crossmatch of ZTF and the SRG/eFEDS X-Ray Catalog. *The Astrophysical Journal*, 945(2):141, Mar. 2023d. 10.3847/1538-4357/acbb6f.

A. C. Rodriguez, K. El-Badry, V. Suleimanov, A. F. Pala, S. R. Kulkarni, B. Gaensicke, K. Mori, R. M. Rich, A. Sarkar, T. Bao, R. Lopes de Oliveira, G. Ramsay, P. Szkody, M. Graham, T. A. Prince, I. Caiazzo, Z. P. Vanderbosch, J. van Roestel, K. K. Das, Y.-J. Qin, M. M. Kasliwal, A. Wold, S. L. Groom, D. Reiley, and R. Riddle. Cataclysmic Variables and AM CVn Binaries in SRG/eROSITA + Gaia: Volume Limited Samples, X-ray Luminosity Functions, and Space Densities. *arXiv e-prints*, art. arXiv:2408.16053, Aug. 2024. 10.48550/arXiv.2408.16053.

A. C. Rodriguez, K. El-Badry, P. Hakala, P. Rodríguez-Gil, T. Bao, I. Galiullin, J. A. Kurlander, C. J. Law, I. Pelisoli, M. R. Schreiber, K. Burdge, I. Caiazzo, J. van Roestel, P. Szkody, A. J. Drake, D. A. H. Buckley, S. B. Potter, B. Gaensicke, K. Mori, E. C. Bellm, S. R. Kulkarni, T. A. Prince, M. Graham, M. M. Kasliwal, S. Rose, Y. Sharma, T. Ahumada, S. Anand, A. Viitanen, A. Wold, T. X. Chen, R. Riddle, and R. Smith. A Link Between White Dwarf Pulsars and Polars: Multiwavelength Observations of the 9.36-Minute Period Variable Gaia22ayj. *arXiv e-prints*, art. arXiv:2501.01490, Jan. 2025a.

A. C. Rodriguez, K. El-Badry, V. Suleimanov, A. F. Pala, S. R. Kulkarni, B. Gaensicke, K. Mori, R. M. Rich, A. Sarkar, T. Bao, R. Lopes de Oliveira, G. Ramsay, P. Szkody, M. Graham, T. A. Prince, I. Caiazzo, Z. P. Vanderbosch, J. van Roes-

tel, K. K. Das, Y.-J. Qin, M. M. Kasliwal, A. Wold, S. L. Groom, D. Reiley, and R. Riddle. Cataclysmic Variables and AM CVn Binaries in SRG/eROSITA + Gaia: Volume Limited Samples, X-Ray Luminosity Functions, and Space Densities. *Publications of the Astronomical Society of the Pacific*, 137(1):014201, Jan. 2025b. 10.1088/1538-3873/ada185.

G. H. A. Roelofs, G. Nelemans, and P. J. Groot. The population of AM CVn stars from the Sloan Digital Sky Survey. *Monthly Notices of the Royal Astronomical Society*, 382(2):685–692, Dec. 2007. 10.1111/j.1365-2966.2007.12451.x.

R. W. Romani and N. Sanchez. Intra-binary Shock Heating of Black Widow Companions. *The Astrophysical Journal*, 828(1):7, Sept. 2016. 10.3847/0004-637X/828/1/7.

R. W. Romani, D. Kandel, A. V. Filippenko, T. G. Brink, and W. Zheng. PSR J0952-0607: The Fastest and Heaviest Known Galactic Neutron Star. *The Astrophysical Journal Letters*, 934(2):L17, Aug. 2022. 10.3847/2041-8213/ac8007.

D. M. Russell, R. P. Fender, R. I. Hynes, C. Brocksopp, J. Homan, P. G. Jonker, and M. M. Buxton. Global optical/infrared-X-ray correlations in X-ray binaries: quantifying disc and jet contributions. *Monthly Notices of the Royal Astronomical Society*, 371(3):1334–1350, Sept. 2006. 10.1111/j.1365-2966.2006.10756.x.

H. N. Russell. Notes on white dwarfs and small companions. *The Astronomical Journal*, 51:13, June 1944. 10.1086/105780.

J. Rybizki, G. M. Green, H.-W. Rix, K. El-Badry, M. Demleitner, E. Zari, A. Udalski, R. L. Smart, and A. Gould. A classifier for spurious astrometric solutions in Gaia eDR3. *Monthly Notices of the Royal Astronomical Society*, 510(2):2597–2616, Feb. 2022. 10.1093/mnras/stab3588.

K. C. Sahu, J. Anderson, S. Casertano, H. E. Bond, A. Udalski, M. Dominik, A. Calamida, A. Bellini, T. M. Brown, M. Rejkuba, V. Bajaj, N. Kains, H. C. Ferguson, C. L. Fryer, P. Yock, P. Mróz, S. Kozłowski, P. Pietrukowicz, R. Poleski, J. Skowron, I. Soszyński, M. K. Szymański, K. Ulaczyk, Ł. Wyrzykowski, R. K. Barry, D. P. Bennett, I. A. Bond, Y. Hirao, S. I. Silva, I. Kondo, N. Koshimoto, C. Ranc, N. J. Rattenbury, T. Sumi, D. Suzuki, P. J. Tristram, A. Vandorou, J.-P. Beaulieu, J.-B. Marquette, A. Cole, P. Fouqué, K. Hill, S. Dieters, C. Coutures,

D. Dominis-Prester, C. Bennett, E. Bachelet, J. Menzies, M. Albrow, K. Pollard, A. Gould, J. C. Yee, W. Allen, L. A. Almeida, G. Christie, J. Drummond, A. Gal-Yam, E. Gorbikov, F. Jablonski, C.-U. Lee, D. Maoz, I. Manulis, J. McCormick, T. Natusch, R. W. Pogge, Y. Shvartzvald, U. G. Jørgensen, K. A. Alsubai, M. I. Andersen, V. Bozza, S. C. Novati, M. Burgdorf, T. C. Hinse, M. Hundertmark, T.-O. Husser, E. Kerins, P. Longa-Peña, L. Mancini, M. Penny, S. Rahvar, D. Ricci, S. Sajadian, J. Skottfelt, C. Snodgrass, J. Southworth, J. Tregloan-Reed, J. Wambsganss, O. Wertz, Y. Tsapras, R. A. Street, D. M. Bramich, K. Horne, I. A. Steele, and RoboNet Collaboration. An Isolated Stellar-mass Black Hole Detected through Astrometric Microlensing. *The Astrophysical Journal*, 933(1):83, July 2022. 10.3847/1538-4357/ac739e.

E. E. Salpeter. The Luminosity Function and Stellar Evolution. *The Astrophysical Journal*, 121:161, Jan. 1955. 10.1086/145971.

M. Salvato, J. Buchner, T. Budavári, T. Dwelly, A. Merloni, M. Brusa, A. Rau, S. Fotopoulou, and K. Nandra. Finding counterparts for all-sky X-ray surveys with NWAY: a Bayesian algorithm for cross-matching multiple catalogues. *Monthly Notices of the Royal Astronomical Society*, 473(4):4937–4955, Feb. 2018. 10.1093/mnras/stx2651.

M. Salvato, J. Wolf, T. Dwelly, A. Georgakakis, M. Brusa, A. Merloni, T. Liu, Y. Toba, K. Nandra, G. Lamer, J. Buchner, C. Schneider, S. Freund, A. Rau, A. Schwope, A. Nishizawa, M. Klein, R. Arcodia, J. Comparat, B. Musiimenta, T. Nagao, H. Brunner, A. Malyali, A. Finoguenov, S. Anderson, Y. Shen, H. Ibarra-Medel, J. Trump, W. N. Brandt, C. M. Urry, C. Rivera, M. Krumpe, T. Urrutia, T. Miyaji, K. Ichikawa, D. P. Schneider, A. Fresco, T. Boller, J. Haase, J. Brownstein, R. R. Lane, D. Bizyaev, and C. Nitschelm. The eROSITA Final Equatorial-Depth Survey (eFEDS). Identification and characterization of the counterparts to point-like sources. *Astronomy & Astrophysics*, 661:A3, May 2022. 10.1051/0004-6361/202141631.

H. Sana, S. E. de Mink, A. de Koter, N. Langer, C. J. Evans, M. Gieles, E. Gosset, R. G. Izzard, J. B. Le Bouquin, and F. R. N. Schneider. Binary Interaction Dominates the Evolution of Massive Stars. *Science*, 337(6093):444, July 2012. 10.1126/science.1223344.

A. Sarkar, H. Ge, and C. A. Tout. Evolved cataclysmic variables as progenitors of AM CVn stars. *Monthly Notices of the Royal Astronomical Society*, 520(2): 3187–3200, Apr. 2023a. 10.1093/mnras/stad354.

A. Sarkar, H. Ge, and C. A. Tout. New insights into the helium star formation channel of AM CVn systems with explanations of Gaia14aae and ZTFJ1637+49. *Monthly Notices of the Royal Astronomical Society*, 519(2):2567–2577, Feb. 2023b. 10.1093/mnras/stac3688.

A. Sarkar, H. Ge, and C. A. Tout. Evolved cataclysmic variables as progenitors of AM CVn stars. *Monthly Notices of the Royal Astronomical Society*, 520(2): 3187–3200, Apr. 2023c. 10.1093/mnras/stad354.

A. Sarkar, A. C. Rodriguez, S. Ginzburg, L. Yungelson, and C. A. Tout. Magnetic braking below the cataclysmic variable period gap and the observed dearth of period bouncers. *Astronomy & Astrophysics*, 686:L19, June 2024. 10.1051/0004-6361/202449345.

R. Sasaki, Y. Tsuboi, W. Iwakiri, S. Nakahira, Y. Maeda, K. Gendreau, M. F. Corcoran, K. Hamaguchi, Z. Arzoumanian, C. B. Markwardt, T. Enoto, T. Sato, H. Kawai, T. Mihara, M. Shidatsu, H. Negoro, and M. Serino. The RS CVn-type Star GT Mus Shows Most Energetic X-Ray Flares Throughout the 2010s. *The Astrophysical Journal*, 910(1):25, Mar. 2021. 10.3847/1538-4357/abde38.

S. Sazonov, M. Revnivtsev, M. Gilfanov, E. Churazov, and R. Sunyaev. X-ray luminosity function of faint point sources in the Milky Way. *Astronomy & Astrophysics*, 450(1):117–128, Apr. 2006. 10.1051/0004-6361:20054297.

J. D. Scargle. Studies in astronomical time series analysis. II. Statistical aspects of spectral analysis of unevenly spaced data. *The Astrophysical Journal*, 263:835–853, Dec. 1982. 10.1086/160554.

S. Scaringi, P. J. Groot, C. Knigge, A. J. Bird, E. Breedt, D. A. H. Buckley, Y. Cavecchi, N. D. Degenaar, D. de Martino, C. Done, M. Fratta, K. Iłkiewicz, E. Koerding, J. P. Lasota, C. Littlefield, C. F. Manara, M. O'Brien, P. Szkody, and F. X. Timmes. Localized thermonuclear bursts from accreting magnetic white dwarfs. *Nature*, 604(7906):447–450, Apr. 2022. 10.1038/s41586-022-04495-6.

S. Scaringi, K. Breivik, T. B. Littenberg, C. Knigge, P. J. Groot, and M. Veresvarska. Cataclysmic variables are a key population of gravitational wave sources for LISA.

Monthly Notices of the Royal Astronomical Society, 525(1):L50–L55, Oct. 2023. 10.1093/mnrasl/slad093.

M. Schaich, D. Wolf, R. Oestreicher, and H. Ruder. Phase resolved linear polarization spectra of AM Herculis. *Astronomy & Astrophysics*, 264:529–535, Oct. 1992.

E. F. Schlafly and D. P. Finkbeiner. Measuring Reddening with Sloan Digital Sky Survey Stellar Spectra and Recalibrating SFD. *The Astrophysical Journal*, 737(2): 103, Aug. 2011a. 10.1088/0004-637X/737/2/103.

E. F. Schlafly and D. P. Finkbeiner. Measuring Reddening with Sloan Digital Sky Survey Stellar Spectra and Recalibrating SFD. *The Astrophysical Journal*, 737(2): 103, Aug. 2011b. 10.1088/0004-637X/737/2/103.

G. D. Schmidt and H. S. Stockman. Synchronization of the Magnetic Nova V1500 Cygni. *The Astrophysical Journal*, 371:749, Apr. 1991. 10.1086/169939.

G. D. Schmidt, P. Szkody, L. Homer, P. S. Smith, B. Chen, A. Henden, J.-E. Solheim, M. A. Wolfe, and R. Greimel. Unraveling the Puzzle of the Eclipsing Polar SDSS J015543.40+002807.2 with XMM and Optical Photometry/Spectropolarimetry. *The Astrophysical Journal*, 620(1):422–431, Feb. 2005. 10.1086/426807.

J. H. M. M. Schmitt, T. A. Fleming, and M. S. Giampapa. The X-Ray View of the Low-Mass Stars in the Solar Neighborhood. *The Astrophysical Journal*, 450:392, Sept. 1995. 10.1086/176149.

M. R. Schreiber, D. Belloni, B. T. Gänsicke, S. G. Parsons, and M. Zorotovic. The origin and evolution of magnetic white dwarfs in close binary stars. *Nature Astronomy*, 5:648–654, Apr. 2021a. 10.1038/s41550-021-01346-8.

M. R. Schreiber, D. Belloni, B. T. Gänsicke, S. G. Parsons, and M. Zorotovic. The origin and evolution of magnetic white dwarfs in close binary stars. *Nature Astronomy*, 5:648–654, Jan. 2021b. 10.1038/s41550-021-01346-8.

M. R. Schreiber, D. Belloni, and J. van Roestel. Period bouncers as detached magnetic cataclysmic variables. *Astronomy & Astrophysics*, 679:L8, Nov. 2023. 10.1051/0004-6361/202347766.

M. R. Schreiber, D. Belloni, and A. D. Schwope. The cataclysmic variable orbital period gap: More evident than ever. *Astronomy & Astrophysics*, 682:L7, Feb. 2024a. 10.1051/0004-6361/202348807.

M. R. Schreiber, D. Belloni, and A. D. Schwope. The cataclysmic variable orbital period gap: More evident than ever. *Astronomy & Astrophysics*, 682:L7, Feb. 2024b. 10.1051/0004-6361/202348807.

E. J. Schreier, K. Swartz, R. Giacconi, G. Fabbiano, and J. Morin. The long-term intensity behavior of Centaurus X-3. *The Astrophysical Journal*, 204:539–547, Mar. 1976. 10.1086/154200.

A. Schwope. CV surveys with eROSITA. *Memorie della Società Astronomica Italiana*, 83:844, Jan. 2012.

A. Schwope, G. Hasinger, I. Lehmann, R. Schwarz, H. Brunner, S. Neizvestny, A. Ugryumov, Y. Balega, J. Trümper, and W. Voges. The ROSAT Bright Survey: II. Catalogue of all high-galactic latitude RASS sources with PSPC countrate CR > $0.2\,s^{-1}$. *Astronomische Nachrichten*, 321(1):1–52, Jan. 2000. 10.1002/(SICI)1521-3994(200003)321:1<1::AID-ASNA1>3.0.CO;2-C.

A. Schwope, D. A. H. Buckley, A. Malyali, S. Potter, O. König, R. Arcodia, M. Gromadzki, and A. Rau. Discovery of eRASSt J192932.9-560346: A bright, two-pole accreting, eclipsing polar. *Astronomy & Astrophysics*, 661:A43, May 2022a. 10.1051/0004-6361/202141653.

A. Schwope, D. A. H. Buckley, A. Malyali, S. Potter, O. König, R. Arcodia, M. Gromadzki, and A. Rau. Discovery of eRASSt J192932.9-560346: A bright, two-pole accreting, eclipsing polar. *Astronomy & Astrophysics*, 661:A43, May 2022b. 10.1051/0004-6361/202141653.

A. Schwope, T. R. Marsh, A. Standke, I. Pelisoli, S. Potter, D. Buckley, J. Munday, and V. Dhillon. X-ray properties of the white dwarf pulsar eRASSU J191213.9−441044. *Astronomy & Astrophysics*, 674:L9, June 2023. 10.1051/0004-6361/202346589.

A. Schwope, K. Knauff, J. Kurpas, M. Salvato, B. Stelzer, L. Stütz, and D. Tubín-Arenas. A first systematic characterization of cataclysmic variables in SRG/eROSITA surveys. *arXiv e-prints*, art. arXiv:2407.20903, July 2024a. 10.48550/arXiv.2407.20903.

A. Schwope, J. Kurpas, P. Baecke, K. Knauff, L. Stütz, D. Tubín-Arenas, A. Standke, S. F. Anderson, F. Bauer, W. N. Brandt, K. Covey, S. Demasi, T. Dwelly, S. Freund, S. Friedrich, B. T. Gänsicke, C. Maitra, A. Merloni, D. Muñoz-Giraldo, A. Rodriguez, M. Salvato, K. Stassun, B. Stelzer, A. Strong, and S. Morrison. Compact white dwarf binaries in the combined SRG/eROSITA/SDSS eFEDS survey. *Astronomy & Astrophysics*, 686:A110, June 2024b. 10.1051/0004-6361/202348426.

A. D. Schwope. Exploring the space density of X-ray selected cataclysmic variables. *Astronomy & Astrophysics*, 619:A62, Nov. 2018. 10.1051/0004-6361/201833723.

A. D. Schwope, A. Staude, D. Koester, and J. Vogel. XMM-Newton observations of EF Eridani: the textbook example of low-accretion rate polars. *Astronomy & Astrophysics*, 469(3):1027–1031, July 2007. 10.1051/0004-6361:20066928.

A. D. Schwope, K. Horne, D. Steeghs, and M. Still. Dissecting the donor star in the eclipsing polar HU Aquarii. *Astronomy & Astrophysics*, 531:A34, July 2011. 10.1051/0004-6361/201016373.

N. I. Shakura and R. A. Sunyaev. Black holes in binary systems. Observational appearance. *Astronomy & Astrophysics*, 24:337–355, Jan. 1973.

C. Shariat, S. Naoz, K. El-Badry, K. Akira Rocha, V. Kalogera, A. P. Stephan, K. B. Burdge, and I. Angelo. Triple Evolution Pathways to Black Hole Low-Mass X-ray Binaries: Insights from V404 Cygni. *arXiv e-prints*, art. arXiv:2411.15644, Nov. 2024. 10.48550/arXiv.2411.15644.

A. I. Sheinis, M. Bolte, H. W. Epps, R. I. Kibrick, J. S. Miller, M. V. Radovan, B. C. Bigelow, and B. M. Sutin. ESI, a New Keck Observatory Echellette Spectrograph and Imager. *Publications of the Astronomical Society of the Pacific*, 114(798): 851–865, Aug. 2002. 10.1086/341706.

T. Shenar, H. Sana, L. Mahy, K. El-Badry, P. Marchant, N. Langer, C. Hawcroft, M. Fabry, K. Sen, L. A. Almeida, M. Abdul-Masih, J. Bodensteiner, P. A. Crowther, M. Gieles, M. Gromadzki, V. Hénault-Brunet, A. Herrero, A. de Koter, P. Iwanek, S. Kozłowski, D. J. Lennon, J. Maíz Apellániz, P. Mróz, A. F. J. Moffat, A. Picco, P. Pietrukowicz, R. Poleski, K. Rybicki, F. R. N. Schneider, D. M. Skowron, J. Skowron, I. Soszyński, M. K. Szymański, S. Toonen, A. Udalski, K. Ulaczyk, J. S. Vink, and M. Wrona. An X-ray-quiet black hole born with a negligible kick

in a massive binary within the Large Magellanic Cloud. *Nature Astronomy*, 6: 1085–1092, July 2022. 10.1038/s41550-022-01730-y.

H. L. Shipman. Masses and Radii of White Dwarfs. *The Astrophysical Journal*, 177:723, Nov. 1972. 10.1086/151752.

A. D. Silber. *Studies of an X-Ray Selected Sample of Cataclysmic Variables.* PhD thesis, Massachusetts Institute of Technology, Jan. 1992.

A. Skumanich. Time Scales for Ca II Emission Decay, Rotational Braking, and Lithium Depletion. *The Astrophysical Journal*, 171:565, Feb. 1972. 10.1086/151310.

K. V. Sokolovsky, J. Strader, S. J. Swihart, E. Aydi, A. Bahramian, L. Chomiuk, C. O. Heinke, A. K. Hughes, K.-L. Li, R. L. de Oliveira, J. C. A. Miller-Jones, K. Mukai, D. J. Sand, L. Shishkovsky, E. Tremou, and K. Voggel. 1RXH J082623.6-505741: A New Long-period Cataclysmic Variable with an Evolved Donor and a Low Mass-transfer Rate. *The Astrophysical Journal*, 934(2):142, Aug. 2022. 10.3847/1538-4357/ac7b25.

J. E. Solheim. AM CVn Stars: Status and Challenges. *Publications of the Astronomical Society of the Pacific*, 122(896):1133, Oct. 2010. 10.1086/656680.

L. Souza and R. Baptista. Cyclical Period Changes in Cataclysmic Variables: A Statistical Study. *The Astrophysical Journal*, 972(1):33, Sept. 2024. 10.3847/1538-4357/ad6b0e.

H. C. Spruit and H. Ritter. Stellar activity and the period gap in cataclysmic variables. *Astronomy & Astrophysics*, 124(2):267–272, Aug. 1983a.

H. C. Spruit and H. Ritter. Stellar activity and the period gap in cataclysmic variables. *Astronomy & Astrophysics*, 124(2):267–272, Aug. 1983b.

E. R. Stanway, T. R. Marsh, P. Chote, B. T. Gänsicke, D. Steeghs, and P. J. Wheatley. VLA radio observations of AR Scorpii. *Astronomy & Astrophysics*, 611:A66, Mar. 2018. 10.1051/0004-6361/201732380.

R. Stehle, U. Kolb, and H. Ritter. Modelling Population II cataclysmic variables. *Astronomy & Astrophysics*, 320:136–146, Apr. 1997.

R. F. Stellingwerf. Period determination using phase dispersion minimization. *The Astrophysical Journal*, 224:953–960, Sept. 1978. 10.1086/156444.

B. Stelzer, A. Marino, G. Micela, J. López-Santiago, and C. Liefke. The UV and X-ray activity of the M dwarfs within 10 pc of the Sun. *Monthly Notices of the Royal Astronomical Society*, 431(3):2063–2079, May 2013. 10.1093/mnras/stt225.

B. Stelzer, A. Klutsch, M. Coffaro, E. Magaudda, and M. Salvato. A first eROSITA view of ultracool dwarfs. *Astronomy & Astrophysics*, 661:A44, May 2022. 10.1051/0004-6361/202141232.

S. Stevenson. Biases in Estimates of Black Hole Kicks from the Spin Distribution of Binary Black Holes. *The Astrophysical Journal Letters*, 926(2):L32, Feb. 2022. 10.3847/2041-8213/ac5252.

J. T. Stocke, S. L. Morris, I. M. Gioia, T. Maccacaro, R. Schild, A. Wolter, T. A. Fleming, and J. P. Henry. The Einstein Observatory Extended Medium-Sensitivity Survey. II. The Optical Identifications. *The Astrophysical Journal Supplement Series*, 76:813, July 1991. 10.1086/191582.

T. Sukhbold, T. Ertl, S. E. Woosley, J. M. Brown, and H. T. Janka. Core-collapse Supernovae from 9 to 120 Solar Masses Based on Neutrino-powered Explosions. *The Astrophysical Journal*, 821(1):38, Apr. 2016. 10.3847/0004-637X/821/1/38.

V. F. Suleimanov, V. Doroshenko, and K. Werner. Hard X-ray view on intermediate polars in the Gaia era. *Monthly Notices of the Royal Astronomical Society*, 482(3): 3622–3635, Jan. 2019. 10.1093/mnras/sty2952.

V. F. Suleimanov, V. Doroshenko, and K. Werner. Hard X-ray luminosity functions of cataclysmic variables: joint Swift/BAT and Gaia data. *Monthly Notices of the Royal Astronomical Society*, 511(4):4937–4945, Apr. 2022. 10.1093/mnras/stac417.

R. Sunyaev, V. Arefiev, V. Babyshkin, A. Bogomolov, K. Borisov, M. Buntov, H. Brunner, R. Burenin, E. Churazov, D. Coutinho, J. Eder, N. Eismont, M. Freyberg, M. Gilfanov, P. Gureyev, G. Hasinger, I. Khabibullin, V. Kolmykov, S. Komovkin, R. Krivonos, I. Lapshov, V. Levin, I. Lomakin, A. Lutovinov, P. Medvedev, A. Merloni, T. Mernik, E. Mikhailov, V. Molodtsov, P. Mzhelsky, S. Müller, K. Nandra, V. Nazarov, M. Pavlinsky, A. Poghodin, P. Predehl, J. Robrade, S. Sazonov, H. Scheuerle, A. Shirshakov, A. Tkachenko, and V. Voron. SRG X-ray orbital observatory. Its telescopes and first scientific results. *Astronomy & Astrophysics*, 656:A132, Dec. 2021. 10.1051/0004-6361/202141179.

D. Sweeney, P. Tuthill, S. Sharma, and R. Hirai. The Galactic underworld: the spatial distribution of compact remnants. *Monthly Notices of the Royal Astronomical Society*, 516(4):4971–4979, Nov. 2022. 10.1093/mnras/stac2092.

P. Szkody. Cataclysmic Variables from SDSS: A Review and A Look Forward to LSST. *Acta Polytechnica CTU Proceedings*, 2(1):55–59, Jan. 2015. 10.14311/APP.2015.02.0055.

P. Szkody, L. Homer, B. Chen, A. Henden, G. D. Schmidt, S. F. Anderson, D. W. Hoard, W. Voges, and J. Brinkmann. XMM-Newton Observations of the Extremely Low Accretion Rate Polars SDSS J155331.12+551614.5 and SDSS J132411.57+032050.5. *The Astronomical Journal*, 128(5):2443–2447, Nov. 2004. 10.1086/424540.

P. Szkody, S. F. Anderson, K. Brooks, B. T. Gänsicke, M. Kronberg, T. Riecken, N. P. Ross, G. D. Schmidt, D. P. Schneider, M. A. Agüeros, A. N. Gomez-Moran, G. R. Knapp, M. R. Schreiber, and A. D. Schwope. Cataclysmic Variables from the Sloan Digital Sky Survey. VIII. The Final Year (2007-2008). *The Astronomical Journal*, 142(6):181, Dec. 2011. 10.1088/0004-6256/142/6/181.

P. Szkody, B. Dicenzo, A. Y. Q. Ho, L. A. Hillenbrand, J. van Roestel, M. Ridder, I. DeJesus Lima, M. L. Graham, E. C. Bellm, K. Burdge, T. Kupfer, T. A. Prince, F. J. Masci, P. J. Mróz, V. Z. Golkhou, M. Coughlin, V. A. Cunningham, R. Dekany, M. J. Graham, D. Hale, D. Kaplan, M. M. Kasliwal, A. A. Miller, J. D. Neill, M. T. Patterson, R. Riddle, R. Smith, and M. T. Soumagnac. Cataclysmic Variables in the First Year of the Zwicky Transient Facility. *The Astronomical Journal*, 159(5): 198, May 2020. 10.3847/1538-3881/ab7cce.

P. Szkody, C. Olde Loohuis, B. Koplitz, J. van Roestel, B. Dicenzo, A. Y. Q. Ho, L. A. Hillenbrand, E. C. Bellm, R. Dekany, A. J. Drake, D. A. Duev, M. J. Graham, M. M. Kasliwal, A. A. Mahabal, F. J. Masci, J. D. Neill, R. Riddle, B. Rusholme, J. Sollerman, and R. Walters. Cataclysmic Variables in the Second Year of the Zwicky Transient Facility. *The Astronomical Journal*, 162(3):94, Sept. 2021. 10.3847/1538-3881/ac0efb.

Y. Tanaka and N. Shibazaki. X-ray Novae. *Annual Review of Astronomy and Astrophysics*, 34:607–644, Jan. 1996. 10.1146/annurev.astro.34.1.607.

P. Tang, J. Eldridge, R. Meyer, A. Lamberts, G. Boileau, and W. van Zeist. Predicting gravitational wave signals from BPASS White Dwarf Binary and Black Hole Binary populations of a Milky Way-like galaxy model for LISA. *arXiv e-prints*, art. arXiv:2405.20484, May 2024. 10.48550/arXiv.2405.20484.

T. M. Tauris and E. P. J. van den Heuvel. *Physics of Binary Star Evolution. From Stars to X-ray Binaries and Gravitational Wave Sources*. 2023. 10.48550/arXiv.2305.09388.

M. B. Taylor. TOPCAT & STIL: Starlink Table/VOTable Processing Software. In P. Shopbell, M. Britton, and R. Ebert, editors, *Astronomical Data Analysis Software and Systems XIV*, volume 347 of *Astronomical Society of the Pacific Conference Series*, page 29, Dec. 2005.

J. R. Thorstensen. Follow-up Studies of Five Cataclysmic Variable Candidates Discovered by LAMOST. *The Astronomical Journal*, 160(4):151, Oct. 2020. 10.3847/1538-3881/aba7c7.

C. G. Tinney, I. N. Reid, and J. R. Mould. The Faintest Stars: From Schmidt Plates to Luminosity Functions. *The Astrophysical Journal*, 414:254, Sept. 1993. 10.1086/173074.

J. L. Tonry, L. Denneau, A. N. Heinze, B. Stalder, K. W. Smith, S. J. Smartt, C. W. Stubbs, H. J. Weiland, and A. Rest. ATLAS: A High-cadence All-sky Survey System. *Publications of the Astronomical Society of the Pacific*, 130(988):064505, June 2018a. 10.1088/1538-3873/aabadf.

J. L. Tonry, L. Denneau, A. N. Heinze, B. Stalder, K. W. Smith, S. J. Smartt, C. W. Stubbs, H. J. Weiland, and A. Rest. ATLAS: A High-cadence All-sky Survey System. *Publications of the Astronomical Society of the Pacific*, 130(988):064505, June 2018b. 10.1088/1538-3873/aabadf.

C. A. Tout, D. T. Wickramasinghe, J. Liebert, L. Ferrario, and J. E. Pringle. Binary star origin of high field magnetic white dwarfs. *Monthly Notices of the Royal Astronomical Society*, 387(2):897–901, June 2008. 10.1111/j.1365-2966.2008.13291.x.

D. M. Townsley and L. Bildsten. Measuring White Dwarf Accretion Rates via Their Effective Temperatures. *The Astrophysical Journal Letters*, 596(2):L227–L230, Oct. 2003. 10.1086/379535.

J. Truemper. The ROSAT mission. *Advances in Space Research*, 2(4):241–249, Jan. 1982. 10.1016/0273-1177(82)90070-9.

A. V. Tutukov, A. V. Fedorova, E. V. Ergma, and L. R. Yungelson. Evolution of Low-Mass Close Binaries - the Minimum Orbital Period. *Soviet Astronomy Letters*, 11:52–56, Feb. 1985.

J. A. Tyson. Large Synoptic Survey Telescope: Overview. In J. A. Tyson and S. Wolff, editors, *Survey and Other Telescope Technologies and Discoveries*, volume 4836 of *Society of Photo-Optical Instrumentation Engineers (SPIE) Conference Series*, pages 10–20, Dec. 2002. 10.1117/12.456772.

S. van der Walt, S. C. Colbert, and G. Varoquaux. The NumPy Array: A Structure for Efficient Numerical Computation. *Computing in Science and Engineering*, 13 (2):22–30, Mar. 2011. 10.1109/MCSE.2011.37.

A. van Maanen. A Very Faint Star of Spectral Type F. *Publications of the Astronomical Society of the Pacific*, 31(179):42, Feb. 1919. 10.1086/122810.

J. van Paradijs and N. White. The Galactic Distribution of Low-Mass X-Ray Binaries. *The Astrophysical Journal Letters*, 447:L33, July 1995. 10.1086/309558.

J. van Paradijs, W. Penninx, and W. H. G. Lewin. On the relation between X-ray burst properties and the persistent X-ray luminosity. *Monthly Notices of the Royal Astronomical Society*, 233:437–450, July 1988. 10.1093/mnras/233.2.437.

J. van Roestel, L. Creter, T. Kupfer, P. Szkody, J. Fuller, M. J. Green, R. M. Rich, J. Sepikas, K. Burdge, I. Caiazzo, P. Mróz, T. A. Prince, D. A. Duev, M. J. Graham, D. L. Shupe, R. R. Laher, A. A. Mahabal, and F. J. Masci. A Systematic Search for Outbursting AM CVn Systems with the Zwicky Transient Facility. *The Astronomical Journal*, 162(3):113, Sept. 2021. 10.3847/1538-3881/ac0622.

J. van Roestel, T. Kupfer, M. J. Green, T. L. S. Wong, L. Bildsten, K. Burdge, T. Prince, T. R. Marsh, P. Szkody, C. Fremling, M. J. Graham, V. S. Dhillon, S. P. Littlefair, E. C. Bellm, M. Coughlin, D. A. Duev, D. A. Goldstein, R. R. Laher, B. Rusholme, R. Riddle, R. Dekany, and S. R. Kulkarni. Discovery and characterization of five new eclipsing AM CVn systems. *Monthly Notices of the Royal Astronomical Society*, 512(4):5440–5461, June 2022. 10.1093/mnras/stab2421.

J. van Roestel, A. C. Rodriguez, P. Szkody, A. J. Brown, I. Caiazzo, A. Drake, K. El-Badry, T. Prince, R. M. R. Rich, J. D. Neill, Z. Vanderbosch, E. C. Bellm, R. Dekany, F. Feinstein, M. Graham, S. L. Groom, G. Helou, S. R. Kulkarni, T. du Laz, A. Mahabal, Y. Sharma, J. Sollerman, and A. Wold. Cyclotron emitting magnetic white dwarfs in post common envelope binaries discovered with the Zwicky Transient Facility. *arXiv e-prints*, art. arXiv:2412.15153, Dec. 2024. 10.48550/arXiv.2412.15153.

J. Vanderplas. gatspy: General tools for Astronomical Time Series in Python, Feb. 2015.

J. VanderPlas. gatspy: General tools for Astronomical Time Series in Python. Astrophysics Source Code Library, record ascl:1610.007, Oct. 2016a.

J. VanderPlas. gatspy: General tools for Astronomical Time Series in Python, Oct. 2016b.

J. T. VanderPlas. Understanding the Lomb-Scargle Periodogram. *The Astrophysical Journal Supplement Series*, 236(1):16, May 2018. 10.3847/1538-4365/aab766.

F. Verbunt and C. Zwaan. Magnetic braking in low-mass X-ray binaries. *Astronomy & Astrophysics*, 100:L7–L9, July 1981.

F. Verbunt, W. H. Bunk, H. Ritter, and E. Pfeffermann. Cataclysmic variables in the ROSAT PSPC All Sky Survey. *Astronomy & Astrophysics*, 327:602–613, Nov. 1997.

P. Virtanen, R. Gommers, T. E. Oliphant, M. Haberland, T. Reddy, D. Cournapeau, E. Burovski, P. Peterson, W. Weckesser, J. Bright, S. J. van der Walt, M. Brett, J. Wilson, K. J. Millman, N. Mayorov, A. R. J. Nelson, E. Jones, R. Kern, E. Larson, C. J. Carey, İ. Polat, Y. Feng, E. W. Moore, J. VanderPlas, D. Laxalde, J. Perktold, R. Cimrman, I. Henriksen, E. A. Quintero, C. R. Harris, A. M. Archibald, A. H. Ribeiro, F. Pedregosa, P. van Mulbregt, and SciPy 1. 0 Contributors. SciPy 1.0: fundamental algorithms for scientific computing in Python. *Nature Methods*, 17: 261–272, Feb. 2020. 10.1038/s41592-019-0686-2.

W. Voges, B. Aschenbach, T. Boller, H. Bräuninger, U. Briel, W. Burkert, K. Dennerl, J. Englhauser, R. Gruber, F. Haberl, G. Hartner, G. Hasinger, M. Kürster,

E. Pfeffermann, W. Pietsch, P. Predehl, C. Rosso, J. H. M. M. Schmitt, J. Trümper, and H. U. Zimmermann. The ROSAT all-sky survey bright source catalogue. *Astronomy & Astrophysics*, 349:389–405, Sept. 1999a.

W. Voges, B. Aschenbach, T. Boller, H. Bräuninger, U. Briel, W. Burkert, K. Dennerl, J. Englhauser, R. Gruber, F. Haberl, G. Hartner, G. Hasinger, M. Kürster, E. Pfeffermann, W. Pietsch, P. Predehl, C. Rosso, J. H. M. M. Schmitt, J. Trümper, and H. U. Zimmermann. The ROSAT all-sky survey bright source catalogue. *Astronomy & Astrophysics*, 349:389–405, Sept. 1999b. 10.48550/arXiv.astro-ph/9909315.

S. S. Vogt, D. R. Soderblom, and G. D. Penrod. Rotational studies of late-type stars. III. Rotation among BY Draconis stars. *The Astrophysical Journal*, 269:250–252, June 1983. 10.1086/161035.

R. A. Wade and K. Horne. The Radial Velocity Curve and Peculiar TiO Distribution of the Red Secondary Star in Z Chamaeleontis. *The Astrophysical Journal*, 324: 411, Jan. 1988. 10.1086/165905.

T. Wagg, K. Breivik, and S. de Mink. LEGWORK: A python package for computing the evolution and detectability of stellar-origin gravitational-wave sources with space-based detectors. *The Journal of Open Source Software*, 7(70):3998, Feb. 2022a. 10.21105/joss.03998.

T. Wagg, K. Breivik, and S. E. de Mink. LEGWORK: A Python Package for Computing the Evolution and Detectability of Stellar-origin Gravitational-wave Sources with Space-based Detectors. *The Astrophysical Journal Supplement Series*, 260(2): 52, June 2022b. 10.3847/1538-4365/ac5c52.

F. M. Walter and S. Bowyer. On the coronae of rapidly rotating stars. I. The relation between rotation and coronal activity in RS CVn systems. *The Astrophysical Journal*, 245:671–676, Apr. 1981. 10.1086/158842.

F. M. Walter and L. D. Matthews. The optical counterpart of the isolated neutron star RX J185635-3754. *Nature*, 389(6649):358–360, Sept. 1997. 10.1038/38682.

Y. M. Wang. Cyclic Magnetic Variations of the Sun. In R. A. Donahue and J. A. Bookbinder, editors, *Cool Stars, Stellar Systems, and the Sun*, volume 154 of *Astronomical Society of the Pacific Conference Series*, page 131, Jan. 1998.

Z. Wang, N. Rea, T. Bao, D. L. Kaplan, E. Lenc, Z. Wadiasingh, J. Hare, A. Zic, A. Anumarlapudi, A. Bera, P. Beniamini, A. J. Cooper, T. E. Clarke, A. T. Deller, J. R. Dawson, M. Glowacki, N. Hurley-Walker, S. J. McSweeney, E. J. Polisensky, W. M. Peters, G. Younes, K. W. Bannister, M. Caleb, K. C. Dage, C. W. James, M. M. Kasliwal, V. Karambelkar, M. E. Lower, K. Mori, S. K. Ocker, M. Pérez-Torres, H. Qiu, K. Rose, R. M. Shannon, R. Taub, F. Wang, Y. Wang, Z. Zhao, N. D. R. Bhat, D. Dobie, L. N. Driessen, T. Murphy, A. Jaini, X. Deng, J. N. Jahns-Schindler, Y. W. J. Lee, J. Pritchard, J. Tuthill, and N. Thyagarajan. Detection of X-ray Emission from a Bright Long-Period Radio Transient. *arXiv e-prints*, art. arXiv:2411.16606, Nov. 2024. 10.48550/arXiv.2411.16606.

B. Warner. *Cataclysmic variable stars*, volume 28. 1995a.

B. Warner. *Cataclysmic variable stars*, volume 28. 1995b.

B. Warner. *Cataclysmic variable stars*, volume 28. 1995c.

R. S. Warwick, R. D. Saxton, and A. M. Read. The XMM-Newton slew survey in the 2-10 keV band. *Astronomy & Astrophysics*, 548:A99, Dec. 2012. 10.1051/0004-6361/201118642.

N. A. Webb, M. Coriat, I. Traulsen, J. Ballet, C. Motch, F. J. Carrera, F. Koliopanos, J. Authier, I. de la Calle, M. T. Ceballos, E. Colomo, D. Chuard, M. Freyberg, T. Garcia, M. Kolehmainen, G. Lamer, D. Lin, P. Maggi, L. Michel, C. G. Page, M. J. Page, J. V. Perea-Calderon, F. X. Pineau, P. Rodriguez, S. R. Rosen, M. Santos Lleo, R. D. Saxton, A. Schwope, L. Tomás, M. G. Watson, and A. Zakardjian. The XMM-Newton serendipitous survey. IX. The fourth XMM-Newton serendipitous source catalogue. *Astronomy & Astrophysics*, 641:A136, Sept. 2020. 10.1051/0004-6361/201937353.

R. F. Webbink. Double white dwarfs as progenitors of R Coronae Borealis stars and type I supernovae. *The Astrophysical Journal*, 277:355–360, Feb. 1984. 10.1086/161701.

B. L. Webster and P. Murdin. Cygnus X-1-a Spectroscopic Binary with a Heavy Companion ? *Nature*, 235(5332):37–38, Jan. 1972. 10.1038/235037a0.

D. T. Wickramasinghe and L. Ferrario. Magnetism in Isolated and Binary White Dwarfs. *Publications of the Astronomical Society of the Pacific*, 112(773):873–924, July 2000. 10.1086/316593.

D. T. Wickramasinghe, J. Bailey, S. M. A. Meggitt, L. Ferrario, J. Hough, and I. R. Tuohy. New polarimetric observations and a two pole model for the cyclotron emission from AM Herculis. *Monthly Notices of the Royal Astronomical Society*, 251:28, July 1991. 10.1093/mnras/251.1.28.

P. K. G. Williams, M. Clavel, E. Newton, and D. Ryzhkov. pwkit: Astronomical utilities in Python. Astrophysics Source Code Library, record ascl:1704.001, Apr. 2017.

J. Wilms, A. Allen, and R. McCray. On the Absorption of X-Rays in the Interstellar Medium. *The Astrophysical Journal*, 542(2):914–924, Oct. 2000. 10.1086/317016.

T. L. S. Wong and L. Bildsten. Mass Transfer and Stellar Evolution of the White Dwarfs in AM CVn Binaries. *The Astrophysical Journal*, 923(1):125, Dec. 2021. 10.3847/1538-4357/ac2b2a.

D. M. Worrall and F. E. Marshall. Stellar contributions to the hard X-ray galactic ridge. *The Astrophysical Journal*, 267:691–697, Apr. 1983. 10.1086/160906.

E. L. Wright, P. R. M. Eisenhardt, A. K. Mainzer, M. E. Ressler, R. M. Cutri, T. Jarrett, J. D. Kirkpatrick, D. Padgett, R. S. McMillan, M. Skrutskie, S. A. Stanford, M. Cohen, R. G. Walker, J. C. Mather, D. Leisawitz, I. Gautier, Thomas N., I. McLean, D. Benford, C. J. Lonsdale, A. Blain, B. Mendez, W. R. Irace, V. Duval, F. Liu, D. Royer, I. Heinrichsen, J. Howard, M. Shannon, M. Kendall, A. L. Walsh, M. Larsen, J. G. Cardon, S. Schick, M. Schwalm, M. Abid, B. Fabinsky, L. Naes, and C.-W. Tsai. The Wide-field Infrared Survey Explorer (WISE): Mission Description and Initial On-orbit Performance. *The Astronomical Journal*, 140(6):1868–1881, Dec. 2010. 10.1088/0004-6256/140/6/1868.

N. J. Wright, J. J. Drake, E. E. Mamajek, and G. W. Henry. The Stellar-activity-Rotation Relationship and the Evolution of Stellar Dynamos. *The Astrophysical Journal*, 743(1):48, Dec. 2011. 10.1088/0004-637X/743/1/48.

G. A. Wynn, A. R. King, and K. Horne. A magnetic propeller in the cataclysmic variable AE Aquarii. *Monthly Notices of the Royal Astronomical Society*, 286(2): 436–446, Apr. 1997. 10.1093/mnras/286.2.436.

F.-G. Xie and F. Yuan. Radiative efficiency of hot accretion flows. *Monthly Notices of the Royal Astronomical Society*, 427(2):1580–1586, Dec. 2012. 10.1111/j.1365-2966.2012.22030.x.

J. M. Yao, R. N. Manchester, and N. Wang. A New Electron-density Model for Estimation of Pulsar and FRB Distances. *The Astrophysical Journal*, 835(1):29, Jan. 2017. 10.3847/1538-4357/835/1/29.

D. G. York, J. Adelman, J. Anderson, John E., S. F. Anderson, J. Annis, N. A. Bahcall, J. A. Bakken, R. Barkhouser, S. Bastian, E. Berman, W. N. Boroski, S. Bracker, C. Briegel, J. W. Briggs, J. Brinkmann, R. Brunner, S. Burles, L. Carey, M. A. Carr, F. J. Castander, B. Chen, P. L. Colestock, A. J. Connolly, J. H. Crocker, I. Csabai, P. C. Czarapata, J. E. Davis, M. Doi, T. Dombeck, D. Eisenstein, N. Ellman, B. R. Elms, M. L. Evans, X. Fan, G. R. Federwitz, L. Fiscelli, S. Friedman, J. A. Frieman, M. Fukugita, B. Gillespie, J. E. Gunn, V. K. Gurbani, E. de Haas, M. Haldeman, F. H. Harris, J. Hayes, T. M. Heckman, G. S. Hennessy, R. B. Hindsley, S. Holm, D. J. Holmgren, C.-h. Huang, C. Hull, D. Husby, S.-I. Ichikawa, T. Ichikawa, Z. Ivezic, S. Kent, R. S. J. Kim, E. Kinney, M. Klaene, A. N. Kleinman, S. Kleinman, G. R. Knapp, J. Korienek, R. G. Kron, P. Z. Kunszt, D. Q. Lamb, B. Lee, R. F. Leger, S. Limmongkol, C. Lindenmeyer, D. C. Long, C. Loomis, J. Loveday, R. Lucinio, R. H. Lupton, B. MacKinnon, E. J. Mannery, P. M. Mantsch, B. Margon, P. McGehee, T. A. McKay, A. Meiksin, A. Merelli, D. G. Monet, J. A. Munn, V. K. Narayanan, T. Nash, E. Neilsen, R. Neswold, H. J. Newberg, R. C. Nichol, T. Nicinski, M. Nonino, N. Okada, S. Okamura, J. P. Ostriker, R. Owen, A. G. Pauls, J. Peoples, R. L. Peterson, D. Petravick, J. R. Pier, A. Pope, R. Pordes, A. Prosapio, R. Rechenmacher, T. R. Quinn, G. T. Richards, M. W. Richmond, C. H. Rivetta, C. M. Rockosi, K. Ruthmansdorfer, D. Sandford, D. J. Schlegel, D. P. Schneider, M. Sekiguchi, G. Sergey, K. Shimasaku, W. A. Siegmund, S. Smee, J. A. Smith, S. Snedden, R. Stone, C. Stoughton, M. A. Strauss, C. Stubbs, M. SubbaRao, A. S. Szalay, I. Szapudi, G. P. Szokoly, A. R. Thakar, C. Tremonti, D. L. Tucker, A. Uomoto, D. Vanden Berk, M. S. Vogeley, P. Waddell, S.-i. Wang, M. Watanabe, D. H. Weinberg, B. Yanny, N. Yasuda, and SDSS Collaboration. The Sloan Digital Sky Survey: Technical Summary. *The Astronomical Journal*, 120(3):1579–1587, Sept. 2000a. 10.1086/301513.

D. G. York, J. Adelman, J. Anderson, John E., S. F. Anderson, J. Annis, N. A. Bahcall, J. A. Bakken, R. Barkhouser, S. Bastian, E. Berman, W. N. Boroski, S. Bracker, C. Briegel, J. W. Briggs, J. Brinkmann, R. Brunner, S. Burles, L. Carey, M. A. Carr, F. J. Castander, B. Chen, P. L. Colestock, A. J. Connolly, J. H. Crocker, I. Csabai, P. C. Czarapata, J. E. Davis, M. Doi, T. Dombeck, D. Eisenstein, N. Ellman, B. R. Elms, M. L. Evans, X. Fan, G. R. Federwitz, L. Fiscelli, S. Friedman,

J. A. Frieman, M. Fukugita, B. Gillespie, J. E. Gunn, V. K. Gurbani, E. de Haas, M. Haldeman, F. H. Harris, J. Hayes, T. M. Heckman, G. S. Hennessy, R. B. Hindsley, S. Holm, D. J. Holmgren, C.-h. Huang, C. Hull, D. Husby, S.-I. Ichikawa, T. Ichikawa, Z. Ivezic, S. Kent, R. S. J. Kim, E. Kinney, M. Klaene, A. N. Kleinman, S. Kleinman, G. R. Knapp, J. Korienek, R. G. Kron, P. Z. Kunszt, D. Q. Lamb, B. Lee, R. F. Leger, S. Limmongkol, C. Lindenmeyer, D. C. Long, C. Loomis, J. Loveday, R. Lucinio, R. H. Lupton, B. MacKinnon, E. J. Mannery, P. M. Mantsch, B. Margon, P. McGehee, T. A. McKay, A. Meiksin, A. Merelli, D. G. Monet, J. A. Munn, V. K. Narayanan, T. Nash, E. Neilsen, R. Neswold, H. J. Newberg, R. C. Nichol, T. Nicinski, M. Nonino, N. Okada, S. Okamura, J. P. Ostriker, R. Owen, A. G. Pauls, J. Peoples, R. L. Peterson, D. Petravick, J. R. Pier, A. Pope, R. Pordes, A. Prosapio, R. Rechenmacher, T. R. Quinn, G. T. Richards, M. W. Richmond, C. H. Rivetta, C. M. Rockosi, K. Ruthmansdorfer, D. Sandford, D. J. Schlegel, D. P. Schneider, M. Sekiguchi, G. Sergey, K. Shimasaku, W. A. Siegmund, S. Smee, J. A. Smith, S. Snedden, R. Stone, C. Stoughton, M. A. Strauss, C. Stubbs, M. SubbaRao, A. S. Szalay, I. Szapudi, G. P. Szokoly, A. R. Thakar, C. Tremonti, D. L. Tucker, A. Uomoto, D. Vanden Berk, M. S. Vogeley, P. Waddell, S.-i. Wang, M. Watanabe, D. H. Weinberg, B. Yanny, N. Yasuda, and SDSS Collaboration. The Sloan Digital Sky Survey: Technical Summary. *The Astronomical Journal*, 120(3):1579–1587, Sept. 2000b. 10.1086/301513.

F. Yuan, E. Quataert, and R. Narayan. Nonthermal Electrons in Radiatively Inefficient Accretion Flow Models of Sagittarius A*. *The Astrophysical Journal*, 598 (1):301–312, Nov. 2003. 10.1086/378716.

F. Yuan, M. Wu, and D. Bu. Numerical Simulation of Hot Accretion Flows. I. A Large Radial Dynamical Range and the Density Profile of Accretion Flow. *The Astrophysical Journal*, 761(2):129, Dec. 2012. 10.1088/0004-637X/761/2/129.

L. R. Yungelson, A. G. Kuranov, and K. A. Postnov. Wind-accreting symbiotic X-ray binaries. *Monthly Notices of the Royal Astronomical Society*, 485(1):851–860, May 2019a. 10.1093/mnras/stz467.

L. R. Yungelson, A. G. Kuranov, and K. A. Postnov. Wind-accreting symbiotic X-ray binaries. *Monthly Notices of the Royal Astronomical Society*, 485(1):851–860, May 2019b. 10.1093/mnras/stz467.

V. E. Zavlin, G. G. Pavlov, D. Sanwal, R. N. Manchester, J. Trümper, J. P. Halpern, and W. Becker. X-Radiation from the Millisecond Pulsar J0437-4715. *The Astrophysical Journal*, 569(2):894–902, Apr. 2002. 10.1086/339351.

I. Zaznobin, S. Sazonov, R. Burenin, G. Uskov, A. Semena, M. Gilfanov, P. Medvedev, R. Sunyaev, and M. Eselevich. Identification of three cataclysmic variables detected by the ART-XC and eROSITA telescopes on board the SRG during the all-sky X-ray survey. *Astronomy & Astrophysics*, 661:A39, May 2022. 10.1051/0004-6361/202141777.

R. Zhai, A. C. Rodriguez, S. Mao, C. Y. Lam, E. C. Bellm, J. Purdum, F. J. Masci, and A. Wold. Microlensing Events in Five Years of Photometry from the Zwicky Transient Facility. *The Astrophysical Journal*, 978(1):76, Jan. 2025. 10.3847/1538-4357/ad94e7.

Y. Zhao, P. Gandhi, C. Dashwood Brown, C. Knigge, P. A. Charles, T. J. Maccarone, and P. Nuchvanichakul. Evidence for mass-dependent peculiar velocities in compact object binaries: towards better constraints on natal kicks. *Monthly Notices of the Royal Astronomical Society*, 525(1):1498–1519, Oct. 2023. 10.1093/mnras/stad2226.

A. G. Zhilkin, A. V. Sobolev, D. V. Bisikalo, and M. M. Gabdeev. Flow Structure in the Eclipsing Polar V808 Aur. Results of 3D Numerical Simulations. *Astronomy Reports*, 63(9):751–777, Sept. 2019. 10.1134/S1063772919090087.

M. Zorotovic and M. R. Schreiber. Cataclysmic variable evolution and the white dwarf mass problem: A Review. *Advances in Space Research*, 66(5):1080–1089, Sept. 2020. 10.1016/j.asr.2019.08.044.

M. Zorotovic, M. R. Schreiber, and B. T. Gänsicke. Post common envelope binaries from SDSS. XI. The white dwarf mass distributions of CVs and pre-CVs. *Astronomy & Astrophysics*, 536:A42, Dec. 2011. 10.1051/0004-6361/201116626.

M. Zorotovic, M. R. Schreiber, S. G. Parsons, B. T. Gänsicke, A. Hardy, C. Agurto-Gangas, A. Nebot Gómez-Morán, A. Rebassa-Mansergas, and A. D. Schwope. Detached cataclysmic variables are crossing the orbital period gap. *Monthly Notices of the Royal Astronomical Society*, 457(4):3867–3877, Apr. 2016a. 10.1093/mnras/stw246.

M. Zorotovic, M. R. Schreiber, S. G. Parsons, B. T. Gänsicke, A. Hardy, C. Agurto-Gangas, A. Nebot Gómez-Morán, A. Rebassa-Mansergas, and A. D. Schwope. Detached cataclysmic variables are crossing the orbital period gap. *Monthly Notices of the Royal Astronomical Society*, 457(4):3867–3877, Apr. 2016b. 10.1093/mnras/stw246.

B. Zuckerman. Recognition of the First Observational Evidence of an Extrasolar Planetary System. In P. Dufour, P. Bergeron, and G. Fontaine, editors, *19th European Workshop on White Dwarfs*, volume 493 of *Astronomical Society of the Pacific Conference Series*, page 291, June 2015. 10.48550/arXiv.1410.2575.